frontiers | Research Topics

Advanced concretes and their structural applications, volume III

Edited by
Zhigang Zhang, Yao Ding, Jialuo He and Yang Zou

Coordinated by
Pengfei Men

Published in
Frontiers in Materials

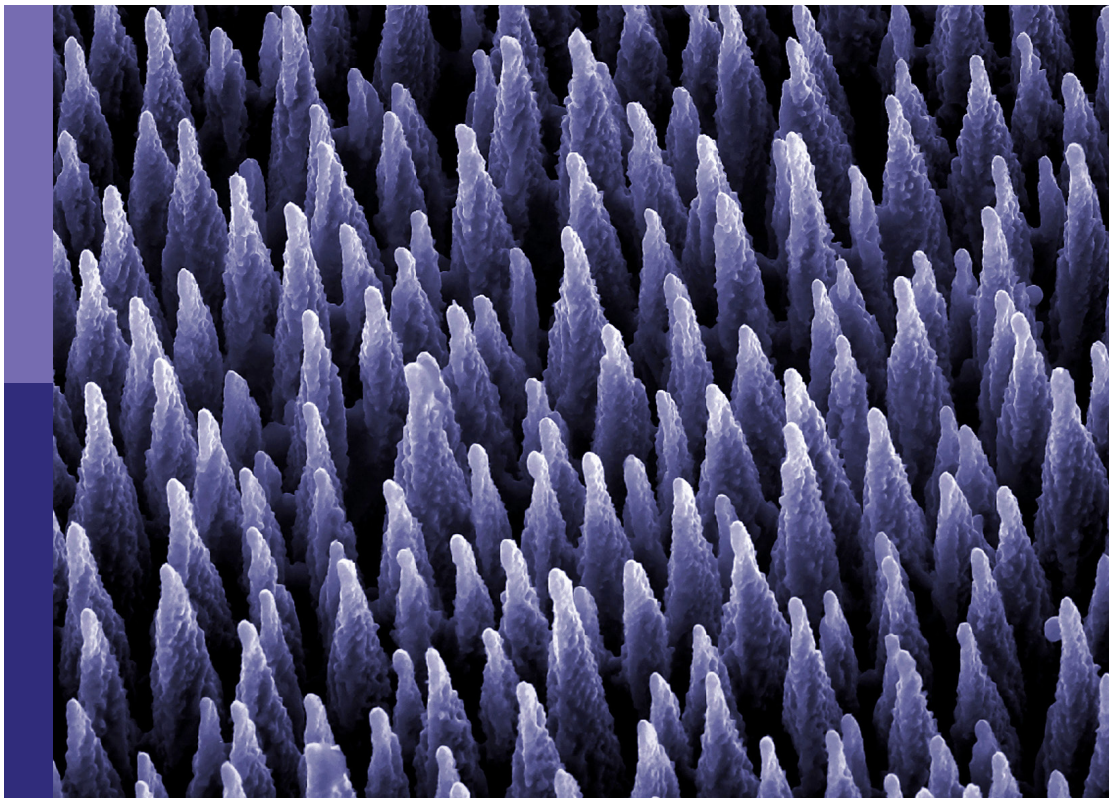

ISSN 1664-8714
ISBN 978-2-8325-5958-1
DOI 10.3389/978-2-8325-5958-1

About Frontiers

Frontiers is more than just an open access publisher of scholarly articles: it is a pioneering approach to the world of academia, radically improving the way scholarly research is managed. The grand vision of Frontiers is a world where all people have an equal opportunity to seek, share and generate knowledge. Frontiers provides immediate and permanent online open access to all its publications, but this alone is not enough to realize our grand goals.

Frontiers journal series

The Frontiers journal series is a multi-tier and interdisciplinary set of open-access, online journals, promising a paradigm shift from the current review, selection and dissemination processes in academic publishing. All Frontiers journals are driven by researchers for researchers; therefore, they constitute a service to the scholarly community. At the same time, the *Frontiers journal series* operates on a revolutionary invention, the tiered publishing system, initially addressing specific communities of scholars, and gradually climbing up to broader public understanding, thus serving the interests of the lay society, too.

Dedication to quality

Each Frontiers article is a landmark of the highest quality, thanks to genuinely collaborative interactions between authors and review editors, who include some of the world's best academicians. Research must be certified by peers before entering a stream of knowledge that may eventually reach the public - and shape society; therefore, Frontiers only applies the most rigorous and unbiased reviews. Frontiers revolutionizes research publishing by freely delivering the most outstanding research, evaluated with no bias from both the academic and social point of view. By applying the most advanced information technologies, Frontiers is catapulting scholarly publishing into a new generation.

What are Frontiers Research Topics?

Frontiers Research Topics are very popular trademarks of the *Frontiers journals series*: they are collections of at least ten articles, all centered on a particular subject. With their unique mix of varied contributions from Original Research to Review Articles, Frontiers Research Topics unify the most influential researchers, the latest key findings and historical advances in a hot research area.

Find out more on how to host your own Frontiers Research Topic or contribute to one as an author by contacting the Frontiers editorial office: frontiersin.org/about/contact

Advanced concretes and their structural applications, volume III

Topic editors
Zhigang Zhang — Chongqing University, China
Yao Ding — Chongqing University, China
Jialuo He — Washington State University, United States
Yang Zou — Chongqing Jiaotong University, China

Topic coordinator
Pengfei Men — Hong Kong Polytechnic University, Hong Kong, SAR China

Citation
Zhang, Z., Ding, Y., He, J., Zou, Y., Men, P., eds. (2025). *Advanced concretes and their structural applications, volume III*. Lausanne: Frontiers Media SA.
doi: 10.3389/978-2-8325-5958-1

Table of contents

frontiers | Frontiers in Materials

TYPE Original Research
PUBLISHED 12 January 2024
DOI 10.3389/fmats.2023.1282919

OPEN ACCESS

EDITED BY
Zhigang Zhang,
Chongqing University, China

REVIEWED BY
Ping Duan,
China University of Geosciences Wuhan, China
Yunchao Tang,
Guangxi University, China

*CORRESPONDENCE
Hui Li,
hla_zyj@qq.com

RECEIVED 25 August 2023
ACCEPTED 22 December 2023
PUBLISHED 12 January 2024

CITATION
Huo G, Jiang X, Sun X, Li H and Shi H (2024), Performance of high-belite calcium sulfoaluminate cement subjected to hydrochloric acid and sulfuric acid. *Front. Mater.* 10:1282919. doi: 10.3389/fmats.2023.1282919

Performance of high-belite calcium sulfoaluminate cement subjected to hydrochloric acid and sulfuric acid

Guang Huo[1,2], Xinchao Jiang[2], Xiaoheng Sun[2], Hui Li[3]* and Hongxing Shi[4]

[1]Shandong Hi-Speed Construction Management Group Co., Ltd., Jinan, China, [2]Shandong Hi-speed Mingdong Expressway Co., Ltd., WeiFang, China, [3]School of Civil and Transportation Engineering, Hebei University of Technology, Tianjin, China, [4]Beijing Zhihuatong Technology Co., LTD., Beijing, China

The high-belite calcium sulfoaluminate cement (HB-CSA) has displayed outstanding acid resistance. However, further research is needed to understand the mechanism behind its acid resistance fully. This study investigates the resistance of a new type of HB-CSA to hydrochloric and sulfuric acid. Additionally, the impact of the ye'elimite ($C_4A_3\bar{S}$)-to-gypsum ($C\bar{S}$) ratio on the acid resistance of HB-CSA is discussed. The resistance performance is investigated by flexural strength and resistance index analyses, X-ray diffraction (XRD), thermogravimetric analysis (TGA), electronic computed tomography (CT) scans, and scanning electron microscopy (SEM). The results show that the HB-CSA exhibits superior resistance to sulfuric acid and hydrochloric acid compared to Portland cement. The absence of portlandite contributes to the enhanced performance of HB-CSA. In addition, as the $C_4A_3\bar{S}$-to-$C\bar{S}$ ratio decreases, the content of Aft in HB-CSA increases, leading to an increase in the acid resistance of HB-CSA.

KEYWORDS

durability, acid attack, high-belite calcium sulfoaluminate cement, ettringite, ye'elimite and gypsum content

1 Introduction

Acid wastewater like domestic wastewater (Congressional budget office, 2002), acid mine drainage (AMD) (Wu et al., 2020a), and cooling towers at power plants (Berndt, 2011) has become a serious global problem due to its adverse impact on the environment and infrastructure (Wu et al., 2020b). As the most widely used structural material, concrete determines the durability of the industrial acidic aqueous treatment (or containment) infrastructure or potentially acid-attack infrastructure (Joorabchian, 2010). However, due to the poor acid corrosion resistance of concrete, repair and reconstruction of acidic aqueous treatment (containment) or acid-attack infrastructure are expensive and time-consuming every year (Congressional budget office, 2002).

The pH of the acid-attack environment usually ranges from 3 to 5 (Larreur-Cayol et al., 2011; Yue et al., 2011; Ninan et al., 2021) or even less than 3 under some special circumstances (Gutiérrez-Padilla et al., 2010). The acid-erosion process of the concrete takes place through a combination of three main mechanisms (Beddoe and Dorner, 2005): 1) the ingress of the acid into the pore solution releases the H^+ ions to decrease the pH in the

TABLE 1 Chemical composition of CSA, HB-CSA-H, HB-CSA-O, and OPC (%).

	SiO_2	Al_2O_3	Fe_2O_3	CaO	MgO	SO_3	TiO_2	LOI	Total
CSA	13.95	22.46	2.67	39.39	2.92	14.34	1.66	1.68	99.07
HB-CSA-H	17.08	15.39	1.37	44.98	4.48	13.80	0.70	1.27	99.05
HB-CSA-O	17.44	15.95	1.35	44.96	4.58	13.04	0.70	1.14	99.16
OPC	23.29	7.47	2.68	55.38	4.22	4.08	0.59	1.8	99.51

TABLE 2 $C_4A_3\bar{S}$-to-C$\bar{S}$ ratio of R-CSA, HB-CSA-H, and HB-CSA-O (-).

	R-CSA	HB-CSA-O	HB-CSA-H
$m(C_4A_3\bar{S})/m$ (C$\bar{S}$)	2.85	0.92	0.60

TABLE 3 Strength development of HB-CSA, CSA, and OPC mortar specimens with a water-to-cement ratio of 0.5 and a sand-to-cement ratio of 2.5 (MPa).

	Flexural strength/compressive strength		
	1 day	7 days	28 days
R-CSA	9.1/39.1	9.5/53.2	9.5/56.0
HB-CSA-O	7.0/37.6	8.0/50.9	8.3/65.0
HB-CSA-H	7.2/36.4	7.8/44.2	7.8/50.3
OPC	3.5/12.1	6.7/36.7	10.7/51.8

pore solution; 2) the free OH^- and alkali in the pore solution are progressively consumed by neutralizing the H^+ ions, reducing the pH of the pore solution and increasing the dissolution of portlandite from the matrix; and 3) C-S-H starts dissolving due to the reduction in pH. In addition, when the concrete made using ordinary Portland cement (OPC) is exposed to a sulfuric acid environment, the dissolution of CH occurs followed by the formation of gypsum ($CaSO_4{\cdot}2H_2O$). This process introduces further damage due to sulfate attack, i.e., expansion due to ettringite formation and subsequent cracking, as reported by Beddoe (2016). Following this, data suggest that the chemical erosion rates of sulfuric acid are faster than those of hydrochloric acid and nitric acid (Bassuoni and Nehdi, 2007). The corrosion of hydration products in the concrete makes the structures looser, reducing the strength and impermeability of concrete, representing a potentially major safety hazard and durability issues (Girardi et al., 2010). Studies on concrete to increase the resistance to acid attack have focused on decreasing the ratio of water to cement (w/c) to make the mortar denser (Kim et al., 2014) and mixing supplementary cementing materials (SCMs), such as fly ash (FA), granulated blast furnace slag (GBFS), and silica fume (SF), to decrease the alkalinity of concrete (Mlinárik and Kopecskó, 2017). However, these methods have little effect on improving the acid resistance since ordinary Portland cement, the most widely used in civil engineering, has poor resistance to acid corrosion (Imbabi et al., 2012; Xu et al., 2017; Maddalena et al., 2018).

Recently, calcium sulfoaluminate (CSA) cement has emerged as an alternative cementing material owing to its advantages, such as low carbon emissions (Glasser and Zhang, 2001; Gartner, 2004), rapid hardening (Hou et al., 2020), and excellent performance in acid environments (Dyer, 2017; Gartner and Sui, 2018; Yang et al., 2018). Although CSA has many advantages, it has obvious shortcomings. The manufacturing of CSA strongly depends on the high quality of bauxite (Chaunsali and Mondal, 2015), which limits large-scale production. In addition, mechanical properties such as the compressive strength and flexural strength of concrete made using CSA may be reduced after long-term aging because of the expansion caused by the production of a large amount of ettringite ($3CaO{\cdot}Al_2O_3{\cdot}3CaSO_4{\cdot}32H_2O$, AFt) (Ogawa and Roy, 1982; Zhang, 2015). To overcome the shortcomings of CSA, a promising alternative with the rapid setting and hardening of high-belite calcium sulfoaluminate (HB-CSA) cement has been developed (Li et al., 2014). The HB-CSA clinker is mainly composed of ye'elimite ($3CaO{\cdot}3Al_2O_3{\cdot}CaSO_4$, $C_4A_3\bar{S}$) and belite ($2CaO{\cdot}SiO_2$, C_2S), and the strength of HB-CSA would not decrease at late ages owing to its increased C_2S content (Wang et al., 2022). However, since the content of $C_4A_3\bar{S}$ decreases, the early and final strength of HB-CSA is lower than that of CSA (Chi et al., 2021). By adjusting the amount of gypsum and mineral admixtures in cement, the early and final strength of HB-CSA has been significantly increased, and a new type of HB-CSA has been proposed (Zhang et al., 2022). The new type of HB-CSA has been successfully used as a repair material, flooring material, and UHPC. It was also used as the activator to increase the blast slag activity and proposed a high-performance cement named calcium sulfoaluminate-activated supersulfated cement (CSA-SSC) (Sun et al., 2022). Since HB-CSA is a type of CSA, HB-CSA is expected to be an ideal material for acidic aqueous treatment (containment) infrastructure. However, because the mineral content of HB-CSA differs somewhat from that of conventional CSA, particularly in terms of the mass ratio of $C_4A_3\bar{S}$-to-C$\bar{S}$, the acid corrosion resistance of HB-CSA must differ from that of CSA.

This study aims to investigate changes in the chemical components and mechanical evolution of the new type of HB-CSA when exposed to the hydrochloric and sulfuric acid solutions and understand the underlying mechanisms of their evolution under such exposure conditions. Specimens were evaluated based on their changes in flexural strength, composition, and microstructure under the coupling effect of sulfuric acid and sulfuric acid attacks. The influence of the mass ratio of $C_4A_3\bar{S}$ to C$\bar{S}$ on the acid corrosion resistance capability of CSA was also discussed.

10.3389/fmats.2023.1282919

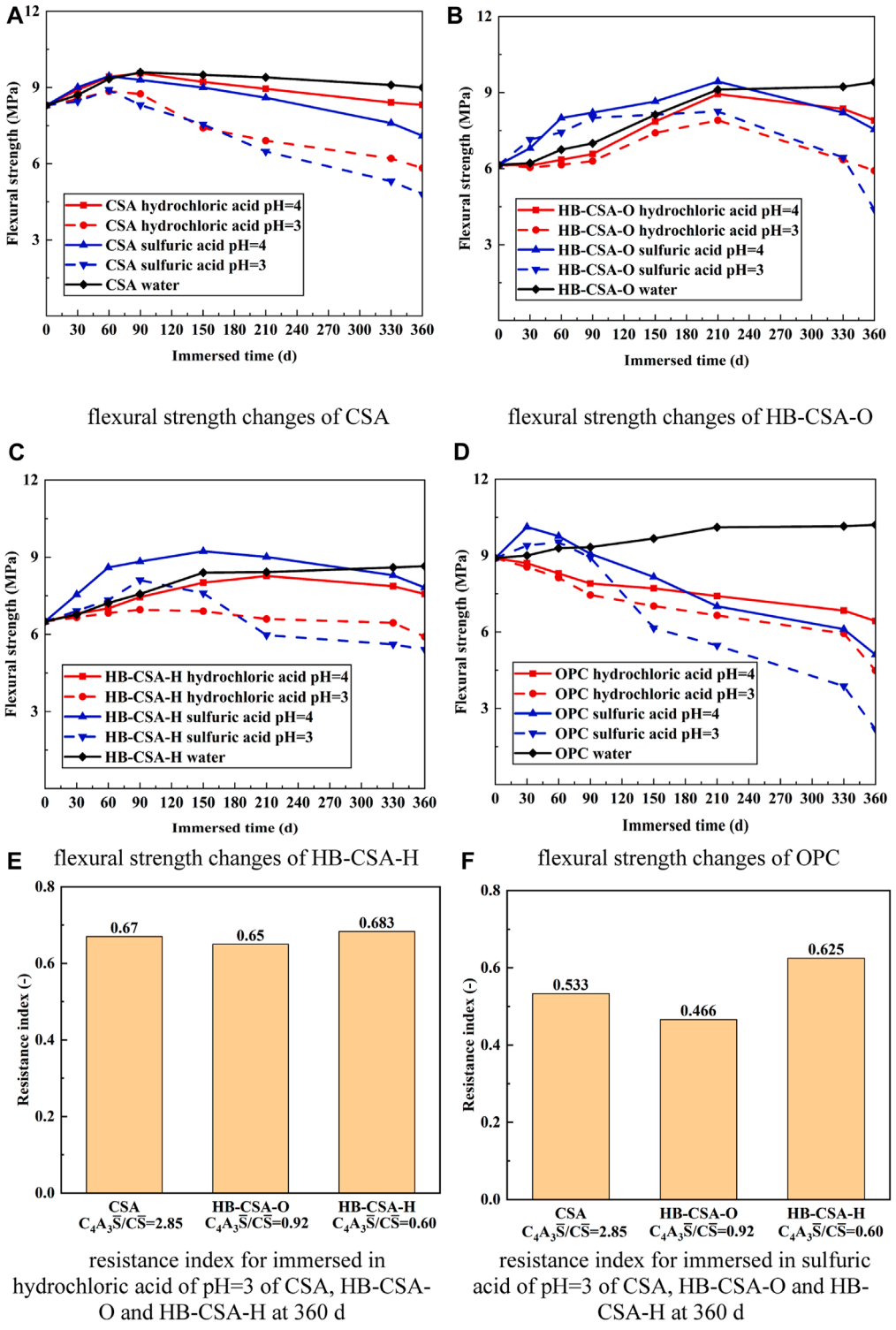

FIGURE 1
Flexural strength changes and resistance indexes of CSA, HB-CSA-O, HB-CSA-H, and OPC immersed in different acid solutions. **(A)** Flexural strength changes in CSA, **(B)** flexural strength changes in HB-CSA-O, **(C)** flexural strength changes in HB-CSA-H, **(D)** flexural strength changes in OPC, **(E)** resistance indexes of CSA, HB-CSA-O, and HB-CSA-H immersed in hydrochloric acid at pH 3 for 360 days, and **(F)** resistance indexes of CSA, HB-CSA-O, and HB-CSA-H immersed in sulfuric acid at pH 3 for 360 days.

10.3389/fmats.2023.1282919

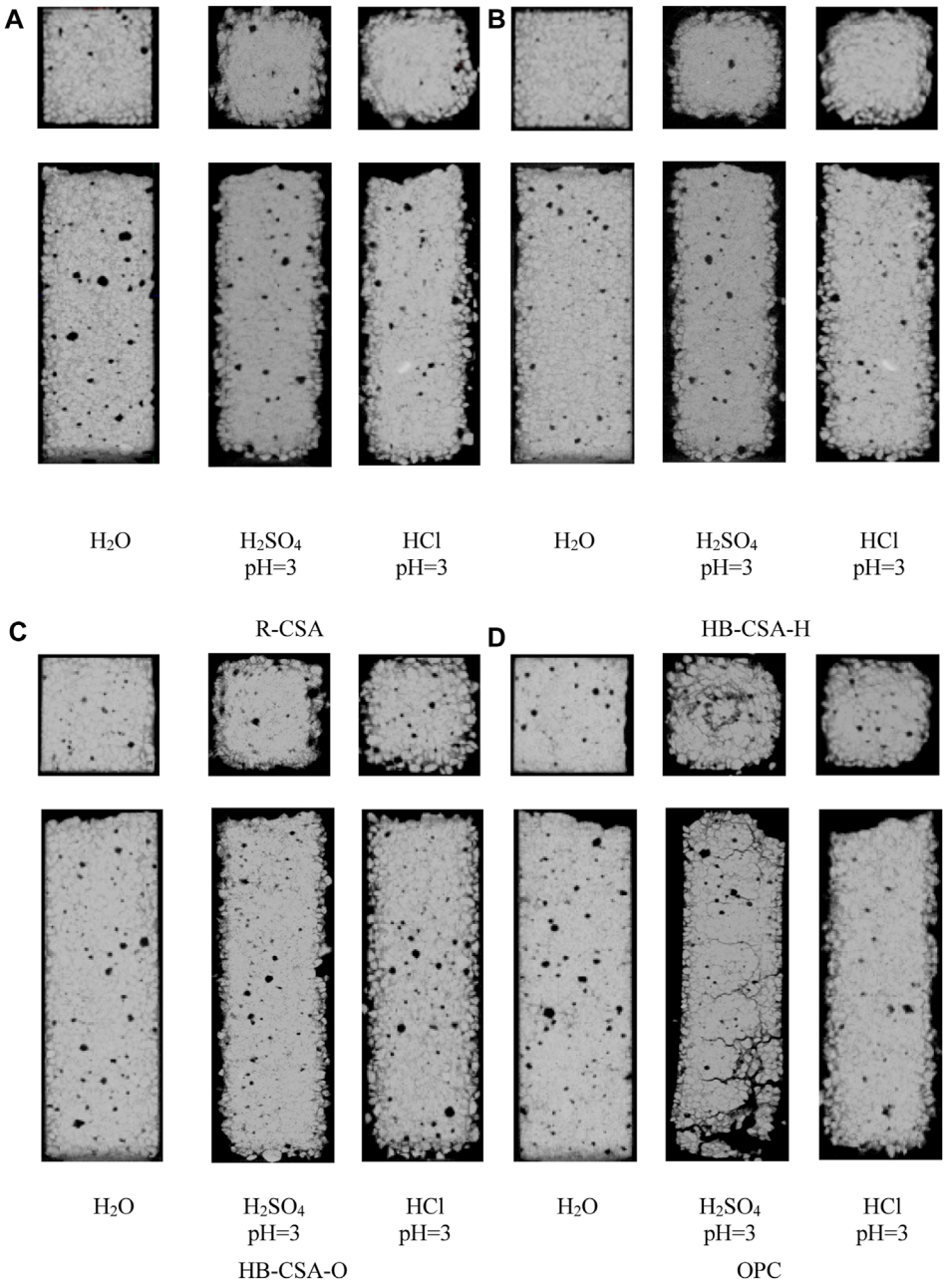

FIGURE 2
Structure morphology obtained by CT for mortar specimens exposed to water, hydrochloric acid solution, and sulfuric acid solution at pH 3 for 360 days. **(A)** R-CSA, **(B)** HB-CSA-H, **(C)** HB-CSA-O, and **(D)** OPC.

2 Experimental

2.1 Materials

OPC, CSA, and HB-CSA were used in this research. OPC was prepared using 42.5 R Portland cement (a Chinese cement standard with a 28-day compressive strength of at least 42.5 MPa obtained based on the given ratio). Two types of HB-CSA, namely, HB-CSA-H and HB-CSA-O, were used in this study to investigate the influence of the mass ratio of $C_4A_3\overline{S}$ to $C\overline{S}$ on the acid resistance behavior of HB-CSA. Table 1 shows the chemical compositions of CSA, HB-CSA-H, HB-CSA-O, and OPC. Table 2 shows the mass ratio of $C_4A_3\overline{S}$ to $C\overline{S}$ for CSA, HB-CSA-H, and HB-CSA-O. It is worth noting that the mass ratio of $C_4A_3\overline{S}$ to $C\overline{S}$ in HB-CSA-O is higher than that in HB-CSA-H. This suggests that the content of $C_4A_3\overline{S}$ is more in HB-CSA-O relative to $C\overline{S}$. The fine aggregate was natural sand of 0–6 mm in diameter and crushed stone dust of 0–6 mm in diameter, with a fineness modulus of 2.5.

The hydrochloric and sulfuric acid solutions were diluted with pure water to obtain the required pH. The hydrochloric

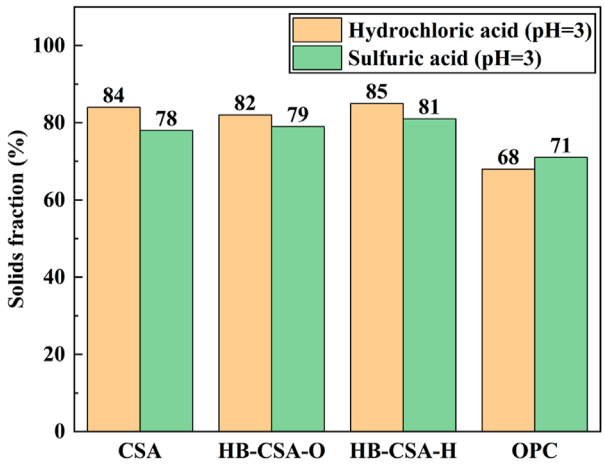

FIGURE 3
Solid fractions of CSA, HB-CSA-O, HB-CSA-H, and OPC immersed in acid at pH 3 for 360 d.

acid solutions with pH 3 and 4 were prepared as the corrosive solutions since the pH of acid wastewater is usually in the range of 3–5 in acidic aqueous treatment (containment) infrastructure (Larreur-Cayol et al., 2011; Yue et al., 2011; Ninan et al., 2021). In addition, the sulfuric acid solutions with pH 4 and 3 were prepared to investigate the chemical components and mechanical evolution of HB-CSA under the coupling effect of acid and sulfate attacks.

2.2 Mix proportion and sample preparation

HB-CSA (HB-CSA-H and HB-CSA-O), CSA, and OPC mortar specimens with a water–cement ratio of 0.5 and sand–cement ratio of 2.5 were prepared using the following procedure: first, water, sand, and cement were combined in a mixer and then stirred for 3 min. After stirring, the mortar was poured into metal molds of dimensions 10 mm × 10 mm × 60 mm. The mortar with molds was cured at a temperature of 20°C and relative humidity of 95% for 24 h. All the specimens were then de-molded and cured in water at a temperature of 20°C for another 27 days.

Plastic containers sealed with lids were used to hold the specimens and corrosive solutions. Each container contained 27 samples and 6 L of acid solution. Meanwhile, samples soaked in water of the same volume were set as the control group. All the containers were maintained at 20°C. A handheld pH meter was used to detect the acidity of the corrosive solutions at regular intervals, and the hydrochloric and sulfuric acid solutions were restored when the pH of the solution increased by 0.5.

2.3 Test methods

The strength development of HB-CSA and OPC mortar during curing was measured according to the Chinese standard GB/T 17671-2021 (ISO679:2009) and is listed in Table 3. The changes in flexural strength, chemical components, and structural morphology of each type were measured after the specimens were immersed in different acid solutions for 30, 60, 90, 120, 150, 210, 330, and 360 days.

As a non-destructive testing method, CT can quickly obtain the realistic internal structure of the specimen after acid erosion for the qualitative characterization of the acid erosion damage degree of the specimen. At the same time, the images obtained by CT can be processed using image processing technology (Li et al., 2022) or computer deep learning (Wu et al., 2003; Que et al., 2023) to quantitatively analyze the width and other related parameters of the cracks and quantitatively evaluate the damage degree of the specimen. In this study, a YXLON FF35 electronic computed tomography (CT) scanner was used for the visual inspection of the specimens before and after being immersed in different acid solutions for different immersion times. The current and voltage used in this test were 120 kV and 200 μA, respectively. The step size was 0.11°, and a two-frame averaging technique was used to form the images.

The average flexural strength of specimens with different immersion times was measured following the three-point bending experiment. The test is performed under load control at a constant rate of 0.78 N/s, and nine specimens were tested per group in this test. The maximum and minimum values were discarded, and the average of the remaining seven values was taken as the test result. The percentage change in flexural strength was also calculated by the strength change between the specimens immersed in acid solutions and water. The percentage change is denoted as the resistance index (K) and can be expressed using Eq. 1 according to the Chinese standard GB/T 50082-2009.

$$K = \frac{F_s}{F_w}, \tag{1}$$

where F_s is the flexural strength of a specimen immersed in acid solutions and F_w is the flexural strength of a specimen immersed in water.

After flexural strength testing, the undamaged part of the specimens was broken into small pieces for chemical and microscopic tests. X-ray diffraction (XRD) was used to analyze the hydration and corrosion products of HB-CSA (HB-CSA-H and HB-CSA-O), CSA, and OPC at the selected ages. Dried samples were ground into a powder with a size of less than 60 μm. The current and voltage of the Bruker D8 Advance 1,600 W instrument were 40 kV and 40 mA, respectively. The radiation source used was Cu-Kα radiation, and the 2θ ranged from 5° to 70°. The step size was 0.01°, and each step took 0.2 s.

Thermogravimetric analysis (TGA) was also used along with XRD to analyze the hydration and corrosion products. A Mettler Toledo TGA/DSC-1600 instrument was used in this test. The ground samples (less than 60 μm) were placed in Al_2O_3 crucibles and heated from 30°C to 600°C with a 10 K/min heating rate in a nitrogen atmosphere.

Image analysis based on scanning electron microscopy (SEM) is used to analyze visual changes in morphology before and after the acid attack. A cross section of the sample was selected for observation. Crushed samples with a size of approximately 5 mm were selected, and gold spray was applied prior to the test to improve

10.3389/fmats.2023.1282919

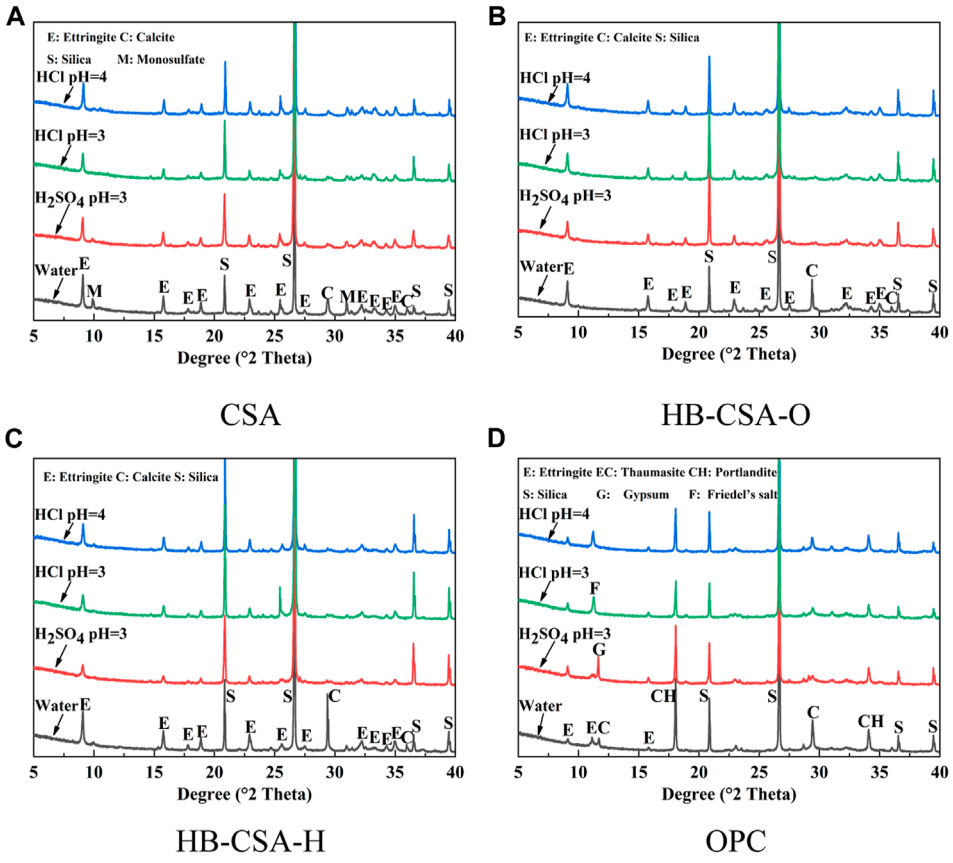

FIGURE 4
XRD patterns of CSA, HB-CSA, and OPC specimens after being immersed in hydrochloric acid at pH 3 and 4 and sulfuric acid at pH 3 for 360 days. **(A)** CSA, **(B)** HB-CSA-O, **(C)** HB-CSA-H, and **(D)** OPC.

the conductivity. A Nova NanoSEM 450 microscope was used, and the voltage was 10 kV.

3 Results and discussion

3.1 Flexural strength evolution

Figure 1 displays the flexural strength changes observed in the specimens immersed in various acid solutions for different immersion times. For specimens immersed in water, the flexural strength of CSA reaches the peak at 90 days and slightly decreases after reaching the peak. The maximum flexural strength of CSA is 9.6 MPa and falls to 9.0 MPa at 360 days of immersion in water. The flexural strength of HB-CSA-H gradually increases as the immersion time increases, reaching stability (approximate peak) after being immersed in water for 360 days. Specifically, the flexural strength of HB-CSA-H increases from 6.50 to 8.65 MPa when the specimens are immersed in water for 360 days. For HB-CSA-O, the trend of flexural strength change in HB-CSA-O is similar to that in HB-CSA-H. However, the early strength of HB-CSA-O (6.15 MPa after 0 days of immersion) is lower than that of HB-CSA-H. On the other hand, the long-term strength of HB-CSA-O (9.41 MPa after 360 days of immersion) is higher than that of HB-CSA-H. The strength increase in HB-CAS-O and HB-CSA-H in the long term may be attributed to the hydration of belite in cement. For OPC, the flexural strength development trends gently after being immersed in water for 360 days. The maximum flexural strength is approximately 10.10 MPa.

When the specimens are immersed in hydrochloric acid, the flexural strength of CSA, HB-CSA-O, and HB-CSA-H show a similar change trend of an increase followed by a decrease in flexural strength. In contrast, the flexural strength of OPC mortar specimens immersed in hydrochloric acid always decreases with the increase in immersion time. Differences in peak flexural strength arrival timing were observed in CSA, HB-CSA-O, and HB-CSA-H. CSA reaches its peak flexural strength after being immersed in hydrochloric acid for 60 days at pH 4 and 3. HB-CSA-O reaches its peak flexural strength after being immersed in hydrochloric acid for 210 days at pH 4 (or 90 days at pH 3), while HB-CSA-H reaches its peak flexural strength after being immersed in hydrochloric acid for 150 days at pH 4 (or 90 days at pH = 3). Based on the test results, it is indicated that CSA, HB-CSA-O, and HB-CSA-H exhibit strong resistance to hydrochloric acid corrosion. Even after being immersed in hydrochloric acid with a pH of 4 for 360 days, the flexural strength of CSA, HB-CSA-O, and HB-CSA-H remains stable at 8.32, 7.57, and 7.9 MPa, respectively. Similarly, after being immersed in hydrochloric acid with a pH of 3 for 360 days, the flexural

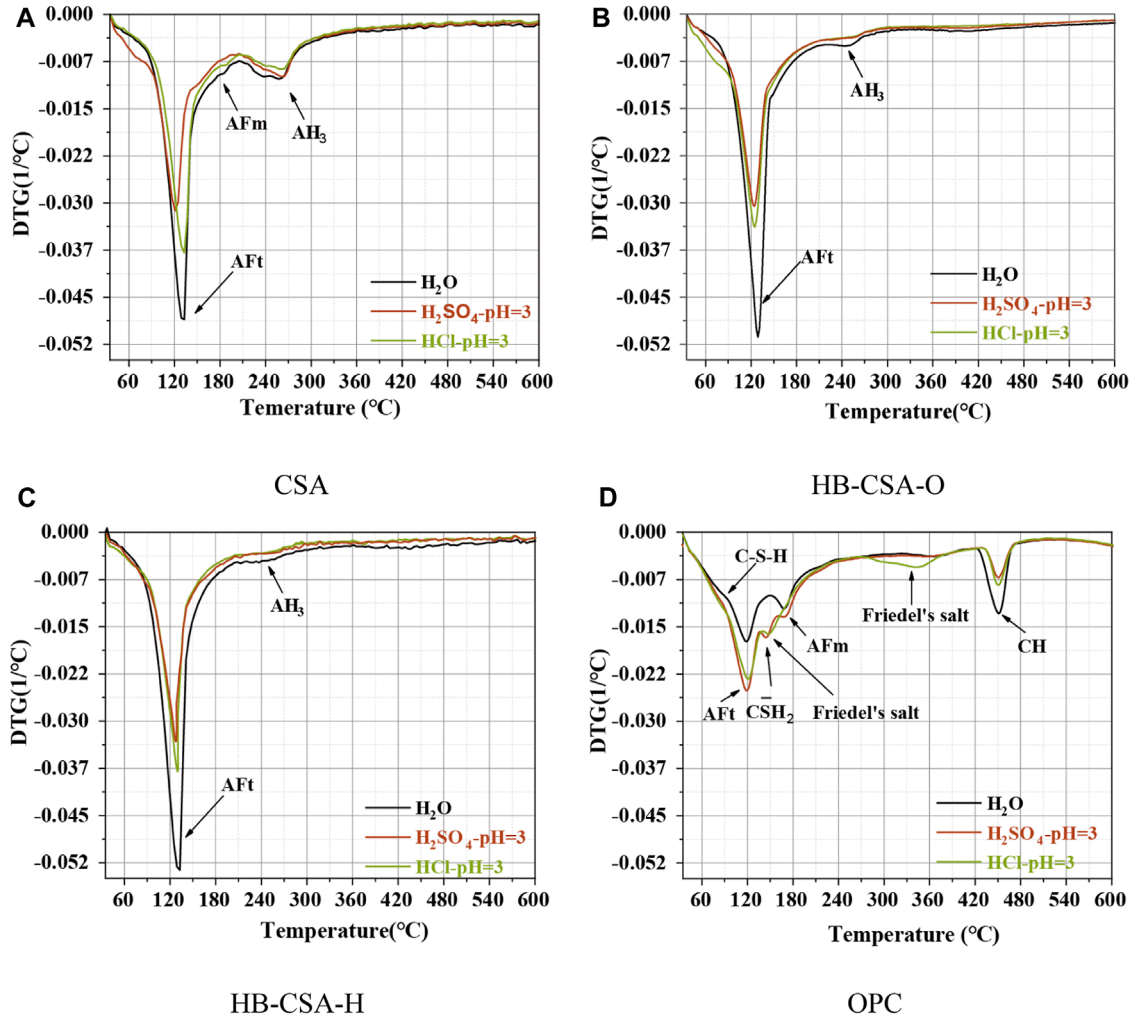

FIGURE 5
DTG patterns of CSA, HB-CSA, and OPC specimens after being immersed in hydrochloric acid and sulfuric acid at pH 3 for 360 days. **(A)** CSA, **(B)** HB-CSA-O, **(C)** HB-CSA-H, and **(D)** OPC.

strength of CSA, HB-CSA-O, and HB-CSA-H remains consistent at 6.02, 5.91, and 5.92 MPa, and the corresponding resistance indexes of CSA, HB-CSA-O, and HB-CSA-H remain 0.670, 0.650, and 0.683, respectively. It is found that the ability of hydrochloric acid corrosion resistance of HB-CSA increases with a decrease in the $C_4A_3\overline{S}$-to-$C\overline{S}$ ratio. After being immersed in hydrochloric acid, the flexural strength of OPC decreases significantly. Specifically, its strength drops from 8.9 to 6.43 MPa after being immersed in hydrochloric acid with a pH of 4 for 360 days and falls from 8.9 to 4.49 MPa after being immersed in hydrochloric acid with a pH of 3 for 360 days.

When immersed in sulfuric acid, the flexural strength of CSA, HB-CSA-O, HB-CSA-H, and OPC experiences an increase in the early stage of immersion. During this stage, the flexural strength of these cement specimens immersed in sulfuric acid is greater than that of the specimens immersed in water for the same time of immersion (except CSA immersed in pH 3 of sulfuric acid). Particularly, for HB-CSA-O and HB-CSA-H, the flexural strength increases notably until 210 days and 150 days of immersion, respectively. However, after reaching the peak of flexural strength, the fall in flexural strength of specimens immersed in sulfuric acid is much faster than that of the specimens immersed in hydrochloric acid. As a result, specimens immersed in sulfuric acid for 360 days have lower flexural strength compared to those immersed in hydrochloric acid with the same pH and immersion time. The resistance indexes of CSA, HB-CSA-O, and HB-CSA-H remain 0.533, 0.466, and 0.625 for specimens immersed in sulfuric acid with a pH of 3 at 360 days. It can be found that the ability of sulfuric acid corrosion resistance of HB-CSA increases with a decrease in the $C_4A_3\overline{S}$-to-$C\overline{S}$ ratio. When OPC is immersed in sulfuric acid, its flexural strength decreases significantly compared to other types of cement. After being immersed in sulfuric acid with a pH of 4 for 360 days, its flexural strength decreases from 8.9 to 5.11 MPa. Similarly, when immersed in sulfuric acid with a pH of 3 for 360 days, its flexural strength drops further to 2.18 MPa.

10.3389/fmats.2023.1282919

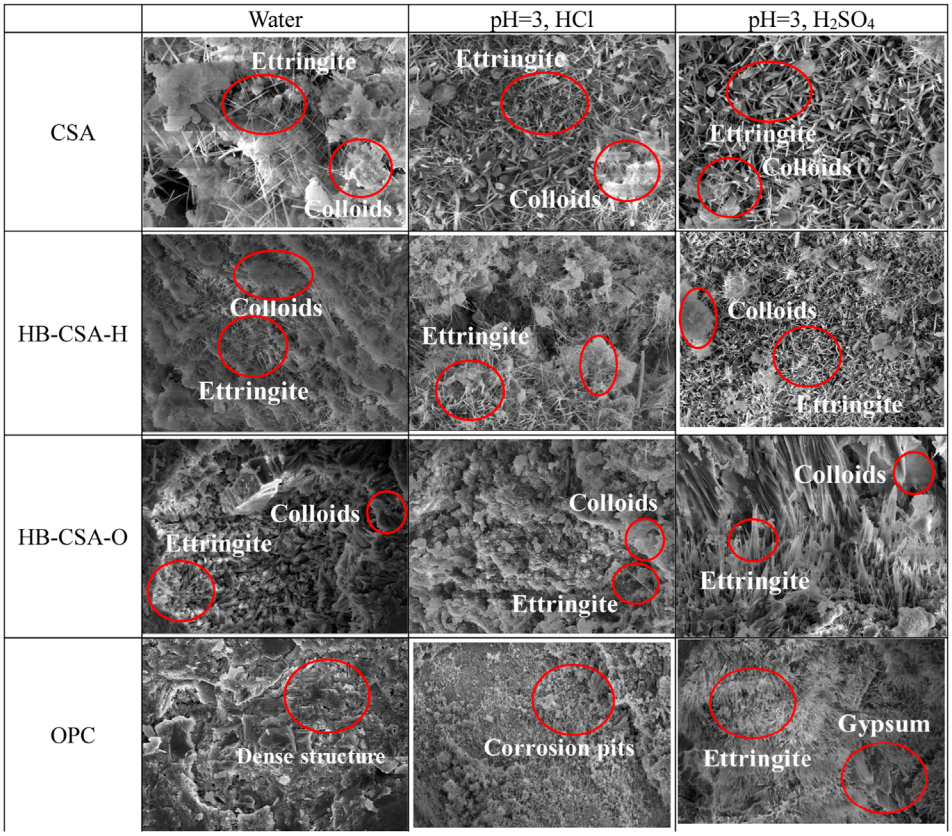

FIGURE 6
SEM images of specimens immersed in water, hydrochloric acid, and sulfuric acid for 360 days.

3.2 Internal structure changing

Figure 2 displays the internal structure morphology obtained by CT for specimens immersed in water, hydrochloric acid solution at pH 3, and sulfuric acid solution at pH 3 for 360 days. The color and density of the samples as shown in the figure positively correlate with the results of CT. Brighter and whiter colors correspond to the matrix, and the black color corresponds to the pores, corrosion pits, and cracks. For CSA and HB-CSA, the corrosion pits and micro-cracks appeared on the surface of the specimens after being immersed in the hydrochloric acid and sulfuric acid solutions at pH 3 for 360 days, which increased the surface roughness of the specimens. However, the morphological integrity in the core of the specimen was well maintained. For OPC mortar specimens, corrosion becomes more severe. Particularly, in the sulfuric acid corrosion, big cracks form on the surface of the specimen and extend into the core of the specimen, which damages the structure of the matrix.

The solid fractions of specimens immersed in hydrochloric acid and sulfuric acid for 360 days are obtained by calculating the brighter and whiter areas in CT images and summarized in Figure 3. The loss of flexural strength in CSA, HB-CSA-O, and HB-CSA-H when immersed in sulfuric and hydrochloric acid solutions is directly related to the reduction in their solid fraction, as observed from the specimens' solid fraction combined with their flexural strength test results. The more the solid loss, the more severe the strength loss. In the case of CSA, HB-CSA-O, and HB-CSA-H, the solid fraction of specimens immersed in hydrochloric acid for 360 days is greater than that of the specimens immersed in sulfuric acid. Therefore, the corresponding flexural strength of specimens immersed in hydrochloric acid is higher than that of the specimens immersed in sulfuric acid with the same pH and immersion time. For OPC, serious cracks tend to form in the specimen immersed in sulfuric acid. As a result, the flexural strength of OPC immersed in sulfuric acid for 360 days is significantly lower than that of the specimens immersed in hydrochloric acid with the same pH and immersion time.

3.3 Changes in microstructure and mineralogy

Figures 4, 5 show the results of XRD and differential thermal analysis (DTG) of specimens immersed in water, hydrochloric acid solution at pH 3 and 4, and sulfuric acid solution at pH 3 for 360 days. For CSA, the main hydration product is AFt. Since gypsum is insufficient to convert all minerals into AFt, some monosulfate (AFm) and alumina gel (AH) are found in the hydration of CSA. In the case of HB-CSA-O and HB-CSA-H, AFt is also the primary product of hydration. However, due to the ample content of gypsum in cement, no AFm is detected in the hydration products. Only a

minimal amount of AH is found. In addition, some calcium silicate hydrates are found since HB-CSA-H and HB-CSA-O contain a certain amount of C_2S. For HB-CSA-H, the content of AFt is higher than that of HB-CSA-O since the gypsum content in HB-CSA-H is higher than that in HB-CSA-O, resulting in the conversion of AH to AFt. Meanwhile, the content of AH in HB-CSA-H is lower than that in HB-CSA-O. No new products are generated during the corrosion process of CSA, HB-CSA-H, and HB-CSA-O in hydrochloric acid and sulfuric acid. The strength loss of these three types of cement can be attributed to the dissolution of the hydration products. Specimens immersed in sulfuric acid have their hydration products more dissolved than those immersed in hydrochloric acid, ultimately resulting in lower flexural strength. For CSA, the acid corrosion causes a large amount of dissolution of AFt and AFm, but the amount of AH dissolved in CSA is minimal. For HB-CSA-H and HB-CSA-O, in addition to the dissolution of AFt, AH also has a certain amount of dissolution. After 360 days of acid corrosion, the residual content of AFt in HB-CSA-H is higher than that in CSA and HB-CSA-O. Due to this, the flexural strength of the HB-CSA-H specimen immersed in acid is higher than that of the other two types of cement with the same immersion time in acid. For OPC, new hydration products are generated along with the acid corrosion, i.e., Friedel's salt for hydrochloric acid corrosion and AFt and gypsum for sulfuric acid corrosion. The expansion of gypsum causes cracking and damage to OPC specimens immersed in sulfuric acid.

SEM images (×3,000 magnification) of mortar specimens immersed in water, hydrochloric acid solution at pH 3, and sulfuric acid solution at pH 3 for 360 days are shown in Figure 6. For OPC mortar specimens, a dense structure consisting of C-S-H is formed in the specimens immersed in water for 360 days. After being corroded by hydrochloric acid and sulfuric acid, the matrix becomes looser and much fibrous product occurs in the specimen immersed in sulfuric acid. Based on the experimental results of TGA, it can be concluded that the fibrous products formed are ettringite and gypsum crystals for OPC immersed in sulfuric acid. The looser structure of OPC immersed in sulfuric acid can be attributed to the production of large-sized gypsum crystals, which cause structural expansion and cracking leading to a decrease in flexural strength. As observed in SEM images, the microstructure of CSA, HB-CSA-H, and HB-CSA-O appears similar when immersed in either hydrochloric acid or sulfuric acid. The only discernible differences are in the size of AFt and the amount of colloidal hydration products. The content of colloidal products in specimens immersed in hydrochloric acid is higher than that in specimens immersed in sulfuric acid. This causes a reduction in the flexural strength of specimens immersed in sulfuric acid compared to those immersed in hydrochloric acid.

4 Conclusion

This study aims to investigate the changes in the chemical components and mechanical evolution of HB-CSA when exposed to sulfuric and hydrochloric acid solutions and understand the underlying mechanisms of their evolution under such exposure conditions. In addition, the influence of the mass ratio of $C_4A_3\overline{S}$ to $C\overline{S}$ on the acid corrosion resistance capability of HB-CSA is also discussed. The following conclusions are drawn:

(1) HB-CSA exhibits superior resistance to sulfuric acid and hydrochloric acid compared to OPC. When the specimens are immersed in hydrochloric acid at a pH of 3 for 360 days, the flexural strength of HB-CSA-O and HB-CSA-H remains 5.91 and 5.92 MPa, respectively. At the same time, the flexural strength of OPC remains only 4.49 MPa. The same results are obtained in the sulfuric acid-corroded specimens.

(2) No new products are generated during the corrosion process of HB-CSA in hydrochloric and sulfuric acid solutions. The strength loss of HB-CSA can be attributed to the dissolution of the hydration products. The HB-CSA specimens immersed in sulfuric acid have a greater dissolution amount of hydration product than those immersed in hydrochloric acid, resulting in lower flexural strength than those immersed in hydrochloric acid.

(3) As the $C_4A_3\overline{S}$-to-$C\overline{S}$ ratio in HB-CSA decreases, the amount of AFt present in HB-CSA increases. AFt has excellent resistance to acid attack, and thus, after being immersed in a certain acid solution for 360 days, the residual content of AFt present in HB-CSA with a lower $C_4A_3\overline{S}$-to-$C\overline{S}$ ratio is greater than that in HB-CSA with a higher $C_4A_3\overline{S}$-to-$C\overline{S}$ ratio. Consequently, after being immersed in a certain acid solution for 360 days, the flexural strength of the HB-CSA specimen with a lower $C_4A_3\overline{S}$-to-$C\overline{S}$ ratio is higher than that of the HB-CSA specimen with a higher $C_4A_3\overline{S}$-to-$C\overline{S}$ ratio.

Data availability statement

The original contributions presented in the study are included in the article/Supplementary Material; further inquiries can be directed to the corresponding author.

Author contributions

GH: data curation and writing–original draft. XJ: investigation, methodology, and writing–original draft. XS: investigation and writing–review and editing. HL: conceptualization and writing–original draft. HS: investigation, methodology, and writing–review and editing.

Funding

The author(s) declare that financial support was received for the research, authorship, and/or publication of this article. This study was financially supported by the National Natural Science Foundation of China (No. 52008150) and the Natural Science Foundation of Hebei Province, China (No. E2021202037).

Acknowledgments

The authors would like to acknowledge the financial support provided by the National Natural Science Foundation of China

(No. 51702082), the Natural Science Foundation of Hebei Province, China (No. E2021202037), and Tangshan Polar Bear Building Materials Co., Ltd., Tangshan, China.

Conflict of interest

Author GH was employed by Shandong Hi-Speed Construction Management Group Co., Ltd., and Shandong Hi-speed Mingdong Expressway Co., Ltd. Authors XJ and XS were employed by Shandong Expressway Mingdong Highway Co., Ltd. Author HS was employed by Beijing Zhihuatong Technology Co., Ltd.

The remaining author declares that the research was conducted in the absence of any commercial or financial relationships that could be construed as a potential conflict of interest.

Publisher's note

All claims expressed in this article are solely those of the authors and do not necessarily represent those of their affiliated organizations, or those of the publisher, the editors, and the reviewers. Any product that may be evaluated in this article, or claim that may be made by its manufacturer, is not guaranteed or endorsed by the publisher.

References

Bassuoni, M. T. T., and Nehdi, M. L. L. (2007). Resistance of self-consolidating concrete to sulfuric acid attack with consecutive pH reduction. *Cem. Concr. Res.* 37, 1070–1084. doi:10.1016/j.cemconres.2007.04.014

Beddoe, R. E. (2016). Modelling acid attack on concrete: part II. A computer model. *Cem. Concr. Res.* 88, 20–35. doi:10.1016/j.cemconres.2015.10.012

Beddoe, R. E., and Dorner, H. W. (2005). Modelling acid attack on concrete: part I. The essential mechanisms. *Cem. Concr. Res.* 35, 2333–2339. doi:10.1016/j.cemconres.2005.04.002

Berndt, M. L. (2011). Evaluation of coatings, mortars and mix design for protection of concrete against sulphur oxidising bacteria. *Constr. Build. Mater.* 25 (10), 3893–3902. doi:10.1016/j.conbuildmat.2011.04.014

Chaunsali, P., and Mondal, P. (2015). Influence of calcium sulfoaluminate (CSA) cement content on expansion and hydration behavior of various ordinary portland cement-CSA blends. *J. Am. Ceram. Soc.* 98 (8), 2617–2624. doi:10.1111/jace.13645

Chi, L., Wang, Z., Lu, S., Wang, H., Liu, K., and Liu, W. (2021). Early assessment of hydration and microstructure evolution of belite-calcium sulfoaluminate cement pastes by electrical impedance spectroscopy. *Electrochimica Acta* 389, 138699. doi:10.1016/j.electacta.2021.138699

Congressional budget office (2002). *Future investment in drinking and wastewater infrastructure*. Washington, DC: Congressional Budget Office. ISBN 0160512433.

Dyer, T. (2017). Influence of cement type on resistance to attack from two carboxylic acids. *Cem. Concr. Compos.* 83, 20–35. doi:10.1016/j.cemconcomp.2017.07.004

Gartner, E. (2004). Industrially interesting approaches to "low-CO_2" cements. *Cem. Concr. Res.* 34, 1489–1498. doi:10.1016/j.cemconres.2004.01.021

Gartner, E., and Sui, T. B. (2018). Alternative cement clinkers. *Cem. Concr. Res.* 114, 27–39. doi:10.1016/j.cemconres.2017.02.002

Girardi, F., Vaona, W., and Maggio, R. D. (2010). Resistance of different types of concretes to cyclic sulfuric acid and sodium sulfate attack. *Cem. Concr. Compos.* 32, 595–602. doi:10.1016/j.cemconcomp.2010.07.002

Glasser, F. P., and Zhang, L. (2001). High-performance cement matrices based on calcium sulfoaluminate-belite compositions. *Cem. Concr. Res.* 31, 1881–1886. doi:10.1016/s0008-8846(01)00649-4

Gutiérrez-Padilla, M. G. D., Bielefeldt, A., Ovtchinnikov, S., Hernandez, M., and Silverstein, J. (2010). Biogenic sulfuric acid attack on different types of commercially produced concrete sewer pipes. *Cem. Concr. Res.* 40, 293–301. doi:10.1016/j.cemconres.2009.10.002

Hou, W., Liu, Z. Q., He, F. Q., Huang, J., and Zhou, J. (2020). Sulfate diffusion in calcium sulphoaluminate mortar. *Constr. Build. Mater.* 234, 117312. doi:10.1016/j.conbuildmat.2019.117312

Imbabi, M. S., Carrigan, C., and McKenna, S. (2012). Trends and developments in green cement and concrete technology. *Int. J. Sustain. Built Environ.* 1, 194–216. doi:10.1016/j.ijsbe.2013.05.001

Joorabchian, S. M. (2010). *Durability of concrete exposed to sulfuric acid attack*. Toronto: Ryerson University.

Kim, Y. Y., Lee, K. M., Bang, J. W., and Kwon, S. J. (2014). Effect of W/C ratio on durability and porosity in cement mortar with constant cement amount. *Adv. Mater. Sci. Eng.* 2014, 1–11. doi:10.1155/2014/273460

Larreur-Cayol, S., Bertron, A., and Escadeillas, G. (2011). Degradation of cement-based materials by various organic acids in agroindustrial waste-waters. *Cem. Concr. Res.* 41, 882–892. doi:10.1016/j.cemconres.2011.04.007

Li, H., Li, L., Li, L., Zhou, J., Mu, R., and Xu, M. (2022). Influence of fiber orientation on the microstructures of interfacial transition zones and pull-out behavior of steel fiber in cementitious composites. *Cem. Concr. Compos.* 128, 104459. doi:10.1016/j.cemconcomp.2022.104459

Li, J., Ma, B., Zhou, C., and Yang, Y. (2014). Study on mechanism of chemical activation for minerals of high belite-calcium sulfoaluminate clinker. *J. Sustain. Cement-Based Mater.* 3 (1), 13–23. doi:10.1080/21650373.2013.843476

Maddalena, R., Roberts, J. J., and Hamilton, A. (2018). Can Portland cement be replaced by low-carbon alternative materials? A study on the thermal properties and carbon emissions of innovative cements. *J. Clean. Prod.* 186, 933–942. doi:10.1016/j.jclepro.2018.02.138

Mlinárik, L., and Kopecskó, K. (2017). The influence of combined application of two SCMs on the corrosion and acid attack durability of mortars. *Period. Polytech. Civ. Eng.* 61 (2), 313–321. doi:10.3311/ppci.9352

Ninan, C. M., Ramaswamy, K. P., and Sajeeb, R. (2021). A critical review on the factors influencing the design of test methods for assessing acid attack in concrete. *IOP Conf. Ser. Mater. Sci. Eng.* 1114 (1), 012013. doi:10.1088/1757-899x/1114/1/012013

Ogawa, K., and Roy, D. M. (1982). C_4A_3S hydration, ettringite formation, and its expansion mechanism: III. Effect of CaO, NaOH and NaCl; conclusions. *Cem. Concr. Res.* 12, 247–256. doi:10.1016/0008-8846(82)90011-4

Que, Y., Dai, Y., Ji, X., Leung, A. K., Chen, Z., Tang, Y., et al. (2023). Automatic classification of asphalt pavement cracks using a novel integrated generative adversarial networks and improved VGG model. *Eng. Struct.* 277, 115406. doi:10.1016/j.engstruct.2022.115406

Sun, Z., Nie, S., Zhou, J., Li, H., Chen, Z., Xu, M., et al. (2022). Hydration mechanism of calcium sulfoaluminate-activated supersulfated cement. *J. Clean. Prod.* 333, 130094. doi:10.1016/j.jclepro.2021.130094

Wang, X., Guo, M., Yue, G., Li, Q., and Ling, T. C. (2022). Synthesis of high belite sulfoaluminate cement with high volume of mixed solid wastes. *Cem. Concr. Res.* 158, 106845. doi:10.1016/j.cemconres.2022.106845

Wu, H., Zhang, D., Du, T. J., and Li, V. C. (2020a). Durability of engineered cementitious composite exposed to acid mine drainage. *Cem. Concr. Compos.* 108, 103550. doi:10.1016/j.cemconcomp.2020.103550

Wu, M., Wang, T., Wu, K., and Kan, L. (2020b). Microbiologically induced corrosion of concrete in sewer structures: a review of the mechanisms and phenomena. *Constr. Build. Mater.* 239, 117813. doi:10.1016/j.conbuildmat.2019.117813

Wu, Z., Tang, Y., Hong, B., Liang, B., and Liu, Y. (2003). Enhanced precision in dam crack width measurement: leveraging advanced lightweight network identification for pixel-level accuracy. *Int. J. Intelligent Syst.* 2023, 9940881. doi:10.1155/2023/9940881

Xu, L. L., Wu, K., Li, N., Zhou, X. Y., and Wang, P. M. (2017). Utilization of flue gas desulfurization gypsum for producing calcium sulfoaluminate cement. *J. Clean. Prod.* 161, 803–811. doi:10.1016/j.jclepro.2017.05.055

Yang, Y., Ji, T., Lin, X. J., Chen, C. Y., and Yang, Z. X. (2018). Biogenic sulfuric acid corrosion resistance of new artificial reef concrete. *Constr. Build. Mater.* 158, 33–41. doi:10.1016/j.conbuildmat.2017.10.007

Yue, Q., Li, L., and He, Z. P. (2011). Experiment research on the steel fiber reinforced concrete in the acid environment. *Adv. Mater. Res.* 224, 224–228. doi:10.4028/www.scientific.net/amr.224.224

Zhang, W., Nie, S., Xu, M., Zhou, J., and Li, H. (2022). Research progress on activation of high belite calcium sulphoaluminate cement. *Bull. Chin. Ceram. Soc.* 41 (9), 2979–2992. doi:10.16552/j.cnki.issn1001-1625.2022.09.002

Zhang, Z. Q. (2015). *Rapid-setting and hardening, high-belite sulfoaluminate cement clinker as well as application and production process thereof*. US Patent 9822036B2.

frontiers | Frontiers in Materials

TYPE Original Research
PUBLISHED 19 January 2024
DOI 10.3389/fmats.2024.1346140

OPEN ACCESS

EDITED BY
Yang Zou,
Chongqing Jiaotong University, China

REVIEWED BY
Xiaohua Li,
Chongqing University, China
Ali Raza,
University of Engineering and Technology, Taxila, Pakistan

*CORRESPONDENCE
Xiang Lyu,
lvxiang18@mails.jlu.edu.cn

RECEIVED 29 November 2023
ACCEPTED 02 January 2024
PUBLISHED 19 January 2024

CITATION
Lyu X, Li W, Hu H, Ding X and Hu X (2024), Cracking characteristics evaluation for reinforcement basalt fiber reactive powder concrete beam using acoustic emission. *Front. Mater.* 11:1346140.
doi: 10.3389/fmats.2024.1346140

Cracking characteristics evaluation for reinforcement basalt fiber reactive powder concrete beam using acoustic emission

Xiang Lyu[1]*, Wenjun Li[2], Hang Hu[1], Xuezheng Ding[3] and Xiaochuan Hu[3]

[1]China Construction Second Engineering Bureau Ltd., Beijing, China, [2]The Department of Bridge Engineering, Tongji University, Shanghai, China, [3]The Civil Engineering Group of China Construction Second Engineering Bureau LTD., Beijing, China

New types of fibers such as basalt fibers are gradually being used to reinforce cement-based concrete materials. To provide a basis for the further popularization of basalt fibers and basalt fiber reinforced reactive powder concrete (BFRPC) materials, the bending mechanical properties and fracture properties of BFRPC beams were investigated by innovatively applying four-point bending test and multiple acoustic parameter analysis methods. On the one hand, the load vs. displacement curve and crack pattern of reinforcement BFRPC beam were obtained from the four-point bending test. On the other hand, Acoustic emission (AE) technology was used to monitor the cracking process of reinforcement BFRPC beam under four-point bending load, and the AE signal was analyzed to illustrate the cracking characteristics of reinforcement BFRPC beam. The results revealed that AE hits, amplitude, counts, duration, and energy have a similar changing trend with bending load. Cumulative hits and cumulative energy are positively linearly related to the displacement and quadratically related to the sum of crack widths, and the correlation coefficients are all above 0.95. Besides, the cracking process of reinforcement BFRPC beam can be divided into four stages by the variation of AE basic parameters with bending load. The main rebars yielding is an important turning point of the crack characteristic of reinforcement BFRPC beam. AE signal data varies greatly in different locations, and it has an obvious advantage to detect the formation of invisible cracks. The results of predicting concrete damage and cracking by AE signal data are consistent with the experimental phenomenon. The low-stress brittle fracture caused by tensile fracture was reduced, and the tensile resistance and flexural bearing capacity of the reinforcement BFRPC beam were increased. The results obtained in this paper support the damage assessment and structural health monitoring for cement base concrete materials under bending load.

KEYWORDS

basalt fiber, reactive powder concrete, acoustic emission, cracking characteristics, damage assessment

1 Introduction

Basalt fiber reactive powder concrete (BFRPC) is a new type of cement-based concrete material with excellent mechanical properties and durability (Li et al., 2020). This is partly because reactive powder concrete (RPC) is prepared by the theory of densified particle packing (Chen et al., 2019; Zdeb, 2019; Sultan and Alyaseri, 2020). RPC replaces the coarse aggregate in ordinary concrete with millimeter-level aggregate (quartz sand) and filled the gap between millimeter-level aggregate with micron particles (cement) and submicron particles (silica fume) (Merdas and Shallal, 2023; Zhang et al., 2023). In this way, the internal defects of concrete are controlled, and both the density and homogeneity are improved. Another reason is that basalt fiber has superior mechanical properties and has good resistance to all kinds of acid and alkaline conditions (Lou et al., 2021; Si et al., 2021). Basalt fiber improves the mechanical properties and durability of RPC (Liu et al., 2020a; Liu et al., 2020b). Based on these obvious advantages, BFRPC has been considered suitable for concrete beam structural materials. On the basis of previous studies on the properties of BFRPC materials, it is very important to study the flexural cracking performance of BFRPC beam structures for their popularization and application. Concrete cracking greatly deteriorates the mechanical properties and durability of reinforcement BFRPC beams, so it is of great significance to evaluate the cracking characteristics to promote the application of BFRPC materials in practical structural engineering. The cracking characteristics of concrete beams are mainly evaluated by crack-related indexes, such as cracking moment, crack propagation, crack spacing, crack width, and so on (Rashid et al., 2020; Li et al., 2021a). However, it is difficult to monitor and evaluate the whole cracking and damage process of concrete beams only by traditional measurements and naked-eye observation, especially concrete beam internal cracking and damage assessment at a low-stress level.

Acoustic emission (AE) is a non-destructive detection tool with the advantages of high sensitivity (Boniface et al., 2020; Zhang et al., 2020; Karimian and Modarres, 2021). Depending on its high efficiency, convenience and accuracy, it has been widely used in cracking and damage assessment of building materials and engineering structures (Dubuc et al., 2020; Fan et al., 2020; Li. et al., 2021b; Mohammadi et al., 2021; Tan et al., 2021). Han et al. (2019) used AE technology to clarify the concrete damage mechanism and proved that the analysis of AE signals was effective in the identification of concrete damage. Xargay et al. (2018) analyzed the concrete damage process under heat-exposure conditions based on AE technology and confirmed the potential of AE technology in the diagnosis of concrete damage levels. Nguyen-Tat et al. (2018) verified the strong correlation between the damage evolution of concrete and the AE activity. Farhidzadeh et al. (2013) monitored the fracture process of concrete construction and illustrated that AE was very effective in determining structural safety. Xargay et al. (2021) used four AE indexes (load ratio, calm ratio, cumulative signal strength ratio, and relaxation ratio) to evaluate the damage of steel fiber reinforced concrete beams; and the test results showed that AE damage indexes have a quite good correlation with cracking initiation and propagation, and AE damage indexes can not only monitor the loading response of reinforced concrete beam but also detect local damage. Li et al. (2018) described the cracking modes of steel fiber reinforced concrete through AE parameters such as average frequency (AF), rise angle (RA) value, and found that the failure of ordinary concrete was mainly caused by tensile cracks. Zhang et al. (2019) used AE technology to perform a laboratory study focus on the bending characteristics of the ordinary RC beam affected by steel corrosion, and described the ordinary concrete cracking process, and determined the cracking modes by the b-value and AF-RA association value analysis method, respectively. Therefore, it is advanced and effective to describe the cracking characteristics of reinforcement BFRPC beams by AE parameters such as b-value and AF-RA association value, *etc.*

In this paper, three reinforcement BFRPC beams with different reinforcement ratios were prepared, and the beams were subjected to a four-point bending test by graded loading. The load vs. displacement curve and crack pattern of reinforcement BFRPC beam were recorded. At the same time, AE technology was used to monitor the AE signal of reinforcement BFRPC beams during the loading process. Besides, the parameters of the AE signal were analyzed to elucidate the damage process and cracking characteristics. The purpose of this paper is to elaborate the cracking characteristics of the new composite material (reinforcement BFRPC beam), which can provide a theoretical basis for the application of reinforcement BFRPC and provide a reference for the damage assessment of cementitious concrete materials under bending loads.

2 Experimental details

2.1 Materials and mixture

Materials required for reinforcement BFRPC beams include quartz sand, quartz powder, cement, silica ash, water reducer, basalt fiber, water, and rebars. The quartz sand has a hardness of 7 and is mainly composed of SiO_2. The quartz sand specifications used in this paper were 20–40, 40–80, 80–120 mesh, and they were filtered by a square hole sieve of 0.6, 0.3 and 0.15 mm respectively. The mixture proportions for the reinforcement BFRPC beam are listed in Table 1. According to the laboratory test, the compressive strength and flexural strength of BFRPC prepared by the mix proportions as shown in Table 1 are 110 and 15 MPa respectively. The basic characteristics of basalt fiber are shown in Table 2.

2.2 Specimen preparation

In this paper, three reinforcement BFRPC beams with different reinforcement ratios were prepared, and the designed size was 1500 mm × 150 mm × 300 mm. Figure 1 shows the dimensions of three test beams and the relative positions of the rebars. The types and diameters of erective steel bars, stirrups, and main rebars of each test beam are shown in Table 3. In each test beam, two HPB300 steel bars with a diameter of 6 mm were used as erecting steel bars; ten HPB300 steel bars with a diameter of 8 mm were used as stirrups; two HRB335 rebars with a diameter of 12, 14, and 16 mm respectively were used as the main rebars.

TABLE 1 Mix proportions of reinforcement BFRPC beam (kg/m^3).

Water	Cement	Silica fume	Quartz sand		Quartz powder	Basalt fiber	Water reducer
			0.15 mm–0.3 mm	0.3 mm–0.6 mm			
151.5	841.8	210.4	364.2	582.8	311.4	12	52.6

TABLE 2 Basic properties of basalt fibers.

Length	Diameter	Linear density	Tensile strength	Elastic modulus	Breaking strength	Elongation
22 mm	23 μm	2,392 tex	2,836 MPa	62 GPa	0.69 N/tex	3%

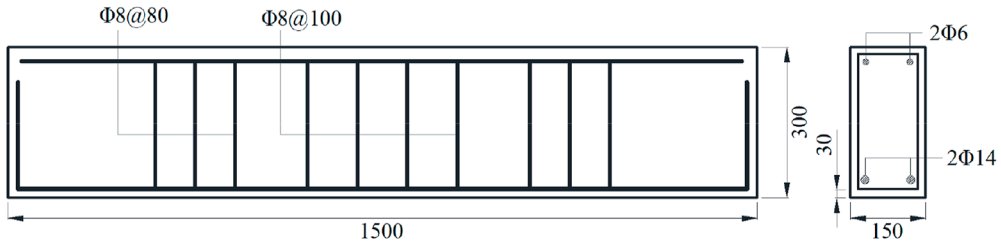

FIGURE 1
Dimension of the specimen (mm).

TABLE 3 Types and diameters of steel bars in test beams.

Teat beam number	Erecting steel bar		Stirrup		Main rebar	
	Type	Diameter	Type	Diameter	Type	Diameter
Beam-1	HPB 300	6 mm	HPB 300	8 mm	HRB 335	12 mm
Beam-2	HPB 300	6 mm	HPB 300	8 mm	HRB 335	14 mm
Beam-3	HPB 300	6 mm	HPB 300	8 mm	HRB 335	16 mm

2.3 Experimental procedure

The experimental flow chart is shown in Figure 2. The prepared test beams firstly underwent curing. The reinforcement BFRPC beams were cured in 90°C steam for 48 h. After curing, all the test beams were performed the four-point bending test; the load vs. displacement curves, cracking patterns, and crack widths of the test beams were measured and recorded. During the bending load process, concurrently, the AE test was conducted for obtaining the AE signals. The parameters including hits, energy, b-value from AE signals were used for analyzing the damage process and the cracking characteristics from the mesoscale.

2.4 Experimental setups

This paper carries out concrete beam stress tests based on Chinese standards (Ministry of Housing and Urban-Rural Development of the People's Republic of China, 2012). A WAW-1000 kN type electro-hydraulic servo universal testing machine was utilized to perform the four-point bending test for the beams. The dial gauges were arranged at the bottom of the 1/2 and 1/4 span of the beams for recording the displacement during the loading process. Simultaneously, the crack width could be tested by the crack testing instrument and the crack pattern was plotted. The measurement accuracy of crack width is 0.01 mm. The AE test was performed simultaneously with the bending test for obtaining AE signals. Four SR150M type AE sensors (produced by Soundwel Technology Co., Ltd., Beijing, China) were attached to the side of test beams by epoxy resin adhesive. Loading device of four-point bending tests and the arrangement of AE sensors are schematically shown in Figure 3. The test loading adopted a multi-step loading process (20 kN for each step), and the loading rate was controlled to be 0.037 kN/s.

The measurement frequency range of the AE sensor was 60–400 kHz. AE sampling frequency was 5 MSPS. The AE signal amplitude threshold was set to 40 dB to filter the environmental noise. To ensure the accuracy of the AE signal, the peak definition

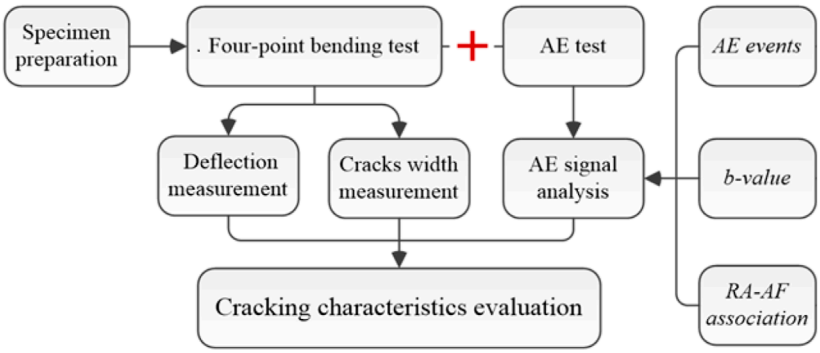

FIGURE 2
Experimental flow chart.

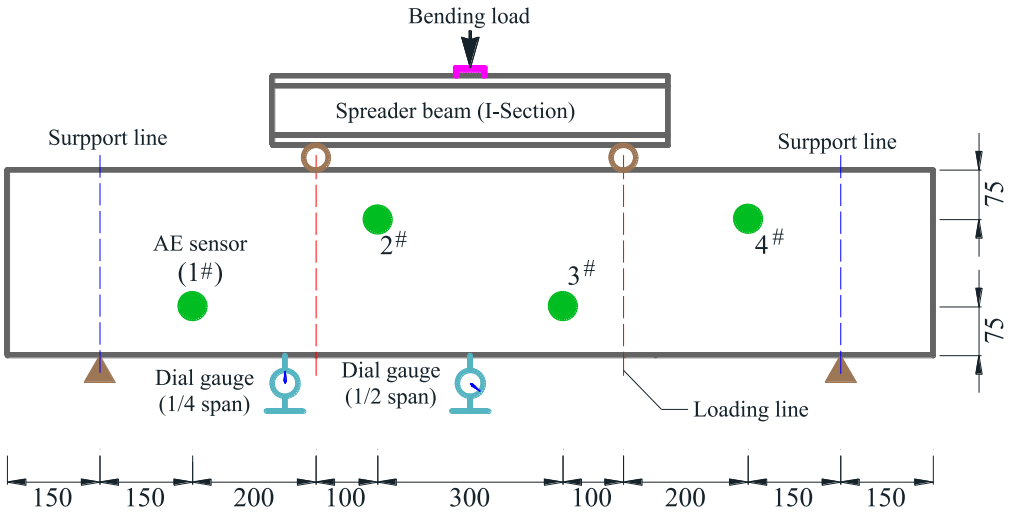

FIGURE 3
Sketch of the experimental setup for the four-point bending test (unit: mm).

time was set at 50 μs, and the hit definition and lock time were set at 150 and 300 μs respectively. The experimental setups are shown in Figure 4.

3 Analysis methods

3.1 AE basic parameters

The elastic wave generated by the crack initiation inside the reinforcement BFRPC beam is transmitted to the surface of the AE sensor to be converted into an electrical signal, which is processed and calculated into a signal parameter by the analytical system and characterised as a digitised AE waveform, so that structural changes inside the concrete can be explored through the changes in acoustic emission signal parameters. The basic parameters (shown in Figure 5) of the AE signal include hit, count, amplitude, duration, rise time, energy, and so on.

The hit is a signal that exceeds the threshold and causes a system channel to accumulate data. In Figure 5, one waveform corresponds to one "hit". Signal amplitude is the sensor output peak voltage, which is the indicator of signal size. Signal count, also known as signal ringing count, is the times that the AE amplitude exceeds the threshold in the duration. The rise time is the time interval between the signal trigger time and the peak amplitude time. And the duration is the time interval between the signal trigger time and the signal disappearance time. Signal energy is defined as the measured area below the AE signal envelope.

3.2 b-value analysis

The b-value analysis method, first applied for analyzing seismic waves, is famous for its advantages in quantifying the distribution of earthquake magnitude. In the past decades, the b-value analysis method was successfully imported into the AE signals analysis field

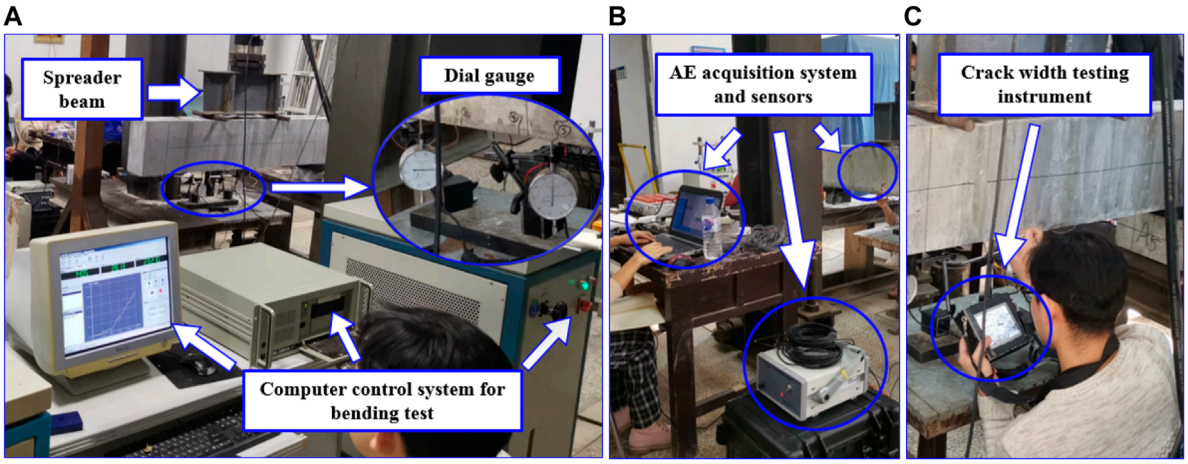

FIGURE 4
Experimental setups. **(A)** Four-point bending test; **(B)** AE test; **(C)** Crack width test.

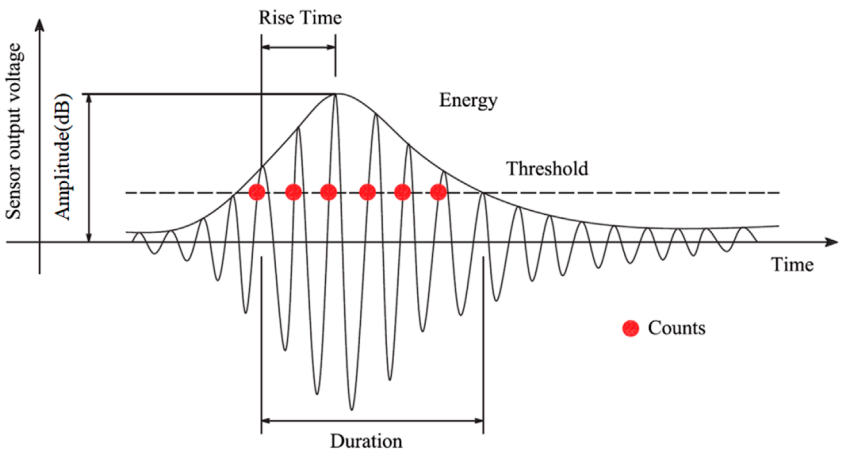

FIGURE 5
AE characteristic parameters.

due to the waves in AE were similar to the earthquake (Jiao et al., 2019). The b-value can be calculated as follows:

$$\log_{10} N = a - b\left(\frac{A_{dB}}{20}\right) \tag{1}$$

where A_{dB} is the amplitude of the AE signal; N is the number of AE signals with the amplitude above the A_{dB}; a is the intercepts of the linear fitting line; and b is the slope of the linear fitting line, which is called the b-value of these AE events.

3.3 AF value and RA value

Both RA and AF values are the statistical parameters of AE signals. AF-RA association analysis, as a statistical parameter-based method, was widely used to classify the cracking modes in concrete in the past few years. The RA and AF values can be calculated by the following equations:

$$AF\,value = Ringing\,counts/Duration, (kHz) \tag{2}$$

$$RA\,value = Rise\,time/Amplitude, (ms/V) \tag{3}$$

Ohtsu et al. (2010) demonstrated that AE signals could be divided into the tensile signals and shear signals, which corresponded to the occurrence of tensile cracks and shear cracks in concrete respectively. Figure 6 shows the schematic of the crack modes classification based on the AF-RA association analysis method. When a tensile crack occurs, the amplitude of the signal wave is large, the rising time is short, and the wave velocity is fast, which is reflected in a large AF value and a small RA value. On the contrary, when a shear crack occurs, the wave velocity of the signal

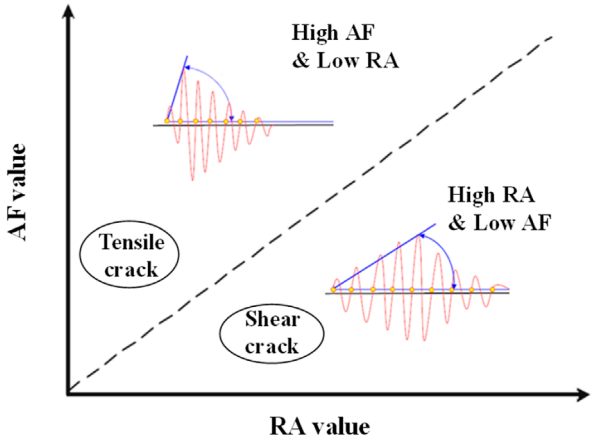

FIGURE 6
Cracking modes classification based on AF-RA association values.

wave is low, the rise time and duration are long, which is reflected in a large RA value and a small AF value.

4 Results and discussion

4.1 Load vs. displacement curve

The load vs. displacement curve of three reinforcement BFRPC simply supported beams are shown in Figure 7, and the load vs. displacement curve can be roughly divided into three stages according to the test beam imminent cracking point and the main rebars yielding point. The first stage is before the test beam cracking; the second stage is from the test beam imminent cracking to the main rebars yielding, and the third stage is from the main rebars yielding to the test beam failure.

Besides, the slopes of the load vs. displacement curve in the first and second stage are the same, while the slope of load vs. displacement curve in the third stage is significantly lower than that in the first and second stages, indicating that reinforcement BFRPC beams have a good ductility after the main rebars yielding. When the bending loads of Beam-1, Beam-2, and Beam-3 reached 40 kN, it can be seen from the test phenomenon that subtle cracks gradually appear on the bottom of the test beams. Therefore, the cracking bending load value of Beam-1, Beam-2, and Beam-3 is 40 kN. Moreover, it can be seen from Figure 7 that the main rebars yielding load values of Beam-1, Beam-2, and Beam-3 are 140 kN, 160 kN, and 180 kN, respectively. And the failure load values of Beam-1, Beam-2, and Beam-3 are 197 kN, 235 kN, and 261 kN, respectively. It is shown that within the range of reinforcement ratio of suitable reinforcement beam, the main rebars yielding load and failure load of the reinforcement BFRPC simply supported beam increase gradually with the increasing of reinforcement ratio.

4.2 Crack pattern

To better describe the cracks propagation, at the end of each loading stage, the testers mapped the crack pattern on the side of the test beam and measured the maximum width of each crack. When the test beam was loaded to 180 kN, the deformation of reinforcement BFRPC beams increased significantly. In order to avoid the damage of the test beam to the test personnel, the crack width of the test beam with the load exceeding 180 kN was not measured. When the bending load was less than 40 kN, there were almost no visible cracks can be checked on the surface of the test beam, while when the load was more than 40 kN, many subtle cracks began to appear at the bottom of the pure bending section of the test beams. Representative crack patterns (Figure 8) with the bending load values of 60, 100, 140, and 180 kN are presented to understand the crack propagation of each test beam in detail.

As shown in Figure 8, Beam-1, Beam-2, and Beam-3 have similar crack patterns under the bending load. When the load reached 60 kN, fine visible cracks were first generated in the pure bending section of the test beam. As the bending load step reached 100 kN, the cracks in the pure bending section of the test beam gradually extended to the top of the beam, while the new cracks began to appear in the shear bending section. As the bending load step reached 140 kN, the cracks in the pure bending section of the test beam extended vertically to the middle part of the beam side, while the cracks in the shear bending section began to extend to the middle part of the beam side toward the loading point. At the load step of 180 kN, the cracks of the test beam continued to form through cracks. As the bending load exceeded 180 kN, the crack width of the bottom part of the beam increased significantly, and an obvious crackling sound could be heard.

Simultaneously, the crack widths at each loading step were measured by the crack width tester. As shown in Figure 9, the sum of crack widths at each loading step of all test beams increases with bending load. After main rebars yielding, the sum of crack widths of all the reinforcement BFRPC beams increased significantly, and the failure process of test beams accelerated.

4.3 AE basic parameters analysis

4.3.1 AE basic parameters

In this section, the AE basic parameters were utilized to describe the craking characteristics of the reinforcement BFRPC beam. Figure 10 taking Beam-3 as an example, AE signals were used to analyze the variation of AE basic parameters with bending load. The units of AE basic parameters are different. To make a comparative analysis in the unified coordinate system, each AE basic parameter should be homogenized.

It can be seen from Figure 10 that the hits and amplitude have a similar variation with bending load, while the counts, duration, and energy have a consistent variation with bending load. Thus, for a clearer and more detailed analysis, the hits and energy parameters were selected to analyze the damage process of the reinforcement BFRPC beam with bending load in Figures 11, 12.

As can be seen from Figure 11, the total hits and total energy gradually increase with bending load, which indicates that the damage degree of the test beam gradually increased with the bending

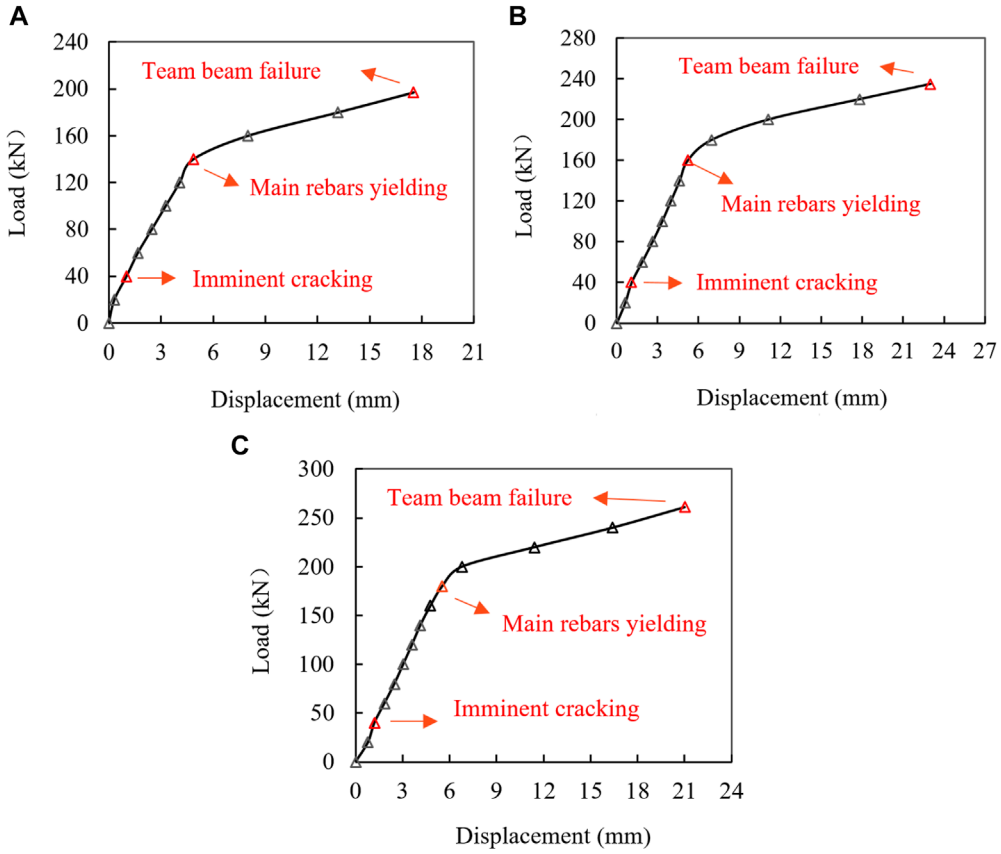

FIGURE 7
Displacement of the test beams. **(A)** Beam-1; **(B)** Beam-2; **(C)** Beam-3.

load. It is especially noteworthy that the AE basic parameters (hits and energy) have an excellent monitoring effect on the initial damage of the test beam. When the bending load reached 40 kN, no visible cracks appeared on the surface of the test beam, while the hits value is larger and the energy value is small, this phenomenon shows that many microcracks formed in the test beam. During the bending load of 80–120 kN, the hits value has a small increase, but the energy value has a significant increase, indicating that the trend of new crack initiation was weakened, the trends of original microcrack propagation and macrocrack formation were increased at this stage, and the test beam entered the stage of microcrack propagation and macrocrack formation. After the bending load reached 120 kN, the hits value and energy value both increase significantly, indicating that there were both new crack initiation and macrocrack formation inside the test beam at this stage, and the test beam entered the critical failure stage. Moreover, it can be seen from the AE sensors at different positions in Figure 11 that the AE hits and energy values collected by sensor 1# and sensor 3# which near the bottom of the test beam are more than that collected by sensor 2# and sensor 4# which near the top of the test beam. Compared with sensor 1# (located in the shear bending section) and sensor 3# (located in the pure bending section), the hits and energy of sensor 1# are greater than that of sensor 3# when the load reached 40 kN and 197 kN. This phenomenon infers that at the beginning and the end of bending load action, the pure bending section of the reinforcement BFRPC beam was more prone to damage, while the shear bending section of the reinforcement BFRPC beam was more prone to damage at the middle of bending load process.

From Figure 12, the variation of the hits and energy for reinforcement BFRPC beams with bending load can be roughly divided into four stages. In the first stage, before visible cracks appeared in the bottom of the test beam (the bending load arrived at almost 60 kN), the hits and energy increased with bending load, and the damage of the reinforcement BFRPC beam was mainly caused by microcracks initiation. The second stage was from the appearance of visible cracks to the main rebars yielding (the bending load from 60 kN to 160 kN). In this stage, the hits and energy show a downward trend, and the damage of the reinforcement BFRPC beam was mainly caused by macrocrack formation. In the third stage, from the main rebars yielding to the formation of critical failure cracks, the hits and energy increased sharply, and a large number of macrocracks formed and gradually expanded into critical failure cracks. The fourth stage was the failure stage, the hits and energy were greatly reduced, and the critical failure crack propagation led to the beam failure.

4.3.2 Cumulative AE characteristic parameters

Taking Beam-3 sensor 3# as an example, cumulative AE parameters were homogenized, and the variation of cumulative AE parameters with bending load was compared and analyzed for

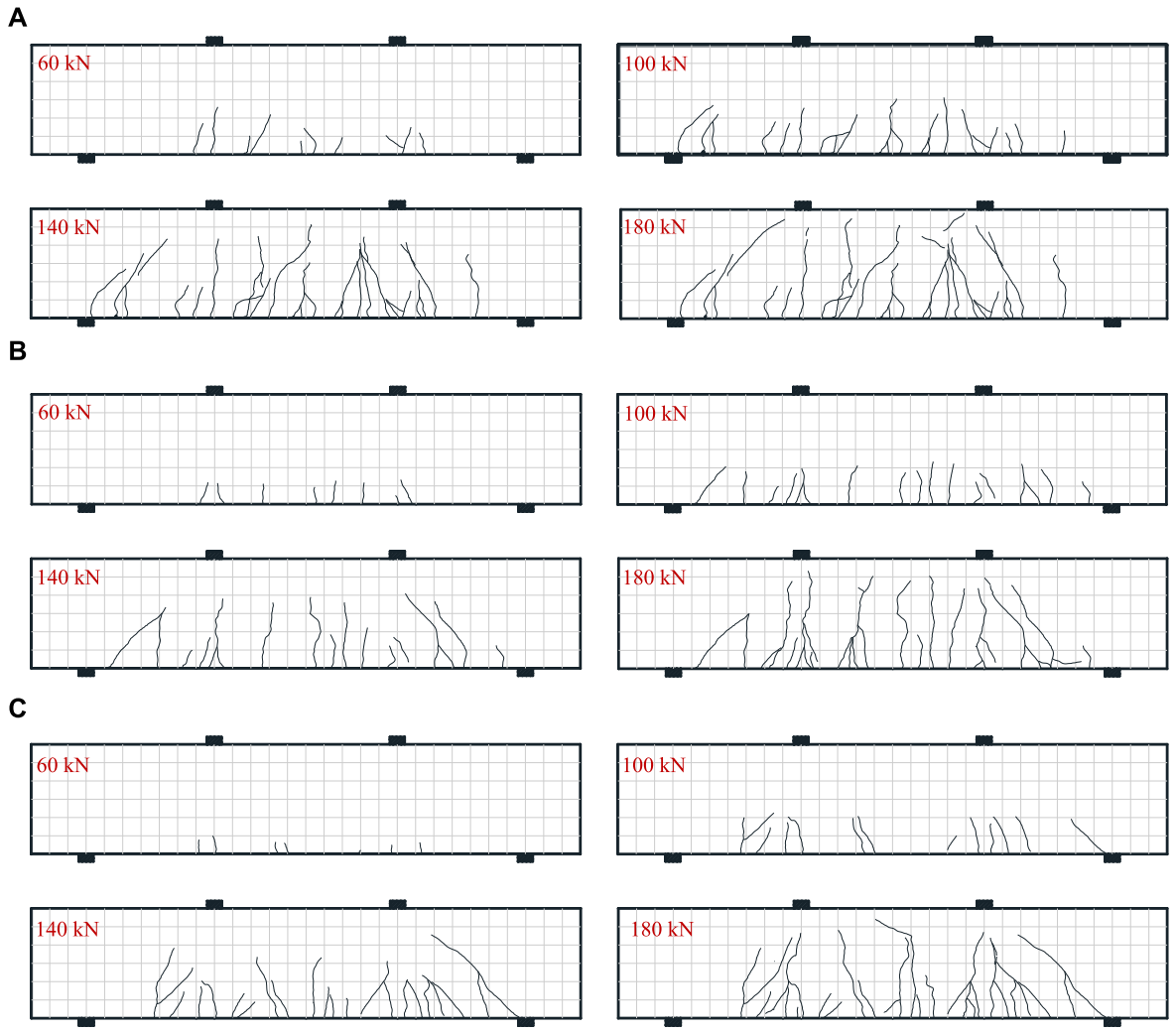

FIGURE 8
The crack pattern of the test beam. **(A)** Beam-1; **(B)** Beam-2; **(C)** Beam-3.

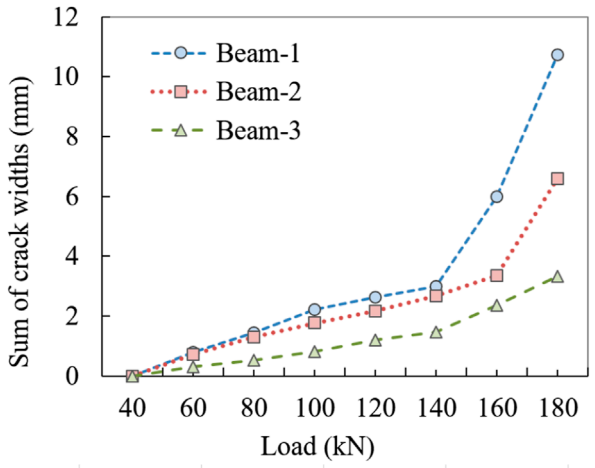

FIGURE 9
The variation of the sum of crack width with bending load.

evaluating the cracking process of the test beams. As can be seen from Figure 13, cumulative AE parameters have similar variation patterns; and thus in this section, the cumulative hits and cumulative energy are selected to focus on the detailed variation of cumulative AE parameters, as shown in Figure 14.

In Figure 14, as the same discussed above, the cumulative hits and cumulative energy can be also divided into four stages. It can be seen that the cumulative hits and cumulative energy are positively linearly correlated with bending load in the four stages, and the correlation coefficients are all above 0.95. Additionally, the slope of the fitting line of stage I is the same as stage II, and the slope of the fitting line of stage III is the same as stage IV. This phenomenon illustrates that the damage rate of the reinforcement BFRPC beam is relatively stable before and after the main rebars yielding point, and the damage rate after the main rebar yielding is significantly higher than that before the main rebar yielding.

To analyze the relationship between cumulative AE parameters and mechanical property parameters of reinforcement BFRPC beam, the relationship between cumulative AE parameters and

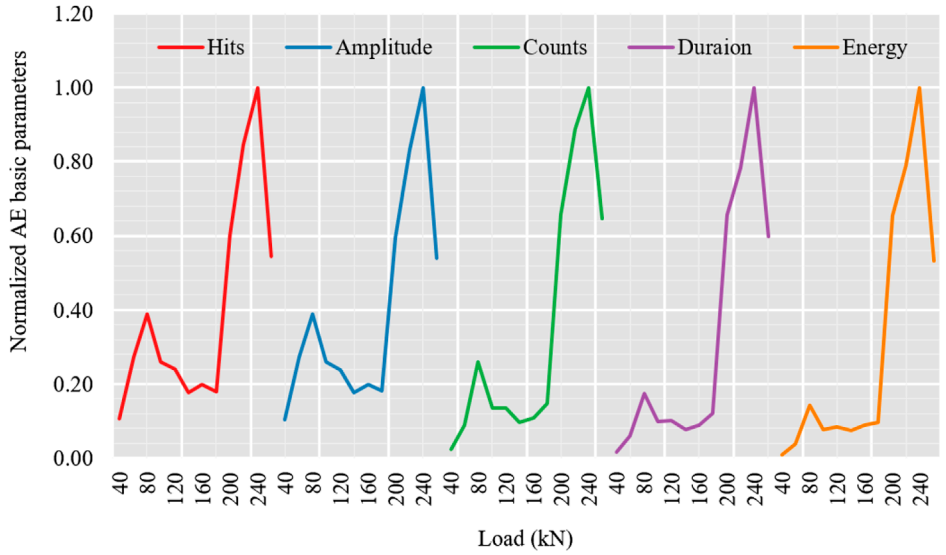

FIGURE 10
The normalized AE basic parameters of the Beam-3.

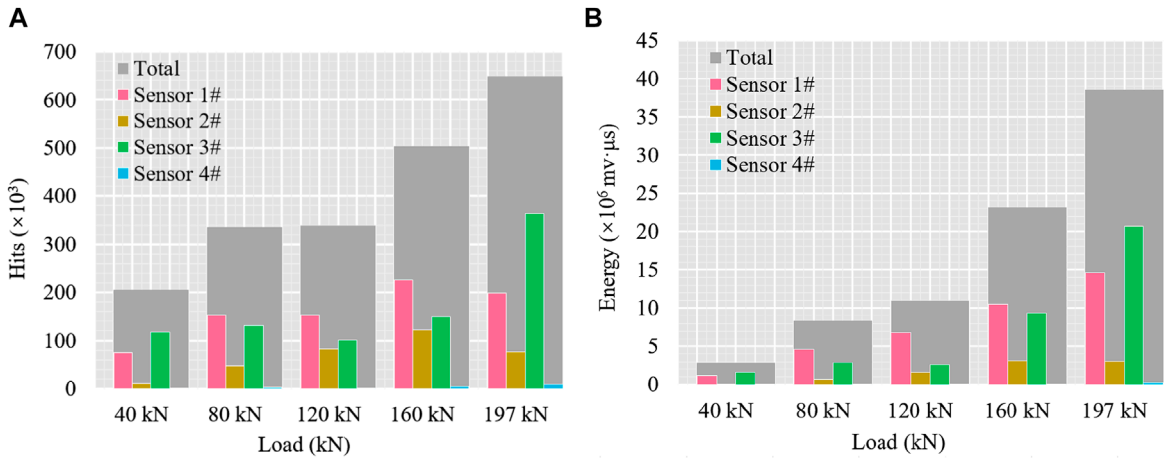

FIGURE 11
Hits and energy collected from different AE sensors of Beam-1 during different load stages. **(A)** Hits; **(B)** Energy.

displacement as well as the relationship between cumulative AE parameters and the sum of crack widths were fitted by stages in Figure 15. It can be seen from Figure 15 that the cumulative AE parameters are positively linearly correlated with the displacement and quadratically correlated with the sum of crack widths, and the correlation coefficients are all above 0.95. Deformation behaviour of reinforcement BFRPC beams and crack propagation can be assessed by monitoring the AE parameters and analysing their cumulative parameters.

4.4 b-value analysis

The b-values presents advantages for monitoring the cracking behaviors of the concrete composites suffered from loads. In general, the b-value increases during the formation of micro-cracks (smaller-scale and weaker damage) and decreases as the micro-cracks coalescent into macrocracks (larger-scale and stronger damage). Thus, the b-value analysis method can effectively evaluate the internal damage degree throughout the entire loading process from a mesoscale perspective. The number (n) of AE amplitude has a great influence on the calculation of the b-value according to Eq. 1. Shiotani et al. (Ohtsu et al., 2010) suggested that the n should be 50 to 100. Hence, for obtaining the accurate results of b-value analysis, the n in this paper was chosen as 50, 70, and 100, respectively. Figure 16 shows the mean value and standard deviation of b-values of all sensors of Beam-3 calculated by the recorded AE amplitude at each bending load step, and the presence of cracks around the sensor is also marked in Figure 16. The number of AE signals collected by sensor 4 in Figure 16E during

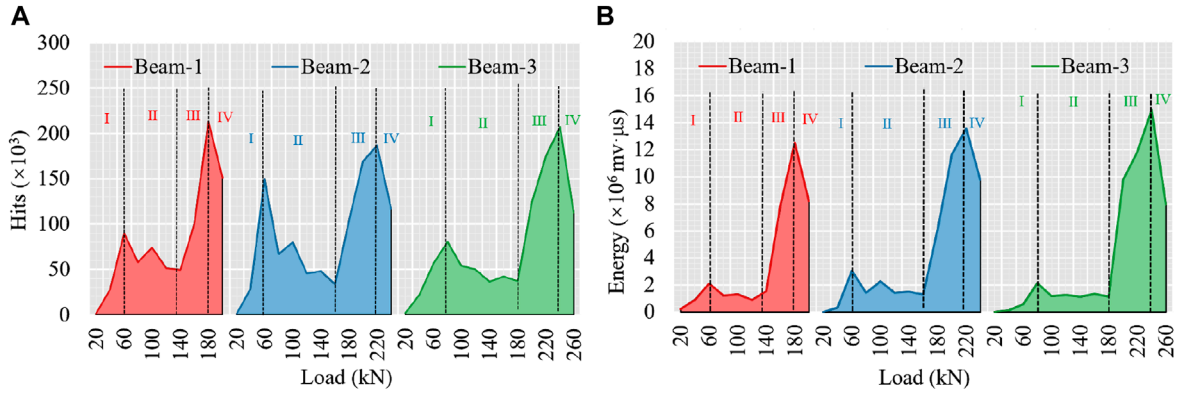

FIGURE 12
Hits and energy collected by different test beams at different load stages. **(A)** Hits; **(B)** Energy.

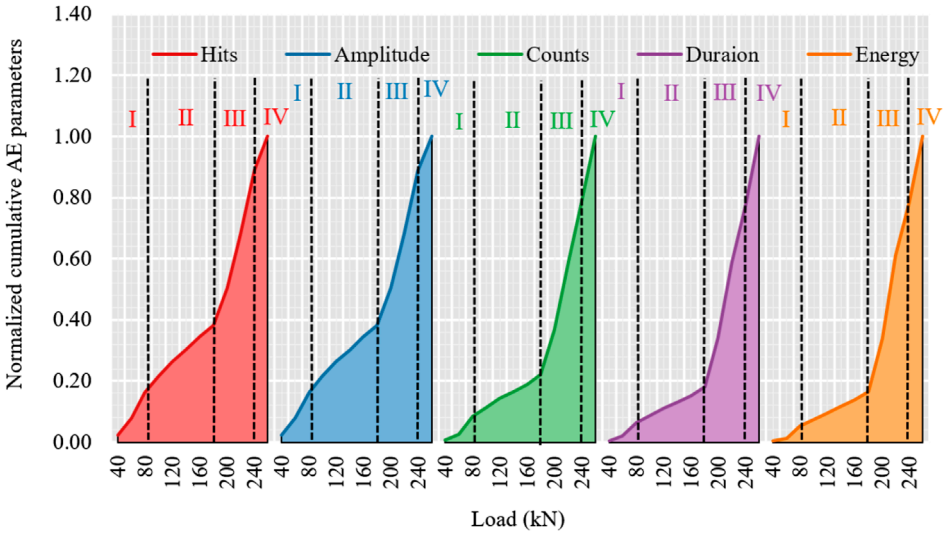

FIGURE 13
The normalized AE basic parameters of the Beam-3.

the loading period from 0 kN to 120 kN is too small to be used for data analysis.

As observed in Figure 16, the b-value calculated from different group sizes varies less. It can be seen from the b-value of all sensors shown in Figure 16A that the b-value presents a fluctuating trend, which illustrates that microcrack activity and macrocrack activity appear alternately. By comparing Figures 16B–E, it can be seen that the cracking characteristics of the reinforcement BFRPC beam are different at different positions. The b-value of sensor 1#, 2#, and 3# all show a downward trend with bending load, while the b-value of sensor 4# increases with the bending load between 120 kN and 260 kN. This phenomenon suggests that the microcrack activity of sensors 1#, 2#, and 3# increases during the whole damage process, while the macrocrack activity of sensor 4# increases between 120 kN and 260 kN. Combined with the crack patterns of Beam-3, it can be seen that sensor 4# located at the upper part of the shear bending section has barely visible cracks, while visible macroscopic cracks appear in other sensor locations. This phenomenon proves the accuracy of the b-value in cracking characterization. As shown in Figure 16B, the b-value of sensor 1# decreases significantly at the load stage of 80–120 kN, showing that an obvious macrocrack is formed at the bottom of the bending shear section of Beam-3. At the load stage after 160 kN, the b-value of sensor 1# is small and gradually tends to be stable, indicating that the macrocrack activity is more prominent and critical failure cracks begin to form at the bottom of the bending shear section of Beam-3. From Figure 16C, the b-value of sensor 2# increases at the load stage before 80 kN, illustrating that microcracks appear on the upper side of the pure bending section. At the load step of 80–200 kN of sensor 2#, the b-value is small and relatively stable, representing that macrocrack activity is large, and the macrocrack gradually forms during this period. At the load stage after 200 kN of sensor 2#, the b-value decreases significantly, stating that critical failure cracks are forming on the upper side of the pure bending section at this stage. As can be

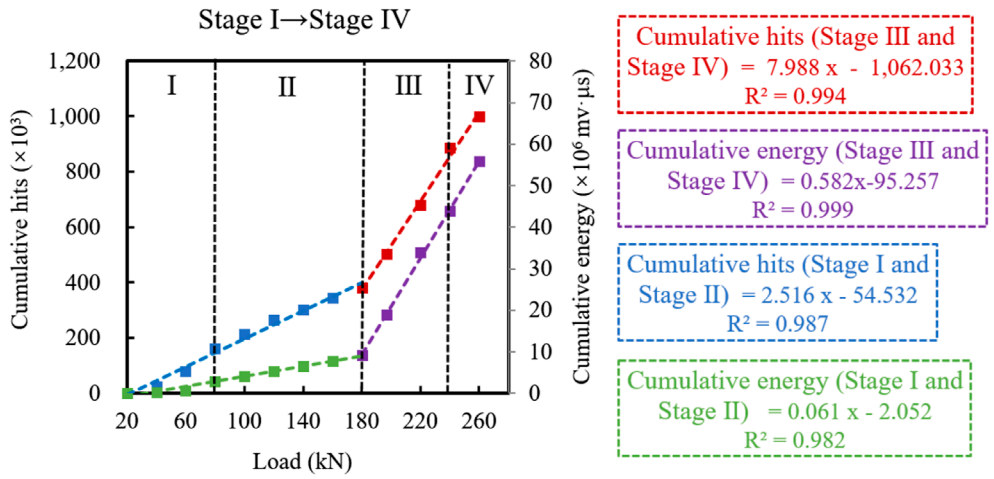

FIGURE 14
The variations of cumulative hits and cumulative energy with bending load.

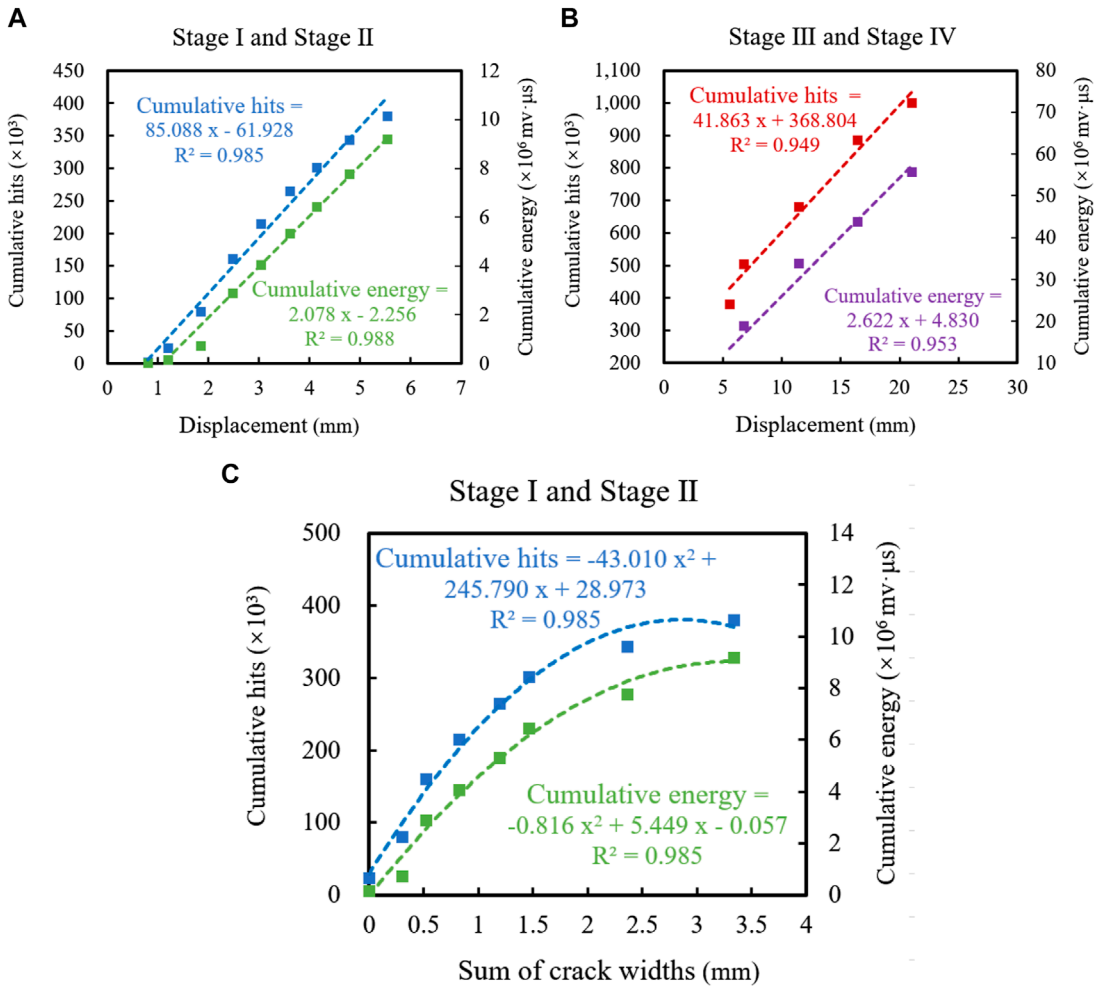

FIGURE 15
Relationship between cumulative AE parameters and mechanical property parameters. **(A)** Displacement in stage I and stage II; **(B)** Displacement in stage III and stage IV; **(C)** Sum of crack widths in stage I and stage II.

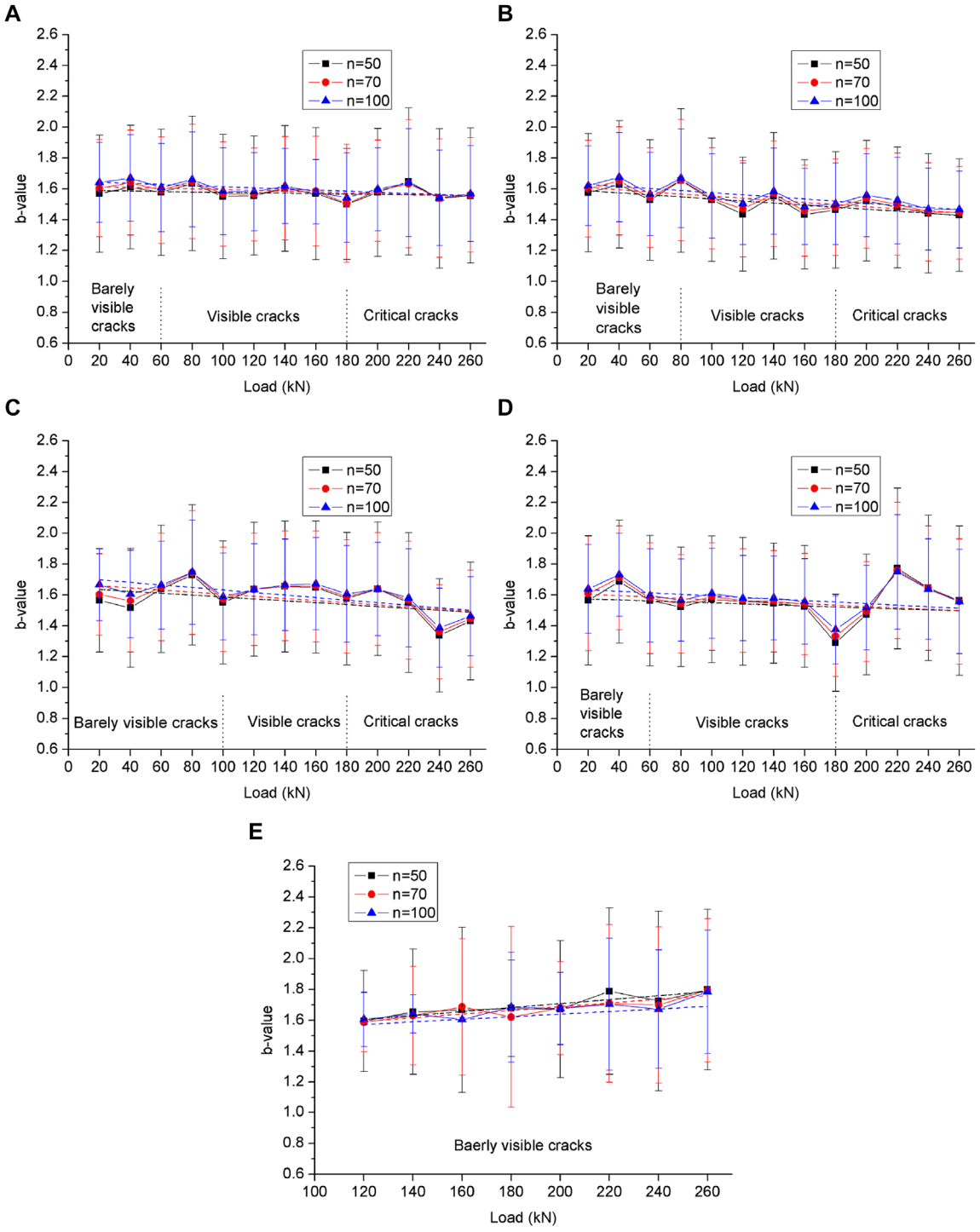

FIGURE 16
Classical b-value obtained from sensors in the Beam-3. **(A)** All sensors; **(B)** Sensor 1#; **(C)** Sensor 2#; **(D)** Sensor 3#; **(E)** Sensor 4#.

seen from Figure 16D, the b-value increases when the bending load is less than 40 kN, indicating that a large number of microcracks are generated at the bottom of the pure bending section. The b-value decreases first and is then gradually maintain at a smaller value between 40 kN and 160 kN, and there is a significant decrease when the load is 180 kN. This indicates that the macrocrack activity at the bottom of the pure bending section is high, and the crack continues to expand steadily, and the critical failure macrocrack is formed when the bending load is 180 kN. The b-value firstly increases and then decreases after 180 kN. This shows that the bottom of the pure bending section once again experiences microcrack initiation and macrocrack formation after main rebars yielding, and more and more fine visible cracks appearing between the earlier visible cracks.

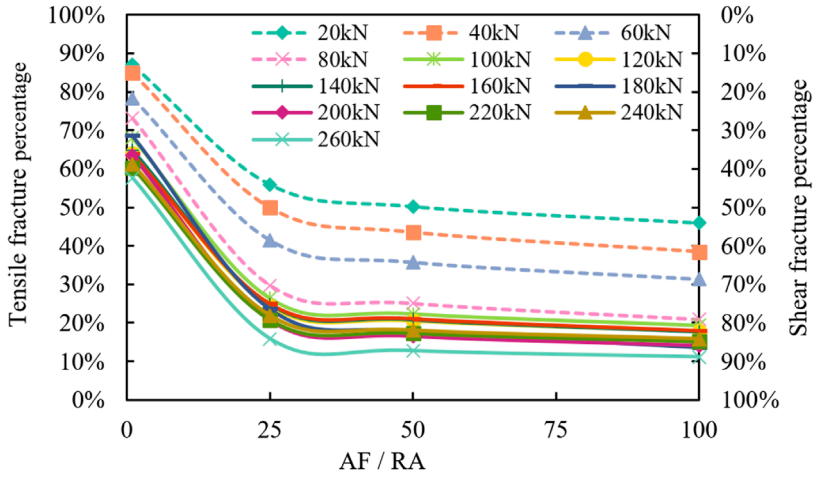

FIGURE 17
Variation of tensile fracture percentage vs. the ratio of AF/RA.

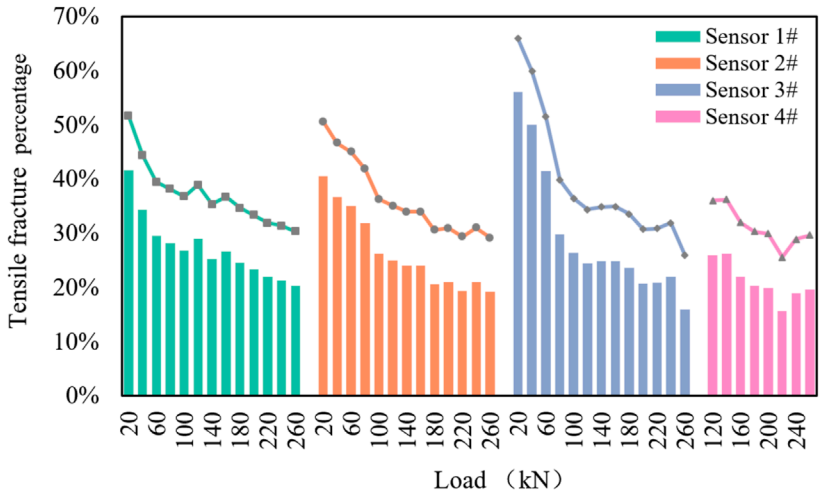

FIGURE 18
Variation of tensile fracture percentage at different positions of beam-3.

4.5 AF-RA analysis

AF value and RA value can be calculated by Eq. 2 and Eq. 3, and the reasonable AF/RA value can distinguish the fracture modes. Ohtsu et al. (Shiotani et al., 2001) suggested that different materials have different AF/RA ratio threshold to distinguish fracture modes, with greater than the critical value being tensile cracking and less than the critical value being shear cracking. BFRPC is a new material and the ratio threshold of AF/RA is unknown. To overcome this limitation, the ratio threshold of 1, 25, 50, and 100 were selected to distinguish fracture modes as tensile fracture and shear fracture, respectively in Figure 17.

As shown in Figure 17, tensile fracture percentage under different loads is similar with the change of AF/RA ratio threshold, and tensile fracture percentage decreases and gradually stabilize with the increase of AF/RA ratio threshold. Although the tensile fracture percentage calculated by different AF/RA ratio threshold is inconsistent, the variation curves of tensile fracture percentage are similar. This indicates that the percentage of tensile and shear cracks in reinforcement BFRPC beams tends to stabilize when the ratio threshold is greater than 25. Therefore, ratio threshold 25 is selected in Figure 18 to analyze the variation trend of tensile fracture percentage at different positions of reinforcement BFRPC beam.

It can be seen from Figure 18 that the tensile fracture percentage of reinforcement BFRPC beam decreases gradually with the increase of bending load. Through calculation, it can be concluded that the tensile fracture percentage of sensor 3# at the bottom of the pure bending section decreases by the most, which is 40%, and that of other positions is reduced by about 25%. During the cracking process of reinforcement BFRPC beam subjected to bending load, the tensile fracture percentage decreased due to the action of basalt fiber and the main rebars, the chemical properties of basalt fiber

and cement are similar, which makes it have great bonding strength with concrete matrix, and gives full play to the bridging effect of fiber to reduce the initiation and expansion of cracks. The low-stress brittle fracture caused by tensile fracture was reduced, and the tensile resistance and flexural bearing capacity of the reinforcement BFRPC beam were increased.

5 Conclusion

Utilizing the AE technology, this paper performed a laboratory investigation to clarify the cracking characteristics of reinforcement BFRPC beams. From the experimental and analytical results, the following conclusions can be drawn:

(1) AE hits, amplitude, counts, duration, and energy have similar changes with bending load. Cumulative AE parameters (cumulative hits and cumulative energy) are positively linearly related to the displacement and quadratically related to the sum of crack widths, and the correlation coefficients are all above 0.95. The cracking process of reinforcement BFRPC beam can be divided into four processes by the variation of AE basic parameters with bending load: microcrack initiation, macrocrack formation, critical failure crack formation, and critical failure crack propagation.

(2) The main rebars yielding is an important turning point of the crack characteristic of reinforcement BFRPC beam. The increase rates of cumulative AE parameters are relatively stable before main rebars yielding and after main rebars yielding, and the increase rate of the latter is significantly higher than that of the former.

(3) AE signal data varies greatly in different locations, and it has an obvious advantage that it can detect the formation of invisible cracks. The results of predicting concrete damage and cracking by AE signal data are consistent with the experimental phenomenon. The b-value calculated by AE amplitude can effectively identify the microcrack and macrocrack activity, and analyze the development of cracks in the beam in detail.

(4) The reinforcement BFRPC beam has good ductility after the main rebars yielding. The low-stress brittle fracture caused by tensile fracture was reduced, and the tensile resistance and flexural bearing capacity of the reinforcement BFRPC beam were increased.

In this study, we innovatively reinforced reactive powder concrete with basalt fiber and analyzed the fracture properties of BFRPC beam by mechanical and acoustic parameters. It can provide a reference for structural performance and damage assessment studies of basalt fiber reinforced cementitious concrete. In the future, it is recommended to use basalt fiber and BFRPC in concrete structural applications and to apply more acoustic techniques in concrete structural health monitoring.

Data availability statement

The datasets presented in this study can be found in online repositories. The names of the repository/repositories and accession number(s) can be found in the article/Supplementary Material.

Author contributions

XL: Conceptualization, Formal Analysis, Methodology, Writing–original draft. WL: Investigation, Software, Writing–review and editing. HH: Formal Analysis, Supervision, Writing–review and editing. XD: Funding acquisition, Resources, Supervision, Writing–review and editing. XH: Writing–review and editing.

Funding

The author(s) declare financial support was received for the research, authorship, and/or publication of this article. This research was funded by the Science and Technology R&D Program of China state Construction Engrg.Corp.Ltd. (CSCEC-2021-S-1), the R&D Program of China Construction Second Engineering Bureau Ltd. (2021ZX050001), and the Funding from China Construction Technology Innovation Platform (CSCEC-PT-017).

Conflict of interest

Authors XL and HH were employed by China Construction Second Engineering Bureau Ltd. Authors XD and XH were employed by The Civil Engineering Group of China Construction Second Engineering Bureau LTD.

The remaining author declares that the research was conducted in the absence of any commercial or financial relationships that could be construed as a potential conflict of interest.

Publisher's note

References

Boniface, A., Saliba, J., Sbartai, Z. M., Ranaivomanana, N., and Balayssac, J. P. (2020). Evaluation of the acoustic emission 3D localisation accuracy for the mechanical damage monitoring in concrete. *Eng. Fract. Mech.* 223, 106742. doi:10.1016/j.engfracmech.2019.106742

Chen, X., Wan, D., Jin, L., Qian, K., and Fu, F. (2019). Experimental studies and microstructure analysis for ultra-high performance reactive powder concrete. *Constr. Build. Mater.* 229, 116924. doi:10.1016/j.conbuildmat.2019.116924

Dubuc, B., Sitaropoulos, K., Ebrahimkhanlou, A., et al. (2020). Acoustic emission diagnostics of corrosion monitoring in prestressed concrete using hidden Markov and semi-Markov models. *Struct. Health. Monit.* 20 (6). doi:10.1177/1475921720976937

Fan, X. Q., Li, S. T., Chen, X. D., Saisai, L., and Yuzhu, G. (2020). Fracture behaviour analysis of the full-graded concrete based on digital image correlation and acoustic emission technique. *Fatigue. Fract. Eng. M.* 4 (6), 1274–1289. doi:10.1111/ffe.13222

Farhidzadeh, A., Salamone, S., Luna, B., and Whittaker, A. (2013). Acoustic emission monitoring of a reinforced concrete shear wall by b-value-based outlier analysis. *Struct. Health. Monit.* 12 (1), 3–13. doi:10.1177/1475921712461162

Han, Q., Yang, G., Xu, J., Fu, Z., Lacidogna, G., and Carpinteri, A. (2019). Acoustic emission data analyses based on crumb rubber concrete beam bending tests. *Eng. Fract. Mech.* 210, 189–202. doi:10.1016/j.engfracmech.2018.05.016

Jiao, Y., Zhang, Y., Shan, W., Han, Q., Zhao, Y., and Liu, S. (2019). Damage fracture characterization of reinforced concrete beam subjected to four-point bending with parametric analysis of static, dynamic, and acoustic properties. *Struct. Health. Monit.* 19 (4), 1202–1218. doi:10.1177/1475921719881756

Karimian, S. F., and Modarres, M. (2021). Acoustic emission signal clustering in CFRP laminates using a new feature set based on waveform analysis and information entropy analysis. *Compos. Struct.* 268, 113987. doi:10.1016/j.compstruct.2021.113987

Li, B., Xu, L., Shi, Y., Chi, Y., Liu, Q., and Li, C. (2018). Effects of fiber type, volume fraction and aspect ratio on the flexural and acoustic emission behaviors of steel fiber reinforced concrete. *Constr. Build. Mater.* 181, 474–486. doi:10.1016/j.conbuildmat.2018.06.065

Li, S. L., Zhang, L. G., Guo, P., Zhang, P., Wang, C., Sun, W., et al. (2021b). Characteristic analysis of acoustic emission monitoring parameters for crack propagation in UHPC-NC composite beam under bending test. *Constr. Build. Mater.* 278, 122401. doi:10.1016/j.conbuildmat.2021.122401

Li, W., Liu, H., Zhu, B., Lyu, X., Gao, X., and Liang, C. (2020). Mechanical properties and freeze-thaw durability of basalt fiber reactive powder concrete. *Appl. Sci-Basel.* 10 (16), 5682. doi:10.3390/app10165682

Li, Z., Zhu, H., Du, C., Gao, D., Yuan, J., and Wen, C. (2021a). Experimental study on cracking behavior of steel fiber-reinforced concrete beams with BFRP bars under repeated loading. *Compos. Struct.* 267, 113878. doi:10.1016/j.compstruct.2021.113878

Liu, H., Lyu, X., Zhang, Y., Luo, G., and Li, W. (2020a). Bending resistance and failure type evaluation of basalt fiber RPC beam affected by notch and interfacial damage using acoustic emission. *Appl. Sci-Basel.* 10 (3), 1138. doi:10.3390/app10031138

Liu, H., Lyu, X., Zhang, Y., Luo, G., and Li, W. (2020b). Steel corrosion evaluation of basalt fiber RPC affected by crack and steel-concrete interface damage using electrochemical methods. *Sensors-Basel.* 20 (18), 5027. doi:10.3390/s20185027

Lou, K., Xiao, P., Kang, A., Wu, Z., and Lu, P. (2021). Performance evaluation and adaptability optimization of hot mix asphalt reinforced by mixed lengths basalt fibers. *Constr. Build. Mater.* 292, 123373. doi:10.1016/j.conbuildmat.2021.123373

Merdas, H. S., and Shallal, M. A. (2023). Shear strength of recycled aggregate concrete beams without shear reinforcement. *IOP Conf. Ser. Earth Environ. Sci.* (1), 1232. doi:10.1088/1755-1315/1232/1/012029

Ministry of Housing and Urban-Rural Development of the People's Republic of China (2012). *Standard for test method of concrete structures (GB/T 50152-2012).* Beijing, China: China Communications Press.

Mohammadi, R., Najafabadi, M. A., Saghafi, H., Saeedifar, M., and Zarouchas, D. (2021). A quantitative assessment of the damage mechanisms of CFRP laminates interleaved by PA66 electrospun nanofibers using acoustic emission. *Compos. Struct.* 258, 113395. doi:10.1016/j.compstruct.2020.113395

Nguyen-Tat, T., Ranaivomanana, N., and Balayssac, J.-P. (2018). Characterization of damage in concrete beams under bending with Acoustic Emission Technique (AET). *Constr. Build. Mater.* 187, 487–500. doi:10.1016/j.conbuildmat.2018.07.217

Ohtsu, M., Shiotani, T., Shigeishi, M., Kamada, T., Yuyama, S., et al. (2010). Recommendation of RILEM TC 212-ACD: acoustic emission and related NDE techniques for crack detection and damage evaluation in concrete Test method for classification of active cracks in concrete structures by acoustic emission. *Mater. Struct.* 43 (9), 1187–1189. doi:10.1617/s11527-010-9640-6

Rashid, K., Li, X. D., Xie, Y., Deng, J., and Zhang, F. (2020). Cracking behavior of geopolymer concrete beams reinforced with steel and fiber reinforced polymer bars under flexural load. *Compos. Part. B-Eng.* 186, 107777. doi:10.1016/j.compositesb.2020.107777

Shiotani, T., Ohtsu, M., and Ikeda, K. (2001). Detection and evaluation of AE waves due to rock deformation. *Constr. Build. Mater.* 15 (5-6), 235–246. doi:10.1016/s0950-0618(00)00073-8

Si, J., Wang, Z., Li, J., Zuo, C., Zhang, P., Wei, C., et al. (2021). Effects of CaO added to raw basalt on producing continuous basalt fibers and their mechanical properties. *J. Non-Cryst. Solids.* 568, 120941. doi:10.1016/j.jnoncrysol.2021.120941

Sultan, H., and Alyaseri, I. (2020). Effects of elevated temperatures on mechanical properties of reactive powder concrete elements. *Constr. Build. Mater.* 261, 120555. doi:10.1016/j.conbuildmat.2020.120555

Tan, G. J., Zhu, Z. Q., Wang, W. S., Wu, C., Ou, J., Cui, G., et al. (2021). Flexural ductility and crack-controlling capacity of polypropylene fiber reinforced ECC thin sheet with waste superfine river sand based on acoustic emission analysis. *Constr. Build. Mater.* 277, 122321. doi:10.1016/j.conbuildmat.2021.122321

Xargay, H., Folino, P., Nuñez, N., Gómez, M., Caggiano, A., and Martinelli, E. (2018). Acoustic emission behavior of thermally damaged self-compacting high strength fiber reinforced concrete. *Constr. Build. Mater.* 187, 519–530. doi:10.1016/j.conbuildmat.2018.07.156

Xargay, H., Ripani, M., Folino, P., Núñez, N., and Caggiano, A. (2021). Acoustic emission and damage evolution in steel fiber-reinforced concrete beams under cyclic loading. *Constr. Build. Mater.* 274, 121831. doi:10.1016/j.conbuildmat.2020.121831

Zdeb, T. (2019). Effect of vacuum mixing and curing conditions on mechanical properties and porosity of reactive powder concretes. *Constr. Build. Mater.* 209, 326–339. doi:10.1016/j.conbuildmat.2019.03.116

Zhang, F. Q., Pahlavan, L., and Yang, Y. G. (2020). Evaluation of acoustic emission source localization accuracy in concrete structures. *Struct. Health. Monit.* 19 (6), 2063–2074. doi:10.1177/1475921720915625

Zhang, K., Zhou, M., Zhang, B., Luan, C., Liu, Y., et al. (2023). Experimental and numerical study of the flexural performance of spontaneous combustion gangue coarse aggregate concrete laminated slab. *Buildings* 13 (7), 1718. doi:10.3390/buildings13071718

Zhang, Y., Tan, G., Wang, S., Cheng, Y., Yang, S., and Sun, X. (2019). Flexural characteristics evaluation for reinforced concrete affected by steel corrosion based on an acoustic emission technique. *Appl. Sci-Basel.* 9 (8), 1640. doi:10.3390/app9081640

frontiers | Frontiers in Materials

TYPE Original Research
PUBLISHED 05 February 2024
DOI 10.3389/fmats.2024.1351938

OPEN ACCESS

EDITED BY
Jialuo He,
Washington State University, United States

REVIEWED BY
Zidong Xu,
Southeast University, China
Xiaohua Li,
Chongqing University, China
Junlin Heng,
University of Birmingham, United Kingdom

*CORRESPONDENCE
Gang Yao,
yaogang@cqu.edu.cn

RECEIVED 07 December 2023
ACCEPTED 09 January 2024
PUBLISHED 05 February 2024

CITATION
Yang Y, Li L, Yao G, Du H, Chen Y and Wu L (2024), An modified intelligent real-time crack detection method for bridge based on improved target detection algorithm and transfer learning.
Front. Mater. 11:1351938.
doi: 10.3389/fmats.2024.1351938

An modified intelligent real-time crack detection method for bridge based on improved target detection algorithm and transfer learning

Yang Yang, Long Li, Gang Yao*, Hongbo Du, Yuxiao Chen and Linjun Wu

Key Laboratory of New Technology for Construction of Cities in Mountain Area, School of Civil Engineering, Chongqing University, Chongqing, China

The combination of UAV camera and intelligent algorithm is a promising method for non-contact bridge crack detection. In this paper, an inspection tool based on UAV Image Acquisition Technology (UAVIAT) and Improved Intelligent Target Detection Technology (IITDT) called Improved Intelligent Real-Time Crack Detection Method for Bridges (IIRTCDMB) is proposed for efficient crack detection. The contributions of this paper are (1) The Squeeze-Excitement (SE) attention module is integrated into the target detection algorithm - You Only Look Once version 7 (YOLOv7) model to improve the learning ability of the feature channel. A Focal-efficient intersection over union (Focal-EIoU) loss function is also introduced to improve the regression accuracy of the model. As a result, a new crack image detection algorithm, YOLOv7-CD, is proposed. (2) A training process based on two-stage transfer learning (TSTL) is established, and hyper-parameter optimization of YOLOv7-CD is carried out. The feasibility and excellent performance of the proposed method are verified by applying it on the Cuntan Yangtze River Bridge. The results show that the average precision (AP) of the YOLOv7-CD model is improved by 3.19% compared with the original YOLOv7 model. After TSTL and hyperparameter optimization, the AP of the YOLOv7-CD model for bridge crack detection reaches 98.01%, which is higher than that of the popular target detection models. The IIRTCDMB proposed in this paper can acquire bridge surface images more safely and efficiently, and provide inspectors with more accurate structural crack information with lower computational and hardware requirements, which can provide technical support for the assessment of structural safety conditions and the formulation of maintenance programs.

KEYWORDS

bridge crack detection, target detection algorithm, transfer learning, hyperparameter optimization, unmanned aerial vehicle

1 Introduction

Crack disease is one of the most common diseases in concrete bridges, which has an essential impact on bridges' structural stability and traffic capacity. Therefore, visually inspecting structures is important for bridge operation and maintenance (Ge et al., 2020; Saidin et al., 2022). With the increase in the

service life of bridges, the demand for crack detection is also increasing (Mohan and Poobal, 2018). Currently, manual inspection and bridge inspection vehicle inspection are the main methods for bridge inspection. Manual detection has high risk, strong subjectivity, and long periods. At the same time, the bridge inspection vehicle method is not conducive to traffic safety, has limited applicable conditions, and is expensive (Tomiczek et al., 2019).

Recently, the rapid development of unmanned aerial vehicles (UAVs) has made collecting images of bridge conditions trivial (Perry et al., 2020). Its high-resolution camera can quickly and safely obtain high-definition images, which serves as an important basis for subsequent analysis of bridge defects. It has been confirmed that the UAS-based bridge inspection is faster and more objective than the existing technology (Kim et al., 2022). Unmanned aerial vehicles (UAVs) are now a viable option for augmenting bridge inspections (Khaloo et al., 2018; Li et al., 2024). Using UAVs for bridge appearance inspection not only has high accuracy and low cost (Seo et al., 2018) but can also perform all-around inspections (Sanchez-Cuevas et al., 2019; Wang et al., 2020; Yao et al., 2023a) and reduce the danger in the inspection work (Liu et al., 2020; Kao et al., 2022).

Currently, there are some things that could be improved in using traditional digital image processing methods to detect cracks. In the crack identification and extraction process, the main methods are the gray threshold segmentation method based on the gray difference between the crack area and the background (Xuhang et al., 2011) and the Canny iterative method based on the linear features of cracks (Xu et al., 2013). The gray threshold segmentation method can only give the general position of the cracks, and the positioning accuracy is insufficient. The Canny iterative method is susceptible to background clutter, resulting in a high rate of false detection and missed detection. With the evolution of machine learning technology, some scholars have implemented crack detection using crack multi-features combined with three statistical classification methods, namely, Support Vector Machine, AdaBoost, and Random Forest, respectively (Prasanna et al., 2016). However, these methods require the manual design of crack features, resulting in poor adaptability and scalability of the algorithm. The tensor voting algorithm (Guan et al., 2015) that enhances crack features by utilizing the linear difference between cracks and background noise has good results in detecting linear cracks, but it is not sensitive to complex cracks and may miss width information.

Deep learning has shown excellent performance in image recognition (Kim et al., 2018; Wei et al., 2019; Chen et al., 2020; Sun et al., 2021; Yang et al., 2021; Chen et al., 2023). Crack detection algorithms based on deep learning can be divided into two categories. The first category uses object detection networks for crack localization and identification, while the other uses semantic segmentation models for pixel-level recognition of crack images. Research has shown that the You Only Look Once (YOLO) series algorithm performs outstandingly among many object detection networks (Du et al., 2021). In the YOLO model, integrating the attention module or improving the feature extraction network can enhance the sensitivity of the model to the target features (Yao et al., 2019; Yang et al., 2022a; Liu et al., 2022; Zhang et al., 2023a; Kao et al., 2023); combining the depth-separable convolution or replacing the lightweight feature extraction network, a lightweight target detection network for real-time detection of cracks on the structure surface can be obtained (Zhang et al., 2020a; Yao et al., 2021a; Yang et al., 2022b; Zhang et al., 2022; Zhang et al., 2023b; Jin et al., 2023); introducing the focal loss function or transfer learning can improve the recognition accuracy of the model. Deep learning has been gradually applied to bridge crack detection (Zhang et al., 2020b; Yao et al., 2021b; Teng et al., 2022). However, there are still problems, such as difficulty in obtaining crack images, excessive training parameters of network models, long inference time, and low detection accuracy.

In order to obtain bridge surface crack images more efficiently and improve the model's detection accuracy of cracks, this study proposed an improved intelligent real-time crack detection method for bridges (IIRTCDMB) based on UAVIAT and improved intelligent target detection technology (IITDT). First, the appearance image of the bridge to be detected was obtained through UAVs. Then, the SE attention module was introduced into the YOLOv7 model to enhance the feature extraction ability of cracks, and the Focal-efficient intersection over union (Focal-EIoU) loss function was used to balance positive and negative samples and accelerate loss convergence. The improved model was defined as YOLOv7-CD. To further improve the average precision (AP), the improved model underwent two-stage transfer learning (TSTL) training. The initial training was performed with the COCO2017 dataset to obtain the initial training weights. Then, the publicly available CRACK500 dataset (Eisenbach et al., 2017) was used for pre-training with different hyperparameters to obtain pre-training weights. Finally, the training is performed on the bridge crack dataset (QL_CRACK dataset), and the error is reduced by adjusting the values of hyperparameters to make the model more suitable for bridge crack detection.

2 Methodologies

The IIRTCDMB proposed in this article mainly includes high-definition image acquisition by UAVs and automatic localization and recognition of bridge cracks based on the YOLOv7-CD model. The specific process is shown in Figure 1.

In the UAVIAT, bridge information review, site risk assessment, flight plan development, and daily environmental monitoring will be conducted. Then, the UAV will be selected, and parameter settings such as shooting distance and flight route will be completed. After camera calibration, the bridge structure's appearance will be captured, and an automatic naming program will be written to assign position and number to each image. The image quality will be judged based on the proposed image quality evaluation function. The images with qualified quality will be stored in the database according to the preset cycle, and finally, the bridge crack dataset will be obtained. The YOLOv7-CD model will be trained with TSTL and hyperparameter optimization. Finally, cracks will be detected in the images, and their corresponding locations in the actual bridge will be obtained.

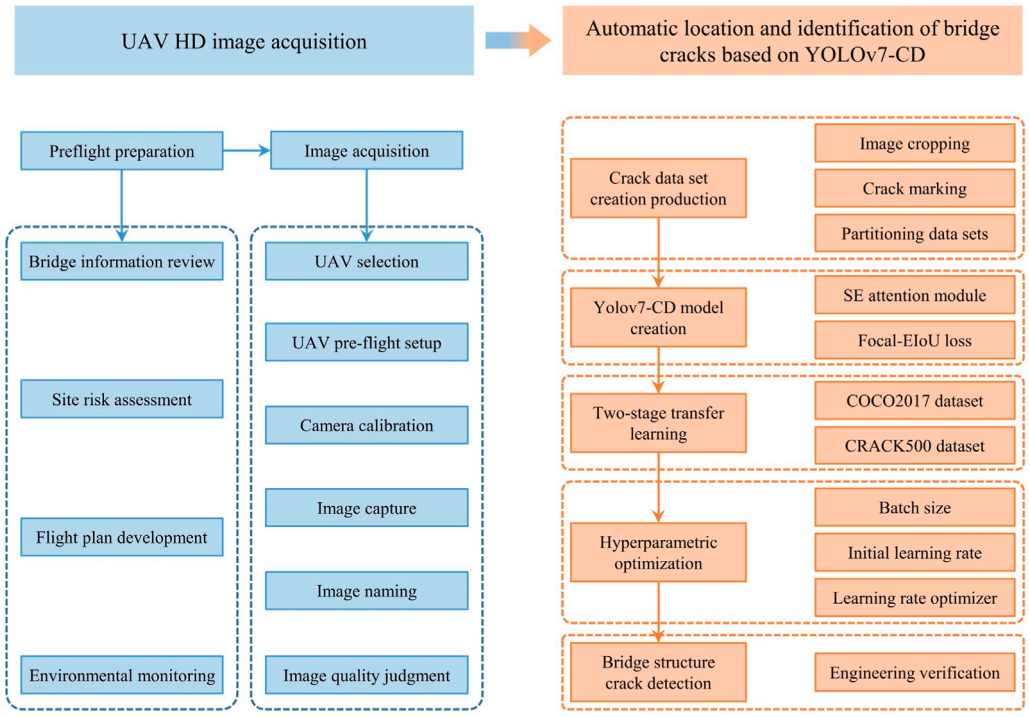

FIGURE 1
The diagram of the improved intelligent real-time crack detection method for bridges.

2.1 Image acquisition method

2.1.1 UAV selection

Currently, the UAVs mainly used for crack detection include DJ Mavic 2 Pro, DJ M210-RTK, DJ Mini 2, and DJ Mavic Air 2 (Xu et al., 2023a). Due to the large span of bridges inspected by UAVs, the main parameters to consider are hovering time and hovering accuracy. Additionally, since it involves storing appearance images of large-span bridges, there is also a high requirement for memory. Through an analysis of the parameters of the four UAVs, DJ Mavic Air 2 is the best option. Its hover time is 33 min, hover accuracy is ± 0.1, and memory size is 8 GB. To ensure consistent experimental conditions, the distance between the UAV and the target surface is fixed at 5.0m, and the normal direction of the lens is perpendicular to the target surface. The images will be taken in clear weather conditions and natural lighting. To ensure sufficient image data, the UAV will cover the entire bridge deck and tower surface, with a 50% overlap in the images taken.

2.1.2 Camera calibration

In the process of picture-taking and crack detection of concrete bridges, a geometric model of camera imaging is required to determine the interrelationship between the three-dimensional geometric position of a point on the surface of the bridge structure and its corresponding point in the image. In the UAVIAT, the calibration of camera parameters is the key link, and its calculation process and calibration results directly affect the authenticity of the crack detection results. The conversion model of the ground coordinate system to the pixel coordinate system is introduced below.

1) Transformation from ground coordinate system to camera coordinate system.

In order to accurately describe the motion trajectory of the UAV and obtain its position information, a transformation model from the ground coordinate system (X_G, Y_G, Z_G) to the camera coordinate system (X_C, Y_C, Z_C) has been established. They represent the angle of camera rotation around the X_G, Y_G, and Z_G axes, respectively (Figure 2). Then, the rotation matrix R from the ground coordinate system to the image coordinate system can be obtained, as shown in Eq. 1.

$$R = \begin{bmatrix} 1 & 0 & 0 \\ 0 & \cos\sigma & \sin\sigma \\ 0 & -\sin\sigma & \cos\sigma \end{bmatrix} \cdot \begin{bmatrix} \cos\mu & 0 & -\sin\mu \\ 0 & 1 & 0 \\ \sin\mu & 0 & \cos\mu \end{bmatrix} \cdot \begin{bmatrix} \cos\varepsilon & \sin\varepsilon & 0 \\ -\sin\varepsilon & \cos\varepsilon & 0 \\ 0 & 0 & 1 \end{bmatrix} \tag{1}$$

In addition to the rotation transformation, there is also a translation transformation between the UAV and the ground. Therefore, the coordinate transformation matrix from the ground coordinate system to the camera coordinate system is given by Eq. 2.

$$M_1 = \begin{bmatrix} R & T \\ O & 1 \end{bmatrix} \tag{2}$$

where $T = [T_x \quad T_y \quad T_z]^T$ is the translation transformation matrix. T_x, T_y and T_z represent the displacement of the UAV in the X_G, Y_G, and Z_G directions, respectively.

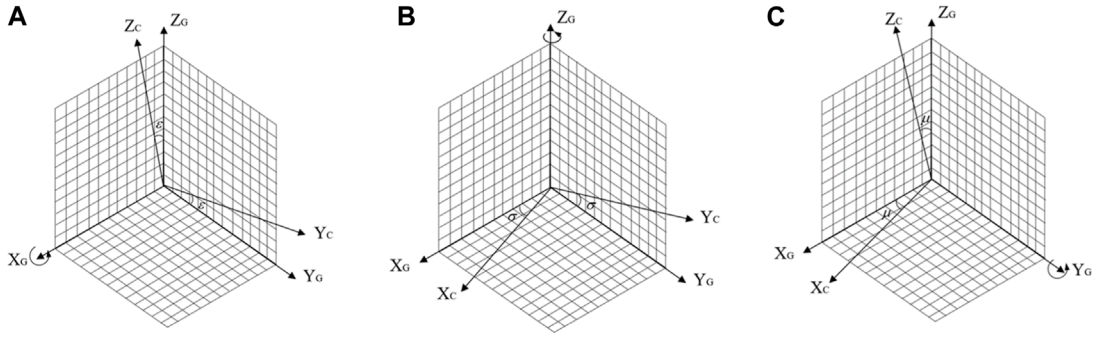

FIGURE 2
UAV motion state description parameters: **(A)** Rotation around XG axis; **(B)** Rotation around YG axis; **(C)** Rotation around ZG axis.

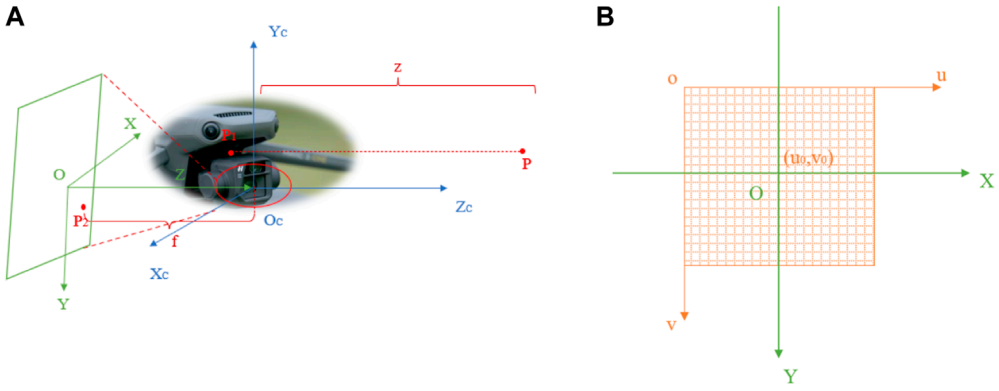

FIGURE 3
Coordinate transformation: **(A)** Transformation from camera coordinate system to image coordinate system; **(B)** Transformation from image coordinate system to pixel coordinate system.

2) Transformation from camera coordinate system to image coordinate system.

As shown in Figure 3A, the transformation from the camera coordinate system to the image coordinate system (X, Y, Z) follows the pinhole imaging principle. The Z_C axis of the camera coordinate system is on the same line as the Z-axis of the image coordinate system. P is a point in space, P_1 is its projection point in the plane $X_C O_C Y_C$, P_2 is the imaging point of P in the XOY plane of the image coordinate system, f is the focal length, and z is the distance from point P to point P_1. The conversion matrix F from camera coordinates to image coordinates is given by Eq. 3.

$$F = \begin{bmatrix} f/z & 0 & 0 & 0 \\ 0 & f/z & 0 & 0 \\ 0 & 0 & 1 & 0 \end{bmatrix} \tag{3}$$

3) Transformation from image coordinate system to pixel coordinate system.

The pixel coordinate system reflects the arrangement of pixels in the CMOS chip of the camera, as shown in Figure 3B. The image coordinate system and the pixel coordinate system (u, v) are in a translation relationship, and the transformation matrix D between them is shown in Eq. 4.

$$D = \begin{bmatrix} 1/dX & 0 & u_0 \\ 0 & 1/dY & v_0 \\ 0 & 0 & 1 \end{bmatrix} \tag{4}$$

where (u_0, v_0) is the coordinate of the image coordinate system origin in the pixel coordinate system; dX and dY represent the physical dimensions of the pixel in the X and Y directions, respectively.

In summary, the formula for transforming the ground coordinate system to the pixel coordinate system is shown in Eq. 5. Eq. 6 represents the calculation of the intrinsic parameter matrix of the camera.

$$\begin{bmatrix} u \\ v \\ 1 \end{bmatrix} = DgFgM_1g \begin{bmatrix} X_G \\ Y_G \\ Z_G \\ 1 \end{bmatrix} = M_2gM_1g \begin{bmatrix} X_G \\ Y_G \\ Z_G \\ 1 \end{bmatrix} \tag{5}$$

$$M_2 = DgF = \begin{bmatrix} f/zdX & 0 & u_0 & 0 \\ 0 & f/zdY & v_0 & 0 \\ 0 & 0 & 1 & 0 \end{bmatrix} \tag{6}$$

where $[u, v, 1]^T$ is the homogeneous coordinate in the pixel coordinate system, and $[X_G, Y_G, Z_G, 1]^T$ is the homogeneous coordinate in the ground coordinate system. M_1 is the external parameter matrix of the camera, and M_2 is the internal parameter matrix of the camera.

2.1.3 Image quality assessment

In this article, entropy and sharpness are utilized as two image quality parameters to assess the quality of the images captured from the UAV.10 (Duque et al., 2018). The formula for judging the image quality is given by Eq. 7 and Eq. 8. The criteria for judging the image quality are:

1) The image sharpness is greater than the average value of sharpness.
2) The image sharpness is less than the average value of sharpness, but the image entropy is less than the average value of entropy.

The image satisfying any of these points is considered a qualified image.

$$S_k \geq \frac{1}{N}\sum_{k=1}^{N}\left(\frac{1}{P_{sum}}\sum_{j=1}^{P_{sum}}\sum_{i=1}^{8}\left|dG_i/dx_i\right|\right) \tag{7}$$

$$S_k \leq \frac{1}{N}\sum_{k=1}^{N}\left(\frac{1}{P_{sum}}\sum_{j=1}^{P_{sum}}\sum_{i=1}^{8}\left|\frac{dG_i}{dx}_i\right|\right), E_k \leq \frac{1}{N}\sum_{k=1}^{N}\left(-\sum_{i=0}^{255}p_i\log_2(p_i)\right) \tag{8}$$

where N is the total number of captured bridge images, S_k is the sharpness of the kth image, P_{sum} is the total number of pixels in the image, dG_i is the amplitude of the grayscale variation, and dx_i is the distance increment between pixels. dG_i/dx_i is the gradient vector between pixels, which is calculated based on the pixel values of the eight neighboring pixels for each pixel. p_i is the occurrence probability of the gray value i in the image, which is obtained from the grayscale histogram.

2.2 Crack detection

2.2.1 YOLOv7-based crack

The bridge surface images that meet the quality requirements are input into the crack detection model YOLOv7. In the beginning, the input image enters the main feature extraction network Backbone, which performs crack feature extraction by convolutional normalization and activation function. In the feature extraction process, the image will be compressed in height and width first, then the channel expansion will be performed, and finally, the three effective crack feature layers will be formed. Then, the three effective crack feature layers obtained at Backbone will be fused by the FPN framework, which aims to combine the crack feature information at different scales for enhanced feature extraction of the image. FPN performs up-sampling and down-sampling on the crack features to achieve the fusion of crack features. After passing through the Backbone and FPN, three enhanced effective crack feature layers will be obtained. Each crack feature layer has a width, height, and number of channels. At this point, the crack feature map can be viewed as a collection of feature points, with three prior boxes at each feature point, each of which has the same number of crack features as the number of channels. Eventually, the RepConv structure is introduced in the Head part to equivalent the complex residual structure to a normal 3 × 3 convolution. This can reduce the complexity of the network while ensuring the same prediction performance.

2.2.2 Attention module

The task of locating and identifying cracks focuses on details such as background color and crack position. Therefore, in order to enhance the model's perception of crack features and improve the detection effect on small targets, three SE channel attention modules were added to the YOLOv7 model. The SE attention module has three steps:

1) Using adaptive global average pooling to compress the length and width of the crack feature layer, leaving only the information of the channel dimension C.
2) Continuously using two fully connected layers to perform self-attention on the channel information and obtaining a feature map with a dimension of 1*1*C.
3) Performing activation by channel-wise multiplication with weight coefficients on the feature map with channel attention (1*1*C) and the original input feature map (H*W*C), and finally outputting a feature map with channel attention.

2.2.3 Loss functions

Neural network model training is the process of optimizing the parameters in the network and reducing the losses using a backpropagation algorithm. Loss is the penalty for inaccurate predictions during the training process and describes the difference between the model's predicted results and the actual results. Eq. 9 is the formula for calculating the loss function of YOLOv7 during the training process.

$$L = L_{CIoU} + L_{obj} + L_{cls} \tag{9}$$

where L is the total loss of the model, L_{CIoU} is the bounding box regression loss used to measure the deviation between the predicted and ground truth crack boxes, L_{obj} is the confidence loss used to measure the accuracy of crack localization, and L_{cls} is the classification loss used to measure the accuracy of predicting the presence of cracks. The calculation formulas for L_{obj} and L_{cls} are shown in Eq. 10 and Eq. 11.

$$\begin{aligned} L_{obj} = &-\sum_{i=0}^{S^2}\sum_{j=0}^{B} I_{i,j}^{ob}\left[C_i^j\log\left(\widehat{C_i^j}\right)+\left(1-C_i^j\right)\log\left(1-\widehat{C_i^j}\right)\right] \\ &-\lambda_{no}\sum_{i=0}^{S^2}\sum_{j=0}^{B} I_{i,j}^{no}\left[C_i^j\log\left(\widehat{C_i^j}\right)+\left(1-C_i^j\right)\log\left(1-\widehat{C_i^j}\right)\right] \end{aligned} \tag{10}$$

$$L_{cls} = -\sum_{i=0}^{S^2} I_{i,j}^{ob}\sum\left[P_i^j\log\left(\widehat{P_i^j}\right)+\left(1-P_i^j\right)\log\left(1-\widehat{P_i^j}\right)\right] \tag{11}$$

where B and S^2 are the priori box and the feature map scale. $I_{i,j}^{ob}$ and $I_{i,j}^{no}$ denote crack and no crack in the jth prior box of the ith grid. C_i^j

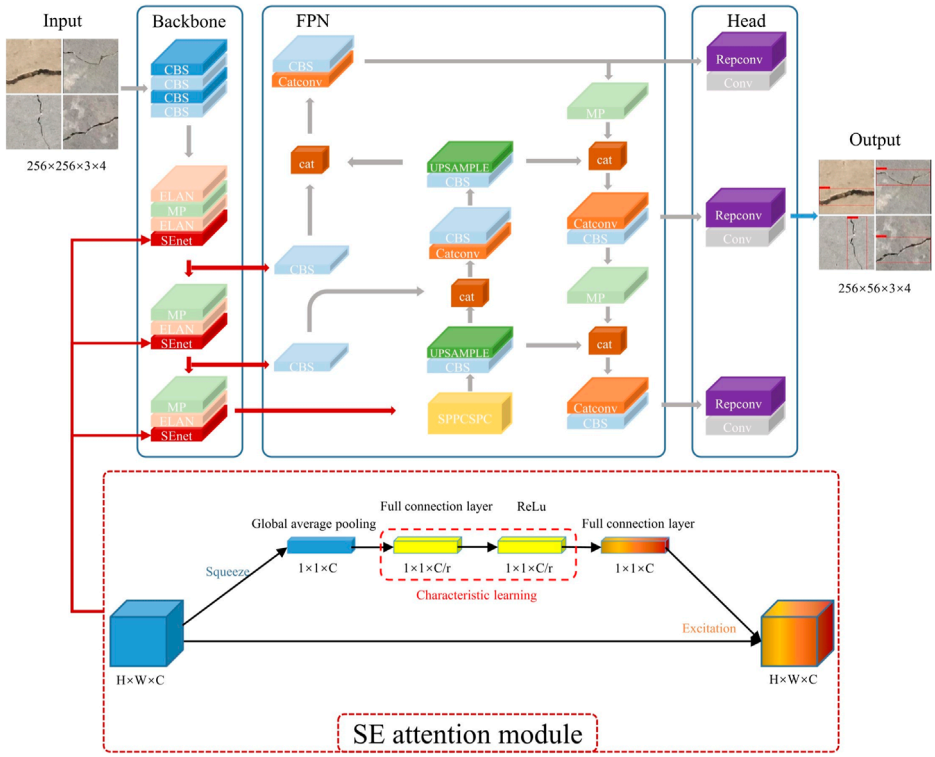

FIGURE 4
YOLOv7-CD model architecture.

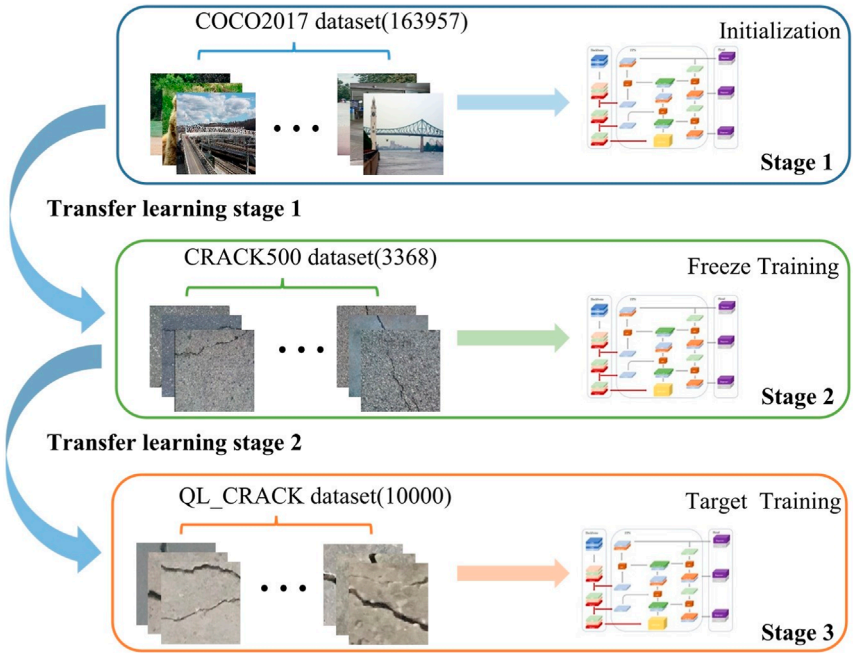

FIGURE 5
Two-stage transfer learning training diagram.

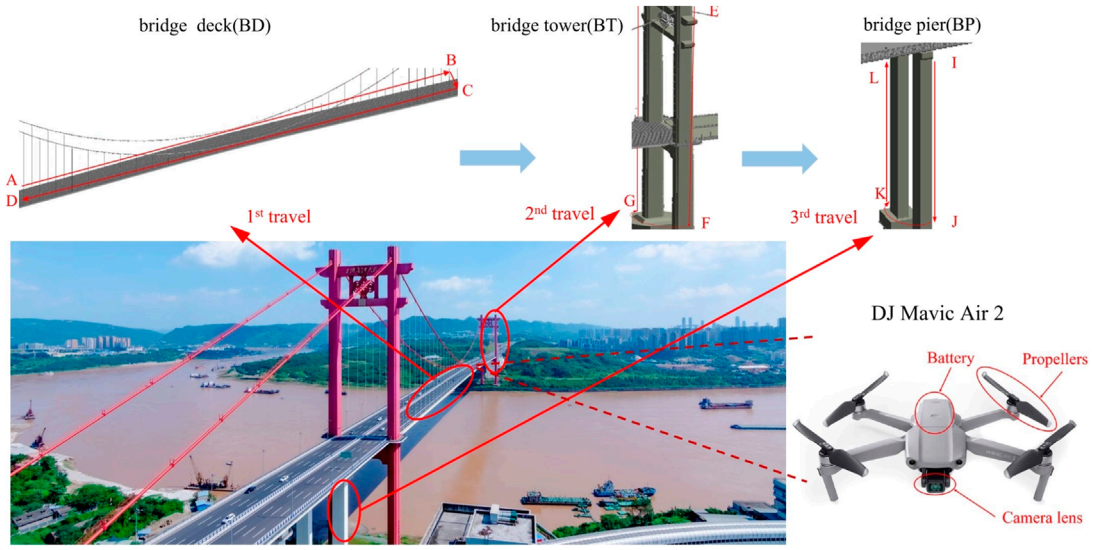

FIGURE 6
UAV shooting route diagram.

and $\widehat{C_i^j}$ denote the confidence of the predicted and labeled box. λ_{no} is the weight coefficient. P_i^j and $\widehat{P_i^j}$ denote the classification probability of the predicted and labeled box.

When calculating the regression loss, the EIoU was used instead of complete intersection over union (CIoU) to consider the effects of overlapping area, centroid distance, and aspect ratio of the target and prediction boxes simultaneously. The EIoU takes into account the width and height loss, which minimizes the difference between the width and height of the target and prediction boxes, thereby accelerating convergence and improving regression accuracy. Since cracks are small and occupy a small proportion of the background, the focal loss function is introduced to balance the proportion of foreground and background data samples (Lin et al., 2020; Wang et al., 2023a). Finally, the Focal-EIoU loss function is obtained, as shown in Eq. 12 and Eq. 13.

$$L_{EIoU} = 1 - IoU + \frac{\rho^2(b, b^{gt})}{{c_w}^2 + {c_h}^2} + \frac{(w - w^{gt})^2}{{c_w}^2} + \frac{(h - h^{gt})^2}{{c_h}^2} \tag{12}$$

$$L_{Focal-EIoU} = IoU^{\gamma} L_{EIoU} \tag{13}$$

where IoU is the ratio of the intersection of the area of the target box and the predicted box to the concatenated set. b, w and h are the coordinates of the center point, width, and height of the predicted box, respectively. b^{gt}, w^{gt} and h^{gt} are the coordinates of the center point, width, and height of the target box, respectively. $\rho^2(b, b^{gt})$ represents the distance between two center coordinates. c_w and c_h are the minimum width and height of the outlier boxes of the target and prediction boxes. λ is a parameter controlling the degree of outlier suppression.

2.2.4 YOLOv7-CD model

The YOLOv7 model, which integrates the SE attention module and the Focal-EIoU Loss, is named YOLOv7-CD, as shown in Figure 4. The red part indicates the added SE attention module, and the red arrow represents the changed computation path.

2.3 Two-stage transfer learning

The hyperparameters for extracting different features in the same neural network model have good interoperability. In order to improve the training efficiency and prediction accuracy of the model, TSTL is used in this study. The transfer learning process is shown in Figure 5. In Stage 1, the initial training weights are obtained by initializing the model parameters on the COCO2017 dataset. In Stage 2, the model backbone network is frozen, and the batch normalization layer is not updated during feature transfer to reduce the model error and to ensure the transfer effect. The pre-trained model parameters are adjusted by training on the publicly available CRACK500 dataset, which is a pavement crack dataset suitable for target detection. In Stage 3, freeze training and then thaw training is performed on the QL_CRACK dataset.

3 Experiments

3.1 Image acquisition

The selected research object of this article is the Cuntan Yangtze River Bridge, which starts from Huangjuewan Interchange in the south, crosses the Yangtze River, and ends at Happy Valley Interchange in the north. The total length of the line is 1.6 km, and the main bridge is 880 m long and 42 m wide.

The DJ Mavic Air 2 UAV was used for bridge crack image acquisition in the experiment, which has high vertical hovering accuracy and horizontal hovering accuracy (Yao et al., 2022). The resolution of captured photos can reach up to 8000*6000, and its

TABLE 1 Performance comparison before and after model improvement.

Method	Precision (%)	Recall (%)	F1	AP (%)	FPS
YOLOv7	89.20	92.07	0.86	94.60	52
YOLOv7-CD	94.70	96.31	0.95	97.79	52

high pixels can meet the data requirements of the experiment. In addition, the excellent endurance and stable flight speed of this UAV can ensure the efficiency of image acquisition.

The flight path of DJ Mavic Air 2 is shown in Figure 6.

1) Flew along the path A-B-C-D on the upper bridge deck, then flew to the lower bridge deck to shoot along the same route. After shooting the bridge deck, retrieved the UAV.
2) Flew from the top point E on one side of the bridge tower pylon to the bottom endpoint F, shot the four sides of the pylon back and forth, then flew to another pylon and flew up from the bottom endpoint G to the top point H. Repeated the appeal operation until all the pylons were shot and retrieved the UAV (this path was E-F-G-H).
3) The bridge pier shooting path (I-J-K-L) was similar to the bridge tower. Started flying from the top point I on one side of a bridge pier to the bottom endpoint J. After shooting four sides, flew to the next pier and repeated the aforementioned shooting operation. Finally, retrieved the UAV.

After each retrieval of the UAV, the acquired image information was read, and the images were numbered in the order in which they were taken. To obtain clear images of cracks, raw images with occlusions were consciously avoided, and images with occlusions were carefully screened and removed during the dataset creation process.

3.2 Dataset creation

In this experiment, a total of 466 raw images were acquired by DJ Mavic Air 2. In order to improve the training efficiency of the model, this article does some processing on the raw images. A raw image with a resolution of 8000 × 6000 was segmented into 713 sample images of 256 × 256, and then 10000 crack images that meet the criteria are selected as training sample images among the sample images according to the image quality ranking from high to low to create the QL_CRACK dataset. To determine the location of the crack images in the bridge structure, the images were named according to "bridge structure - raw image number - segmented image number". The bridge structure includes a bridge deck (BD), a bridge tower (BT), and a bridge pier (BP). After obtaining the QL_CRACK dataset, Lamblmg software was used to annotate the image crack areas, and 10,000 annotation files in XML format were obtained after annotation. The COCO2017 public dataset and the publicly available CRACK500 crack dataset were downloaded from the internet as the datasets for transfer learning, with a total of 163,957 images in the COCO2017 dataset and 3,368 images in the CRACK500 dataset. To evaluate the generalization ability of the YOLOv7-CD model, 80% of the 10,000 images were used as the training and validation sets (with 80% of the training set and 20% of the validation set), and 20% were used as the test set according to the five-fold cross-validation principle.

3.3 Model training

The training process of the network model in this study was implemented in the Pytorch deep learning framework built in Windows 11, NVIDIA GeForce RTX 3060 was used for the GPU, AMD Ryzen 7 5800H with Radeon Graphics at 3.20 GHz was used for the CPU, CUDA11.0 and CUDNN8.0 were selected for the calculation platform, RAM specification was 16 GB, and the Deep learning framework was built by PyTorch 1.7.1. Development environment was based on Visual Studio Code 1.73, python3.9.

When training the model, the batch size can only be set to 2, 4, and 8 due to the limitation of the experimental platforms, and a small batch size setting can lead to a large model error and slow down the training speed during the batch normalization operation (Ioffe and Szegedy, 2015; Wu and He, 2018). However, the TSTL approach adopted in this study can solve this problem well. As shown in Figure 5, the approach first trained on the COCO2017 dataset to obtain the initial weights; then froze the backbone network and trained 50 epochs on the CRACK500 dataset to obtain the pre-training weights; and finally froze the backbone network to train 50 epochs on the QL_CRACK dataset and then unfroze it to train 250 epochs.

In order to compare the performance of the YOLOv7-CD model under different conditions, a total of 16 sets of working conditions were set up for comparison experiments, which were (SGD$10^{-2.0}$)LR-(2 or 4 or 8)BS-(0)TL, (Adam$10^{-2.0}$)LR-(2 or 4 or 8)BS-(0)TL, (SGD$10^{-5.0}$)LR-(4)BS-(0) TL, (SGD$10^{-4.0}$)LR-(4)BS-(0)TL, (SGD$10^{-3.0}$)LR-(4)BS-(0)TL, (SGD$10^{-1.0}$)LR-(4)BS-(0)TL, (Adam$10^{-5.0}$)LR-(4)BS-(0)TL, (Adam$10^{-4.0}$)LR-(4)BS-(0)TL, (Adam$10^{-3.0}$)LR-(4)BS-(0)TL, (Adam$10^{-1.0}$)LR-(4)BS-(0)TL and (Adam$10^{-3.0}$)LR-(4)BS-(1or2)TL. "LR" and "BS" represent the learning rate and batch size, respectively. "SGD" and "Adam" are shorthand for stochastic gradient descent algorithm and adaptive descent algorithm, respectively. The corresponding parameters are in the front brackets. For example, "(SGD$10^{-2.0}$)LR-(2)BS" indicates that the SGD learning rate optimization algorithm is chosen with an initial learning rate of 10^{-2} and a batch size of 2. "(0)TL" denotes TSTL training, "(1)TL" denotes no second stage of transfer learning training, and "(2)TL" denotes no TSTL was performed.

4 Results and discussion

In this article, Precision, Recall, F1, and AP were selected as accuracy evaluation indexes, and frames per second (FPS) were selected as model inference speed evaluation indexes to analyze the performance of the YOLOv7-CD model.

Before introducing the evaluation metrics, we should first introduce the confusion matrix. The confusion matrix itself is a rough evaluation of the prediction results, which can give us a macro understanding of the prediction results and the original data.

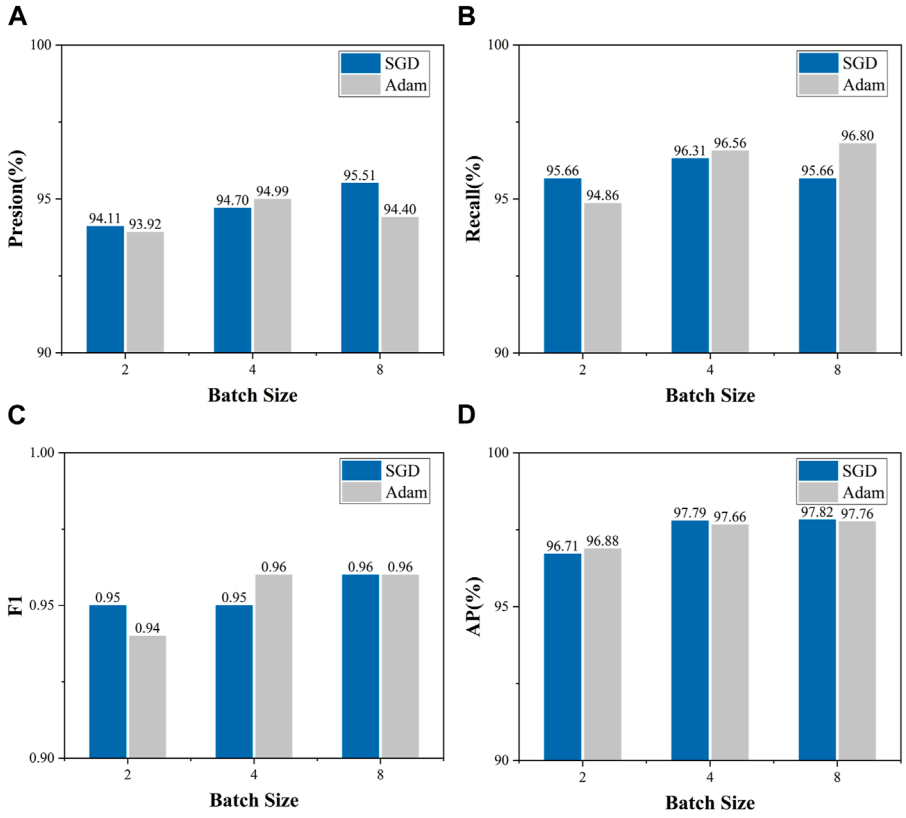

FIGURE 7
Variation of Precision, Recall, F1, and AP with batch size for different learning rate optimization algorithms: **(A)** Variation of Precision with batch size; **(B)** Variation of Recall with batch size; **(C)** Variation of F1 with batch size; **(D)** Variation of AP with batch size.

TABLE 2 Precision, Recall, F1, and AP for different working conditions.

Number	Working condition	Precision (%)	Recall (%)	F1	AP (%)
1	(SGD$10^{-2.0}$)LR-(2)BS-(0)TL	94.11	95.66	0.95	96.71
2	(SGD$10^{-2.0}$)LR-(4)BS-(0)TL	94.70	96.31	0.95	97.79
3	(SGD$10^{-2.0}$)LR-(8)BS-(0)TL	95.51	95.66	0.96	97.82
4	(Adam$10^{-2.0}$)LR-(2)BS-(0)TL	93.92	94.86	0.94	96.88
5	(Adam$10^{-2.0}$)LR-(4)BS-(0)TL	94.99	96.56	0.96	97.66
6	(Adam$10^{-2.0}$)LR-(8)BS-(0)TL	94.40	96.80	0.96	97.76

We will also use the data in the confusion matrix to calculate the evaluation index.

The confusion matrix has four compartments that contain all the possible scenarios of the prediction result when we make a binary prediction.

True Positive (abbreviated as TP) means that the sample is actually Positive and the model predicts the sample as Positive.

True Negative (abbreviated as TN) means that the sample is actually Negative and the model predicts the sample as Negative.

False Positive (abbreviated as FP) means that the sample is actually Negative, but the model predicts it as Positive.

False Negative (abbreviated as FN) means that the sample is actually Positive, but the model predicts it to be Negative.

Precision, also known as the check rate, indicates the proportion of samples predicted to be Positive that are actually Positive. Precision can be seen as a measure of quality. Higher precision means that an algorithm returns more relevant results than irrelevant ones.

The formula is:

$$\text{Precision} = \frac{\text{TP}}{\text{TP} + \text{FP}} \tag{14}$$

TABLE 3 Train loss under different working conditions.

Number	Working condition	Train loss
7	(SGD$10^{-5.0}$)LR-(4)BS-(0)TL	0.0221
8	(SGD$10^{-4.0}$)LR-(4)BS-(0)TL	0.0187
9	(SGD$10^{-3.0}$)LR-(4)BS-(0)TL	0.0175
2	(SGD$10^{-2.0}$)LR-(4)BS-(0)TL	0.0194
10	(SGD$10^{-1.0}$)LR-(4)BS-(0)TL	0.0224
11	(Adam$10^{-5.0}$)LR-(4)BS-(0)TL	0.0135
12	(Adam$10^{-4.0}$)LR-(4)BS-(0)TL	0.0130
13	(Adam$10^{-3.0}$)LR-(4)BS-(0)TL	0.0100
5	(Adam$10^{-2.0}$)LR-(4)BS-(0)TL	0.0129
14	(Adam$10^{-1.0}$)LR-(4)BS-(0)TL	0.0175

Recall, also known as the rate of checking for completeness, indicates the proportion of the number of actual positive samples in the positive sample that the prediction results in a positive sample to the proportion of positive samples in the full sample. Recall can be seen as a measure of quantity. High recall means that an algorithm returns most of the relevant results (whether or not irrelevant ones are also returned).

The formula is:

$$\text{Recall} = \frac{\text{TP}}{\text{TP} + \text{FN}} \tag{15}$$

AP is the area under the Precision-recall curve, usually the better a classifier is, the higher the AP value is.

F1 is a weighted average of precision and recall.

The formula for F1 is as follows:

$$\text{F1} = 2 \times \frac{\text{P} \times \text{R}}{\text{P} + \text{R}} \tag{16}$$

4.1 Comparative results of YOLOv7 and YOLOv7-CD

To verify the effectiveness of the improvement of the YOLOv7 model, the AP and FPS before and after the improvement with default parameters (batch size = 4, initial learning rate = 0.01 and SGD learning rate optimization algorithm) were compared, and the comparison results are shown in Table 1. Although the inference speed did not change after the model improvement, Precision, Recall, F1, and AP were improved. Among them, Precision improved by 5.50%, Recall improved by 4.24%, F1 improved by 0.09, and AP improved by 3.19%. This indicates that integrating the SE attention module and introducing the Focal-EIoU loss function in the YOLOv7 model can improve detection accuracy. The AP value before model improvement is 94.60% and the AP value after model improvement is 97.79%.

4.2 Hyperparameter optimization results

The parameters of the neural network are the internal variables of the neural network model, such as weights (w) and bias (b), and they can be obtained by training. The hyperparameters of the neural network are the external parameters of the model, such as learning rate, batch size, number of hidden layers, number of hidden layer units, activation function, momentum, etc. These parameters cannot be obtained from training and must be set manually, and they will affect the values of the obtained parameters w and b. The hyperparameters of the neural network have an important impact on the prediction results, and the appropriate hyperparameters will greatly improve the accuracy and efficiency of the network model.

In structured data, optimizing the batch size and learning rate are effective ways to achieve good performance in deep learning networks. Within a certain range, increasing batch size can improve convergence stability and reduce training time, but as the batch size increases, the number of iterations per epoch decreases, and the model's accuracy decreases accordingly. The impact of the learning rate on model performance is reflected in two aspects: the size of the initial learning rate and the optimization algorithm for the learning rate. The initial learning rate usually has an optimal value. When the initial learning rate is too small, the model converges slowly, and when it is too large, the model does not converge. The convergence of the model will be different when different learning rate optimization algorithms are chosen. In this article, two optimizers, SGD and Adam, were used to investigate (Shafi and Assad, 2023).

In order to make the model more suitable for bridge crack detection, this method conducts comparison experiments on three variables, batch size, learning rate, and optimization algorithm. In the experiments, the minimum learning rate was always 0.01 times the initial learning rate. A loss function is used to determine the convergence of the model during the hyperparameter optimization.

4.2.1 Batch size optimization

The larger the batch size, the higher the GPU performance requirements and the batch size is usually a power of 2 (Dong et al., 2021). Therefore, in this experiment, the batch size was set to 2, 4, and 8 based on the actual hardware configuration. And the performance of two learning rate optimization algorithms, SGD and Adam, was compared simultaneously. To ensure the reliability of batch size optimization, the initial learning rate was set to 0.01, and 50 epochs were trained in the freezing phase and 250 epochs in the thawing phase on the QL_CRACK dataset. Figure 7 shows the relationship between Precision, Recall, F1, and AP with different batch sizes for different learning rate optimization algorithms. The blue color represents the SGD optimization algorithm, and the grey color represents the Adam optimization algorithm. The results are also summarized in Table 2.

Combined with Figure 7 and Table 2, it can be seen that Precision is the largest for Number 3 and Number 5, with 95.51% and 94.99%, respectively; Recall is the largest for Number 5 and Number 6, with 96.56% and 96.80%, respectively; F1 is the largest for Number 3, Number 5 and Number 6, all with 0.96. When the batch size is 4 and 8, the precision, recall, and F1 are all higher than when the batch size is 2.

When the batch size is increased from 2 to 4, the AP for SGD and Adam optimization algorithms improved by 1.08% and 0.76%,

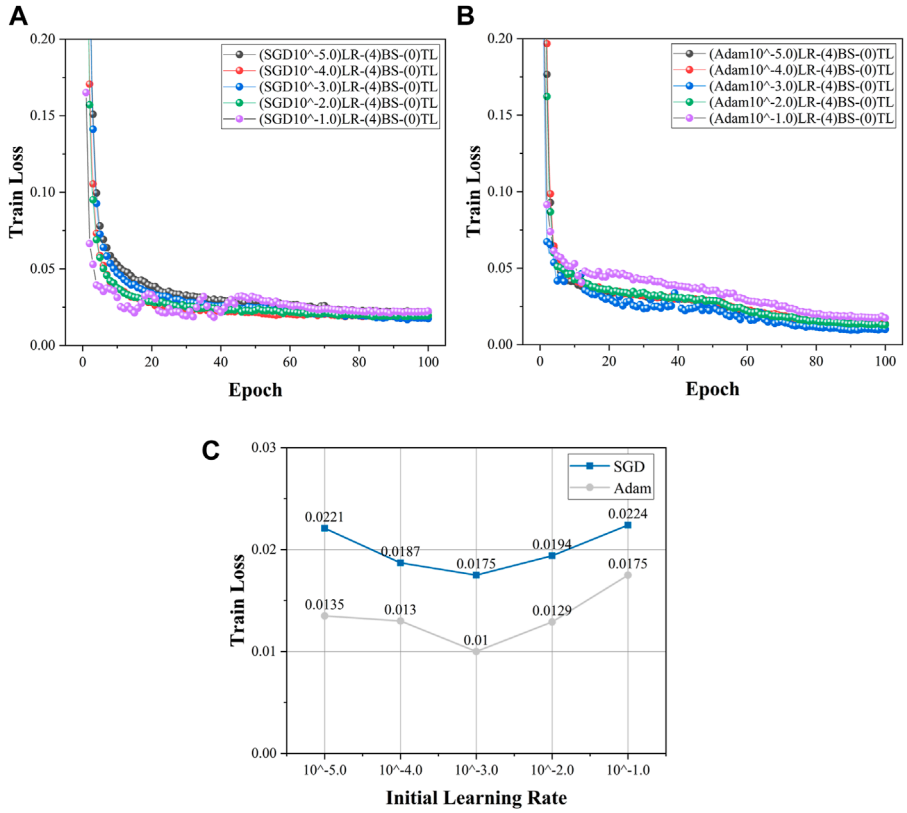

FIGURE 8
Learning rate optimization process: **(A)** loss variation of SGD optimization algorithm with different initial learning rates; **(B)** loss variation of Adam optimization algorithm with different initial learning rates; **(C)** Variation of the loss function with initial learning rate.

respectively, while when the batch size is increased from 4 to 8, the AP only improved by 0.03% and 0.1%, respectively. This indicates that the AP obtained by different optimization algorithms (SGD and Adam) have similar trends with the batch size, both of which have a large change in the batch size from 2 to 4 and a small change in the batch size from 4 to 8. The AP for the SGD and Adam optimization algorithms are the largest at a batch size of 8, but the difference with a batch size of 4 is small. Considering both the saving of video memory and the speed of training, the batch size of the freezing phase was set to 8, and the training batch size of the thawing phase was set to 4 during the experiment.

4.2.2 Learning rate optimization

The learning rate affects how fast the algorithm converges to the regionally minimal value. A suitable learning rate allows the algorithm to descend in the direction of the maximum gradient in appropriate steps, and the learning rate can be effectively optimized by the decreasing gradient of the loss function. Since the YOLOv7 model uses the learning rate optimization algorithm, only the initial learning rate and the optimization algorithm can be considered in the optimization (Wang et al., 2023b).

In this manuscript, the range of the initial learning rate was set from $10^{-5.0}$ to $10^{-1.0,}$ with a step size of 10 set in sequence (Mayr et al., 2018; Xu et al., 2023b; Yao et al., 2023b). The minimum learning rate was set to 0.01 times the initial learning rate. The batch size follows the optimal solution mentioned above (batch size = 4), and the Epoch is set to 100. Table 3 shows the training loss under different working conditions. Figures 8A, B show the convergence of the loss function values with the initial learning rate for the SGD and Adam optimization algorithms, respectively. From Figure 8A, it can be seen that the loss function converges fastest when the initial learning rate is set to 10^{-3} when the SGD optimization algorithm is used, and the loss function fluctuates more in the early stage when the initial learning rate is 10^{-1}, indicating that the learning rate is set too large at this time and the model does not converge well. From Figure 8B, it can be seen that the convergence curves of the loss function are smooth when the Adam optimization algorithm is used, but in the convergence process, the loss function values of each working condition have the following relationships: Number 14>Number 5, 11and 12>No. 14. When the initial learning rate is 10^{-3}, the model convergence effect is obviously better than other working conditions.

Figure 8C shows the variation of the loss function with the initial learning rate when the SGD and Adam optimization algorithms were used. Combining Figure 8C and Table 3, it can be seen that the minimum loss is 0.0175 for an initial learning rate of 10^{-3}, and the maximum is 0.0224 for an initial learning rate of 10^{-1} when the SGD optimization algorithm was used. And the minimum loss is 0.0100 for an initial learning rate of 10^{-3}, and the maximum is 0.0175 for an initial learning rate of 10^{-1} when the Adam

optimization algorithm was used. The trend of the loss curve with the initial learning rate is similar for the SGD and Adam optimization algorithms, both decreasing first and then increasing, and there is an optimal initial learning rate. In addition, the loss functions of the Adam optimization algorithm are lower than those of the SGD optimization algorithm. The optimal result is that the learning rate optimization algorithm is set to Adam, and the initial learning rate is set to 0.001.

4.3 Transfer learning results

In order to demonstrate the enhancement effect brought by the TSTL approach, a comparison experiment was conducted. The AP under different working conditions are counted in Table 4. "(0)TL" represents TSTL, "(1)TL" represents only transfer learning stage 1, and " (2)TL" represents no transfer learning. The AP of YOLOv7-CD is 98.01% with TSTL, 97.75% with only transfer learning stage 1, and 96.23% with the model without transfer learning.

AP of the YOLOv7-CD model with TSTL is 98.01%, AP of the YOLOv7-CD model with only transfer learning stage 1 is 97.75%, AP of the YOLOv7-CD model without transfer learning is 96.23%. For more visual observation of the effect of transfer learning, Figure 9 shows the convergence of the loss function for different transfer learning cases. It can be seen from Figure 9 that there is a relationship of "(2)TL < (1)TL < (0)TL" in the training loss during convergence, indicating that both phases of transfer learning can reduce the value of the loss function of the model and thus improve the model accuracy.

TABLE 4 AP under different transfer learning conditions.

Number	Working condition	AP (%)
13	(Adam$10^{-3.0}$)LR-(4)BS-(0)TL	98.01
15	(Adam10^{-3}.0)LR-(4)BS-(1)TL	97.75
16	(Adam$10^{-3.0}$)LR-(4)BS-(2)TL	96.23

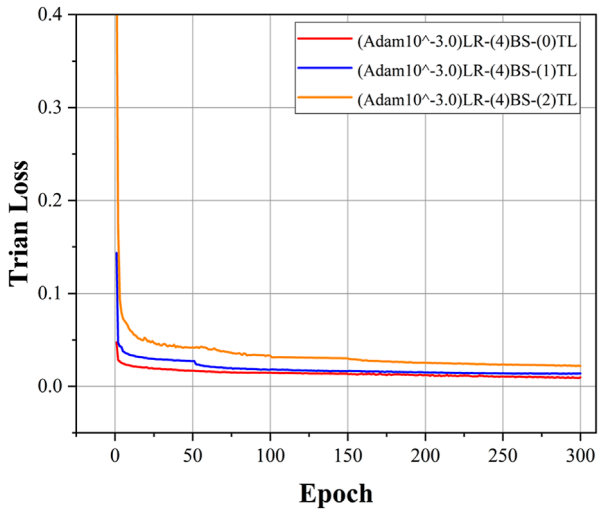

FIGURE 9
YOLOv7-CD model convergence process under different transfer learning cases.

4.4 Crack detection results

In YOLO, confidence is a value between 0 and 1 that indicates how sure the model is about the detected target (Yang et al., 2022c; Yang et al., 2022d; Yang et al., 2023a; Yang et al., 2023b; Yang et al., 2023c; Yang et al., 2024). This method has a good effect on bridge crack detection, and some of the detection results are shown in Figure 10. The naming rule in the figure is "bridge structure location - original image number - segmented image number" For example, "BR-095–164" means the crack is located in the 164th segmented image of the 95th captured image of the bridge deck. This is a good way to determine the location of the crack in the bridge structure. The red box in the image indicates the location of the crack, and the confidence level is marked in the lower left corner.

From Figure 10, it can be seen that YOLOv7-CD model has a good detection effect on transverse cracks, vertical cracks, and oblique cracks. The mean confidence rate is 0.83, ranging from 0.60 to 0.96. The cracks in Figures 10A, E, and Figure 10H all have certain curvature, similar to U-shape, and their confidence levels are above 0.9. For the oblique cracks, whether it is the southwest-northeast-trending crack in Figures 10B, G or the northwest-southeast-trending crack "crack-2" in Figure 10D, the confidence level is above 0.8. In contrast, for the transverse crack in Figure 10F and the vertical crack in Figure 10C, the confidence levels are below 0.8. The lowest confidence level is for transverse and vertical cracks, higher for diagonal cracks, and the highest confidence level is for U-shaped cracks, indicating that the model believes that bridge cracks should be more irregularly oriented through crack feature learning. Two cracks are present in Figure 10D, and the model accurately identifies the number and extent of cracks with confidence levels of 0.70 and 0.83. For fine cracks, the confidence level is 0.92 in Figure 10A and 0.64 in Figure 10C; for wide cracks, the confidence level is 0.93 in Figure 10E and 0.79 in Figure 10F. This indicates that the width of the crack does not have a significant effect on the confidence level of crack detection. Overall, YOLOv7-CD can quickly and accurately locate and identify cracks in the acquired images.

4.5 Comparison of different models

The improved model in this study was compared with five currently common target detection networks (YOLOv4, YOLOv5m, YOLOv4-tiny, and MobileNet-SSD) for experiments. The AP, number of parameters (#Param), computation volume (FLOPs), and FPS were used as evaluation metrics, and the comparison results are tallied in Table 5.

From Table 5, the AP of YOLOv4, YOLOv5m, YOLOv4-tiny, MobileNet-SSD, and YOLOv7-CD are 95.5%, 85.58%, 72.22%, 84.28%, and 98.01%, respectively. The prediction accuracy of YOLOv7-CD is higher than the remaining four target detection models. The parameters of YOLOv4, YOLOv5m, YOLOv4-tiny, MobileNet-SSD, and YOLOv7-CD are 64, 21.4, 5.9, 8.85, and

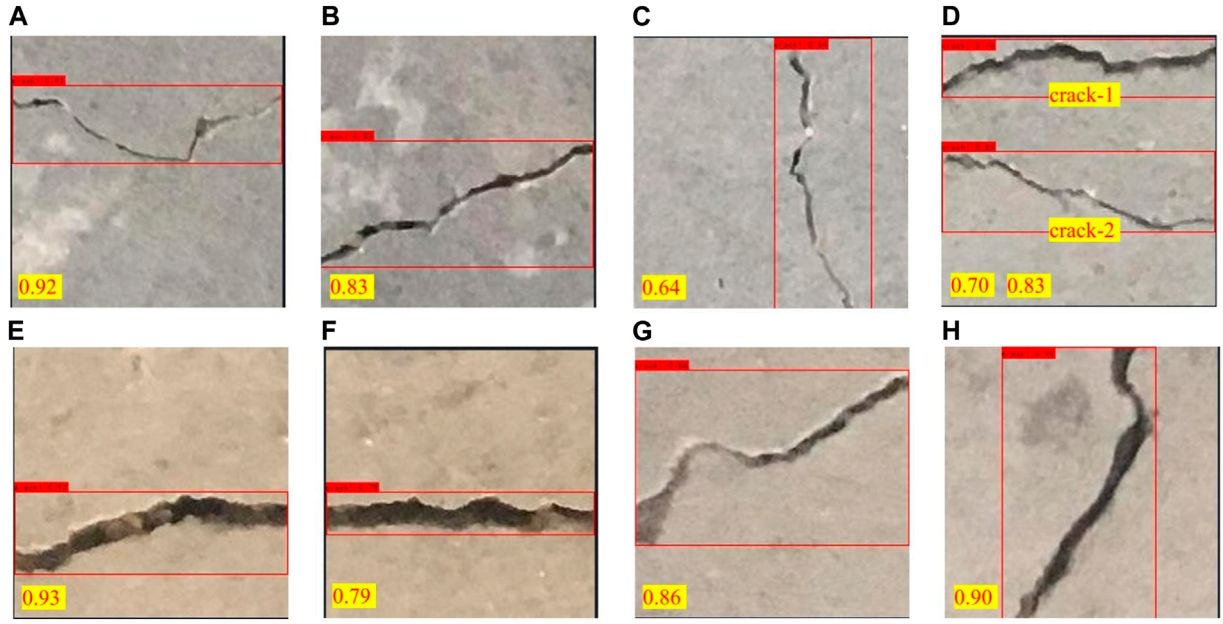

FIGURE 10
Bridge crack detection results: **(A)** BD-095-164; **(B)** BD-095-168; **(C)** BD-107-017; **(D)** BD-105-13; **(E)** BP-400-093; **(F)** BP-400-094; **(G)** BT-380-283; **(H)** BT-380-059.

TABLE 5 Performance comparison of different target detection models.

Model	AP (%)	#Param (M)	FLOPs (GMacs)	FPS
YOLOv4	95.50	64.00	63.92	16
YOLOv5m	85.58	21.40	51.30	39
YOLOv4-tiny	72.22	5.90	4.31	56
MobileNet-SSD	84.28	8.85	12.40	48
YOLOv7-CD	98.01	37.65	17.04	52

37.65 M, respectively; the computational volume were 63.92, 51.3, 4.31, 12.4 and 17.04 GMacs, respectively; the ratio of parameter number to the computational volume were 1.00, 0.42, 1.37, 0.71, and 2.21, respectively.

YOLOv7-CD has the largest ratio of parameters to computation volume, and its higher number of parameters maintains a lower computation volume, which will ensure its fast inference capability to a certain extent. The FPS of YOLOv4, YOLOv5m, YOLOv4-tiny, MobileNet-SSD, and YOLOv7-CD are 16, 39, 56, 48, and 52, respectively. YOLOv4-tiny has the fastest inference speed of 56, followed by 52 for YOLOv7-CD. In terms of inference speed, YOLOv7-CD is 7.6% lower than YOLOv4-tiny, but in terms of AP, YOLOv7-CD is 25.79% higher than YOLOv4-tiny. Therefore, among the five object detection models, YOLOv7-CD has the best comprehensive performance in both prediction accuracy and inference speed.

5 Conclusion

In response to the current problems in intelligent bridge crack detection, such as difficulties in acquiring high-quality crack images, long inference time of network models, and detection accuracy to be improved, this article proposes an IIRTCDMB based on UAVIAT and IITDT.

The method proposed in this article can effectively detect cracks with different morphologies and complex backgrounds and has strong robustness as well as background noise filtering capability, which can reduce the problems of noise interference and blurring of UAV images due to the influence of environmental conditions. The adopted crack image naming method can quickly find out the actual location where the cracks appear and maintain them in time.

In order to verify the excellent performance of this method, it was applied to the Cuntan Yangtze River Bridge, and the following conclusions were obtained:

1) The YOLOv7-CD model, which integrates the SE attention module and introduces the Focal EIOU loss function, has an AP improvement of 3.19% compared to the original YOLOv7 model. The comparison experiments of transfer learning show that both stages of transfer learning can reduce the loss of model convergence.
2) The hyperparameter optimization of the YOLOv7-CD model can reduce the model loss to a certain degree and improve the accuracy of the model in detecting bridge cracks. The model performs best when the batch size is 8, the initial learning rate is 0.001, and the learning rate optimization algorithm is Adam. Because the AP difference between the batch size of 4 and 8 is small, the batch size of the freezing phase is set to 8, and

the batch size of the thawing phase is set to 4 in order to save computational performance.

3) In the crack localization and identification results, the confidence level of horizontal and vertical cracks is the lowest, the confidence level of oblique cracks is higher, and the confidence level of U-shaped cracks is the highest, which indicates that the model believes that the bridge cracks should be more irregularly oriented through crack feature learning. The average value of the crack detection confidence is 0.83. Overall, the YOLOv7-CD model can quickly and accurately perform crack location and identification on the acquired images.
4) Under the conditions of this article, the AP of the YOLOv7-CD model is 98.01%, and the FPS is 52. Its comprehensive performance is all the better than the current popular target detection models YOLOv4, YOLOv5m, YOLOv4-tiny, and MobileNet-SSD.

In conclusion, the method proposed in this paper solves the current problems of difficult crack image acquisition and high cost of image labeling while improving the performance of the model. The model can focus on the relationship between pixels, improve the robustness of the model, and reduce the time cost of sample labeling. In the future, the model can be further optimized toto improve the segmentation ability of the model for crack edges and small cracks, and to improve the generalization ability of the model.

Data availability statement

The data analyzed in this study is subject to the following licenses/restrictions: The datasets used and analyzed during the current study are available from the corresponding author on reasonable request. Requests to access these datasets should be directed to GY, yaogang@cqu.edu.cn.

Author contributions

YY: Writing–review and editing, Conceptualization, Methodology. LL: Writing–original draft, Formal Analysis, Software. GY: Writing–review and editing, Conceptualization, Methodology. HD: Writing–original draft. YC: Writing–original draft. LW: Writing–original draft.

Funding

The author(s) declare financial support was received for the research, authorship, and/or publication of this article. This research was funded by Chongqing City Infrastructure Construction Investment Co., Ltd. Grant number CQCT-JSA-GC-2021-0140 and Central Universities Basic Research Operating Expenses (2023CDJXY-031).

Conflict of interest

The authors declare that the research was conducted in the absence of any commercial or financial relationships that could be construed as a potential conflict of interest.

The reviewer [XL] declared a shared affiliation with the authors to the handling editor at the time of review.

The author(s) declare financial support was received for the research, authorship, and/or publication of this article. This research was funded by Chongqing City Infrastructure Construction Investment Co., Ltd. Grant number CQCT-JSA-GC-2021-0140 and Central Universities Basic Research Operating Expenses (2023CDJXY-031). The funder had the following involvement in the study: data collection and analysis.

Publisher's note

References

Chen, L. K., Chen, W. X., Wang, L., Zhai, C. C., Hu, X. L., Sun, L. L., et al. (2023). Convolutional neural networks (CNNs)-based multi-category damage detection and recognition of high-speed rail (HSR) reinforced concrete (RC) bridges using test images. *Eng. Struct.* 276, 115306. doi:10.1016/j.engstruct.2022.115306

Chen, X. X., Ye, Y., Zhang, X., and Yu, C. C. (2020). Bridge damage detection and recognition based on deep learning. *J. Phys. Conf. Ser.* 1626 012151 doi:10.1088/1742-6596/1626/1/012151

Dong, X. P., Shen, J. B., Wang, W. G., Shao, L., Ling, H. B., and Porikli, F. (2021). Dynamical hyperparameter optimization via deep reinforcement learning in tracking. *Ieee Trans. Pattern Analysis Mach. Intell.* 43 (5), 1515–1529. doi:10.1109/tpami.2019.2956703

Du, Y. C., Pan, N., Xu, Z. H., Deng, F. W., Shen, Y., and Kang, H. (2021). Pavement distress detection and classification based on YOLO network. *Int. J. Pavement Eng.* 22 (13), 1659–1672. doi:10.1080/10298436.2020.1714047

Duque, L., Seo, J., and Wacker, J. (2018). Bridge deterioration quantification protocol using UAV. *J. Bridge Eng.* 23 (10). doi:10.1061/(asce)be.1943-5592.0001289

Eisenbach, M., Stricker, R., Seichter, D., Amende, K., Debes, K., Sesselmann, M., et al. (2017). "How to get pavement distress detection ready for deep learning? A systematic approach," in Proceedings of the 2017 International Joint Conference on Neural Networks (IJCNN), Anchorage, AK, USA, May 2017.

Ge, L., Dan, D., and Li, H. (2020). An accurate and robust monitoring method of full-bridge traffic load distribution based on YOLO-v3 machine vision. *Struct. Control Health Monit.* 27 (12). doi:10.1002/stc.2636

Guan, H. Y., Li, J., Yu, Y. T., Chapman, M., Wang, H. Y., Wang, C., et al. (2015). Iterative tensor voting for pavement crack extraction using mobile laser scanning data. *Ieee Trans. Geoscience Remote Sens.* 53 (3), 1527–1537. doi:10.1109/tgrs.2014.2344714

Ioffe, S., and Szegedy, C. (2015). Batch normalization: accelerating deep network training by reducing internal covariate shift. Available at: https://arxiv.org/abs/1502.03167.

Jin, Q. L., Han, Q. B., Su, N. A., Wu, Y., and Han, Y. F. (2023). A deep learning and morphological method for concrete cracks detection. *J. Circuits Syst. Comput.* 32. doi:10.1142/s0218126623502717

Kao, S. P., Chang, Y. C., and Wang, F. L. (2023). Combining the YOLOv4 deep learning model with UAV imagery processing technology in the extraction and quantization of cracks in bridges. *Sensors* 23 (5), 2572. doi:10.3390/s23052572

Kao, S.-P., Wang, F.-L., Lin, J.-S., Tsai, J., Chu, Y.-D., and Hung, P.-S. (2022). Bridge crack inspection efficiency of an unmanned aerial vehicle system with a laser ranging module. *Sensors* 22 (12), 4469. doi:10.3390/s22124469

Khaloo, A., Lattanzi, D., Cunningham, K., Dell'Andrea, R., and Riley, M. (2018). Unmanned aerial vehicle inspection of the Placer River Trail Bridge through image-based 3D modelling. *Struct. Infrastructure Eng.* 14 (1), 124–136. doi:10.1080/15732479.2017.1330891

Kim, I. H., Jeon, H., Baek, S. C., Hong, W. H., and Jung, H. J. (2018). Application of crack identification techniques for an aging concrete bridge inspection using an unmanned aerial vehicle. *Sensors* 18 (6), 1881. doi:10.3390/s18061881

Kim, I.-H., Yoon, S., Lee, J. H., Jung, S., Cho, S., and Jung, H.-J. (2022). A comparative study of bridge inspection and condition assessment between manpower and a UAS. *Drones* 6 (11), 355. doi:10.3390/drones6110355

Li, Q., Yang, Y., Yao, G., Wei, F., Xue, G., and Qin, H. (2024). Multiobject real-time automatic detection method for production quality control of prefabricated laminated slabs. *J. Constr. Eng. Manag.* 150 (3), 05023017. doi:10.1061/jcemd4.coeng-14089

Lin, T.-Y., Goyal, P., Girshick, R., He, K., and Dollar, P. (2020). Focal loss for dense object detection. *IEEE Trans. pattern analysis Mach. Intell.* 42 (2), 318–327. doi:10.1109/tpami.2018.2858826

Liu, L. S., Ke, C. Y., Lin, H., and Xu, H. (2022). Research on pedestrian detection algorithm based on MobileNet-YoLo. *Comput. Intell. Neurosci.* 2022, 1–12. doi:10.1155/2022/8924027

Liu, Y.-F., Nie, X., Fan, J.-S., and Liu, X.-G. (2020). Image-based crack assessment of bridge piers using unmanned aerial vehicles and three-dimensional scene reconstruction. *Computer-Aided Civ. Infrastructure Eng.* 35 (5), 511–529. doi:10.1111/mice.12501

Mayr, A., Klambauer, G., Unterthiner, T., Steijaert, M., Wegner, J. K., Ceulemans, H., et al. (2018). Large-scale comparison of machine learning methods for drug target prediction on ChEMBL. *Chem. Sci.* 9 (24), 5441–5451. doi:10.1039/c8sc00148k

Mohan, A., and Poobal, S. (2018). Crack detection using image processing: a critical review and analysis. *Alexandria Eng. J.* 57 (2), 787–798. doi:10.1016/j.aej.2017.01.020

Perry, B. J., Guo, Y., Atadero, R., and van de Lindt, J. W. (2020). Streamlined bridge inspection system utilizing unmanned aerial vehicles (UAVs) and machine learning. *Measurement* 164, 108048. doi:10.1016/j.measurement.2020.108048

Prasanna, P., Dana, K. J., Gucunski, N., Basily, B. B., La, H. M., Lim, R. S., et al. (2016). Automated crack detection on concrete bridges. *Ieee Trans. Automation Sci. Eng.* 13 (2), 591–599. doi:10.1109/tase.2014.2354314

Saidin, S. S., Jamadin, A., Abdul Kudus, S., Mohd Amin, N., and Anuar, M. A. (2022). An overview: the application of vibration-based techniques in bridge structural health monitoring. *Int. J. Concr. Struct. Mater.* 16 (1), 69. doi:10.1186/s40069-022-00557-1

Sanchez-Cuevas, P. J., Ramon-Soria, P., Arrue, B., Ollero, A., and Heredia, G. (2019). Robotic system for inspection by contact of bridge beams using UAVs. *Sensors* 19 (2), 305. doi:10.3390/s19020305

Seo, J., Duque, L., and Wacker, J. (2018). Drone-enabled bridge inspection methodology and application. *Automation Constr.* 94, 112–126. doi:10.1016/j.autcon.2018.06.006

Shafi, S., and Assad, A. (2023). "Exploring the relationship between learning rate, batch size, and epochs in deep learning: an experimental study," in *Soft computing for problem solving* (Singapore: Springer Nature Singapore).

Sun, Y. J., Yang, Y., Yao, G., Wei, F. J., and Wong, M. P. (2021). Autonomous crack and bughole detection for concrete surface image based on deep learning. *Ieee Access* 9, 85709–85720. doi:10.1109/access.2021.3088292

Teng, S., Liu, Z. C., and Li, X. D. (2022). Improved YOLOv3-based bridge surface defect detection by combining high- and low-resolution feature images. *Buildings* 12 (8), 1225. doi:10.3390/buildings12081225

Tomiczek, A. P., Whitley, T. J., Bridge, J. A., and Ifju, P. G. (2019). Bridge inspections with small unmanned aircraft systems: case studies. *J. Bridge Eng.* 24 (4). doi:10.1061/(asce)be.1943-5592.0001376

Wang, C. Y., Bochkovskiy, A., and Liao, H. Y. M. (2023a). "YOLOv7: trainable bag-of-freebies sets new state-of-the-art for real-time object detectors," in Proceedings of the IEEE/CVF Conference on Computer Vision and Pattern Recognition (CVPR), Vancouver, CANADA.

Wang, H.-F., Zhai, L., Huang, H., Guan, L.-M., Mu, K.-N., and Wang, G.-p. (2020). Measurement for cracks at the bottom of bridges based on tethered creeping unmanned aerial vehicle. *Automation Constr.* 119, 103330. doi:10.1016/j.autcon.2020.103330

Wang, Z.-J., Gao, H.-B., Wang, X.-H., Zhao, S.-Y., Li, H., and Zhang, X.-Q. (2023b). Adaptive learning rate optimization algorithms with dynamic bound based on Barzilai-Borwein method. *Inf. Sci.* 634, 42–54. doi:10.1016/j.ins.2023.03.050

Wei, F. J., Yao, G., Yang, Y., and Sun, Y. J. (2019). Instance-level recognition and quantification for concrete surface bughole based on deep learning. *Automation Constr.* 107, 102920. doi:10.1016/j.autcon.2019.102920

Wu, Y., and He, K. (2018). *Group normalization*.

Xu, H. K., Tian, Y., Lin, S., and Wang, S. C. (2013). "Research of image segmentation algorithm applied to concrete bridge cracks," in Proceedings of the International Conference on Information Science and Technology (ICIST), Yangzhou, China, March 2013.

Xu, Z., Wang, H., Xing, C., Tao, T., Mao, J., and Liu, Y. (2023b). Physics guided wavelet convolutional neural network for wind-induced vibration modeling with application to structural dynamic reliability analysis. *Eng. Struct.* 297, 117027. doi:10.1016/j.engstruct.2023.117027

Xu, Z., Wang, Y., Hao, X., and Fan, J. (2023a). Crack detection of bridge concrete components based on large-scene images using an unmanned aerial vehicle. *Sensors (Basel)* 23 (14), 6271. doi:10.3390/s23146271

Xuhang, T., Jie, G., Yun, L., and Zhouping, Y. (2011). "A new image-based method for concrete bridge bottom crack detection," in Proceedings of the 2011 International Conference on Image Analysis and Signal Processing, Hubei, October 2011.

Yang, Y., Li, Q., and Yao, G. (2022b). Intelligent identification and detection method of prefabricated laminated slab. *J. Civ. Environ. Eng.* 44 (01), 87–93. doi:10.11835/j.issn.2096-6717.2020.187

Yang, Y. Y., Ling, Y., Tan, X., Wang, S., and Wang, R. Q. (2022d). Damage identification of frame structure based on approximate metropolis–hastings algorithm and probability density evolution method. *Int. J. Struct. Stab. Dyn.*

Yang, Y. H., Lu, X., Tan, H. K., Chai, R., Wang, and Zhang, Y. (2022c). Fundamental mode shape estimation and element stiffness evaluation of girder bridges by using passing tractor-trailers. *Mech. Sys. Sig. Pr.* 169.

Yang, Y. H., Lu, X., Tan, R., Wang, and Zhang, Y. (2023b). Mode shape identification and damage detection of bridge by movable sensory system. *IEEE trans. Intell. Transp. Syst.* 24 1299–1313.

Yang, Y. Z., Wang, Q., Yang, X., Tan, and Gao, Y. (2024). Bridge bearing damage identification based on statistical moment change rate. *Mech. Sys. Sig. Pr.* 206, 110898.

Yang, Y. Z., Wang, B., Xian, H. K., Chai, Z., Yu, Y., Zhang, et al. (2023a). Baseline-free detection method for change of lateral stiffness of high-rise building based on statistical moment curvature. *Struct. Control. Health Monit.* 4373174.

Yang, Y., Yang, L., and Yao, G. (2021). Post-processing of high formwork monitoring data based on the back propagation neural networks model and the autoregressive—moving-average model. *Symmetry* 13 (8), 1543. doi:10.3390/sym13081543

Yang, Z., Ni, C. S., Li, L., Luo, W. T., and Qin, Y. (2022a). Three-stage pavement crack localization and segmentation algorithm based on digital image processing and deep learning techniques. *Sensors* 22 (21), 8459. doi:10.3390/s22218459

Yao, G., Li, R., and Yang, Y. (2023a). An improved multi-objective optimization and decision-making method on construction sites layout of prefabricated buildings. *Sustainability* 15 (7), 6279. doi:10.3390/su15076279

Yang, Y., Xu, W., Gao, Z., Yu, Z., and Zhang, Y. (2023c). Research progress of SHM system for super high-rise buildings based on wireless sensor network and cloud platform. *Remote Sens.* 15 (6) 1473.

Yao, G., Sun, W., Yang, Y., Wang, M., Li, R., and Zheng, Y. (2023b). Multi-volume variable scale bitmap data object classification algorithm architectural concrete color difference detection. *J. Intelligent Constr.* 1 (2), 9180010. doi:10.26599/jic.2023.9180010

Yao, G., Sun, W. T., Yang, Y., Sun, Y. J., Xu, L. J., and Zhou, J. (2022). Chromatic aberration identification of fair-faced concrete research based on multi-scale lightweight structured data algorithm. *Front. Mater.* 9. doi:10.3389/fmats.2022.851555

Yao, G., Sun, Y. J., Wong, M. P., and Lv, X. N. (2021b). A real-time detection method for concrete surface cracks based on improved YOLOv4. *Symmetry-Basel* 13 (9), 1716. doi:10.3390/sym13091716

Yao, G., Sun, Y. J., Yang, Y., and Liao, G. (2021a). Lightweight neural network for real-time crack detection on concrete surface in fog. *Front. Mater.* 8. doi:10.3389/fmats.2021.798726

Yao, G., Wei, F., Yang, Y., and Sun, Y. (2019). Deep-learning-based bughole detection for concrete surface image. *Adv. Civ. Eng.* 2019, 1–12. doi:10.1155/2019/8582963

Zhang, C. B., Chang, C. C., and Jamshidi, M. (2020b). Concrete bridge surface damage detection using a single-stage detector. *Computer-Aided Civ. Infrastructure Eng.* 35 (4), 389–409. doi:10.1111/mice.12500

Zhang, J., Qian, S. R., and Tan, C. (2022). Automated bridge surface crack detection and segmentation using computer vision-based deep learning model. *Eng. Appl. Artif. Intell.* 115, 105225. doi:10.1016/j.engappai.2022.105225

Zhang, J., Qian, S. R., and Tan, C. (2023b). Automated bridge crack detection method based on lightweight vision models. *Complex and Intelligent Syst.* 9 (2), 1639–1652. doi:10.1007/s40747-022-00876-6

Zhang, Y., Sun, Y. P., Wang, Z., and Jiang, Y. (2023a). YOLOv7-RAR for urban vehicle detection. *Sensors* 23 (4), 1801. doi:10.3390/s23041801

Zhang, Y. X., Huang, J., and Cai, F. H. (2020a). On bridge surface crack detection based on an improved YOLO v3 algorithm. *J. Phys. Conf. Ser.* 1626 (1), 012151.

frontiers | Frontiers in Materials

TYPE Original Research
PUBLISHED 14 February 2024
DOI 10.3389/fmats.2023.1347176

OPEN ACCESS

EDITED BY
Yang Zou,
Chongqing Jiaotong University, China

REVIEWED BY
Xiaohua Li,
Chongqing University, China
Kun Xu,
Beijing University of Technology, China
Lei Yan,
Central South University, China

*CORRESPONDENCE
Mingyu Fan,
ff98@163.com
Ke Li,
keli-bridge@cqu.edu.cn

RECEIVED 30 November 2023
ACCEPTED 26 December 2023
PUBLISHED 14 February 2024

CITATION
Chen B, Fan M, Li K, Gao Y, Wang Y, Chen Y, Yin S and Sun J (2024), The PFILSTM model: a crack recognition method based on pyramid features and memory mechanisms. *Front. Mater.* 10:1347176. doi: 10.3389/fmats.2023.1347176

The PFILSTM model: a crack recognition method based on pyramid features and memory mechanisms

Bin Chen[1], Mingyu Fan[2]*, Ke Li[3]*, Yusheng Gao[2], Yifu Wang[4], Yiqian Chen[1], Shuohui Yin[5] and Junxia Sun[6]

[1]National Engineering Research Center for Highways in Mountainous Areas, Chongqing, China, [2]School of Computer Science and Engineering, University of Electronic Science and Technology of China, Chengdu, China, [3]College of Civil Engineering, Chongqing University, Chongqing, China, [4]Department of Mechanical Engineering, Guangzhou City Polytechnic, Guangzhou, China, [5]Engineering Research Center of Complex Tracks Processing Technology and Equipment of Ministry of Education, Xiangtan University, Xiangtan, China, [6]Chongqing College of Architecture and Technology, Chongqing, China

Crack detection is a crucial task for the structural health diagnosis of buildings. The current widely used manual inspection methods have inherent limitations and safety hazards, while traditional digital image processing methods require manual feature extraction and also have substantial limitations. In this paper, we propose a crack recognition method based on pyramid features and memory mechanisms that leverages a U-shaped network, long short-term memory mechanisms, and a pyramid feature design to address the recognition accuracy, robustness, and universality issues with deep learning-based crack detection methods in recent years. Experiments were conducted on four publicly available datasets and one private dataset. Compared with the commonly used FCN8s, SegNet, UNet, and DeepLabv3+ models and other related studies using the same evaluation criteria and datasets, our proposed model shows better overall performance in terms of all metrics evaluated.

KEYWORDS

crack detection, deep learning, neural network, image segmentation, PFILSTM

1 Introduction

With the development of the economy and the extensive and lasting use of concrete in construction facilities, the possible harmfulness of building structures are becoming more and more serious, so it is increasingly important and urgent to diagnose and maintain the health of structures. Crack detection is an important part of structural health diagnosis and has become a research focus (Deng et al., 2023).

Over the past two decades, a variety of image-based detection methods have provided a safe, efficient, and cost-effective approach to crack detection techniques.

With the emergence of fully convolutional neural networks, deep learning has been applied to image semantic segmentation. The goal of building crack image recognition is to detect whether there are cracks on the surface of the building structure and the location of the cracks. Image semantic segmentation technology divides the image into different blocks according to the content. Compared with image classification and detection, image

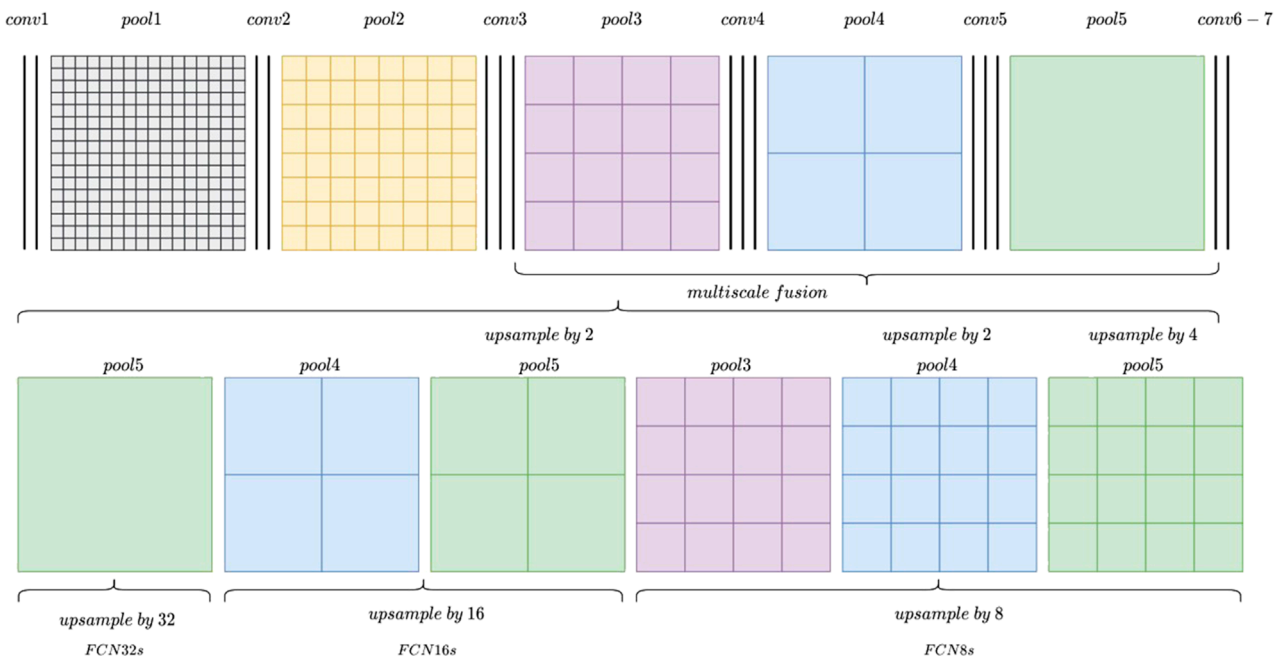

FIGURE 1
FCN8s, FCN16s, and FCN32s models.

segmentation is a more delicate work, including image semantics and location issues. Image segmentation can be divided into semantic segmentation and instance segmentation. Semantic segmentation simply classifies each pixel in an image, but instance segmentation needs to distinguish different objects. This paper considers semantic segmentation. The semantic problem is the "what" problem in the image classification task, while the location problem is the "where" problem in the image target detection task (Long et al., 2015), which is very suitable for crack detection.

Aiming at the problems of the low accuracy and poor robustness of current semantic segmentation methods for building crack images, this paper proposes a new crack recognition model based on memory mechanisms and pyramid features which adopts multi-scale feature fusion and cross-layer feature fusion methods to improve segmentation accuracy. In addition, long and short-term memory mechanisms are used to learn the correlation between feature maps to remove disturbing features. Finally, comparative experiments are designed on multiple datasets to test the effect of the proposed model.

The structure of this paper is as follows: the Section 2 is the research status analysis, the Section 3 is the model design, the Section 4 is the experimental design and experimental results analysis, and the Section 5 is the conclusion.

2 Research status analysis

At present, there is a lot of research in the field of crack identification (Jieh-Haur et al., 2017; Li et al., 2017; Liu et al., 2021; Asadi Shamsabadi et al., 2022; Liu et al., 2023).

Among them, literature Jieh-Haur et al. (2017) adopted self-organizing map optimization (SOMO) integrated with image processing techniques to develop a crack recognition model for bridge inspection. Bridge crack data from 216 images were collected from the database of the Taiwan Bridge Management System, which provides detailed information on the condition of bridges. Its methods and datasets are different from those in this paper. Literature Li et al. (2017) developed a machine learning-based algorithm for extracting cracks from concrete bridge images which combines a modified region-based active contour model for image segmentation and the linear support vector machine using a greedy search strategy for noise elimination. Literature Liu et al. (2021) proposed an approach to recognize concrete crack patterns from images. By analyzing the characteristics of structural and non-structural cracks, a binary classification of crack patterns into isolated patterns and map patterns was proposed. The recognition of crack patterns was performed through similarity comparisons using the Differentiable-Image-Saliency-Transform-for-Improved-Scalability-and-Portability-of-Image-Quality-Assessment (DISTS) index. Various parameters that may affect the performance were investigated through several experiments conducted using real-world images. The methods and purposes in literatures Li et al. (2017), Liu et al. (2021) are different from those of this paper. Literature Asadi Shamsabadi et al. (2022) proposed a vision transformer (ViT)-based framework for crack detection on asphalt and concrete surfaces. With transfer learning and the differentiable intersection over union (IoU) loss function, the encoder-decoder network equipped with ViT could achieve an enhanced real-world crack segmentation performance. Compared to the Convolutional-Neural-Networks (CNN) based models (DeepLabv3+ and U-Net), TransUNet with a CNN-ViT backbone achieved up to ~61% and ~3.8% better mean IoU on the original images of

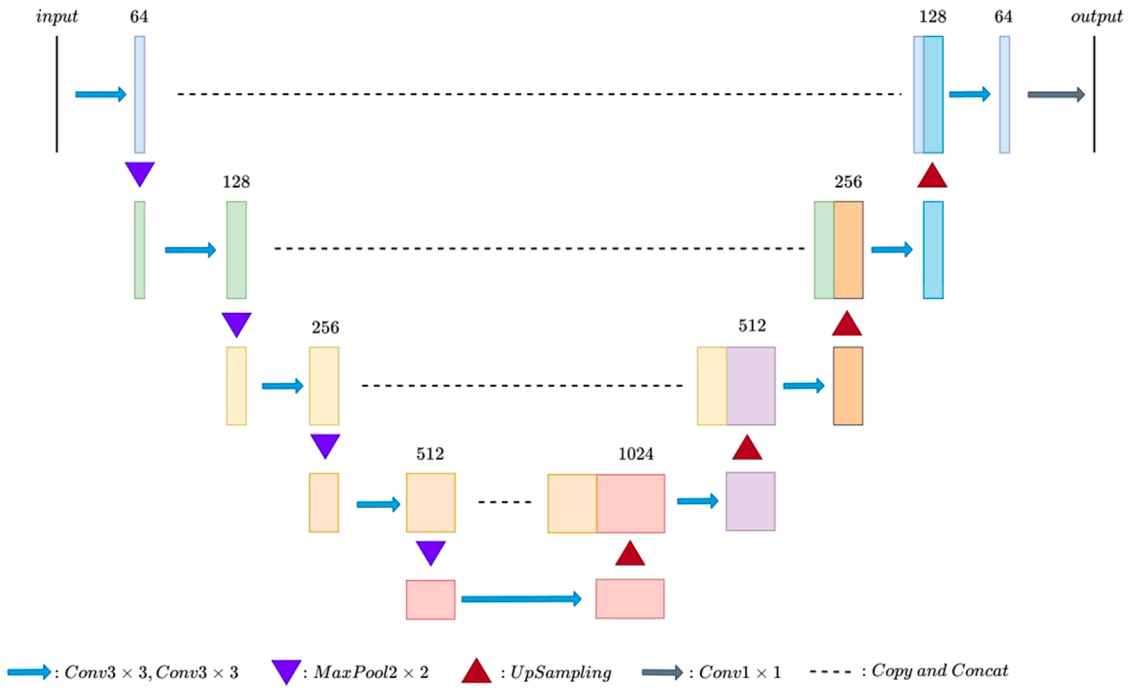

FIGURE 2
UNet model.

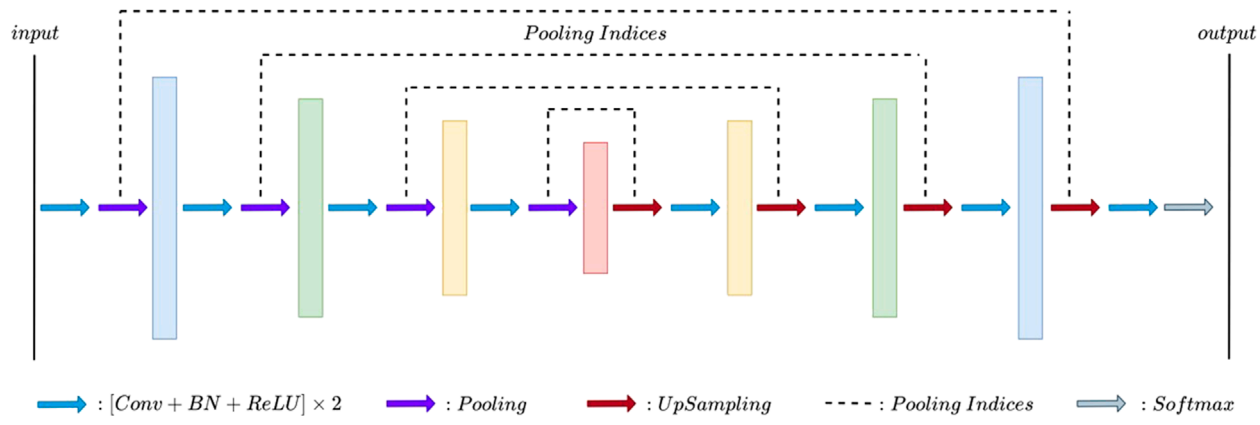

FIGURE 3
SegNet model.

the respective datasets with very small and multi-scale crack semantics. The model principle and mechanism of literature Asadi Shamsabadi et al. (2022) is different from that of this paper. Literature Liu et al. (2023) described a You-Only-Look-Once-version-three (YOLOv3) model with four-scale detection layers (FDL) to detect combined B-scan and C-scan ground-penetrating-radar (GPR) images subject to poor detection effects and a high missed detection rate of small crack feature sizes. Multiscale fusion structures, efficient intersection over union (EIoU) loss function, K-means++ clustering, and hyperparameter optimization were used in this proposed model to further improve detection performance.

We focus on the models in literature Cao et al. (2020), Xiang et al. (2020), Berman et al. (2018), Zhu et al. (2022), Qu et al. (2022) using the same evaluation index and datasets in the application of research into building crack identification.

Literature (Cao et al., 2020), the attention mechanism was joined to the encoder and decoder of the nerual network structure for road surface crack detection. Compared with other advanced detection methods, this method achieved the highest F1 score of 0.69.

Literature Xiang et al. (2020) proposed an end-to-end convolutional neural network based on pyramid features and attention mechanisms for pavement crack detection. The spatial

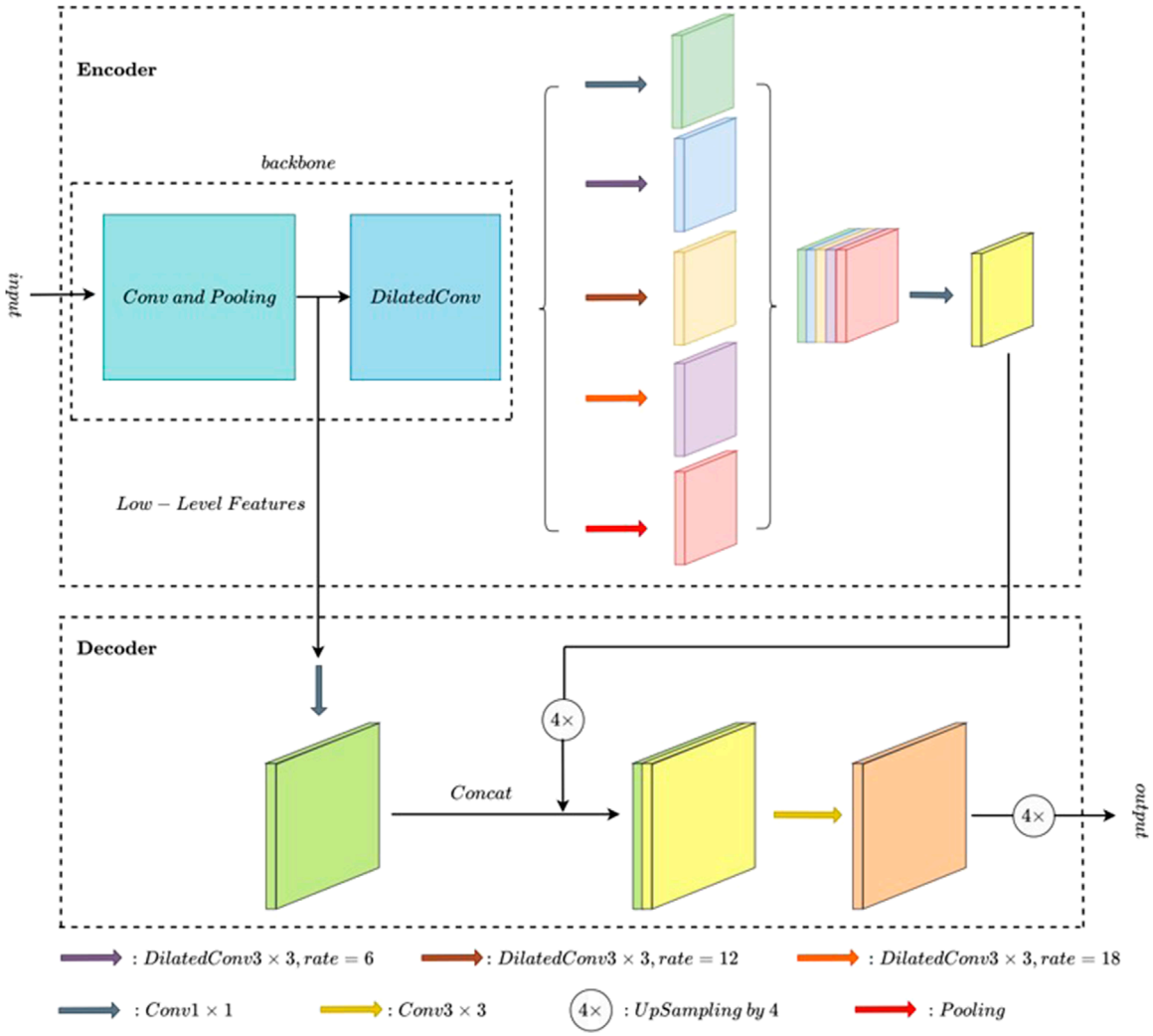

FIGURE 4
DeepLabv3+ model.

channel combination attention module is introduced in the Fully-Convolutional-Networks (FCN) network to refine the fracture characteristics. Extended convolution is used to reduce the loss of crack detail due to pooling operation in encoder networks. In addition, the hinge loss function (Berman et al., 2018) is introduced to apply to small objects. Experimental results showed that it has a better effect.

In 2022, the study of the literature (Zhu et al., 2022) in the UNet model based on intensive connection and supervision mechanism to detect road surface crack, and obtained F1 score of 0.684 and 0.654 on two datasets respectively.

Literature Qu et al. (2022) proposed a convolutional neural network with the method of the transformer to capture the image with more long-term dependence and global context information to detect cracks; the experimental results showed that the method on the three datasets achieved *F1 scores* of 0.86, 0.71, and 0.64, respectively.

In summary, the mainframes of image segmentation in deep learning include the FCN (Long et al., 2015), UNet (Ronneberger et al., 2015), SegNet (Badrinarayanan et al., 2017), and DeepLabv3+ (Chen et al., 2018), as shown in Figures 1–4, respectively. Among them, the FCN (fully convolutional network) classifies the images at the pixel level (Long et al., 2015) to solve the image segmentation problem at the semantic level. Different from classic CNNs (convolutional neural networks), which use the full connection layer after the convolutional layer to obtain the feature vector of fixed length for classification, FCNs accept an input image of any size. The deconvolution layer is used to upsample the feature map of the last convolutional layer to restore it to the same size as the input image so that a prediction can be generated for each pixel while retaining the spatial information in the original input image. Finally, pixel-by-pixel classification is carried out on the upsampled feature map. According to the granularity of its segmentation, FCN8s, FCN16s, and FCN32s can be used, in which FCN32s restore the size of the original input graph from the feature graph sampled 32 times down, and FCN16s and FCN8s recover the size of the original input graph from the feature graph sampled 16 times down and 8 times down, respectively. The smaller the number

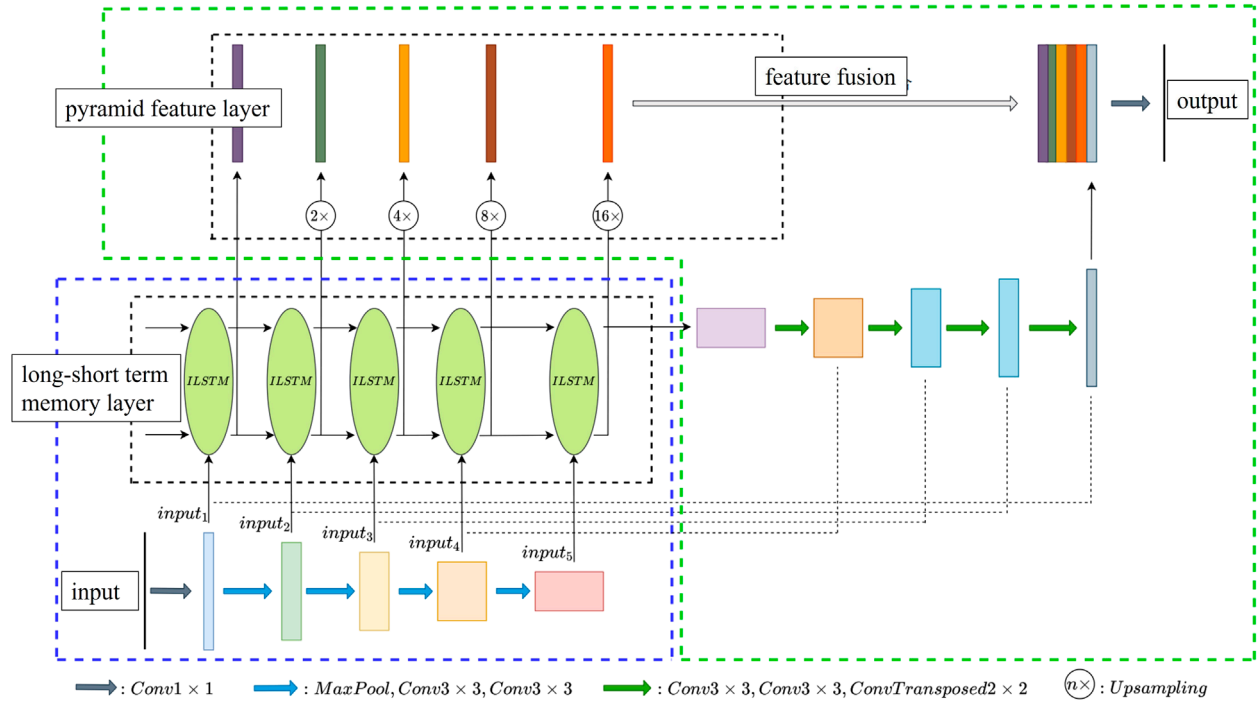

FIGURE 5
PFILSTM model structure.

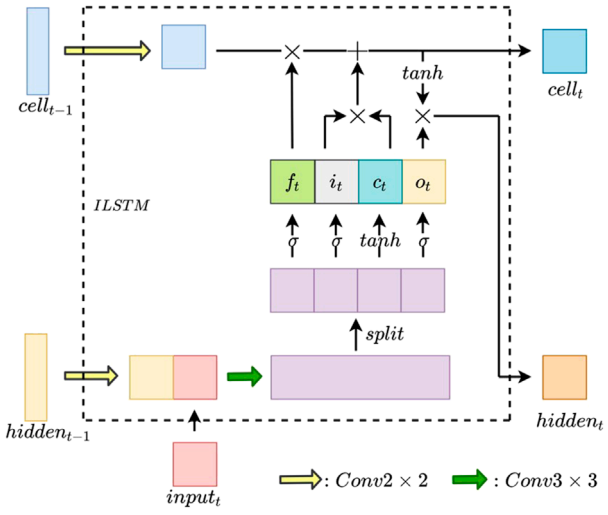

FIGURE 6
ILSTM unit structure.

of the model, the more operations are used in the upsampling and the more complex the corresponding model structure.

The UNet model (Ronneberger et al., 2015) was first released in 2015, and its network topology is shaped like "U." It consists of a contraction path (downsampling) and an expansion path (upsampling). The contraction path is used to capture context Fully-Convolutional-Networks (FCN) information in the image, while the opposite extension path is used to accurately locate the parts that need to be segmented in the image. A total of four times upsampling were performed, and a skip connection was used at the same stage. Compared with FCNs, the UNet model has two differences. First, the FCN model only uses one upsampling operation to restore image resolution, while the UNet model uses four upsampling operations to restore image solution, forming a symmetrical structure with left and right subnetworks. Second, the jump connection of the UNet model uses a vector splicing operation, while the multi-scale fusion of the FCN model uses a vector addition operation.

There is a problem in that the perception field and positioning accuracy cannot be achieved simultaneously in the UNet. When the perception field is large, the dimension reduction multiple of the pooling layer will be increased, which will lead to the reduction of positioning accuracy. However, if the perception field is small, the classification accuracy will be reduced.

The key component of the SegNet model is the decoder network (Badrinarayanan et al., 2017); each decoder corresponds to an encoder. Its main feature is to save the source information of all feature points after the maximum pooling operation in the process of encoding subsampling and achieve the upper sampling by using the index of maximum pooling (anti-pooling) in the process of encoding. The objective is to accurately restore the correct positions of the feature points within the output feature map region. SegNet maximum pooling and noise removal are not considered; the use of two consecutive 4x upsamples to restore resolution also results in less detailed predictions.

The DeepLab model series is a semantic segmentation algorithm proposed by Google. DeepLabv3+ was published in 2018 (Chen et al., 2018). Deeplabv3 + uses atrous convolution to reduce the downsampling rate while maintaining the sensitivity field. The semantics of the final feature map are rich and relatively fine, and the

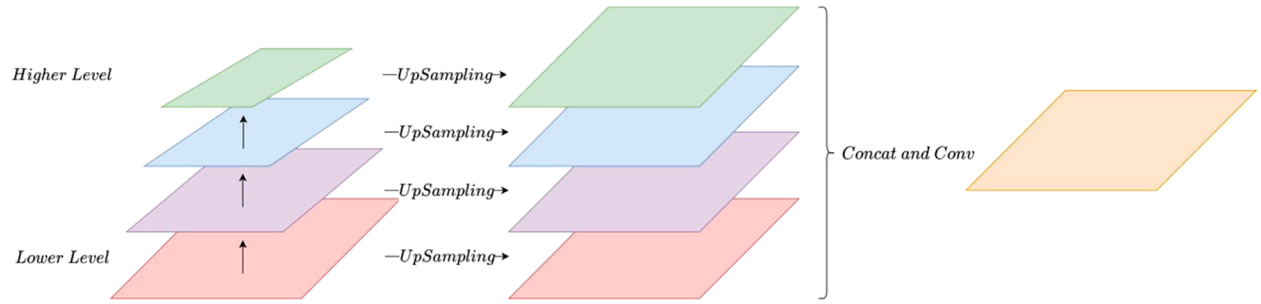

FIGURE 7
Pyramid feature fusion.

TABLE 1 Experimental environment.

Attribute	Value
OS	Ubuntu18.04 kernel 5.4.0-137
CPU	Intel(R) Xeon(R) Platinum 8269CY CPU @ 2.50 GHz
GPU	NVIDIA GeForce RTX 3080 Ti
VRAM	12G
RAM	64G
Python	3.7.10
PyTorch	1.9

original resolution can be restored directly by interpolation. Atrous convolution is one of the keys to the DeepLab model. It controls the receptive fields without changing the size of the feature map, which is advantageous for extracting multi-scale information. The space pyramid module is another key technology in DeepLab's model to further extract multi-scale information.

There is a limit on the size of the input image, which is one of the drawbacks of this architecture.

In summary, the recognition accuracy of the above method is still not ideal, and the evaluation index is low, which is reflected in the difficulty to identify the invisible fine cracks in the image and the sensitivity to the noise in the image. Secondly, the universality of the model is poor, which is reflected in that the model only has a good effect on a certain dataset and cannot achieve good performance on all datasets. Finally, some studies did not use public datasets, making it difficult to compare.

3 The PFILSTM method

As can be seen from the above analysis, the semantic segmentation model is based on the classification model (like the detection model), that is, the CNN is used to extract features for classification.

When the FCN is used to classify each pixel, the relationship between pixels is not fully considered. It also ignores the spatial normalization step used in the segmentation methods based on pixel classification, which lacks spatial consistency. In addition, the way of reusing the encoder feature map in the decoder makes it consume a lot of video memory during testing.

There is a problem with the UNet, that is, it cannot realize both the sensing field and positioning accuracy. When the perception field is large, the dimension reduction multiple of the pooling layer is increased, which leads to the reduction of positioning accuracy. However, if the perception field is small, the classification accuracy is reduced.

SegNet's maximum pooling approach does not consider denoising.

In DeepLabv3+, the size of the input image is a restriction in addition to the calculation requirements, which must have a specific size.

3.1 Overall structure of the model

In order to address the aforementioned problems, this paper introduces a Feature Pyramid Image-based Long Short-Term Memory (LSTM) (PFILSTM). This is a semantic segmentation model for architectural crack images, which leverages memory mechanisms and pyramid features. The main design concept is that the UNet model is adopted, and to retain the dependence between crack pixels during the downsampling process, each layer of long short-term memory is introduced to extract features, aiming to prevent the loss of crack features and interference features. To meet the requirements of multi-scale receptive fields, pyramid feature layers are introduced for fusion. Finally, the two are fused in the last layer of upsampling, so that the lost shallow features can be retrieved from the deep layer of the network, and the recognition ability of the model for fine cracks is further improved.

The overall structure of the PFILSTM model is shown in Figure 5, where the blue box area is the encoder part and the green box area is the decoder part. The PFILSTM adds a long short-term memory layer and a pyramid feature layer based on the UNet model. The difference between the PFILSTM model and the UNet model is that each layer of the PFILSTM model decoder uses the long and short-term memory layer as the input of the pyramid feature layer rather than the output after continuous downsampling. Second, the decoder of the PFILSTM model also integrates the feature map of the pyramid feature layer in the last layer.

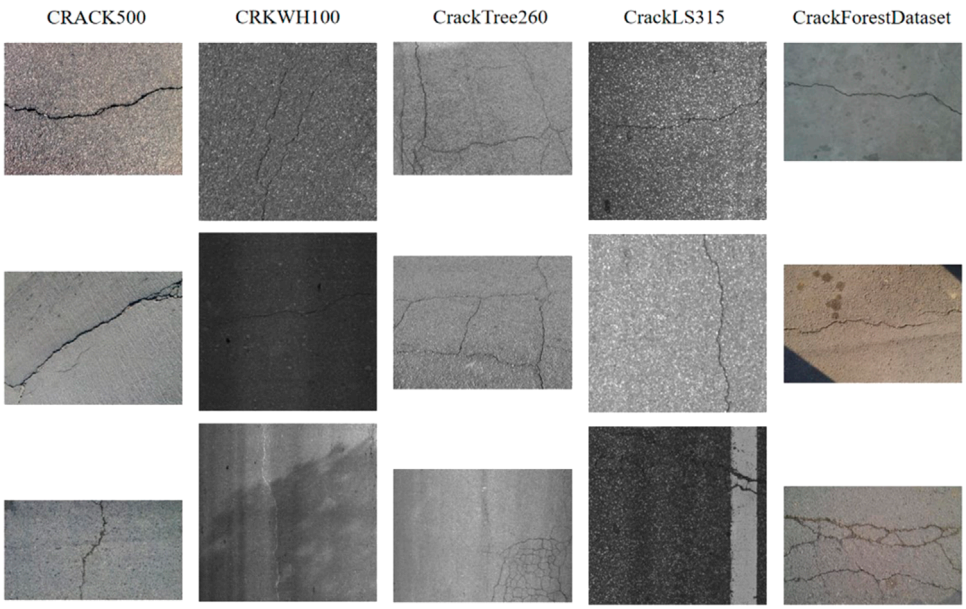

FIGURE 8
Samples from publicly available road crack datasets.

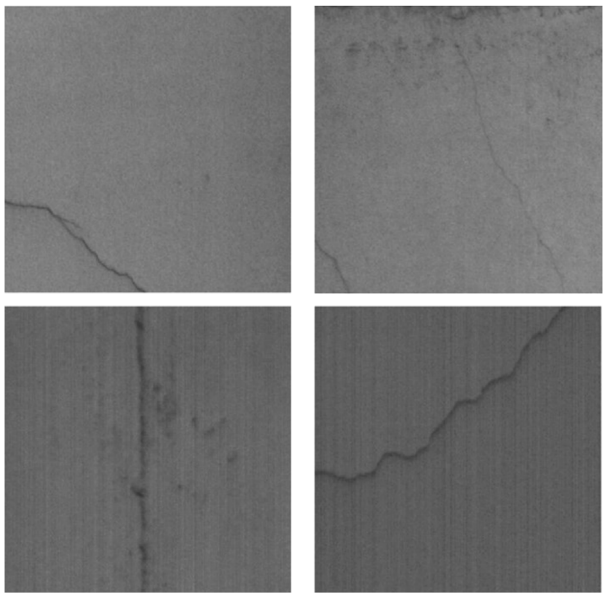

FIGURE 9
Samples of crack images (private dataset) of an abandoned residential building.

The ILSTM (Image-based LSTM) layer and pyramid layer of the PFILSTM model is analyzed in detail.

3.2 ILSTM unit

The network composed of long- and short-term memory units can remember information from different parts of the input sequence and learn the relationship between each element in the input sequence as well as the long-term dependence among them, so that the neural network does not lose the previously learned information and updates the saved information according to the existing information. The LSTM layer possesses the capability to dynamically modify its internal state in response to the input data. This unique feature enables it to adapt to a variety of input data, learning distinct features at various time steps. Given that different images may necessitate unique features for effective segmentation, this adaptability is crucial for the task of segmenting crack images. At present, there have been studies using its memory retention ability to successfully apply it to computer vision tasks, such as image semantic segmentation (Stollenga et al., 2015; Xu et al., 2019) and target tracking (Gao et al., 2019; Liu et al., 2020).

Inspired by the above research, the PFLSTM incorporates an image long-short memory ILSTM unit using convolution operation based on the standard LSTM layer, as shown in Figure 6. A series of ILSTM units are used to model multi-level feature maps at different levels of the same image, learn the correlation between different levels of features, extract important features related to cracks from the image according to the correlation, and filter out the interference information. Similar to standard LSTM cells, ILSTM cells also contain forget gates, input gates, output gates, candidate states, hidden states, and cell states, and the update mechanism is the same; the difference is that ILSTM units do not model the subregions of the same image but the feature maps of the same image at different levels of the convolutional neural network. During model training, each memory unit saves the historical feature information extracted from the same picture so that the subsequent network layer can capture useful historical features from these memory units to help understand the current state and semantics. The memory unit can also filter the interference feature information in the historical feature information according to the current input so that the neural network can make more accurate semantic annotations for the input image.

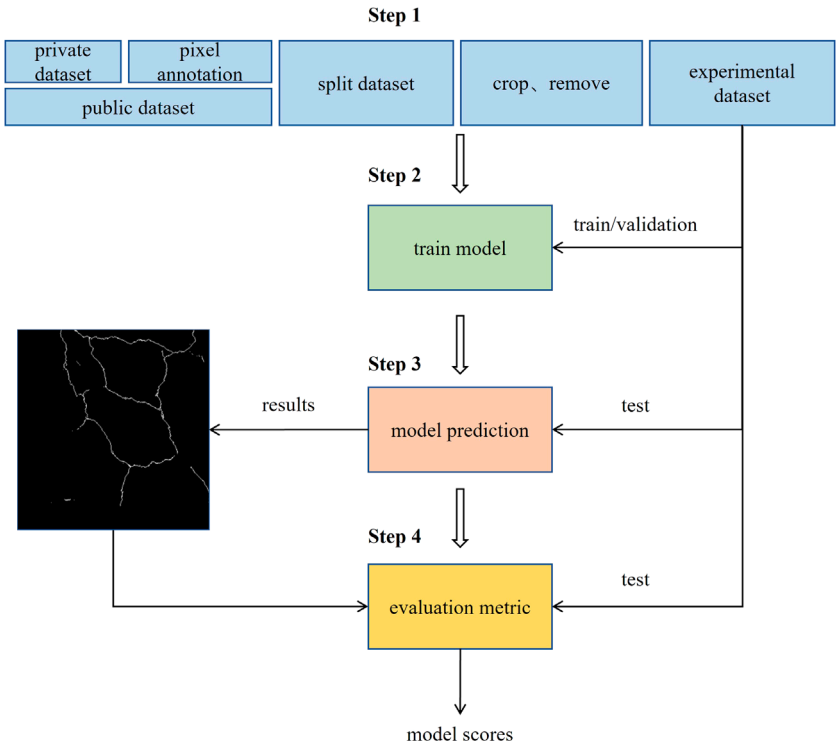

FIGURE 10
Process of experiment.

3.3 Pyramid unit

The current semantic segmentation model either directly adds (FC model) or stitches together (UNET model) the same feature maps from each layer of the encoder and decoder. However, there is a deficiency in passing the feature map from the shallow network to mitigate the impact of reducing feature maps in the deeper network on the edge detail information of the target in the image. However, because the important features of different sizes in the image may appear on the feature diagrams of different scales, it is difficult to identify and divide objects of different scales in the image (Yu and Koltun, 2016; Chen et al., 2017; Zhao et al., 2017). In addition, when detecting the targets with different scales in the image, different degrees of context information also are required (Qu et al., 2022).

The feature maps of targets at different scales extracted from images by the pyramid layer can be used to detect targets in images because each feature map contains different information (Lin et al., 2017). These feature maps with different scales have different receptive fields and contain different levels of context information (Liu et al., 2016). The fusion of these features extracted at different scales can improve the recognition and segmentation ability of the model for objects of different scales. The fusion process is shown in Figure 7. Through the above analysis, it can be seen that when generating the final feature map of the PFILSTM, the feature map information of each layer of the network is fully utilized, which is conducive to eliminating the local features with ambiguity in the low-level feature map, making the edge details of the segmentation results more abundant and less noisy. It also helps to improve the scale robustness and accuracy of the model.

4 Experimental design and experimental results analysis

To test the crack identification effectiveness of the proposed PFILSTM model, two experiments were designed. One was to compare the PFILSTM with the popular FCN8s model, SegNet model, UNet model, and DeepLabv3+ model on multiple datasets. Secondly, the PFILSTM was compared with other studies using the same evaluation indicators and datasets.

4.1 Experimental environment

All experimental models were developed and trained utilizing Python version 3.7.10 within the Pytorch framework. The computational resources employed included an Intel® Xeon® Platinum 8269CY CPU, 64GB of RAM, and an NVIDIA Geforce RTX 3080 Ti graphics card equipped with 12GB of memory. Comprehensive specifications are tabulated in Table 1.

4.2 Datasets and their preprocessing

Concrete buildings can be mainly divided into bridges, roads, and buildings. Limited by space, this paper starts with the

TABLE 2 The dataset preprocessing segmentation results.

Dataset name	Total number of the images	Cut size	Cut step size	Partition type	Partition quantity
BUILDINGS	200	360 × 360	360	Train	1,032
				Validation	318
				Test	341
CRACK675	675	360 × 360	120	Train	2,977
				Validation	2,207
				Test	2,194
CRACK500	500	360 × 360	360	Train	3,044
				Validation	542
				Test	2,623
CFD	118	160 × 160	160	Train	492
				Validation	72
				Test	144

TABLE 3 Confusion matrix.

Predicted values	Actual values	
	Positive (1)	Negative (0)
Positive (1)	TP	FP
Negative (0)	FN	TN

concrete public crack dataset and combines private residential buildings and roads crack datasets to conduct experiments and analysis.

4.2.1 Public and private dataset

For concrete road cracks, several open datasets of the CRKWH100 (Zou et al., 2019; Lau et al., 2020), CrackTree260 (Lau et al., 2020), CrackLS315 (Zou et al., 2019), CRACK500 (Yang et al., 2019), and CrackForestDataset (CFD) (Cuilimeng, 2023) were adopted. Finally, these datasets were integrated according to their characteristics. Some images of each dataset are shown in Figure 8.

Among them, the CRACK500 dataset comes from the crack images of concrete roads in literature (Yang et al., 2019), and the total number of crack pixels in each image is more than 1,000. The dataset was divided into a training set, verification set, and test set, which contain 3,792, 696, and 2,248 images, respectively, totaling 6,736 images.

The CFD dataset, which is open source on Github, is small and contains only 118 images of cracks in urban concrete roads with a resolution of about 480 × 320.

The images in CRKWH100 and CrackLS315 were taken using linear array cameras and contain 100 and 315 images of road cracks, respectively. CrackTree260 contains 260 images of road cracks taken using a front array camera. In this paper, these three datasets were combined and named the CRACK675 dataset.

After the above integration, the final datasets used in the experiment are BUILDINGS, CRACK675, CRACK500, and CFD. Among them, the BUILDINGS dataset is the private dataset manually marked in this paper and the CRACK675 dataset contains many pictures of fine cracks. The CRACK500 dataset contains more wide-crack images, while the CFD dataset contains the least number of images and has the lowest resolution. The four datasets have different styles that allow for a more comprehensive assessment of the model's performance in different scenarios.

Our private Residential Building Crack Dataset comprises 200 high-resolution images of fissures in deserted residential structures. These images, captured by our research team using state-of-the-art industrial cameras, are of 1,000 × 1,000 pixel resolution. Each image has been meticulously annotated with relevant labels by a team of researchers. To ensure the utmost accuracy of these annotations, we have implemented a rigorous cross-validation process on this proprietary dataset.

4.2.2 Dataset preprocessing

Preprocessing included two steps: first was the annotation of the private dataset; the second was image size cutting.

The images in the private dataset were manually marked by LabelMe software (Labelme, 2023) to obtain the crack image dataset of residential BUILDINGS

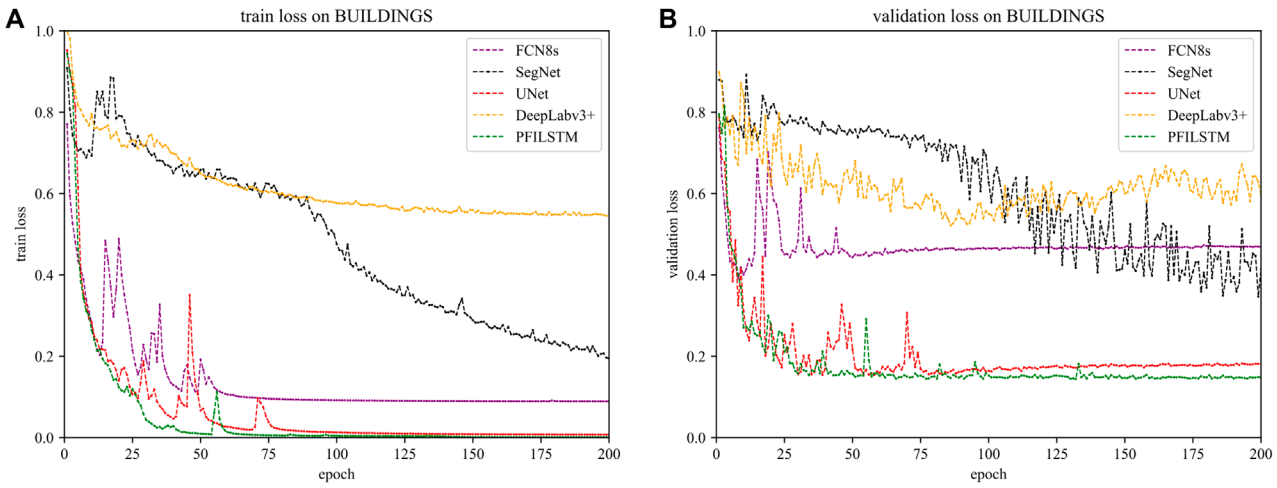

FIGURE 11
The loss of training processes **(A)** and verification process **(B)** on the BUILDINGS dataset.

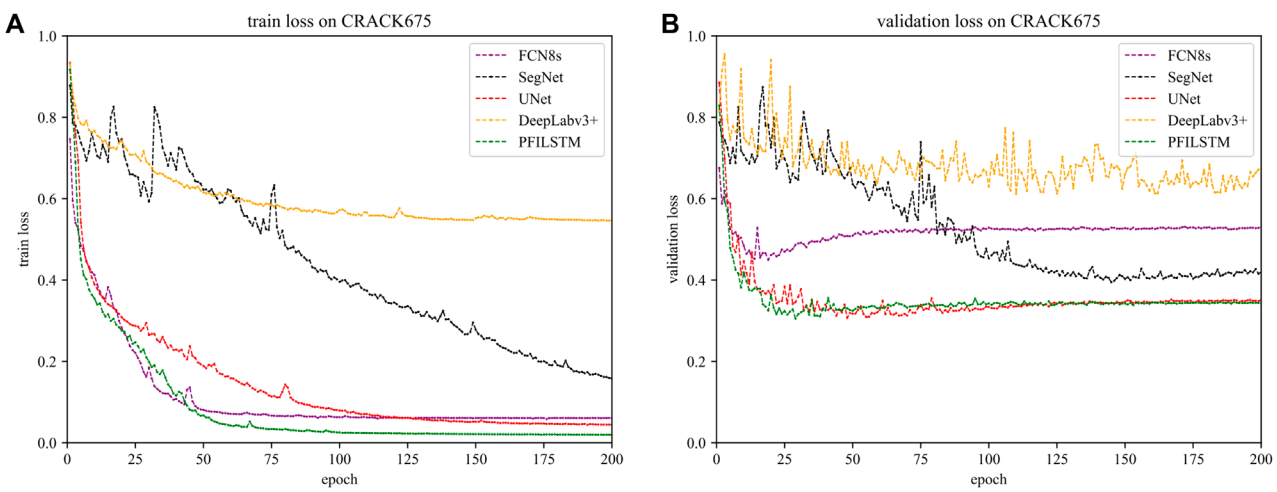

FIGURE 12
Training **(A)** and verification **(B)** loss on the CRACK675 dataset for each model.

used in the experiment, hereinafter referred to as the Buildings dataset.

However, the images in Figures 9, 10 have different sizes and resolutions, which will affect the subsequent deep learning algorithm, so they need to be converted into a standard format with uniform size and resolution. The pre-processing process is as follows:

(1) Divide the dataset into the training set, verification set, and test set.
(2) Cut the dataset according to the fixed size.
(3) Eliminate the images without cracks.

Since the CRACK500 dataset is pre-divided into training, verification, and test sets, the process for the CRACK500 dataset does not include step (1). At the same time, to maintain the original characteristics of the CRACK500 dataset, images with less than 1,000 crack pixels are removed in step (3). Table 2 shows the final partitioning results after data set preprocessing.

4.3 Process of experiment

The experimental process is shown in Figure 10. The first step is to build the dataset for the experiment, as described in Section 4.2. The second step is the training of the model so that each model is trained on the same dataset. The third step is to use trained models to make predictions. The final step is to calculate the score of the predicted results of each model according to the evaluation index.

To compare the performance of various models, the FCN8s, UNet, SegNet, and DeepLabv3+, the PFILSTM model proposed in this paper is used to conduct experiments on the dataset

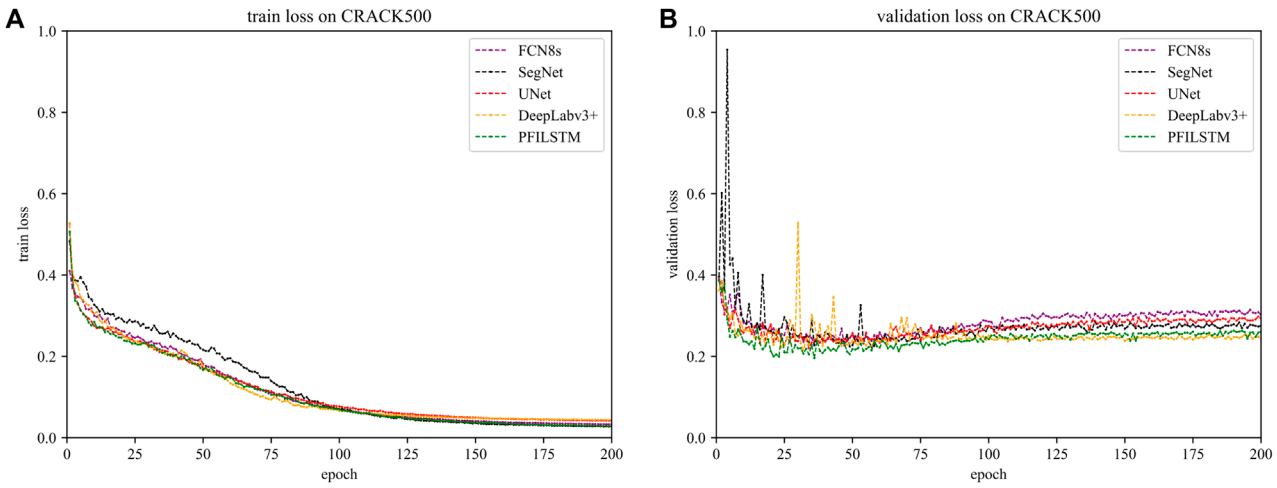

FIGURE 13
Training **(A)** and verification **(B)** on the training of each model on the CRACK500 dataset.

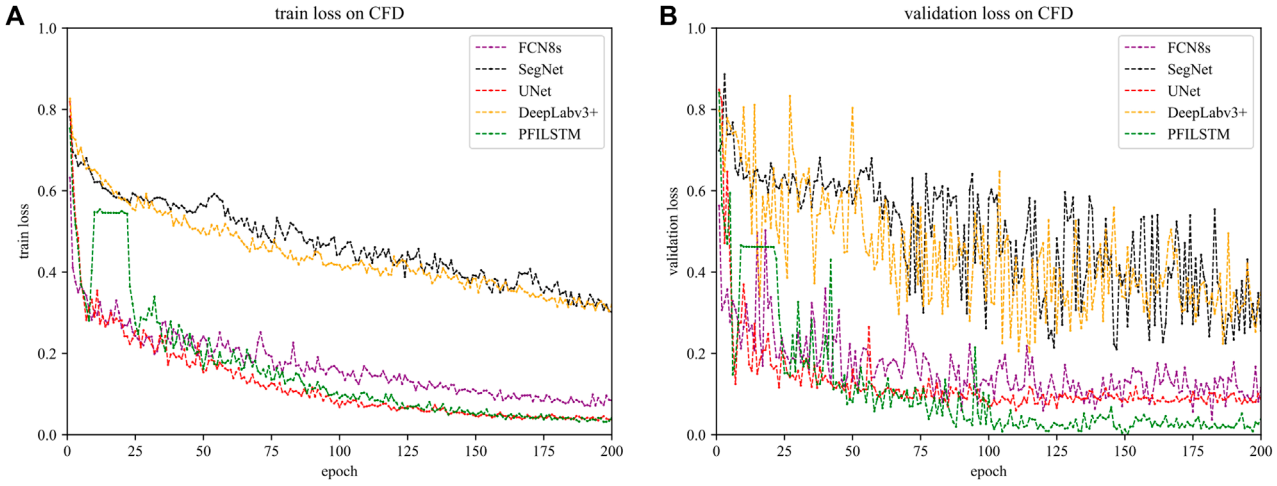

FIGURE 14
Training **(A)** and verification **(B)** loss of each model on CFD datasets.

in Section 4.2, and the hyperparameters of each model in the experiment are adjusted from various aspects. The hyperparameters of each model in the experiment are adjusted from various perspectives to ensure that all models are ultimately obtained under relatively optimal conditions in all aspects. Finally, batch_size was determined to be 8, the learning rate was 0.00075, and the learning rate attenuation coefficient was 0.875. In the experiment, each model was trained on all datasets for a maximum of 200 rounds, and the learning rate was attenuated when the loss on the verification set did not decrease for five consecutive rounds. Because the data in the training set, verification set, and test set do not have exactly the same distribution, a model that performs well on the verification set in a certain round does not necessarily mean that it performs well on the test set, so the experiment uses the optimal results in the last 10 training rounds in the model prediction evaluation stage.

4.4 Loss functions and optimizers

It is not difficult to see that the number of background pixels in the crack image far exceeds the number of crack pixels. For this imbalance distribution, the loss function Dice loss (Milletari et al., 2016) has been shown to handle this type of dataset well. It is a loss function for image segmentation tasks, and the basic idea is to calculate the overlapping part of the predicted result and the real result and optimize the model by minimizing the difference between the two.

The optimizer uses Adam (Kingma and Ba, 2015). It is a momentum-based algorithm which uses the historical gradient information of each parameter to ensure a smooth iteration. Compared to other optimizers, the Adam optimizer is less sensitive to the initial learning rate and the selection of hyperparameters, so it is easier to use. In addition, the Adam optimizer can converge

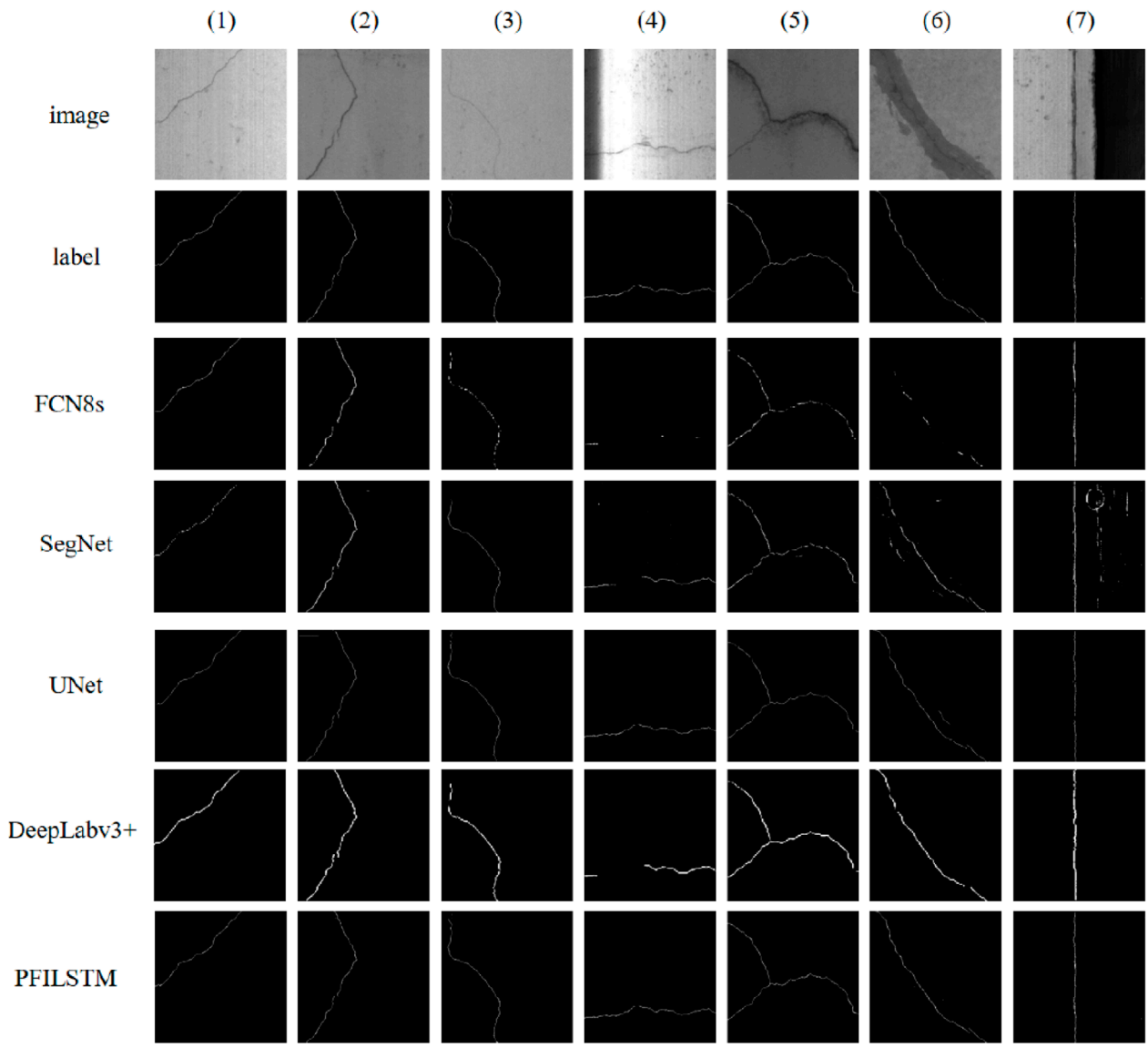

FIGURE 15
Part of the prediction results of each model on the Buildings dataset.

quickly to the optimal solution, especially when dealing with large-scale data and high-dimensional parameters, and it can better adapt to different datasets and models.

4.5 Evaluation index of quantitative analysis

The *F1score*, the mean intersection over union (mIoU), and the confusion matrix as shown in Table 3 are commonly used as indicators of the image semantic segmentation model. Next, we will separately delve into the interconnectedness and computational methodologies of three distinct evaluation metrics.

The confusion matrix serves as the foundation for computing the F1 score and mIoU, effectively highlighting the discrepancies between the pixel blocks of the model's forecasted image and the labeled image, where T/F means that the prediction result is correct/wrong and P/N means that the sample is predicted to be correct/wrong. The combination of the two results produces four kinds of results: TP, TN, FP, and FN. The accuracy rate of prediction is defined as the proportion of samples with correct prediction results in the total number of samples, and its calculation method is shown in Formula 1. The Precision is defined as the proportion of true positive samples among the samples predicted as positive. And the calculation method as shown in Formula 2:

$$Accuracy = (TP + TN)/(TP + TN + FP + FN) \quad (1)$$

$$Precision = TP/(TP + FP) \quad (2)$$

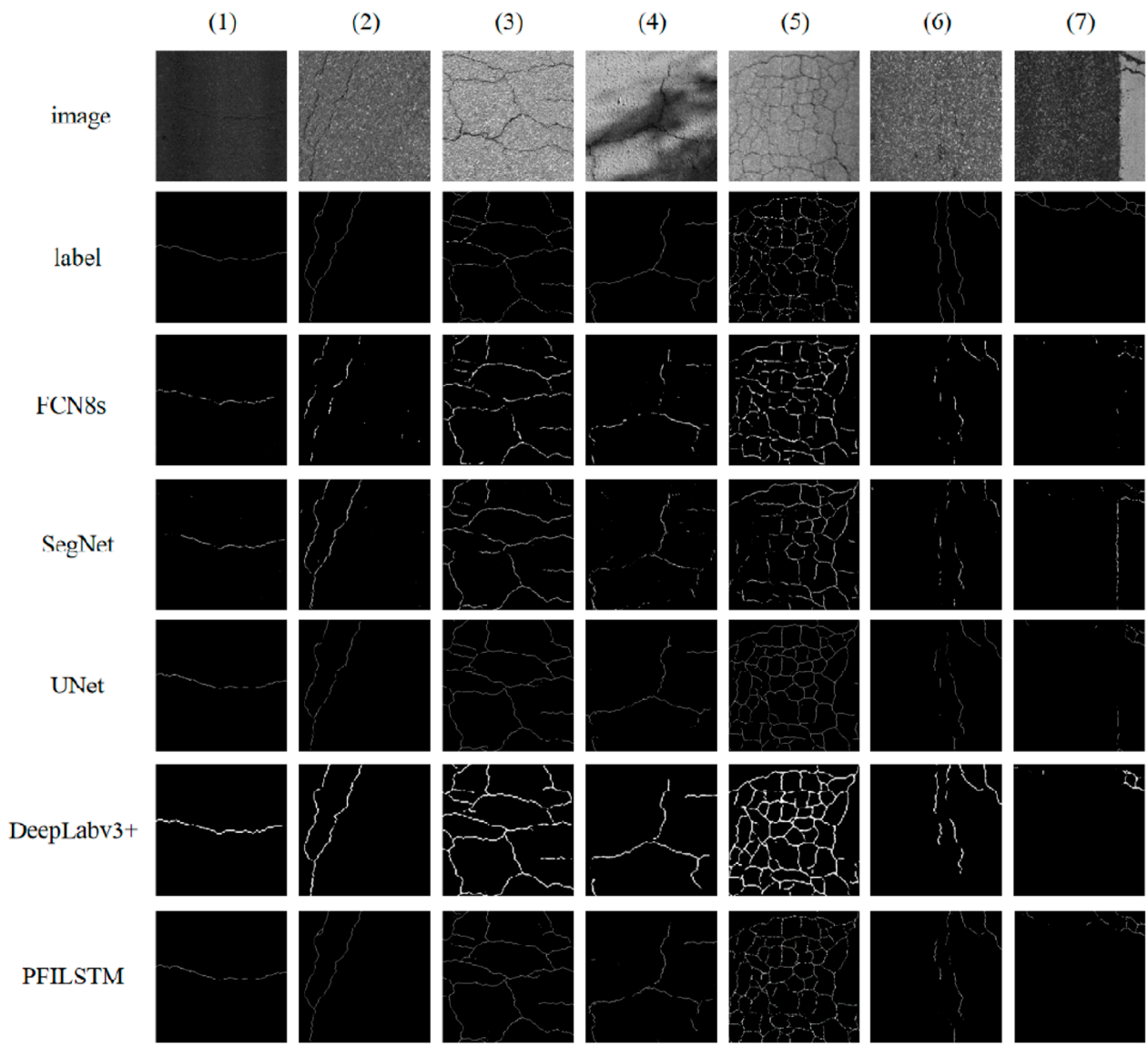

FIGURE 16
Part of the prediction results of each model on the Crack675 dataset.

The predicted recall rate is defined as the proportion of the samples that are positive samples that are predicted to be positive the calculation method as shown in Formula 3:

$$Recall = TP/(TP + FN) \tag{3}$$

Typically, precision and recall are considered contradictory measures bound by a certain degree of mutual constraint. To encapsulate the learner's performance in terms of precision and recall more effectively, we introduce the $F1_{score}$, which is the harmonic mean of precision and recall. This score amalgamates the two evaluation indicators. The calculation method as shown in Formula 4, its calculation precision rate and recall rate of harmonic mean, Only when both precision rate and recall rate are high, the harmonic mean F1score will be higher.

$$F1_{score} = 2 \times Precision \times Recall/(Precision + Recall) \tag{4}$$

Unlike F1, MIoU measures the performance of the model from another perspective, using the calculation of the intersection and union of two sets as the evaluation metric. In the semantic segmentation problem, the two sets are the sample set that is truly positive and the sample set that is predicted to be positive. The mIoU is calculated by the confusion matrix, as shown in Formula 5.

$$mIoU = (1/k)\left(\sum_{i=1}^{k}\left(TP_i/\left(TP_i + FPi + FN_i\right)\right)\right) \tag{5}$$

When the semantic segmentation of the cracks of the building, there is a highly unbalanced distribution of the number of pixels between cracks and background likely, more than 90% of the pixels in the crack image belong to the background, and the calculation result of Eq. 5 is usually high, so using the *F1score* to measure the prediction is somewhat more convincing than using the mIoU.

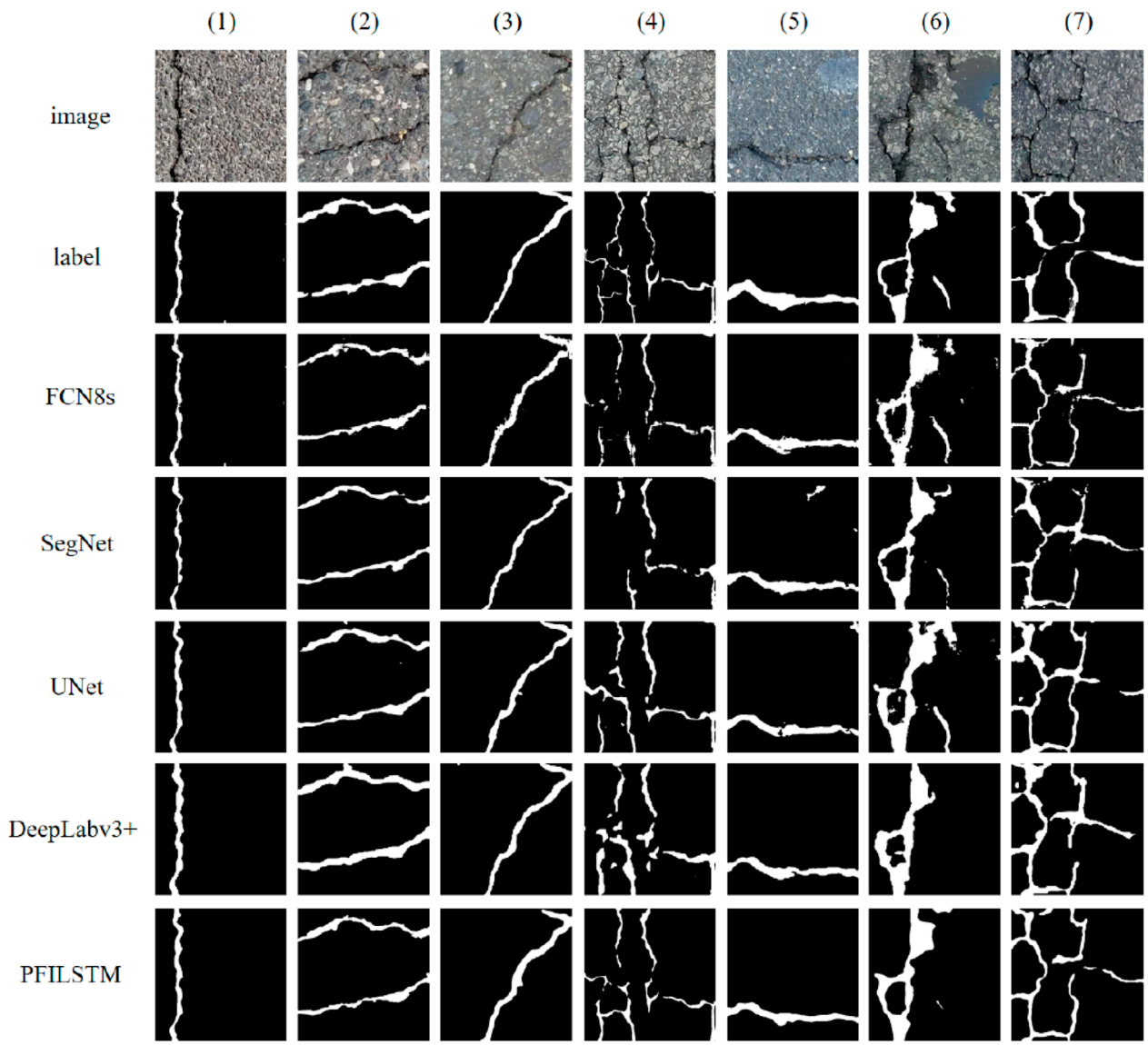

FIGURE 17
Partial predictions of each model on the CRACK500 dataset.

4.6 Training and prediction process

Figures 11–14 are the average loss curves of each model in the BUILDINGS dataset, CRACK675 dataset, CRACK500 dataset, and CFD datasets. The subdiagram (a) on the left is average training loss on the set, the subdiagram (b) on the right is the average validation loss on the set.

It can be seen from Figure 11 that on the Buildings dataset, after 200 rounds of iteration, in contrast, the UNET model and the PFILSTM model training loss have fallen to a very low, but the PFILSTM model has the lowest verification loss. The training loss of the SEGNET model continues to decline. The DeepLabv3+ model is the model with the highest training loss and verification loss.

It can be seen from Figure 12A that on the CRACK675 dataset, the FCN8S model and the PFLSTM model reached fit in about 50 rounds of training, and the training loss and verification loss will be slowly reduced. To converge, the SEGNET model still has a downward trend after 200 rounds of training, but the validation loss curve does not change after 125 training rounds. It can also be seen from Figure 12B that although the training loss is relatively low, the verification loss is relatively high. This is not an overfitting phenomenon, because the verification loss and training loss curve of the FCN8S model are synchronized. In the first 40 rounds of model training, both training loss and validation loss are declining, and there is not much fluctuation afterward. The reason for this phenomenon may be that it is not uniform when dividing the dataset. There is a large gap between the distribution of training images and verification images, resulting in the FCN8S model not learning the relevant characteristics of the test set image from the training set. The PFILSTM and UNET models have low final training

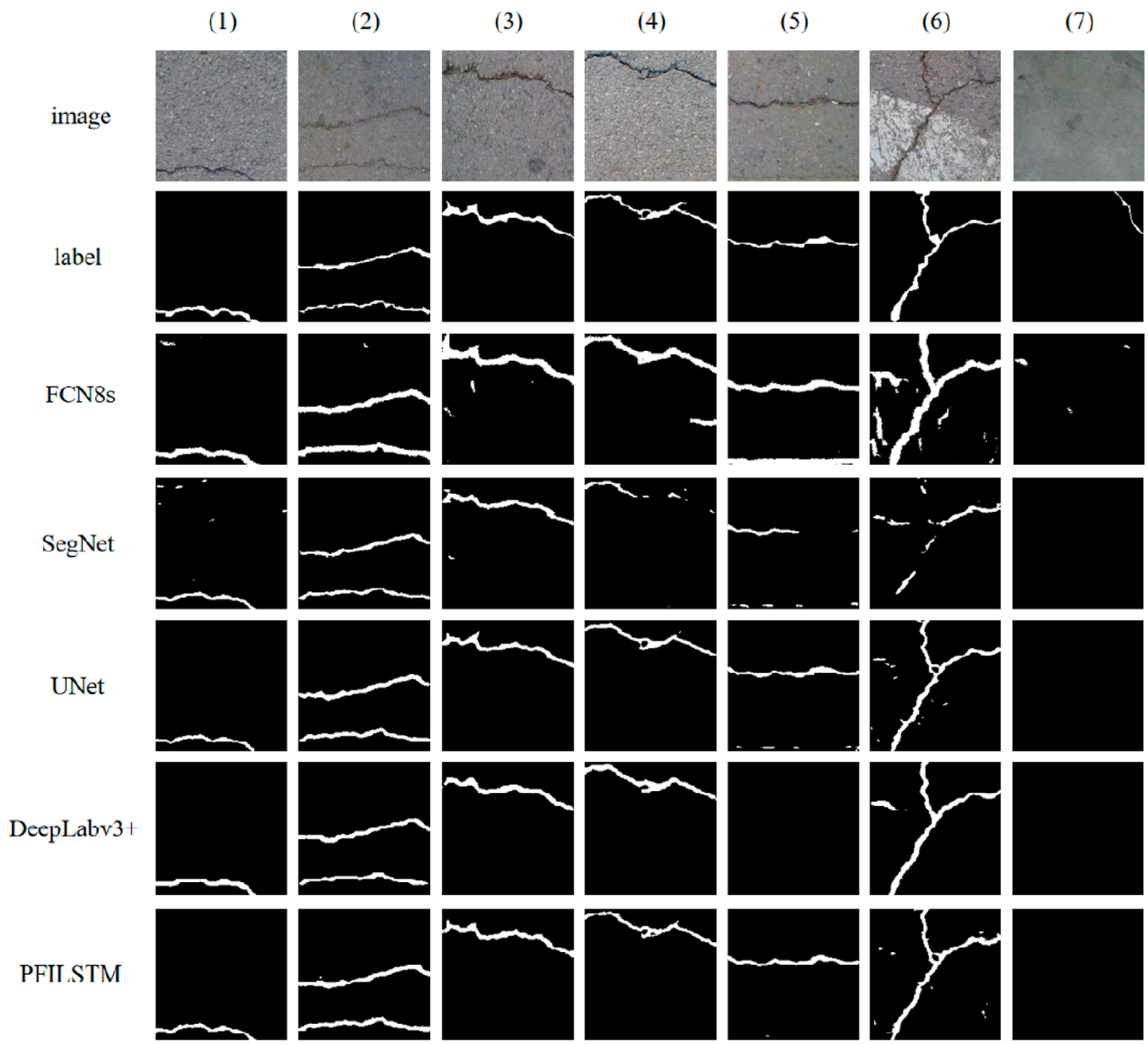

FIGURE 18
Partial predictions for each model on a CFD dataset.

loss and verification loss. In contrast, PFILSTM performance is better.

It can be seen from Figure 13 that on the CRACK500 dataset, the training loss curve and verification loss curve change of the five models in the experiment are the same. SegNet verified that the loss fluctuated in the first 10 rounds of training, and the DeepLabv3+ model also appeared. It can be speculated that this was caused by a slightly higher initial learning rate because, after 25 rounds and 100 rounds of training, all models were verified. The average losses on the set and the training set have almost no significant fluctuations.

It can be seen from Figure 14 that the verification loss of the FCN8S model on the CFD dataset is also declining. It is speculated that the reason for this phenomenon is that the number of images in the CFD dataset is small and the style is relatively singular, while the CRACK675 dataset is composed of three types of datasets with a large number and changing style. Therefore, the FCN8S model can easily learn the relevant features from the training set image of the CFD dataset to fit the verification set. The volatility of the verification of the loss curve becomes larger because the number of images of the CFD dataset is too small. After 200 rounds of training, the UNET and PFILSTM models are the lowest in training. The loss of PFLSTM model is the lowest, which verifies that its strongest detection ability.

4.7 Result analysis

Figures 15–18 lists some of the prediction results on the models on the Buildings, Crack675, Crack500, and CFD datasets, and the performance of each model is judged according to subjective intuition and experience.

In Figure 15, the FCN8S model leaks more cracks, especially in images 4 and 6. The SegNet model also leaks prediction in the fourth

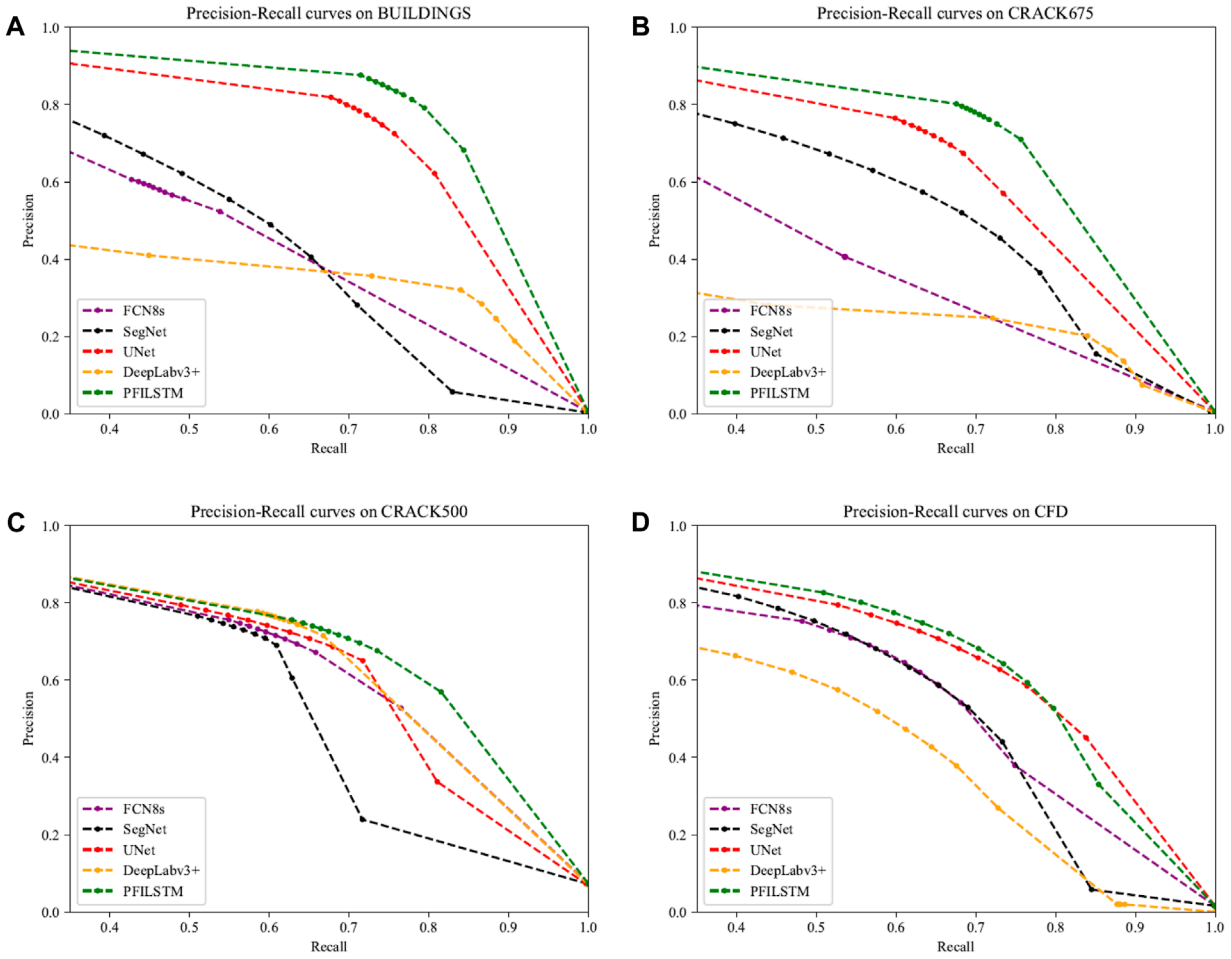

FIGURE 19
PR curves for each model on the four data sets.

column, but its main problem is that it is easy to be disturbed. The interference identification is identified as cracks on the images in columns 6 and 7. The UNET model has a few predictions error on the column 6 images. DeepLabv3+ models have not all the cracks are predicted on the fourth column image, and the PFILSTM model predicts all cracks.

The FCN8s model's predictions are found to be deficient in crack representation, thereby overlooking numerous intricate details of the cracks. This could potentially be attributed to the model's approach when handling complex scenarios such as concrete cracks. It employs multiple rounds of downsampling and upsampling, which diminishes the resolution of the output image. This results in a loss of detailed information about the cracks and introduces a blurring effect. Furthermore, the model's convolutional network structure might have an inadequate receptive field size, hindering its ability to perform precise segmentation. Consequently, the model's predictions suggest a lack of sufficient learning of crack characteristics, rendering it incapable of identifying all the detailed features of the cracks in the image.

The prediction results of the SegNet model exhibit more noise compared to other models, which could be a detrimental effect of "up-pooling." Given the uneven surface of concrete roads and the presence of disturbances such as stains and shadows that are not cracks, these pseudo-cracks interfere with the neural network's learning of correct crack features during the model's learning process. This ultimately leads to the model learning some noise features and making predictions based on them. The encoder of the SegNet model is likely to "store" some noise locations during pooling, and subsequent sampling operations use these locations to restore the resolution of the image. Therefore, this model cannot effectively filter out the noise in the image, ultimately learning the features of the noise and displaying them in the prediction result map.

The prediction results of the UNET model lack a few cracks, but roughly determine the location of all cracks in the image.

The Crack675 dataset is a dataset composed of three datasets and the visual gaps between each model can be seen in Figure 16.

The prediction results of the DeepLabv3+ model are wider than the cracks in the label image. This analysis may have occurred because the decoder uses four times the sampling four consecutive times, causing the model to lose the detailed information on the crack edge.

From a subjective perspective, the prediction results of the PFILSTM model are generally better than the prediction results of

TABLE 4 Experimental results for each model on four datasets.

Dataset	Model	Accuracy	Precision	Recall	$F1_{Score}$	mIoU
Buildings	FCN8s	0.9961	0.5229	0.5380	0.5304	0.6785
	SegNet	0.9964	0.5547	0.5496	0.5521	0.6888
	UNet	0.9980	0.7729	0.7222	0.7467	0.7969
	DeepLabv3+	0.9959	0.3565	0.7285	0.4787	0.6472
	PFILSTM	**0.9986**	**0.8255**	**0.7680**	**0.7957**	**0.8152**
CRACK675	FCN8s	0.9941	0.4056	0.5364	0.4619	0.6472
	SegNet	0.9964	0.5736	0.6330	0.6019	0.7134
	UNet	0.9974	0.7093	0.6563	0.6818	0.7743
	DeepLabv3+	0.9884	0.2473	**0.7208**	0.3683	0.6070
	PFILSTM	**0.9976**	**0.7713**	0.7164	**0.7382**	**0.7913**
CRACK500	FCN8s	0.9514	0.6719	0.6581	0.6649	0.7235
	SegNet	0.9513	0.6900	0.6090	0.6470	0.7136
	UNet	0.9538	0.6866	0.6792	0.6829	0.7349
	DeepLabv3+	0.9573	**0.7152**	0.6675	0.6906	0.7413
	PFILSTM	**0.9579**	0.6963	0.7130	**0.7046**	**0.7498**
	CrackT-net (Gao et al., 2019)	—	—	—	0.6370	—
	(Chen et al., 2018)	—	—	—	—	0.7360
	CrackU-Net (Xu et al., 2019)	—	0.6500	**0.7720**	0.6840	—
	ACNet (Badrinarayanan et al., 2017)	—	0.6805	0.7489	0.6982	—
CFD	FCN8s	0.9888	0.6454	0.6105	0.6275	0.7229
	SegNet	0.9893	0.6816	0.5744	0.6234	0.7210
	UNet	0.9901	0.6818	**0.6787**	0.6803	0.7527
	DeepLabv3+	0.9844	0.5751	0.5267	0.5499	0.6817
	PFILSTM	**0.9908**	**0.7208**	0.6661	**0.6924**	**0.7601**
	(Chen et al., 2018)	—	—	—	—	0.6200

The bold values indicate the model presented in this paper.

all other models: in the first column image with lower brightness, all models can accurately predict the position of the crack; the FCN8S model is the only one that did not completely predict the cracks; the fourth column is an image of a crack with shadows. Apart from the PFILSTM model, none of the other models were able to successfully predict this image. Interestingly, the crack in the sixth column is so subtle that it is even unrecognizable to the human eye, yet all models managed to predict the location of the crack to some extent. In the seventh column image, both the SegNet model and the UNET model incorrectly predicted the presence of cracks in the sidewalk image where there were none. In contrast, the PFILSTM model predicts all the cracks, except for the cracks in columns 6 and 7 of the image there are some that are not fully predicted.

In Figure 17, all models have leakage prediction on the images in column 4, but the PFILSTM model has the least number of cracks predicted by leakage. The SegNet model predicted significant noise in the upper right of the image in column 5 under the influence of interferers; the DeepLabv3+ model and the PFILSTM model did not predict the crack in the lower right corner of the image in column 6; the cracks predicted by the PFILSTM model in the seventh column mesh image have stronger continuity.

In Figure 18, the FCN8s and SegNet models predicted more noise. The UNet model also showed noise on the predictions of images in columns 5 and 6; the FCN8s model predicts the interference under the image in column 5 as a crack; in column 6, although all models are affected by sidewalks, making the predictions noisy, the PFILSTM model gives the clearest predictions and the least interference. None of the models accurately predicted cracks in the seventh column image, which may be because the CFD dataset is too small.

The qualitative analysis above is a subjective evaluation. Figure 19 shows the precision-recall curve (PR curve) for each model on the four datasets. The closer the PR curve is to the upper right corner of the table, the larger the area enclosed by the coordinate axis, which represents the better the overall performance of the model.

In Figure 19, the PFILSTM model presented in this paper shows the greatest advantage, and the PR curves on the four datasets of the experiment are the closest to the upper right corner of the table, indicating that its performance is the best in the comparison model. In addition, the PR curves of the DeepLabv3+ model in Figures 19A, B are closest to the axes, which indicates poor performance. However, as can be seen from Figures 15, 16, the DeepLabv3+ model accurately predicts the location of the crack, but it is wider than the crack on the label, which results in a high recall, low accuracy, and therefore low overall performance, which is supported by the distribution of the individual data points in the graph. On the CRACK500 dataset with wide cracks, it can be seen from Figure 19C that the DeepLabv3+ model also performs well. In Figure 19D, it can be seen that the PR curves of the UNet model and the PFILSTM model are relatively close, so their performance is not far different on the CFD dataset.

Table 4 shows the accuracy, precision, recall, F1 score, and mIoU data of the four datasets: FCN8s, SegNet, UNet, DeepLabv3+, the PFILSTM model proposed in this paper, as well as the models from the literature (Cao et al., 2020; Xiang et al., 2020; Zhu et al., 2022; Qu et al., 2022), using the same evaluation indices and datasets.

As can be seen from Table 4, the PFILSTM model proposed in this paper is optimal for both the F1score and mIoU on the four datasets. On the CRACK675 dataset, the F1score and mIoU of the PFILSTM model reached 0.7382 and 0.7913, respectively, which is 8.27% and 2.20% higher than the next highest UNet model, respectively. On the CRACK500 dataset, the F1score and mIoU of the PFILSTM model reached 0.7046 and 0.7498, respectively, which is 2.03% and 1.15% higher than the next highest DeepLabv3+ model, respectively. On the CFD dataset, the PFILSTM model F1score and mIoU reached 0.6924 and 0.7601, respectively, which is 1.78% and 0.98% higher than the next highest UNet model, respectively.

Compared with other methods of researchers using the same evaluation index and dataset, the F1score of the PFILSTM model is improved by 10.61% compared with the CrackT-Net (Qu et al., 2022) on the CRACK500 dataset. Compared with the literature (Xiang et al., 2020), the mIoU of the PFILSTM model is improved by 1.88%.

Compared to the CrackU-Net (Zhu et al., 2022), the $F1_{score}$ of the PFILSTM is 3.01% better. Compared to the ACNet (Cao et al., 2020), the F1score of the PFILSTM model is improved by 0.92%. Compared to the CrackU-Net (Zhu et al., 2022), *F1score* is 3.01% higher. Compared to the ACNet (Cao et al., 2020), the $F1_{score}$ of the PFILSTM model is 0.92% higher.

On the CFD dataset, the mIoU of the PFILSTM model increased by 22.60% compared to the literature (Xiang et al., 2020). On the BUILDINGS dataset, the F1score and mIoU of the PFILSTM model reached 0.7957 and 0.8152, respectively, which is 6.56% and 2.30% higher than the next highest UNet model, respectively.

It can also be seen from the table that the UNet model is suboptimal on the three datasets, the CRACK675, CFD, and BUILDINGS. The FCN8s model and DeepLabv3+ model are more suitable for the CRACK500 datasets, but their performance on other datasets is not good. The performance of the SegNet model does not have many bright spots.

Comprehensive analysis of experimental comparison results shows that the PFILSTM model designed in this paper can learn better crack features and can better eliminate the influence of interference factors in the image, which is a great improvement on the problems of the low recognition accuracy and poor robustness in existing studies.

5 Conclusion

Focusing on the problems of low accuracy and poor robustness in existing building crack identification research, this paper proposes a PFILSTM model. Based on the "U" model, the model introduces the advantages of long short-term memory mechanisms and pyramid features, uses the memory mechanisms to learn the correlation between features at all levels of the image, optimizes the crack feature information, screens the interference feature information, and then uses the pyramid feature to further integrate the multi-scale context information, so that the final semantic segmentation result is better.

To test the effect of the PFILSTM model, the comparison experiments with the FCN8s, SegNet, UNet, DeepLabv3+, and literature (Cao et al., 2020; Xiang et al., 2020; Zhu et al., 2022; Qu et al., 2022) models were completed on three public datasets and one private dataset, and the qualitative and quantitative analysis results showed that the PFILSTM model had the best effect.

As for the CFD and CRACK500 datasets, the effect of the PFILSTM model does not differ from other models, indicating that there is still room for improvement in the model designed in this paper, and this problem will continue to be studied in the future.

Data availability statement

The original contributions presented in the study are included in the article/Supplementary Material, further inquiries can be directed to the corresponding authors.

Author contributions

BC: Writing–original draft, Funding acquisition. MF: Writing–original draft. KL: Writing–review and editing. YG: Writing–original draft. YW: Writing–review and editing. YC:

Validation, Writing–review and editing. SY: Writing–review and editing. JS: Writing–review and editing.

Funding

The author(s) declare financial support was received for the research, authorship, and/or publication of this article. This work was supported by the Fund of National Engineering and Research Center for Mountainous Highways (GSGZJ-2022-04), Key Laboratory of Wind Resistance Technology of Bridge Structure and Transportation Industry (Tongji University) open project (KLWRTBMC22-01), Chongqing Construction Science and Technology Plan Project (2023-0069), Water Resources Science and Technology Program of Hunan Province (XSKJ2023059-32), and National Science Foundation of China (60272091, 60373109, and 51808075).

Conflict of interest

The authors declare that the research was conducted in the absence of any commercial or financial relationships that could be construed as a potential conflict of interest.

The reviewer XL declared a shared affiliation with the author KL to the handling editor at the time of review.

Publisher's note

References

Asadi Shamsabadi, E., Xu, C., Rao, A. S., Nguyen, T., Ngo, T., and Dias-da-Costa, D. (2022). Vision transformer-based autonomous crack detection on asphalt and concrete surfaces. *Automation Constr.* 140, 104316, 104316. doi:10.1016/j.autcon.2022.104316

Badrinarayanan, V., Kendall, A., and Cipolla, R. (2017). Segnet: a deep convolutional encoder-decoder architecture for image segmentation. *IEEE Trans. pattern analysis Mach. Intell.* 39 (12), 2481–2495. doi:10.1109/tpami.2016.2644615

Berman, M., Triki, A. R., and Blaschko, M. B. (2018). "The lovasz-softmax loss: a tractable surrogate for the optimization of the intersection-overunion measure in neural networks," in IEEE/CVF Conference on Computer Vision and Pattern Recognition, Salt Lake City, UT, USA, 18-23 June 2018 (IEEE), 4413–4421.

Cao, J., Yang, G., and Yang, X. (2020). Deep learning pavement crack detection based on attention mechanism. *J. Computer-Aided Des. Comput. Graph.* 32 (8), 10. doi:10.1109/AEECA55500.2022.9918950

Chen, L. C., Papandreou, G., Kokkinos, I., Murphy, K., and Yuille, A. L. (2017). Deeplab: semantic image segmentation with deep convolutional nets, atrous convolution, and fully connected crfs. *IEEE Trans. pattern analysis Mach. Intell.* 40 (4), 834–848. doi:10.1109/tpami.2017.2699184

Chen, L. C., Zhu, Y., and Papandreou, G. (2018). "Encoder-decoder with atrous separable convolution for semantic image segmentation," in The European Conference on Computer Vision (Spinger), 801–818. doi:10.1007/978-3-030-01234-2_492

Cuilimeng (2023). CrackForest dataset. Avaliable at: https://github.com/cuilimeng/CrackForest-dataset.

Deng, L., Chu, H., and Long, L. (2023). Review of crack detection in civil infrastructure based on deep learning. *China J. Highw. Transp.* 36 (2), 1–21. doi:10.3969/j.issn.1001-7372.2023.02.001

Gao, C., Yan, J., Zhou, S., Varshney, P. K., and Liu, H. (2019). Long short-term memory-based deep recurrent neural networks for target tracking. *Inf. Sci.* 502, 279–296. doi:10.1016/j.ins.2019.06.039

Jieh-Haur, C., Su, M.-C., Cao, R., Hsu, S.-C., and Lu, J.-C. (2017). A self organizing map optimization based image recognition and processing model for bridge crack inspection. *Automation Constr.* 73, 58–66. doi:10.1016/j.autcon.2016.08.033

Kingma, D. P., and Ba, J. (2015). Adam: a method for stochastic optimization. arXiv. doi:10.48550/arXiv.1412.6980

Labelme (2023). Wkentaro. Avaliable at: https://github.com/wkentaro/labelme/releases.

Lau, S. L., Chong, E. K., Yang, X., and Wang, X. (2020). Automated pavement crack segmentation using u-net-based convolutional neural network. *IEEE Access* 8, 114892–114899. doi:10.1109/access.2020.3003638

Li, G., Zhao, X., Du, K., Ru, F., and Zhang, Y. (2017). Recognition and evaluation of bridge cracks with modified active contour model and greedy search-based support vector machine. *Automation Constr.* 78, 51–61. doi:10.1016/j.autcon.2017.01.019

Lin, T. Y., Dollár, P., and Girshick, R. (2017). "Feature pyramid networks for object detection," in 2017 IEEE Conference on computer vision and pattern recognition, Honolulu, HI, USA, 21-26 July 2017 (IEEE), 2117–2125.

Liu, J., Wang, Z., and Xu, M. (2020). DeepMTT: a deep learning maneuvering target-tracking algorithm based on bidirectional LSTM network. *Inf. Fusion* 53, 289–304. doi:10.1016/j.inffus.2019.06.012

Liu, W., Anguelov, D., and Erhan, D. (2016). "SSD: single shot multibox detector," in *Proceedings, Part I computer vision–ECCV 2016: 14th European conference* (Amsterdam, The Netherlands: Spinger), 21–37.

Liu, Y., Justin, K., and Yeoh, W. (2021). Automated crack pattern recognition from images for condition assessment of concrete structures. *Automation Constr.* 128, 103765. doi:10.1016/j.autcon.2021.103765

Liu, Z., Gu, X., Chen, J., Wang, D., Chen, Y., and Wang, L. (2023). Automatic recognition of pavement cracks from combined GPR B-scan and C-scan images using multiscale feature fusion deep neural networks. *Automation Constr.* 146, 104698, 104698. doi:10.1016/j.autcon.2022.104698

Long, J., Shelhamer, E., and Darrell, T. (2015). Fully convolutional networks for semantic segmentation[C]. *IEEE Conf. Comput. Vis. pattern Recognit.* 2015, 3431–3440. doi:10.1109/CVPRW.2017.156

Milletari, F., Navab, N., and Ahmadi, S. A. (2016). "V-net: fully convolutional neural networks for volumetric medical image segmentation," in 4th International Conference on 3D Vision (3DV), Stanford, CA, USA, 25-28 October 2016 (IEEE), 565–571.

Qu, Z., Li, Y., and Zhou, Q. (2022). Crackt-net: a method of convolutional neural network and transformer for crack segmentation. *J. Electron. Imaging* 31 (2), 23040. doi:10.1117/1.JEI.31.2.023040

Ronneberger, O., Fischer, P., and Brox, T. (2015). "U-net: convolutional networks for biomedical image segmentation," in *Medical Image Computing and Computer-Assisted Intervention—MICCAI* (Spinger), 234–241. doi:10.1007/978-3-319-24574-4_28

Stollenga, M. F., Byeon, W., and Liwicki, M. (2015). "Parallel multi-dimensional LSTM, with application to fast biomedical volumetric image segmentation," in The 28th International Conference on Neural Information Processing Systems (ACM), 2998–3006. doi:10.1007/978-3-319-24574-4_282

Xiang, X., Zhang, Y., and El Saddik, A. (2020). Pavement crack detection network based on pyramid structure and attention mechanism. *IET Image Process.* 14 (8), 1580–1586. doi:10.1049/iet-ipr.2019.0973

Xu, F., Ma, H., and Sun, J. (2019). "LSTM multi-modal unet for brain tumor segmentation," in 4th international conference on image, vision, and computing (ICIVC), Xiamen, China, 05-07 July 2019 (IEEE), 236–240.

Yang, F., Zhang, L., Yu, S., Prokhorov, D., Mei, X., and Ling, H. (2019). Feature pyramid and hierarchical boosting network for pavement crack detection. *IEEE Trans. Intelligent Transp. Syst.* 21 (4), 1525–1535. doi:10.1109/tits.2019.2910595

Yu, F., and Koltun, V. (2016). Multi-scale context aggregation by dilated convolutions. arXiv. doi:10.48550/arXiv.1511.07122

Zhao, H., Shi, J., and Qi, X. (2017). "Pyramid scene parsing network," in 2017 IEEE Conference on computer vision and pattern recognition, Honolulu, HI, USA, 21-26 July 2017 (IEEE), 2881–2890.

Zhu, Y., Wang, H., and Li, K., (2022). A High-precision pavement crack detection network structure:crack U-Net. *Comput. Sci.* 49 (01), 204–211. doi:10.7544/issn1000-1239.2022.20210122

Zou, Q., Zhang, Z., Li, Q., Qi, X., Wang, Q., and Wang, S. (2019). DeepCrack: learning hierarchical convolutional features for crack detection. *IEEE Trans. Image Process.* 28 (3), 1498–1512. doi:10.1109/tip.2018.2878966

frontiers | Frontiers in Materials

TYPE Original Research
PUBLISHED 26 March 2024
DOI 10.3389/fmats.2024.1380316

OPEN ACCESS

EDITED BY
Zhigang Zhang,
Chongqing University, China

REVIEWED BY
Fan Bai,
Beijing Jiaotong University, China
Xiaoqing Xu,
Tongji University, China

*CORRESPONDENCE
Zhongya Zhang,
zhangzhongya@cqjtu.edu.cn

RECEIVED 01 February 2024
ACCEPTED 01 March 2024
PUBLISHED 26 March 2024

CITATION
Zhou X, Jiang J, Liu L, Wang S, Deng X, Li Y and Zhang Z (2024), Bending performance of prefabricated ultra-thin UHPC unit plate reinforced orthotropic steel bridge decks. *Front. Mater.* 11:1380316.
doi: 10.3389/fmats.2024.1380316

Bending performance of prefabricated ultra-thin UHPC unit plate reinforced orthotropic steel bridge decks

Xiang Zhou[1,2], Jinlong Jiang[1,2], Le Liu[1,2], Shan Wang[1,2], Xilei Deng[1,2], Yong Li[1,2] and Zhongya Zhang[1,2]*

[1]State Key Laboratory of Mountain Bridge and Tunnel Engineering, Chongqing Jiaotong University, Chongqing, China, [2]School of Civil Engineering, Chongqing Jiaotong University, Chongqing, China

To address the challenges related to lengthy construction period, complex maintenance requirement, and the elevated risk of shrinkage cracking associated with cast-in-place UHPC reinforcement of orthotropic steel bridge decks. This paper proposes a novel solution that prefabricated ultra-high-performance concrete (UHPC) slab with epoxy bond connection is used as a reinforcement layer for orthotropic steel bridge decks. Four sets of bending tests on composite bridge deck were carried out to compare the flexural performance of composite bridge decks under different joint forms and loading patterns. The results indicate that the precast UHPC decks delaminated from the epoxy bonding layer without failure of the epoxy layer itself in all cases. The positive bending capacity of the jointless composite bridge deck is approximately 27.67 kN, while the negative bending capacity is around 16.58 kN. For the composite bridge deckwith epoxy adhesive joints (EA-J-Ln), the negative bending capacity is 2.54 kN, and the negative bending capacity of the joint area reinforced with carbon fiber cloth (EA-JC-Ln) is increased to 4.17 kN. Therefore, the use of carbon fiber cloth can significantly improve the bending resistance of the joints. Finally, numerical model of the composite deck based on Cohesive Zone Model (CZM) was established, validating the applicability of this simulation method in the novel composite bridge deck.

KEYWORDS

ultra-high-performance concrete (UHPC), bridge deck joints, epoxy adhesive, flexural performance, numerical simulation

1 Introduction

Ultra-high-performance concrete (UHPC) is an advanced construction material known as its high strength, high ductility and excellent durability (Du et al., 2021; 2022; Jia et al., 2023). It is widely used in fields such as bridge structures, house construction, maintenance and reinforcement, etc (Shao et al., 2018; Wang et al., 2021; Zhang Z. et al., 2023; Zou et al., 2023b). It is worth noting that concrete shrinkage can significantly impact the long-term performance of NC structures (Hung et al., 2021; Men et al., 2023). However, this influence can be mitigated in UHPC components treated with steam curing (Yoo et al., 2014a; 2014b), enabling the rapid achievement of desired high strength within approximately 72 days. Therefore, UHPC is an exceptional material for prefabricated structural components, which can saved time costs (Zhang et al.,

2022; Benedetty et al., 2023) and provide higher strength, superior durability, and lower life-cycle costs (Wang et al., 2021; Fang et al., 2022; Jia et al., 2023).

Shear studs, one of the commonly used connecting components between orthotropic steel bridge deck and UHPC (Jiang et al., 2022), are widely used in composite structures due to their convenient installation (Fang et al., 2022), simple load transferring pathway (Hu et al., 2023), and cost-effectiveness, among other characteristics (Shi et al., 2022; Bu et al., 2023). However, the extensive use of shear studs inevitably introduces welding defects and residual stresses (Khorramian et al., 2017; Ding et al., 2023; Liu et al., 2023), which may pose inconvenience during the later disassembly or replacement of the structure (Li Y. et al., 2023). Furthermore, the availably shortest height of shear studs in the market is currently 35 mm (Shao et al., 2018), thereby limiting the development of ultra-thin UHPC panels (Bu et al., 2023; Leng et al., 2024).

In the field of Prefabricated Concrete Segmental Bridges (PCSB), the concept, development, and global acceptance of segmental structures represent one of the most remarkable achievements in civil engineering (Jiang et al., 2015). The use of prefabricated UHPC segmental bridge decks can significantly shorten construction time and improve the efficiency of bridge structure construction (Yu et al., 2022). However, the inevitable issue of joints between prefabricated UHPC bridge decks poses a challenge. Figure 1 illustrates the novel assembly of prefabricated UHPC bridge decks were proposed in this study for reinforcing orthotropic steel bridge decks. By adopting this system, the limitations posed by shear stud connections on bridge structures can be effectively overcome, and the construction of bridge decks using prefabricated components can be realized. This approach not only reduces construction time and economic costs but also facilitates the reinforcement of orthotropic steel bridge decks. Additionally, the connection between prefabricated UHPC decks and steel bridge decks can be achieved using an epoxy bonding layer (Zou et al., 2021a). The joints of prefabricated UHPC bridge decks are divided into wet joints and epoxy joints. Ahmed and Aziz (2019) demonstrated through direct shear tests that the shear resistance of epoxy resin joints is 25%–28% higher than that of wet joints, with a more uniform distribution of shear stress. Pan et al. (2023) studied the shear performance of epoxy-bonded joints with large teeth, considering parameters such as shear teeth. The study showed that the large teeth has a significant impact on the shear performance of joints, and proposed relevant specifications for the teeth size. Connecting prefabricated UHPC decks with steel plates using epoxy bonding (Sun et al., 2021; Li et al., 2022a) can reduce damage to the steel bridge deck and satisfy load-bearing capacity and construction convenience (Pang et al., 2022; Zhang P. et al., 2023). Additionally, as a rigid connection layer, bond can significantly reduce interfacial slippage and improve the overall performance of composite structures (Luo et al., 2012; Fang et al., 2024). Li C. et al. (2023) conducted experiments and found that the shear performance using epoxy bonding interface is related to the bonding area, and summarized various factors affecting shear bond strength, such as the strength of epoxy bonding agents, roughness of bonding surfaces, concrete strength, and temperature. Further research on steel-UHPC components under bending was conducted by Wang et al. (2019) and Duan et al. (2020), who studied the interfacial bonding performance under combined bending and bending-shear actions based on three-point bending and four-point bending tests. The extensive researches on epoxy bonding interfaces in steel-UHPC composite bridge decks evident that epoxy bonding interfaces can provide high load-bearing capacity to meet the requirements of practical engineering applications.

To investigate the flexural performance of the novel assembly-type epoxy-bonded prefabricated UHPC bridge deck (Figure 1) proposed in this study, four sets of bending performance tests on composite bridge deck were conducted. Joints in the negative bending moment zone often experience tension, and the bonding performance of the interface at the joints needs to be verified. Therefore, the bending performance of epoxy-bonded joints in prefabricated UHPC panels under different joint forms, positive bending moment loading, and negative bending moment loading were discussed. Experimental failure modes, load-deflection curves, load-interface slip curves, and strain distribution were evaluated to determine appropriate epoxy bonding joint forms for prefabricated UHPC panels. Furthermore, a numerical simulation method based on Cohesive Zone Model (CZM) is proposed for analyzing this bonding joint.

2 Materials and methods

2.1 Specimen design

To investigate the bending performance of steel- UHPC composite bridge decks with epoxy bonded joints, four sets of bending tests were designed. The overall specimen design is illustrated in Figure 2, consisting of a steel plate, epoxy adhesive, carbon fiber cloth, and precast UHPC slab. The overall dimensions are 800 mm in length, 150 mm in width, and 42 mm in height. The steel plate dimensions are 800 mm in length, 150 mm in width, and 10 mm in thickness. The precast UHPC slab dimensions are 800 mm in length, 150 mm in width, and 30 mm in thickness. The epoxy bonded layer dimensions are 800 mm in length, 150 mm in width, and 2 mm in thickness, and the carbon fiber cloth dimensions are 150 mm in length, 20 mm in width, and 2 mm in thickness. To simulate the actual joints between precast UHPC slabs in bridge structures, two sets of specimens with 2 mm thick epoxy bonded joints were designed, and one set was reinforced with a 20 mm width carbon fiber cloth in the joint area. The specimens without joints were subjected to both positive and negative bending moments, while the specimens with joints were subjected to negative bending moments. All precast UHPC slabs had smooth surfaces, and epoxy bonded joints were used to naturally bond the precast UHPC slabs to the steel plates. Specific specimen parameters are detailed in Table 1.

2.2 Material properties

2.2.1 UHPC and steel

The mixture proportions for the UHPC raw materials used in the experiments are provided in Table 2. The UHPC mix

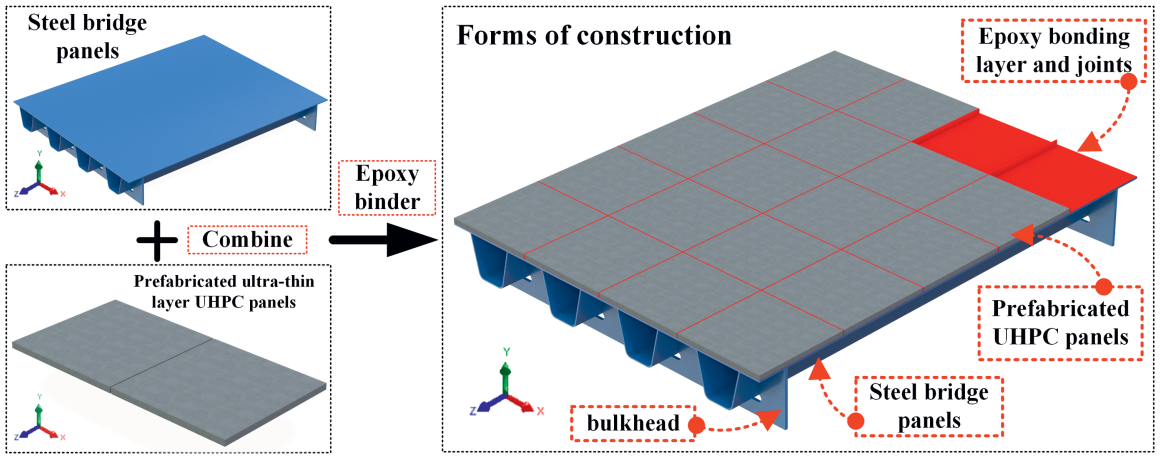

FIGURE 1
OSD-UHPC epoxy bonding layer connection solution.

TABLE 1 Test specimen parameters.

Specimen number	Joints	Reinforcement type	Loading mode	Number of specimens
EA-Lm	-	-	Positive bending moment	3
EA-Ln	-	-	Negative bending moment	1
EA-J-Ln	Rectangular joint	-	Negative bending moment	3
EA-JC-Ln	Rectangular joint	Carbon fiber cloth	Negative bending moment	3

The specimen identification follows the naming convention of interface type + joint type + loading mode + loading step. EA represents the epoxy adhesive interface, J represents the mid-span adhesive joint, JC represents the joint reinforced with carbon fiber cloth, Lm represents positive bending moment loading, and Ln represents negative bending moment loading.

includes a volume fraction of 3% of straight steel fibers (yield strength greater than 1,200 MPa) with a diameter of 0.12 mm and a length of 8 mm. The manufacturing process of UHPC is as follows: first, the dry materials are mixed according to the proportions in Table 3, and then they are dry mixed in a mixer for 2 min to ensure even mixing of the dry ingredients. After that, water and a water-reducing agent are added evenly and mixed for 1 min. Once the dry materials are thoroughly mixed with water and the water-reducing agent, steel fibers are evenly sprinkled and mixing continues for 6 min to complete the preparation of UHPC. Additionally, the strength grade of steel used for the specimens was Q345.

UHPC and steel were tested according to the standards "High-Performance Concrete" (GB/T31387-2015) (GB/T31387-2015 (General Administration of Quality Supervision, 2015)) and "Metallic Materials - Tensile Testing - Part 1: Method of Test at Room Temperature" (GB/T 228.1-2010) (GB/T 228.1-2010 (General Administration of Quality Supervision, 2010)), respectively. The schematic representation of the tests and the material properties are shown in Figure 3 and Table 4, respectively. In the table, f_y, f_u, and E_s represent the yield strength, ultimate strength, and elastic modulus of Q345 steel. f_c, f_t, and E_c represent the compressive strength, tensile strength, and elastic modulus of UHPC.

TABLE 2 Specific mix proportion of UHPC.

Component	Weight (kg)	Ratio of weight (%)
Dry material	100.000	82.09
Steel fiber	12.232	10.04
Water reducer	0.672	0.55
Water	8.916	7.32
Total	121.82	100

2.2.2 Epoxy binder and carbon fiber cloth

The epoxy adhesive used is CBSR-A/B Steel Filling Adhesive produced by Cabon Technology Group Co., Ltd. The primary components are the base agent CBSR-A and the hardener CBSR-B, with a material weight mixing ratio of 2:1. According to the "Test Methods for Properties of Resin Castings" (GB/T 2567-2021) (Test methods for properties of resin casting body: GB/T 2567-2021) ([in Chinese]), tensile and compression tests on the epoxy adhesive are conducted using an electronic

10.3389/fmats.2024.1380316

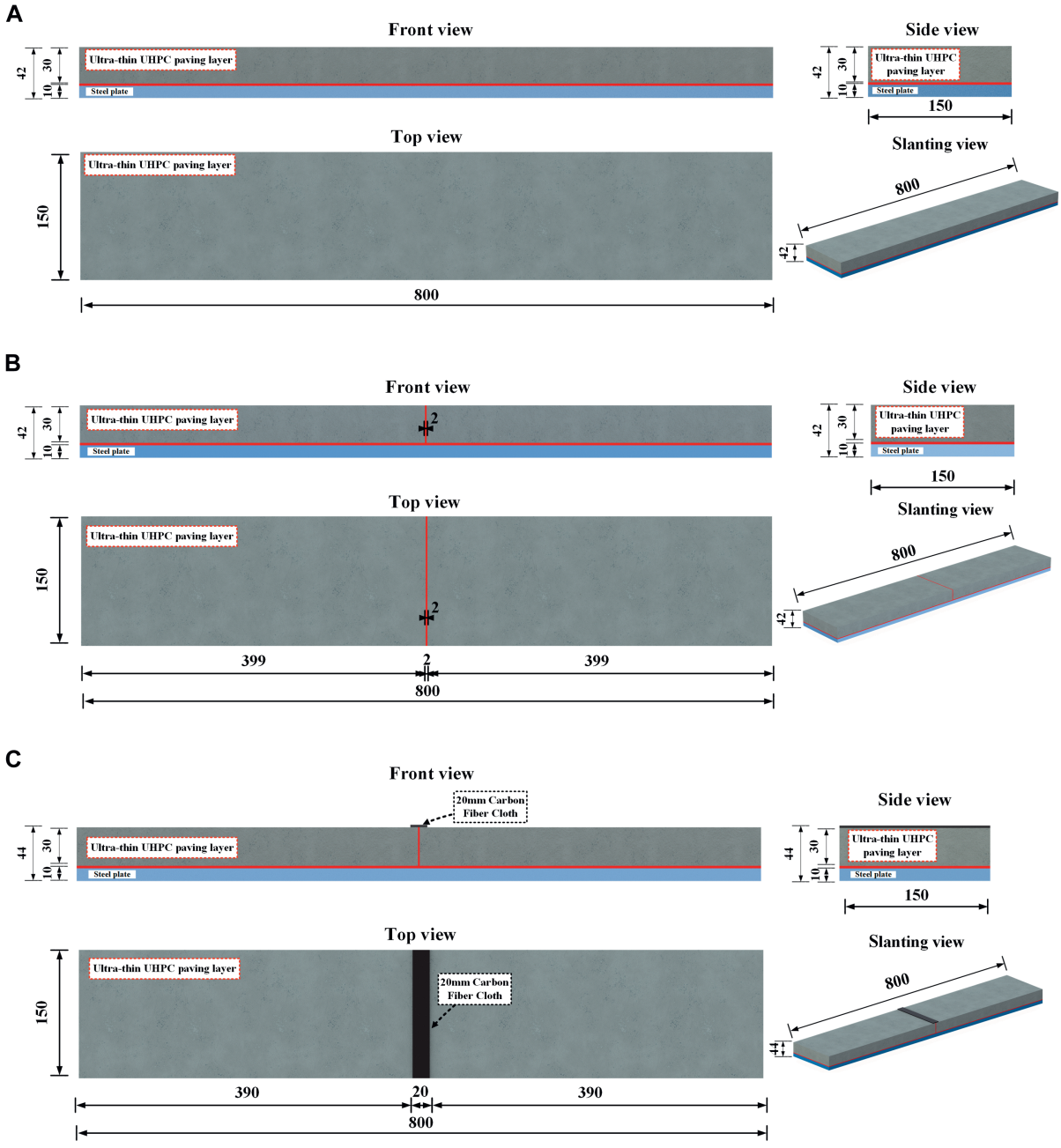

FIGURE 2
Test specimen construction details (units: mm). **(A)** Specimen of EA; **(B)** Specimen of EA-J; **(C)** Specimen of EA-JC.

universal testing machine. The mechanical properties are detailed in Table 5.

The carbon fiber fabric used in this study was acquired from Shanghai Yuezi Industrial Co., Ltd. (Shanghai, China). The fabric is woven from 12K carbon fiber filaments, with a carbon content of more than 98%, a thickness of 0.167 mm, and a density of 300 g/cm³. According to the "Code for acceptance of construction quality of strengthening building structures, 2010" (GB 50550-2010 ([in Chinese]), tensile tests on the carbon fiber fabric were conducted using an electronic universal testing machine. The mechanical properties are detailed in Table 5.

2.3 Specimen preparation

The precast UHPC slabs were naturally bonded to the steel plates using an epoxy bonded layer. The specific procedure was as follows: a) Fabrication of molds and casting of precast UHPC slabs; b) After casting, the UHPC required 48 h of curing at room

TABLE 3 Dry material mix ratio of UHPC.

Component	Cement	Silica fume	Quartz sand	Quartz powder	Water reducing agent	Water
Mass ratio	1.000	0.250	1.100	0.300	0.019	0.225
The volume content of steel fiber				3%		

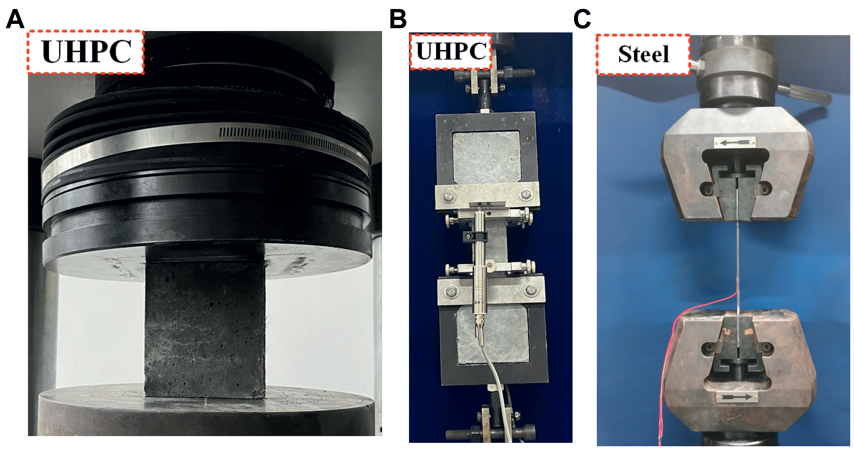

FIGURE 3
Steel and UHPC material properties tests. **(A)** UHPC compressive test; **(B)** UHPC tensile test; **(C)** Steel tensile test.

TABLE 4 Material properties of steel and UHPC.

Material	f_c (MPa)	f_t (MPa)	E_c (GPa)
UHPC	128.5	10.43	44.3
	f_y (MPa)	f_u (MPa)	E_s (GPa)
Q 345	359.5	494.4	202.2

temperature, followed by demolding and 72 h of steam curing at 95°C; c) Cleaning the surface of the steel plates with acetone to remove all debris and rust; d) Fixing the precast UHPC slabs onto the steel plates with a 2 mm gap maintained between them; e) Preparation of epoxy adhesive; f) Injecting the epoxy adhesive into the 2 mm gap through pre-drilled holes until a small amount of adhesive overflowed from the edges; g) Curing the specimens at room temperature for 7 days until the epoxy bonded layer reached its full strength. The preparation process of the specimens is illustrated in Figure 4.

2.4 Loading scheme and measurement method

Figure 5A illustrates the loading method and measurement point arrangement for the specimens. All composite bridge decks are subjected to a four-point loading scheme, enabling a pure bending region of 300 mm at the midspan using a distributing beam. The load is applied using an electronic universal testing machine (MTS Exceed E45.205) at a loading rate of 0.01 mm/s. Displacement sensors D-4 and D-5 are placed 50 mm from the edge of the composite plate to measure deflections at the supports, while displacement sensor D-1 was positioned at the midspan of the specimen to measure midspan deflection. Displacement sensors S-1 to S-2 are arranged on the edge of the side of the specimen to measure the slip at the interface between the UHPC layer and the steel plate. Strain gauges are installed at the top, bottom, and sides of the midspan region to measure strains in the UHPC layer and the steel plate within the pure bending zone.

For specimens subjected to positive bending moment loading, the UHPC is positioned on top with the steel plate underneath. Conversely, for specimens subjected to negative bending moment loading, the arrangement is reversed. The bending tests of the steel-UHPC composite bridge decks follow the loading scheme used by Zou et al. (2021b). As shown in Figure 5B, preloading with an amplitude of 30% of the ultimate load (Pu) was applied three times to check the potential effects during the loading process. Subsequently, continuous loading is applied until specimen failure, with the observation and recording of crack propagation during the loading process.

3 Results

3.1 Failure mode

The failure characteristics of the specimens under positive bending moment without joints (EA-Lm) are as follows: as the load

10.3389/fmats.2024.1380316

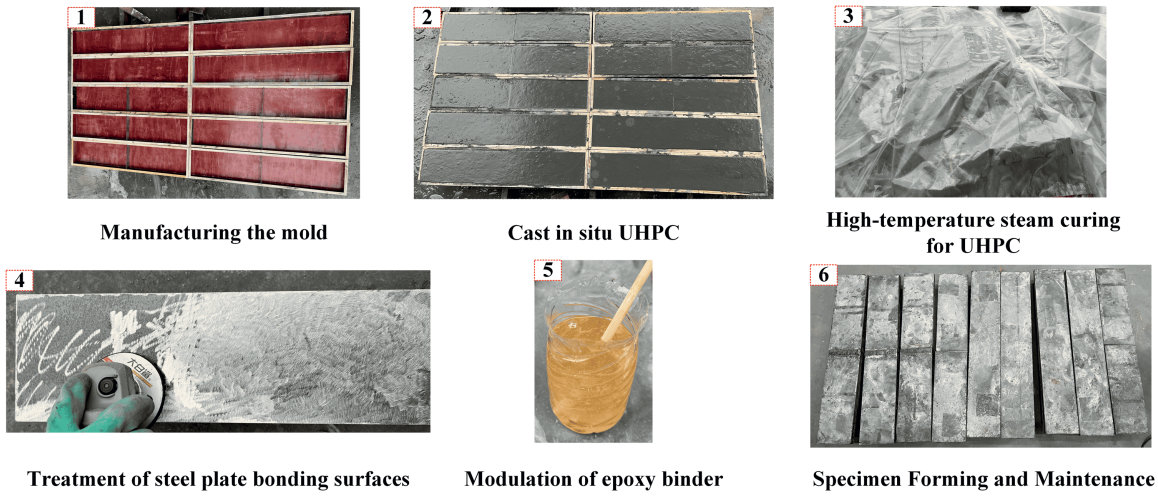

FIGURE 4
Test specimen fabrication process.

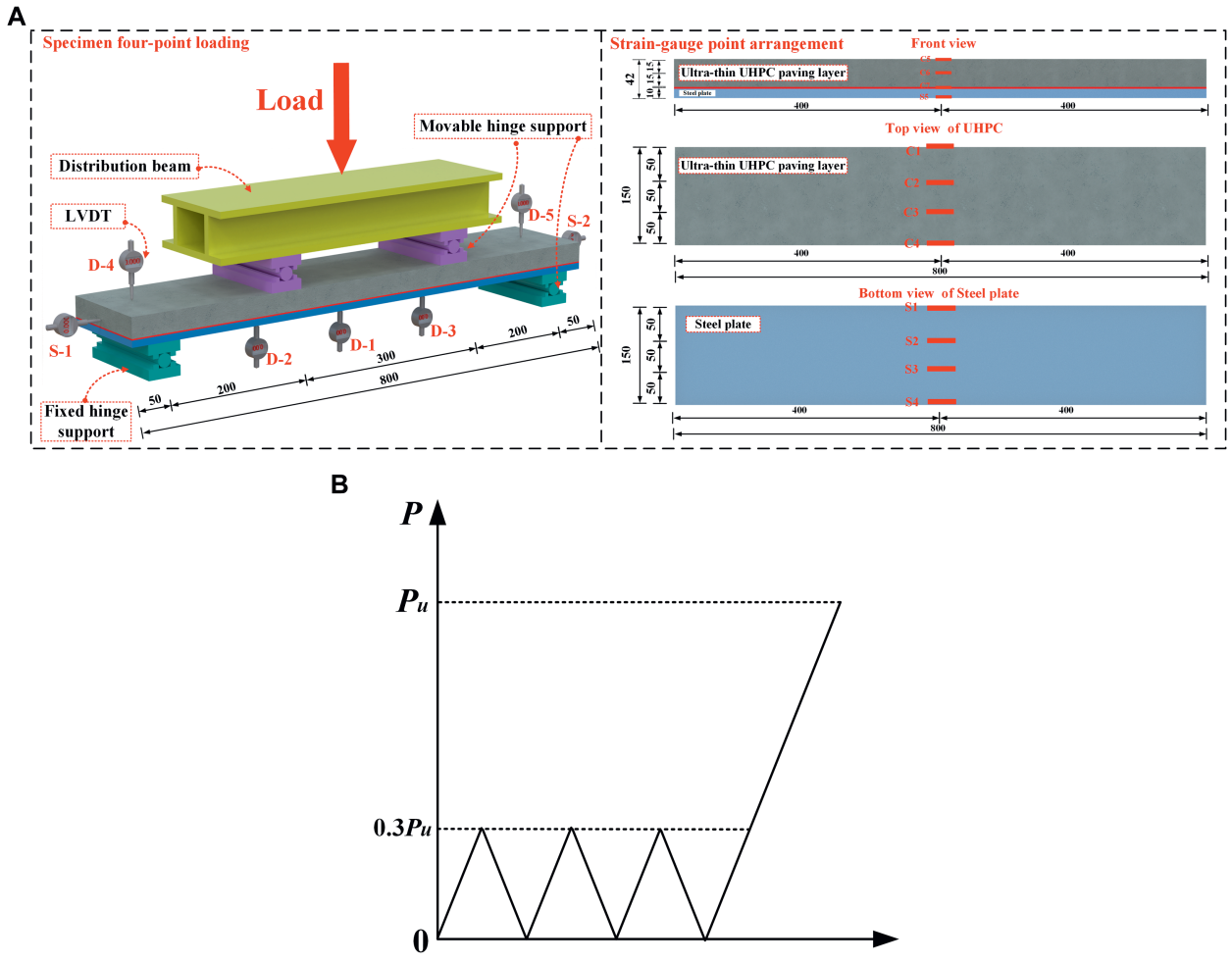

FIGURE 5
Test loading scheme and measurement point arrangement. **(A)** Specimen loading device and measurement point arrangement; **(B)** Monotonic loading process.

10.3389/fmats.2024.1380316

TABLE 5 Epoxy adhesive and carbon fiber cloth material properties.

Material	Tensile strength (MPa)	Bending strength (MPa)	Compressive strength (MPa)	Elastic modulus (MPa)
CBSR-A/B	62	55.0	70	3,920
Carbon fiber cloth	2,840	-	-	45,300

increases, cracks begin to appear in the pure bending region at mid-span. When the ultimate load P_u is reached, the UHPC slab delaminates from the epoxy bonding layer, accompanied by a "bang" sound. The top of UHPC slab in the pure bending section of the specimen collapses under pressure. The failure mode of this type of specimen indicates excellent bonding performance between the epoxy bonding layer and the steel plate, while the bonding strength between the smooth UHPC slab and the epoxy bonding layer is significantly insufficient, resulting in separation of the steel plate from one side of the UHPC slab. The failure mode of the EA-Lm specimen is shown in Figure 6A.

The failure mode of the specimens under negative bending moment without joints (EA-Ln) is shown in Figure 6B. This type of specimen exhibits UHPC rupture and exposed steel fibers on the basis of the failure mode of the EA-Lm specimen. After reaching the peak load P_u, cracks extend upward along the main crack at mid-span, ultimately resulting in rupture of the UHPC slab along the mid-span. At the same time, the bonding strength between the UHPC slab and the epoxy bonding layer is completely lost, leading to separation between the steel plate and the UHPC slab.

The failure modes of the specimens under negative bending moment with joints (EA-J-Ln) and the specimens with joints reinforced with carbon fiber cloth under negative bending moment (EA-JC-Ln) are shown in Figures 6C, D, respectively. The failure characteristics of the two types of specimens are consistent: once the joint cracks, the cracks continue to extend upward, eventually leading to delamination of the prefabricated UHPC slab from the epoxy bonding layer near the joint, while the interface far from the joint remains intact.

3.2 Load-deflection curve

Figure 7A presents the load-deflection curves for the EA-Lm specimen, which can be divided into three stages: a) Elastic stage: Before reaching the ultimate load P_u, the interface of the specimen remains undamaged, and it is in the elastic stage. During this stage, the load continues to increase, and the deflection increases slowly. b) After reaching the ultimate load P_u, there is a sudden failure at the interface, resulting in a sharp drop in load, indicating irreversible damage to the interface. c) Continued loading: The upper load is borne by the steel plate, and the deflection of the specimen continues to increase, but the load increases slowly. Local fragmentation occurs in the UHPC layer near the loading point, resulting in bending failure of the composite bridge deck. The load-deflection curves for these three types of specimens exhibit a similar trend, and their ultimate load P_u is approximately 27.67 kN.

The load-deflection curves for the negative bending moment tests are shown in Figure 7B, including three types of specimens: EA-Ln, EA-J-Ln, and EA-JC-Ln. It can be observed that the specimen EA-Ln without joint is capable of resisting external loads under negative bending moment loading, with an ultimate load P_u of approximately 16.58 kN. Before reaching the ultimate load P_u, the composite bridge deck is able to jointly bear the external load, and a primary crack appears at the mid-span of the UHPC board and continues to propagate upwards during this process. After reaching the ultimate load P_u, the UHPC board detaches from the epoxy bonding layer in the mid-span bending section. As the load continues to increase, the UHPC board is pulled apart along the primary crack at the mid-span, eventually the composite function was lost, and only the steel plate beared the external load.

The load-deflection curves for EA-J-Ln and EA-JC-Ln specimens exhibit similarities and can be analyzed in three stages: a) Elastic Stage: During this stage, the load continues to increase gradually, and the deflection increases slowly, resulting in a straight upward-sloping curve. The composite bridge deck are jointly stressed and the interface is intact in this stage. b) Ultimate Load P_u Stage: When reaching the ultimate load P_u, cracks propagate upward along the seam near the mid-span. The load experiences a sudden drop, and the deflection increases rapidly, leading to a steep decline in the curve. This phase continues until the UHPC board detaches from the epoxy bonding layer near the seam. c) After Reaching Ultimate Load: In this phase, the UHPC board and epoxy bonding layer at the seam have detached. The composite structure loses its capacity, and all external loads are borne by the steel plate. Comparing the test results of all specimens, it is evident that the failure of EA-J-Ln and EA-JC-Ln specimens occurs at the seam. This indicates that the composite bridge deck has poor resistance under negative bending moment loading, whereas the seam-less specimen EA-Ln can effectively resist external loads in negative bending moment mode. Additionally, the epoxy bonding layer-bonded composite bridge deck exhibits effective resistance to external loads in positive bending moment mode. Therefore, in the design of orthotropic steel bridge decks using prefabricated UHPC deck combined with epoxy bonding layers, it is recommended to place the seam at the location where positive bending moments are generated in the bridge deck. From Figure 7B, it can be observed that the ultimate load of the EA-JC-Ln specimen is approximately twice as high as that of the EA-J-Ln specimen. This indicates that reinforcing the joint area with carbon fiber cloth can enhance its bending performance.

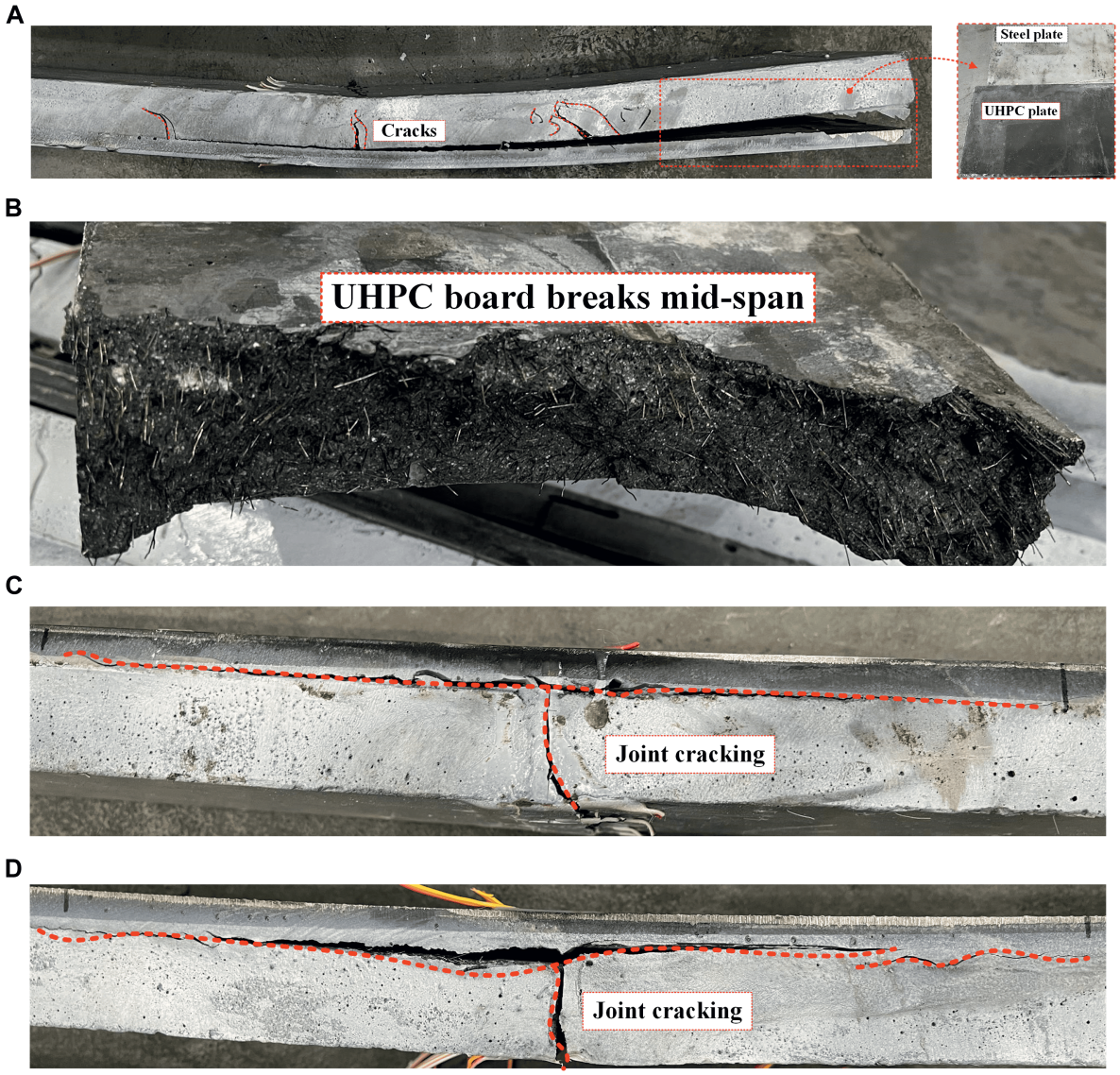

FIGURE 6
Specimen damage model. **(A)** EA-Lm; **(B)** EA-Ln; **(C)** EA-J-Ln; **(D)** EA-JC-Ln.

3.3 Load-slip curve

Figure 8 shows the load-slip curves of the specimens. As shown in Figure 8A, the load-slip curve of the EA-Lm specimen indicates that, prior to reaching the ultimate load, the epoxy adhesive layer ensures an effective connection between the UHPC panel and the steel plate, with negligible slip occurring at this stage. Subsequently, upon reaching the ultimate load, the slip at both ends of the specimen escalates and continues to increase. Larger slip occurs on the S-1 side, with a maximum slip value of S-1 = 13.9 mm. Hence, a smooth UHPC panel can achieve effective bonding through the epoxy adhesive layer. The load-slip curves of the EA-Ln, EA-J-Ln, and EA-JC-Ln specimens, as shown in Figures 8B, C, are characterized by the fact that the failure of all three types of specimens occurs at the mid-span joint, and debonding occurs between the UHPC panel and the epoxy layer at the joint, resulting in minimal and almost negligible slip at the ends. The maximum slip value for specimens with only epoxy joints is S-1 = 0.08 mm. For the EA-JC-Ln specimen, which was reinforced at the joint with carbon fiber cloth, the slip at the ends is significantly larger, indicating that the reinforcement of the joint with carbon fiber cloth enhances the bending performance of the epoxy joint, with a maximum slip value of only S-1 = 0.31 mm.

3.4 Strain distribution

The strain distribution curves were drawn after averaging the values for specimens in the same group. However, the strain distribution curve for the EA-JC-Ln specimen could not be plotted due to damage to the strain gauges during initial loading. Figure 9A

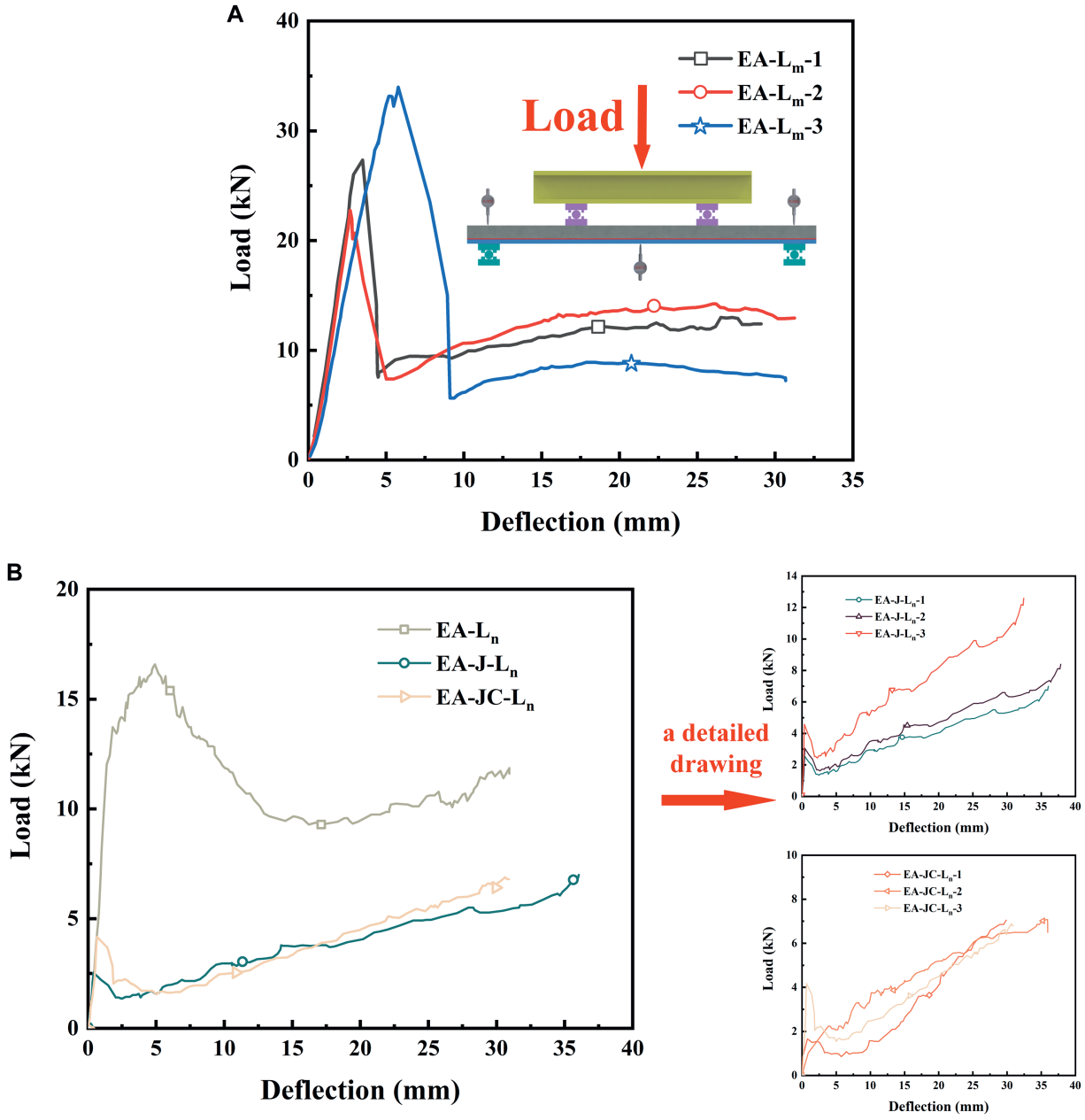

FIGURE 7
Load-deflection curve. **(A)** Positive bending moment test. **(B)** Negative bending moment test.

shows the strain distribution curve along the height direction at mid-span for the EA-Lm specimen. Before the applied load reaches the ultimate load P_u = 27.3 kN, the strain at mid-span exhibits a linear distribution. As the load continues to increase, the strain at mid-span shows an increasingly evident nonlinear distribution. However, the strain distribution across the mid-span section always remains linear. The distribution is discontinuous at the steel-UHPC interface, where both the thin UHPC panel and the steel plate exhibit a linear strain distribution. Once the ultimate load P_u = 27.3 kN is reached and the epoxy adhesive layer interface is damaged, the assumption of plane sections being plane no longer holds.

Figure 9B depicts the strain distribution curve along the height direction at mid-span for the EA-Ln specimen. Throughout the loading process, the strain distribution of the specimen consistently adheres to the plane section assumption, with the neutral axis maintaining a constant position as theoretically expected, as shown in Figure 13B. This is consistent with the low level of interfacial slip for the EA-Ln specimen shown in Figure 8B. In Figure 9C, for the EA-J-Ln specimen, when the load is below 2.5 kN, the strain distribution at mid-span is approximately linear. Before reaching the ultimate load, the epoxy adhesive interface can achieve reliable connection between the thin UHPC panel and the steel plate. After the load exceeds 2.5 kN, sudden extensive

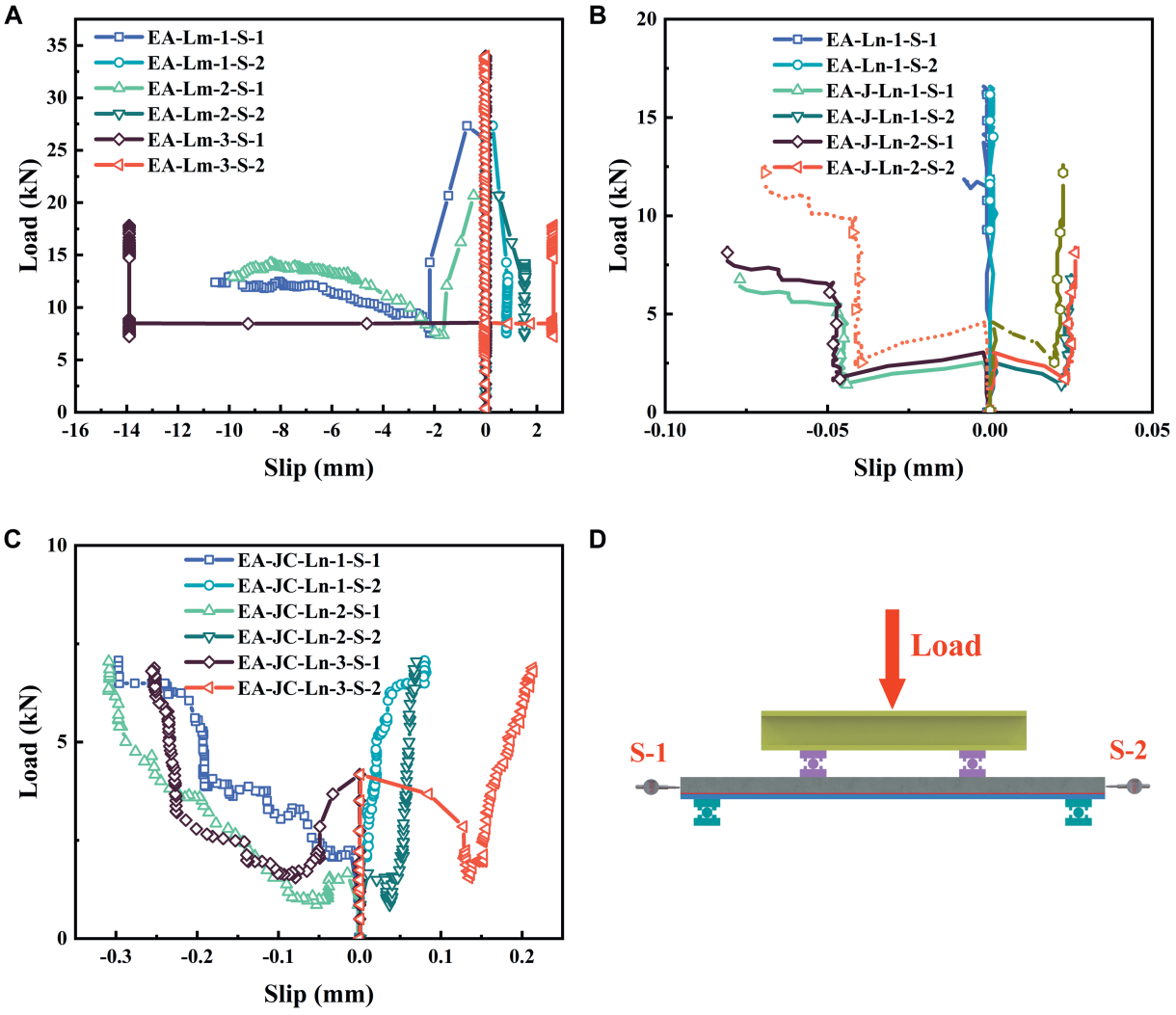

FIGURE 8
Load-slip curve. **(A)** EA-Lm interfacial slip curve; **(B)** EA-J-Ln interfacial slip curve; **(C)** EA-Ln and EA-JC-Ln interfacial slip curve; **(D)** Interface slip measurement point location.

damage occurs at the interface around the joint, leading to a sharp increase in strain, which indicats that the joint has fractured and damaged.

4 Numerical simulation

4.1 Finite element models

In this study, a finite element model of the steel-UHPC composite bridge deck was established using the static analysis method in ABAQUS. Based on the symmetry of the steel-UHPC composite bridge deck, a half-model was developed to improve computational efficiency. The symmetrical plane is the x-plane. The steel plate, ultra-thin UHPC, and epoxy adhesive layer were simulated using C3D8R (three-dimensional, 8-node linear solid integrated elements). According to the experimental results, the bonding behavior between the UHPC panel and the epoxy adhesive layer was simulated using cohesive contact properties. The specific finite element model is shown in Figure 10.

4.2 Material constitutive model

4.2.1 UHPC

The damage and cracking behavior of UHPC can be defined in ABAQUS by defining the concrete plastic damage (CDP) model. Its constitutive model (Li et al., 2022b) is shown in Figure 11. For the elastic parameters of UHPC, the modulus of elasticity is 42.1 GPa and the Poisson's ratio is 0.3. The plastic parameters include the dilation angle, eccentricity, the ratio of biaxial to uniaxial compressive strength, K, and the viscosity parameter, with values of 36°, 0.1, 1.16, 0.6667, and 0.0005, respectively. The remaining parameters are all displayed in the figure.

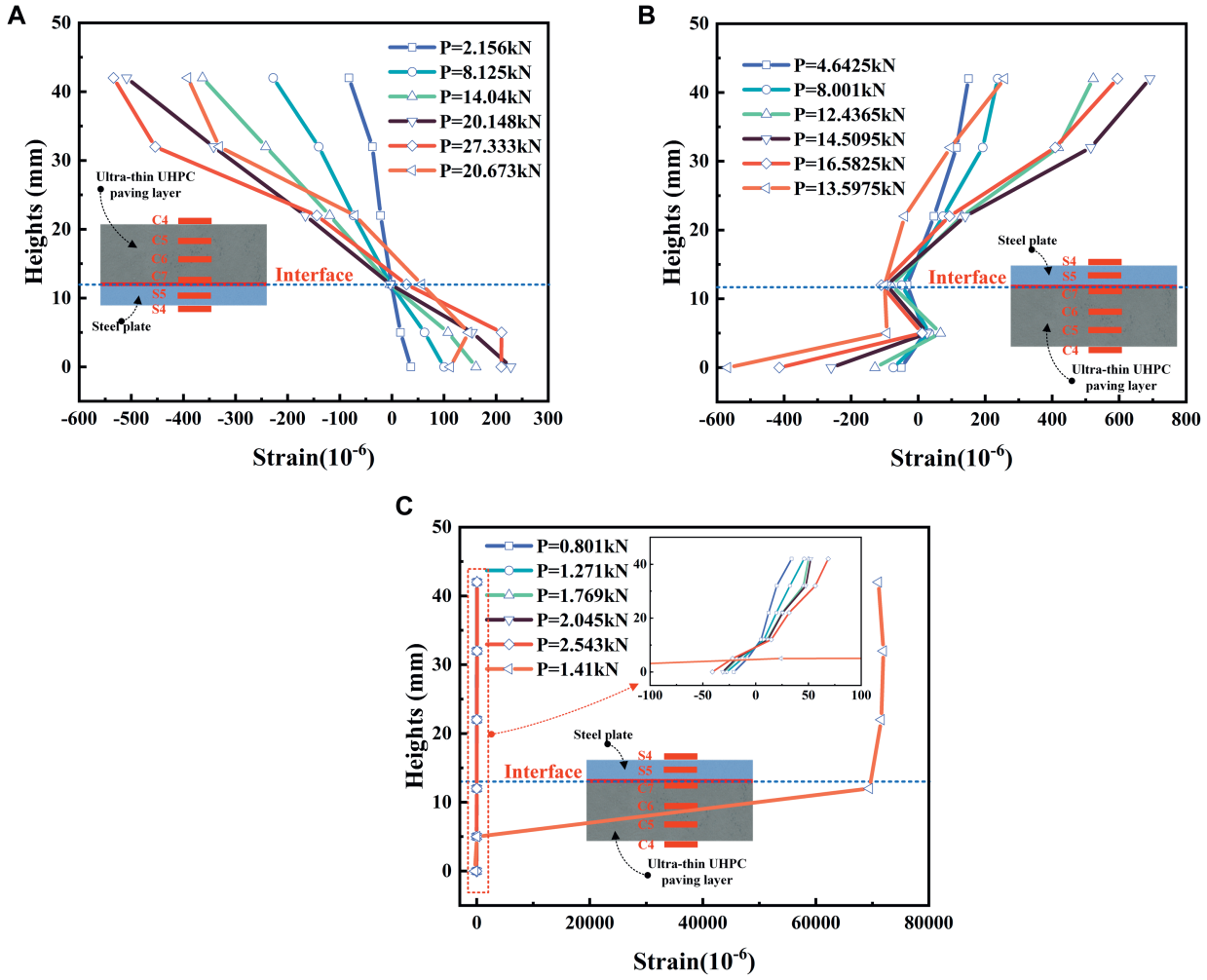

FIGURE 9
Strain distribution. **(A)** EA-Lm strain distribution; **(B)** EA-Ln strain distribution; **(C)** EA-J-Ln strain distribution.

4.2.2 Steel

The steel material is primarily referenced from the existing literature (Cao and Shao, 2019), and the stress-strain curve is shown in Figure 12. Experimental results indicate that the steel plate undergoes yielding during the bending failure process of the composite bridge deck, thus a trilinear hardening elastic-plastic constitutive model is adopted for simulation. All steel components have a material strength grade of Q345, with a yield strength of 387.1 MPa, an ultimate strength of 542.3 MPa, and an elastic modulus of 202.2 GPa based on material testing results.

4.2.3 Interfaces

The cohesive zone model is applicable for numerical analysis of the steel-concrete interface (Yin et al., 2019). Complex interface behaviors can be simulated by the traction-separation relationship of nodes in the cohesive elements (Ranz et al., 2020). In Figure 13, the thickness of the interface is much smaller than that of the composite bridge deck. Therefore, a cohesive contact behavior is employed to simulate the interface elements of the epoxy bonding layer. Additionally, referring to previous research, the shear stress-slip curve is bilinear (Zou et al., 2023a; Fang et al., 2024), suggesting that the cohesive model should adopt a bilinear stress-separation relationship. The stress-displacement relationship of the bonding elements can be determined by a bilinear traction-separation relationship, achieving the simulation of complex interface behavior in the local model, as detailed in Table 6.

4.3 Model validation

Figure 14 displays the load-deflection curves for both the EA-Lm and EA-J-Ln specimens (experimental and modeled). Both types of specimens exhibit good consistency in their curves. Compared to the experiment, the finite element model for the EA-Lm specimen exhibits debonding between the UHPC panel and the epoxy

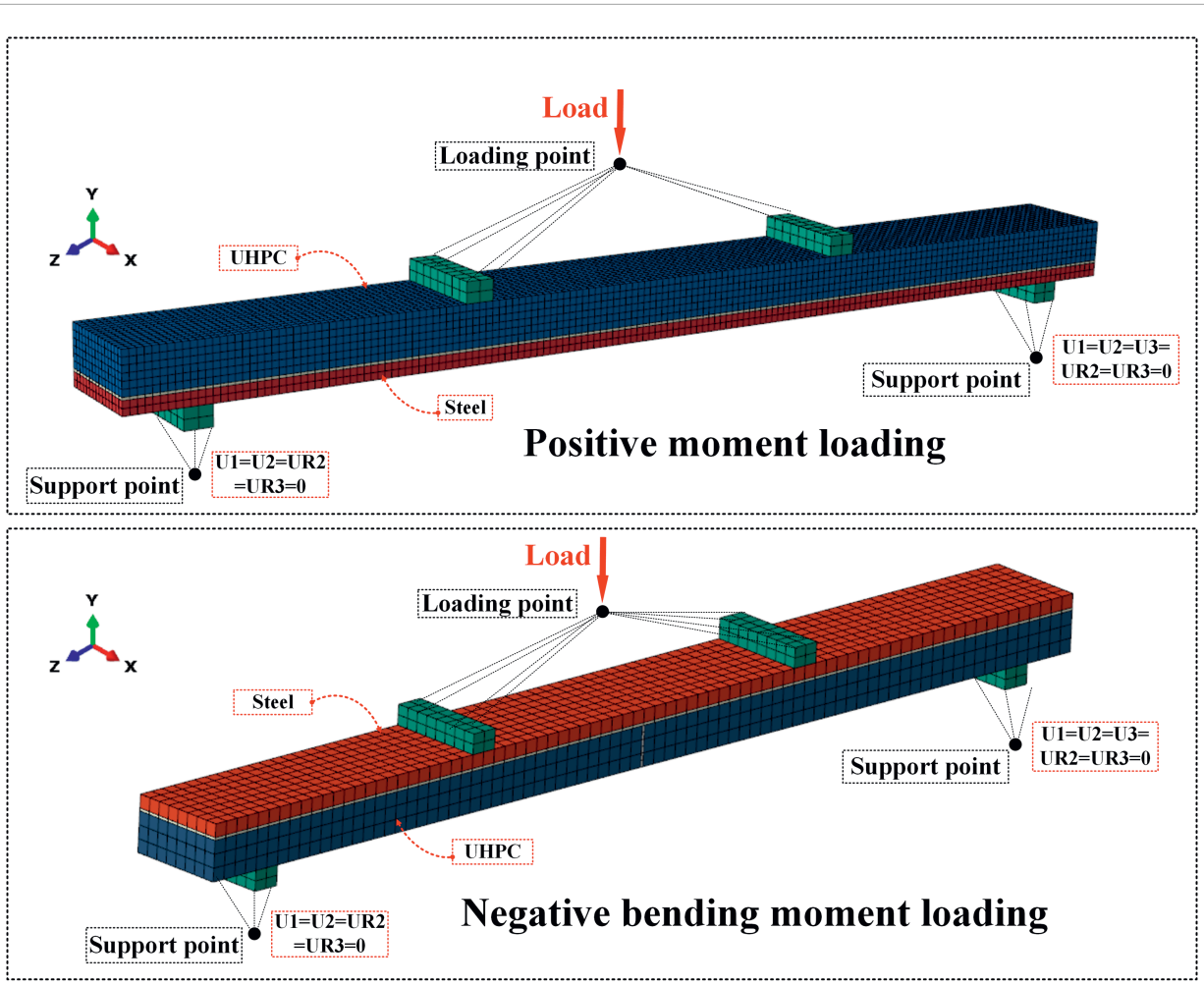

FIGURE 10
Introduction to models.

TABLE 6 Cohesion model ontology parameters.

Direction	$t^0_{n,s,t}$ (MPa)	$K_{nn,ss,tt}$ (N/mm^3)	$G_{n,s,t}$ (N/mm)
Normal	3.74	174.33	0.06
Tangential I	5.3	209.28	0.1224
Tangential II	5.3	209.28	0.1224

adhesive layer, while for the EA-J-Ln specimen, debonding occurs at the joint between the UHPC panel and the epoxy adhesive layer, with the area of failure being consistent. This indicates that the bending behavior of the composite bridge deck can be simulated by Cohesive Zone Model (CZM) to represent the bonding between the UHPC panel and the epoxy adhesive layer. The deviation between the experimental ultimate load and the model calculated value is within 5%, demonstrating that the finite element analysis can accurately simulate the bending behavior of the EA-Lm and EA-J-Ln specimens.

4.4 Discussion

Figure 15 presents the numerical simulation results of the EA-Lm and EA-J-Ln specimens. CSDMG is an indicator used to determine the degree of interface damage. When CSDMG reaches 1, it indicates delamination between the interface layers, and when its value ranges between 0 and 1, it signifies interface damage. DAMAGEC and DAMAGET represent the indices for evaluating compression and tensile damage in UHPC, respectively. Their values also range between 0 and 1, indicating damage to the UHPC matrix

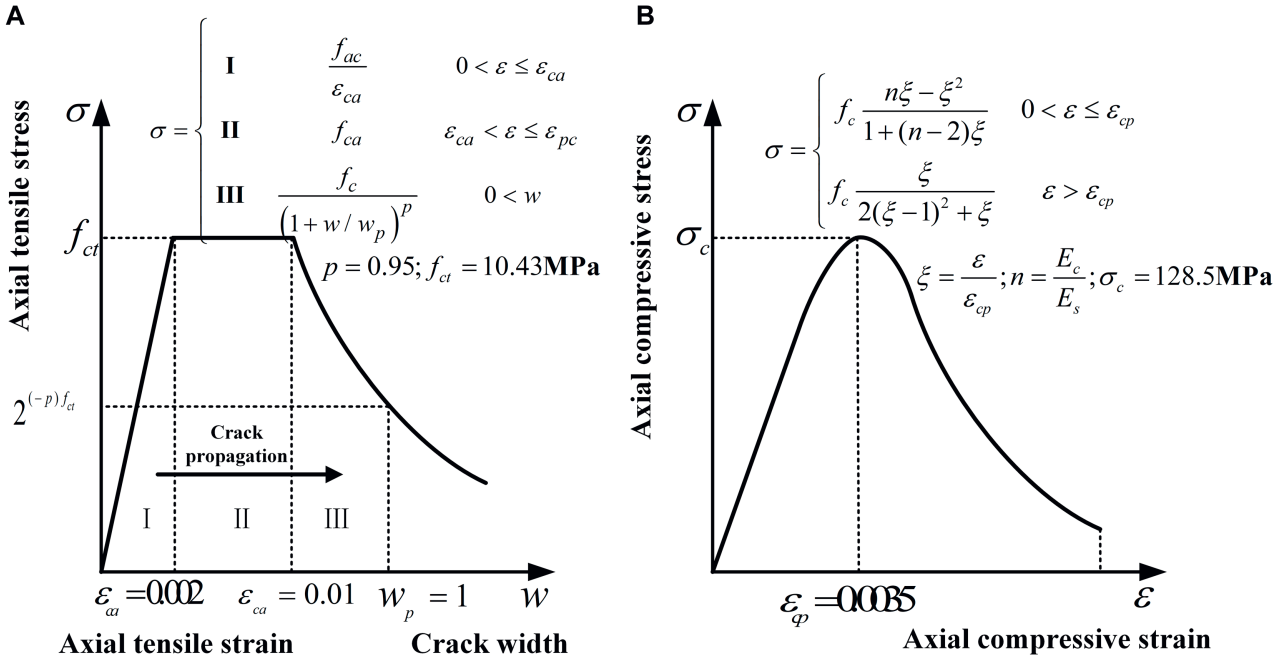

FIGURE 11
Stress-strain relationship of UHPC. **(A)** UHPC Tensile Constitutive Model; **(B)** Compresssive stress-strain relationship.

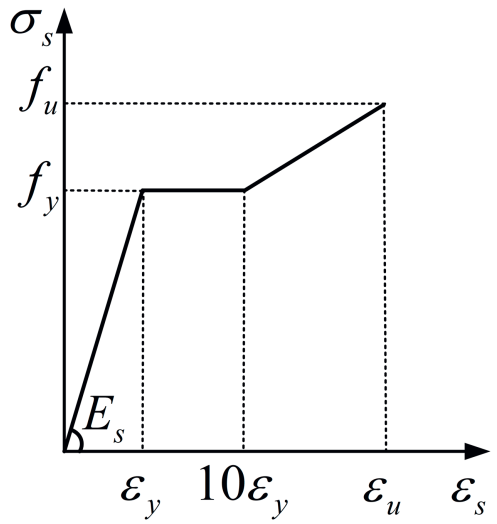

FIGURE 12
Stress-strain relationship of Steel.

when they reach 1. According to Figure 15A, under the ultimate load P_u = 24.87 kN, there is extensive debonding between the epoxy adhesive layer and the UHPC panel, rendering them ineffective in working together. Additionally, significant tensile damage and minor compressive damage are observed near the loading point on the UHPC panel, but no destruction occurs. From Figure 15B, it can be seen that under the ultimate load P_u = 2.45 kN, extensive debonding occurs between the UHPC panel and the epoxy adhesive layer near the joint, while the UHPC matrix exhibits only minor tensile damage and no compressive damage.

5 Conclusion

The following conclusions are drawn.

(1) For specimens using smooth surface UHPC bridge deck without joints under positive bending loading mode, the epoxy adhesive layer interface can provide a load-bearing capacity of approximately 27.67 kN. However, there is a risk of debonding between the UHPC panel and the epoxy adhesive layer, which prevents the full utilization of the material properties of UHPC. It is recommended to roughen the surface of prefabricated UHPC panels to ensure effective bonding with the epoxy adhesive layer.

(2) For specimens containing epoxy glue joints, under the negative bending moment loading mode, the interface damage first started at the joint position, and after the joint damage, the UHPC board close to the joint position and the epoxy adhesive layer debonded.

(3) Under the negative bending moment loading mode, the ultimate bearing capacity of the jointless specimen is 16.58 kN, which is about 6.5 times lower than the ultimate bearing capacity of the specimen containing epoxy joints.

(4) The use of carbon fiber cloth to enhance the epoxy glue joints can effectively improve the bending resistance of the joints and increase the ultimate bearing capacity by about 2 times. However, the width of the carbon fiber cloth has a significant impact on the bending performance of the composite plate joints.

(5) Establishing a numerical model for composite panels based on CZM can effectively simulate the bonding behavior between UHPC panels and steel plates. Using

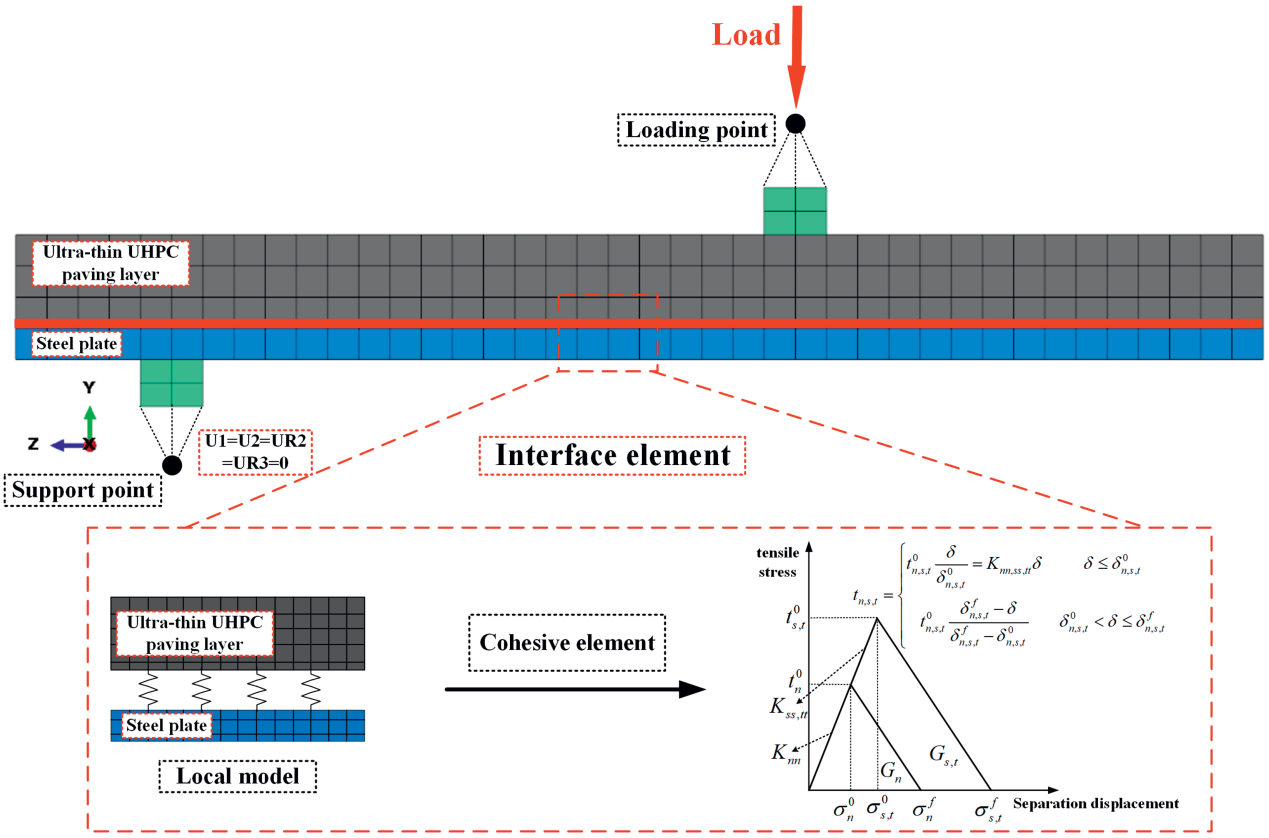

FIGURE 13
Constitutive model of cohesive element.

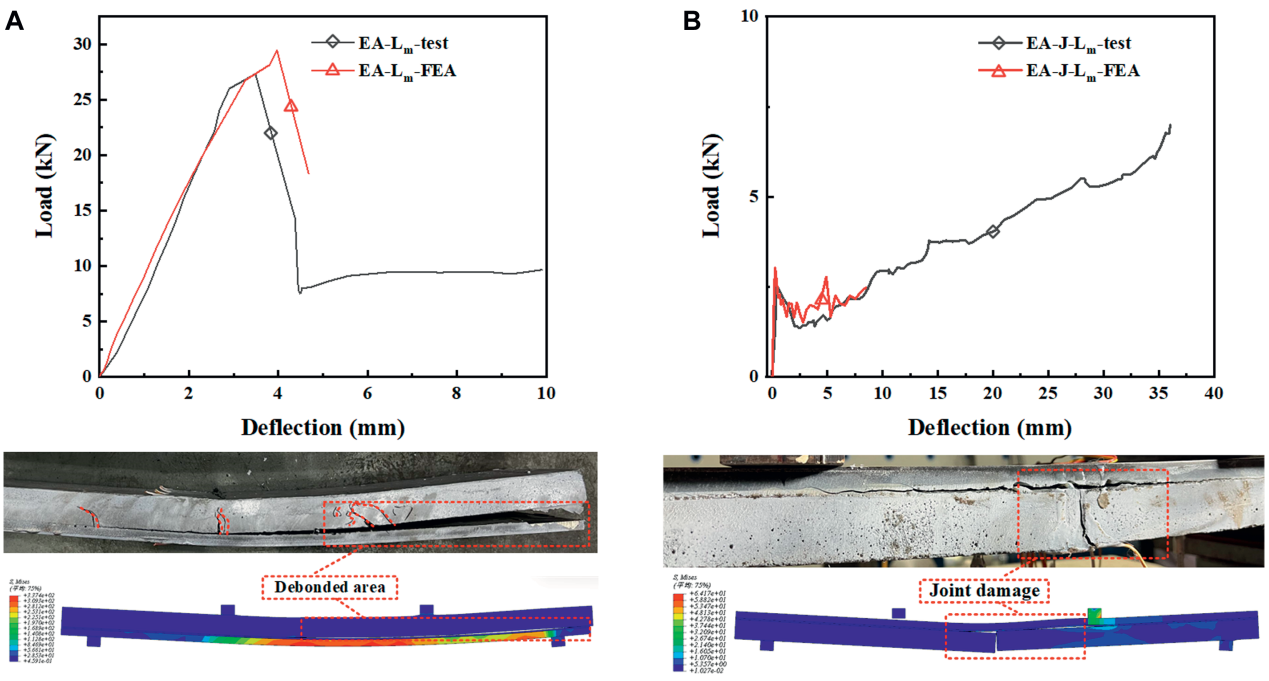

FIGURE 14
Model verification. **(A)** EA-Lm; **(B)** EA-J-Ln.

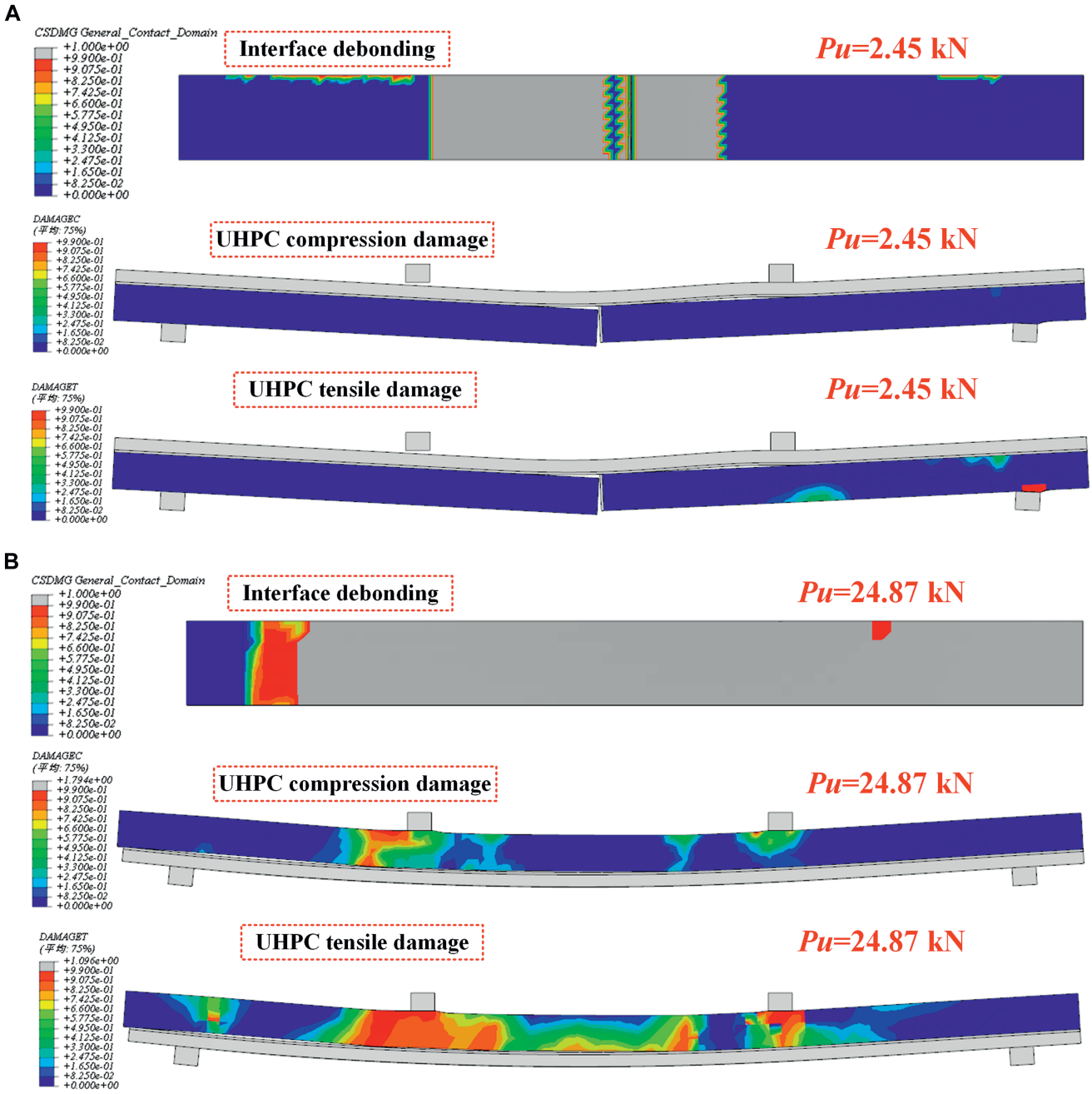

FIGURE 15
Numerical simulation results. **(A)** EA-Lm; **(B)** EA-J-Ln.

epoxy adhesive layers to connect steel plates with prefabricated UHPC bridge deck ensures more uniform stress transfer at the steel-UHPC interface. Additionally, the ultra-thin UHPC panel does not fail before interface failure occurs.

Data availability statement

The original contributions presented in the study are included in the article/Supplementary material, further inquiries can be directed to the corresponding author.

Author contributions

XZ: Data curation, Software, Validation, Visualization, Writing–original draft, Writing–review and editing. JJ: Conceptualization, Data curation, Investigation, Writing–original draft. LL: Investigation, Methodology, Writing–review and editing. SW: Methodology, Project administration, Writing–review and editing. XD: Software, Validation, Visualization, Writing–review and editing. YL: Formal Analysis, Investigation, Writing–review and editing. ZZ: Funding acquisition, Project administration, Resources, Supervision, Writing–review and editing, Writing–original draft.

Funding

The author(s) declare that financial support was received for the research, authorship, and/or publication of this article. The authors express their sincere gratitude for the financial support provided by the Natural Science Foundation of Chongqing, China (CSTB2023NSCQ-MSX0019), the National Nature Science Foundation of China (Grant Nos. 52208302, 52278293) and Science and Technology Research Program of Chongqing Municipal Education Commission (KJZD-M202300706).

Conflict of interest

The authors declare that the research was conducted in the absence of any commercial or financial relationships that could be construed as a potential conflict of interest.

Publisher's note

References

Ahmed, G. H., and Aziz, O. Q. (2019). Shear behavior of dry and epoxied joints in precast concrete segmental box girder bridges under direct shear loading. *Eng. Struct.* 182, 89–100. doi:10.1016/j.engstruct.2018.12.070

Benedetty, C. A., Dos Santos, V. B., Krahl, P. A., Rossi, A., Silva, F. D. A., Cardoso, D. C. T., et al. (2023). Flexural and shear behavior of steel-UHPC composite beams: a review. *Eng. Struct.* 293, 116649. doi:10.1016/j.engstruct.2023.116649

Bu, Y., Li, M., Wei, C., Cheng, Z., Cui, C., and Bao, Y. (2023). Experimental and analytical studies on flexural behavior of composite bridge decks with orthotropic steel deck and ultra-high-performance concrete (UHPC) slab under negative moment. *Eng. Struct.* 274, 115190. doi:10.1016/j.engstruct.2022.115190

Cao, J., and Shao, X. (2019). Finite element analysis of headed studs embedded in thin UHPC. *J. Constr. Steel Res.* 161, 355–368. doi:10.1016/j.jcsr.2019.03.016

Code for acceptance of construction quality of strengthening building structures (2010). *Code for acceptance of construction quality of strengthening building structures (GB 50550-2010) [in Chinese]*.

Ding, J., Zhu, J., and Shi, T. (2023). Performance of grouped stud connectors in precast steel-UHPC composite bridges under combined shear and tension loads. *Eng. Struct.* 277, 115470. doi:10.1016/j.engstruct.2022.115470

Du, J., Meng, W., Khayat, K. H., Bao, Y., Guo, P., Lyu, Z., et al. (2021). New development of ultra-high-performance concrete (UHPC). *Compos. B Eng.* 224, 109220. doi:10.1016/j.compositesb.2021.109220

Du, L., Qi, J., Cheng, Z., and Wang, J. (2022). Finite element modeling of UHPC slabs with dovetail joints and steel wire mesh using an innovative interfacial treating method. *Structures* 37, 745–755. doi:10.1016/j.istruc.2022.01.057

Duan, L., Brühwiler, E., and Wang, C. (2020). Cold stiffening of orthotropic steel decks by a composite UHPFRC layer. *J. Constr. Steel Res.* 172, 106209. doi:10.1016/j.jcsr.2020.106209

Fang, Z., Wu, J., Xu, X., Ma, Y., Fang, S., Zhao, G., et al. (2024). Grouped rubber-sleeved studs–UHPC pocket connections in prefabricated steel–UHPC composite beams: Shear performance under monotonic and cyclic loadings. *Eng. Struct.* 305, 117781. doi:10.1016/j.engstruct.2024.117781

Fang, Z. C., Wu, J. P., Zhao, G. F., Fang, S., Ma, Y. H., and Jiang, H. B. (2024). Shear performance and design recommendations of single embedded nut bolted shear connectors in prefabricated steel–UHPC composite beams. *Steel Compos. Struct.* 50 (3), 319–336. doi:10.12989/scs.2024.50.3.319

Fang, Z., Fang, S., and Liu, F. (2022). Experimental and numerical study on the shear performance of short stud shear connectors in steel–UHPC composite beams. *Buildings* 12, 418. doi:10.3390/buildings12040418

General Administration of Quality Supervision (2010). *Inspection and Quarantine, beijing, China. Metallic materials-Tensile testing-Part 1:Method of test at roomtemperature (GB/T 228.1-2010) ([in Chinese]).*

General Administration of Quality Supervision (2015). *Inspection and quarantine, beijing, China*. Reactive powder concrete (GB/T 31387-2015) ([in Chinese]).

Hu, W., Li, C., Chen, B., and Liu, Y. (2023). Finite element analysis on shear behavior of headed studs in steel-UHPC composite slab. *Structures* 52, 464–475. doi:10.1016/j.istruc.2023.03.185

Hung, C.-C., El-Tawil, S., and Chao, S.-H. (2021). A review of developments and challenges for UHPC in structural engineering: behavior, analysis, and design. *J. Struct. Eng.* 147, 03121001. doi:10.1061/(asce)st.1943-541x.0003073

Jia, J., Ren, Z., Bai, Y., Li, J., Li, B., Sun, Y., et al. (2023). Tensile behavior of UHPC wet joints for precast bridge deck panels. *Eng. Struct.* 282, 115826. doi:10.1016/j.engstruct.2023.115826

Jiang, H., Chen, L., Ma, Z. J., and Feng, W. (2015). Shear behavior of dry joints with castellated keys in precast concrete segmental bridges. *J. Bridge Eng.* 20, 04014062. doi:10.1061/(ASCE)BE.1943-5592.0000649

Jiang, L., Nie, L., Zhou, W., Wu, X., and Liu, L. (2022). Distortional buckling analysis of steel-concrete composite box beams considering effect of stud rotational restraint under hogging moment. *J. Cent. South Univ.* 29, 3158–3170. doi:10.1007/s11771-022-5130-6

Khorramian, K., Maleki, S., Shariati, M., Jalali, A., and Tahir, M. M. (2017). Numerical analysis of tilted angle shear connectors in steel-concrete composite systems. *Steel compos. Struct.* 23, 067–085. doi:10.12989/scs.2017.23.1.067

Leng, J., Yang, J., Zhang, Z., Du, J., Zou, Y., and Zhou, J. (2024). Effect of vehicle-induced vibration on the strength, nano-mechanical properties, and microstructural characteristics of ultra-high-performance concrete during hardening process. *Cem. Concr. Compos.* 148, 105487. doi:10.1016/j.cemconcomp.2024.105487

Li, B., Jiang, J., Deng, Z., Zhou, H., Wang, H., Jiang, H., et al. (2022a). Bending behavior of steel-UHPC composite bridge deck based on epoxy adhesive. *Front. Mater.* 9. doi:10.3389/fmats.2022.1023886

Li, C., Chen, B., Hu, W., and Sennah, K. (2023a). Push-out test of hybrid shear connector in steel-precast UHPC composite slab. *Structures* 50, 1767–1782. doi:10.1016/j.istruc.2023.02.113

Li, Y., Ma, X., Li, H., Li, C., Hu, Z., and Li, Z. (2023b). Experimental study on flexural and interfacial shear properties of the steel-UHPC glued composite deck. *Eng. Struct.* 293, 116643. doi:10.1016/j.engstruct.2023.116643

Liu, Y., Bao, Y., Deng, L., and Zhang, Q. (2023). Numerical study on the effects of stud degradation and stud arrangement on the fatigue performance of steel-UHPC composite decks. *Eng. Struct.* 292, 116549. doi:10.1016/j.engstruct.2023.116549

Luo, Y., Li, A., and Kang, Z. (2012). Parametric study of bonded steel–concrete composite beams by using finite element analysis. *Eng. Struct.* 34, 40–51. doi:10.1016/j.engstruct.2011.08.036

Men, P., Di, J., Qin, F., and Su, Y. (2023). Experimental investigation of the shear behavior of slender continuous steel–concrete composite girders in hogging moment. *J. Struct. Eng.* 149, 04022218. doi:10.1061/JSENDH.STENG-11537

Pan, R., He, W., Cheng, L., Su, M., and Li, C. (2023). Experimental investigation on the shear performance of UHPC large-keyed epoxy joints subjected to direct shear loading. *Structures* 54, 171–182. doi:10.1016/j.istruc.2023.05.050

Pang, B., Jin, Z., Zhang, Y., Xu, L., Li, M., Wang, C., et al. (2022). Ultraductile waterborne epoxy-concrete composite repair material: epoxy-fiber synergistic effect on flexural and tensile performance. *Cem. Concr. Compos.* 129, 104463. doi:10.1016/j.cemconcomp.2022.104463

Ranz, D., Cuartero, J., Castejon, L., Miralbes, R., and Malon, H. (2020). A cohesive zone model approach to interlaminar behaviour of carbon/epoxy laminated curved beams. *Compos. Struct.* 238, 111983. doi:10.1016/j.compstruct.2020.111983

Shao, X., Qu, W., Cao, J., and Yao, Y. (2018). Static and fatigue properties of the steel-UHPC lightweight composite bridge deck with large U ribs. *J. Constr. Steel Res.* 148, 491–507. doi:10.1016/j.jcsr.2018.05.011

Shi, Z., Su, Q., Kavoura, F., and Veljkovic, M. (2022). Behavior of short-headed stud connectors in orthotropic steel-UHPC composite bridge deck under fatigue loading. *Int. J. Fatigue* 160, 106845. doi:10.1016/j.ijfatigue.2022.106845

State Administration for Market Regulation (2021). *Standardization Administration, beijing, China. Test methods for properties of resin casting body (GB/T 2567-2021) ([in Chinese])*.

Sun, N., Song, Y., Hou, W., Zhang, H., Wu, D., Li, Y., et al. (2021). Interfacial bond properties between normal strength concrete and epoxy resin concrete. *Adv. Mater. Sci. Eng.* 2021, 1–14. doi:10.1155/2021/5561097

Wang, Y., Shao, X., Chen, J., Cao, J., and Deng, S. (2021). UHPC-based strengthening technique for orthotropic steel decks with significant fatigue cracking issues. *J. Constr. Steel Res.* 176, 106393. doi:10.1016/j.jcsr.2020.106393

Wang, Z., Nie, X., Fan, J.-S., Lu, X.-Y., and Ding, R. (2019). Experimental and numerical investigation of the interfacial properties of non-steam-cured UHPC-steel composite beams. *Constr. Build. Mater.* 195, 323–339. doi:10.1016/j.conbuildmat.2018.11.057

Yin, H., Shirai, K., and Teo, W. (2019). Numerical model for predicting the structural response of composite UHPC–concrete members considering the bond strength at the interface. *Compos. Struct.* 215, 185–197. doi:10.1016/j.compstruct.2019.02.040

Yoo, D.-Y., Min, K.-H., Lee, J.-H., and Yoon, Y.-S. (2014a). Shrinkage and cracking of restrained ultra-high-performance fiber-reinforced concrete slabs at early age. *Constr. Build. Mater.*73, 357–365. doi:10.1016/j.conbuildmat.2014.09.097

Yoo, D.-Y., Park, J.-J., Kim, S.-W., and Yoon, Y.-S. (2014b). Influence of reinforcing bar type on autogenous shrinkage stress and bond behavior of ultra high performance fiber reinforced concrete. *Cem. Concr. Compos.* 48, 150–161. doi:10.1016/j.cemconcomp.2013.11.014

Yu, K., Zhang, Z., Zou, Y., Jiang, J., Zeng, X., and Tang, L. (2022). Interfacial shear performance of epoxy adhesive joints of prefabricated elements made of ultra-high-performance concrete. *Polymers* 14, 1364. doi:10.3390/polym14071364

Zhang, B., Yu, J., Chen, W., Sun, H., Chen, S., and Wang, H. (2022). Interfacial properties between ultra-high performance concrete (UHPC) and steel: from static performance to fatigue behavior. *Eng. Struct.* 273, 115145. doi:10.1016/j.engstruct.2022.115145

Zhang, P., Xu, F., Peng, E., Liu, Y., and Sheikh, S. A. (2023a). Shear performance of the epoxy-bolt interface between UHPC slabs and GFRP girder. *Structures* 54, 263–279. doi:10.1016/j.istruc.2023.05.014

Zhang, Z., Pang, K., Xu, L., Zou, Y., Yang, J., and Wang, C. (2023b). The bond properties between UHPC and stone under different interface treatment methods. *Constr. Build. Mater.* 365, 130092. doi:10.1016/j.conbuildmat.2022.130092

Zou, Y., Jiang, J., Yang, J., Zhang, Z., and Guo, J. (2023a). Enhancing the toughness of bonding interface in steel-UHPC composite structure through fiber bridging. *Cem. Concr. Compos.* 137, 104947. doi:10.1016/j.cemconcomp.2023.104947

Zou, Y., Jiang, J., Zhou, Z., Wang, X., and Guo, J. (2021a). Study on the static performance of prefabricated UHPC-steel epoxy bonding interface. *Adv. Civ. Eng.* 2021, 1–15. doi:10.1155/2021/6663517

Zou, Y., Zhou, H., Yang, J., Zhang, Z., Zheng, K., and Jiang, J. (2023b). Mechanical behavior of natural bonding interface in hollow steel-UHPC composite bridge deck. *J. Constr. Steel Res.* 210, 108093. doi:10.1016/j.jcsr.2023.108093

frontiers | Frontiers in Materials

TYPE Original Research
PUBLISHED 04 April 2024
DOI 10.3389/fmats.2024.1367600

OPEN ACCESS

EDITED BY
Jialuo He,
Washington State University, United States

REVIEWED BY
Hui Li,
Hebei University of Technology, China
Chongsheng Cheng,
Chongqing Jiaotong University, China

*CORRESPONDENCE
Hong Liao,
liaohong2024@126.com

RECEIVED 09 January 2024
ACCEPTED 18 March 2024
PUBLISHED 04 April 2024

CITATION
Han B, Wang H, Liao H, Dai C, Zhao Y, Xu W, Zhou G and Shi C (2024), Investigation into the seamless construction for hundred-meter scale super-length raft structure based on magnesia expansive agent concrete. *Front. Mater.* 11:1367600. doi: 10.3389/fmats.2024.1367600

Investigation into the seamless construction for hundred-meter scale super-length raft structure based on magnesia expansive agent concrete

Bin Han, Huichao Wang, Hong Liao*, Chao Dai, Yunpeng Zhao, Wenlong Xu, Guojing Zhou and Chuandong Shi

China Construction Third Engineering Bureau Group Co., Ltd., Chongqing, China

This research introduces an innovative construction method based on magnesia expansive agent concrete for the seamless construction of hundred-meter scale super-length raft structures, corroborated by the on-site test. The basic principle of this construction method is to use the pre compression stress generated by magnesia expansive agent to offset temperature and shrinkage stress. A temperature-strain monitoring system was employed to gather data, affirming the technique's applicability and safety. Through the examination of temperature and strain dispersion trends in super-length raft structure, recommendations for the configuration of temperature-strain sensors have been put forth. Through the scrutiny of the temporal evolution pattern of temperature, the specific temporal and spatial coordinates that warrant particular vigilance during the surveillance of the raft's inner-surface temperature difference were identified. Upon evaluating the correlation between strain dispersion and strain-temperature differential in the raft's thickness dimension, a novel temperature control index (the bottom-surface temperature difference) was introduced. The threshold for this metric was established at 30°C, derived from empirical test outcomes conducted on-site. Furthermore, the critical regions for monitoring the bottom-surface temperature difference were specified.

KEYWORDS

super-length raft structure, seamless construction, expansive strengthening band, on-site test, temperature-strain monitoring system

1 Introduction

Within the realm of contemporary construction engineering, the utilization of mass concrete edifices is progressively pervasive, encompassing the raft foundations of ultra-tall structures, piers of substantial bridges, dams, and so forth (Ming et al., 2022). Owing to the considerable structural dimensions and the immense quantity of concrete casting associated with these projects, a multitude of challenges frequently arise during the construction phase, one notable issue being the formation of thermal cracks (Xin et al., 2021).

Throughout the solidification phase, mass concrete engenders a substantial quantity of heat as a result of the exothermic hydration reaction of cement (Liu et al., 2022). If this heat is not dispersed promptly, it will instigate a swift escalation in the internal temperature of the concrete. Nevertheless, due to the concrete

surface being in contact with the environment, its heat dissipation rate is accelerated, thereby establishing a temperature gradient with a high internal temperature and a low external temperature. When this temperature disparity surpasses the concrete's tolerance threshold, thermal stress will be induced within the concrete, culminating in the emergence of thermal cracks. The manifestation of these thermal cracks could gravely compromise the safety and durability of the concrete structures (Tatro et al., 2007).

Furthermore, shrinkage stress constitutes a significant concern during the preservation procedure of super-length concrete structures. Concrete undergoes contraction throughout the solidification process. When the contraction process of concrete is restricted, shrinkage stress is engendered within the structure, and the elongation of the structure directly correlates with the magnitude of the shrinkage stress (Jin, 2002). If this shrinkage stress surpasses the tensile resilience of the concrete, it will instigate the concrete to fracture, resulting in the formation of shrinkage cracks.

Super-length raft structures are classified under both mass concrete structures and super-length structures. Consequently, the effective management of their thermal cracks and shrinkage cracks is a crucial challenge that necessitates resolution in the contemporary realm of construction engineering. This issue has been the subject of investigation by scholars from diverse nations.

An automated preservation apparatus was devised to address the issue of thermal cracks during the construction of mass concrete (Ha et al., 2014). This apparatus maintains the temperature gradient between the internal and external milieu of the edifice beneath a specified threshold, and it has been efficaciously examined in simulations and field implementations.

An investigation into the influence of cement and aggregate varieties on the hydration temperature and mechanical attributes of concrete was conducted (Batog and Giergiczny, 2014). They employed six varieties of cement and four types of aggregates. The findings indicated that low-clinker cement can markedly diminish the hydration temperature of concrete, thereby mitigating the likelihood of fissure development. While the type of aggregate does not impact the hydration temperature, it can influence the magnitude of thermal stress due to varying thermal expansion coefficients.

A case study on the construction of mass concrete bridge foundations in Iowa, USA, with an emphasis on averting the emergence of thermal cracks was conducted (by Sargam et al., 2019). They employed ConcreteWorks software to prognosticate the thermal performance of the edifice. The forecasted temperature evolution curves and temperature disparities were juxtaposed with the real-time measurements of the bridge foundation, demonstrating a commendable match. They also executed a sensitivity analysis of various mass concrete parameters.

A framework utilizing a Distributed Temperature Sensing (DTS) system to regulate cracks in mass concrete edifices in reservoir ventures was proposed (Ouyang et al., 2019). The DTS system is employed to monitor the temperature of the concrete, and the thermal performance of the cast-in-place concrete is ascertained through a reverse analysis technique. Subsequently, the risk of concrete cracking under diverse construction and environmental conditions is prognosticated and evaluated.

A nonlinear incremental structural analysis of mass concrete was performed (Truman et al., 1991), taking into account thermal effects, to assess the impact of creep, shrinkage, adiabatic temperature rise, and the construction process on tensile stress. The findings indicated that mass concrete edifices are susceptible to cracking. The paper furnished stress and strain time-history diagrams at typical locations of mass concrete, underscoring the importance of these diagrams in determining the impact of the construction sequence.

The pivotal issue of the spacing between post-pouring strips in mass concrete edifices was investigated (Zhou et al., 2019). The research centered on a 100 m long inverted T-shaped concrete edifice on a soft soil foundation in the Yangtze River Delta region. They utilized the finite element method to simulate the temperature and stress field of the concrete under various construction conditions, and proffered recommended spacing for the post-pouring strips.

However, extant research has not been successful in accomplishing the seamless construction of hundred-meter scale super-length raft structures. The conventional construction methodologies of super-length raft structures predominantly encompass the "Sequential Placement Method" and the "Post Pouring Strip Method." The former method partitions the extensive concrete blocks into multiple smaller units for phased construction during the initial stage of high-temperature shrinkage stress. Following a brief period of stress alleviation, these smaller units are amalgamated into a single entity during the subsequent stage of reduced shrinkage stress, leveraging the tensile strength of the concrete to counteract the temperature and shrinkage stress of the ensuing stage. The specific construction sequence involves pouring the initial batch, followed by the second batch after a minimum interval of 7 days. This approach capitalizes on the inherent principle that the performance of concrete remains unstable during the initial 5–10 days, facilitating the easy release of internal stress prior to complete solidification. However, the compartment length in the "Sequential Placement Method" should not surpass 40 m (Ministry of Housing and Urban Rural Development of the People's Republic of China, 2023). For super-length raft structures, it necessitates the division and pouring of multiple compartments multiple times, leading to an extended construction period and intricate construction organization design. The "Post Pouring Strip Method" involves the creation of temporary construction joints at corresponding locations, temporarily segregating the structure into several sections, shrinking the internal components, and pouring and compacting the concrete of the construction joint after a certain duration, thereby integrating the structure as a whole. Nevertheless, the interface between the new and old concrete at the construction joint is susceptible to quality issues such as cracking and water seepage, and the construction joint necessitates secondary pouring, which prolongs the construction period and hampers the construction progress.

To address these issues, this paper introduces a seamless construction method for hundred-meter scale super-length raft structures predicated on expansive strengthening bands. The basic principle of this construction method is to use the pre compression stress generated by magnesia expansive agent to offset temperature and shrinkage stress. Magnesium oxide (MgO), characterized by its

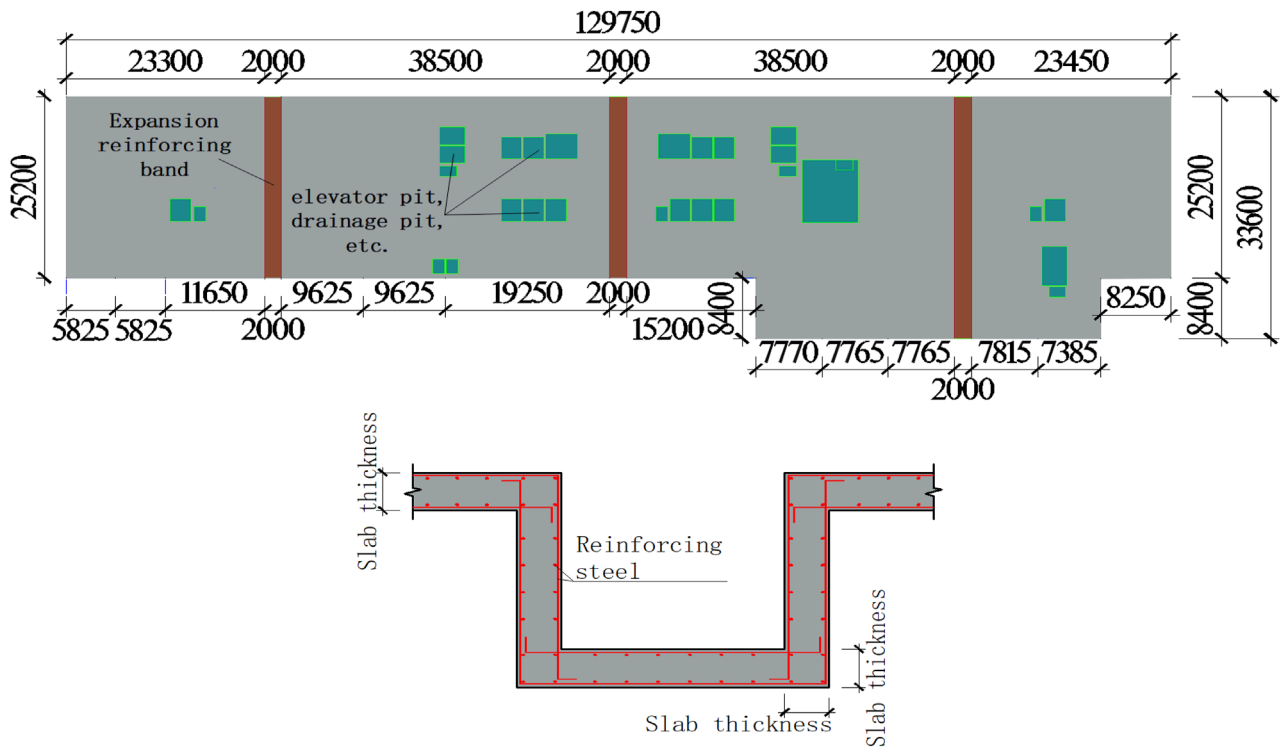

FIGURE 1
Dimensional drawing of the raft and the elevator, catchment well pit (unit mm).

white, powdery form, exhibits significant hygroscopic and expansive properties. When incorporated into concrete as an expansion agent, it absorbs the inherent moisture, leading to an expansion of the MgO and the generation of a specific pressure. A chemical interaction between MgO and water results in the formation of magnesium hydroxide ($Mg(OH)_2$). The resultant $Mg(OH)_2$ occupies a volume that is 3–4 times greater than the initial MgO, facilitating the expansion of the material.

In contrast to the conventional technique, this construction method circumvents secondary construction and independent support, thereby diminishing construction expenses and abbreviating the construction duration. The primary limitation of this construction method is that the induction of preloading stress is contingent upon the expansion rate and the interstitial distance of the expansive strengthening band. The expansion rate of the concrete within the expansive strengthening band is capped at 0.8% (Li et al., 2021). If the expansion rate surpasses this threshold, the alterations in porosity induced by expansion can compromise the mechanical attributes and longevity of the concrete. Consequently, the spacing of the expansive strengthening band is also subject to an upper limit. Leveraging a construction venture of the China Construction Third Engineering Bureau Group Co., Ltd., an on-site test was executed on a raft structure that spans 130 m in length and varies from 1.9 m to 3.55 m in thickness. A temperature-strain monitoring system was employed to monitor the raft concrete, substantiating the practicability and safety of this construction method.

2 Materials and methods

2.1 Project overview

The construction venture encompasses an region of 186,000 m^2, with the cumulative edifice region amounting to 563,000 m^3. The tower of the project employs a raft foundation, with its load-bearing stratum situated in the middle weathered mudstone, and the characteristic value of the foundation load-bearing capacity is 1,205 kPa. Notably, the tower raft of the A, B, and C edifices of the hospital is super-length, with a raft thickness of 1900 mm, and at the elevator and catchment well pit, the maximal thickness of the raft escalates to 3,550 mm. The length of the raft extends to about 130 m at its longest, and the width ranges between 25–34 m. The dimensions of the raft and the large sample of the elevator and catchment well pit are depicted in Figure 1.

The raft was fabricated with C35 concrete, and 3 expansive strengthening bands were incorporated into the raft. The concrete grade of the expansive strengthening band was designated as C40, and a MgO expansion agent was integrated. The mix proportion and compressive strength at varying ages (7-day and 28-day) of C35 and C40 concrete are illustrated in Supplementary Tables S1, S2. For the sake of differentiation, the raft exterior to the expansive strengthening band was denoted as the "standard region." The expansive strengthening band and the raft concrete were cast concurrently, accomplishing the seamless construction of the hundred-meter scale super-length raft, as depicted in Figure 2.

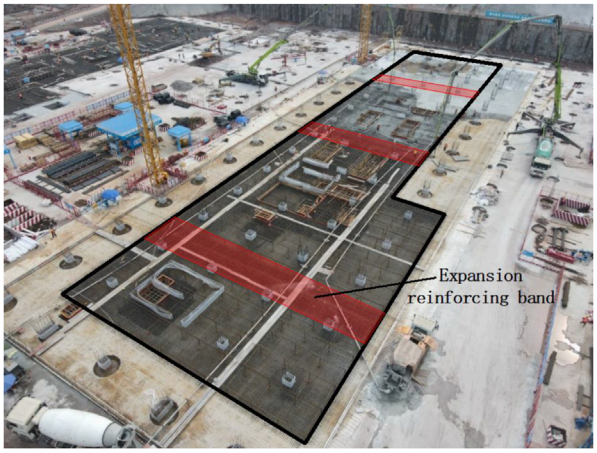

FIGURE 2
On-site casting diagram of the raft.

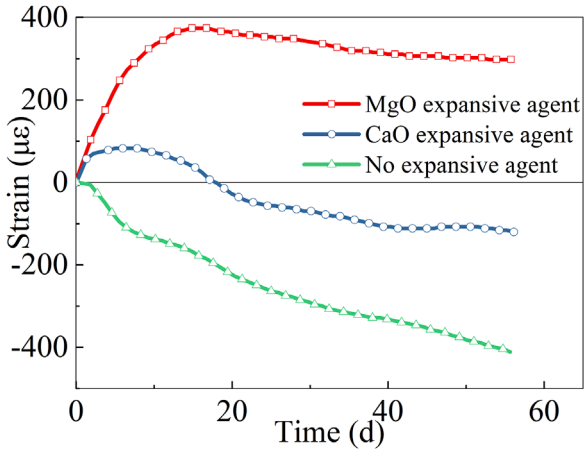

FIGURE 3
Comparison of the effects of expansion agents.

In the conventional methodology for seamless construction of super-length structures, calcium sulfoaluminate ($Ca_4Al_6SO_{16}$) and calcium oxide (CaO) serve as the primary expansion agents. The underlying principle of expansion involves hydration, leading to the formation of ettringite and calcium hydroxide. However, this approach exhibits several limitations: under standard temperature and water curing conditions, the expansion reaction culminates within a span of 7 days, rendering it incapable of compensating for subsequent shrinkage; the initial expansion rate is excessively rapid, and the plastic stage depletes a significant amount of expansion energy, thereby posing challenges in compensating for the shrinkage due to temperature drop and subsequent drying of concrete; the expansion products, namely calcium hydroxide and ettringite, exhibit a solubility of 0.17 g/100 g for calcium hydroxide at room temperature, while ettringite decomposes above 80°C.

To address the issues associated with traditional expansion agents, this construction technique innovatively incorporates MgO expansion agents into the seamless construction of super-length structures. The principle of expansion, as elucidated in the preceding chapter, endows MgO expansion agents with several advantages: they offer the flexibility to regulate the expansion characteristics of concrete through various combinations of dosages and activities, thereby synchronizing the expansion energy with concrete shrinkage; it allows for the customization of product types based on environmental conditions, controls the pattern of expansion and development, and compensates for self-shrinkage, temperature shrinkage, and drying shrinkage throughout the entire cycle, thereby achieving superior resistance to cracking and seepage; the expansion is conspicuous, and the solubility of the product is extremely low. The expansion product is $Mg(OH)_2$, with a solubility of 0.0009 g/100 g, and its expansion performance remains stable at elevated temperatures.

To comprehensively comprehend the efficacy and benefits of the MgO expansion agent, a series of concrete expansion experiments were executed, with the type of expansion agent serving as the variable. The experimental variables for the 3 concrete groups were: absence of an expansion agent, incorporation of a CaO expansion agent, and addition of an MgO expansion agent. The outcomes of these tests are depicted in Figure 3.

The graphical representation reveals that the concrete devoid of an expansion agent did not undergo expansion, but initiated contraction subsequent to the initial setting. Concrete supplemented with a CaO expansion agent exhibited substantial expansion during the initial phase, attaining its peak expansion rate on the 8th day, followed by contraction. Conversely, concrete supplemented with an MgO expansion agent demonstrated significant expansion during the initial 17 days. Post this period, the expansion rate experienced a slight decline, yet maintained a relatively elevated level of expansion rate. From the perspective of the "full pouring maintenance cycle" theory, it is evident that the MgO expansion agent possesses significant benefits.

The experimental location was situated in the Jiulongpo District of Chongqing City, with the experimental duration extending from 24 June 2023, to 23 August 2023. Throughout this timeframe, the maximum recorded temperature was 39°C, observed on July 12 and August 11, while the minimum temperature of 20°C was noted on July 14. Predominantly, the wind conditions were classified as first-class, with velocities ranging between 0.3 and 1.5 m/s. The initial experimental design proposed the utilization of wired temperature-strain sensors. However, during the implementation phase, two significant challenges emerged: the extensive length of the raft structure necessitated a substantial quantity of wires, escalating the testing expenses; additionally, the construction process posed a risk of wire damage, leading to potential measurement point failures. To address these issues, the decision was made to employ wireless sensors. Subsequent on-site testing and verification confirmed the efficacy of this solution.

2.2 Temperature-strain monitoring system

2.2.1 Temperature-strain sensor

In this investigation, the SZZX-A150 embedded strain gauge was employed as a temperature-strain sensor, as depicted in Figure 4. This sensor operates on the principle of wire vibration, where a

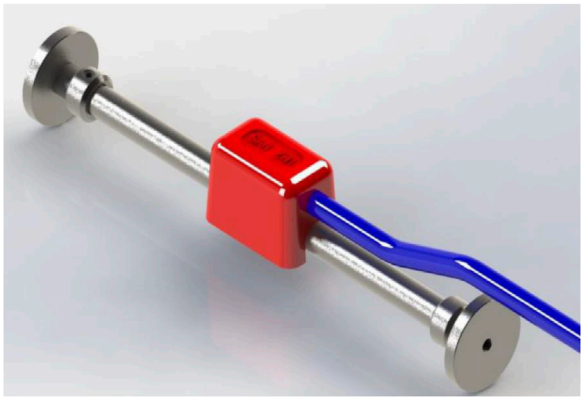

FIGURE 4
SZZX-A150 embedded strain gauge.

specified length of steel wire is tensioned between two terminal blocks (steel wire clamping pins). The terminal blocks are intimately affixed to the concrete under examination, and the deformation of the concrete can be comprehensively reflected to the two terminal blocks, instigating relative movement between them and leading to alterations in the tension of the steel wire. This shift in tension induces a change in the natural resonance frequency of the steel wire. The instrument quantifies this change in the natural resonance frequency to ascertain the change in stress and strain within the concrete. The standard range of the sensor is ±1,500 με, and the sensitivity is 1 με. Additionally, this sensor utilizes the DS18B20 digital temperature sensor, which can measure the temperature of the measurement point in real time. The applicable temperature range is −20°C–80°C, and the temperature measurement accuracy attains ± 0.5°C.

Throughout the embedding procedure, rebar functioned as a support carrier, and the temperature-strain sensor was affixed to the rebar to guarantee that the sensor did not directly interact with the wall panel and the supporting rebar, as illustrated in Figure 5. During the concrete casting procedure, particular care was taken to avoid directly impacting the temperature-strain sensor and the wire; during the tamping procedure, the tamper was strictly prohibited from contacting the sensor and the wire. Throughout the casting procedure, a dedicated individual was assigned for real-time surveillance to ensure the precision and safety of the operation.

2.2.2 Temperature-strain system arrangement

In accordance with the stipulations for temperature monitoring in the "Standard for Construction of Mass Concrete" GB50496-2018 (Ministry of Housing and Urban-Rural Development of the People's Republic of China, 2018), a total of 123 temperature-strain sensors were systematically positioned within the raft foundation, as depicted in Figure 6. At each designated measurement point, a trio of sensors was arranged in alignment with the thickness of the raft. The uppermost and lowermost measurement points were situated 50 mm from the concrete surface, while the median measurement point was located at the midpoint of the raft thickness.

In alignment with the central axis of the raft in the direction of its length, 21 measurement points were systematically positioned, and they were densified at the expansive strengthening band, with a trio of measurement points arranged at each expansive strengthening band. At a distance of 11.65 m from the leftmost edge of the raft, a quintet of measurement points was arranged in alignment with the width of the raft, and an additional quintet of measurement points was arranged in alignment with the width of the raft at the second expansive strengthening band. Additionally, measurement points were positioned at the corner points of the raft. Prior to the pouring of the concrete, the sensor layout was finalized, the wires were bundled and organized, and ultimately gathered to the data collection chamber.

3 Results and discussions

3.1 Principle of temperature distribution

The temperature distribution along the longitudinal axis of the raft, as depicted in Figure 7, evolved in 3 distinct phases:

1) Thermal accumulation phase: In the initial 48 h post-casting, the temperature of the raft escalated swiftly.
2) Thermal transfer and release phase: From the 72 nd h to the 7th day post-casting, the temperature of the raft progressively declined, with the surface temperature exhibiting the most significant decrease.
3) Thermal balance phase: From the 28th to the 60th day post-casting, the cement hydration reaction was fundamentally complete, and the temperature of the raft exhibited a tendency towards stabilization.

During the thermal accumulation phase, the central temperature exceeded the surface and bottom temperatures. Owing to the relatively suboptimal heat dissipation conditions in the center, an excess of heat accumulated, instigating a rise in temperature (Xie et al., 2023). The surface temperature along the longitudinal axis of the raft exhibited a relatively uniform distribution, but in the 80 m–96 m region, the surface temperature declined by 6.75°C. This region of the surface encompassed a lowering plate region, which might have contributed to this temperature distribution characteristic. The lowering plate region on the surface augmented the contact region with the environment, which might have enhanced the heat dissipation efficiency of the local region. Hence, in the process of architecting a temperature-strain monitoring system, it is imperative to enhance the density of sensors within the surface lowering plate region. This augmentation is crucial to promptly detect alterations in the inner-surface temperature difference.

The central temperature exhibited a distribution characteristic of being elevated in the middle and diminished at both ends along the longitudinal direction, with the middle being approximately 16°C higher than both ends. This phenomenon can be attributed to the larger contact region with the environment at both ends, permitting heat to be dissipated to the environment more rapidly through convection and radiation. In the process of positioning temperature-strain sensors centrally, it is essential to implement encryption at the terminal point of the raft. This measure is crucial to circumvent imprecise monitoring of the inner-surface temperature difference,

FIGURE 5
Temperature-strain sensor layout.

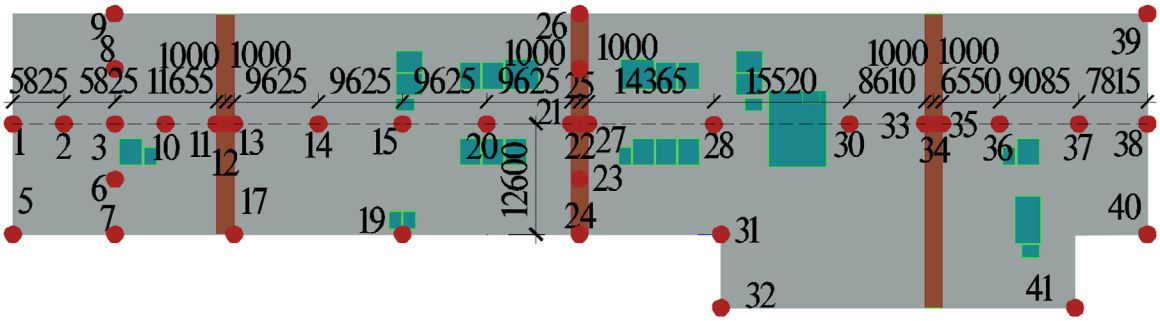

FIGURE 6
Temperature-strain sensor arrangement (Unit mm).

which could potentially resulted by substantial alterations in the temperature gradient within the central space.

The bottom temperature escalated by approximately 15°C and 20°C respectively at 63.8 m and 80.2 m, which might be associated with the increase in the thickness of the raft in these regions. This alteration in thickness was induced by the layout of the elevator and catchment well pits. In these dense well pit regions, the thickening of the raft caused heat to accumulate in these local regions, thereby causing the temperature to escalate. The temperature gradient in the bottom of the elevator and catchment well pits exhibits considerable spatial variation. To ensure precise measurement of the bottom-surface temperature difference, it is recommended to implement encryption for the temperature-strain sensor situated at the bottom in this specific location.

During the thermal transfer and release phase, the mean temperatures of the surface, center, and bottom declined by 14.3°C, 11.5°C, and 3.6°C, respectively. The pronounced reduction in surface temperature was attributable to the direct interaction of the concrete surface with the external environment, facilitating effective heat dissipation via convection and radiation mechanisms. The elevated heat dissipation efficiency of the surface region was due to its larger surface region and direct interaction with the ambient environment, particularly following the deceleration of the hydration reaction, the temperature decrease was more conspicuous. The larger decline in central temperature indicated that as the hydration reaction decelerated, the accumulated heat commenced conducting outward through the concrete. A pronounced reduction in the raft's surface temperature engenders a substantial spatial temperature differential between its center and surface. This differential facilitates thermal conduction from the center towards the surface, culminating in a marked diminution of the center temperature. The smaller decline in bottom temperature was attributable to its contact with the foundation, which restricted the heat dissipation from the bottom.

During the thermal balance phase, the mean temperatures of the surface, center, and bottom declined by 7.9°C, 26.8°C, and 20.3°C, respectively. Figure 7F illustrates that at 60 days, the temperatures of the surface, center, and bottom exhibited a tendency towards consistency and proximity to the environmental temperature. This convergence phenomenon reflected the gradual establishment of thermal equilibrium, indicating that the heat exchange between various parts inside the concrete reached a balanced state, rendering the temperature distribution of the entire structure to be uniform (Yang et al., 2022). In addition, the heat exchange between the raft and its surrounding environment also reached a dynamic balance, causing the concrete temperature to be close to the environmental temperature, indicating that the hydration heat of the concrete was entirely over.

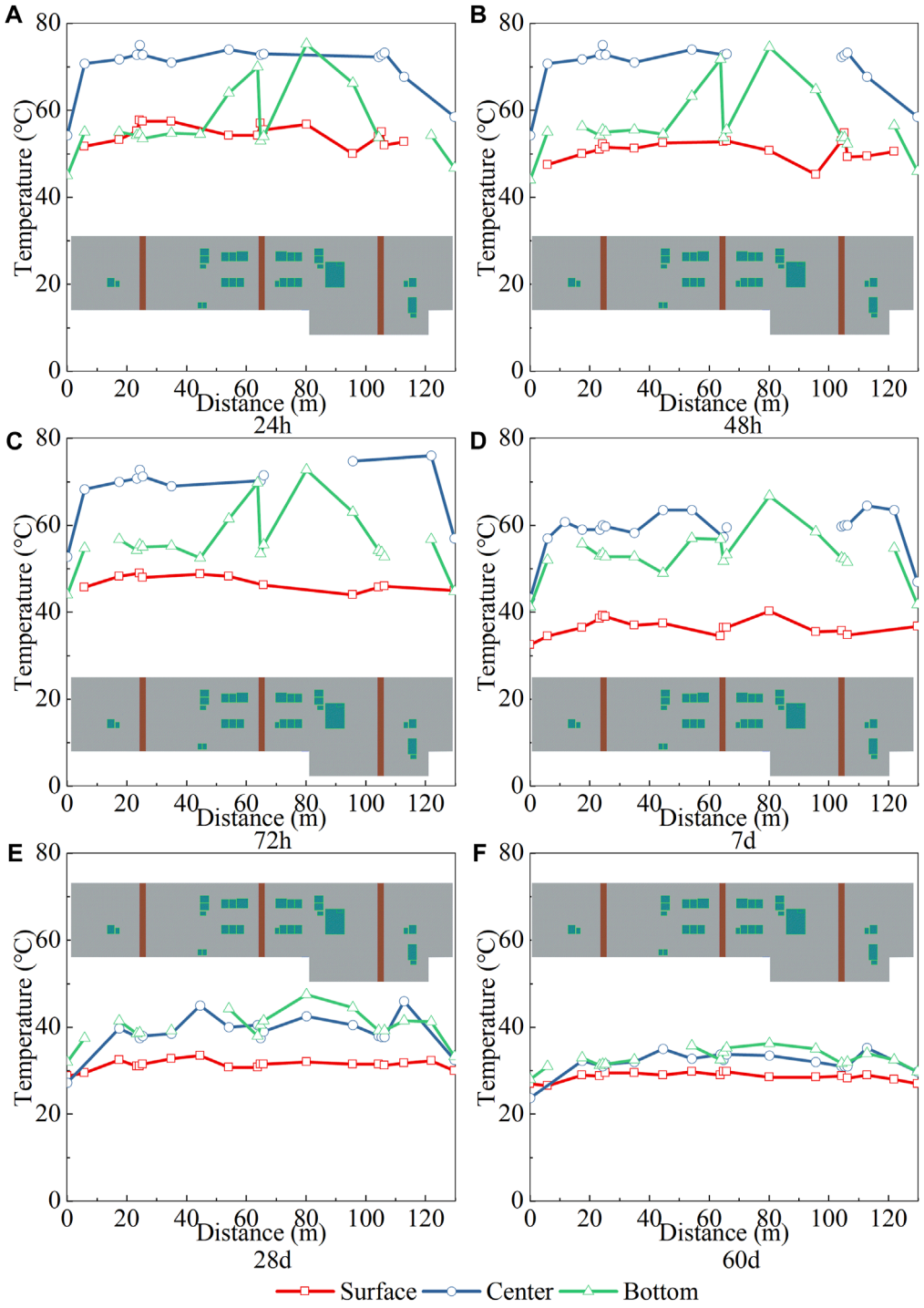

FIGURE 7
Principle of temperature distribution. **(A)** 24 h, **(B)** 48 h, **(C)** 72 h, **(D)** 7 d, **(E)** 28 d, **(F)** 60 d.

3.2 Principle of strain distribution

The strain distribution along the longitudinal axis of the raft, as depicted in Figure 8, was predominantly instigated by temperature fluctuations during the thermal accumulation phase (Liu et al., 2020). As discernible from Section 3.1, the temperature in the central region was typically superior to the surface and bottom, inducing a more pronounced expansion of its concrete volume. However, this expansion was restrained, culminating in a maximum compressive strain of −560 με in the central region. The mean compressive strain in the central region was 282 με and 223 με greater than the surface and bottom, respectively.

In the vicinity of the expansive strengthening band, a substantial escalation in compressive strain was observed in the surface, center,

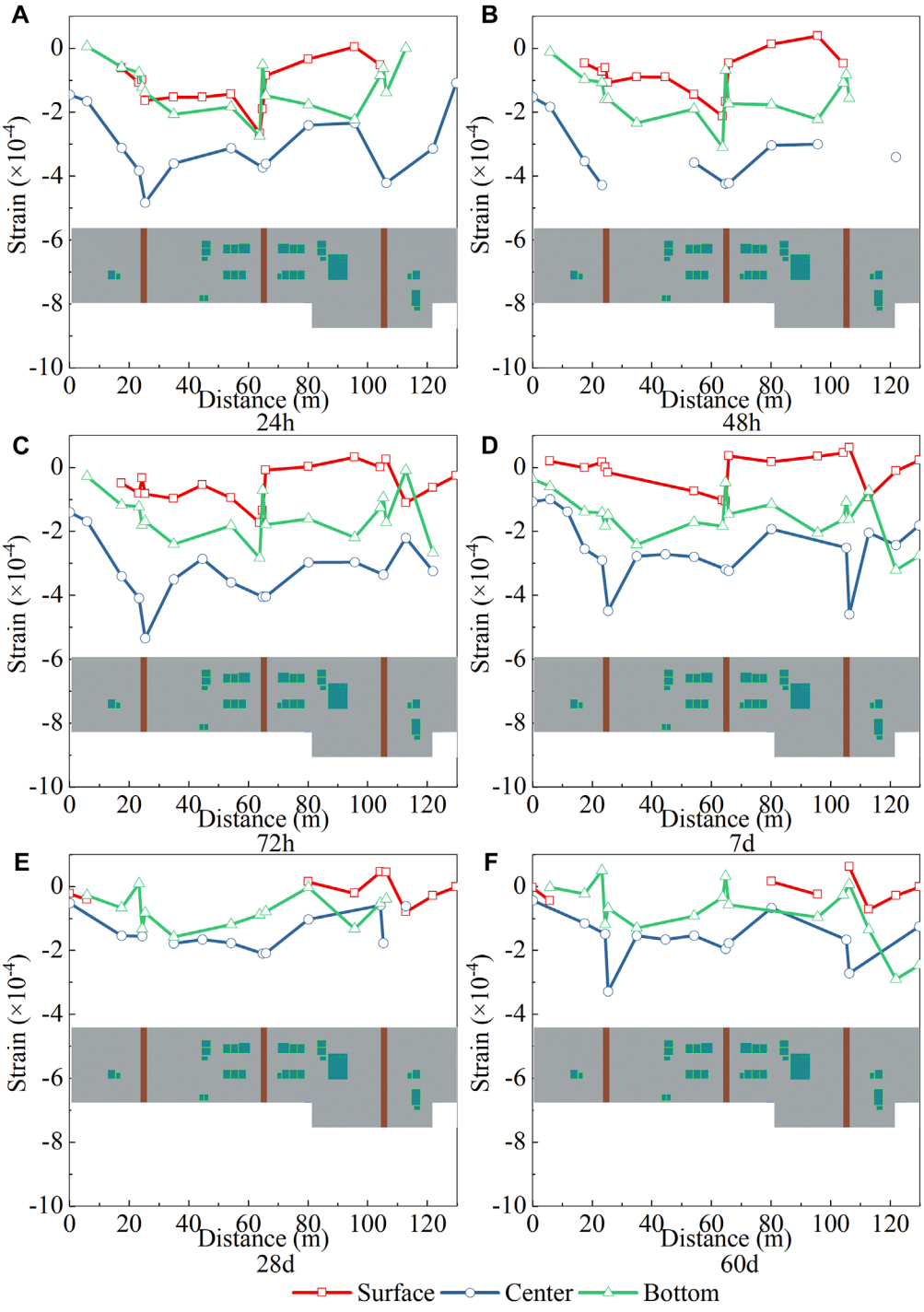

FIGURE 8
Principle of strain distribution. **(A)** 24 h, **(B)** 48 h, **(C)** 72 h, **(D)** 7 d, **(E)** 28 d, **(F)** 60 d.

and bottom regions of the concrete. This phenomenon can be ascribed to two primary factors: Firstly, due to the superior grade of concrete in the expansive strengthening band, the quantity of heat engendered by hydration is elevated (Wang et al., 2022), which significantly escalates the temperature in this region, leading to a higher degree of thermal expansion. Secondly, the MgO expander induces the concrete in the expansive strengthening band to expand (Tian et al., 2022), which is restrained by the adjacent standard region concrete, resulting in compressive strain (Myint et al., 2021).

Within the 63.8 m–96 m region, the strain on the surface of the structure exhibited a shift from −265 με to 4 με, a total increment of 269 με, as shown in Figure 8A. In contrast, the strain in the bottom region declined from −52 με to −224 με, a total decrement of 172 με. The rationale for this strain distribution pattern can be

attributed to the lowering plate region at 96 m, which caused the surface to possess a larger heat dissipation region, and the increased thickness of the raft at the bottom, rendering the surface temperature relatively lower and the bottom temperature relatively higher. The strain dispersion in the raft's thickness dimension suggests that the raft experiences comprehensive deformation due to the influence of the bottom-surface temperature difference. This deformation results in an escalation of surface strain and a reduction in bottom strain. If the bottom-surface temperature difference is excessively large, leading to an overly substantial deformation of the raft, it may cause the tensile strain on the raft's surface to surpass its threshold. Consequently, it is imperative to employ the bottom-surface temperature difference as a surveillance parameter.

During the thermal transfer and release phase, the mean strain of the surface and center escalated by 73 με and 109 με respectively, while the bottom strain remained virtually unchanged. This strain development rule is intimately related to the temperature development rule described in Section 3.1. During this stage, the mean temperatures of the surface and center declined by 14.3°C and 11.5°C respectively, while the mean temperature of the bottom only declined by 3.6°C. This suggests that throughout the thermal transfer and release phase, the raft's strain was predominantly influenced by alterations in temperature, while the strain engendered by contraction remains a subordinate factor.

During the thermal balance phase, due to severe damage to the surface strain gauge, it was not feasible to procure valid mean strain data for this stage. The mean strain in the center and bottom escalated by 93 με and 77 με respectively. During this stage, the mean temperatures of the center and bottom declined by 26.8°C and 20.3°C respectively. The decline in temperature and the shrinkage effect led to an increment in strain (Qin, 2006).

Throughout the entire strain development process, the maximum strain value of the raft was 61 με. This value is significantly inferior to the standard limit of 95 με stipulated in the "Code for design of concrete structures " (Ministry of Housing and Urban-Rural Development of the People's Republic of China, 2010). This indicates that the risk of cracking in the raft concrete is extremely low, thereby verifying the feasibility and safety of using a expansive strengthening band to achieve seamless construction for super-length raft structures of the 130 m class.

3.3 Temperature-time characteristic

3.3.1 Expansive strengthening band and standard region

To scrutinize the temperature-time attributes of the raft, measurement points situated on 3 expansive strengthening bands (specifically measurement points 12, 22, 34) and measurement points in 3 standard regions (namely, measurement points 15, 28, 36) were selected. The corresponding data outcomes are exhibited in Figure 9. The surface temperature displays conspicuous minor waveform fluctuations, and during the local time period of the temperature descent phase (for instance, 10–20 days), it anomalously ascends due to the influence of the ambient temperature. This signifies that the surface temperature of the concrete is exceedingly sensitive to the ambient temperature. Consequently, when constructing super-length raft structures, it is imperative to fortify maintenance measures, such as employing sunshades, sprinkler systems, or insulation materials, to mitigate the impact of the environment on the surface temperature.

Upon analyzing the 3 measurement points on the expansive strengthening band, it was discerned that the highest temperature all manifested in the central region, transpiring between 36 and 48 h, with the temperature reaching 73–75°C. This observation is congruent with the summary of the temperature development process of the raft in Section 3.1. Notably, the temperature in the central region exhibited a rapid decline subsequently, and by the 12th day, the temperature had descended from 73 to 75°C to 48–50°C. Additionally, it was observed that in the initial 48 h, the temperature curves of the surface and bottom of the concrete displayed a high degree of consistency. However, after the surface temperature reached its zenith, the rate of decline was significantly swifter than that of the bottom, which can be ascribed to the disparate heat dissipation conditions of the surface and bottom discussed earlier.

In the standard region, the temperature-time curves observed at measurement points 15 and 36 exhibit a pattern akin to the expansive strengthening band, but the temperature is lower, with the highest temperature only being 67.8°C, which is 9.7% lower than the highest temperature of the expansive strengthening band. This discrepancy can be attributed to the inferior grade of concrete utilized in the standard region, which engenders less heat of hydration (Wang et al., 2022). However, measurement point 28 presents a unique pattern, where the temperature curves of its bottom and center almost coincide. This anomaly can be attributed to the large quantity of elevator and catchment well pits near measurement point 28. These structures augment the thickness of the raft, leading to an increase in the heat of hydration, thereby elevating the bottom temperature. This will engender a more substantial bottom-surface temperature difference in this region relative to other regions. Hence, when executing temperature surveillance, it is not only essential to ensure that the inner-surface temperature difference does not surpass the prescribed threshold, but it is also crucial to ascertain that the bottom-surface temperature difference remains within the specified limit.

During the temperature development process in the expansive strengthening band and the standard region, the maximum inner-surface temperature difference is significant. The surface temperature reaches its zenith after about 48 h, and then commences to decline, while the center temperature is still ascending. When the center temperature reaches its zenith, the temperature difference between the center and the surface also reaches its maximum. For instance, the internal surface temperature difference of measurement point 22 reaches its maximum value of 24.5°C at 72 h. This observation elucidates the temporal evolution of the inner-surface temperature difference, and establishes that the apex of this differential is reached during the thermal transfer and release phase. Consequently, during temperature surveillance, it is imperative to rigorously monitor the inner-surface temperature difference during the thermal transfer and release phase, particularly when the surface temperature attains its zenith and commences to decline. If the inner-surface temperature difference approaches or even meets the standard threshold, it becomes necessary to implement insulation and maintenance procedures on the raft surface to mitigate the inner-surface temperature difference.

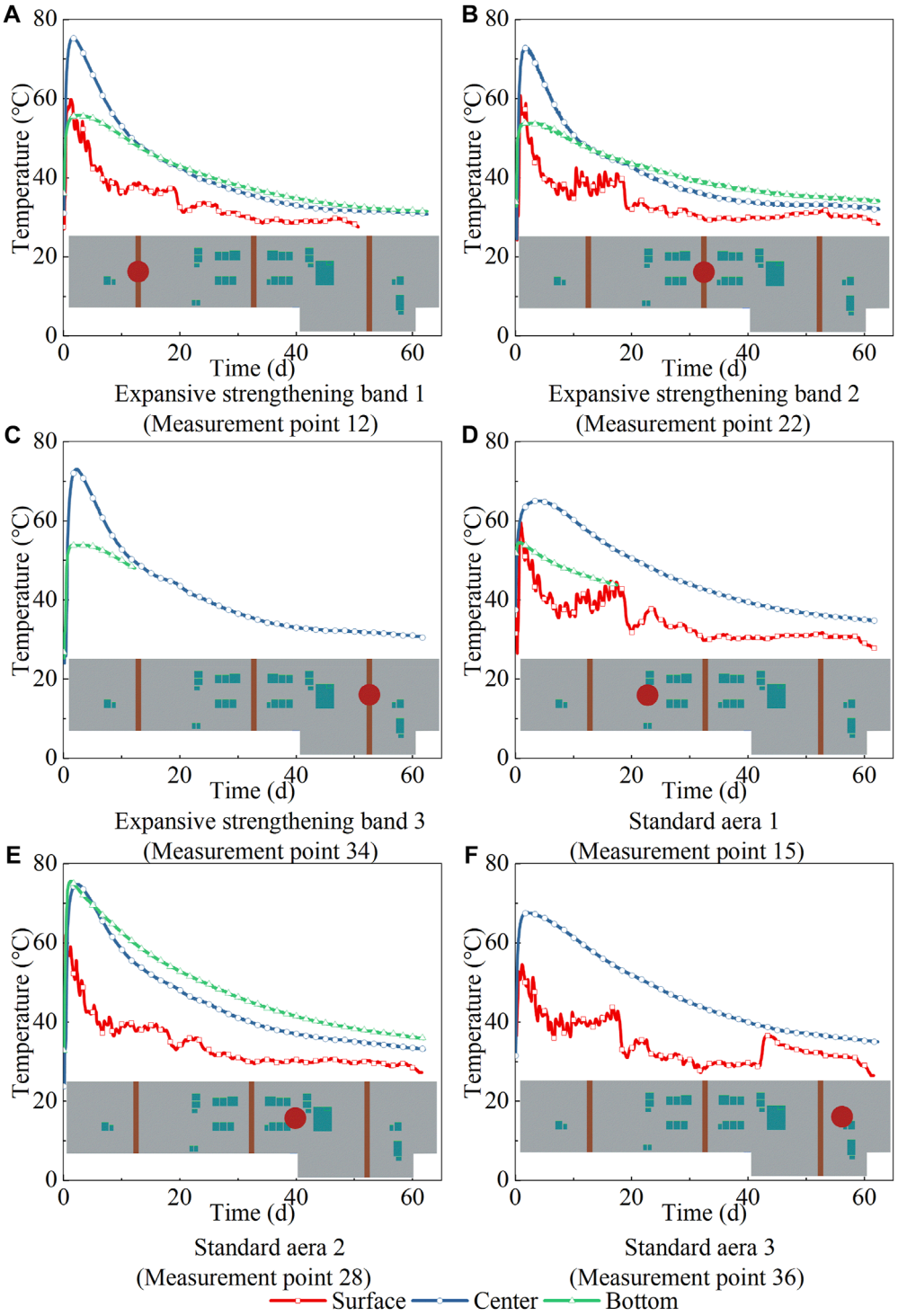

FIGURE 9
Temperature-time curves of expansion reinforcement band and standard area.

3.3.2 Corner point of the raft

To scrutinize the temperature and strain temporal characteristics of the raft's corner points, specific measurement points were selected for in-depth analysis, encompassing measurement points 5, 19, 31, 32, 41, and 40. Measurement points 5, 32, 41, and 40 are situated at the positive corners of the raft, measurement point 19 is positioned at the edge of the raft, and measurement point 31 is located at the negative corner of the raft. The temperature-time curve of the corner points is illustrated in Figure 10.

There exists a significant disparity between the temperature-time characteristics of the positive and negative corners. The

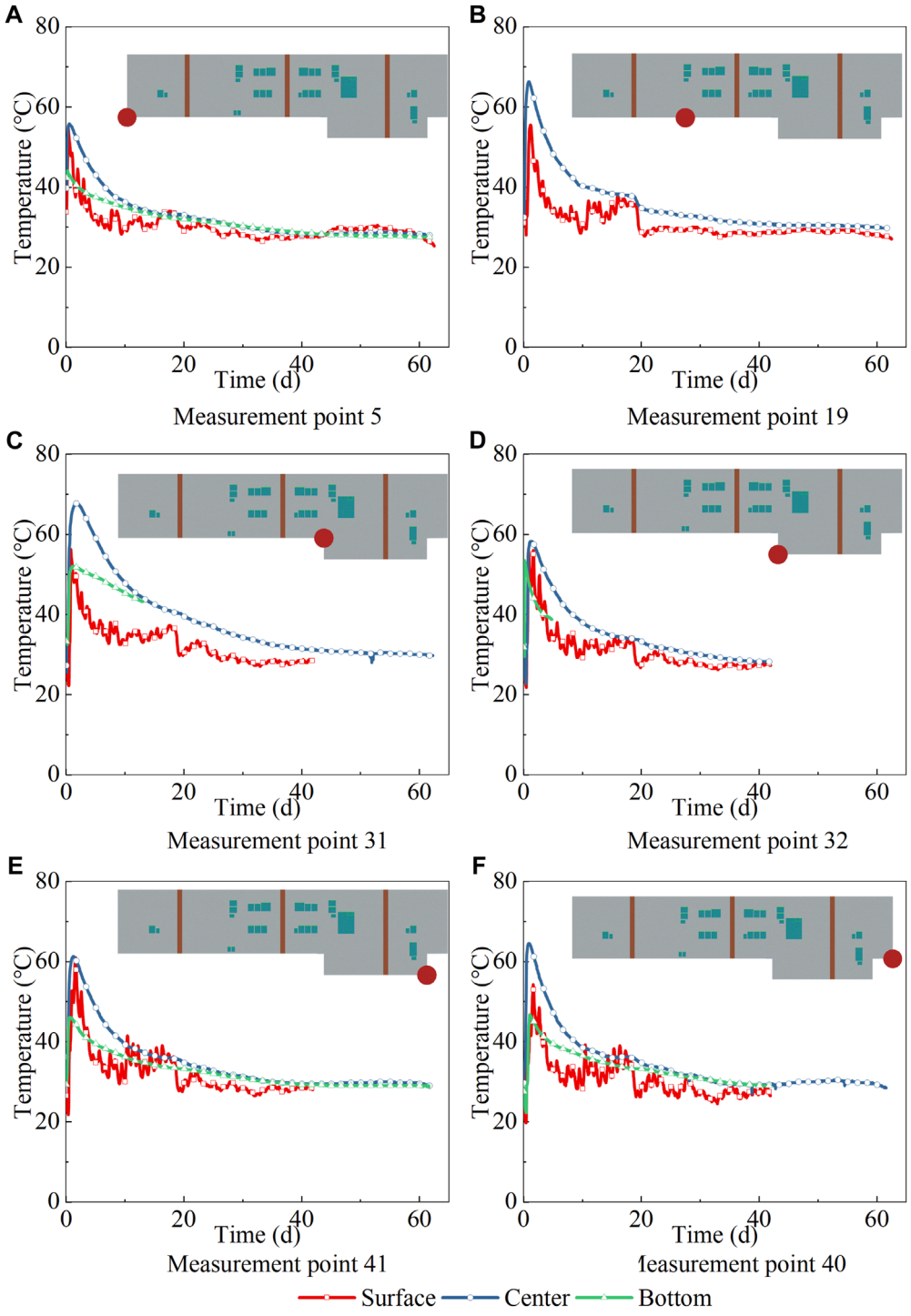

FIGURE 10
Temperature-time curves of corner point.

positive corners exhibit a superior heat dissipation efficiency, the central temperature descends rapidly, and the inner-surface temperature difference of the measurement points is minimal, with a maximum of merely 17°C. In contrast, the negative corners display an inferior heat dissipation efficiency, the central temperature descends slowly, and the internal surface temperature difference is substantial, reaching a maximum of 24.8°C. These findings suggest that when conducting temperature monitoring, special attention should be accorded to monitoring the temperature evolution at the negative corners to prevent the internal surface temperature difference from exceeding an acceptable limit.

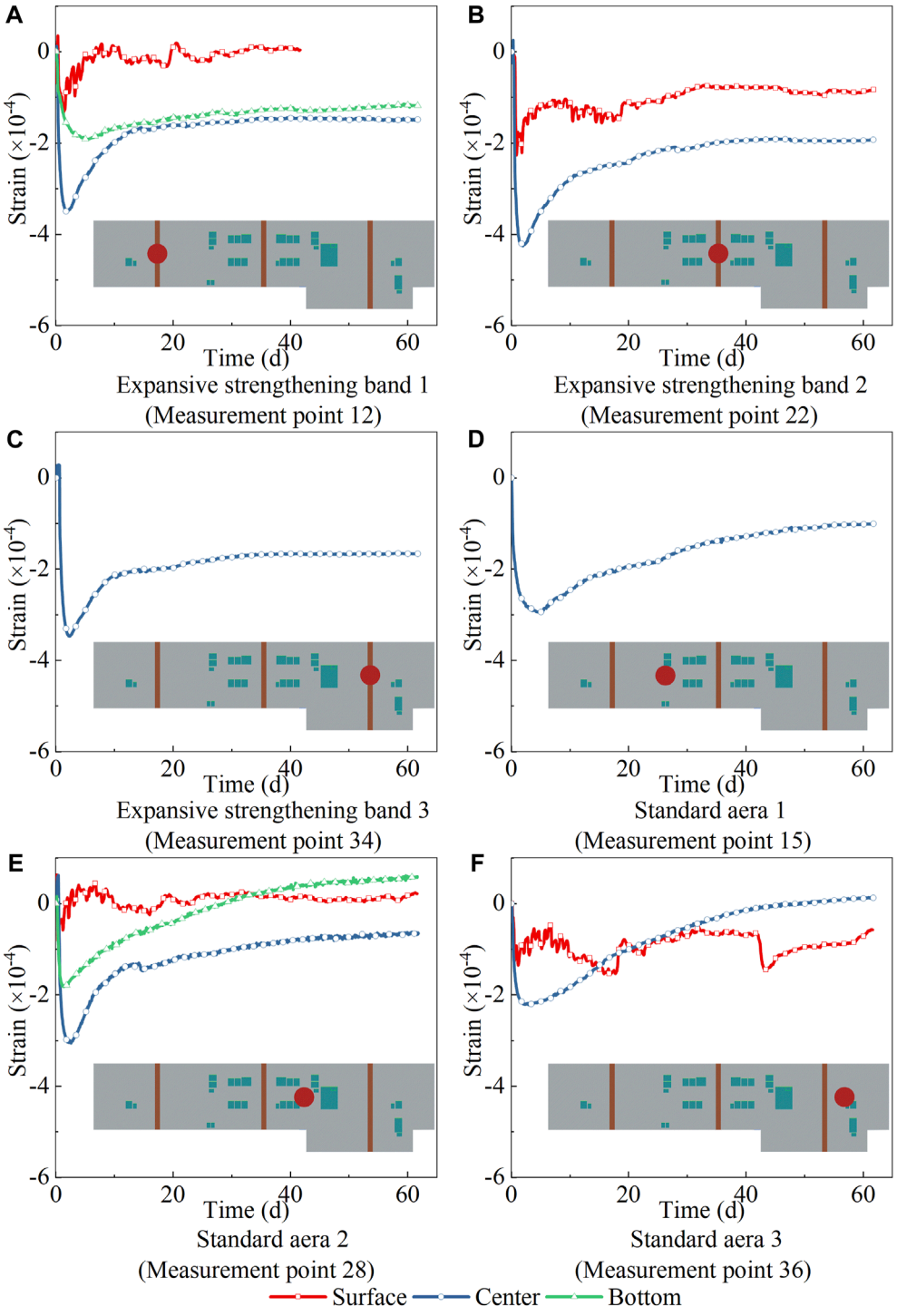

FIGURE 11
Strain-time curves of expansion reinforcement band and standard area.

3.4 Strain-time characteristic

3.4.1 Expansive strengthening band and standard region

To delve deeper into the strain-time attributes of the raft, specific measurement points situated on 3 expansive strengthening bands (namely measurement points 12, 22, 34) and measurement points in 3 standard regions (specifically, measurement points 15, 28, 36) were selected for additional analysis, as depicted in Figure 11. Corresponding to the temperature-time characteristics, compressive strain would be engendered during the heating process. The highest temperature and the maximum compressive strain

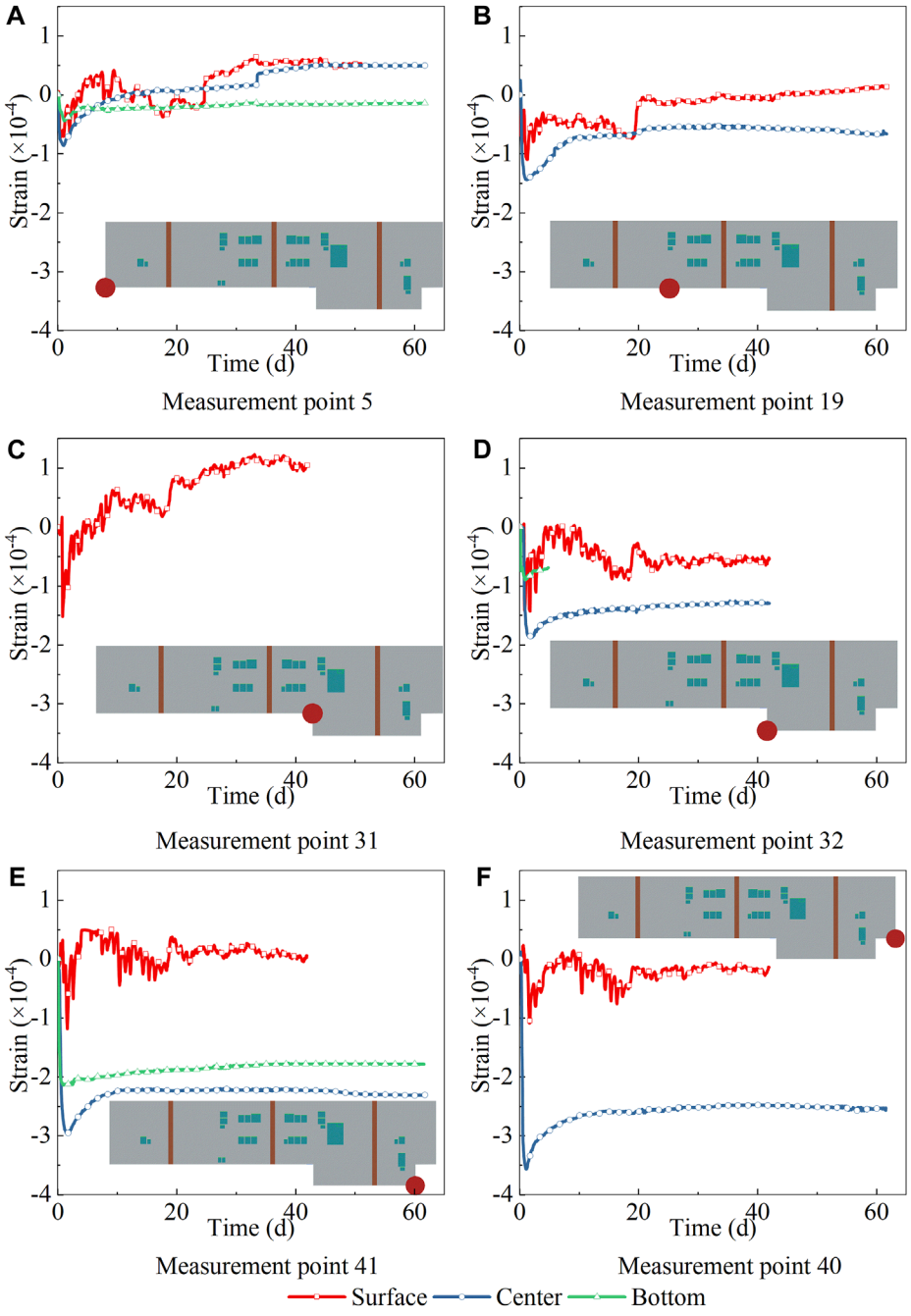

FIGURE 12
Strain-time curves of corner point.

both transpired in the central region, which was attributable to the thermal expansion being constrained by factors such as the foundation and reinforcement, thereby generating compressive strain. The maximum compressive strain in the center of the expansive strengthening band could reach −425~−350 με, while the maximum compressive strain in the center of the standard region could only reach −300~−220 με. One aspect of the reason is that the temperature of the expansive strengthening band is higher and the thermal expansion is larger, and another aspect of the reason is that the concrete of the expansive strengthening band has an expansion effect. In addition, due to this expansion effect, the strain growth of the concrete in the expansive strengthening band is less during the temperature reduction stage, that is, the shrinkage effect is not very pronounced. The strain of the concrete in the expansive strengthening band increased from −425~−350 με to −191~−144 με, and the concrete in the expansive strengthening band was consistently in a state of compression. Concurrently, the strain of the concrete in the standard region increased from −300~−220 με

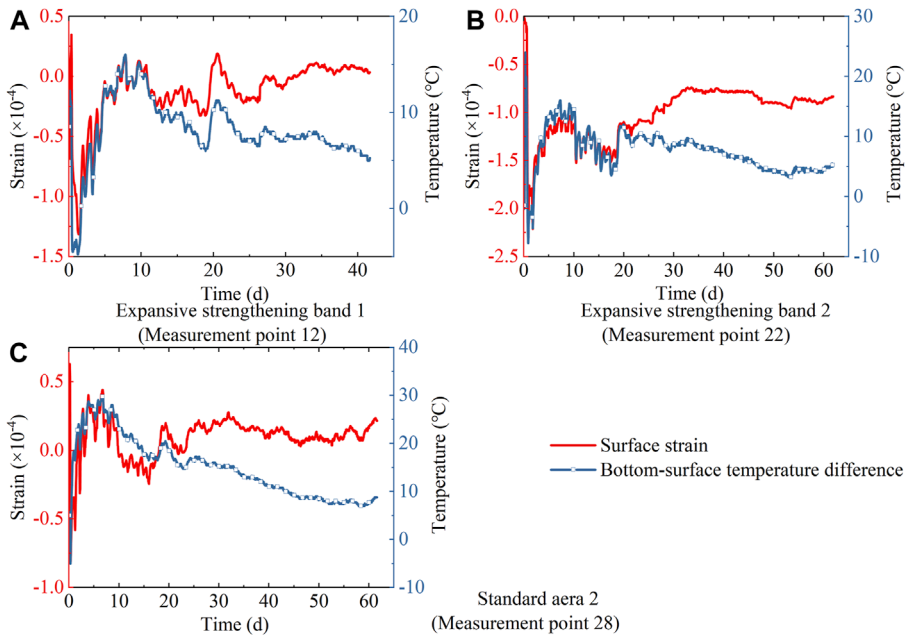

FIGURE 13
The correlation between surface strain and bottom-surface temperature difference.

to −101–14 με, and tensile strain appeared in the concrete in the standard region.

For measurement point 28, during the thermal accumulation phase, the temperature rise at the bottom was akin to that at the center. However, the constraint conditions at the bottom were not as robust as those at the center, resulting in a compressive strain at the bottom that only reached −182 με, which is 40.5% less than the maximum compressive strain of −306 με at the center. When the temperature descended, the strain at the bottom escalated, reaching a maximum of 61 με. Commencing from the 30th day, the bottom strain surpassed the surface strain, a unique phenomenon observed across all measurement points. This can be attributed to the fact that from the 1st to the 30th day, the surface temperature descended from 56.8°C to 31°C, a cumulative decrease of 25.8°C, while the bottom temperature descended from 75.3°C to 46.3°C, a cumulative decrease of 29°C, thereby exhibiting a larger temporal gradient of the bottom temperature.

The maximum strain range of the expansive strengthening band is −74–19 με, all appearing on the surface, while the maximum strain range in the standard region is 13–61 με. Within 60 days post the completion of the concrete pouring, the tensile strain of the concrete in the expansive strengthening band and the standard region did not exceed the standard limit of 95 με stipulated in the "Code for design of concrete structures" (Ministry of Housing and Urban-Rural Development of the People's Republic of China, 2010). Furthermore, the raft exhibited no signs of cracking during empirical testing conducted on-site. This indicates that the method proposed in this paper to achieve seamless construction of a hundred-meter scale super-length raft using a expansive strengthening band is feasible and has value for further promotion.

3.4.2 Corner point of the raft

The strain-time trajectory of the raft corner points is depicted in Figure 12. During the cooling phase, certain distinct strain patterns were discerned. The positive corner, which experiences less constraint during the shrinkage process, exhibits a reduced tensile strain, with the peak tensile strain being 65 με, which is within the standard threshold of 95 με stipulated in the "Code for design of concrete structures" (Ministry of Housing and Urban-Rural Development of the People's Republic of China, 2010). Conversely, due to the potential stress concentration at the negative corner (Pilkey, 1999), the negative corner is subject to greater constraint. As the negative corner undergoes shrinkage, it exhibits an increased tensile strain, with the peak tensile strain reaching 123 με, surpassing the standard threshold of 95 με. This implies that particular attention should be devoted to the potential issue of concrete cracking at the negative corner of the raft.

3.5 A novel temperature control index: bottom-surface temperature difference

Currently, the temperature gradient index delineated in the regulations predominantly pertains to the inner-surface temperature difference (Ministry of Housing and Urban Rural Development of the People's Republic of China, 2018). The fundamental tenet of this thermal control index is that when the inner-surface temperature difference surpasses the standardized

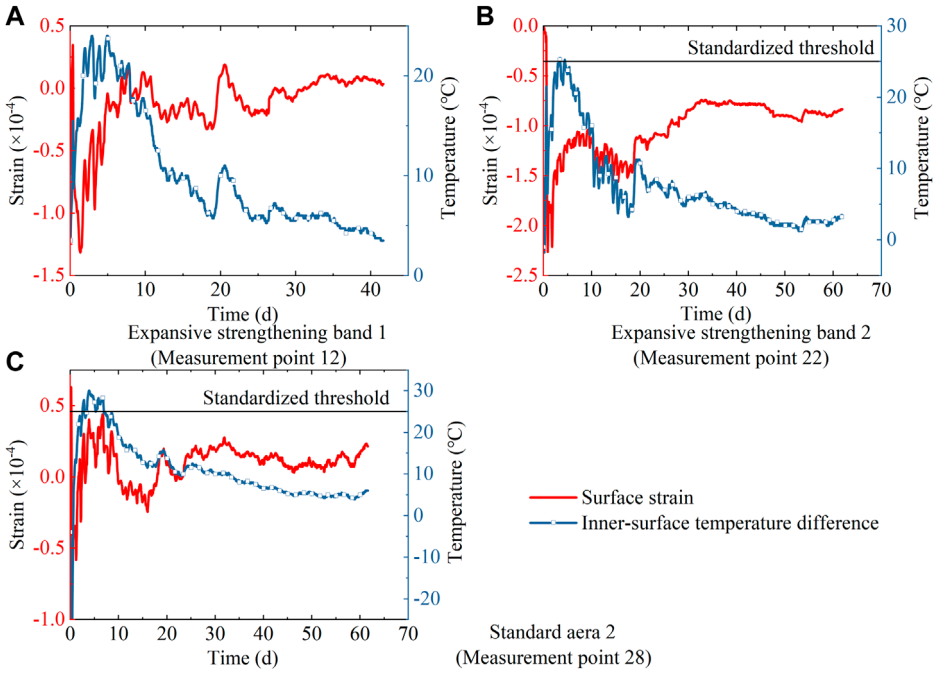

FIGURE 14
The correlation between surface strain and inner-surface temperature difference.

threshold, i.e., when the surface temperature is excessively low and the center temperature is high, the surface concrete undergoes cooling and shrinkage due to the fundamental principle of thermal expansion and contraction. However, this shrinkage is constrained by the central concrete, leading to tensile stress on the surface. This temperature control index, however, overlooks a significant influencing factor, which is the bottom temperature. The deformation coordination of raft concrete due to thermal disparity is a holistic effect, rather than merely involving the surface and center of the concrete. Although the bottom temperature is relatively low compared to the center temperature, it will also undergo cooling shrinkage. However, on one hand, due to the lowest surface temperature, and on the other hand, due to the overall deformation coordination of the raft, the overall deformation of the raft remains surface shrinkage, but is constrained by the center and bottom. Therefore, the bottom-surface temperature difference is also a significant temperature control index. To substantiate this theory, this manuscript scrutinizes the correlation between the surface strain of raft concrete and the bottom-surface temperature difference and inner-surface temperature difference, as depicted in Figure 13 and Figure 14.

From Figure 13, it is evident that in the initial 20 days post-pouring, the evolution of surface strain mirrors the evolution of the bottom-surface temperature difference. Post the 20-day mark, the surface strain is primarily influenced by drying shrinkage, and the impact of cooling shrinkage progressively diminishes. From Figure 14, it is observable that the evolution of surface strain does not align perfectly with the evolution of the inner-surface temperature difference. For instance, for expansive strengthening band 1, from the 5th to the 8th day, the inner-surface temperature difference descends from 24°C to 21°C, but the surface strain paradoxically escalates from −5 με to 17 με. Furthermore, the inner-surface temperature difference of the expansive strengthening band 2 and the standard region 2 surpassed the standardized threshold during certain time periods, but the surface strain during this period was still less than the ultimate tensile strain of the concrete. Based on the conclusions and analysis of these monitoring data, this manuscript advocates the use of the bottom-surface temperature difference as a novel temperature control index, and based on the monitoring data of this on-site test, the threshold is determined to be 30°C.

4 Conclusion

This manuscript presents a methodology for the seamless construction of a hundred-meter scale super-length raft structure. This approach was empirically tested on a raft that spans 130 m in length and 1.9 m in thickness in a construction project executed by the China Construction Third Engineering Bureau Group Co., Ltd. A temperature-strain monitoring system was employed to track the temperature and strain of the raft, furnishing experimental data to validate the feasibility and safety of this construction methodology. The pivotal conclusions derived from this research are enumerated as follows:

(1) Commencing from the inception of the raft pouring to 60 days subsequent to the pouring, the peak tensile strain of the raft was 65 με, barring a few corner points. Furthermore, the raft exhibited no signs of cracking during empirical testing conducted on-site. This signifies that the seamless construction methodology proposed in this manuscript for hundred-

meter scale super-length raft structures is both feasible and safe, and possesses substantial potential for promotion in this domain.

(2) Upon evaluating the correlation between strain dispersion and strain-temperature differential in the raft's thickness dimension, Relative to the inner-surface temperature difference, the surface strain exhibits a more potent association with the bottom-surface temperature difference. Therefore, a novel temperature control index (the bottom-surface temperature difference) was introduced. In light of the empirical test outcomes obtained on-site, the threshold for the temperature control index is established at 30°C.

(3) In the process of architecting a temperature-strain monitoring system, it is imperative to enhance the density of sensors within the surface of lowering plate region, the center of the raft terminal point, and the bottom of the elevator and catchment well pits. Owing to the substantial spatial gradient of temperature present in these regions, these augmentations are crucial to promptly detect alterations in the inner-surface temperature difference and bottom-surface temperature difference.

(4) The apex of the inner-surface temperature difference is reached during the thermal transfer and release phase. During temperature surveillance, it is imperative to rigorously monitor the inner-surface temperature difference during this phase, particularly when the surface temperature attains its zenith and commences to decline. If the inner-surface temperature difference approaches or even meets the standard threshold, it becomes necessary to implement insulation and maintenance procedures on the raft surface to mitigate the inner-surface temperature difference.

(5) The subsequent phase in the research agenda entails the establishment of a finite element model and the execution of parameter analysis predicated on the verification of the model's reliability. This encompasses the analysis of the functional correlation between the spacing, breadth, and concrete expansion rate of the expansive strengthening bands with the length and thickness of the raft. The objective is to broaden the application parameters of the seamless construction methodology for super-length raft structures, thereby facilitating its application to more extensive and thicker raft structures.

Data availability statement

The original contributions presented in the study are included in the article/Supplementary Material, further inquiries can be directed to the corresponding author.

Author contributions

BH: Conceptualization, Data curation, Investigation, Software, Visualization, Writing–original draft, Writing–review and editing. HW: Funding acquisition, Resources, Supervision, Writing–review and editing. HL: Conceptualization, Project administration, Supervision, Writing–original draft. CD: Funding acquisition, Supervision, Writing–review and editing. YZ: Funding acquisition, Investigation, Supervision, Writing–review and editing. WX: Data curation, Methodology, Writing–review and editing. GZ: Conceptualization, Writing–review and editing. CS: Software, Writing–review and editing.

Funding

The author(s) declare that financial support was received for the research, authorship, and/or publication of this article. This research was funded by Chongqing Construction Science and Technology Plan Project, grant number Chengke Zi 2023 No. 8–6.

Acknowledgments

The authors express their gratitude to the reviewers for their valuable feedback and suggestions aimed at enhancing the paper's quality.

Conflict of interest

Authors BH, HW, HL, CD, YZ, WX, GZ, and CS were employed by the China Construction Third Engineering Bureau Group Co., Ltd.

Publisher's note

Supplementary material

The Supplementary Material for this article can be found online at: https://www.frontiersin.org/articles/10.3389/fmats.2024.1367600/full#supplementary-material

References

Batog, M., and Giergiczny, Z. (2014). Influence of mass concrete constituents on its properties. *Constr. Build. Mater.* 146, 221–230. doi:10.1016/j.conbuildmat.2017.04.085

Ha, J.-H., Jung, Y. S., and Cho, Y.-G. (2014). Thermal crack control in mass concrete structure using an automated curing system. *Autom. Constr.* 45, 16–24. doi:10.1016/j.autcon.2014.04.014

Jin, J. (2002). Design suggestion about crack precaution and reduction caused by temperature and shrinkage jointly in over-long concrete structure. *Ind. Constr.* 2002 (06), 57–59. doi:10.13204/j.gyjz2002.06.019

Li, S., Feng, Y., and Yang, J. (2021). Expansion mechanism and properties of magnesium oxide expansive hydraulic cement for engineering applications. *Adv. Mater. Sci. Eng.* 2021, 1–9. doi:10.1155/2021/5542072

Liu, J., Liu, Y., Zhang, N., Ma, Z., and Bai, Y. (2020). Research on temperature action and cracking risk of steel–concrete composite girder during the hydration process. *Arch. Civ. Mech. Eng.* 47, 47. doi:10.1007/s43452-020-00050-0

Liu, Y., Zhang, J., Chang, J., and Zhao, Y. (2022). Use of cement hydration heat as heating resource in curing of precast concrete - temperature rise simulation. *J. Adv. Concr. Technol.* 20, 564–580. doi:10.3151/jact.20.564

Ming, X., Huang, J. C., and Li, Z. (2022). Materials-oriented integrated design and construction of structures in civil engineering—a review. *Front. Struct. Civ. Eng.* 16, 24–44. doi:10.1007/s11709-021-0794-9

Ministry of Housing and Urban-Rural Development of the People's Republic of China (2010). *GB 50010-2010 Code for design of concrete structures*. Beijing: China Architecture and Building Press.

Ministry of Housing and Urban-Rural Development of the People's Republic of China (2018). *Standard for construction of mass concrete*. Beijing: China Architecture and Building Press.

Ministry of Housing and Urban-Rural Development of the People's Republic of China (2023). *Standard for seamless construction for super-length concrete structure*. Beijing: China Construction Publishing Media Co, Ltd.

Myint, S. H., Tanapornraweekit, G., and Tangtermsirikul, S. (2021). Investigation of expansive concrete structures through strain monitoring in field structures. *Asian J. Civ. Eng.* 22, 565–578. doi:10.1007/s42107-020-00332-1

Ouyang, J., Chen, X., Huangfu, Z., Lu, C., Huang, D., and Li, Y. (2019). Application of distributed temperature sensing for cracking control of mass concrete. *Constr. Build. Mater.* 197, 778–791. doi:10.1016/j.conbuildmat.2018.11.221

Pilkey, W. D. (1999). *Peterson's stress concentration factors*. 2nd ed. Wiley.

Qin, W. (2006). Shrinkage and cracking of concrete and its evaluation and prevention. *Concrete* 04, 19–23.

Sargam, Y., Faytarouni, M., Riding, K., Wang, K., Jahren, C., and Shen, J. (2019). Predicting thermal performance of a mass concrete foundation – a field monitoring case study. *Case Stud. Constr. Mater.* 11, e00289. doi:10.1016/j.cscm.2019.e00289

Tatro, S. B., Allen, J. C., Arnold, T. E., Bass, R. P., Best, F. J., Bombich, A. A., et al. (2007). Report on thermal and volume change effects on cracking of mass concrete. *ACI Comm.* 207.

Tian, C. J., Wang, Y. Z., Qiu, K., and Yang, Q. l. (2022). Effects of submicron-MgO and nano-MgO on the expansion and microscopic properties of high-performance concrete. *J. Cent. South Univ.* 29, 3186–3200. doi:10.1007/s11771-022-5090-x

Truman, K. Z., Petruska, D. J., and Norman, C. D. (1991). Creep, shrinkage, and thermal effects on mass concrete structure. *J. Eng. Mech.* 117 (6), 1274–1288. doi:10.1061/(ASCE)0733-9399(1991)117:6(1274)

Wang, Y., Tian, Q., Li, H., and Wang, Y. (2022). Humidity sensitivity of hydration of expansive agent and its expansive efficiency in ultra-high performance concrete. *Crystals* 12 (2), 195. doi:10.3390/cryst12020195

Xie, Y., Du, W., Xu, Y., Peng, B., and Qian, C. (2023). Temperature field evolution of mass concrete: from hydration dynamics, finite element models to real concrete structure. *J. Build. Eng.* 65, 105699. doi:10.1016/j.jobe.2022.105699

Xin, J., Liu, Y., Zhang, G., Wang, Z., Yang, N., Qiao, Y., et al. (2021). Comparison of thermal cracking potential evaluation criteria for mass concrete structures. *Mater. Struct.* 54, 243. doi:10.1617/s11527-021-01840-5

Yang, Z., Yang, Y., Ji, X., Xu, K., and Wang, H. (2022). Experimental and numerical simulation study on hydration heat of expansive mass concrete. *Mater. Res. Appl.* 16 (2), 222–227.

Zhou, Y., Leng, X., Xu, P., Wang, X., and Qiang, S. (2019). Research on the reasonable spacing of post-casting belt of 100m long inverted-T shape concrete structures on soft foundation. *IOP Conf. Ser. Earth Environ. Sci.* 304, 052008. doi:10.1088/1755-1315/304/5/052008

frontiers | Frontiers in Materials

TYPE Original Research
PUBLISHED 05 April 2024
DOI 10.3389/fmats.2024.1378089

OPEN ACCESS

EDITED BY
Zhigang Zhang,
Chongqing University, China

REVIEWED BY
Hui Li,
Hebei University of Technology, China
Mingfeng Xu,
State Key Laboratory of Building Safety and Environment, China

*CORRESPONDENCE
Jin Hou,
houjin1976@hotmail.com

RECEIVED 29 January 2024
ACCEPTED 18 March 2024
PUBLISHED 05 April 2024

CITATION
Hou J, Bai J, Mou H and Xiang Z (2024), Tensile properties and constitutive model of cost-effective multiscale hybrid fiber reinforced strain hardening cementitious composites.
Front. Mater. 11:1378089.
doi: 10.3389/fmats.2024.1378089

Tensile properties and constitutive model of cost-effective multiscale hybrid fiber reinforced strain hardening cementitious composites

Jin Hou*, Jianjun Bai, Hongmei Mou and Zhisuo Xiang

Zhenjiang Port Group Co., Ltd., Zhenjiang, Jiangsu, China

To enhance the mechanical properties and cost-effectiveness of conventional polyvinyl alcohol fiber reinforced strain hardening cementitious composite (PVA-SHCC), a modified version called multiscale hybrid fiber reinforced SHCC (MsHySHCC) was developed. This new composite incorporates a combination of steel fiber, PVA fiber and calcium carbonate ($CaCO_3$) whisker. Uniaxial direct tensile behaviors (stress-strain relationship, tensile strength, tensile deformation capacity and tensile toughness) of designed MsHySHCCs were investigated and evaluated. The results show that the PVA fibers dominate the ductile behavior and the steel fibers and $CaCO_3$ whiskers effectively affect the strength of MsHySHCCs. The PVA fibers can be partially replaced by $CaCO_3$ whisker and steel fiber, along with an increase in tensile strength and ductility of designed composites. The findings suggest that the configuration of MsHySHCC proves to be a viable approach in simultaneously enhancing the strength and ductility of PVA-SHCC. A semi-theoretical prediction model for tensile constitutive relationship was derived. The comparison of the theoretical results with the experimental data shows that this semi-theoretical model is applicable for determining the tensile constitutive relationship of PVA-SHCCs and MsHySHCCs.

KEYWORDS

strain hardening cementitious composite, tensile behavior, hybrid fiber, calcium carbonate whisker, constitutive relationship

1 Introduction

Strain hardening cementitious composite (SHCC) is a kind of cementitious composite with high ductility (Liu et al., 2020; Arain et al., 2023). In SHCC preparation, PVA fiber and PE fiber are commonly utilized (Zhang et al., 2021; Zhang et al., 2023a; Khalil and Atta, 2023; Tran and Nguyen, 2023). Out of all these, PVA-SHCC stands as the extensively researched and utilized fiber reinforced material. Nevertheless, the high expense remains a significant obstacle for PVA-SHCC to be implemented in extensive engineering projects (Zhang et al., 2020).

Hybrid use of low cost fibers is one of the effective ways to decrease the material cost of PVA-SHCC (Maalej et al., 2012; Liu et al., 2020; Rawat et al., 2022; Qasim et al., 2023), especially for the hybridization of PVA fiber and micro steel fiber (SF/PVA-SHCC). A lot of previous literatures have reported the tensile performance of SF/PVA-SHCCs. Ramasamy

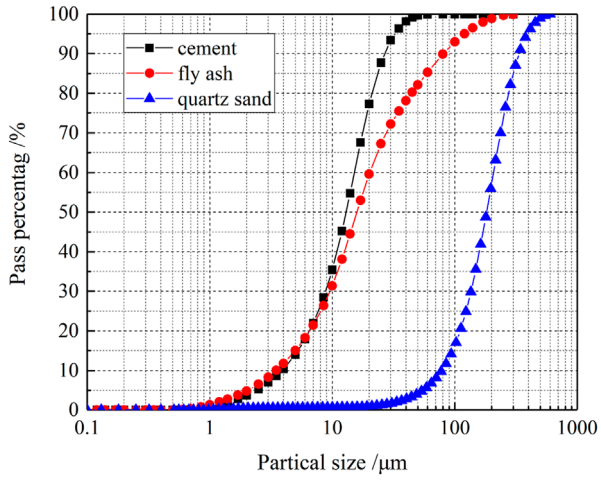

FIGURE 1
Particle size distribution curves of raw materials.

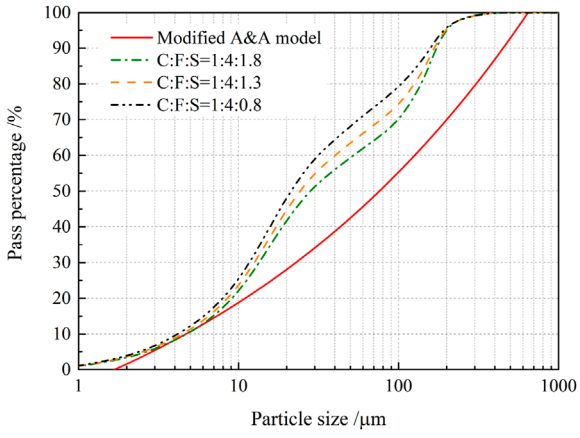

FIGURE 2
Calculation curves based on modified A&A model (C, cement; F, fly ash; S, sand).

and Shanmughasundaram, (2018) reported the mechanical properties of SF/PVA-SHCC containing 0.65% PVA fibers and 1.35% steel fibers. The experimental tensile strength and ultimate tensile strain are 6.78 MPa and 0.98%, respectively. Ramasamy's research found that the steel fiber content exceeded that of PVA fiber, resulting in a comparatively elevated tensile strength but relatively limited tensile ductility. Similar results were also noted in other studies (Hermes et al., 2012; Feng, 2019). It seems that the tensile ductility of SF/PVA-SHCC isn't mainly dominated by steel fibers. Wang et al. (2014) studied the tensile behavior of SF/PVA-SHCCs made by 0.3% steel+1.7% PVA fibers and 0.6% steel+1.7% PVA fibers. The tensile strength of these two kinds of SF/PVA-SHCCs is 3.72 and 4.02 MPa, respectively, while the ultimate tensile strain is 2.39% and 1.97%, respectively. It seems that the combination of high content of PVA fiber and low content of steel fiber can obtain a relatively high tensile ductility, but can't achieve a relatively high tensile strength. Similar experimental results were also pointed out by Liu and Tan. (2017a); Pourfalah (2018); Zhao et al. (2020); Tinoco and Silva (2021).

However, the influence of the content of steel fiber and PVA fiber on the tensile behaviors of SHCC is not completely consistent with the change laws discussed above. A lot of studies have attempted to achieve both high tensile strength and ductility via further adjusting fiber content, introducing highly reactive mineral admixtures, lowing water-binder ratio and optimizing the sand-binder ratio (Zhang et al., 2016; Liu et al., 2017b; Deshpande et al., 2019). However, it is regrettable that we are still far from this idea. Despite the high concentration of steel fibers and PVA fibers in certain research studies, the obtained experimental outcomes remain dissatisfactory (Zhang et al., 2016; Deshpande et al., 2019). As has been reported in Zhang's study, the combination of 1% steel fiber and 2% PVA fiber obtained a very high tensile strength (7.22 MPa), while the ultimate tensile strain was relatively low (0.8%) (Zhang et al., 2016). Therefore, it still needs to find an effective way to optimize the tensile strength and ductility of SF/PVA-SHCC.

It is widely recognized that cementitious materials possess distinct structural characteristics at multiple levels, including the levels of cement hydration products, cement paste, mortar, and concrete (Koichi et al., 2003; Kang and Bolander, 2016). Theoretically, the performance of cementitious materials can be significantly improved by incorporating multi-scale hybrid fibers, spanning from the microscopic to the macroscopic level (Parant and Rossi, 2007a; Parant and Rossi, 2007b; Pierre and Edouard, 2008; Rossi and Parant, 2008; Zhang and Cao, 2014; Cao et al., 2015). However, it is clear that achieving this task solely with steel fiber and PVA fiber is challenging. According to reports, it is believed that the size of fibers, particularly their diameter, has an inverse relationship with their ability to delay the development of microscopic cracks (Betterman et al., 1995; Cao et al., 2013). The dimensions of commonly used PVA fiber and steel fiber do not align well with the microscopic scale of cement hydration product and microscopic cracks, consequently failing to effectively improve the microscopic characteristics of cementitious materials. Hence, it is imperative to discover a viable approach to further augment the microscopic properties of SF/PVA-SHCC.

In recent times, SHCC's mechanical properties were improved using calcium carbonate ($CaCO_3$) whiskers with dimensions of about 30 μm in length and 1 um in diameter. Meanwhile, the cost of $CaCO_3$ whiskers is only about 230 $/t. The enhancement is achieved through microscopic mechanisms such as whisker pull-out, bridging, and crack deflection (Ma et al., 2017; Pan et al., 2018; Cao et al., 2019; Xie et al., 2020). As a result, a composite material named MsHySHCC, which consists of multiple scales of hybrid fibers and exhibits strain hardening properties, was developed. There are two main kinds of MsHySHCC now. The initial type of MsHySHCC solely comprises of PVA fiber and $CaCO_3$ whisker, whereas the second type of MsHySHCC is created by simultaneously incorporating two macro fibers (steel fiber and PVA fiber) and one microscopic fiber ($CaCO_3$ whisker). Mechanical performance and reinforcing mechanism of these two kinds of MsHySHCC have been widely studied. Ma et al. (2017) tested the tensile properties of the aforementioned first kind of MsHySHCC. The experimental findings indicated that $CaCO_3$ whisker increased the tensile strain capacity of PVA-SHCC. However, the strength of the MsHySHCC is comparatively weak, with a compressive

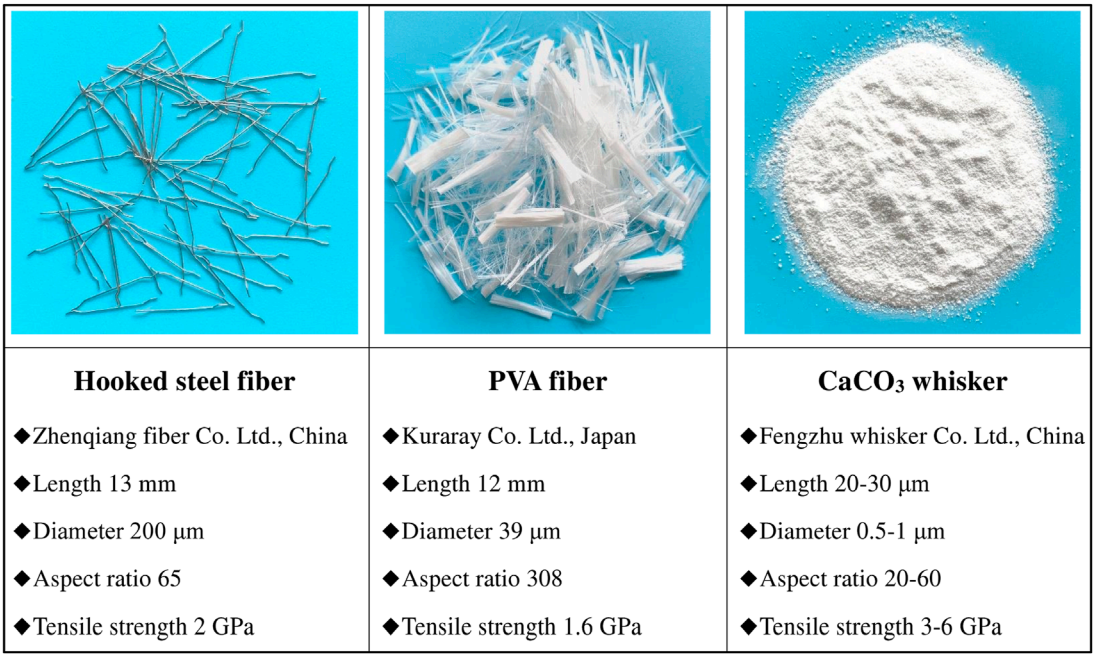

FIGURE 3
Whisker, steel fiber and PVA fiber employed in this paper.

TABLE 1 Fiber content in each designed groups.

Groups	Specification	Steel fiber (SF)/Vol.%	PVA fiber (PVA)/Vol.%	$CaCO_3$ whisker (CW)/Vol.%	Compressive strength/MPa
Control-1	Matrix	0	0	0	39.6
Control-2	CW1	0	0	1	42.8
Control-3	CW2	0	0	2	44.1
PVA-SHCC	PVA2	0	2	0	36.6
MsHySHCC-1	SF0.25PVA1.75CW1	0.25	1.75	1	38.8
MsHySHCC-2	SF0.5PVA1.5CW1	0.5	1.5	1	40.5
MsHySHCC-3	SF0.75PVA1.25CW1	0.75	1.25	1	41.3
MsHySHCC-4	SF0.25PVA1.5CW2	0.25	1.5	2	40.8
MsHySHCC-5	SF0.5PVA1.25CW2	0.5	1.25	2	42.2
MsHySHCC-6	SF0.75PVA1CW2	0.75	1	2	43.7

strength of about 25 MPa and a tensile strength of about 3 MPa. Consequently, this aspect hinders the practical implementation of the designed MsHySHCC. Mechanical properties of PVA-SHCC, which was modified by $CaCO_3$ whiskers (the aforementioned initial type of MsHySHCC), were also documented in Pan's study. It was discovered that the $CaCO_3$ whiskers can be used as a partial replacement for the PVA fibers, resulting in further improvement of the tensile and flexural characteristics of the designed MsHySHCC. However, the concentration of $CaCO_3$ whisker in their research is exceedingly high, consequently elevating the likelihood of whisker agglomeration (Cao et al., 2013). Cao et al. (2019) and Xie et al. (2020) studied the rheological behaviors, mechanical properties and shrinkage performances of MsHySHCC containing steel fiber, PVA fiber and $CaCO_3$ whisker (the aforementioned second kind of MsHySHCC). The researchers discovered that the engineered MsHySHCCs improved the abiligy of the mortar matrix against cracking at multiple scales. However, despite their initial intention to create the SHCC substance through the incorporation of

FIGURE 4
Preparation steps for MsHySHCC.

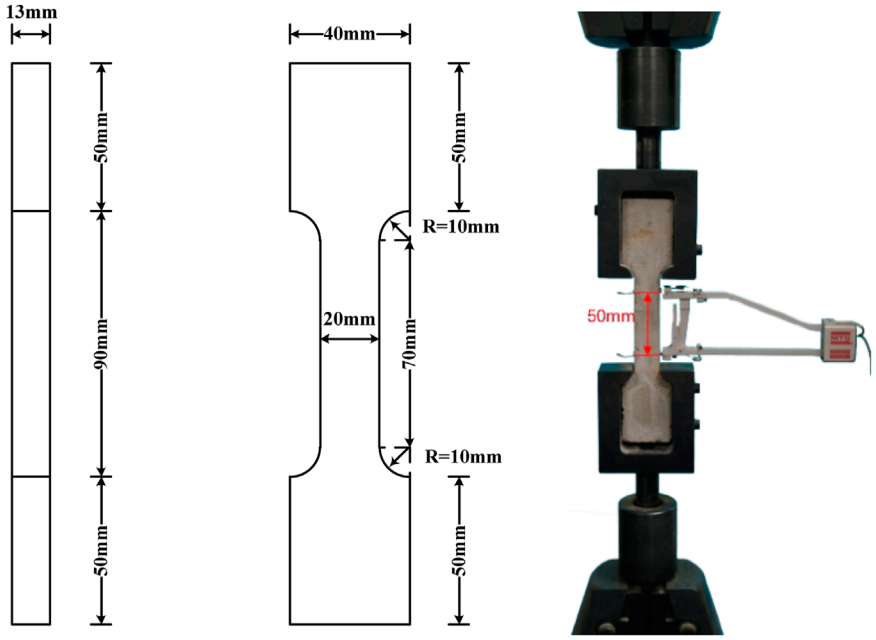

FIGURE 5
Dimension of tensile specimen and tensile test set-ups.

fibers at various scales, the strain hardening characteristics of the developed MsHySHCCs did not meet expectations. Due to the improper consideration of the steel fiber's role in controlling the hardening performance of cementitious materials in their study, the content of steel fiber is higher than that of PVA fiber, resulting in the inability to achieve a high ductility for MsHySHCCs.

From the above previous literatures, it can be noticed that although previous studies focused on MsHySHCC have obtained some relatively rich achievements, there are three basic questions still need to be well responded. (a) What methods can be used to simultaneously enhance the strength and ductility of existing MsHySHCCs? (b) Most of the literatures are experimental studies focus on mechanical properties of MsHySHCC, it still lacking an

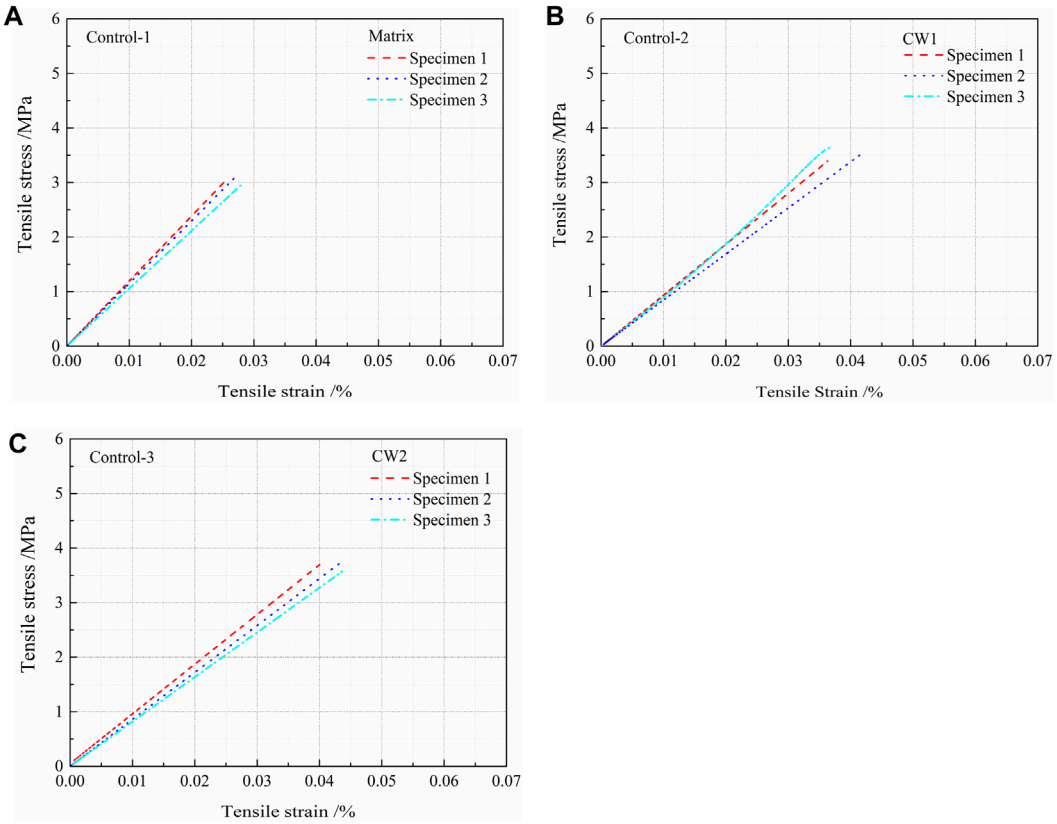

FIGURE 6
Tensile stress-strain relationships of **(A)** matrix; **(B)** 1% $CaCO_3$ whisker and **(C)** 2% $CaCO_3$ whiskers.

TABLE 2 Average values of tensile parameters for control groups.

Groups	Tensile strength/MPa	Ultimate strain/%	Tensile toughness/(N·mm/mm^3)
Control-1	3.027	0.027	0.041
Control-2	3.509	0.038	0.067
Control-3	3.751	0.042	0.079

effective constitutive model to describe the tensile behavior of MsHySHCC, although some micromechanical models and fractural models have been proposed for single fiber type SHCC. To this question, the main difficulties are how to consider the effect of hybrid fibers and most importantly how to take the action of $CaCO_3$ whisker into consideration.

In order to answer the above questions, the following two main works were carried out in this paper. By reasonably adjusting the ratio of matrix, steel fiber, PVA fiber, and $CaCO_3$ whisker, a novel form of MsHySHCC was achieved. Direct tensile performance of this kind of MsHySHCC was characterized, and the balance of strength and ductility of the designed composites was verified. By considering the impact of hybrid fibers and $CaCO_3$ whisker, a semi-theoretical prediction model was given to describe the tensile constitutive relationship of the designed MsHySHCC.

2 Material and experiment

2.1 Raw materials and mix proportion

The components utilized in the matrix included P·O 42.5 cement, fly ash, and fine quartz sand with a particle size ranging from 100 to 210 μm and an average size of 150 μm. Figure 1 displays the particle size distribution curves for fly ash, sand and cement. The particle size of fly ash is finer compared to cement. It can be used to make the particles of the raw material pack more closely, meanwhile, it has higher hydration activity than low grade fly ash, thus improving the strength of the composite material to a certain extent. Referred to the previous research results (Ma et al., 2017; Zhang et ak., 2020a), the mass ratio of fly ash and cement was set as 4:1 to guarantee a substantial ductility for the designed composite material.

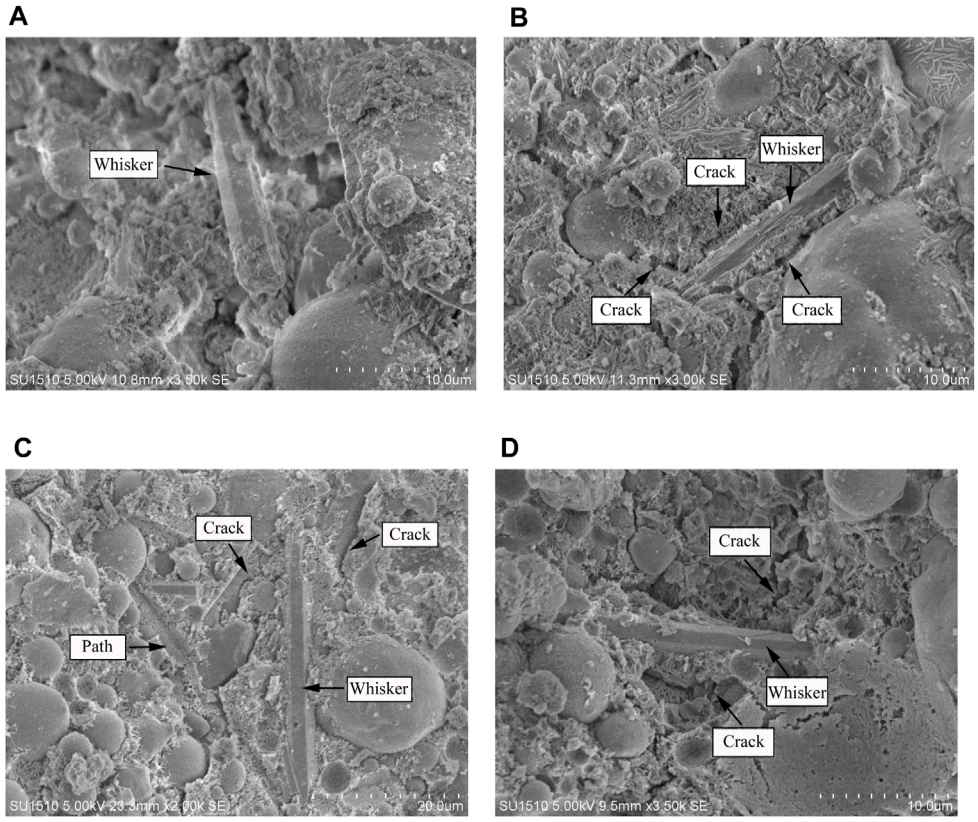

FIGURE 7
Micro-mechanisms of calcium carbonate whisker **(A)** pull-out; **(B)** crack deflection; **(C)** crack deflection and **(D)** bridging.

Previous literatures suggested that the optimal proportion of cement to fine sand should be between 0.6 and 1.8 (Liu and Tan, 2017a; Liu et al., 2017; Ramasamy and Shanmughasundaram, 2018; Tinoco and Silva, 2021; Arain et al., 2023). This study set the mass ratio of sand and cement as 1.8:1 in order to increase the density of the particles, bringing them closer to the theoretical curve, as depicted in Figure 2. More details about the modified A&A model can be obtained in previous literatures (Andreasen and Andersen, 1930; Funk and Dinger, 1994; Hunger, 2010; Karim et al., 2019).

The water to binder ratio was set as 0.34. The fresh MsHySHCC's workability was modified using superplasticizer at 0.5 wt% of binder. Three kinds of reinforcing fibrous materials were employed in this study, as shown in Figure 3. Table 1 displays the composition of various fibers in each designed group. Meanwhile, the 28 days compressive strength (70.7 mm^3 cube) of each group is also give in Table 1. It can be seen that the designed composites had a relative high compressive strength.

2.2 Specimen preparation and testing method

The process of preparing the specimen is illustrated in Figure 4. Dog-bone-shaped specimen was prepared. The tension specimen size is shown in Figures 4, 5. To ensure the precision of the experimental findings, three samples were prepared for every design mixture.

Tensile test set-ups are shown in Figure 5. A 15 mm range extensometer was used to monitor the tensile deformation of the specimen. The tensile loading rate is 0.1 mm/min.

3 Results and discussion

3.1 Tensile stress-strain relationships

Figure 6 shows the tensile stress-strain relationships of control groups with or without $CaCO_3$ whiskers. Table 2 summarizes the average tensile values of strength, ultimate strain and toughness of the three groups of materials. This paper quantifies the tensile toughness by calculating the enclosed region beneath the tensile stress-strain graph, which is employed to assess the specimen's ability to absorb energy under tensile force. By observing Figure 6; Table 2, it becomes evident that $CaCO_3$ whiskers can enhance both the tensile strength and tensile strain capacity of the mortar matrix. And the tensile strength and ultimate strain are further improved with increasing the content of $CaCO_3$ whiskers from 1% to 2%. The enhancements can be explained by the micro-mechanisms of $CaCO_3$ whiskers as illustrated in Figure 7. However, it is worth mentioning that despite the enhancement of tensile properties in the mortar matrix due to the utilization of $CaCO_3$ whisker, the

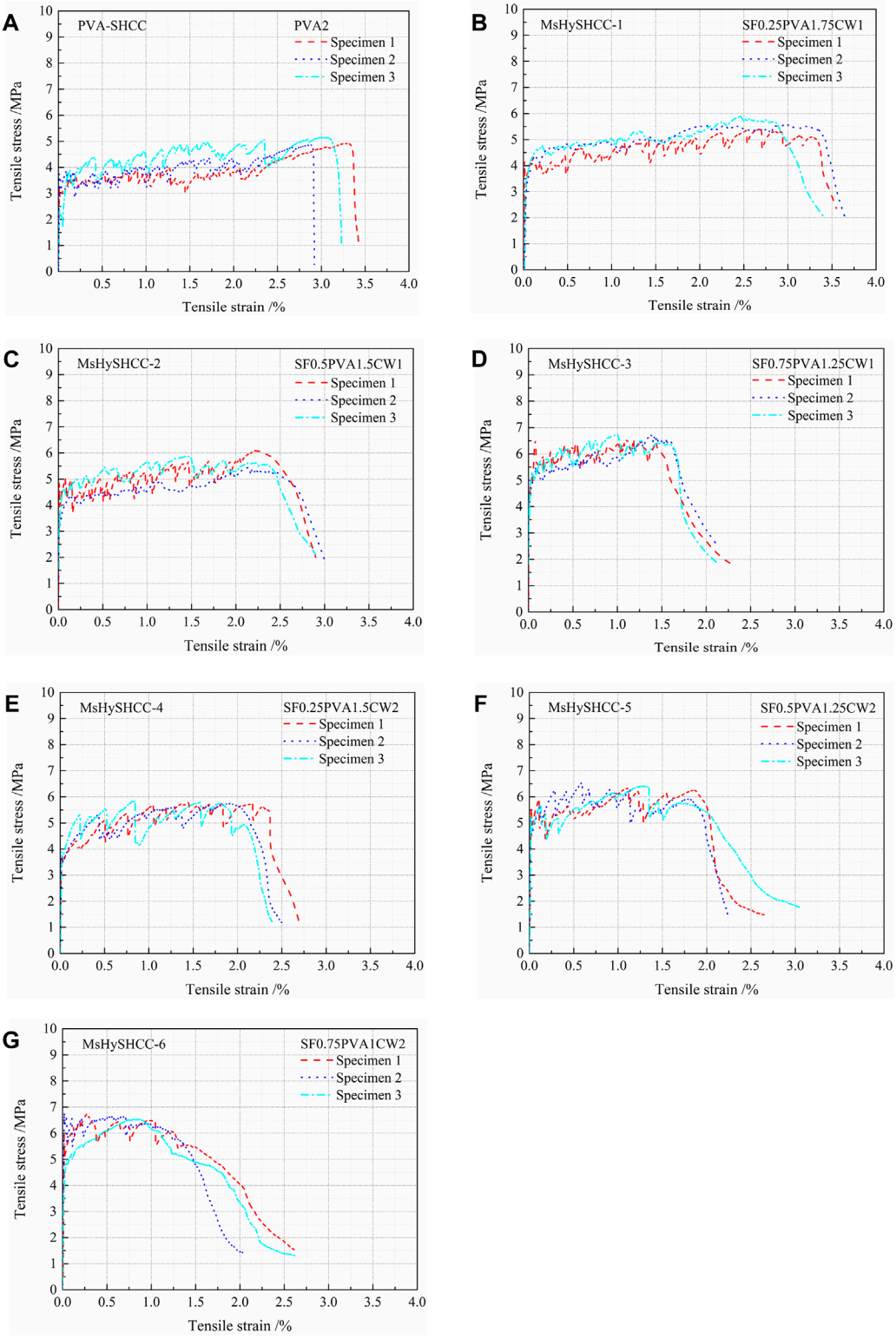

FIGURE 8
Tensile stress-strain relationship curves of MsHySHCCs and PVA-SHCC.

failure process still exhibited evident brittleness and lacked post peak toughness (Cao et al., 2013; Cao et al., 2019). Because the particle size of $CaCO_3$ whisker is small, it can only strengthen and toughen the mortar matrix at the microscopic level, thus can't improve the post peak toughness of the matrix like other macro fibers.

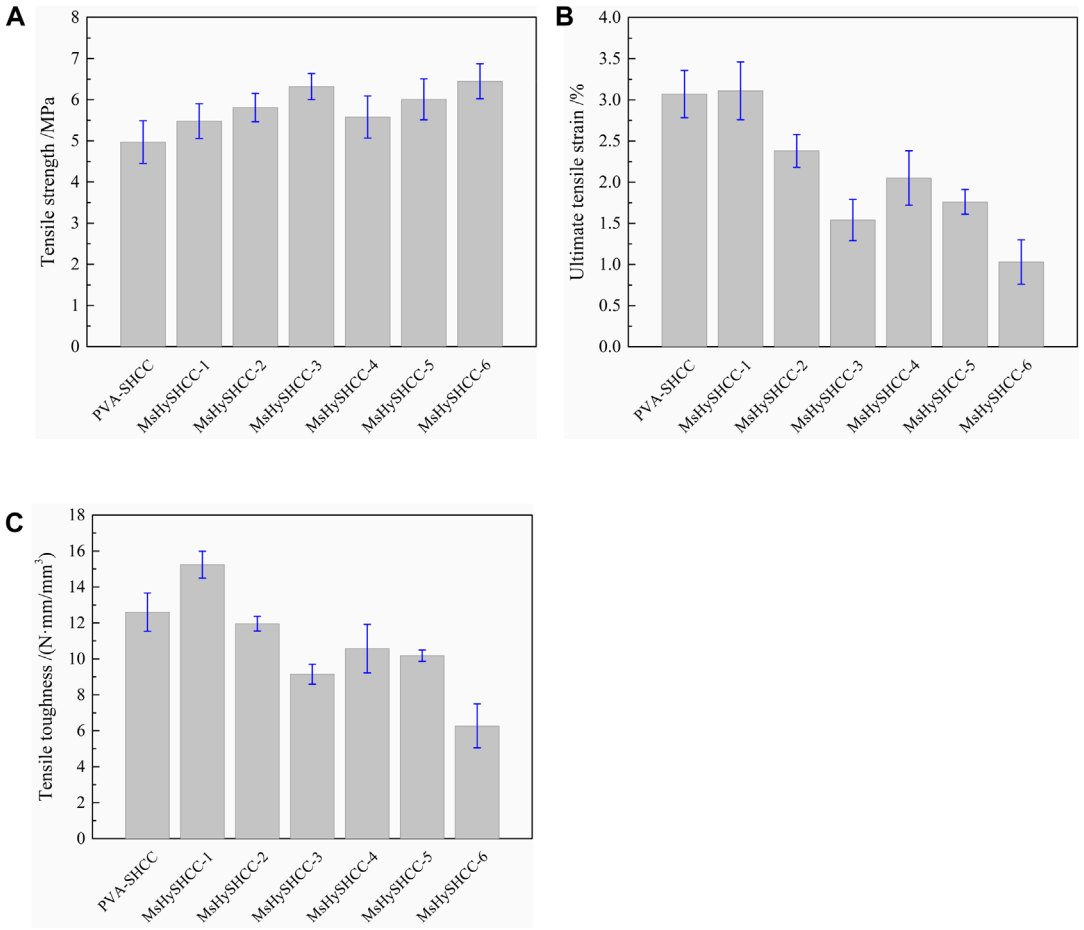

FIGURE 9
Experimental tensile results of **(A)** strength; **(B)** ultimate strain and **(C)** toughness for PVA-SHCC and MsHySHCCs.

The relationship between tensile stress and strain is depicted in Figure 8. Experimental tensile results of strength, ultimate strain and toughness for each group are provided in Figure 9. Experimental data of tensile parameters in previous available literatures are summarized in Table 3. Figure 10 illustrates the comparisons of the experimental findings between previous literature and the current study. From Figures 8–10; Table 3, the following findings can be addressed.

The experimental curves exhibited a slight improvement in robustness when PVA fibers were partially replaced with $CaCO_3$ whiskers and micro hooked steel fibers, as depicted in Figures 8A–G. The microscopic mechanisms of $CaCO_3$ whisker shown in Figure 7 have the potential to enhance the quantity and evenness of micro-cracks within the mortar matrix (Cao et al., 2015; Ma et al., 2017; Pan et al., 2018). Ma et al. (2017) discovered that additional crack sources could potentially contribute to the multiple cracking performance of SHCC (Pan et al., 2018). As a result, it is possible to improve the robustness of the tensile stress-strain curves.

The addition of steel fibers and $CaCO_3$ whiskers to replace some PVA fibers increased the tensile strength of PVA-SHCC. Compared to PVA-SHCC, when the whisker content maintained at 1%, the tensile strength exhibited an increase from 5.48 MPa to 6.32 MPa with the steel fiber content ranging from 0.25% to 0.75%. Increasing the amount of whiskers further enhanced the tensile strength to a small extent, despite the further reduction in PVA fiber content. The enhancements could be credited to the higher peak stress for crack bridging offered by steel fibers with hooks and the reinforcing effect at a microscopic level provided by $CaCO_3$ whiskers. The whiskers and steel fibers have greater modulus of elasticity and stiffness compared to PVA fibers. By limiting the development of cracks, these rigid fibers can effectively improve the principal tensile stress of the material, thus increasing its tensile strength (Rawat et al., 2022; Qasim et al., 2023). On the contrary, PVA fiber is a kind of flexible synthetic fiber that has a lesser impact on the tensile strength compared to steel fiber and $CaCO_3$ whisker.

As depicted in Figure 8; Table 3, MsHySHCC-1 exhibited greater tensile strength and ultimate tensile strain in comparison to PVA-SHCC, with 1% $CaCO_3$ whiskers hybrid 0.25% steel fibers partially replacing 0.25% PVA fibers. Nevertheless, a gradual deterioration in strain hardening behavior of SHCCs was observed when the PVA fiber content was reduced while the steel fiber and $CaCO_3$ whisker amounts were increased. It implies the strain hardening behavior dominates by the PVA fibers. The discrepancy in total quantity between PVA fiber and hooked steel fiber arises due to the constant

TABLE 3 Summary of tensile properties in available literatures and in present study.

Researcher	V_f/%			σ_{tu}/MPa	ε_{tu}/%	Other descriptions
	SF	PVA	CW			
Hermes (2012)	0.75	1.25	—	4.16	0.81	C:FA:S:W = 1:1.2:0.8:0.56
Soe et al. (2013)	0.5	1.5	—	4.73	0.34	C:FA:S:W = 1:1.2:0.8:0.56
	0.58	1.75	—	5.60	0.52	
Wang et al. (2014)	0.3	1.7	—	3.72	2.39	C:S:W = 1:0.3:0.35
	0.6	1.7	—	4.02	1.97	
Tinoco and Silva. (2021)	0.5	1.5	—	4.59	1.88	C:FA:S:W = 1:1.23:1.06:0.665
	1	1	—	4.82	1.79	
Liu and Tan. (2017a)	0.5	1.5	—	5.50	0.8	C:FA:S:W = 1:1.22:1:0.62
Liu et al. (2017b)	0.5	1.5	—	5.48	0.63	C:FA:S:W = 1:1.22:1:0.62
	0.5	1.5	—	4.25	2.08	C:FA:S:W = 1:1.86:0.72:1.03
Zhang et al. (2016)	1	2	—	7.22	0.8	B:S:W = 1:0.833:0.18
Pourfalah (2018)	0.75	1.75	—	4.36	3.0	C:FA:S:W = 1:1.81:0.6:0.78 and l_{sf} = 6 mm
	0.75	1.75	—	4.71	2.5	C:FA:S:W = 1:1.81:0.6:0.78 and l_{sf} = 12 mm
Pan et al. (2018)	—	1.5	2	3.92	2.8	B:S:W = 1:0.2:0.28
	—	1.25	2	3.41	3.22	
	—	1.5	4	3.02	1.97	
	—	1.5	4	3.75	2.15	
Ramasamy and Shanmughasundaram. (2018)	1	1	—	6.30	1.08	C:FA:S:W = 1:0.43:0.71:0.5
	1.35	0.65	—	6.78	0.98	
Liu et al. (2018)	1	1.5	—	5.25	0.65	C:FA:S:W = 1:3:1.4:1.28
Deshpande et al. (2019)	1	2	—	5.85	1.51	C:FA:S:W = 1:2.2:1.3:1.06
Ma et al. (2017)	—	2	0.5	3.29	6.3	C:FA:S:W = 1:4:1.8:1.5
	—	2	1	2.34	6.76	
	—	2	2	2.15	6.77	
	—	5	0.5	2.95	3.43	C:FA:S:W = 1:2.2:1.2:0.96
Zhao et al. (2020)	0.5	2.2	—	3.75	2.95	B:S:W = 1:0.28:0.31
	1	2.2	—	4.71	1.48	
	1.5	2.2	—	4.57	0.82	
Feng (2019)	1.25	0.75	—	5.8	0.13	B:S:W = 1:0.5:0.3
	1.25	0.55	2	5.85	0.16	

(Continued on the following page)

TABLE 3 (*Continued*) Summary of tensile properties in available literatures and in present study.

Researcher	V_f/%			σ_{tu}/MPa	ε_{tu}/%	Other descriptions
	SF	PVA	CW			
Present study	0.25	1.75	1	5.48	3.11	B:S:W = 1:0.36:0.34
	0.5	1.5	1	5.81	2.38	
	0.75	1.25	1	6.32	1.54	
	0.25	1.5	2	5.58	2.05	
	0.5	1.25	2	6.01	1.76	
	0.75	1	2	6.45	1.03	

Note: V_f is the volume fraction of fiber; σ_{tu} is the tensile strength; ε_{tu} is the ultimate tensile strain; l_{sf} is the length of steel fiber; C, cement; FA, fly ash; S, sand; W, water; B, binder.

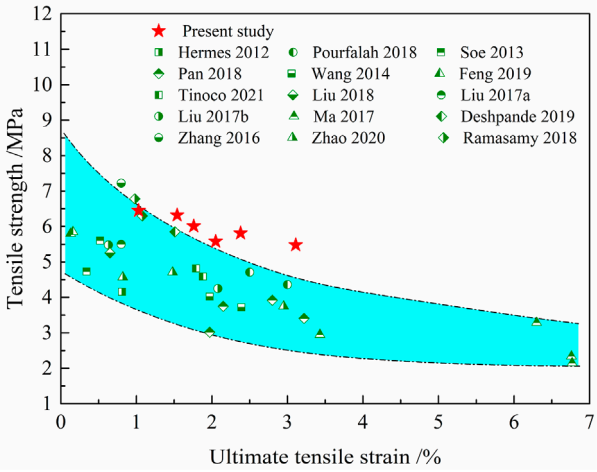

FIGURE 10
Tensile parameters in previous literatures and present study.

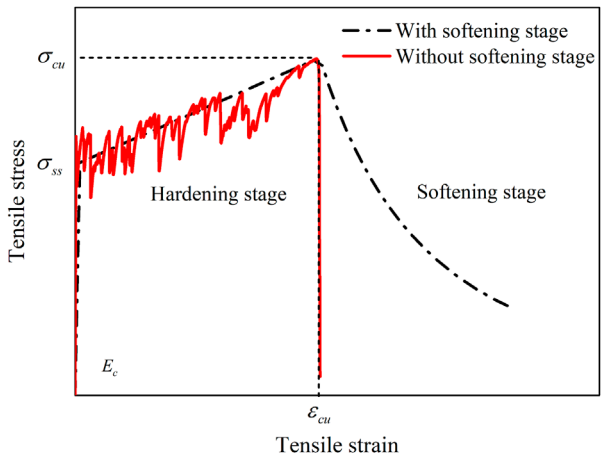

FIGURE 11
Double-line model and triple-line model for SHCC with or without softening stage.

volume content condition. The main determinant for enhancing hardening performance primarily relies on the quantity of fibers rather than just the fiber content. A decrease in the number of fiber pieces results in a reduction in the effective stress caused by fibers, consequently resulting in an unsaturated cracking performance and an unstable hardening process. Meanwhile, although the number of whiskers is very high, the size of the whiskers is tens of times smaller than that of the PVA fibers, so the whiskers can only have a positive effect on microscopic cracks in the matrix. Consequently, the SHCCs don't exhibit significant ductility due to the excessive replacement of PVA fibers with whiskers and hooked steel fibers.

As shown in Table 3; Figure 10, based on the findings, it can be inferred that incorporating PVA fiber, steel fiber, and $CaCO_3$ whisker in the design process of multi-scale fibers is a viable approach to simultaneously enhance the strength and ductility in SHCC.

3.2 Semi-theoretical prediction model

Available literatures have confirmed that double-line model can be used to describe the tensile constitutive relationship of PVA-SHCC, as illustrated in Figure 11. To the SHCC reinforced by steel and PVA hybrid fibers, it may have obvious post-peak softening stage due to the introduction of hooked steel fibers. Generally, the parameter of fiber reinforcing factor RI_v dominates the softening behavior. Previous literatures (Ramasamy and Shanmughasundaram, 2018; Tinoco and Silva, 2021; Deshpande et al., 2019.) show that the softening stage should be considered when $RI_v \geq 1$, which is presented as a triple-line constitutive model, as illustrated in Figure 11. However, through the experimental results in this paper, it is found that when $CaCO_3$ whiskers are added, a relatively obvious softening behavior begins to appear when $RI_v \geq 0.876$. This is because the microscopic reinforcing and toughening effects of $CaCO_3$ whiskers improves the matrix properties and then enhances the pullout behavior of steel fibers and PVA fibers (Cao et al., 2015; Pan et al., 2018). Therefore, a higher residual bearing capacity for post-peak stage can be achieved, i.e., a more noticeable softening stage for tensile stress-strain curves.

TABLE 4 Interfacial bonding strength of steel fiber and PVA fiber.

Fiber type	0% whisker	1% whisker	2% whisker	Reference
Hooked steel fiber	7.0	7.2	7.5	Wu and Li. (1999), Voo and Foster. (2003)
PVA fiber	1.37	1.45	1.85	Ma et al. (2017)

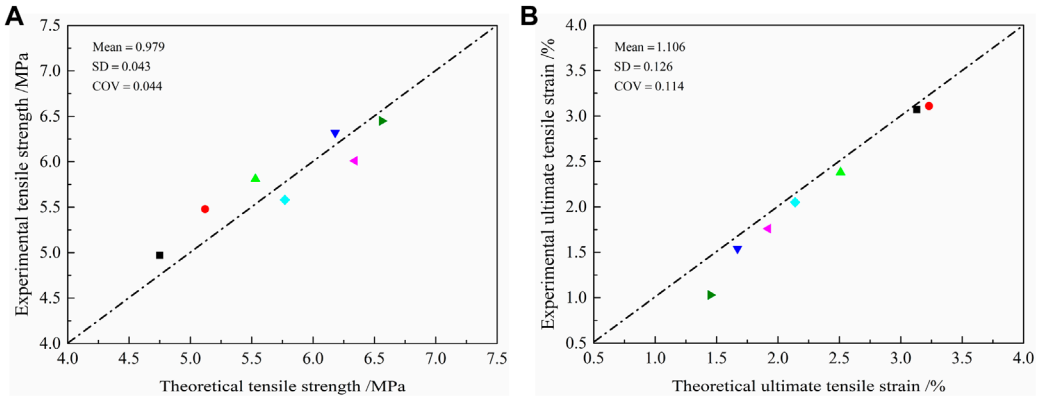

FIGURE 12
Calculation results of tensile strength and ultimate tensile strain.

The triple-line model needs to determine three key parameters, namely, stable cracking stress σ_{ss}, ultimate tensile stress σ_{cu} and ultimate tensile strain ε_{cu}, as illustrated in Figure 11. For the convenience of calculation, the first-peak stress σ_0 is numerically equal to the stable cracking stress σ_{ss} approximately, that is, the stress at the beginning of the strain hardening behavior. Therefore, the relationship of tensile stress $\sigma(\varepsilon)$ and tensile strain ε for MsHySHCCs can be expressed as Eq. 1.

$$\sigma(\varepsilon) = \begin{cases} E_c\varepsilon & 0 \le \varepsilon < \frac{\sigma_{ss}}{E_c} \\ \sigma_{ss} + k_1\left(\varepsilon - \frac{\sigma_{ss}}{E_c}\right) & \frac{\sigma_{ss}}{E_c} \le \varepsilon < \varepsilon_{cu} \\ k_2\sigma_{cu} & \varepsilon_{cu} \le \varepsilon \end{cases} \tag{1}$$

Where k_1 is the hardening coefficient, $k_1 = \frac{\sigma_{cu}-\sigma_{ss}}{\varepsilon_{cu}-\sigma_{ss}/E_c}$; E_c is the elastic modulus of designed MsHySHCCs, which can be empirically obtained by fitting experimental data in this study and $E_c = -10.3RI_v^2 + 27.8RI_v + 1.8$; k_2 is the softening coefficient, $k_2 = \left(\frac{\varepsilon_{cu}}{\varepsilon}\right)^{\frac{4}{RI_v^2}}$; RI_v is the fiber reinforcing parameter (Ou et al., 2011; Ning et al., 2015), and RI_v can be obtained by Eq. 2.

$$RI_v = \sum_{i=1}^{n} \beta V_i \frac{l_i}{d_i}\left(\frac{E_i}{E_{sf}}\right)^p \tag{2}$$

The interfacial bonding parameter β can be considered as 1.0 for PVA fiber and 1.2 for steel fiber with hooked shape. Additionally, a stiffness factor p can be set as 1.3 for PVA fiber. The fiber volume fraction, fiber geometric length, and diameter are denoted as V_i, l_i, and d_i, respectively. Furthermore, E_i represents the fiber elastic modulus, while E_{sf} signifies the elastic modulus of hooked steel fiber.

The ultimate tensile stress σ_{tu} can be calculated by using the equation provided by Li and Leung in 1992, as shown in Eq. 3. The first-peak stress σ_0 can be calculated by Eq. 4. The hardening coefficient g can be determined by Eq. 5. The interfacial bonding strength τ_i can be determined according to Table 4.

$$\sigma_{tu} = g\sigma_0 \tag{3}$$

$$\sigma_0 = \frac{V_{i,pva}\tau_{i,pva}}{2}\left(\frac{l_{i,pva}}{d_{i,pva}}\right) + \frac{V_{i,sf}\tau_{i,sf}}{2}\left(\frac{l_{i,sf}}{d_{i,sf}}\right) \times F_{be} \tag{4}$$

$$g = \frac{2}{4+f^2}\left(1 + e^{\pi f/2}\right) \tag{5}$$

The hooked steel fiber characteristic parameter F_{be} was set as 1.7. Additionally, the hardening effect was taken into consideration using the factor f (Ahmed et al., 2007). In this study, the f values assigned to the matrix with 0%, 1%, and 2% $CaCO_3$ whiskers were 0.085, 0.105, and 0.125 respectively.

To characterize the ductility of SHCC, it is necessary to theoretically calculate the ultimate tensile strain ε_{tu} (Lin and Li, 1997), as provided in Eq. 6.

$$\varepsilon_{tu} = \frac{\delta_{tu}}{x_d} \tag{6}$$

Based on earlier research (Li and Stang, 1997; Lin and Li, 1997; Kanda and Li, 2000), the ultimate crack opening displacement δ_{tu} can be calculated by Eq. 7.

$$\delta_{tu} = \frac{\tilde{l}_f}{2}\left(\frac{c-2}{3c}\right) \tag{7}$$

Where $c = \frac{\gamma\tilde{l}_f}{2\tilde{d}_f}$; γ is a dimensionless factor (Wang et al., 1988; Shao et al., 1993), set as 0.5 in this study (Wu and Li, 1999). The

10.3389/fmats.2024.1378089

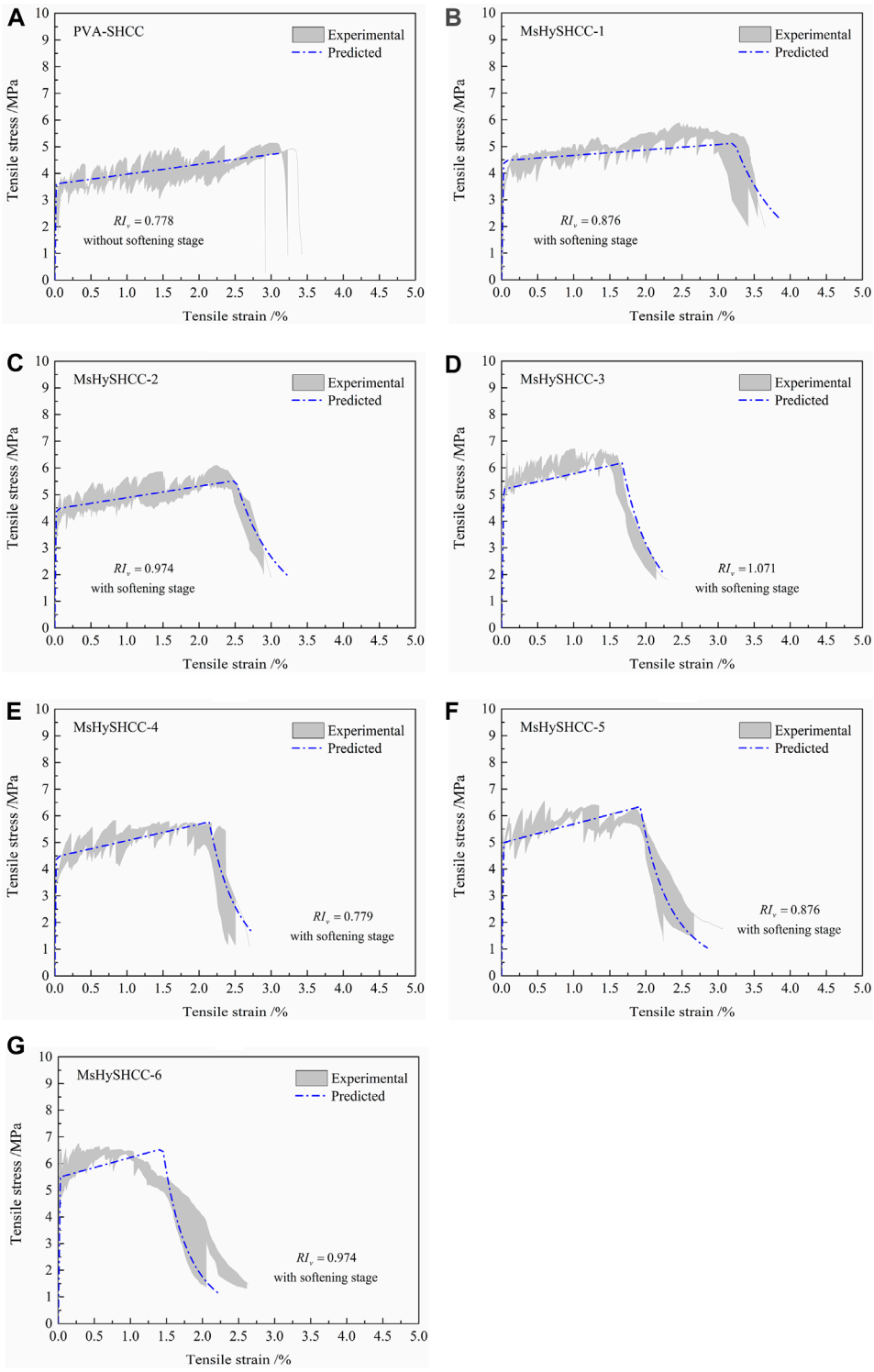

FIGURE 13
Calculation results of tensile constitutive relationship curves.

parameter $\tilde{l}_f$ and $\tilde{d}_f$ signifies the generalized mean value of fiber length and fiber diameter, respectively.

According to previous literature (Wu and Li, 1992; Alwan, 1994; Kanda and Li, 1998; Wu and Li, 1995), the crack spacing value x_d can be determined by Eq. 8.

$$x_d = \frac{\tilde{l}_f - \sqrt{\tilde{l}_f^2 - 2\pi\psi\tilde{l}_f x}}{2 - 2F(\bar{\varepsilon}_{mc})} \tag{8}$$

Where $\psi = \frac{4}{\pi g}$, $x = \frac{V_m \sigma_{mu} \tilde{d}_f}{4 V_f \tilde{\tau}_f}$, $F(\bar{c}_{mc}) = \exp\left[-\frac{1}{\lambda}\left(\frac{\bar{c}_0}{\bar{c}_{mc}}\right)^m\right]$ and $\bar{c}_0 = \left(\frac{\sqrt{\pi}}{2}\frac{K_m}{\sigma_{mu}}\right)^2$. The tensile strength of mortar σ_{mu} for 0%, 1% and 2% whiskers is taken as 3.0, 3.5, and 3.75 MPa, respectively; V_m is the volume fraction of mortar; the Weibull parameter m is taken as 2 and the normalized flaw size is set as 10 μm (Wu and Li, 1992); the fracture toughness of mortar is set as 0.37 MPa·m$^{1/2}$ (Ahmed et al., 2007).

Figures 12, 13 showcase the theoretical findings related to the tensile parameters and stress-strain curves. It can be seen that the proposed model adequately characterizes the tensile stress-strain correlation of MsHySHCC. Nevertheless, to a certain degree, the proposed model overestimates the cracking saturation degree of MsHySHCC and traditional PVA-SHCC during the experiment. Consequently, the calculated ultimate tensile strain values surpass the corresponding experimental measurements.

4 Conclusion

The aim of this study was to examine the tensile characteristics of SHCC reinforced with hybrid fibers at multiple scales (MsHySHCC). Two main questions were responded in this study. The initial step involves achieving a kind of MsHySHCC with both high strength and ductility. The second one is how to predict the tensile behaviors of MsHySHCC. This study yields the subsequent fundamental findings.

(1) PVA fibers control the tensile ductility of MsHySHCC. Steel fibers have a more pronounced effect on the tensile strength, but do not improve the tensile ductility of MsHySHCC. The tensile strength and tensile deformation capacity of the SHCC matrix can be significantly enhanced due to the micro-mechanisms involving $CaCO_3$ whiskers. The improved effect of whiskers on the mechanical properties of the matrix can further strengthen the pull-out mechanism of PVA fibers and steel fibers.

(2) Designing MsHySHCC is one of the effective ways to simultaneously enhance the strength and ductility of PVA-SHCC. The designed MsHySHCC shows higher tensile strength than that of traditional PVA-SHCC. Replacing some of the PVA fibers with $CaCO_3$ whiskers and hooked steel fibers at a volume fraction of 0.25% can result in increased tensile strength and ultimate tensile strain. However, a substantial decrease in the PVA fiber amount will greatly diminish the tensile ductility.

(3) By considering the impact of hybrid fibers and $CaCO_3$ whiskers, a semi-theoretical model was developed to describe the tensile constitutive relationship of the designed MsHySHCC. The comparison between the theoretical and experimental findings leads to the conclusion that this semi-theoretical model is capable of determining the tensile stress-strain relationships of MsHySHCC.

Data availability statement

The original contributions presented in the study are included in the article/Supplementary material, further inquiries can be directed to the corresponding author.

Author contributions

JH: Investigation, Writing–original draft, Writing–review and editing. JB: Investigation, Writing–review and editing. HM: Investigation, Writing–review and editing. ZX: Investigation, Writing–review and editing.

Funding

The author(s) declare that no financial support was received for the research, authorship, and/or publication of this article.

Conflict of interest

Authors JH, JB, HM, and ZX were employed by Zhenjiang Port Group Co., Ltd.

Publisher's note

All claims expressed in this article are solely those of the authors and do not necessarily represent those of their affiliated organizations, or those of the publisher, the editors and the reviewers. Any product that may be evaluated in this article, or claim that may be made by its manufacturer, is not guaranteed or endorsed by the publisher.

References

Ahmed, S. F., Maalej, M., and Paramasivam, P. (2007). Analytical model for tensile strain hardening and multiple cracking behavior of hybrid fiber-engineered cementitious composites. *J. Mater. Civ. Eng.* 19 (7), 527–539. doi:10.1061/(asce)0899-1561(2007)19:7(527)

Alwan, J. M. (1994). *Modeling of the mechanical behavior of fiber reinforced cement based composites under tensile loads*. PH.D. Dissertation. Michigan: University of Michigan.

Andreasen, A., and Andersen, J. (1930). About the relationship between grain and gradation gap in products of loose grains (with a few experiments). *Kolloid-Zeitschrift* 50 (3), 217–228. doi:10.1007/bf01422986

Arain, M. F., Memon, H., Wang, M., Ahmed, A., Chen, J., and Zhang, H. (2023). Matrix tailoring for polyvinyl alcohol (PVA) fiber-reinforced ductile cementitious composites. *AATCC J. Res.* 10 (2), 63–72. doi:10.1177/24723444221147982

ASTM (2010). *Standard test method for flexural performance of fiber-reinforced concrete (using beam with third-point loading)*. C1609/C1609M. West Conshohoken, PA: ASTM.

Betterman, L., Ouyang, C., and Shah, S. (1995). Fiber-matrix interaction in microfiber reinforced mortar. *Adv. Cem. Based Mater.* 2, 53–61. doi:10.1016/1065-7355(94)00027-b

Cao, M., Xie, C., Li, L., and Khan, M. (2019). Effect of different PVA and steel fiber length and content on mechanical properties of $CaCO_3$ whisker reinforced cementitious composites. *Mater. Construcc.* 69 (336), 200. doi:10.3989/mc.2019.12918

Cao, M., Zhang, C., Li, Y., and Wei, J. (2015). Using calcium carbonate whisker in hybrid fiber-reinforced cementitious composites. *J. Mater. Civ. Eng.* 27 (4), 1–13. doi:10.1061/(asce)mt.1943-5533.0001041

Deshpande, A., Kumar, D., and Ranade, R. (2019). Influence of high temperatures on the residual mechanical properties of a hybrid fiber-reinforced strain-hardening cementitious composite. *Constr. Build. Mater.* 208 (30), 283–295. doi:10.1016/j.conbuildmat.2019.02.129

Ding, Y., Yu, J., Yu, K., and Xu, S. l. (2018). Basic mechanical properties of ultra-high ductility cementitious composites: from 40 MPa to 120 MPa. *Compo. Struct.* 185, 634–645. doi:10.1016/j.compstruct.2017.11.034

Feng, J. Q. (2019). *Tensile properties of new hybrid fiber reinforced cementitious composites (NHyFRCC)*. Ph.D. Dissertation. Dalian: Dalian University of Technology.

Funk, J., and Dinger, D. (1994). *Predictive process control of crowded particulate suspensions*. New York, NY, USA: Springer.

Hermes, P., Zhang, Y., Soe, K., and Bell, J. (2012). Material properties of a new hybrid-fiber engineered cementitious composite. *Adv. Mater. Res.* 450-451, 433–438. 10.4028/www.scientific.net/amr.450-451.433.

Huang, T., Zhang, Y. X., and Yang, C. H. (2016). Multiscale modelling of multiple-cracking tensile fracture behaviour of engineered cementitious composites. *Eng. Fract. Mech.* 160, 52–66. doi:10.1016/j.engfracmech.2016.04.006

Hunger, M. (2010). *An integral design concept for ecological self-compacting concrete*. Ph.D. Dissertation. Eindhoven: Eindhoven University of Technology.

Kabele, P. (2007). Multiscale framework for modeling of fracture in high performance fiber reinforced cementitious composites. *Eng. Fract. Mech.* 74, 194–209. doi:10.1016/j.engfracmech.2006.01.020

Kanda, T., and Li, V. C. (1998). Multiple cracking sequence and saturation in fiber reinforced cementitious composites. *Concr. Res. Tech.* 9 (2), 19–32. doi:10.3151/crt1990.9.2_19

Kanda, T., and Li, V. C. (2000). Tensile stress-strain modeling of pseudo-strain hardening cementitious composites. *J. Mater. Civ. Eng.* 12 (2), 147–156. doi:10.1061/(asce)0899-1561(2000)12:2(147)

Kang, J., and Bolander, J. E. (2016). Multiscale modeling of strain-hardening cementitious composites. *Mech. Res. Commun.* 78, 47–54. doi:10.1016/j.mechrescom.2015.08.004

Karim, R., Najimi, M., and Shafei, B. (2019). Assessment of transport properties, volume stability, and frost resistance of non-proprietary ultra-high performance concrete. *Constr. Build. Mater.* 227, 117031. doi:10.1016/j.conbuildmat.2019.117031

Khalil, A. A., Atta, A. M., Baraghith, A. T., Behiry, R. N., and Soliman, O. E. (2023). Shear strengthening of concrete deep beams using pre-fabricated strain-hardening cementitious composite plates. *Eng. Struct.* 278, 115548. doi:10.1016/j.engstruct.2022.115548

Koichi, M., Tetsuya, I., and Toshiharu, K. (2003). Multi-scale modeling of concrete performance. *J. Adv. Concr. Technol.* 1, 91–126.

Li, V. C., and Leung, C. K. Y. (1992). Steady-state and multiple cracking of short random fiber composites. *J. Eng. Mech.* 11 (118), 2246–2264. doi:10.1061/(asce)0733-9399(1992)118:11(2246)

Li, V. C., and Stang, H. (1997). Interface property characterization and strengthening mechanisms in fiber reinforced cement based composites. *Adv. Cem. Based Mater.* 6 (1), 1–20. doi:10.1016/s1065-7355(97)90001-8

Lin, Z., and Li, V. C. (1997). Crack bridging in fiber reinforced cementitious composites with slip-hardening interfaces. *J. Mech. Phys. Solids* 45 (5), 763–787. doi:10.1016/s0022-5096(96)00095-6

Liu, J. C., and Tan, K. H. (2017a). Fire resistance of strain hardening cementitious composite with hybrid PVA and steel fibers. *Constr. Build. Mater.* 135, 600–611. doi:10.1016/j.conbuildmat.2016.12.204

Liu, J. C., Tan, K. H., and Fan, S. (2018). Residual mechanical properties and spalling resistance of strain-hardening cementitious composite with Class C fly ash. *Constr. Build. Mater.* 181 (30), 253–265. doi:10.1016/j.conbuildmat.2018.06.009

Liu, J. C., Tan, K. H., and Zhang, D. (2017b). Multi-response optimization of post-fire performance of strain hardening cementitious composite. *Cem. Concr. Compos.* 80, 80–90. doi:10.1016/j.cemconcomp.2017.03.001

Liu, T., Yang, Y., Chen, Z., Li, Y., and Bai, R. (2020). Optimization of fiber volume fraction to enhance reinforcing efficiency in hybrid fiber reinforced strain hardening cementitious composite. *Cem. Concr. Compos.* 113, 103704. doi:10.1016/j.cemconcomp.2020.103704

Ma, H., Cai, J., Lin, Z., Qian, S., and Li, V. C. (2017). $CaCO_3$ whisker modified engineered cementitious composite with local ingredients. *Constr. Build. Mater.* 151, 1–8. doi:10.1016/j.conbuildmat.2017.06.057

Maalej, M., Quek, S. T., Ahmed, S. F. U., Zhang, J., Lin, V., and Leong, K. (2012). Review of potential structural applications of hybrid fiber engineered cementitious composites. *Constr. Build. Mater.* 36, 216–227. doi:10.1016/j.conbuildmat.2012.04.010

Ning, X., Ding, Y., and Zhang, F. (2015). Experimental study and prediction model for flexural behavior of reinforced SCC beam containing steel fibers. *Constr. Build. Mater.* 93 (0), 644–653. doi:10.1016/j.conbuildmat.2015.06.024

Ou, Y., Tsai, M., Liu, K., and Chang, K. C. (2011). Compressive behavior of steel-fiber-reinforced concrete with a high reinforcing index. *J. Mater. Civ. Eng.* 24 (2), 207–215. doi:10.1061/(asce)mt.1943-5533.0000372

Pan, J., Cai, J., Ma, H., and Leung, C. K. Y. (2018). Development of multiscale fiber-reinforced engineered cementitious composites with PVA fiber and $CaCO_3$ whisker. *J. Mater. Civ. Eng.* 30 (6), 04018106. doi:10.1061/(asce)mt.1943-5533.0002305

Pan, Z., Wu, C., Liu, J., and Wang, W. (2015). Study on mechanical properties of cost-effective polyvinyl alcohol engineered cementitious composites (PVA-ECC). *Constr. Build. Mater.* 78, 397–404. doi:10.1016/j.conbuildmat.2014.12.071

Parant, E., Rossi, P., and Boulay, C. (2007a). Fatigue behavior of a multi-scale cement composite. *Cem. Concr. Res.* 37, 264–269. doi:10.1016/j.cemconres.2006.04.006

Parant, E., Rossi, P., and Maou, F. L. (2007b). Durability of a multiscale fibre reinforced cement composite in aggressive environment under service load. *Cem. Concr. Res.* 37, 1106–1114. doi:10.1016/j.cemconres.2006.02.021

Pierre, R., and Edouard, P. (2008). Damage mechanisms analysis of a multi-scale fibre reinforced cement-based composite subjected to impact and fatigue loading conditions. *Cem. Concr. Res.* 38, 413–421. doi:10.1016/j.cemconres.2007.09.002

Pourfalah, S. (2018). Behaviour of engineered cementitious composites and hybrid engineered cementitious composites at high temperatures. *Constr. Build. Mater.* 158, 921–937. doi:10.1016/j.conbuildmat.2017.10.077

Qasim, M., Lee, C. K., and Zhang, Y. X. (2023). Flexural strengthening of reinforced concrete beams using hybrid fibre reinforced engineered cementitious composite. *Eng. Struct.* 284, 115992. doi:10.1016/j.engstruct.2023.115992

Ramasamy, K. A., and Shanmughasundaram, K. (2018). Flexural performance of hybrid engineered cementitious composite layered reinforced concrete beams. *Period. Polytech. – Civ.* 62 (4), 921–929. doi:10.3311/ppci.11748

Rawat, S., Zhang, Y. C., and Lee, C. K. (2022). Multi-response optimization of hybrid fibre engineered cementitious composite using Grey-Taguchi method and utility concept. *Constr. Build. Mater.* 319, 126040. doi:10.1016/j.conbuildmat.2021.126040

Rossi, P., and Parant, E. (2008). Damage mechanisms analysis of a multi-scale fibre reinforced cement-based composite subjected to impact and fatigue loading conditions. *Cem. Concr. Res.* 38, 413–421. doi:10.1016/j.cemconres.2007.09.002

Shao, Y., Li, Z., and Shah, S. P. (1993). Matrix cracking and interface debonding in fiber-reinforced cement-matrix composites. *Adv. Cem. Based Mater.* 1 (2), 55–66. doi:10.1016/1065-7355(93)90010-l

Soe, K., Zhang, Y., and Zhang, L. (2013). Material properties of a new hybrid fibre-reinforced engineered cementitious composite. *Constr. Build. Mater.* 43, 399–407. doi:10.1016/j.conbuildmat.2013.02.021

Tinoco, M. P., and Silva, F. D. A. (2021). On the mechanical behavior of hybrid fiber reinforced strain hardening cementitious composites subjected to monotonic and cyclic loading. *J. Mater. Res. Tech.* 11, 754–768. doi:10.1016/j.jmrt.2021.01.053

Tran, N. T., Nguyen, T. K., Nguyen, D., and Le, Q. H. (2023). Assessment of fracture energy of strain-hardening fiber-reinforced cementitious composite using experiment and machine learning technique. *Struct. Concr.* 24 (3), 4185–4198. doi:10.1002/suco.202200332

Voo, J., and Foster, S. (2003). *Variable engagement model for fiber reinforced concretein tension UNICIV Report No. R-420*. Sydney: The University of New South Wales.

Wang, Y., Li, V. C., and Backer, S. (1988). Modelling of fibre pull-out from a cement matrix. *Int. J. Cem. Compos. Lightweight Concr.* 10 (3), 143–149. doi:10.1016/0262-5075(88)90002-4

Wang, Z., Zhang, J., and Wang, J. (2014). Tensile performance of polyvinyl alcohol–steel hybrid fiber reinforced cementitious composite with impact of water to binder ratio. *J. Compos. Mater.* 49 (18), 1–19. doi:10.1177/0021998314542450

Wu, H., and Li, V. C. (1992). Snubbing and bundling effects on multiple crack spacing of discontinuous random fiber-reinforced brittle matrix composites. *J. Am. Ceram. Soc.* 75 (12), 3487–3489. doi:10.1111/j.1151-2916.1992.tb04457.x

Wu, H., and Li, V. C. (1995). Stochastic process of multiple cracking in discontinuous random fiber reinforced brittle matrix composites. *Int. J. Damage Mech.* 4 (4), 83–102. doi:10.1177/105678959500400105

Wu, H., and Li, V. C. (1999). Fiber/cement interface tailoring with plasma treatment. *Cem. Concr. Compos.* 21 (3), 205–212. doi:10.1016/s0958-9465(98)00053-5

Xie, C., Cao, M., Si, W., and Khan, M. (2020). Experimental evaluation on fiber distribution characteristics and mechanical properties of calcium carbonate whisker modified hybrid fibers reinforced cementitious composites. *Constr. Build. Mater.* 265, 120292. doi:10.1016/j.conbuildmat.2020.120292

Zhang, C., and Cao, M. (2014). Fiber synergy in multi-scale fiber-reinforced cementitious composites. *J. Reinf. Plast. Comp.* 33 (9), 862–874. doi:10.1177/0731684413514785

Zhang, J., Wang, Q., and Wang, Z. (2016). Properties of polyvinyl alcohol-steel hybrid fiber reinforced composite with high-strength cement matrix. *J. Mater. Civ. Eng.* 29 (7), 1–9. doi:10.1061/(asce)mt.1943-5533.0001868

Zhang, Y., Deng, M., and Dong, Z. (2019). Seismic response and shear mechanism of engineered cementitious composite (ECC) short columns. *Eng. Struct.* 192, 296–304. doi:10.1016/j.engstruct.2019.05.019

Zhang, Z. G., Li, Z., He, J., and Shi, X. (2023b). High-strength engineered cementitious composites with nanosilica incorporated: mechanical performance and autogenous self-healing behavior. *Cem. Concr. Compos.* 135, 104837. doi:10.1016/j.cemconcomp.2022.104837

Zhang, Z. G., Liu, J., Li, J., Qin, F., and Di, J. (2023a). Micromechanics-based analysis of PVA-ECC after thermal exposure. *Arch. Civ. Mech. Eng.* 23, 213. doi:10.1007/s43452-023-00736-1

Zhang, Z. G., Liu, S., Yang, F., Weng, Y., and Qian, S. (2021). Sustainable high strength, high ductility engineered cementitious composites (ECC) with substitution of cement by rice husk ash. *J. Clean. Prod.* 317, 128379. doi:10.1016/j.jclepro.2021.128379

Zhang, Z. G., Qin, F., Ma, H., and Xu, L. (2020a). Tailoring an impact resistant engineered cementitious composite (ECC) by incorporation of crumb rubber. *Constr. Build. Mater.* 262, 120116. doi:10.1016/j.conbuildmat.2020.120116

Zhang, Z. G., Yang, F., Liu, J., and Wang, S. (2020b). Eco-friendly high strength, high ductility engineered cementitious composites (ECC) with substitution of fly ash by rice husk ash. *Cem. Concr. Res.* 137, 106200. doi:10.1016/j.cemconres.2020.106200

Zhao, X., Li, Q., and Xu, S. (2020). Contribution of steel fiber on the dynamic tensile properties of hybrid fiber ultra-high toughness cementitious composites using Brazilian test. *Constr. Build. Mater.* 246, 118416. doi:10.1016/j.conbuildmat.2020.118416

Zhou, J., Pan, J., and Leung, C. (2015). Mechanical behavior of fiber reinforced engineered cementitious composites in uniaxial compression. *J. Mater. Civ. Eng.* 27 (1), 04014111. doi:10.1061/(asce)mt.1943-5533.0001034

frontiers | Frontiers in Materials

TYPE Original Research
PUBLISHED 10 June 2024
DOI 10.3389/fmats.2024.1410016

OPEN ACCESS

EDITED BY
Zhigang Zhang,
Chongqing University, China

REVIEWED BY
Shaorui Wang,
Chongqing Jiaotong University, China
Shi Jun,
Central South University, China

*CORRESPONDENCE
Pengfei Men,
menpengfei185811@163.com

RECEIVED 31 March 2024
ACCEPTED 14 May 2024
PUBLISHED 10 June 2024

CITATION
Huang S, Xi Y, Li X, Men P and Wu G (2024), Flexural behaviour of damaged concrete T-beams reinforced with ultra-high performance concrete filling.
Front. Mater. 11:1410016.
doi: 10.3389/fmats.2024.1410016

Flexural behaviour of damaged concrete T-beams reinforced with ultra-high performance concrete filling

Shuai Huang[1], Yonglei Xi[2], Xin Li[3], Pengfei Men[4]* and Gangan Wu[3]

[1]Shanxi Transportation New Technology Development Co., Ltd., Taiyuan, China, [2]China Communications 2nd Navigational Bureau 2nd Engineering Co., Ltd., Chongqing, China, [3]CSCEC Xinjiang Construction and Engineering (group) Co., Ltd. Southwest Company, Chengdu, Sichuan, China, [4]Department of Civil and Environmental Engineering, The Hong Kong Polytechnic University, Kowloon, Hong Kong SAR, China

To improve the flexural performance of damaged reinforced concrete T-beams, a method of filling ultra-high performance concrete (UHPC) in the damaged area was adopted. Experimental studies were conducted on two UHPC-reinforced concrete T-beams with different lengths of damaged areas and one undamaged concrete T-beam as a reference. Crack distribution, failure modes, cracking loads, flexural capacities, and strain variation of the specimens were analyzed. Subsequently, a nonlinear finite element (FE) model of the UHPC-reinforced T-beam was developed using ABAQUS, and the FE model results were compared with the experimental results to validate the accuracy of the FE simulation method. The results indicated that the two UHPC-reinforced T-beams exhibited a similar flexural failure process to the undamaged T-beam. The longitudinal tensile strain distribution at the mid-span section showed that the composite section formed by the filling of UHPC in the damaged region still adhered the assumption of the planar section. Owing to the excellent bond performance between UHPC and the existing concrete, the main cracks of the UHPC-reinforced T-beams appeared in the chiseled area, and the crack widths of the UHPC-reinforced T-beams under the same load were smaller than those of the reference T-beam. Overall, the reinforcing method of filling UHPC in the damaged region can restore or even enhance the flexural performance of the damaged reinforced concrete T-beams.

KEYWORDS

damaged reinforced concrete T-beam, reinforcement by ultra-high performance concrete (UHPC) filling, flexural performance, experiments, finite element model

1 Introduction

It is widely recognized that bridge safety is influenced by two major factors: natural factors and human factors. Among the human factors, vehicle collisions pose a significant threat to bridge structures and should not be ignored. However, it is important to note that not all bridges collapse when struck by vehicles, particularly in cases where high vehicles collide with overpass bridges. In most instances, these collisions result in localized damage to the upper structure of bridges. Figure 1 depicts a typical bridge collision accident that took place in China, where it is evident that collisions with high vehicles primarily caused

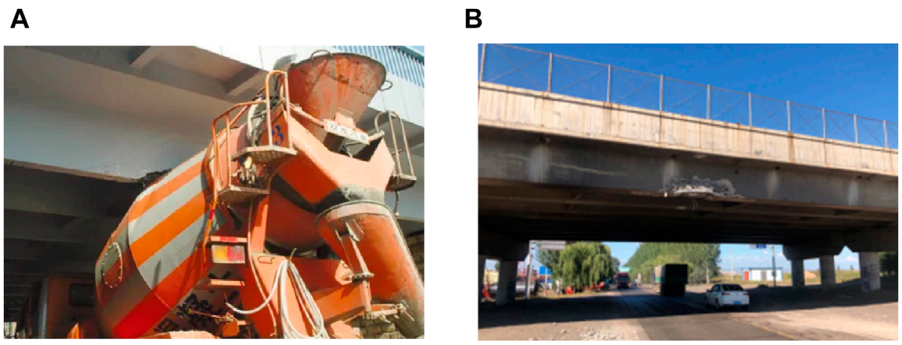

FIGURE 1
Typical accidents caused by vehicle impact on bridges. **(A)** Concrete T-beam bridge **(B)** Small box girder bridge.

localized concrete failure, fractures in ordinary rebars, and breakage of limited prestressed tendons. Typically, such damage does not result in a loss of bearing capacity or collapse of the bridge. However, before the damaged beams are repaired or replaced, the traffic of the damaged bridge needs to be closed for an extended period.

Regarding the issue of vehicle collisions with bridges, current research primarily focuses on the damage mechanisms of bridge structures after impact and numerical simulations of the collision process (Xu et al., 2012; Xu et al., 2013). It is difficult to find research literature specifically addressing reinforcement techniques for damaged bridges caused by collisions. However, extensive studies (Ngidi and Dundu, 2018; Di et al., 2020; Qin et al., 2020) have been conducted on concrete bridges that do not meet the normal serviceability requirements in terms of load capacity, which can provide references for the reinforcement research of collision-damaged bridges. In recent years, new types of cementitious materials, such as engineered cementitious composites (ECC) (Zhang et al., 2023a; 2023b; Liu et al., 2023; Men et al., 2024) Ultra-high performance concrete (UHPC) (Leng et al., 2024) concrete have been studied and used in civil engineering. UHPC exhibits high tensile strength, good flowability, and high bond strength with existing concrete (Zou et al., 2023a; Zou et al., 2023b). The application of UHPC for retrofitting existing bridges has become a significant reinforcement method (Zhu et al., 2020).

Zhang et al. (2020a; 2020b) conducted a series of push-out tests to investigate the effects of various parameters, including the of normal concrete strength, interface treatment methods, the age of UHPC, and the moisture level on the surface of normal concrete, on the shear performance of the interface between UHPC and normal concrete. M.A. Al-Osta et al. (2017) conducted experimental investigations on the flexural performance of reinforced concrete beams strengthened with ultra-high performance fiber-reinforced concrete (UHPFRC) using two interface treatment methods: sandblasting treatment on the surface of the reinforced concrete beams and applying epoxy adhesive at the interface. The results indicated that the flexural performance of the beams under both strengthening methods was similar, with the three-sided U-shaped UHPFRC reinforcement method showing the highest increase in the bearing capacity. Paschalis et al. (2018) conducted a comparative study to evaluate the effectiveness of non-reinforced UHPFRC strengthening layers and reinforced UHPFRC strengthening layers on the flexural behaviour of reinforced concrete beams. They found that the non-reinforced UHPFRC layer had a minimal impact on the flexural capacity of the beams but delayed crack formation and enhanced beam stiffness, while the reinforced UHPFRC layer significantly increased the flexural capacity of the test beams. Zhang et al. (2020c; 2023) investigated the flexural performance of damaged reinforced concrete beams strengthened with reinforced UHPC layers, and they found that the reinforced UHPC layers increased the flexural capacity of the beams by 71.4%–126.3% and effectively delayed the development of cracks. P. Ganesh and Murthy. (2021) used precast UHPC strips to strengthen the tension region of reinforced concrete beams and studied the reinforcement effects of different thicknesses of UHPC strips through static load tests. The results demonstrated that the interface between the UHPC strip and concrete beam remained intact throughout the entire loading process. Although the precast UHPC strips increased the flexural stiffness of the beams, the improvement in flexural capacity was not significant. Safdar et al. (2016) replaced the concrete at the top and bottom of reinforced concrete beams with UHPFRC layers of varying thicknesses to investigate their influence on flexural performance, and the study indicated that the UHPFRC s reinforcement layer enhanced the stiffness, ultimate flexural capacity, and delayed crack initiation, thereby improving the durability of the concrete beams. Yin et al. (2017) conducted flexural performance tests on reinforced concrete slabs using UHPC. The results showed that the UHPC reinforcement layer improved the failure mode of the reinforced concrete slabs and increased their flexural capacities.

According to the available literature, numerous studies have been conducted on the flexural performance of existing bridges reinforced with UHPC. However, there is a lack of research specifically addressing the reinforcement of damaged bridges using UHPC. To bridge this gap, this study conducted experimental investigations and nonlinear finite element (FE) model to study the flexural behaviour of damaged concrete T-beams reinforced with UHPC filling, and the findings in this paper can provide guidance for reinforcing this type of damaged bridge.

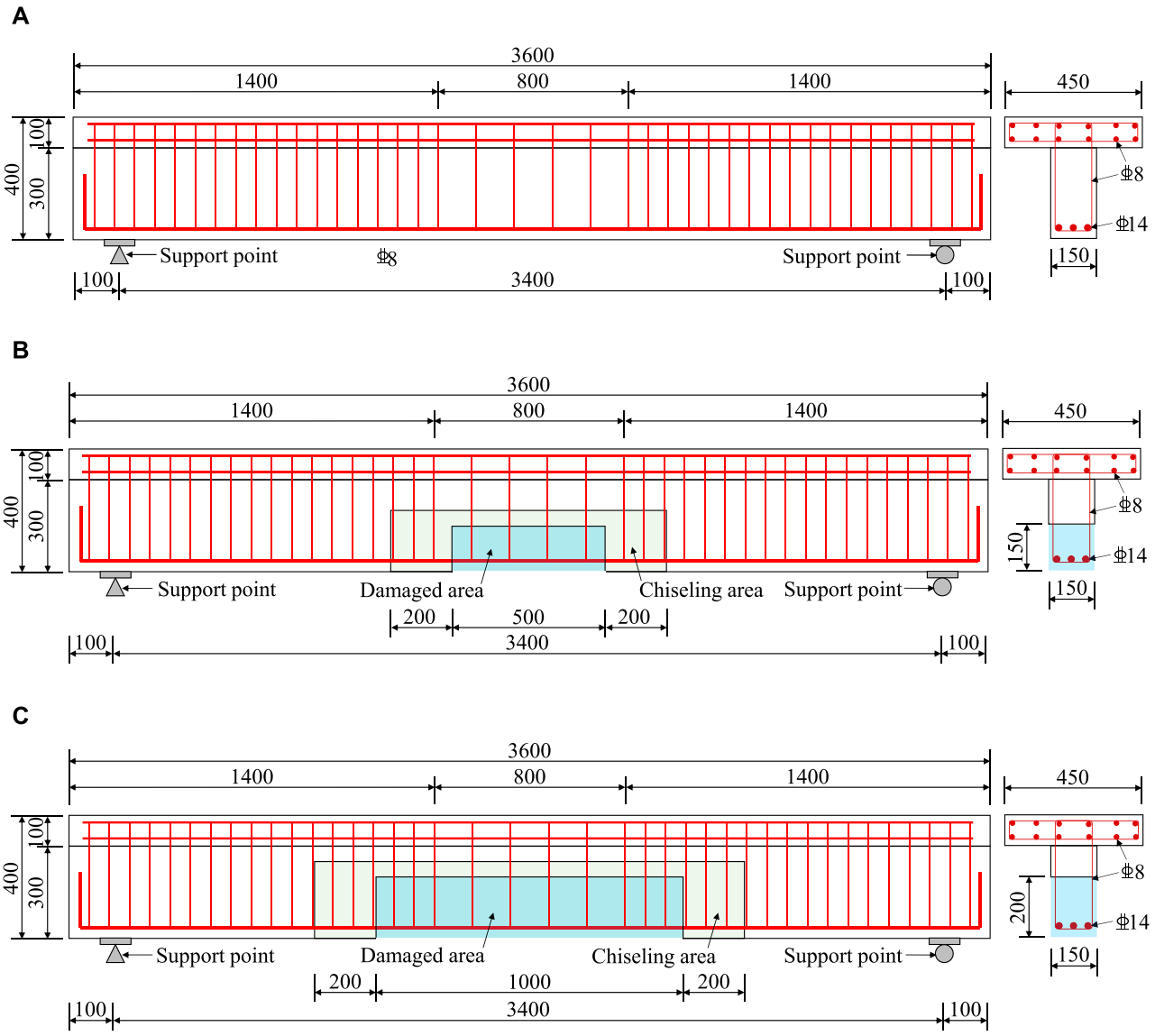

FIGURE 2
Dimensional parameters of the specimens (unit: mm). **(A)** NC **(B)** NU-0.5 **(C)** NU-1.0.

2 Experimental programme

2.1 Specimen design

A total of three T-beam specimens were designed, including one undamaged specimen as a reference and two damaged specimens reinforced with UHPC. For each T-beam, the width and thickness of the top flange were 450 mm and 100 mm, respectively, while the height and width of the web were 300 mm and 150 mm, respectively. The damage areas of the two reinforced specimens were arranged on the web, both located near the mid-span section, with dimensions of 150 mm × 500 mm and 200 mm × 1,000 mm, respectively, in the elevation view. For the actual impact-damaged bridge depicted in Figure 1, prior to reinforcement implementation, it was necessary to remove the damaged rebars and weld new rebars. As the overlapping welding of reinforcing bars is a well-established technique ensuring the strength of the welded joints, this study omitted the step of welding new rebars and used intact rebars in the fabrication process of the specimen. The details of the specimens are illustrated in Figure 2. The dimensions of the damaged and reinforced areas of the specimens are presented in Table 1. In Table 1, the label of the specimen consists of two parts: the first part denotes the reinforcement form of the specimens, where "NC" represents unreinforced T-beam and "NU" represents reinforced beam, and the second part of "NU" represents the length of the reinforced area were 0.5 m or 1.0 m.

During the specimen fabrication, to ensure the enough bond between the UHPC in the damaged region and the normal concrete of the existing beam, the concrete at the damage area was completely removed, and simultaneously, a certain area around the damaged

TABLE 1 Primary test parameters of specimens.

Specimen	Damaged region $l \times h$ (m × m)	Strengthened length l_s (m)	Strengthened height h (mm)	Reinforcement scheme
NC	/	/	/	Comparison specimen
NU-0.5	0.5 × 0.15	0.5	150	Fill the damaged area with UHPC
NU-1.0	1.0 × 0.20	1.0	250	

region of the beam was chiseled to create a rough surface. As shown in Figures 2, 3, the height of the chipped area of the beam was 50 mm higher than that of the damaged region, and each end of the chiseled area was extended 200 mm beyond the damaged region. The chiseling depth on the side and bottom surfaces of the web was controlled at 15 mm and 20 mm, respectively. Through this chiseling process, the normal tensile interface between the UHPC at the damaged region and the existing concrete of the T-beam was transformed into two types of interfaces: the normal tensile interface between the UHPC filling and the existing concrete and the tangential shear interface between the chipped U-shaped UHPC and the existing concrete. This approach helped to weaken or even eliminate the vulnerability of the UHPC-concrete interface to normal tensile strength, which was susceptible to construction quality and material shrinkage deformation. And consequently, the strength of the strengthening interface was improved.

2.2 Material properties

In this experiment, commercial concrete with a concrete grade of C50 was used. The average cubic compressive strength f_{cu}, obtained from six 150 mm × 150 mm × 150 mm cubic specimens, was 51.0 MPa. The average axial compressive strength f_c, measured from three 150 mm × 150 mm × 300 mm prismatic specimens, was 43.0 MPa. The elastic modulus E_c, determined from six prismatic specimens of the same dimensions, was 36.3 GPa. Rebars with diameters of 14 mm and 8 mm, both of grade HRB400, were used in the experiment. Material properties of the rebars, including elastic modulus E, average yield strength f_y, average ultimate tensile strength f_u, yield strain ε_y, and peak strain ε_u, were determined through tensile tests on three rebar coupons. Material properties of rebar are summarized in Table 2.

Furthermore, UDC(II)-150 type UHPC pre-mixed material was adopted. Prior to conducting the experiment, the material properties of UHPC were evaluated in accordance with T/CCPA 7-2018 (T/CBMF 37, 2018). The tensile properties of UHPC, including cracking strain ε_t, peak strain ε_{tu}, and tensile strength f_t, were determined through uniaxial tensile tests on six dog-bone coupons. Moreover, the elastic modulus and axial compressive strength of UHPC were measured using six cylindrical specimens with diameters of 100 mm and heights of 200 mm. The compressive strength of UHPC was evaluated through testing six 100 mm × 100 mm × 100 mm cubes. The material test results of UHPC are presented in Table 3.

2.3 Loading and testing programme

As depicted in Figure 4, four-point bending tests were conducted for all specimens. The distance between the loading points was 550 mm, and the distance between the support points was 3,400 mm. Consequently, the shear span ratio was 3.56. A hydraulic jack was used for loading, and the single-point concentrated load was transformed into two equal point loads using a distribution beam. The applied load was obtained through a load sensor under the jack. The loading process included two steps: pre-loading and formal loading. During the pre-loading, the load was applied to 0.6 times of the estimated cracking load and then unloaded. For the formal loading, at the early loading stages, load control was adopted. Before reaching the cracking load, the load was increased in an increment of 2.5 kN. After the cracking load reached, the increment was adjusted to 5.0 kN. Once the load-displacement curve exhibited a yield turning point, the loading control switched to displacement control. Until the load-displacement curve exhibited a significant yield segment or started to decline, the experiment was stopped. During each loading increment, the load was held for 5 min before colleting the test data. Meanwhile, the development of cracks was recorded and the width of these crack was also measured.

As shown in Figure 5, three linear variable differential transformers (LVDTs) were arranged at the mid-span and two loading points to measure the vertical displacement of the specimen, while one dial gauge was set at each support to measure the settlement of the respective supports. Strain gauges were used to measure the strain of the rebar and concrete. The strain gauge arrangement for the tensile main steel bars is illustrated in Figure 5A, while the strain gauge arrangement for the mid-span section of the specimen is illustrated in Figure 5B.

3 Experimental results

3.1 Cracking and failure modes

Figure 6 illustrates the failure modes of the reference specimen NC and the reinforced specimens NU-0.5 and NU-1.0. Apparently, none of the top flanges of the specimens experienced concrete crushing failure when the specimens reached their flexural capacity. This was attributed to the large compressive area of the top flange in the T-beam. When the load-displacement curves of the specimens exhibited a significant yield segment or started to decline, it was considered that the specimens reached their flexural capacities.

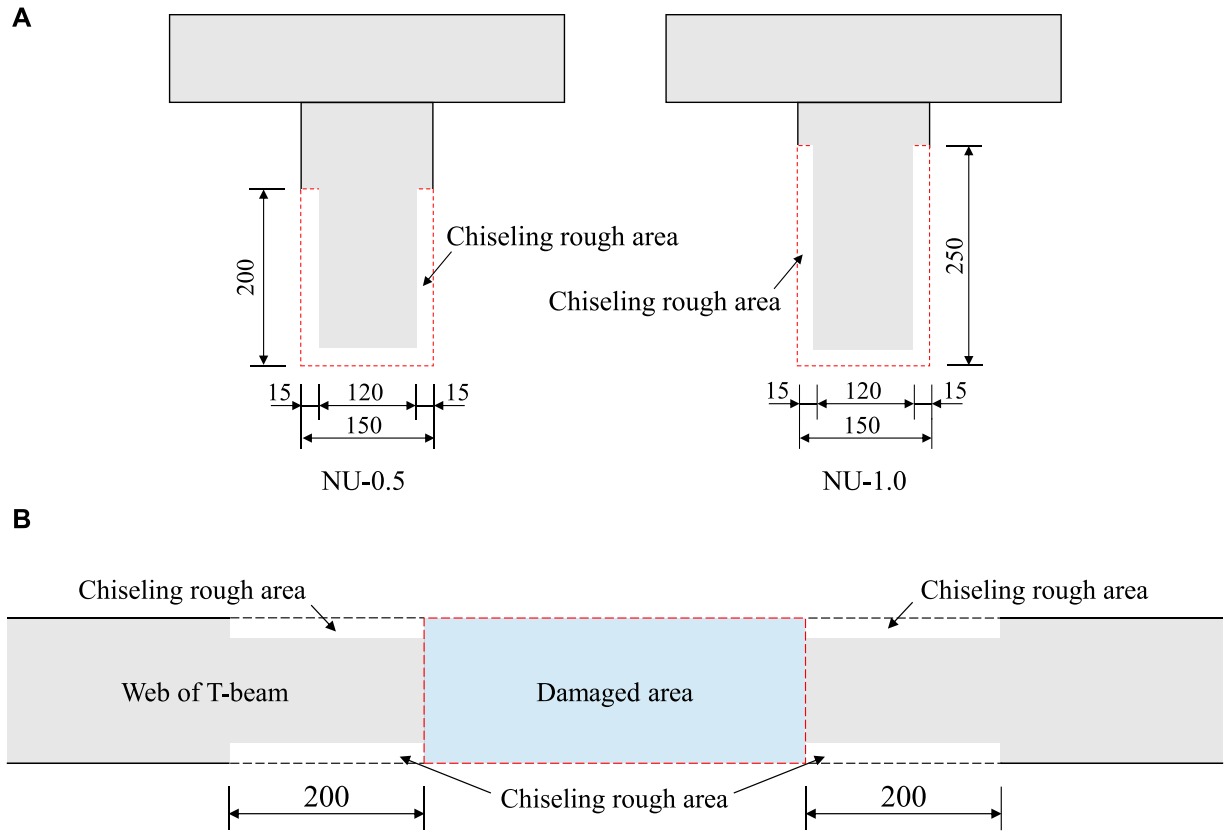

FIGURE 3
Chiseling rough scheme for reinforcing area (unit: mm). **(A)** Cross section of chiseling rough area **(B)** Layout of the web plate in the reinforcement area.

TABLE 2 Material properties of rebar.

Rebar (mm)	E (GPa)	f_y (MPa)	f_u (MPa)	εy (%)	εu (%)
φ-8	200	456.5	699.2	0.23	8.32
φ-14	200	436.6	605.7	0.22	8.65

TABLE 3 Material Properties of UHPC.

Item	E_c (GPa)	f_t (MPa)	ε_t (%)	ε_{tu} (%)	f_{cy} (MPa)	f_{cu} (MPa)
UHPC	42.2	11.0	0.026	0.25	126.1	133.7

A comparative analysis of the crack distributions of the specimens after failure revealed that the specimen NC exhibited extensive crack development. When it reached its flexural capacity, four wide primary cracks appeared in the section outside the two loading points of the specimen. Furthermore, some cracks extended upwards to the top flange, with the majority of these cracks being primarily distributed between the two loading points. In contrast, the specimens NU-0.5 and NU-1.0 exhibited only one wide primary crack when reaching their flexural capacities. These cracks occurred within the tangential shear interface between the UHPC filling and the existing concrete. Notably, the UHPC-reinforced region did not show significant wide cracks. Specifically, specimen NU-0.5 had fewer cracks in the reinforced region, while the NU-1.0 specimen showed well-developed cracks with larger widths in that area. The observed variation in crack width was related to the length of the damaged zone.

During the loading process, the development of crack width under various levels of applied load was measured using a crack observation instrument. The crack width development curves of the specimens were shown in Figure 7. According to the design

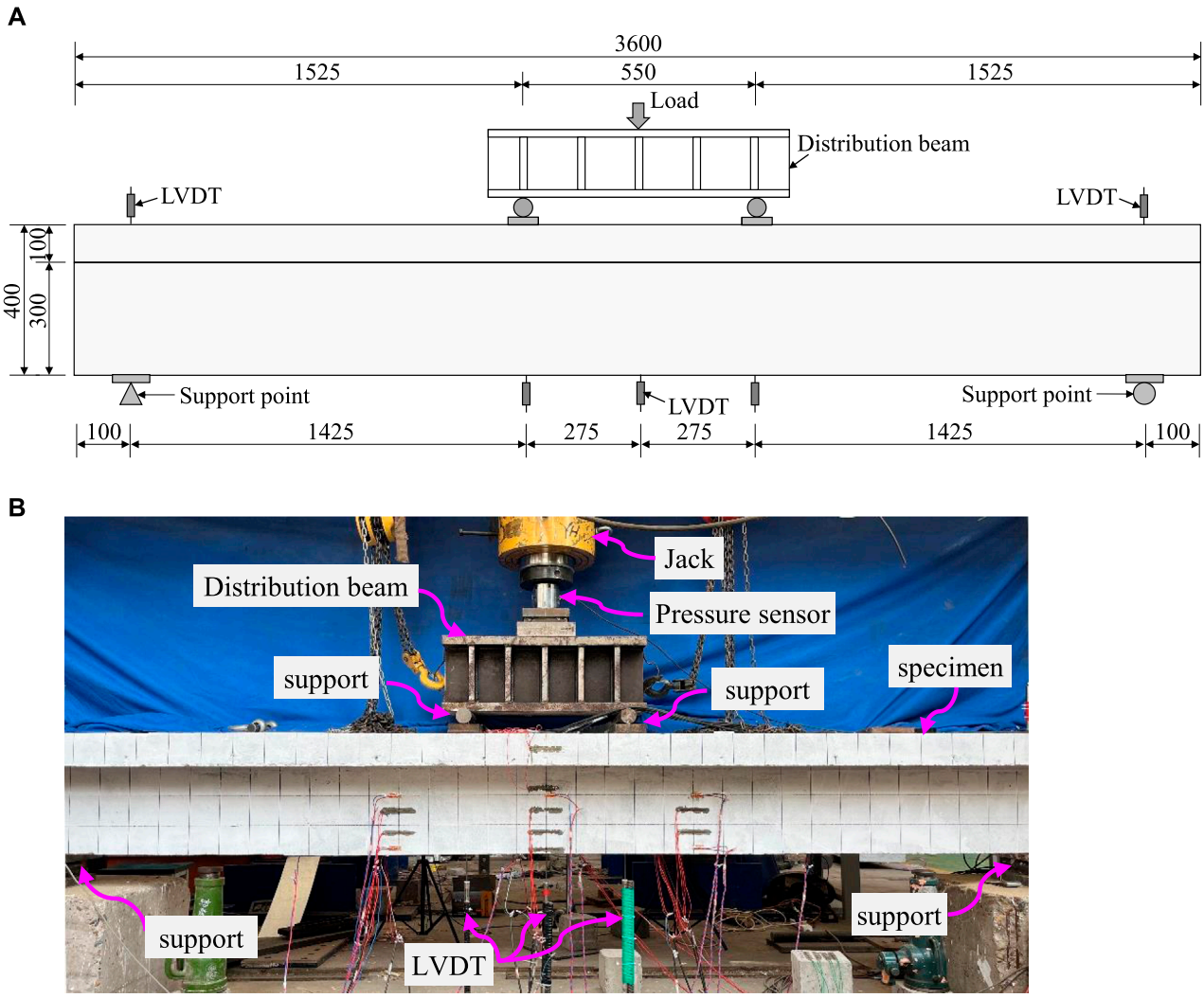

FIGURE 4
Loading scheme of T-beam specimen (unit: mm). **(A)** Arrangement of loading and displacement points **(B)** Experimental loading photographs.

code GB 50010-2010 (Code for Design of Concrete Structures, 2010), the maximum allowable crack width for reinforced concrete structures under various quasi-permanent load combinations in the serviceability limit state is 0.3 mm. From Figure 7, it can be observed that specimen NU-1.0, which had a longer UHPC filling region to bear the bending load, fully utilized the excellent tensile properties of the UHPC in the filling region. As a result, the load at which the crack width reached the 0.3 mm limit was higher for specimen NU-1.0 compared to specimen NC. Conversely, for specimen NU-0.5, the length of the UHPC filling region was smaller than the distance between the two loading points. Consequently, at lower load levels, the corresponding crack width of NU-0.5 exceeded that of specimen NC. However, at higher load levels or when the crack width reached the 0.3 mm limit, the applied load for specimens NU-0.5 and NC were similar. Therefore, for T-beams reinforced with UHPC filling, the chiseling method adopted in this study ensured that the interface strength between the UHPC and the existing concrete reached or even exceeded the strength of the concrete, thereby ensuring reliable force transfer at the interface.

3.2 Load-displacement curves

Figure 8 shows the load-displacement curves of the specimens. The flexural failure process of the specimens reinforced with UHPC filling was similar to that of the reference specimen NC. Both can be divided into three stages: elastic stage, cracking stage, and yielding failure stage, which was typical characteristics of flexural failure in reinforced concrete beams.

Table 4 summarizes bending test results of T beam specimens, including the loads and mid-span vertical displacements. The symbols used in the table are defined as follows: F_c denotes the cracking load, F_u denotes the ultimate load, and Δ_u denotes the mid-span vertical displacement corresponding to the ultimate load. ΔF_c

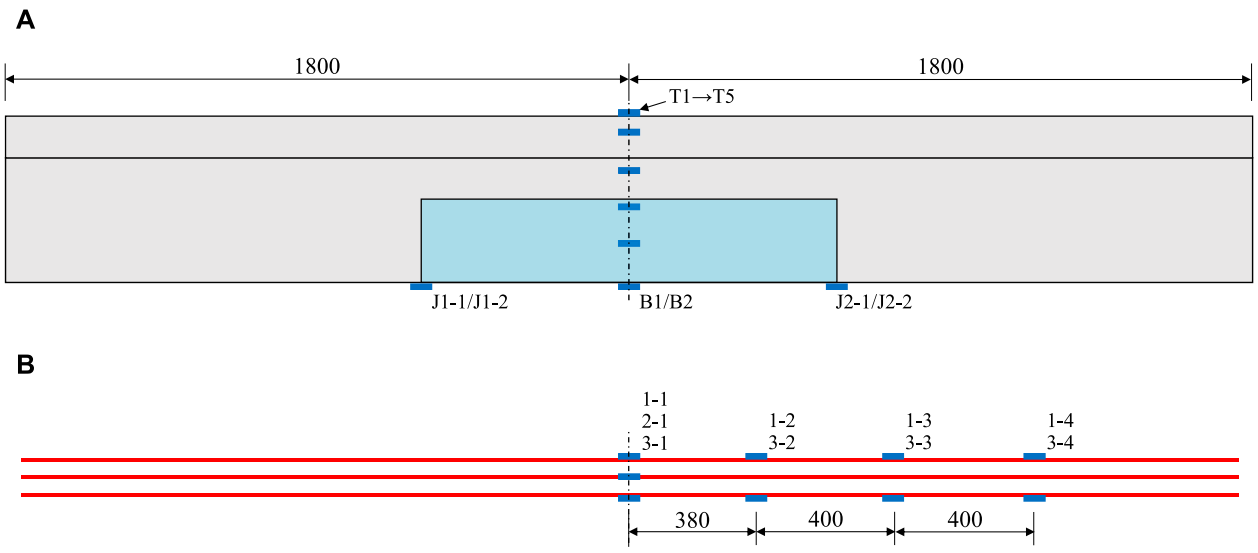

FIGURE 5
Arrangement of strain gauges of T-beam specimen (unit: mm). **(A)** Measurement points on the surface **(B)** Measurement points for rebars.

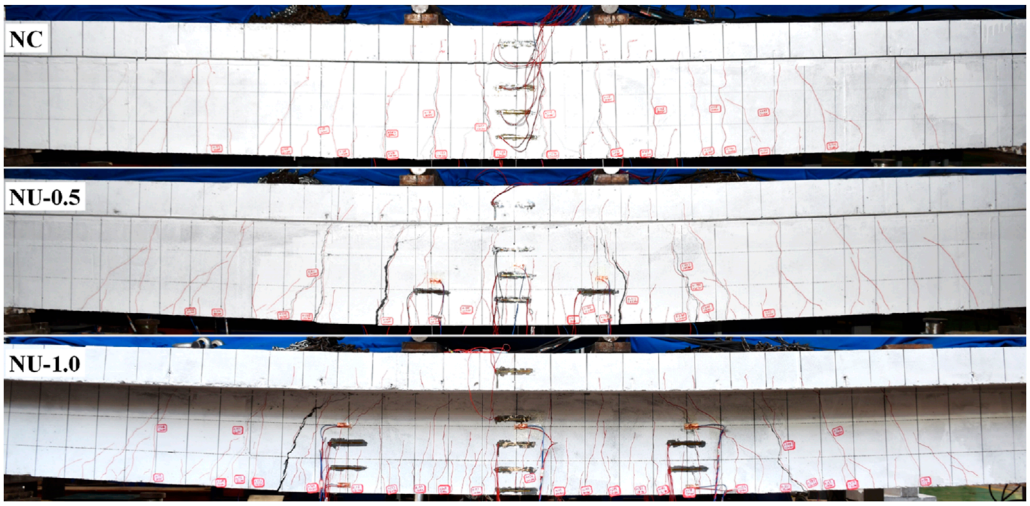

FIGURE 6
Failure modes of T-beam specimens.

and ΔF_u represent the increases in cracking load and ultimate load, respectively, for the reinforced specimens compared to the reference specimens. As shown in Table 4, the cracking loads of specimens NU-0.5 and NU-1.0 increased by 19.52% and 39.84%, respectively, compared to specimen NC. The ultimate loads of specimens NU-0.5 and NU-1.0 increased by 5.73% and 34.11%, respectively. The cracking load and ultimate load of specimen NU-1.0 were higher than those of specimen NU-0.5, with increases of 17.00% and 26.85%, respectively. The flexural stiffness of specimen NU-1.0 was significantly higher than that of specimen NC, while the flexural stiffness of specimen NU-0.5 was only slightly higher than that of specimen NC. This indicated that increasing the UHPC filling area enhanced the flexural capacity and stiffness of the T-beam specimens. In summary, increasing the filling area can significantly improve the flexural stiffness and capacity of damaged T-beams, while also enhancing the ductility of the damaged beams to some extent.

3.3 Load-strain relationship

Figure 9 shows the variation in midspan section strains along the height direction of reinforced specimens under different loading stages, where F_u represents the ultimate load of the reinforced

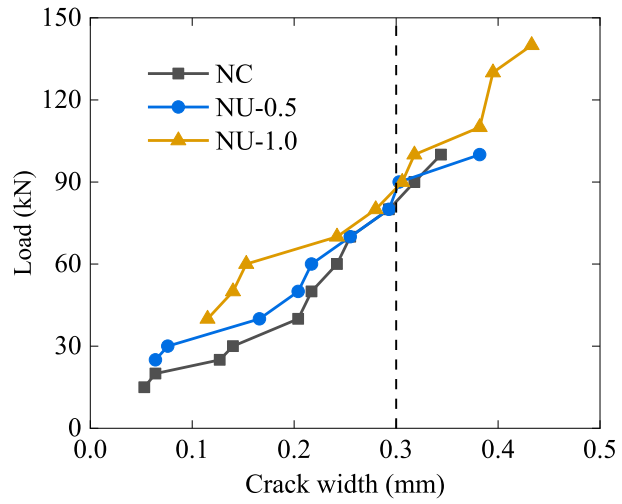

FIGURE 7
Crack width development law of T-beam specimens.

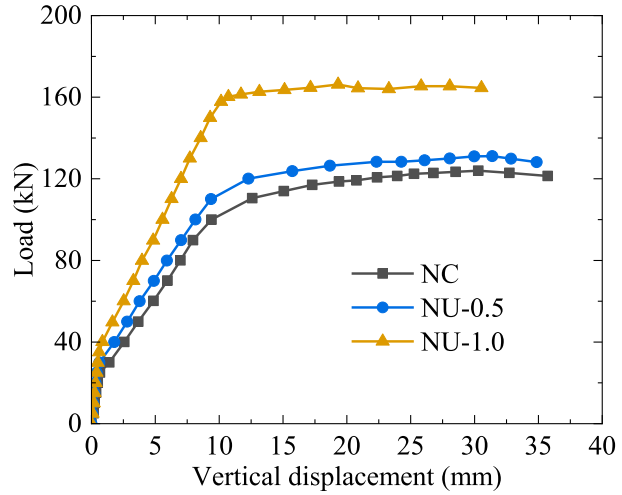

FIGURE 8
Load-displacement curves of specimens.

specimens. During the loading process, the strain distribution along the height of the midspan section of the specimen approximately exhibited a linear pattern, indicating that the composite section formed by the filling of UHPC in the damaged region still adhered the assumption of the planar section composed of two different materials.

Figure 10 presents the load-strain curves of the top flange at midspan section of the specimens. It can be observed that the compressive strain values of the concrete in the width direction of the top flange of the specimens were similar. This indicated that the shear-lag effect of the T-beam section was minimal, and thus, the top flange of the specimens can effectively participate in the overall bending resistance of the beam. A comparison of the specific strain values revealed that, except for reference specimen NC, the compressive strain values of the top flange at midspan section of the other two reinforced specimens did not exceed 1,000 με. This aligned with the pattern of no principal crack in the UHPC filling region of the reinforced specimens.

Figure 11 illustrates the load-strain curves at the bottom surface of UHPC for the reinforced specimens. It was found that both specimens NU-0.5 and NU-1.0 exhibited higher strain values at the interface between UHPC and the existing concrete, in the tensile direction. In contrast, the strain values at the mid-span section of the bottom surface were relatively smaller. This indicated that the primary cracks and the yielding of the tension steel reinforcement of the specimens both occurred near the interface between UHPC and the existing concrete. Compared to specimen NU-0.5, specimen NU-1.0 exhibited higher surface strain on the UHPC at the midspan section of the bottom of the beam. This indicated that a longer UHPC filling region contributed to the full utilization of the tensile performance of the UHPC. Conversely, a shorter UHPC reinforcement region hindered the utilization of tensile performance of the UHPC.

4 Numerical simulations

4.1 FE model

4.1.1 Element and boundary conditions

A FE model was developed using ABAQUS, as depicted in Figure 12. The model adopted C3D8R elements to simulate the T-beam, including normal concrete, loading and support blocks, and UHPC filling in the damaged region. The rebar skeleton was modelled using T3D2 elements. The loading and support blocks were tied to the T-beam, while rebar skeleton was embedded within the surrounding concrete or UHPC. To simulate the potential interface debonding between the UHPC filling and the existing concrete in the damaged region, a surface-to-surface contact approach was employed, and the contact constraint effectively captured the debonding phenomenon. The FE was established with simply supported boundary conditions, mirroring the experimental setup. During the analysis, vertical displacement loads were applied to the reference points located above the mid-span section of the specimen.

4.1.2 Constitutive models of materials

The concrete constitutive model was defined using the Concrete Damage Plasticity (CDP) model within ABAQUS, with stress, strain, and damage parameters of concrete referenced from GB50010-2010 (GB 50010, 2010). There are various models, such as the elastoplastic model, bilinear model (Men et al., 2022; Men et al., 2023a), and trilinear model (Men et al., 2023b), used to simulate the stress-strain behaviour of steel. In this study, the rebars and steel blocks were modelled using an ideal elastoplastic constitutive model. The constitutive models for concrete and steel are illustrated in Figure 13.

After experiencing tensile cracking, UHPC does not immediately lose its load-bearing capacity. Its uniaxial tensile stress-strain curve exhibits a strain-hardening stage after reaching the peak tensile strength. In this study, the constitutive model for UHPC was

TABLE 4 Bending test results of T beam specimens.

Specimens	F_c (kN)	F_u (kN)	ΔF_c (%)	ΔF_u (%)	Δ_u (mm)	Failure modes
NC	25.1	124.0	/	/	35.7	Bending failure
NU-0.5	30.0	131.1	19.52	5.73	34.9	Bending failure
NU-1.0	35.1	166.3	39.84	34.11	30.6	Bending failure

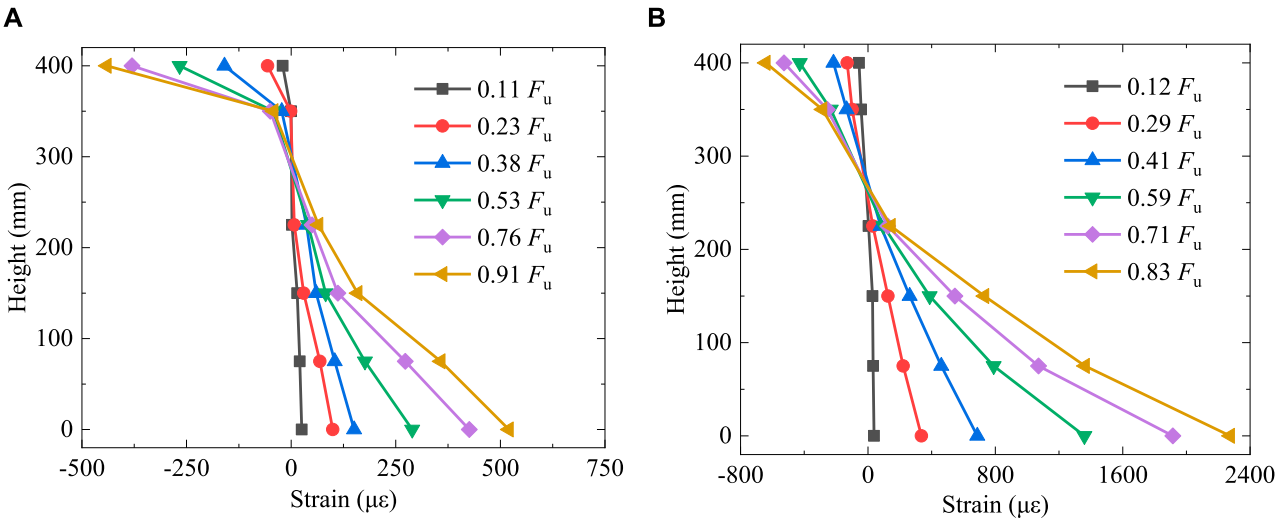

FIGURE 9
Strain distribution along the height of T-beam specimens at the midspan section. **(A)** NU-0.5 **(B)** NU-1.0.

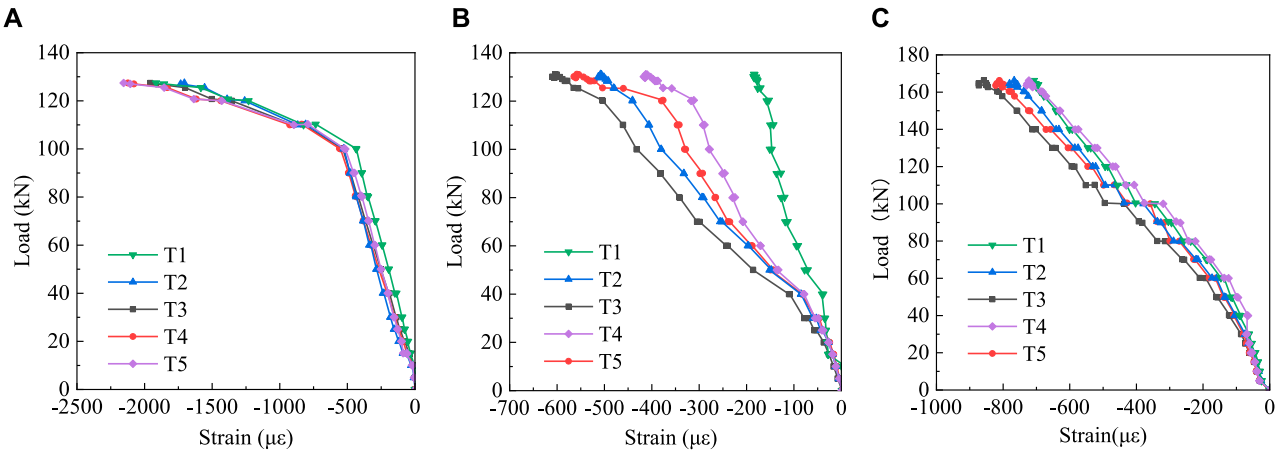

FIGURE 10
Load-strain curves of top flange of T-beam specimens. **(A)** NC **(B)** NU-0.5 **(C)** NU-1.0.

defined using the CDP model in ABAQUS. The compressive and tensile constitutive models for UHPC, as shown in Figure 14, were defined based on the references (Hussein et al., 2017; Sargand et al., 2017). The specific constitutive equations were determined by Eqs 1, 2, with all material parameters obtained from the material properties tests.

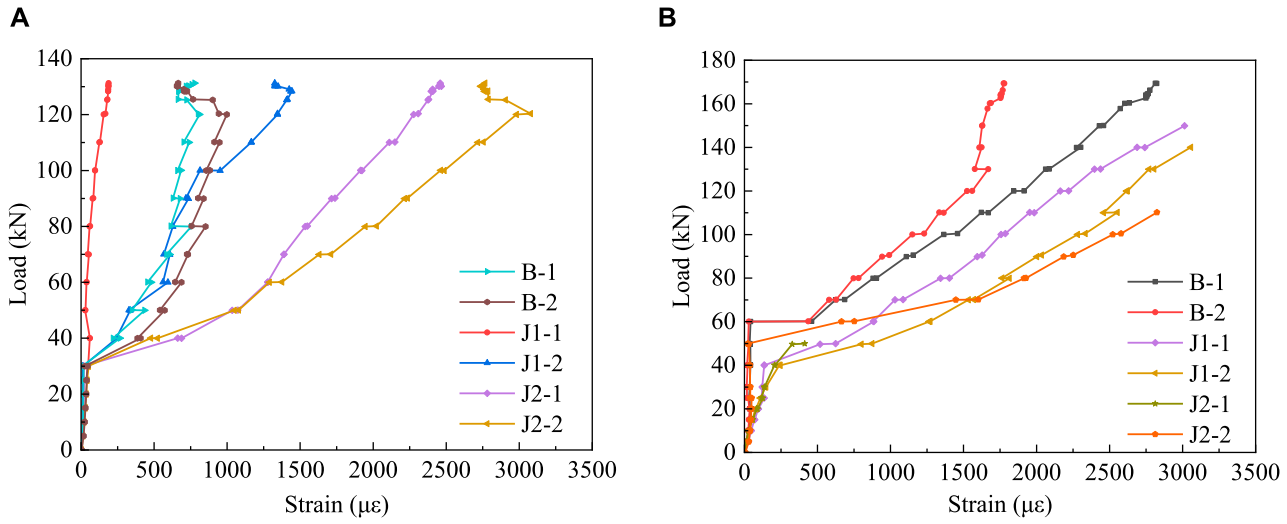

FIGURE 11
Load-strain curves of UHPC surface of T-beam specimens. **(A)** NU-0.5 **(B)** NU-1.0.

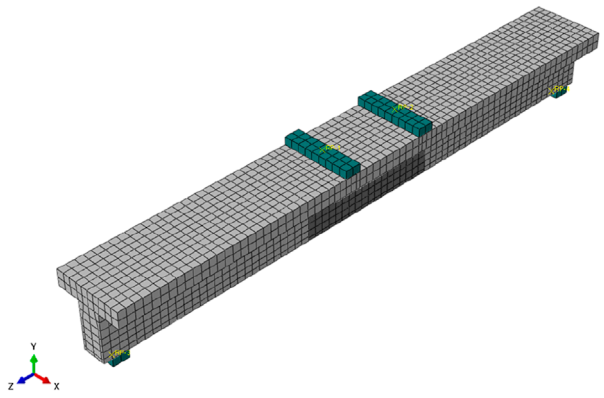

FIGURE 12
Finite element model.

$$y = \begin{cases} \sigma_c \dfrac{Ax - x^2}{1 + (A-2)x} & (0 \le x \le 1) \\ \sigma_c \dfrac{x}{2(x-1)^2 + x} & (x \ge 1) \end{cases} \quad (1)$$

$$\sigma_t = \begin{cases} \dfrac{f_{ct}}{\varepsilon_{ca}} \varepsilon_t & 0 < \varepsilon_t \le \varepsilon_{ca} \\ f_{ct} & \varepsilon_{ca} < \varepsilon_t < \varepsilon_{cp} \end{cases} \quad (2)$$

where, x represents the ratio of compressive strain to peak compressive strain of UHPC; σ_c denotes the peak compressive strength of UHPC; y represents the compressive stress of UHPC; A denotes the ratio of the tangent modulus at the origin to the secant modulus at the peak point of the compressive constitutive curve, with a value of 1.05 in this paper; σ_t and ε_t are the tensile stress and strain of UHPC, respectively; f_{ct} denotes the peak tensile strength of UHPC; ε_{ca} is the initial cracking strain of UHPC; and ε_{cp} is the ultimate strain of UHPC.

4.1.3 Properties of UHPC-NC interface

When simulating the loading conditions of reinforced specimens, it is important to consider the interface behaviour between new and existing materials. In this study, a surface-based cohesive behaviour model in ABAQUS was employed to simulate the bonding behaviour between UHPC and the existing beam. The surface-to-surface contact was used to constrain the UHPC-NC interface, incorporating the corresponding cohesive behavior and damage criterion. Based on the references (Hussein et al., 2017; Sargand et al., 2017), the maximum contact stress before damage at the interface was determined through calculations, resulting in a maximum value of 4.00 MPa, with a corresponding relative displacement of 0.068 mm.

4.2 Analysis of flexural process of specimens

Figure 15 presents a comparison load-displacement curves between the finite element analysis (FEA) and experiments. It can be observed that the simulated load-displacement curves of the three specimens generally follow the same trend as the experimental results. The simulated flexural stiffness after cracking but before yielding was slightly higher that the measured flexural stiffness, which can be attributed to the simplifications of the UHPC constitutive model in the FE model. It should be noted that the focus of this section was primarily on the ultimate load of the specimens. As indicated in Table 5, the deviations between the simulated and experimental values for the ultimate loads of specimens NC, NU-0.5, and NU-1.0 were −4.52%, 1.75%, and −1.38%, respectively. This demonstrated that the FEA method employed in this study effectively predicted the ultimate load of the tested beams.

Furthermore, the FE model was capable of simulating the crack development of the test beams. Taking the NU-0.5 specimen as an example, Figure 16 compares the crack propagation and failure modes between the FEA and experiment. It can be observed that

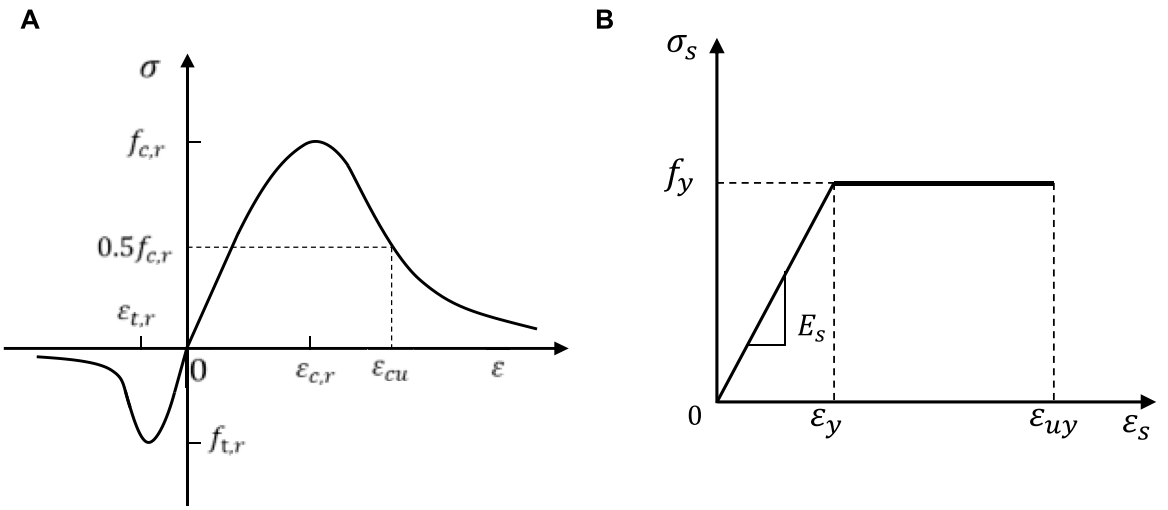

FIGURE 13
Constitutive models for concrete and steel. **(A)** Concrete **(B)** Steel.

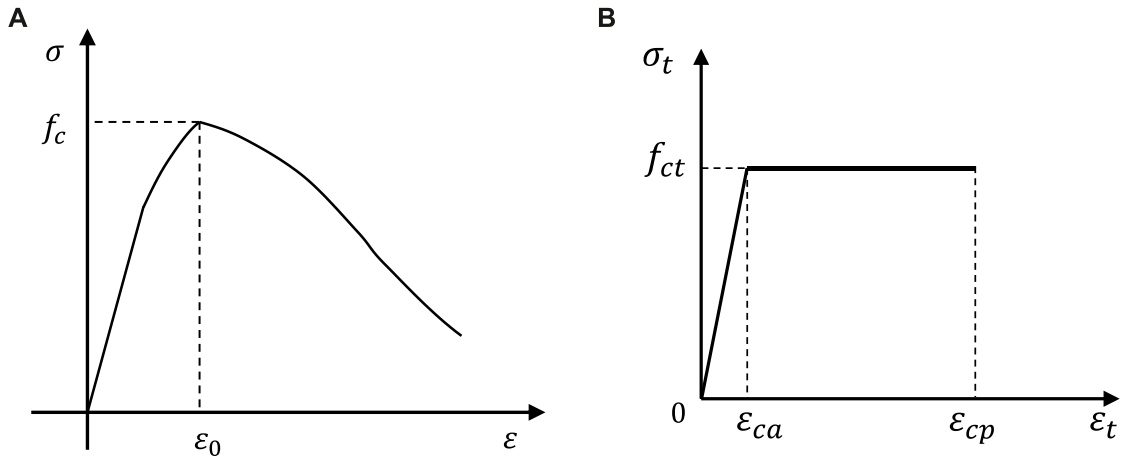

FIGURE 14
Constitutive model of UHPC. **(A)** Compressive stress-strain curve **(B)** Tensile stress-strain curve.

during the loading process of specimen NU-0.5, there was no occurrence of debonding at the interface between the UHPC and the existing concrete. By considering both the load-displacement curve and the simulated failure process, it can be concluded that the FEA employed in this study accurately simulated the flexural performance of the reinforced concrete T-beams strengthened with UHPC filling.

To further understand the failure modes of the specimens, Figure 17 provides the distribution of rebar stresses when specimens NC, NU-0.5, and NU-1.0 reached their flexural ultimate loads. It can be observed that all three specimens experienced flexural failure due to yielding of the tension rebars. Due to the higher tensile strength and elastic modulus of UHPC compared to normal concrete, the yielding zones of the tensile rebars varied among the three specimens. As only normal concrete was used for specimen NC, the crack distribution was uniform, and the yielding zones of the tension rebars occurred between the loading points and in localized areas outside the loading points. In contrast, for specimens NU-0.5 and NU-1.0, as UHPC-filled region exhibited higher stiffness and strength than the existing concrete, the yielding zones of the tension rebars were closer to the interface between UHPC and the existing concrete. The stress level of the tension rebars in the UHPC filling region was relatively low. Further comparison of the distribution of stirrup stress revealed that since the flexural cracks in the NC specimen fully developed across the entire span, the stresses of the stirrups were minimal. However, for specimens NU-0.5 and NU-1.0, the limited cracking in the UHPC-filled region caused higher stresses on the stirrups in the shear

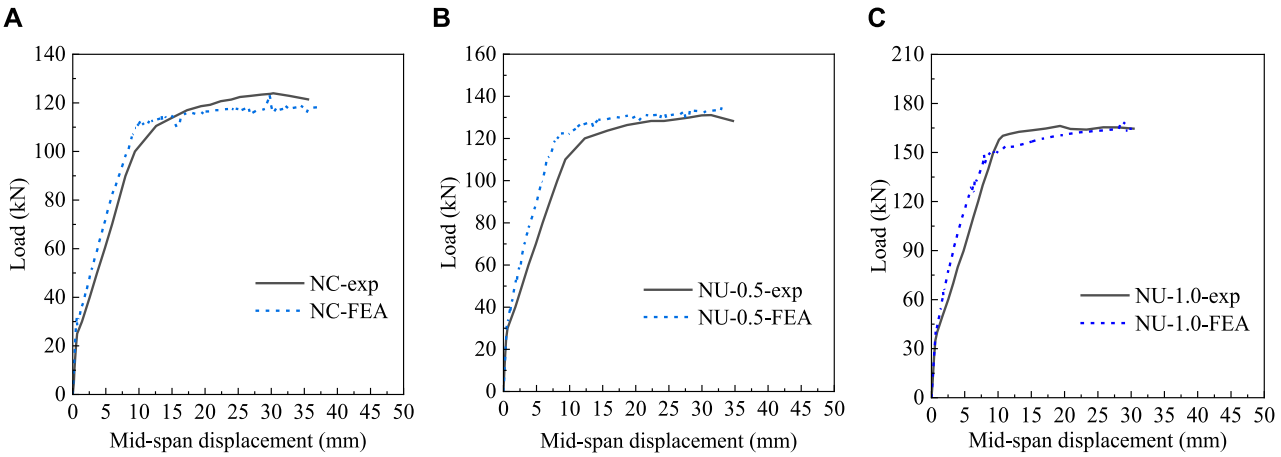

FIGURE 15
Comparison of load-displacement curves between FEA and experiment. **(A)** NC **(B)** NU-0.5 **(C)** NU-1.0.

TABLE 5 Comparison of ultimate loads between FEA and experiment.

Specimen	$F_{u,exp}$ (kN)	$F_{u,FEA}$ (kN)	$(F_{u,FEA}-F_{u,exp})/F_{u,exp}$ (%)	Failure mode
NC	124.0	118.4	−4.52	Bending failure
NU-0.5	131.1	133.4	1.75	Bending failure
NU-1.0	166.3	164.0	−1.38	Bending failure

span. This indicates that when filling damaged concrete beams with UHPC to reinforce them, it is necessary to assess the risk of shear failure in the reinforced beam.

5 Analysis of the failure mechanism of reinforced specimens

Figure 18 illustrates the relative positions of the main cracks, UHPC-filled area, and chiseling rough area in specimens NU-0.5 and NU-1.0. The purple dashed box represents the UHPC-filled area, and the positions of the two short sides of the purple box correspond to the interface between the UHPC and the existing concrete. The region between the red dashed box and the purple dashed box represents the chiseling rough area of the existing beam.

From Figure 18A, it can be observed that the length of the UHPC-filled area of specimen NU-0.5 was smaller than the distance between the two loading points. The interface between the UHPC and the existing concrete was always located in the region of maximum bending moment. To address this, the interface treatment scheme shown in Figure 19 was adopted, which converted a portion of the normal tension reinforcing interface into the tangential shear reinforcing interface. With an increase in the load, the shear interface between the UHPC and the existing concrete in specimen NU-0.5 did not experience shear failure. However, defects in the tension interface were continuously exposed, and the thin U-shaped UHPC layer in the chiseling rough area gradually fractured. Ultimately, the tension interface between the UHPC and the existing concrete separated, and the main rebars near the tension interface yielded. The failure zone of specimen NU-0.5 was limited to the vicinity of the tension interface between the two loading points. This also explained why the ultimate load of the specimen NU-0.5 was not significantly different from that of the reference specimen NC. The UHPC in the reinforced area continued to work together with the rebars even after cracking, resulting in a stiffness greater than the post-cracking stiffness of the tension interface cross-section. The overall bending deformation of the specimen was equivalent to the bending of the low-stiffness beam segment on the outer side of the tension interface, driving the bending of the high-stiffness beam segment on the inner side of the tension interface. The deformation of the high-stiffness beam segment on the inner sider was relatively small. Based on the assumption of the plane section, it can be inferred that the compressive strain level of the top flange at the mid-span section of the specimen was not high, which was consistent with the strain levels measured in the experiment.

As indicated in Figure 18B, the length of the UHPC-filled area of specimen NU-1.0 exceeded the distance between the two loading points. The tension interface between the UHPC and the existing concrete of the NU-1.0 specimen was located in a region with a relatively low bending moment. This allowed the tension interface between the UHPC and the existing concrete to bear higher loads without premature separation. Due to the significantly higher tensile strength of UHPC compared to normal concrete, the failure of specimen NU-1.0 also occurred at the tension interface between

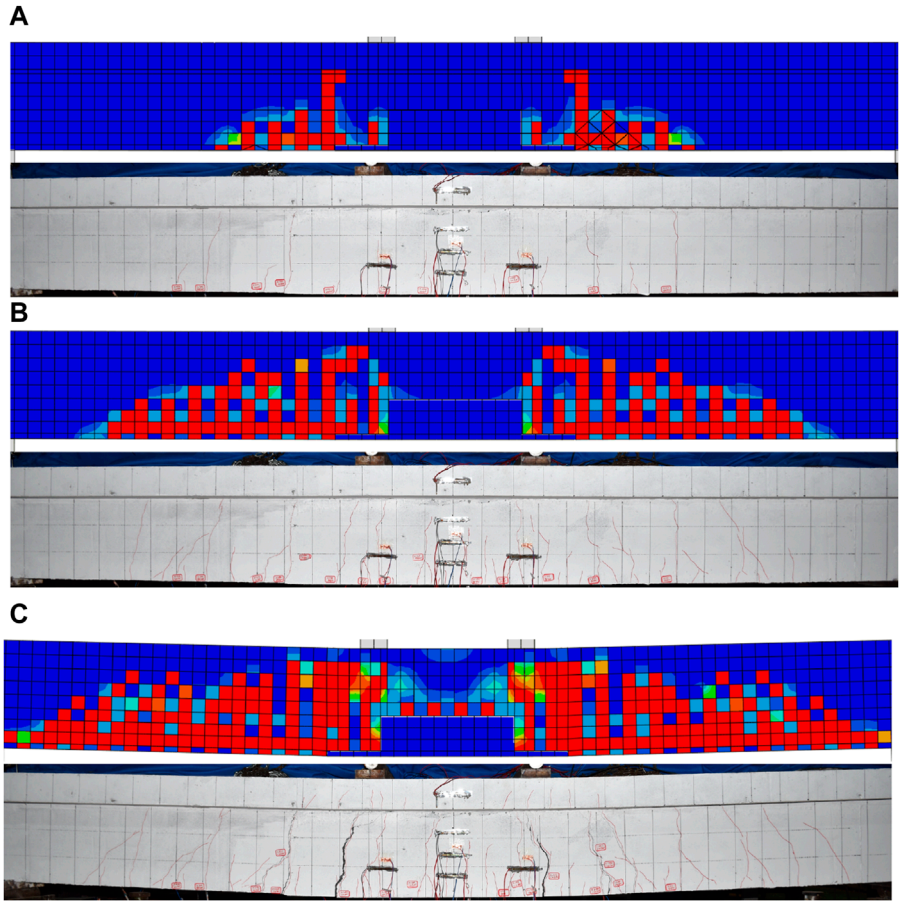

FIGURE 16
Comparison of failure modes between FEA and experiment for specimen NU-0.5. **(A)** 0.3 *Pn* **(B)** 0.7 *Pn* **(C)** *Pn*.

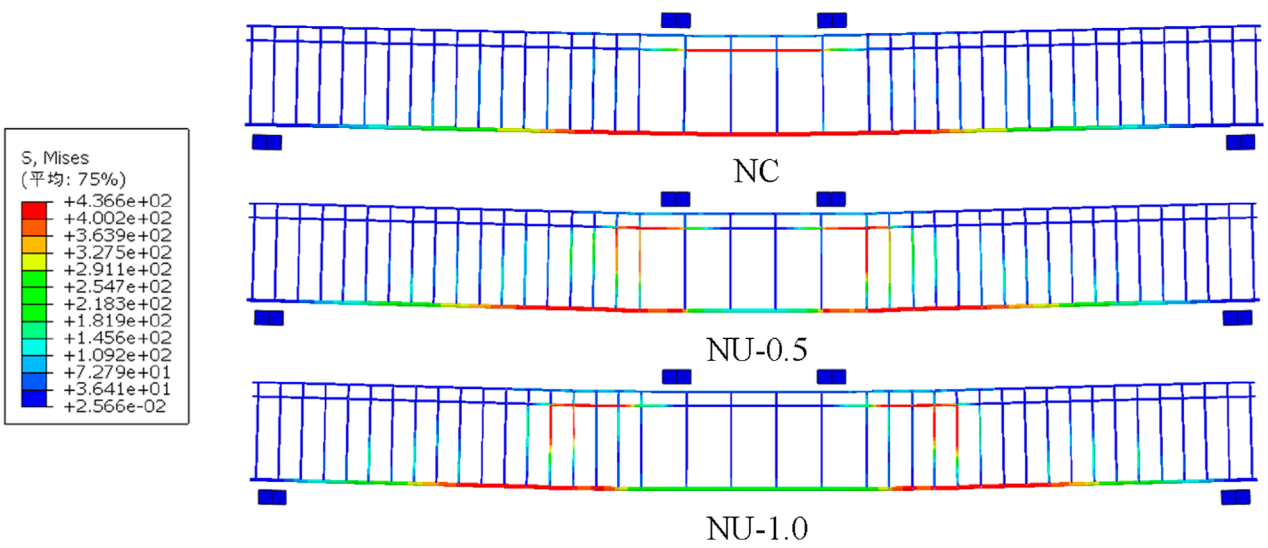

FIGURE 17
Von Mises stresses distribution of rebars of T-beam specimens.

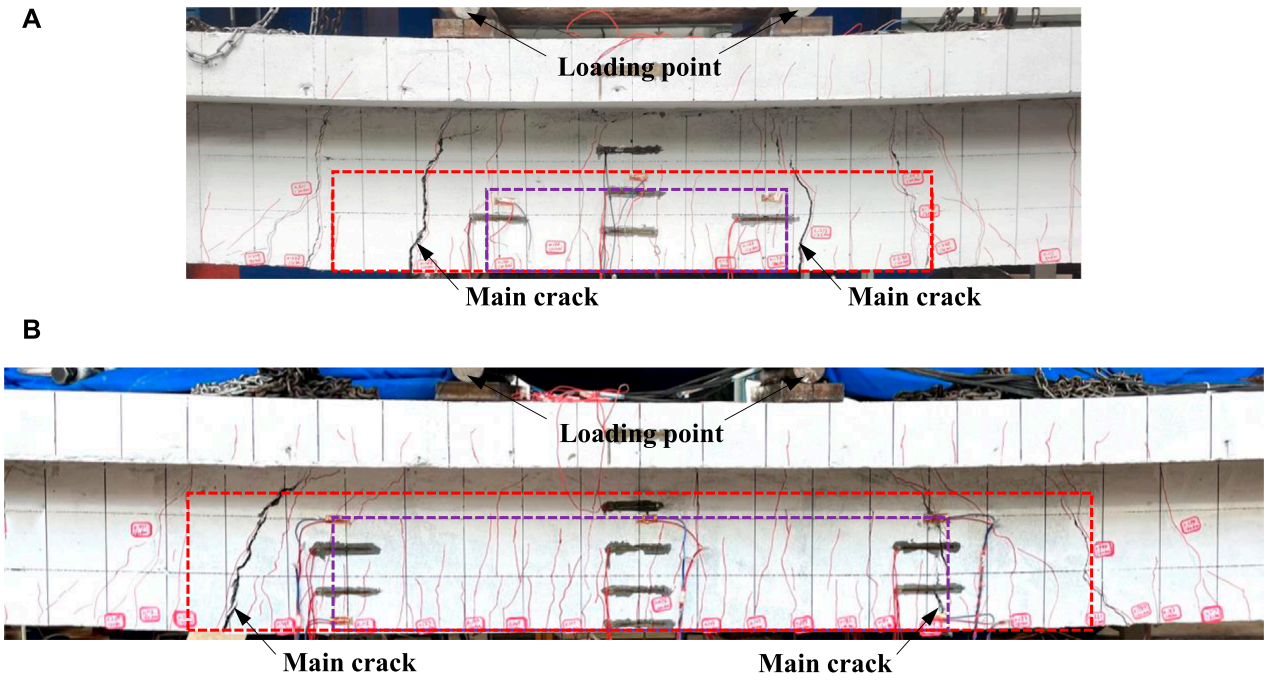

FIGURE 18
Local cracking behaviour of UHPC-reinforced specimens. **(A)** NU-0.5 **(B)** NU-1.0.

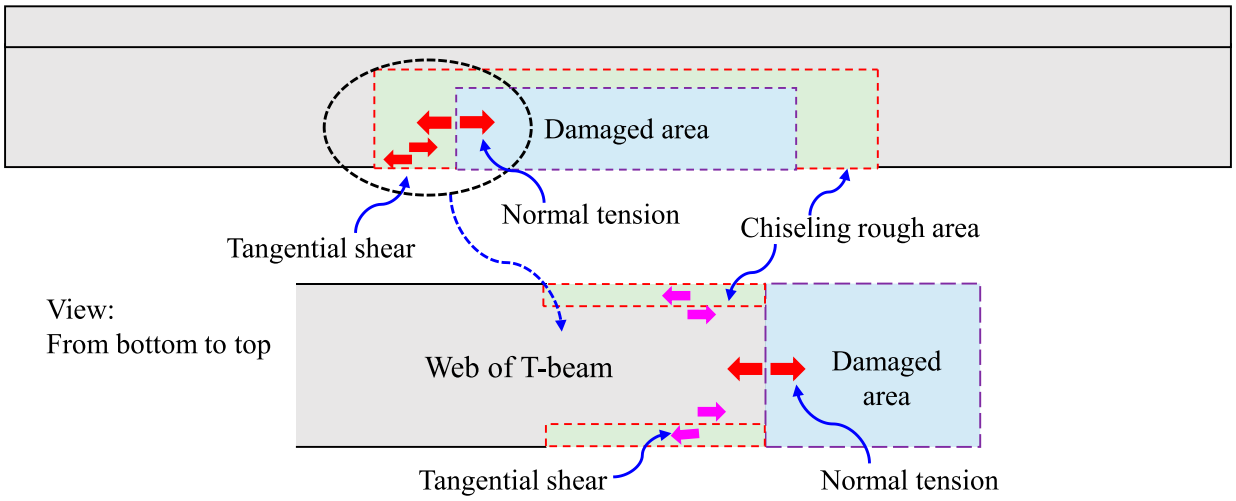

FIGURE 19
Stress mechanism of reinforced region interface.

the UHPC and the existing concrete. The failure process resembled that of the NU-0.5 specimen, where the U-shaped UHPC layer in the chiseling rough area experienced tension-induced fracture, leading to the separation of the tension interface and yielding of the main rebars near the interface. The extended reinforced area of specimen NU-1.0 enabled the UHPC-filled region to bear a larger bending moment. Compared to specimen NU-0.5, specimen NU-1.0 exhibited a higher number of cracks within the reinforced area, with more extensive vertical propagation of these cracks. As the flexural stiffness of the reinforced area was higher than that of the unreinforced area, the local bending deformation in the reinforced area was not significant. Consequently, the compressive strain in the concrete on the top flange of the mid-span section of the specimen remained relatively small, and the cracks in the top flange primarily distributed in the unreinforced region outside the two loading points region.

6 Conclusion

This study investigates the flexural performance of damaged reinforced concrete T-beams reinforced with UHPC filling through experiments and nonlinear FEA. The following key conclusions are drawn:

(1) The method of filling UHPC in the damaged region of the reinforced concrete T-beams effectively restored or enhanced the flexural stiffness, cracking load, and ultimate load of the damaged beams. Compared to the unreinforced specimen NC, the cracking load of the reinforced specimens NU-0.5 and NU-1.0 increased by 19.52% and 39.84%, and the ultimate load increased by 5.73% and 34.11%, respectively.

(2) By implementing chiseling rough area treatment around the UHPC-reinforced region, a portion of the tension interface between UHPC and the existing concrete was transformed into a shear interface between UHPC and the chiseled area. This approach restricted the tendency of separation at the tension interface, thereby increasing the cracking load. The reinforced specimens exhibited smaller surface crack widths compared to the reference specimen before reaching the yield turning point on the load-displacement curve.

(3) A nonlinear FE model of the T-beam was developed using ABAQUS, considering the tensile hardening behaviour of UHPC and employing a cohesive zone model to simulate the bond behaviour between UHPC and the existing concrete. Through comparison with experimental load-displacement curves, ultimate loads, and failure modes, the FE model was validated to accurately simulate the flexural performance of T-beams reinforced with UHPC filling.

Data availability statement

The original contributions presented in the study are included in the article/Supplementary material, further inquiries can be directed to the corresponding author.

Author contributions

SH: Writing–original draft, Resources, Investigation. YX: Writing–review and editing, Validation, Resources, Investigation. XL: Writing–review and editing, Validation, Investigation. PM: Writing–review and editing, Writing–original draft, Software, Methodology, Investigation, Conceptualization. GW: Writing–review and editing, Validation, Investigation.

Funding

The author(s) declare that no financial support was received for the research, authorship, and/or publication of this article.

Acknowledgments

The authors express their sincere gratitude for the financial support provided by Research project of Shanxi Transportation New Technology Development Co., Ltd. (21-XJSKJ-1), and Science and Technology Research and Development Project of CSCEC Xinjiang Construction and Engineering (group) Co., Ltd. (65000022859700230167).

Conflict of interest

Author SH was employed by Shanxi Transportation New Technology Development Co., Ltd. Author YX was employed by China Communications 2nd Navigational Bureau 2nd Engineering Co., Ltd. Authors XL and GW were employed by CSCEC Xinjiang Construction and Engineering (group) Co., Ltd. Southwest Company.

The handling editor ZZ is currently organizing a Research Topic with the author PM.

The remaining author declares that the research was conducted in the absence of any commercial or financial relationships that could be construed as a potential conflict of interest.

Publisher's note

References

Al-Osta, M. A., Isa, M. N., Baluch, M. H., and Rahman, M. K. (2017). Flexural behavior of reinforced concrete beams strengthened with ultra-high performance fiber reinforced concrete. *Constr. Build. Mater.* 134, 279–296. doi:10.1016/j.conbuildmat.2016.12.094

Di, J., Sun, Y., Yu, K., Liu, L., and Qin, F. (2020). Experimental investigation of shear performance of existing PC hollow slab. *Eng. Struct.* 211, 110451. doi:10.1016/j.engstruct.2020.110451

Ganesh, P., and Murthy, A. R. (2021). Static and fatigue responses of retrofitted RC beams with GGBS based UHPC strips. *Eng. Struct.* 240, 112332. doi:10.1016/j.engstruct.2021.112332

GB 50010 (2010) *Code for design of concrete structures*. China: Ministry of Housing and Urban-Rural Development of the People's Republic of China.

Hussein, H. H., Walsh, K. K., Sargand, S. M., Al Rikabi, F. T., and Steinberg, E. P. (2017). Modeling the shear connection in adjacent box-beam bridges with ultrahigh-performance concrete joints. I: model calibration and validation. *J. Bridge Eng.* 22 (8), 04017043. doi:10.1061/(ASCE)BE.1943-5592.0001070

Leng, J., Yang, J., Zhang, Z., Du, J., Zou, Y., and Zhou, J. (2024). Effect of vehicle-induced vibration on the strength, nano-mechanical properties, and microstructural characteristics of ultra-high-performance concrete during hardening process. *Cem. Concr. Compos.* 148, 105487. doi:10.1016/j.cemconcomp.2024.105487

Liu, D., Yu, J., Qin, F., Zhang, K., and Zhang, Z. (2023). Mechanical performance of high-strength engineering cementitious composites (ECC) with hybriding PE and steel fibers. *Case Stud. Constr. Mat.* 18, e01961. doi:10.1016/j.cscm.2023.e01961

Men, P., Di, J., Qin, F., and Su, Y. (2023a). Experimental investigation of the shear behavior of slender continuous steel–concrete composite girders in hogging moment. *J. Struct. Eng-ASCE* 149 (1), 04022218. doi:10.1061/JSENDH.STENG-11537

Men, P., Liang, B., He, W., Di, J., Qin, F., and Zhang, Z. (2023b). Vertical shear resistance of noncompact steel–concrete composite girders under combined positive moment and shear. *Case Stud. Constr. Mat.* 18, e01835. doi:10.1016/j.cscm.2023.e01835

Men, P., Wang, X. M., Liu, D., Zhang, Z., Zhang, Q., and Lu, Y. (2024). On use of polyvinylpyrrolidone to modify polyethylene fibers for improving tensile properties of high strength ECC. *Constr. Build. Mater.* 417, 135354. doi:10.1016/j.conbuildmat.2024.135354

Men, P., Zhou, X., Ye, J., Di, J., and Qin, F. (2022). Shear capacity investigation of steel-concrete composite girders in hogging moment regions. *J. Constr. Steel Res.* 194, 107341. doi:10.1016/j.jcsr.2022.107341

Ngidi, S. D., and Dundu, M. (2018). Composite action of pre-cracked reinforced concrete beams repaired with adhesive bonded steel plates. *Structures* 14, 400–408. doi:10.1016/j.istruc.2018.04.005

Paschalis, S. A., Lampropoulos, A. P., and Tsioulou, O. (2018). Experimental and numerical study of the performance of ultra high performance fiber reinforced concrete for the flexural strengthening of full scale reinforced concrete members. *Constr. Build. Mater.* 186, 351–366. doi:10.1016/j.conbuildmat.2018.07.123

Qin, F., Zhang, Z., Yin, Z., Di, J., Xu, L., and Xu, X. (2020). Use of high strength, high ductility engineered cementitious composites (ECC) to enhance the flexural performance of reinforced concrete beams. *J. Build. Eng.* 32, 101746. doi:10.1016/j.jobe.2020.101746

Safdar, M., Matsumoto, T., and Kakuma, K. (2016). Flexural behavior of reinforced concrete beams repaired with ultra-high performance fiber reinforced concrete (UHPFRC). *Compos. Struct.* 157, 448–460. doi:10.1016/j.compstruct.2016.09.010

Sargand, S. M., Walsh, K. K., Hussein, H. H., Al Rikabi, F. T., and Steinberg, E. P. (2017). Modeling the shear connection in adjacent box-beam bridges with ultrahigh-performance concrete joints. II: load transfer mechanism. *J. Bridge Eng.* 22 (8), 04017044. doi:10.1061/(ASCE)BE.1943-5592.0001071

T/CBMF 37 (2018) *Fundamental characteristics and test methods of ultra-high performance concrete*. China: China Building Materials Federation.

Xu, L., Lu, X., Guan, H., and Zhang, Y. (2013). Finite-element and simplified models for collision simulation between overheight trucks and bridge superstructures. *J. Bridge Eng.* 18 (11), 1140–1151. doi:10.1061/(ASCE)BE.1943-5592.0000472

Xu, L. J., Lu, X. Z., Smith, S. T., and He, S. T. (2012). Scaled model test for collision between over-height truck and bridge superstructure. *Int. J. Impact Eng.* 49, 31–42. doi:10.1016/j.ijimpeng.2012.05.003

Yin, H., Teo, W., and Shirai, K. (2017). Experimental investigation on the behaviour of reinforced concrete slabs strengthened with ultra-high performance concrete. *Constr. Build. Mater.* 155, 463–474. doi:10.1016/j.conbuildmat.2017.08.077

Zhang, Y., Huang, S., Liu, Y., Fan, W., and Shao, X. (2023). Flexural behavior of damaged RC beams strengthened with prestressed UHPC layer. *Eng. Struct.* 283, 115806. doi:10.1016/j.engstruct.2023.115806

Zhang, Y., Li, X., Zhu, Y., and Shao, X. (2020c). Experimental study on flexural behavior of damaged reinforced concrete (RC) beam strengthened by toughness-improved ultra-high performance concrete (UHPC) layer. *Compos. Part B-Eng.* 186, 107834. doi:10.1016/j.compositesb.2020.107834

Zhang, Y., Zhang, C., Zhu, Y., Cao, J., and Shao, X. (2020a). An experimental study: various influence factors affecting interfacial shear performance of UHPC-NSC. *Constr. Build. Mater.* 236, 117480. doi:10.1016/j.conbuildmat.2019.117480

Zhang, Y., Zhu, P., Wang, X., and Wu, J. (2020b). Shear properties of the interface between ultra-high performance concrete and normal strength concrete. *Constr. Build. Mater.* 248, 118455. doi:10.1016/j.conbuildmat.2020.118455

Zhang, Z., Li, Z., He, J., and Shi, X. (2023b). High-strength engineered cementitious composites with nanosilica incorporated: mechanical performance and autogenous self-healing behavior. *Cem. Concr. Compos.* 135, 104837. doi:10.1016/j.cemconcomp.2022.104837

Zhang, Z., Liu, J. C., Li, J., Qin, F., and Di, J. (2023a). Micromechanics-based analysis of PVA–ECC after thermal exposure. *Arch. Civ. Mech. Eng.* 23 (3), 213. doi:10.1007/s43452-023-00736-1

Zhu, Y., Zhang, Y., Hussein, H. H., and Chen, G. (2020). Flexural strengthening of reinforced concrete beams or slabs using ultra-high performance concrete (UHPC): a state of the art review. *Eng. Struct.* 205, 110035. doi:10.1016/j.engstruct.2019.110035

Zou, Y., Jiang, J., Yang, J., Zhang, Z., and Guo, J. (2023a). Enhancing the toughness of bonding interface in steel-UHPC composite structure through fiber bridging. *Cem. Concr. Compos.* 137, 104947. doi:10.1016/j.cemconcomp.2023.104947

Zou, Y., Zheng, K., Zhou, Z., Zhang, Z., Guo, J., and Jiang, J. (2023b). Experimental study on flexural behavior of hollow steel-UHPC composite bridge deck. *Eng. Struct.* 274, 115087. doi:10.1016/j.engstruct.2022.115087

frontiers | Frontiers in Materials

TYPE Original Research
PUBLISHED 17 June 2024
DOI 10.3389/fmats.2024.1392372

OPEN ACCESS

EDITED BY
Yang Zou,
Chongqing Jiaotong University, China

REVIEWED BY
Amir Ali Shahmansouri,
Washington State University, United States
V. R. Prasath Kumar,
SRM Institute of Science and Technology, India
L. Krishnaraj,
SRM Institute of Science and Technology, India

*CORRESPONDENCE
Junfei Zhang,
junfeizhang@hebut.edu.cn

RECEIVED 27 February 2024
ACCEPTED 27 May 2024
PUBLISHED 17 June 2024

CITATION
Wang J, Pang S, Ji S, Li X, Wang L and Zhang J (2024), Weathering resistance of novel sustainable prefabricated thermal insulation wall.
Front. Mater. 11:1392372.
doi: 10.3389/fmats.2024.1392372

Weathering resistance of novel sustainable prefabricated thermal insulation wall

Jian Wang[1], Sen Pang[1], Shengjie Ji[1], Xiaoxiao Li[1], Ling Wang[2] and Junfei Zhang[3]*

[1]Beijing Building Research Institute Corporation Ltd. of China State Construction Engineering Corporation, Beijing, China, [2]Huabei Ltd., China Construction First Group Corporation Ltd., Beijing, China, [3]School of Civil and Transportation Engineering, Hebei University of Technology, Tianjin, China

External walls, serving as the primary medium for heat exchange between the building and the external environment, has its thermal loss comprising the largest proportion of building energy consumption. Therefore, enhancing the thermal insulation capacity of the wall is of great significance in reducing building energy consumption. In this paper, a novel sustainable prefabricated expanded polystyrene (EPS) thermal insulation wall panel with irregular column frame structures was developed. And weathering tests combined with finite element simulations were conducted to investigate its weathering performance and degradation patterns. The results revealed that In the weathering test, the panel surfaces did not exhibit apparent water seepage cracks, powdering, hollowing, peeling, etc. There was no occurrence of facing brick detachment or damage. The outer surface concrete of the wall panel experienced resistance during normal thermal expansion and contraction, generating compressive stress during expansion and tensile stress when contracted. In addition, the bond strength of the specimens decreased by 8.1% after the thermal-rain cycles, 5.1% after the thermal-cold cycles, and 12.1% after the freeze-thaw cycles. In the numerical simulations, the temperature stress at various positions on the concrete wall had a noticeable mutual restraining effect on the force deformation of the nearby concrete. There was a significant risk of cracking in the middle and around the opening, particularly in the lower part of the wall panel. This study serves as a basis for the degradation analyses and optimization design of the sandwich insulation wall panels for sustainability.

KEYWORDS

prefabricated concrete, sandwich insulation wall panel, weathering resistance, temperature effects, concrete

1 Introduction

The building sector, among the most energy-consuming sectors, is under scrutiny owing to its environmental issues such as high energy consumption, carbon dioxide (CO_2) emissions, resource depletion, waste disposal, etc (Dickson and Pavía, 2021). In 2017, United Nations Environment and International Energy Agency released a report stating that building energy consumption accounted for more than 35% of the total energy use (Abergel et al., 2017). Therefore, the compelling demand for saving building energy has motivated researchers to take energy-saving renovation of the building sector.

To address the aforementioned issues, prefabricated construction has been adopted worldwide recently. Prefabricated construction refers to a modern construction technology that uses building components manufactured off-site in a factory and then transported and assembled on-site (Sparksman et al., 1999; Tam et al., 2007; Jiang et al., 2018; Zhang et al., 2022). Prefabricated construction can be classified into four levels depending on the product's degree of fabrication: 1) components are always manufactured and assembled in factories without considering on-site production, 2) non-volumetric pre-assembled units with unenclosed and usable space, such as timber roof trusses, 3) volumetric pre-assembled units enclosing usable space, such as the toilet and bathroom, and 4) entire buildings forming the actual structure and fabric, such as motel rooms (Goodier and Gibb, 2007; Hong et al., 2018). Compared to conventional construction, prefabricated construction improves construction efficiency (Lawson and Ogden, 2010), life cycle environmental performance, and quality control process (Jaillon and Poon, 2008), as well as standards for health and safety (Jaillon and Poon, 2009; López-Mesa et al., 2009; Li et al., 2011; Pons and Wadel, 2011). In addition, the inherent superiority of prefabricated construction includes a reduction in waste, noise, operation time and costs, labour demand, resource depletion, etc (Nadim and Goulding, 2010; Pons and Wadel, 2011; Aye et al., 2012). Most importantly, prefabricated construction is much less energy-intensive. For example, statistical results revealed that the total energy consumption of prefabricated construction was 20.5% lower than that of conventional construction (Cao et al., 2015). As such, advancing prefabricated technology is essential to conserve energy and mitigate carbon dioxide emissions.

As the primary medium for heat exchange between buildings and the outside environment, exterior walls account for the largest proportion of building energy assumption regarding heat loss (Ozel, 2014). Therefore, enhancing the thermal insulation capability of the exterior walls is indispensable for building energy conservation. Highly efficient and energy-saving wall insulation materials are widely adopted internationally to enhance the thermal insulation performance of walls.

Currently, there are three main forms of insulation systems for exterior walls in buildings: external wall insulation (Rodrigues et al., 2018; Axaopoulos et al., 2019; Kon and Caner, 2022), internal wall insulation (Marincioni et al., 2018; Xu et al., 2019; Martel et al., 2021), and sandwiched wall insulation (Hou et al., 2019b; Qiao et al., 2020; Shin and Kim, 2020). Among the three types of insulation systems, sandwiched wall is popular in cold regions of Europe and North America. A sandwich wall panel involves insulation materials between two layers of non-combustible materials, connecting them into a unified structure with connectors, forming a sandwich-like insulated wall panel. This design maximizes the insulation properties of the materials, ensuring thermal efficiency. In addition, it effectively protects both the insulation materials and the underlying wall structure, ensuring the longevity of the wall. The performance of sandwiched wall panels has been intensively investigated in the past few years. For example, Naito et al. (2012) assessed the shear tie performance of 14 insulated precast concrete sandwich wall panels with varied shear tie types. The results revealed noteworthy variations in the strength, stiffness, and deformability of shear ties employed in sandwich wall construction. The observed responses included elastic-brittle, elastic-plastic, and plastic-hardening behaviors. In another study conducted by Hassan and Rizkalla (2010), the degree of mutual interaction in precast concrete sandwich wall panels was analyzed based on the interaction theory of composite steel beams. This approach allows for determining the composite interaction percentage of precast concrete sandwich wall panels under different load conditions. The feasibility of this method was validated through experiments. The theory is applicable to precast concrete sandwich wall panels with various configurations and can be used to quantify various shear transfer mechanisms. Under ultimate load conditions, the overall composite performance of the Expanded Polystyrene (EPS) board (Lafond and Blanchet, 2020; Lakatos and Kovács, 2021; Meddage et al., 2022) with the wall surpassed that of the Extruded Polystyrene (XPS) board (Cai et al., 2019; Li et al., 2019; Park et al., 2020). Asan (2000) investigated the optimal insulation position of a sandwich wall panel concerning both maximum time lag and minimum decrement factor. The one-dimensional transient heat conduction equation was solved for a composite wall using Crank–Nicolson's scheme under periodic convection boundary conditions. It was observed that remarkably high time lags and low decrement factors (close to optimum values) when half of the insulation was placed in the mid-center plane of the wall and the other half on the outer surface. Some studies on sandwich panels have been conducted by integrating agricultural byproducts. For instance, Sharma and Kumar (2023a, 2023b) developed a novel sandwich panel employing calcium silicate board as the facing material, bonded together with a combination of waster coconut husk and polyurethane foam (PU). Based on their testing results, it was found that 20% of the waste coconut husk was the optimum percentage for achieving excellent mechanical properties. In addition, incorporating waste coconut husk into the PU resulted in a reduction in cell size and led to a notable enhancement in acoustic performance, particularly up to a frequency of 1,600 Hz.

Weatherability of wall panels has been attracting remarkable attention for its applications in various construction. Extensive research for investigating weathering resistance of wall panels and related temperature effects has been undertaken. For example, Balocco et al. (2008) analyzed the temperature field and thermal deformation of external wall insulation systems using transient simulations with ANSYS under high-temperature conditions in summer. The results revealed that external wall insulation systems effectively mitigated the impact of outdoor temperature changes, ensuring indoor thermal comfort. The wall panels did not exhibit significant fatigue stress at locations with fixed constraints. However, substantial tensile stresses and fatigue cracks were observed at the free ends of the wall panels. In another study by Daniotti et al. (2013), two sets of weathering tests on external wall insulation systems were conducted to investigate the impact of temperature changes and moisture content on the thermal performance. The results indicated that with the aging of the wall and increasing moisture content, the thermal resistance of the wall decreased while the thermal capacity increased. In addition, Mahaboonpachai et al. (2008), Mahaboonpachai et al. (2010) investigated the bonding failure of concrete walls and mortars under temperature effects through heating experiments. The degradation and durability performance of the interface under prolonged temperature exposure were analyzed. To address the tensile stress ratio of concrete and

polymer cement mortar at different shear strengths, a constitutive model for the interface between the two was established using the finite element method, which successfully obtained the interface fracture toughness.

As a protective structure in buildings, sandwich insulation wall panels primarily bear their own weight, vertical wind loads, seismic forces perpendicular to the panel surface, and temperature effects (Choi et al., 2015; O'Hegarty and Kinnane, 2020; Choi et al., 2016). Due to the presence of insulation material in the middle, the temperatures on the inner and outer sides of the sandwich insulation wall panel differ, causing unequal temperature-induced stresses and deformations on both sides of the panel. This can lead to thermal bending, thus impacting the service life of the wall panel. Temperature effects are often overlooked in the design of structural elements, making it essential to study the impact of temperature on the durability of sandwich insulation wall panels. Currently, there are only weathering test methods for external thermal insulation systems based on foreign standards and domestic experience in the existing Chinese codes. There is limited research and application of sandwich insulation wall panels domestically, making it crucial to explore their durability under climatic and temperature conditions.

In this study, the weathering resistance of a novel prefabricated concrete sandwich insulation wall panel with irregular column frame structures was conducted to analyze its weathering performance and degradation patterns. The structure system utilizes beams, columns, walls, and slabs prefabricated in factories and assembled on-site. Except for the overlapping layers of floor slabs and frame beams, the remaining walls, beams, slabs, and stairs are prefabricated components, with a prefabrication rate of over 75%, thereby realizing the development of residential industrialization towards rural dwellings. This study aims to provide reference data and evaluation criteria for the practical application. In addition, simulations and analyses of temperature effects on this insulation wall panel under weathering test conditions were performed using finite element analysis software ABAQUS. This serves as a basis for the degradation analysis and optimization design of the wall panel.

2 Experimentals

2.1 Materials for the insulation panels

For the precast wall panel, self-compacting concrete with a strength grade of C30 was used to achieve good homogeneity and fluidity. Bi-directional cold-rolled smooth steel bars ($f_y = 360N/mm^2$) were used in inner and outer steel mesh of the precast wall panels. And the connector truss reinforcement employed HRB400 steel bars with a diameter of 8 mm. Expanded Polystyrene (EPS) insulation boards were Class I polystyrene boards with a density, thermal conductivity coefficient, and combustion performance meeting B2 standards, and a thickness of 190 mm.

2.2 Design of the wall panel

2.2.1 Concrete-based wall

According to the current domestic industry standard JG/T 429-2014 "Weather Resistance Test Method for External Thermal Insulation Composite Systems," the concrete-based wall used in this experiment has a width of 3.3 m, height of 2.3 m, with a reserved opening in the upper right corner, 0.85 m from the top of the wall panel and 0.45 m from the right side. The opening has dimensions of 0.52 mm in width and 0.32 mm in height, and an aluminum alloy framed glass window was installed. The test wall panel is installed on the testing equipment based on these specifications.

2.2.2 Construction of the wall panel

The specification of the wall panel is shown in Figure 1. The sandwich insulation wall panel specimen is mainly composed of the following parts: inner leaf wall (C30 self-compacting concrete), insulation layer (EPS insulation board), outer leaf wall (C30 self-compacting concrete), connectors (truss reinforcement), anti-cracking layer (steel mesh), finish layer (flexible waterproof putty, coating, and finish tiles). The upper half of the external finish consists of coated finish, while the lower half is composed of finish tiles.

2.3 Insulation wall cubic specimens

To obtain the bonding strength between finish tiles and wall panels at different stages of the experimental process and analyze their variation patterns, synchronous test blocks were tested during the weathering resistance test. At each stage of the experiment, samples of the finish tiles were taken out for testing without damaging the wall panel specimen. Although the bonding strength obtained by this method may not entirely represent the overall changes in the wall panel, it can significantly reflect the damage to the material and interface strength caused by the experimental conditions. Nine sets of sandwich insulation cubic specimens with pasted finish tiles were produced, with dimensions of 200 mm × 200 mm × 290 mm. Except for the absence of truss reinforcement, the procedures for each layer were consistent with the insulation wall panel. The testing block specimen is shown in Figure 2. It is noted that except for the surface covered by finishing tiles, both sides of the other surfaces were coated with waterproof material. This step ensures that moisture only enters from the external finish surface during the test period, making it more representative of the conditions affecting the wall panel.

2.4 Construction of the wall panel

2.4.1 Reverse attachment of finishing tiles

The traditional method of applying finishing tiles involves bonding them to the concrete wall using mortar, and the construction quality is significantly influenced by the skill level of the workers. Regardless of whether the bond between the mortar and the wall or between the mortar and the facing tile is compromised, it can result in the detachment of finishing tiles, therefore posing safety risks. In this experiment, the technique of reverse attachment of finishing tiles was adopted in the wall panel. This involves arranging the finishing tiles at the bottom of the formwork and then directly pouring concrete to integrate them. This method offers advantages such as a smooth surface, secure adhesion, and efficiency regarding time and labor.

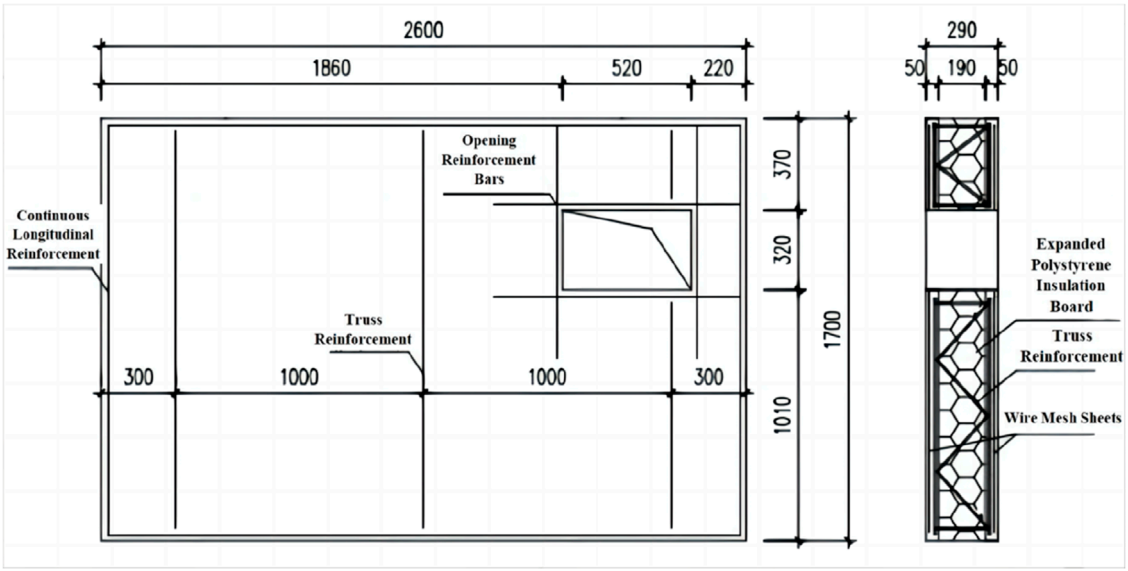

FIGURE 1
Design illustration of the insulation wall panel.

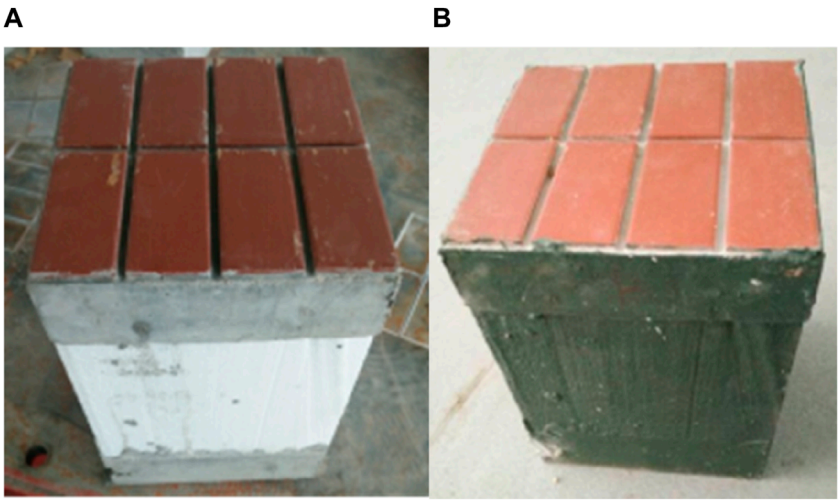

FIGURE 2
Insulation wall cubic specimens: **(A)** before waterproof treatment and **(B)** after waterproof treatment.

2.4.2 Production of the outer wall

As shown in Figure 3, the pre-bound wire mesh and truss reinforcement was placed into the wall panel mold. It is recommended to add small spacers for proper positioning. The concrete was poured starting from the side with finishing tiles, manually controlling the thickness and smoothing the surface.

2.4.3 Placement of EPS insulation board

The openings for embedded parts were reserved. The pre-cut and arranged EPS insulation boards were inserted, and manually compacted and pressed tightly, as shown in Figure 4.

2.4.4 Production of the inner wall

The inner wall wire mesh and the embedded parts for wall panel installation were inserted. The wire mesh was properly bound with the truss reinforcement, then the concrete was poured and the surface was smoothed, as shown in Figure 5.

2.4.5 Curing of the wall panel

Given the small size of the wall panel specimens in this study, manual steam curing was adopted, which was divided into four stages, namely, pre-curing (30°C for 2 h), temperature rise for 2 h (heated at a rate of 15°C/h until reaching a constant temperature of 65°C), constant temperature for 3 h, and temperature reduction for 4 h. Additionally, to mitigate the adverse effects of steam curing

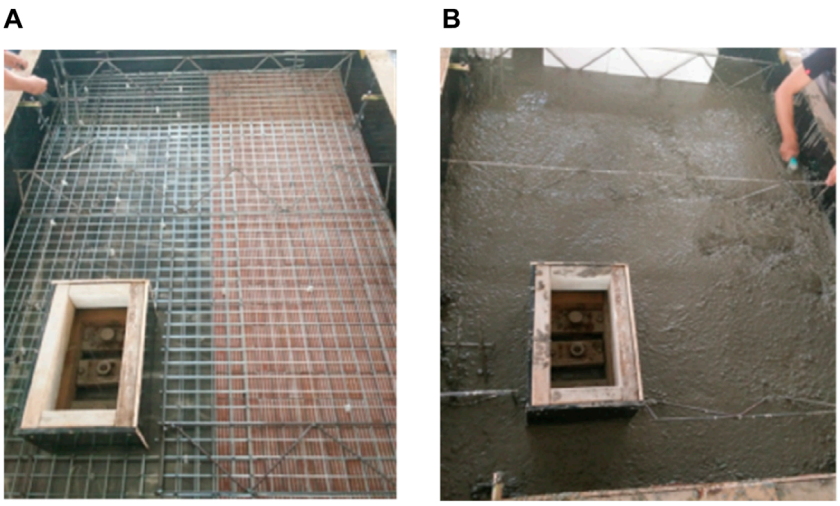

FIGURE 3
The outer wall production. **(A)** Placement of wire mesh and truss reinforcement; **(B)** Pouring of concrete and smoothing.

FIGURE 4
Installment of the insulation board.

on concrete, the specimens were subjected to supplementary curing, i.e., covered with a film for 48 h.

2.4.6 Demolding and hoisting the wall panel

As shown in Figure 6, the wall panel mold was removed, and the wall panel was lifted horizontally using a crane. The insulation boards were placed at both ends of the wall panel after demolding. Then the wall panel was lifted vertically and positioned on the wall panel supports.

2.4.7 Installation of the wall panel

The sandwich insulation wall panel was secured to the base wall using expansion bolts around the perimeter of the test base. The gaps between the inner leaf of the test wall panel and the surrounding base wall were filled with adhesive to prevent unnecessary moisture from affecting the test results. The installed wall panel and instruments are depicted in Figure 7, with the test wall panel positioned inside the box for the next steps of the test.

2.5 Weathering resistance tests of the sandwich insulation wall panel

2.5.1 Weathering test protocol

Thermal-rain cycling was conducted for a total of 80 cycles, with each cycle lasting 6 h. The sample temperature was raised to (70 ± 5)°C within 1 h and maintained for 2 h in an environment with a temperature of (70 ± 5)°C and relative humidity of 10%–30%. Then water spraying was performed for 1 h at a water temperature of (15 ± 5)°C, with each wall panel sample sprayed with a volume of (1.0 ± 0.1) L/(m^2·min), followed by a 2-h resting period. Thermal-cold cycling was conducted for a total of 5 cycles, with each cycle lasting 24 h. The specimen temperature was raised to (50 ± 5)°C within 1 h and maintained for 7 h in an environment with a temperature of (50 ± 5)°C and a maximum relative humidity of 30%. Then the sample temperature was lowered to (−20 ± 5)°C within 2 h and maintained for 14 h in an environment with a temperature of (−20 ± 5)°C. Freeze-thaw cycling was performed for 30 cycles, with each cycle lasting 8 h. Water was sprayed for 1 h at a water temperature of (15 ± 5)°C, with each wall panel sample sprayed with a volume of (1.0 ± 0.1) L/(m^2·min). The sample temperature was maintained for 1 h at a temperature of (20 ± 5)°C. The sample temperature was lowered to −20°C within 1 h and maintained for 4 h in an environment with a temperature of (−20 ± 5)°C. The sample temperature was raised to 20°C within 0.5 h. Finally, the sample was left to rest for 0.5 h.

2.5.2 Strain monitoring scheme of the wall panel

To monitor the strain variations at different locations of the sandwich thermal insulation wall panel throughout the entire experiment (Hou et al., 2019a), strain gauges were affixed to the concrete surface of the external leaf wall, as illustrated in Figure 8. Positions 1, 6, and 7 were primarily designated for detecting strains near the window openings. Positions 2 and 4 were located on the concrete outside the truss steel bars, position 3 was in the concrete be tween two truss steel bars, and positions 2 and 8 were

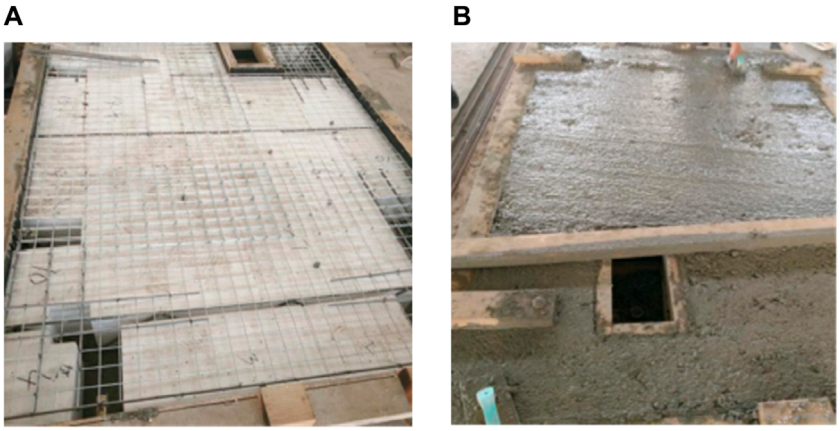

FIGURE 5
Installment of the insulation board. **(A)** Placement of wire mesh and embedded parts; **(B)** Pouring of concrete and smoothing.

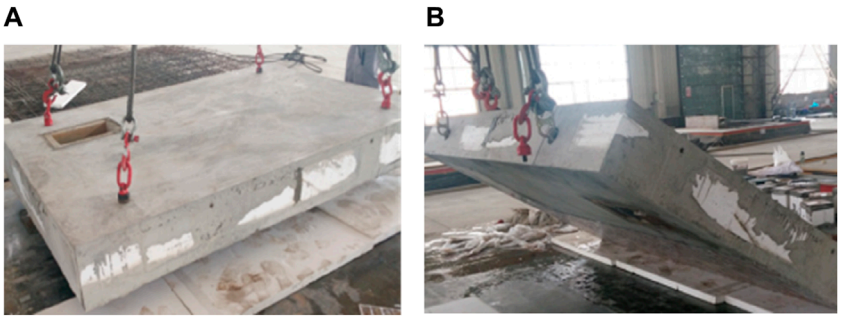

FIGURE 6
Hoisting and installment of the wall panel. **(A)** Horizontal lifting of the wall panel; **(B)** Vertical hoisting of the wall panel.

FIGURE 7
The wall panel and testing equipment after installation.

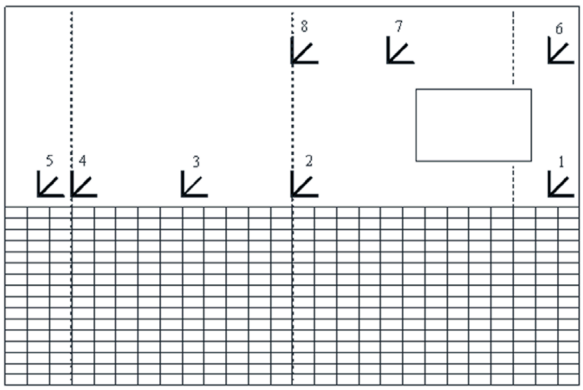

FIGURE 8
Illustration of strain gauge positions.

at different locations on the same truss steel bar. These positions were mainly utilized to analyze the stress impact of truss steel bars on the external leaf concrete. This approach aimed to analyze the strain variations at different positions and different cycle counts, providing a microscopic perspective on the structural deformation characteristics of the wall panel.

2.5.3 Loading procedures

2.5.3.1 Thermal rain cycle: 80 cycles, each lasting 6 h

Elevate the sample temperature to (70 ± 5)°C within 1 h, maintaining it in an environment of (70 ± 5)°C and relative humidity of 10%–30% for 2 h; spray water for 1 h at a temperature of (15 ± 5)°C, with each wall panel receiving water at a rate of (1.0 ± 0.1) L/(m^2·min); then allow a 2-hour rest.

2.5.3.2 Thermal cold cycle: 5 cycles, each lasting 24 h.

Increase the sample temperature to (50 ± 5)°C within 1 h, maintaining it in an environment of (50 ± 5)°C and maximum relative humidity of 30% for 7 h; decrease the sample temperature to (−20 ± 5)°C within 2 h, maintaining it in an environment of (−20 ± 5)°C for 14 h.

2.5.3.3 Freeze-thaw cycle: 15 cycles, each lasting 8 h

Water the sample for 1 h at a temperature of (15 ± 5)°C, with each wall panel receiving water at a rate of (1.0 ± 0.1) L/(m^2·min); maintain the sample temperature at (20 ± 5)°C for 1 h; decrease the sample temperature to −20°C within 1 h, maintaining it in an environment of (−20 ± 5)°C for 4 h; increase the sample temperature to 20°C within 0.5 h; allow it to stand for 0.5 h.

2.5.4 Observation and records during the test

After the thermal rain cycle was completed, a thermal-cold cycle was initiated 2 days later. A freeze-thaw cycle was conducted 2 days later as well. After every 4 thermal rain cycles, every 5 thermal-cold cycles, and every 3 freeze-thaw cycles, observations were made regarding changes such as surface cracks, powdering, hollowness, peeling, etc. The locations and dimensions of these changes were recorded. The specimens were divided into 9 groups, each consisting of 5 blocks. Samples were retrieved before the start of the test (0 cycles), after 28, 56, and 80 thermal rain cycles, after 2 and 5 thermal-cold cycles, and after 3, 9, and 15 freeze-thaw cycles. After 7 days of static adjustment, the tensile bond strength between the facing bricks and concrete was tested. Following the completion of the experiment, the insulation wall panel were left in place for 7 days. Based on the visual inspection, tensile bond strength measurements were conducted in accordance with JGJ110-2008 "Test Standard for Bond Strength of Facing Bricks in Building Construction."

2.6 Simulation of weathering resistance tests of the panel

The numerical simulation of the nonlinear surface temperature field and temperature stress was conducted using the finite element simulation software ABAQUS. Sequential coupled thermal-stress analyses was required, which involved the initial separate analyses of the heat conduction issue. Subsequently, the temperature field distribution was used as a known load for stress analyses. In addition, the temperature variation values on the surface of the wall panel, collected by the computer during the experimental process, were imported into the model as known conditions.

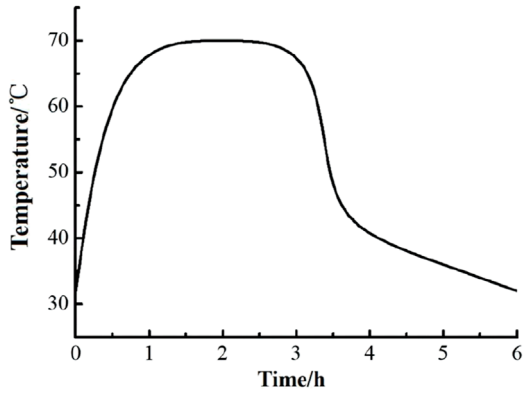

FIGURE 9
Thermal-rain cycle temperature loading curve.

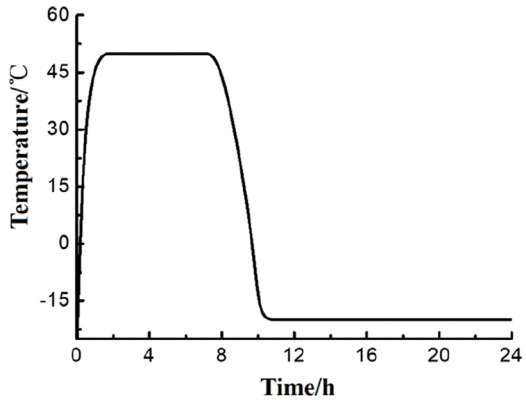

FIGURE 10
Thermal-cold cycle temperature loading curve.

3 Results and discussion

3.1 Temperature and cracking of the sandwich insulation wall panel

The temperature curves of the wall panel's outer surface during one cycle of hot-rain and hot-cold cycles obtained from temperature sensor data are depicted in Figures 9, 10.

During the hot-rain cycle, some visible small cracks appeared on the surface of the wall panel. However, the cracks did not show significant growth in length and width, and no water-seeping cracks occurred. No noticeable concrete cracks were observed after manually peeling off the coating putty layer at the location of the small cracks. Therefore, the conclusion can be drawn that throughout the entire weathering test, there were no apparent changes such as water seepage cracks, powdering, hollowing, peeling on the surface of the wall panel. No issues like the detachment of facing bricks or other safety concerns occurred. The wall panel passed the inspection of the weathering test, indicating good weathering performance.

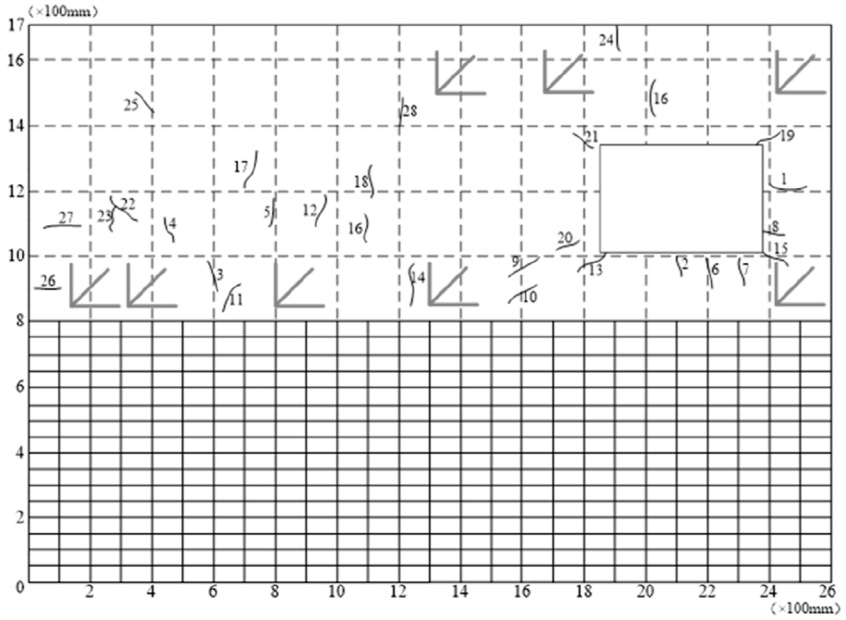

FIGURE 11
Illustration of cracks distribution.

The cracks on the outer surface of the wall panel are mostly shrinkage cracks generated by the high-temperature water spraying of the putty layer, and this is closely related to the quality of materials and construction. In actual construction, it is necessary to control construction quality, and the use of sprayed granular coatings should be considered to enhance the durability of the external finish. Therefore, representative crack positions and directions were selected for summary, and corresponding cracks were surveyed, as shown in Figure 11.

Cracking distribution can be summarized as follows. Overall, the cracks were relatively short and fine, with no significant trend in length and width growth. The crack development was stable, with no water seepage, indicating that the cracks in the wall panel were harmless, and they did not affect the safety performance and normal use of the wall panel. The locations with more cracks were near windows where stress concentration was prone, and there were more cracks in the middle than in the upper part, mainly because the middle received a larger and more sufficient amount of sprayed water. The cracks on the left and right sides of the wall panel were mainly horizontal, while those on the upper and lower sides were mainly vertical. Diagonal cracks mainly appeared near the corners. There were more vertical cracks in the middle part, and cracks on the left side of the wall panel appeared later and were fewer, mainly near the opening of the box on the left side, where temperature fluctuations and sprayed water were relatively less. In the initial stage, the cracks grew rapidly, but in the later stage, the growth slowed down, and deformation basically stopped. Cracks were more densely distributed in locations with larger water amounts than in locations with less water. There was no significant change in cracks after entering the hot-cold cycle. Therefore, it could be inferred that rainfall had a significant impact on the durability performance of the wall panel.

3.2 Strain analyses under weathering test conditions

Based on the theoretical foundation of temperature effects, it is known that the thermal deformation and thermal stress at any point inside a solid do not directly correspond. The deformation of the wall panel under temperature action is formed by the combined effects of the wall panel's free expansion (or contraction) during temperature changes, expansion (or contraction) caused by surrounding constraints, and deformation caused by uneven surface temperature distribution.

3.2.1 Strain analyses under thermal-rain cycles

3.2.1.1 Strain comparison at different locations on the outer surface of the wall during the same cycle

To analyze the strain characteristics at different positions during the same cycle, the strain values at each point in the 16th cycle of the thermal rain cycle were taken, and the strain-tim relationship curve was obtained, as shown in Figure 12.

It was found that the strain at each point changed significantly during the 0–60 min heating stage. During the 60–180 min high-temperature constant stage, the strain at each point did not completely stop changing but continued to change with slight fluctuations in temperature. During the 180–240 min water-spraying stage, the temperature dropped sharply, and the strain at each point also changed sharply. During the 240–360 min drying stage, the strain continued to change but with a smaller amplitude. Tensile strain showed in position 7 with the increase in temperature and compressive strain with the decrease in temperature, while the other points showed the opposite trend. Compressive strain occurred during the heating stage and tensile strain during the cooling stage. It can be seen that, unlike the thermal expansion and

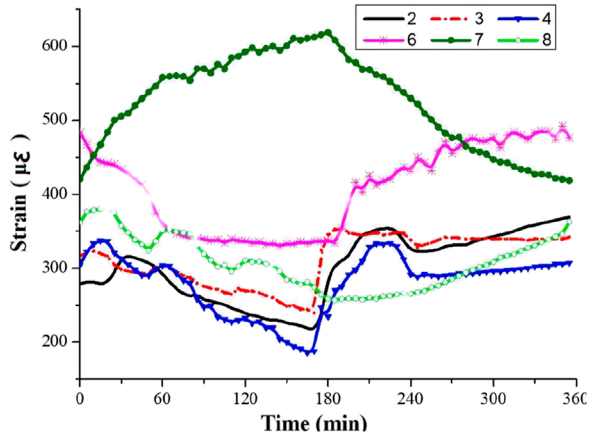

FIGURE 12
Strain-time curve of each point during thermal-rain cycle of 16 times.

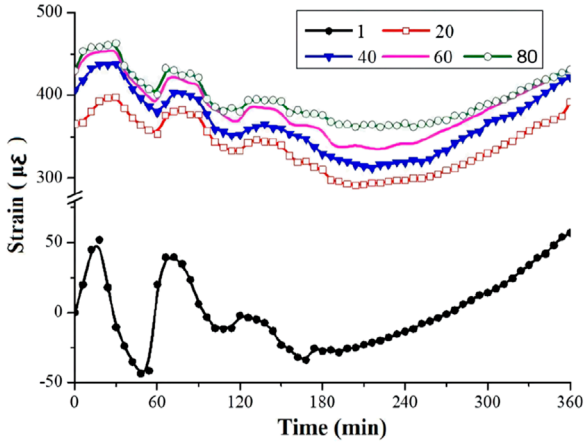

FIGURE 13
Strain-time curve of position 8 at different times of the thermal-rain cycle.

contraction deformation of external thermal insulation wall panel in the past, the total strain at some positions on the outer surface of this sandwich insulation wall panel showed thermal contraction and cold expansion. Since the deformation of the wall panel under temperature action is determined by both temperature difference and constraints (constraints of the entire wall panel and mutual constraints between different parts of the wall panel), during the heating stage, the wall panel underwent free deformation, resulting in tensile strain.

3.2.1.2 Strain comparison at the same location on the outer surface of the wall panel after different numbers of cycles

To analyze the influence of different numbers of cycles on the concrete strain, strain curves at position 8 in the 1st, 20th, 40th, 60th, and 80th thermal rain cycles were taken, as shown in Figure 13. It was found that in the 1st thermal rain cycle, at the beginning of the test, the heating instrument inside the box had just started working, and the temperature rise process had not reached a relatively uniform and stable state compared to later cycles. Therefore, the initial fluctuation was relatively large, but the overall trend was consistent. In addition, the strain growth during the first 20 cycles was significant, and after 20 cycles, the strain continued to increase, but the growth rate was very small, and the deformation amplitude decreased with more cycles. This indicates that the strain and deformation at this location mainly occurred in the early cycles, and there was residual strain and deformation at the end of each cycle, continuously accumulating to produce plastic deformation. Point 8 was located at the upper part of the wall panel. During the initial temperature rise, this location experiences thermal expansion, but it was then constrained, and the expansion cannot proceed freely, resulting in compressive stress. However, its deformation was influenced and constrained by the surrounding concrete and window openings, showing fluctuating changes. In the high-temperature stage, the final trend was still dominated by expansion being restricted, with the concrete under compression. Conversely, in the later cooling stage, the concrete undergoes tension, and its changes are much smoother than in the heating stage.

3.2.2 Strain analyses under thermal-rain cycles

3.2.2.1 Strain comparison at different locations on the outer surface of the wall during the same cycle

The strain analyses was conducted on points 3, 6, 7, and 8 on the outer surface of the wall panel during the third cycle of thermal-cold cycles. The strain-time relationship curve is shown in Figure 14. It was found that each point exhibited a consistent trend of strain variation with the thermal-cold cycle, changing periodically along with the temperature curve. During the 0–1-hour heating phase, significant strain changes occurred at all points. In the 1–8-hour high-temperature constant phase, the strain at each point did not completely cease; initially, it continued to change with minor temperature fluctuations and later tended to stabilize with increasing time. In the 8–10-hour cooling phase, a rapid temperature drop resulted in a sharp change in strain at all points. In the 10–24-hour low-temperature constant phase, strain continued to change but with a smaller amplitude, and later, strain almost ceased to change. Point 6 exhibited the largest amplitude and maximum strain value among all measured points, with the greatest changes during the heating and cooling phases. This point is located at the corner near the window, constrained by the edge of the wall panel and the middle of the truss reinforcement. Therefore, during the heating and high-temperature phases, the concrete expansion is significantly constrained, leading to compressive strain. In the cooling and low-temperature phases, the concrete shrinkage is restricted, resulting in a tensile state, and the residual strain after one cycle reaches 150 με. At point 7, there is an accumulation of compressive strain during thermal-cold cycles, which may contribute to the healing of fine cracks. The deformation trends at points 3, 6, and 8 are relatively consistent, with point 3 exhibiting the smallest change and point 6 the largest.

3.2.2.2 Strain comparison at the same location on the outer surface of the wall panel after different numbers of cycles

To analyze the impact of different cycle numbers on concrete strain, the strain curves for the 1st, 3rd, and 5th thermal-cold cycles at point 8 are shown in Figure 15. It was observed that the

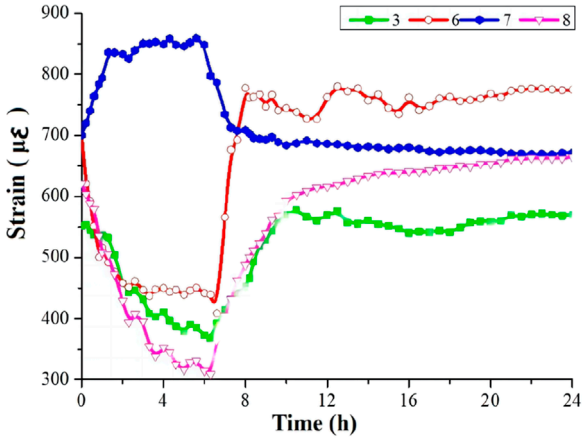

FIGURE 14
Strain-time curve of each point during 3 thermal-cold cycles.

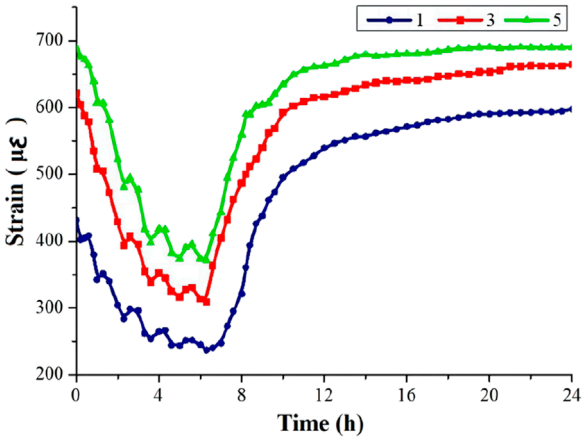

FIGURE 15
Strain-time curve at position 8 during different times of thermal-cooling cycles.

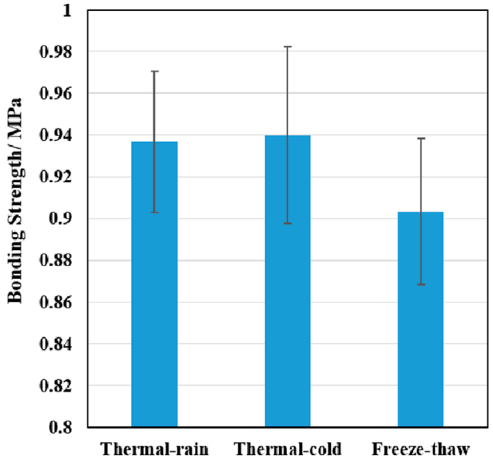

FIGURE 16
Bonding strength of the testing blocks under three cycles.

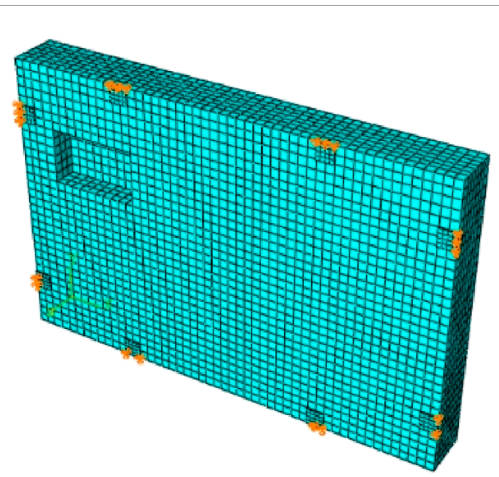

FIGURE 17
Finite element model for stress field analysis of the wall panels.

initial temperature of the 1st thermal-cold cycle was the same as room temperature, while the subsequent cycles were continuous and started from −20°C. Therefore, during the heating phase, the strain values in the first cycle changed significantly less than in the later cycles, and the later trends were basically consistent. In addition, the strain growth during the 1st cycle was relatively large, and after the 3rd and 5th cycles, the strain values continued to increase, but the growth rate was significantly smaller. Additionally, with more cycles, the deformation amplitude decreased. The distance between the 5th and 3rd cycles was noticeably smaller than that between the 1st and 3rd cycles. This indicates that strain and deformation primarily occur in the early cycles and accumulate certain plastic deformation.

3.3 Tensile bond strength of the test blocks

Prior to the experiment (0 cycles), specimens were subjected to 28, 56, and 80 cycles of hot-rain, 2 and 5 cycles of hot-cold, and 3, 9, and 15 cycles of freeze-thaw. Afterward, the specimens were retrieved and allowed to settle in a quiescent state for 7 days, and then tested for the tensile bond strength between facing bricks and concrete. As can be seen in Figure 16, the bond strength of facing bricks decreased by 8.1% following the completion of the hot-rain cycles, after the hot-cold cycles, it decreased by 5.1%, and after the freeze-thaw cycles, it decreased by 12.1%. Overall, the reduction in bond strength was not substantial. In comparison, the freeze-thaw cycles had the most significant impact, followed by the hot-rain cycles, while the hot-cold cycles had the least effect. This can be attributed primarily to moisture infiltration, leading to inadequate dissipation of thermal and moisture-induced stresses. The interface between facing bricks and concrete experienced freeze-thaw cycles, resulting in a certain degree of reduction in bond strength.

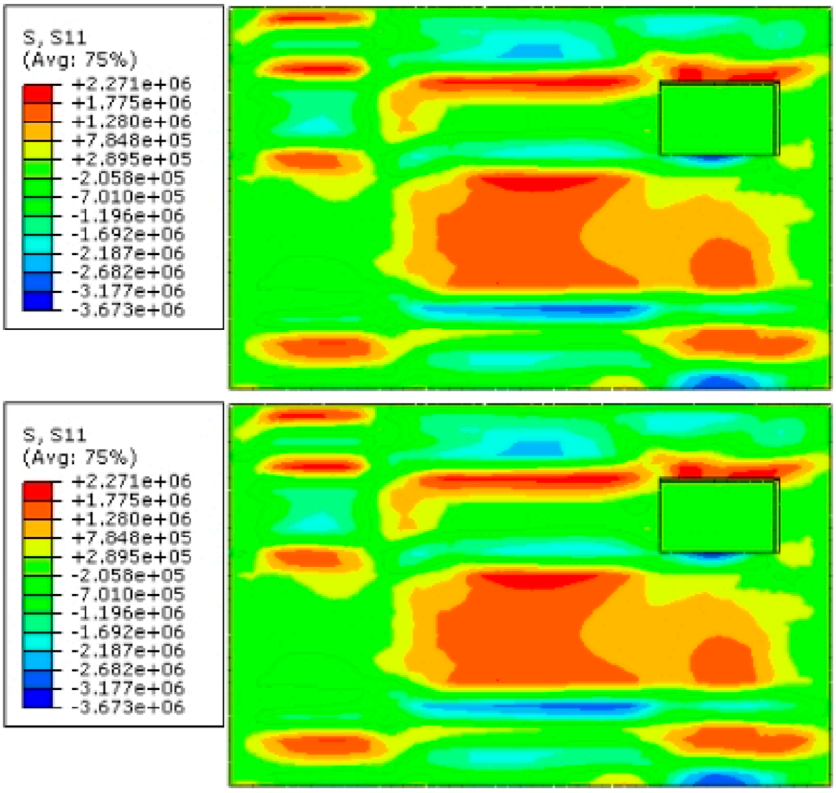

FIGURE 18
Finite element model for stress field analysis of the wall panels.

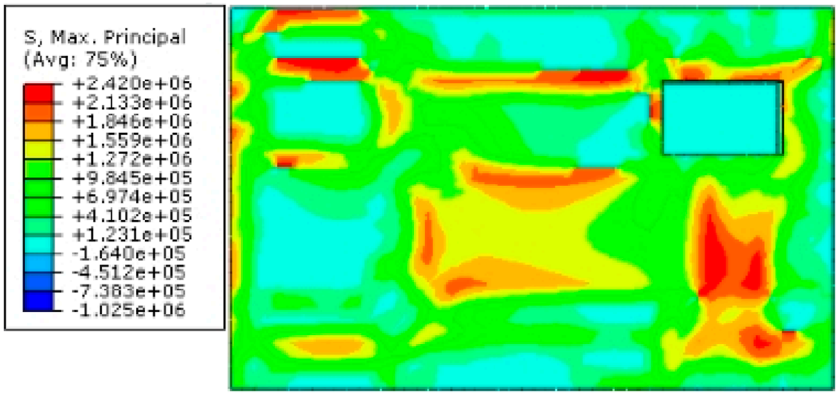

FIGURE 19
Principal stress distribution diagram of the wall panel during high temperature stage.

3.4 Simulations for stress and deformation analyses

The calculation of temperature-induced stresses employed sequential coupled thermal stress analyses. The temperature field data obtained from the analysis were loaded into the model to solve for stress and strain. The stress and displacement of the wall panel under temperature effects are closely related to the constraints it experiences. In the experiment, the wall panel was connected to the base wall using angle steel and bolts. Due to the focus on analyzing the external surface of the wall panel in the weathering test, constraints were simplified by treating them as hinged with additional steel plates. The mesh division and constraint conditions are illustrated in Figure 17.

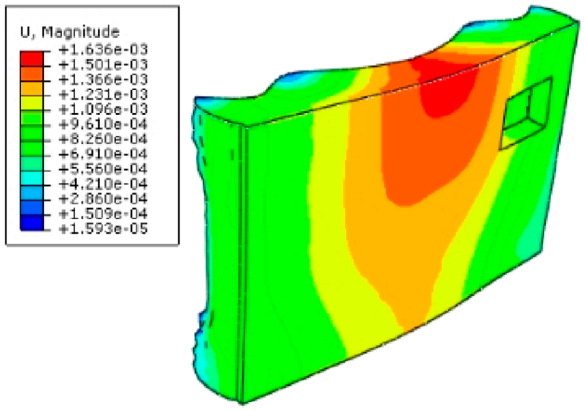

FIGURE 20
Wall panel deformation and displacement diagram at high temperature stage.

3.4.1 Stress and deformation analyses under thermal-rain cycles

3.4.1.1 Wall panel stresses

The obtained S11 and S22 in the simulation represent the stress distribution along the length and width directions of the wall panel, as shown in Figure 18. In the S22 graph, it was assumed that there was no window opening in the upper right corner of the wall panel, the model should be symmetrical, and under the influence of uniformly distributed temperature, the stress distribution on both sides should be relatively consistent. However, small tensile stresses appear on both sides of the window opening in the model, with a significant area of higher tensile stress below the opening. It can be inferred that the opening has a significant impact on the distribution of temperature-induced stresses. In S22, the left half of the wall panel from the constrained position to the vicinity of the truss steel reinforcement showed noticeable compressive stresses. The right half of the wall panel, except for the lower part of the window opening (considered as influenced by the window opening), also exhibited significant compressive stresses at the constrained and truss steel reinforcement positions. This indicates that both the truss steel reinforcement and bolt constraints had a pronounced restraining effect on the wall panel's expansion deformation during the high-temperature stage, resulting in a state of constrained expansion and compression. This is consistent with the conclusions drawn from the earlier analysis of strain variations in the experiment. The middle position of the wall panel still showed a tensile state. The concrete constraints at the middle position are relatively small, and the compressive forces on both sides of the concrete also indirectly induced tensile stresses. Thus, even though there is tension in the truss steel reinforcement at the middle part of this wall panel, its effect on altering the concrete stress state was minimal. Combining the S11 and S22 graphs, it can be seen that during the temperature rise stage, the upper half of the wall panel was mostly subjected to compression, with a certain area near the window opening showing tension. This aligns with the observed strain variations during the experiment, where position 7 near the window opening experienced tension during the high-temperature stage, while other positions were under compression.

Figure 19 shows the distribution of the maximum principal stress in the entire concrete wall panel. Typically, the maximum principal stress is used to assess the cracking of brittle materials such as concrete. It can be observed that the maximum principal stress in the inner leaf wall was distributed in a ring shape, following the positions constrained by the surroundings. However, the external leaf wall was less affected by the constraints from the surroundings. The uneven distribution of temperature-induced stresses in the external leaf wall is evident, with red areas indicating tensile stresses with relatively large values, and blue areas indicating the transition from tensile to compressive stresses. This suggests a significant mutual inhibitory effect of temperature stresses at various positions on the deformation of the nearby concrete. Overall, areas with larger regions of tensile stresses were found in the middle and lower parts of the window, thus indicating a higher risk of concrete cracking in these regions.

3.4.1.2 Deformation of the wall panel

Finite element simulation results for the deformation and displacement of the wall panel during the high-temperature stage are shown in Figure 20. Along the thickness direction of the wall panel, it can be observed that during the expansion deformation caused by temperature rise, the deformation of the wall panel was significantly constrained at the positions with truss steel reinforcement in the length direction of the wall panel. However, in the height direction of the wall panel, where there was no tensile reinforcement, no similar phenomenon occurs. Therefore, it can be seen that the tensile reinforcement effect of the truss steel restricts the free deformation of the wall panel, ensuring that the three parts of the wall panel behave as a whole. In addition, the constraints from bolts around the perimeter mainly restricted the deformation of the inner leaf wall, while the deformation of the outer leaf wall was relatively free. Notably, the overall behavior of the wall panel showed maximum displacement in the middle-upper part, gradually decreasing from the center to the sides, with an overall displacement ranging from 0.67 to 1.6 mm.

3.4.2 Stress and deformation analyses under thermal-cold cycles

The temperature effects during the high-temperature stage of the thermal-cold cycle are consistent with the temperature actions during the thermal-rain cycle, and are not reiterated here. This section specifically analyzes the low-temperature stage (−20°C) during the hot-cold cycle. The simulated results of the plane stress, maximum principal stress, displacement, and deformation are illustrated in Figures 21–23, respectively.

It was found that in contrast to the stress state of concrete during the high-temperature stage, the left half of the wall, from the constrained position to the vicinity of the truss steel, exhibited significant tensile stress. The right half of the wall, except for the lower part of the window opening, was in a compressive state (attributed to the influence of the window opening), and also in a tensile state at the constrained and truss steel locations. This indicates that during the contraction deformation of the wall in the low-temperature stage, both truss steel and bolts had a notable constraining effect, resulting in restrained contraction and a tensile state. In addition, the middle part of the wall is mainly in a compressive state, gradually changing to a tensile state towards the upper and lower sides. Combining the S11 and S22 graphs, during

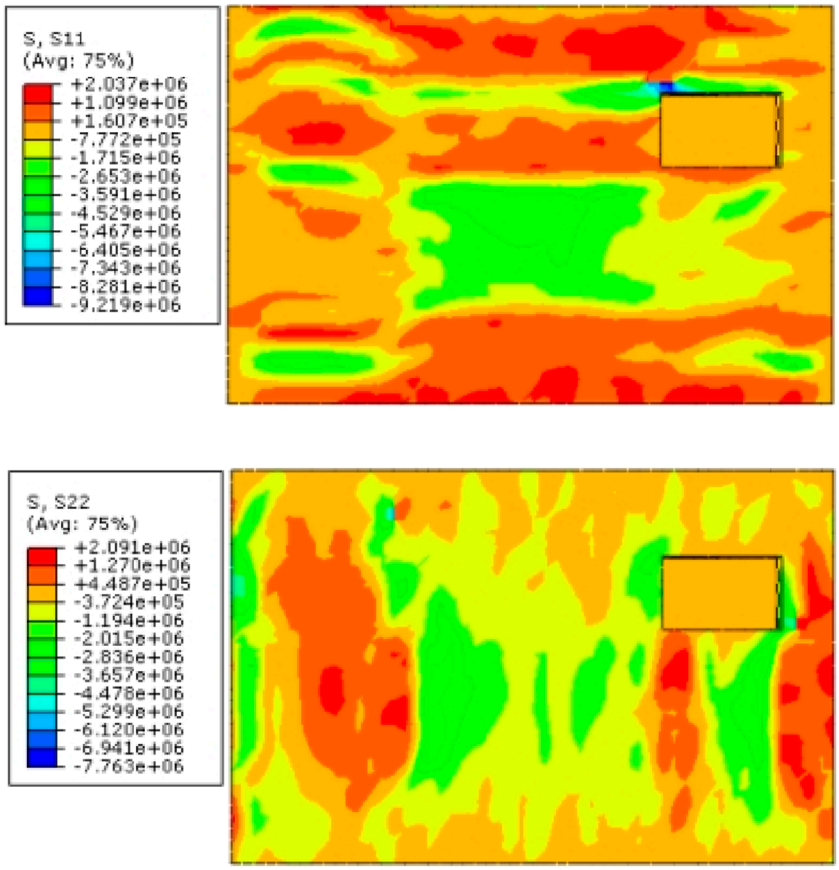

FIGURE 21
Plane stress in the low-temperature stage of the thermal-cold cycle.

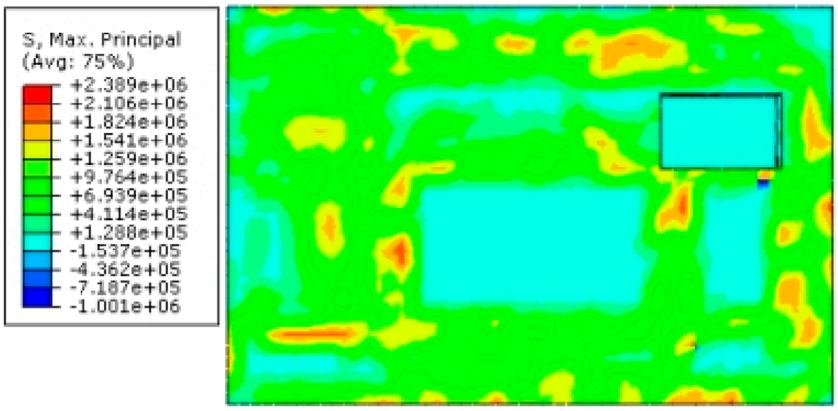

FIGURE 22
Principal stress distribution diagram of the wall panel at low temperature stage.

the temperature decrease stage, the upper part of the wall is mostly in tension, with the concrete being compressed at the upper-left corner of the window. This is consistent with the earlier experimental strain change conclusions. Also, the middle part and the area below the window of the wall have principal stresses smaller than those in the surrounding regions. Overall, the likelihood of cracking in the winter low-temperature climate is much smaller than in the hot summer climate. Notably, In the low-temperature stage, the wall did not exhibit significant deformation compared to the high-temperature stage, and the displacement mostly ranged from 0.55 to 0.63 mm.

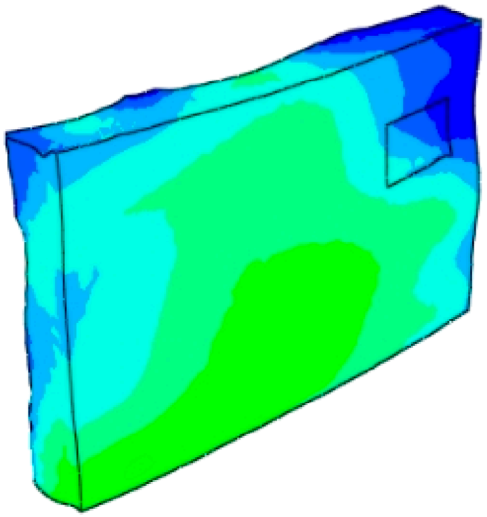

FIGURE 23
Wall panel deformation and displacement diagram at low temperature stage.

4 Conclusion

This paper focuses on exploring weathering resistance of a novel prefabricated EPS sandwich insulation wall panel with irregular column frame structures. The study involves comprehensive analyses of weather resistance and stress characteristics through visual inspections of the panel, determination of the bond strength of facing bricks, and analyses of strain data. Additionally, finite element analysis software ABAQUS was employed to simulate and analyze the temperature effects under weathering test conditions. The conclusions drawn from the study are as follows.

(1) In the weathering test, the panel surfaces did not exhibit apparent water seepage cracks, powdering, hollowing, peeling, etc. There was no occurrence of facing brick detachment or damage. This indicates that the tested wall panels passed the inspection of weathering tests, demonstrating good weather resistance. The strain variation patterns of the wall panels were analyzed at various locations and cycles. The data revealed the impact of the tensile reinforcement of the framework steel and the constraints from the surroundings. The outer surface concrete of the wall panel exhibited resistance during typical thermal expansion and contraction, resulting in compressive stress during expansion and tensile stress during contraction.

(2) The bond strength of the specimens decreased by 8.1% after the thermal-rain cycles, 5.1% after the thermal-cold cycles, and 12.1% after the freeze-thaw cycles, with concrete being the primary mode of failure. It is evident that the reduction in bond strength is not significant. In contrast, the freeze-thaw cycles had the most substantial impact, followed by the thermal-rain cycles, while the thermal-cold cycles had the smallest effect. This is mainly attributed to the entry of moisture, resulting in thermal and moisture-induced stresses and the loss of bond strength due to freeze-thaw cycles at the interface.

(3) The temperature effects on the wall panel under weathering conditions were simulated using ABAQUS. During the expansion deformation of the wall panel in the high-temperature phase, the restraint from the truss reinforcement and bolts significantly constrained it, resulting in restrained expansion and a compressive state. Conversely, during the contraction deformation in the low-temperature phase, it exhibited restrained contraction and a tensile state. It is evident that the results of numerical simulation using the finite element method for nonlinear surface temperature effects were reliable.

(4) In the numerical simulation, the temperature stress at various positions on the concrete wall had a noticeable mutual restraining effect on the force deformation of the nearby concrete. There was a significant risk of cracking in the middle and around the opening, particularly in the lower part of the wall panel. During the high-temperature phase of the thermal rain cycle, the overall deformation of the wall panel was characterized by maximum displacement in the upper-middle section. However, during the low-temperature phase of the thermal-cold cycle, the wall panel did not exhibit significant deformation observed during the high-temperature phase.

5 Future research suggestions

(1) In addition to temperature variations, loads and water spraying, factors such as solar radiation intensity, duration of water spraying, and the content of eroding impurities in the water can also influence the external surface of the wall panel. If these factors can be taken into account in weather resistance tests, the results will be more realistic, enhancing the credibility of the experimental outcomes.

(2) Regarding this novel prefabricated concrete sandwich insulation wall panel with irregular column frame structures itself, different thicknesses and materials of concrete could be investigated to identify the most suitable external wall material and thickness, therefore ensuring both durability and safety.

Data availability statement

The original contributions presented in the study are included in the article; further inquiries can be directed to the corresponding author.

Author contributions

JW: Writing–original draft, Investigation. SP: Conceptualization, Writing–review and editing. SJ: Investigation, Software, Writing–review and editing. XL: Data curation, Methodology, Writing–review and editing. LW: Supervision, Validation, Writing–original draft. JZ: Funding acquisition, Writing–review and editing.

Funding

The author(s) declare that financial support was received for the research, authorship, and/or publication of this article. The research work was supported by CSCEC-PT-015CSCEC City Renovation and Intelligent Operation Engineering Research Center (Building Health Diagnosis and Treatment).

Acknowledgments

The authors would like to acknowledge the support provided by Hebei University of Technology for guidance and greatly appreciate for providing the research facilities.

Conflict of interest

Authors JW, SP, SJ, and XL were employed by Beijing Building Research Institute Corporation Ltd. of China State Construction Engineering Corporation. Author LW was employed by China Construction First Group Corporation Ltd.

The remaining author declares that the research was conducted in the absence of any commercial or financial relationships that could be construed as a potential conflict of interest.

Publisher's note

All claims expressed in this article are solely those of the authors and do not necessarily represent those of their affiliated organizations, or those of the publisher, the editors and the reviewers. Any product that may be evaluated in this article, or claim that may be made by its manufacturer, is not guaranteed or endorsed by the publisher.

References

Abergel, T., Dean, B., and Dulac, J. (2017) *Towards a zero-emission, efficient, and resilient buildings and construction sector: global Status Report 2017*. Paris, France: UN Environment and International Energy Agency.

Asan, H. J.,(2000). Investigation of wall's optimum insulation position from maximum time lag and minimum decrement factor point of view. *Energy Build.* 32 (2), 197–203. doi:10.1016/s0378-7788(00)00044-x

Axaopoulos, I., Axaopoulos, P., Gelegenis, J., and Fylladitakis, E. D. J. J. o.B. P. (2019). Optimum external wall insulation thickness considering the annual CO2 emissions. *J. Build. Phys.* 42 (4), 527–544. doi:10.1177/1744259118774711

Aye, L., Ngo, T., Crawford, R. H., Gammampila, R., and Mendis, P. (2012). Life cycle greenhouse gas emissions and energy analysis of prefabricated reusable building modules. *Energy Build.* 47, 159–168. doi:10.1016/j.enbuild.2011.11.049

Balocco, C., Grazzini, G., and Cavalera, A. J. E. (2008). Transient analysis of an external building cladding. *Energy Build.* 40 (7), 1273–1277. doi:10.1016/j.enbuild.2007.11.008

Cai, M., Chen, S., Tang, Y., Li, Q., and An, W. J. C. S. i.T. E., Study on the influence of enclosed vertical channels on downward flame spread over XPS thermal insulation materials, , 14 (2019) 100486, doi:10.1016/j.csite.2019.100486

Cao, X., Li, X., Zhu, Y., and Zhang, Z. (2015). A comparative study of environmental performance between prefabricated and traditional residential buildings in China. *J. Clean. Prod.* 109, 131–143. doi:10.1016/j.jclepro.2015.04.120

Choi, I., Kim, J., and Kim, H.-R. J. M., Composite behavior of insulated concrete sandwich wall panels subjected to wind pressure and suction, , 8(3) (2015) 1264–1282. doi:10.3390/ma8031264

Choi, I., Kim, J., and You, Y.-C. J. C. P. B. E., Effect of cyclic loading on composite behavior of insulated concrete sandwich wall panels with GFRP shear connectors, , 96 (2016) 7–19. doi:10.1016/j.compositesb.2016.04.030

Daniotti, B., Paolini, R., and Re Cecconi, F. J. D. o.B. M., Effects of ageing and moisture on thermal performance of ETICS cladding, (2013) 127–171. doi:10.1007/978-3-642-37475-3_6

Dickson, T., and Pavía, S. (2021). Energy performance, environmental impact and cost of a range of insulation materials. *Renew. Sustain. Energy Rev.* 140, 110752. doi:10.1016/j.rser.2021.110752

Goodier, C., and Gibb, A. (2007). Future opportunities for offsite in the UK. *Constr. Manag. Econ.* 25 (6), 585–595. doi:10.1080/01446190601071821

Hassan, T. K., and Rizkalla, S. H. J. P. J. (2010). Analysis and design guidelines of precast, prestressed concrete, composite load-bearing sandwich wall panels reinforced with CFRP grid. *pcij.* 55 (2), 147–162. doi:10.15554/pcij.03012010.147.162

Hong, J., Shen, G. Q., Li, Z., Zhang, B., and Zhang, W. (2018). Barriers to promoting prefabricated construction in China: a cost–benefit analysis. *J. Clean. Prod.* 172, 649–660. doi:10.1016/j.jclepro.2017.10.171

Hou, H., Ji, K., Wang, W., Qu, B., Fang, M., and Qiu, C. (2019a). Flexural behavior of precast insulated sandwich wall panels: full-scale tests and design implications. *Eng. Struct.* 180, 750–761. doi:10.1016/j.engstruct.2018.11.068

Hou, H., Ji, K., Wang, W., Qu, B., Fang, M., and Qiu, C. J. E. S. (2019b). Flexural behavior of precast insulated sandwich wall panels: full-scale tests and design implications. *Eng. Struct.* 180, 750–761. doi:10.1016/j.engstruct.2018.11.068

Jaillon, L., and Poon, C. S. (2008). Sustainable construction aspects of using prefabrication in dense urban environment: a Hong Kong case study. *Constr. Manag. Econ.* 26 (9), 953–966. doi:10.1080/01446190802259043

Jaillon, L., and Poon, C. S. (2009). The evolution of prefabricated residential building systems in Hong Kong: a review of the public and the private sector. *Automation Constr.* 18 (3), 239–248. doi:10.1016/j.autcon.2008.09.002

Jiang, L., Li, Z., Li, L., and Gao, Y. J. S. (2018). Constraints on the promotion of prefabricated construction in China. *Sustainability* 10 (7), 2516. doi:10.3390/su10072516

Kon, O., and Caner, İ. J. B. (2022). The effect of external wall insulation on mold and moisture on the buildings. *Build. (Basel).* 12 (5), 521. doi:10.3390/buildings12050521

Lafond, C., and Blanchet, P. J. B. (2020). Technical performance overview of bio-based insulation materials compared to expanded polystyrene. *Build. (Basel).* 10 (5), 81. doi:10.3390/buildings10050081

Lakatos, Á., and Kovács, Z. J. E. (2021). Comparison of thermal insulation performance of vacuum insulation panels with EPS protection layers measured with different methods. *Energy Build.* 236, 110771. doi:10.1016/j.enbuild.2021.110771

Lawson, R., and Ogden, R. (2010). "Sustainability and process benefits of modular construction," in Proceedings of the 18th CIB World Building Congress, Salford, UK, 10–13.

Li, H., Guo, H., Skitmore, M., Huang, T., Chan, K., and Chan, G. (2011). Rethinking prefabricated construction management using the VP-based IKEA model in Hong Kong. *Constr. Manag. Econ.* 29 (3), 233–245. doi:10.1080/01446193.2010.545994

Li, Q., Wei, H., Han, L., Wang, F., Zhang, Y., and Han, S. J. S. (2019). Feasibility of using modified silty clay and extruded polystyrene (XPS) board as the subgrade thermal insulation layer in a seasonally frozen region, northeast China. *Sustainability* 11 (3), 804. doi:10.3390/su11030804

López-Mesa, B., Pitarch, Á., Tomás, A., and Gallego, T. (2009). Comparison of environmental impacts of building structures with *in situ* cast floors and with precast concrete floors. *Build. Environ.* 44 (4), 699–712. doi:10.1016/j.buildenv.2008.05.017

Mahaboonpachai, T., Kuromiya, Y., Matsumoto, T. J. C., and Materials, B. (2008). Experimental investigation of adhesion failure of the interface between concrete and polymer-cement mortar in an external wall tile structure under a thermal load. *Constr. Build. Mater.* 22 (9), 2001–2006. doi:10.1016/j.conbuildmat.2007.07.002

Mahaboonpachai, T., Matsumoto, T., and Inaba, Y. J. I. J. o.A. (2010). Investigation of interfacial fracture toughness between concrete and adhesive mortar in an external wall tile structure. *Int. J. Adhes. Adhes.* 30 (1), 1–9. doi:10.1016/j.ijadhadh.2009.06.005

Marincioni, V., Marra, G., and Altamirano-Medina, H. J. B. (2018). Development of predictive models for the probabilistic moisture risk assessment of internal wall insulation. *Build. Environ.* 137, 257–267. doi:10.1016/j.buildenv.2018.04.001

Martel, T., Rirsch, E., Simmonds, A., and Walker, C. J. C. S. i.C. M., The monitoring of wall moisture in a property retrofitted with Internal Wall Insulation, , 14 (2021) e00520. doi:10.1016/j.cscm.2021.e00520

Meddage, D., Chadee, A., Jayasinghe, M., and Rathnayake, U. J. C. S. i.C. M., Exploring the applicability of expanded polystyrene (EPS) based concrete panels as roof slab insulation in the tropics, , 17 (2022) e01361, doi:10.1016/j.cscm.2022.e01361

Nadim, W., and Goulding, J. S. (2010). Offsite production in the UK: the way forward? A UK construction industry perspective. *Constr. Innov.* 10, 181–202. doi:10.1108/14714171011037183

Naito, C., Hoemann, J., Beacraft, M., and Bewick, B. (2012). Performance and characterization of shear ties for use in insulated precast concrete sandwich wall panels. *J. Struct. Eng.* 138 (1), 52–61. doi:10.1061/(asce)st.1943-541x.0000430

O Hegarty, R., and Kinnane, O. J. C. (2020). Review of precast concrete sandwich panels and their innovations. *Constr. Build. Mater.* 233, 117145. doi:10.1016/j.conbuildmat.2019.117145

Ozel, M. J. E. (2014). Effect of insulation location on dynamic heat-transfer characteristics of building external walls and optimization of insulation thickness. *Energy Build.* 72, 288–295. doi:10.1016/j.enbuild.2013.11.015

Park, S.-H., Lee, M., Seo, P.-N., and Kang, E.-C. J. B. (2020). Effect of resin content on the physiochemical and combustion properties of wood fiber insulation board. *Bioresources* 15 (3), 5210–5225. doi:10.15376/biores.15.3.5210-5225

Pons, O., and Wadel, G. (2011). Environmental impacts of prefabricated school buildings in Catalonia. *Habitat Int.* 35 (4), 553–563. doi:10.1016/j.habitatint.2011.03.005

Qiao, W., Yin, X., Zhang, H., and Wang, D. (2020) *Experimental study of insulated sandwich concrete wall connections under cyclic loading, Structures*. Amsterdam, Netherlands: Elsevier, 2000–2012.

Rodrigues, L., White, J., Gillott, M., Braham, E., and Ishaque, A. J. E. (2018). Theoretical and experimental thermal performance assessment of an innovative external wall insulation system for social housing retrofit. *Energy Build.* 162, 77–90. doi:10.1016/j.enbuild.2017.10.020

Sharma, P., and Kumar, V. P. (2023a). Fabrication of a sandwich panel by integrating coconut husk with polyurethane foam and optimization using R2. *Constr. Build. Mater.* 409, 133929. doi:10.1016/j.conbuildmat.2023.133929

Sharma, P., and Kumar, V. P. (2023b). Amelioration of sandwich panels by replacing polyurethane foam with coconut husk and study on computational prediction using ANN and LR. *Innov. Infrastruct. Solutions* 8 (12), 331. doi:10.1007/s41062-023-01284-6

Shin, D.-H., and Kim, H.-J. J. J. o.B. E., Composite effects of shear connectors used for lightweight-foamed-concrete sandwich wall panels, , 29 (2020) 101108, doi:10.1016/j.jobe.2019.101108

Sparksman, G., Groak, S., Gibb, A., and Neale, R. (1999) *Standardisation and pre-assembly: adding value to construction projects*. CIRIA Report 176. London: Construction Industry Research & Information Association.

Tam, V. W., Tam, C. M., Zeng, S., and Ng, W. C. (2007). Towards adoption of prefabrication in construction. *Build. Environ.* 42 (10), 3642–3654. doi:10.1016/j.buildenv.2006.10.003

Xu, C., Li, S., and Zou, K. J. J. o.B. E., Study of heat and moisture transfer in internal and external wall insulation configurations, , 24 (2019) 100724. doi:10.1016/j.jobe.2019.02.016

Zhang, Z., Tan, Y., Shi, L., Hou, L., and Zhang, G. J. B. (2022). Current state of using prefabricated construction in Australia. *Build. (Basel).* 12 (9), 1355. doi:10.3390/buildings12091355

frontiers | Frontiers in Materials

TYPE Original Research
PUBLISHED 04 September 2024
DOI 10.3389/fmats.2024.1443517

OPEN ACCESS

EDITED BY
Yao Ding,
Chongqing University, China

REVIEWED BY
Ming-Feng Kai,
Hong Kong Polytechnic University, Hong Kong SAR, China
Honglei Chang,
Shandong University, China

*CORRESPONDENCE
Zhen Wang,
zhenwang25@126.com
Qi-Hang Zhang,
xzxynxn@163.com

RECEIVED 04 June 2024
ACCEPTED 21 August 2024
PUBLISHED 04 September 2024

CITATION
Yang X, Ren J-G, Li L-X, Wang Z, Zhang Q-H and Liu Q-L (2024) A preliminary investigation of incorporating cellulose nanocrystals into engineered cementitious composites.
Front. Mater. 11:1443517.
doi: 10.3389/fmats.2024.1443517

A preliminary investigation of incorporating cellulose nanocrystals into engineered cementitious composites

Xiao Yang[1], Jian-Guo Ren[2], Lian-Xu Li[3], Zhen Wang[1,4]*, Qi-Hang Zhang[1]* and Qiao-Ling Liu[1,2,4]

[1]School of Civil Engineering, Shandong Jianzhu University, Jinan, China, [2]Engineering Research Institute of Appraisal and Strengthening of Shandong Jianzhu University Co., Ltd., Jinan, China, [3]Jinan Cigarette Factory, China Tobacco Shandong Industrial Co., Ltd., Jinan, China, [4]Key Laboratory of Building Structural Retrofitting and Underground Space Engineering of Ministry of Education, Jinan, China

This paper explored the effects of various amounts of cellulose nanocrystals (CNCs), namely 0%, 0.1%, 0.2%, and 0.4% of binder weight, on the rheology, pore structure, mechanical properties, and 3D distribution of fibers of an engineered cementitious composite (ECC). The two rheological parameters, namely the yield stress and plastic viscosity, of the matrix containing the CNCs increased. Low-field nuclear magnetic resonance (LF-NMR) analysis, as a non-destructive method, proved that the addition of the CNCs to the ECC could reduce the porosity of the material and refine its pore size distribution. The addition of the CNCs enhanced the compressive strength of the ECC by 19.6%–33%. The results from uniaxial tensile tests showed incorporating the CNCs into the matrix could enhance the initial cracking strength and ultimate tensile strength of the ECC but reduce their tensile strain-hardening capacity. The optimal addition of 0.1% CNCs could effectively offset the decrease in strength due to increasing FA content, and maintain a relatively high level of tensile strain capacity of over 3%. Finally, X-ray micro-computed tomography (micro-CT) with ORS Dragonfly software was employed to reconstruct 3D images of the ECC to present the improvement in the fiber distribution due to the addition of the CNCs.

KEYWORDS

cellulose nanocrystals (CNCs), engineered cementitious composites (ECC), rheology, pore size distribution, tensile strain-hardening capacity, fiber distribution

1 Introduction

Engineered cementitious composites (ECC) are a specific category of fiber-reinforced cementitious composites with high tensile strain capacity (Li, 2019). By incorporating about 2% volume dosage of polyvinyl alcohol (PVA) or polyethylene (PE) short-fibers, ECC exhibits a tensile strain-hardening behavior with the ultimate tensile strain of exceeding 2%, multiple cracking characteristics, high deformation capacity, and so forth. ECC has been developing rapidly in numerous fields due to its excellent deformation capacity, high toughness, and good energy dissipation capacity.

Since the invention of PVA-ECC, they have been continuously modified and improved through, for instance, improving the surface treatment of PVA fibers and the properties of the matrix. Various types of modifying agents were applied to the surface treatment

of PVA fibers to reduce the chemical bonding significantly and thus provide higher tensile ductility (Arain et al., 2019; Ding et al., 2019). Compared with the modification of the surface of fibers, the treatment of the matrix would be easier to achieve. For example, incorporating high volumes of fly ash (Yang et al., 2007) and some particles with low bonding to the cementitious matrix (Wang and Li, 2004; Pang et al., 2014) into the matrix of an ECC could improve its ductility. Ma et al. (2017) and Pan et al. (2018) improved the compressive strength and tensile strain-hardening behavior of an ECC by incorporating an optimal content of $CaCO_3$ whisker and PVA fibers, greatly reducing the cost of production. The microstructural images in their work confirmed that embedding $CaCO_3$ whiskers in the matrix inhibited the initiation and propagation of microscopic cracks, and PVA fibers prevented macroscopic cracks.

In recent years, applying nanomaterials to cementitious composites has increasingly been a popular topic. Adding nano-particles, including multi-walled carbon nanotubes (MWCNTs) (Xu et al., 2019), graphene oxide (GO) (Lu et al., 2016), nano-SiO_2 (NS) (Li et al., 2016; Xi et al., 2020), and nano-$CaCO_3$ (NC) (Ding et al., 2020), has proved to be an effective method for improving the properties of, for instance, high ductility cementitious composites. Further, these nanoparticles could act as nucleation sites and thus accelerate the hydration rate, which produces more hydrated calcium silicate gels to fill the micro-pores of the matrix and hence refines its pore size distribution. The interface between the matrix and fibers could be improved by the addition of nanoparticles, thereby modifying the microscopic properties of the matrix and improving its mechanical properties.

Cellulose stands as the most plentiful among all renewable and biodegradable natural resources. Many methods have been developed for producing nanocellulose from natural cellulose materials, which is in accord with the concept of green development. Nanocellulose materials mainly consist of cellulose nanofibrils (CNF), cellulose nanocrystal (CNC), and bacterial nanocellulose (BNC). Cellulose nanocrystals (CNCs) which are rod-like and whisker-shaped nanoparticles with a length of several microns and a diameter of 5–50 nm can be extracted from plants, woods, etc. on a nanoscale. Compared with macroscale fibers, CNCs have a number of unique features such as a high aspect ratio, low density (1.3 g/m^3), a high elastic modulus, and high crystallinity (54%–88%). However, there are few studies on the effect of CNCs on cementitious materials. Some works have investigated the influence of CNCs on the mechanical and microscopic properties of cement paste. CNCs exert an effect on accelerating the hydration reactions of cement, their nucleation effect has been also verified (Zheng et al., 2023). According to the short circuit diffusion, CNCs can adhere to the surface of cement particles, and act as a transmission path, carrying curing water to unhydrated cement because of their hydrophilicity (Cao et al., 2016). Cao et al. (2015) found that an ideal CNC dosage could enhance the cement hydration degree and the strength development of cement paste; they also investigated the influence of CNCs on the rheology of the cement paste. Moreover, CNCs could hold cement paste from cracking under a low-temperature environment (Liu et al., 2019).

Across the existing studies, no research has been reported on the application of CNCs in ECC yet. This paper preliminarily studies the effect of CNCs on the properties of ECC through rheological analysis, uniaxial direct tensile test, and compressive strength evaluation. On a microscale, the effect of the CNCs on the distribution of PVA fibers in the ECC was studied by X-ray micro-computed tomography (micro-CT) and 3D reconstruction of the captured slices of the samples. Moreover, the porosity tests were conducted using the low-field nuclear magnetic resonance (LF-NMR) method to evaluate the influence of the CNCs on the pore size distribution of the ECC.

2 Materials and methods

2.1 Materials

The materials used in all the mixtures were ordinary 42.5 Portland cement, fly ash, and quartz sand (with a particle size of 120–212 μm). Table 1 lists the chemical compositions of the cement and fly ash. Moreover, a proper high-range water-reducing admixture (HRWRA) was employed to maintain an appropriate flowability of the mixtures. The polyvinyl alcohol (PVA) fibers (KURALON K-II) used in all the mixtures were also supplied by the Japanese Kuraray Company, and they possessed a diameter of 40 μm, a length of 12 mm, and a density of 1,300 kg/m^3. The mixture proportions adopted are listed in Table 2.

The CNCs used in this research were supplied by Qihong Company of Technology, Guilin, China in the form of suspensions with a weight content of 9.3%; it was extracted from waste paper pulp through the TEMPO oxidation method. Figure 1 shows the features of CNCs. CNCs had a diameter of 10–50 nm and a length of 100–1,000 nm. From the Fourier transform infrared (FT-IR) spectra of CNCs, the peaks at 3,340 and 1,600 cm^{-1} were associated with -OH (from hydroxyl group) and -COO^- (from carboxylic salt), respectively.

The CNCs were added to the matrix at different amounts of 0%, 0.1%, 0.2%, and 0.4% of the total weight of the binder. In order to more uniformly disperse the CNC suspensions in the mortar, they must be homogenized in advance by magnetic stirring and ultrasonic dispersion in water [21].

2.2 Mixing procedure

A mortar mixer with a capacity of 15 L was used. All the dry raw materials including the cement, fly ash, and quartz sand were dry mixed for 2 min. Subsequently, water and the admixtures, including the CNC suspensions and HRWRA, were added and mixed for another 6 min to ensure the homogeneity of the fresh mortar. To ensure the workability of the ECC, the fluidity of all the mixtures, measured by the reciprocating flow table method, should reach nearly the same value of about 180–200 mm by adjusting the content of the HRWRA, and no bleeding phenomenon should be seen in all the mixture proportions. Finally, the PVA fibers were added slowly and stirred quickly for 2 min until achieving uniform dispersion. The fresh mixture was cast into molds and demolded after curing for 24 h. Then, all the specimens were cured in a air curing room at a relative humidity of more than 60% and a temperature of 20°C ± 2°C for 28 days before testing.

TABLE 1 Chemical compositions of the cement and fly ash (wt%).

Material	CaO	SiO_2	Al_2O_3	Fe_2O_3	MgO	SO_3	Ignition loss
Cement	60.3	21.2	3.2	3.98	1.53	2.55	1.63
Fly ash	7.53	52.35	28.44	4.87	2.58	1.09	—

TABLE 2 Mixture proportions.

Mixture Id	Cement	FA	Sand	Water	PVA fiber (%)	CNC (wt%)	HRWR (%)
ECC2-C1	0.3	0.7	0.35	0.3	2	0.1	0.09
ECC2	0.3	0.7	0.35	0.3	2	0	0.06
ECC1	0.4	0.6	0.35	0.3	2	0	0.07
ECC1-C1	0.4	0.6	0.35	0.3	2	0.1	0.14
ECC1-C2	0.4	0.6	0.35	0.3	2	0.2	0.19
ECC1-C4	0.4	0.6	0.35	0.3	2	0.4	0.31

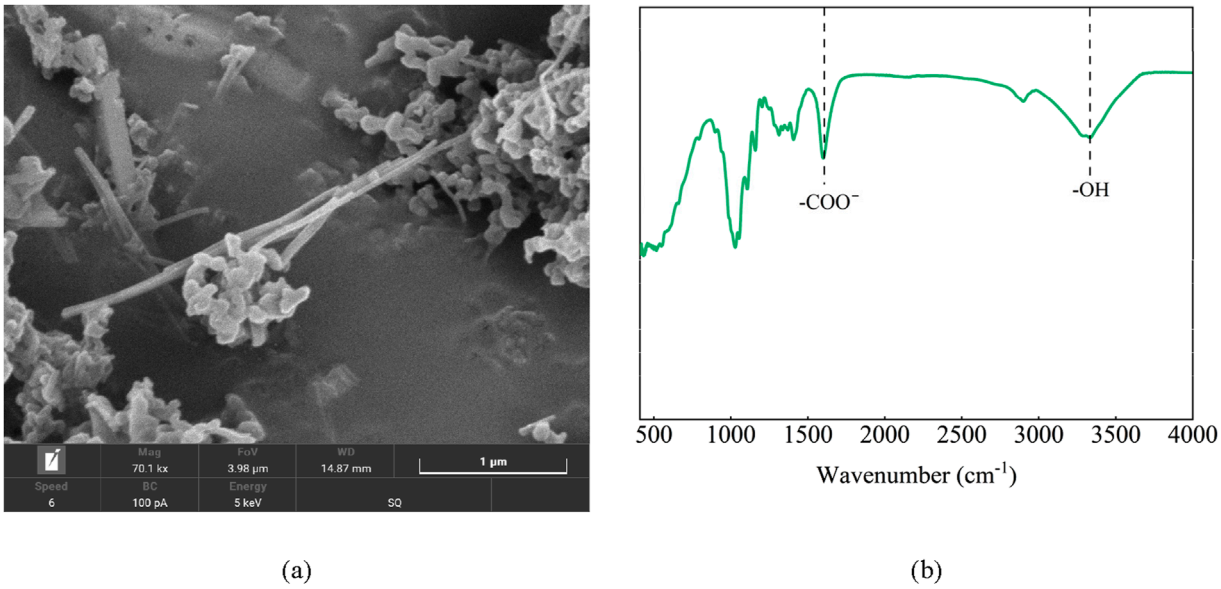

FIGURE 1
Features of CNCs: **(A)** SEM image and **(B)** FT-IR.

2.3 Testing methods

2.3.1 Rheology

The fresh mortar with different amounts of the CNCs was immediately transferred to a container for rheological analysis before adding the PVA fibers, and all tests were performed after 10 min of adding water. A rotary rheometer (Kinexus, Malvern, United Kingdom) was utilized to measure the rheological properties of the mortar at a steady shear rate (see Figure 2). Figure 2B delineates the rheological test program, which mainly includes two stages of pre-shearing and data-logging (Keskinateş and Felekoğlu, 2018). In the pre-shearing stage, the shear rate was increased from 0 to 25 s^{-1} within 30 s and then decreased to 0 s^{-1} within 30 s. The purpose of pre-shearing is to make each group of the mortar have the same initial shearing state during the rheological analysis. In the data-logging stage, after completion of the pre-shearing step, and waiting for 30 s, the shear rate was increased from 0 to 50 s^{-1} within 60 s and then dropped to 0 within 60 s. A total of 120 data points were collected to draw the shear rate–shear stress curve.

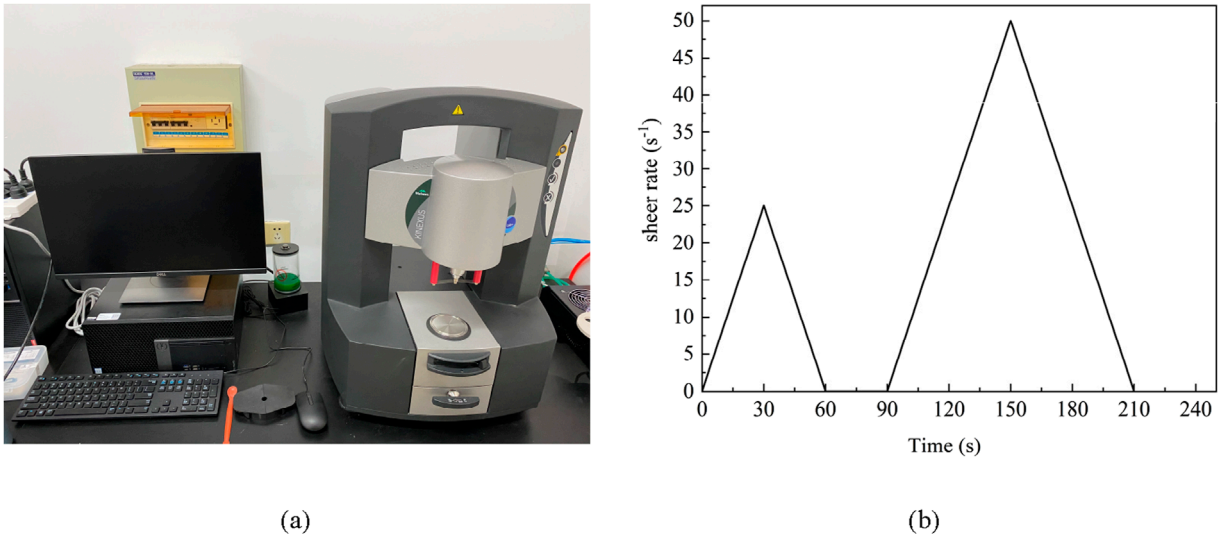

FIGURE 2
Rheology test: **(A)** setup and **(B)** program.

2.3.2 Pore structure

LF-NMR as a non-destructive technology was employed to measure the pore size distribution of the specimens (Wang et al., 2020). The cylindrical samples with a diameter and a length of 50 mm were used. First, the connected pores of the specimens were saturated with water. Then, the signal intensity of the hydrogen protons of water was recorded and converted to the porosity and pore size distribution of the specimens by LF-NMR. The LF-NMR instrument (MacroMR12-150H-I, Suzhou Niumag Analytical Instrument Corporation, Jiangsu, China) employed had a resonance frequency of 12.75 MHz and a radio frequency (RF) coil of 110 mm.

2.3.3 Uniaxial direct tensile test

The uniaxial direct tensile test adopted a type of dog-bone specimen (see Figure 3) to measure the tensile stress-strain curves. At least four specimens were prepared for every mixture proportion. All the tests were conducted using a 600 kN microcomputer-controlled hydraulic servo test machine at a constant-velocity displacement of 0.5 mm/min, and the variation in the tensile length of the middle-cross-section was measured with an electronic extensometer in a gauge length of 100 mm.

2.3.4 Compressive strength test

Three cube specimens with the dimensions 70.7 mm × 70.7 mm × 70.7 mm were prepared to measure the compressive strength after 28 days of curing. A 3,000 kN microcomputer-controlled hydraulic servo test machine was employed to measure the compressive strength of the samples at a stress control of 0.6 MPa/s.

2.3.5 Fiber distribution

In the fiber distribution analysis, to avoid error in the sides of the specimens, cylinders with a diameter of 10 mm and a height of

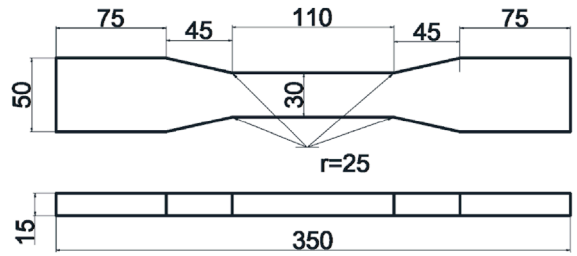

FIGURE 3
The dog-bone specimen for tensile tests (all the dimensions are in mm).

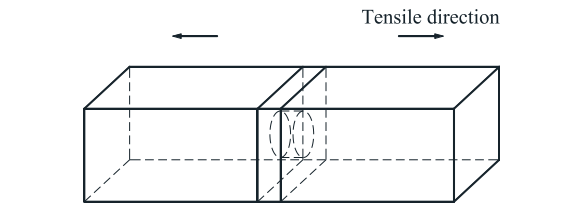

FIGURE 4
The location of the core extracted from the composites.

10 mm were cored from the specimens cured for 28 days by water jet saw, as shown in Figure 4. Then, the samples were scanned by X-ray computed tomography using Zeiss Xradia 510 Versa, Germany. The voltage and current of the X-ray tubes were 80 kV and 87 μA, respectively. A total of 819 2D slices with an image size of 1,000 × 1,024 pixels were obtained, and ORS Dragonfly software was utilized for processing the 2D slices of the samples to obtain the 3D reconstruction images.

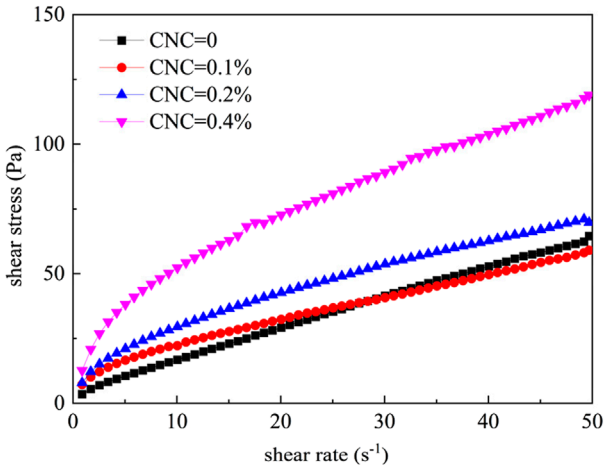

FIGURE 5
Rheological curves at different amounts of the CNCs.

3 Results and discussion

3.1 Rheology

The tensile strain-hardening behavior of ECC is closely related to the uniformity of fiber dispersion, and excellent mechanical properties could be obtained by achieving uniform fiber dispersion within a reasonable range (Sahmaran et al., 2013). Poor fiber dispersion will result in a reduced effective fiber volume fraction, which forms sections with weak bridging capacity, thereby leading to a lower tensile strain capacity (Li and Li, 2013). Since various measurement methods can produce a different result, an optimal range of mortar (without fiber) viscosity should be found for reaching uniform fiber dispersion.

Both shear rate-shear stress upward and downward curves can be obtained by matrix rheology tests. Herein, the rheological downward curves are selected for analysis. Since the uniformity of the mortar was ensured by its shear behavior at a higher shear rate before reaching the given rate, the data obtained from the downward curves are more reliable and repeatable (Cappellari et al., 2013). The rheological downward curves of the samples are presented in Figure 5. After regression analysis by Origin software (OriginLab Corporation), the rheological curve of each group conforms to the modified Bingham model equation ($\tau = \tau_0 + \mu\gamma + c\gamma^2$) where τ is the shear stress (Pa), τ_0 is the yield stress (Pa), μ represents the plastic viscosity (Pa·s), γ stands for the shear rate (s^{-1}), and c denotes the regression coefficient.

According to the regression formulas and rheological parameters of the modified Bingham plastic model listed in Table 3, the fitting correlation coefficients of the rheological curves of the mixtures in each group are 0.99, showing a high correlation, which proves that the modified Bingham plastic model accurately fits the experimental data.

Figure 6 displays the trends of yield stress and plastic viscosity of the cementitious composite matrix with the CNC content. As mentioned in Section 2.1, the HRWRA was used to maintain the flowability of the fresh mortar. In fact, incorporating the HRWRA into the cement could break down the cement flocculation structure to release free water, thereby improving the flowability, and thus reducing the yield stress and plastic viscosity, of the fresh mortar. Considering the interaction influence of both the HRWARA and CNC, it still can be seen that the addition of the CNCs has an impact on yield stress and plastic viscosity.

The yield stress, which is produced by the absorption and friction between particles inside the mixture, is the minimum shear stress which causes the mortar to flow and undergo deformation. The variation of the yield stress measured in a fresh state of the mortar with the CNC content is delineated in Figure 6A; generally, the yield stress increased steadily as the CNC content rose. When the CNCs were added, the water requirement of the fresh mortar obviously increased in the process of stirring. Then, the HRWRA was needed to improve the flowability of the mortar. There is an exception to the trend of the effect of the CNCs on the yield stress of the mortar; indeed, the yield stress of the mortar containing 0.1% of the CNCs is slightly lower than that of the mortar without the CNCs, which might indicate that the effect of the corresponding content of the HRWRA is slightly stronger than that of the CNCs. Nonetheless, because of the satisfaction of the workability and flowability, this result is considered to be reasonable. The mechanism of the CNCs appears to be similar to that of viscosity-enhancing admixtures based on cellulose ether, the role of which is to increase the viscosity of cementitious composites. On the one hand, CNCs are rod-like and whisker-shaped particles, so the specific surface area of them is higher than that of most of nano-particles. Moreover, CNCs provide for surface distinctive chemistries because of hydroxyl groups on their surface; in fact, the hydroxyl groups on the surface of CNCs are generally regarded as the initial sites of water sorption. Therefore, the surface of CNCs can absorb plenty of water and reduce the effective water used for stirring mixtures, resulting in an increase in the friction between particles inside the mixtures. However, another possible explanation for water absorption is that the absorbed water is insignificant and considered to be negligible compared to the total mixing water (Cao et al., 2015). Hence, the effect of water absorption into CNCs could be neglected when discussing the rheology of the fresh mortar. A higher CNC content (0.4%) gave rise to a very high yield stress, which was attributed to the agglomeration of the CNCs. On the other hand, CNCs as nanowhiskers could fill smaller spaces between other particles, and thus increase the probability of collision between particles during rotating (Jiang et al., 2018). Meanwhile, CNCs could retard the cement reactions by adhering to the cement particles and reducing the reaction surface area between the cement and water (Cao et al., 2015), which was also consistent with the practical phenomenon. Additionally, Francisco Montes (Montes et al., 2020) found that, at a lower content (smaller than 0.2 vol% relative to dry cement, which is equivalent to about 0.1 wt% relative to dry cement), CNCs act as water reducers to improve the flowability of the cement paste by decreasing its yield stress, which could be attributed to the steric stabilization reducing the positive-negative interactions between the hydration products; their results also confirmed that the performance of the CNCs was similar to a viscosity-enhancing admixture.

The plastic viscosity parameter denoting the ability to resist the flow inside the fresh mortar is related to the shape, size, and concentration of the mixing particles. The plastic viscosity

TABLE 3 Rheological parameters of each group of the specimens.

CNC content (%)	Plastic viscosity (Pa·s)	Yield stress (Pa)	Regression formula	R^2
0	8.62	1.18	$\tau = 1.18 + 8.62\gamma - 0.00168\gamma^2$	0.99583
0.1	10.31	1.17	$\tau = 10.31 + 1.17\gamma - 0.00456\gamma^2$	0.99572
0.2	11.59	1.79	$\tau = 11.59 + 1.79\gamma - 0.01262\gamma^2$	0.99628
0.4	22.23	2.93	$\tau = 22.23 + 2.93\gamma - 0.02134\gamma^2$	0.99158

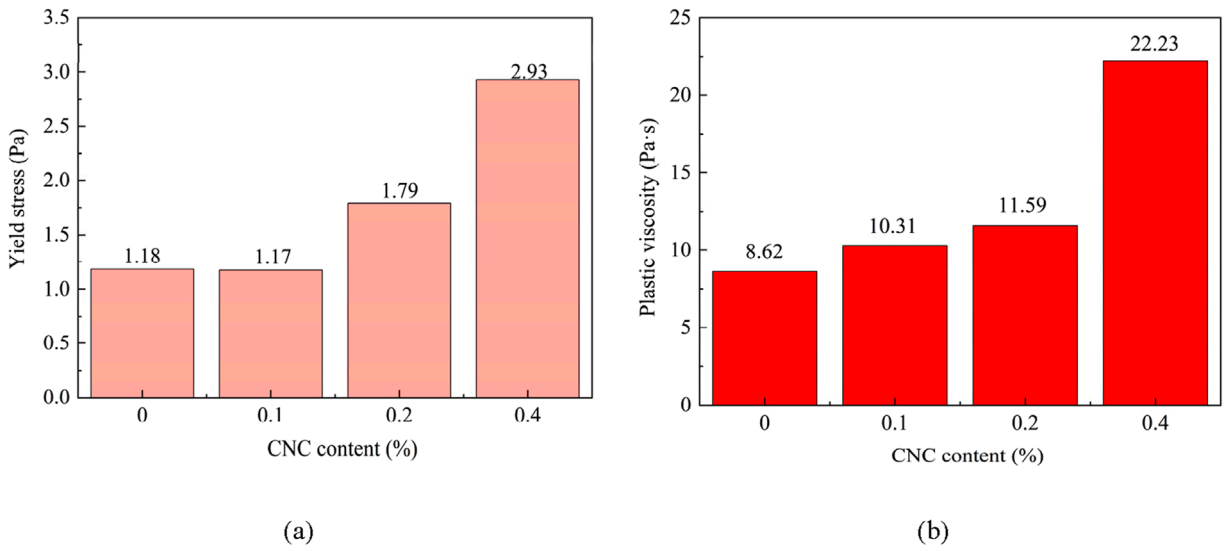

FIGURE 6
Variation of **(A)** yield stress and **(B)** plastic viscosity of the fresh matrix with the CNC content.

increased steadily with the addition of the CNCs in Figure 6B. It should be noted that this result also depended on the special characteristics of the CNCs. As previously mentioned, CNCs could absorb free water, fill smaller spaces between particles, and agglomerate, so they could raise the flow resistance. It could be observed that when the CNC content was higher than 0.2%, the agglomeration of the CNCs was likely to further increase the yield stress of the mortar, and a larger force was required for breaking down the agglomerate. Furthermore, the amount of air entrapped in the mortar increased with a rise in the CNC content, which could lead to enhancing the growth rate of viscosity (Struble and Jiang, 2004).

3.2 Pore structure

Pore distribution is of great importance in improving the mechanical properties and durability of cementitious composites. The addition of nanoparticles is considered to be an effective method for enhancing the pore structure of cementitious composites (Ghafari et al., 2015). Pores are classified on the basis of the pore radius (Kumar and Bhattacharjee, 2003) as gel pores (0.5 nm < radius <10 nm), fine capillary pores (10–50 nm), large capillary pores (50–5,000 nm), and non-capillary pores (radius >5,000 nm).

The pore size distribution and pore volume distribution of the prepared specimens at different amounts of the CNCs, namely 0%, 0.2%, and 0.4%, are plotted in Figure 7. It can be inferred from Figure 7A that the values for the total porosity of the composites containing 0%, 0.2%, and 0.4% of the CNCs were 8.707%, 6.439%, and 6.274% respectively, which represented the area enclosed by the pore size distribution curves. When the content of the CNCs increased from 0% to 0.4%, the total porosity of the specimens kept decreasing, and the pore size distribution was also refined. Also, the peak of the pore size distribution curve moved to the left, which indicated that the most probable pore size dropped with an increase in the CNC content. The most probable pore size was around 10 nm and corresponded to a critical position between gel pores and fine capillary pores at a CNC content of 0%. However, the most probable pore size at a CNC content of 0.2% and 0.4% was around 7 nm and 6 nm respectively, both corresponding to gel pores; it is obvious that the most probable pore size decreased as the CNC content of the composites increased.

Figure 7B illustrates the pore volume distribution of three specimens divided into four types. As the CNC content increased

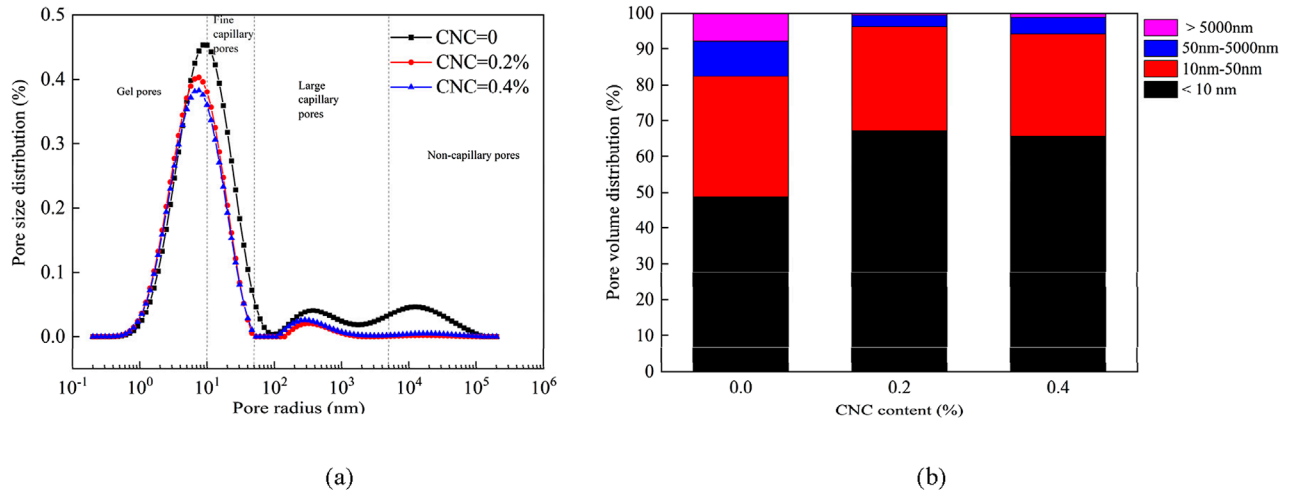

FIGURE 7
Variation of **(A)** pore size distribution and **(B)** pore volume distribution of the engineered cementitious composites with the CNC content.

from 0% to 0.4%, various pores were refined. At a CNC content of 0.2%, the total volume of the gel pores and fine capillary pores was the maximum compared with the two other groups. Moreover, these results indicated that the addition of the CNCs refined the microstructure of the ECC and improved its compactness.

3.3 Compressive strength

The variation of the average compressive strength of all the specimens cured for 28 days with the CNC content is presented in Figure 8. The compressive strength of the ECC1 without CNCs was 49.6 MPa, and the addition of the CNCs significantly enhanced the compressive strength of the ECC1. When 0.1%, 0.2%, and 0.4% of the CNCs were added, the average compressive strength of the ECC was respectively 59.3, 62.8, and 66.0 MPa, indicating an increase of 19.6%, 26.6%, and 33% respectively. The improvement in the compressive strength might be attributed to CNCs accelerating the cement hydration and filling the smaller spaces, as proved in Section 3.2. The porosity of the specimens decreased at a higher CNC content, which increased the compactness of the matrix and then enhanced its compressive strength. Although the average compressive strength increased steadily with the CNC content, the rate of increase in the compressive strength fell relatively at higher amounts of the CNCs. We could speculate that when the CNC content was higher than 0.2%, the CNCs could easily agglomerate, thereby influencing the uniform dispersion of the PVA fibers and leading to a smaller rate of increase in the compressive strength of ECC1. Additionally, a higher replacement of OPC by FA reduced the compressive strength of ECC2 due to a decreasing cement hydration degree. Further, incorporating 0.1% CNCs obtained a compressive strength of 47 MPa with a 23.7% enhancement compared to ECC2. The compressive strength of ECC2-C1 was slightly lower than that of ECC1.

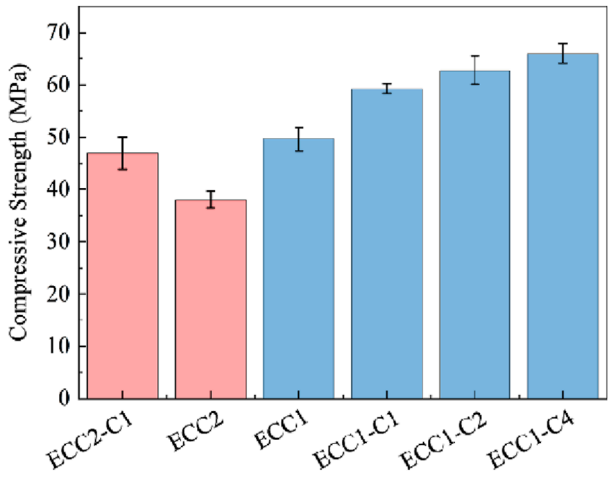

FIGURE 8
Variation of the average compressive strength of the ECC with different the CNC content.

3.4 Uniaxial tensile behavior

The uniaxial tensile stress-strain curves of all the specimens at various amounts of the CNCs are delineated in Figure 9. The initial cracking strength, the ultimate tensile strength, and the tensile strain were used to characterize the tensile behavior capacity of the ECC. As tabulated in Table 4, the average initial cracking strength at a CNC content of 0%, 0.1%, 0.2%, and 0.4% was 3.6, 4.6, 4.9, and 5.1 MPa respectively; obviously, the average initial cracking strength of the composites increased significantly with the addition of the CNCs. Compared with the blank group, the average initial cracking strength of the ECC containing 0.1%, 0.2%, and 0.4% of the CNCs increased by 28%, 36%, and 41% respectively. The initial cracking strength of the ECC is mainly determined by the matrix.

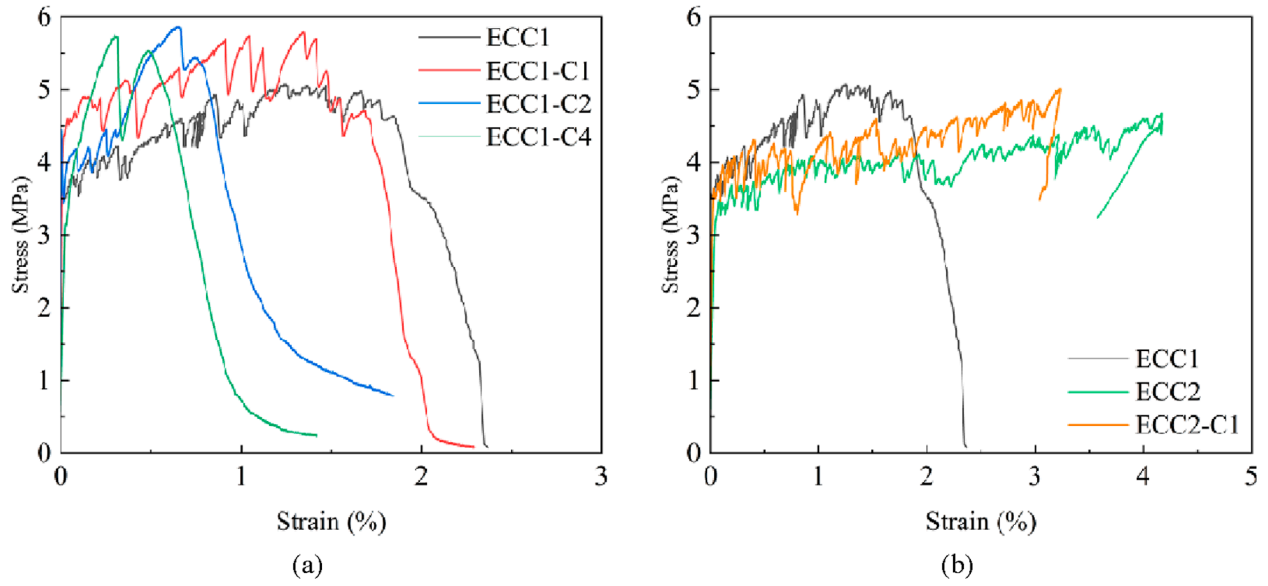

FIGURE 9
Tensile stress-strain curves of all the specimens at different amounts of the CNCs: **(A)** ECC1 series; **(B)** ECC2 series.

TABLE 4 Tensile parameters of all the specimens.

Mixture Id	Tensile strain (%)	Initial cracking strength (MPa)	Tensile strength (MPa)	Crack number	Crack width (μm)
ECC2-C1	3.2 ± 0.2	3.5 ± 0.4	5.0 ± 0.3	44 ± 3	60 ± 4
ECC2	4.1 ± 0.2	3.2 ± 0.2	4.6 ± 0.1	64 ± 5	52 ± 3
ECC1	1.6 ± 0.2	3.6 ± 0.3	5.1 ± 0.3	19 ± 5	71 ± 6
ECC1-C1	0.9 ± 0.3	4.6 ± 0.1	6.0 ± 0.5	10 ± 3	71 ± 3
ECC1-C2	0.8 ± 0.1	4.9 ± 0.3	5.7 ± 0.3	8 ± 2	81 ± 8
ECC1-C4	0.5 ± 0.1	5.1 ± 0.4	5.5 ± 0.5	4 ± 1	85 ± 17

The rise in the initial cracking strength could be attributed to the increase in the compactness, and the role of the CNCs with whisker-shaped particles in bridging the initial flaws of the matrix at a microscopic level.

Table 4 also compares the average ultimate tensile strength of all the specimens. It can be noticed that the trend of the variation in the average ultimate tensile strength was similar to that of the initial cracking strength. However, the enhancement of the initial cracking strength was more obvious, and the ultimate tensile strength improved by only 20%, 14.3%, and 8.6% respectively at a CNC content of 0.1%, 0.2%, and 0.4%. The fiber bridging capacity that depends on the frictional bonding strength governs this value. Meanwhile, the frictional bonding strength is determined by the interface between the matrix and fibers. Adding the CNCs might form stronger frictional bonding between the matrix and fibers, which could further increase the ultimate tensile strength of the ECC. Moreover, higher concentrations of the CNCs would lead to the non-uniform dispersion of the fibers, resulting in a lesser enhancement of the ultimate tensile strength of the ECC.

The tensile strain capacity is considered to be the most important index of ECCs. Under uniaxial tensile conditions, all the specimens presented a strain-hardening behavior to varying degrees, which was caused by the cracking of the matrix, the propagation of cracks, and the debonding and rupture processes of the fibers. With an increase in the CNC content, the tensile strain-hardening capacity dropped continuously from 1.6% to 0.5%. In the microscopic design of pseudo-strain hardening, an energy criterion should be satisfied to ensure a cracking mode, as expressed in Equation 1:

$$J_{tip} = \frac{K_m^2}{E_m} \le J_b' = \sigma_o \delta_0 - \int_0^{\delta_0} \sigma(\delta) d\delta \tag{1}$$

where J_b' is the complementary energy, J_{tip} represents the crack tip toughness, σ_o stands for the maximum stress, δ_0 indicates cracking opening displacement corresponding to σ_o, K_m is the matrix fracture toughness, and E_m stands for the composite elastic

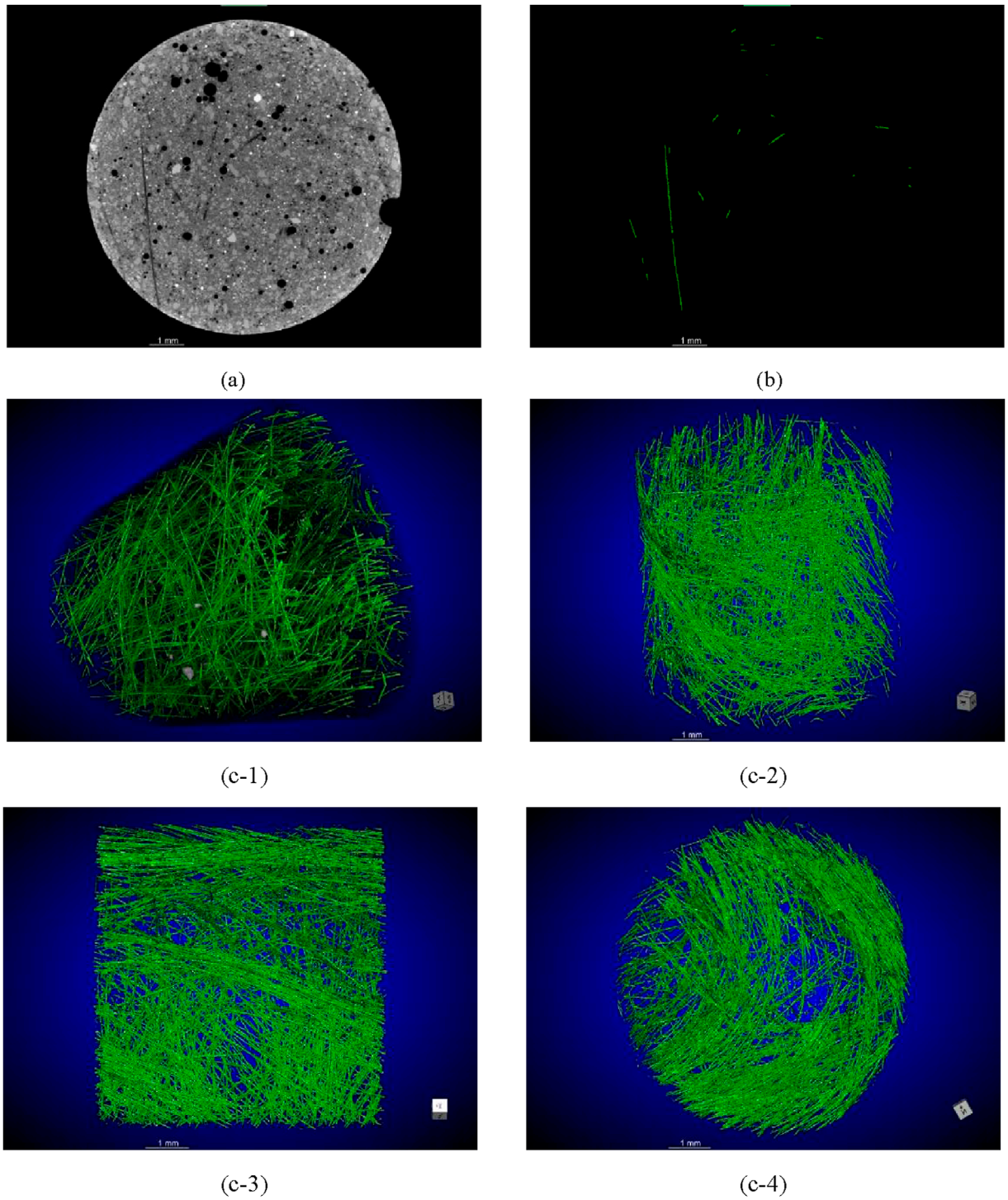

FIGURE 10
ROI segmentation and 3D reconstruction of the ECC without CNCs: **(A)** original 2D slice image; **(B)** ROI segmentation by the deep learning model; **(C)** 3D reconstruction of the fibers at different angles.

modulus. Due to the addition of the CNCs, the matrix strength was enhanced, which could influence the pullout of the fibers. On the one hand, in the uniaxial tensile test, before the initial cracks occurred in the ECC, the load was borne mainly by the matrix. When the initial flaws of the weakest cross-section of the matrix had a tendency to expand, the CNC whiskers might exert their ability to form bridges on a nanoscale and thus hinder the development of cracks, thereby leading to an increase in the initial cracking strength of the ECC. On the other hand, there were chemical bonding and frictional bonding between the matrix and fibers during pullout.

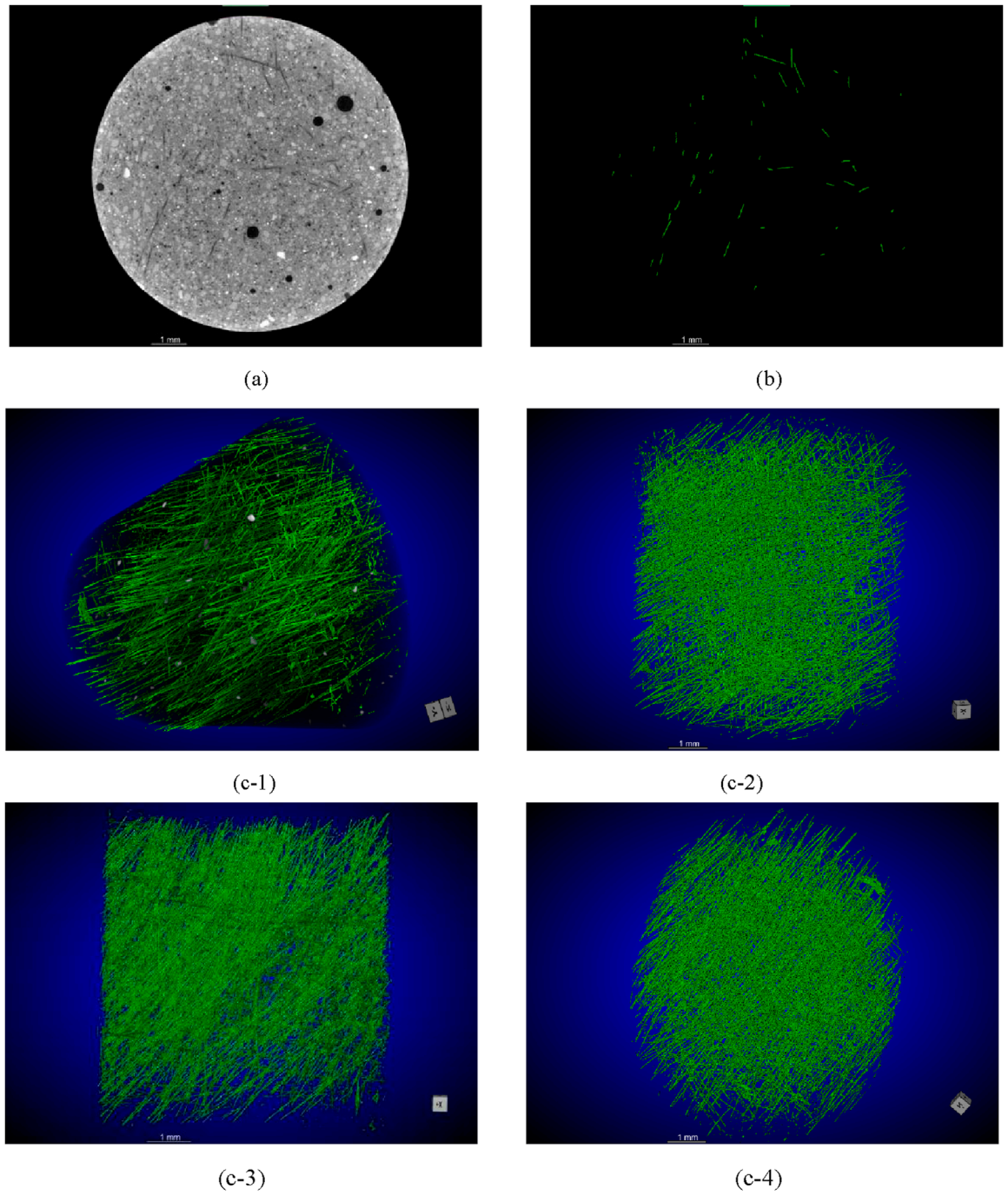

FIGURE 11
ROI segmentation and 3D reconstruction of the ECC with 0.2% of the CNCs: **(A)** original 2D slice image; **(B)** ROI segmentation by the deep learning model; **(C)** 3D reconstruction of the fibers at different angles.

The PVA fibers tend to form chemical bonding with the matrix due to the presence of the hydroxyl groups; it should be noted that the chemical bonding is basically independent of water-to-cement ratio and fiber type (Horikoshi et al., 2006). Generally, the pullout of more fibers, rather than their rupture, is conducive to obtaining a larger ductility for the ECC since the pullout of the fibers will generate higher energy consumption (Li, 2001). The presence of stronger chemical bonding tends to decrease the value of J_b' (Li et al., 2002), which reduces the upper limit of Equation 1, thereby leading to lowering the tensile capacity. Moreover, the value of J_{tip} is correlated positively with the material strength, and the properties of the matrix almost determine the frictional bonding strength between the fibers and matrix. Hence, the CNCs influenced the pullout of the fibers due to the improvement in the matrix strength,

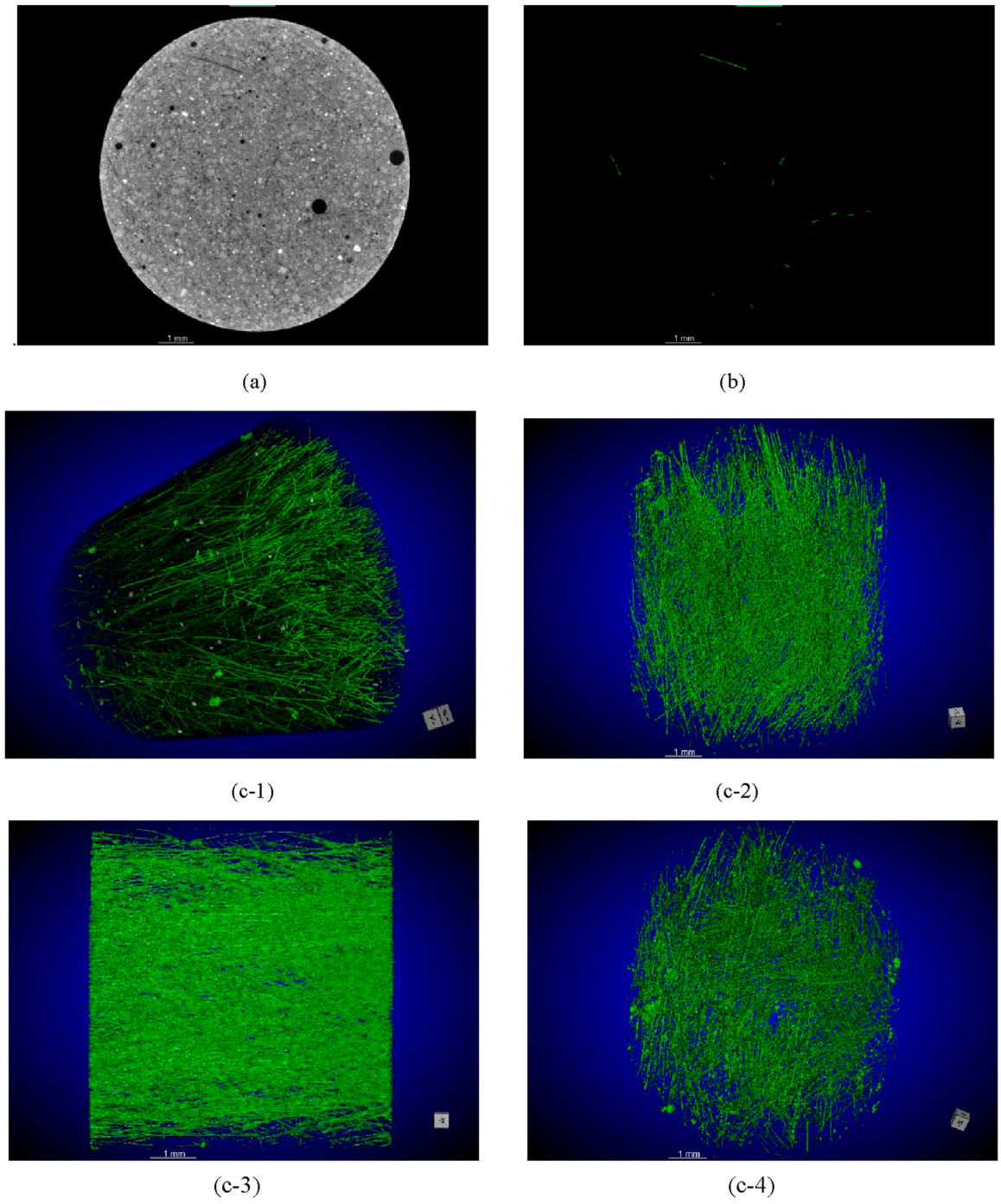

FIGURE 12
ROI segmentation and 3D reconstruction of the ECC with 0.4% of the CNCs: **(A)** original 2D slice image; **(B)** ROI segmentation by the deep learning model; **(C)** 3D reconstruction of the fibers at different angles.

and the PVA fibers tended to rupture instead of pullout during the uniaxial tensile tests. Additionally, it was found that the crack number greatly decreased with the CNC addition, leading to a larger crack width.

Although adding more FA reduced the tensile strength of ECC2, the tensile strain capacity significantly enhanced to 4.1%, and the crack width decreased. This is due to a dropping chemical bond between fiber and matrix with the increasing FA content (Yang et al., 2007). Compared to ECC1, ECC2-C1 achieved a comparable value of initial cracking strength and tensile strength as 0.1% CNCs were incorporated. Specifically, the tensile strain capacity of ECC2-C1 was nearly two times that of ECC1, and ECC2-C1 possessed a tighter crack width than ECC1, which was conducive to self-healing capacity and durability.

3.5 Fiber dispersion

To obtain the internal characteristics of the fiber distribution, the fibers were reconstructed and extracted by utilizing ORS Dragonfly software. X-CT micro-computed tomography can identify different materials based on their density and provide a gray-scale presentation in which the greater the density is, the higher the gray scale is. All the fibers regarded as the regions of interest (ROI) should be separated from the matrix by threshold segmentation. It should be noted that the density of the PVA fibers was close to the other components, so an initial threshold segmentation might include much unwanted noise. ORS Dragonfly software provides a deep learning tool based on artificial intelligence (AI) to denoise and enhance images, improving the precision of segmentation. The deep learning steps were as follows:

a. Selecting 10 serial 2D slices with distinct fiber characteristics from all the 2D slices.
b. Marking accurately all the fibers as ROI in these 10 slices by an ROI painter tool.
c. Using the deep learning tool and training the data of these 2D slices for creating a specific deep learning model.
d. Applying the model to all the 2D slices and checking the accuracy of the result.
e. Adjusting some parameters influencing the accuracy of the deep learning and choosing the best optimal parameter.

It should be noted that due to the limited number of slices used to perform the deep learning, the data perpendicular to the XY plane slices could not be correctly identified. Therefore, we must extract the ROI in the XY, XZ, and YZ planes respectively, and then unite the three ROI.

Figures 10–12 present the ROI segmentation and 3D reconstruction of the composites having 0%, 0.2%, and 0.4% of the CNCs respectively. It can be seen in Figures 10C, 11C, 12C that the distribution of fibers in the matrix was not uniform in the 3D images. During pouring the fresh material into the mold, we ensured that the fresh materials freely flowed into the models as much as possible, so the fibers were more likely to be parallel to the tensile direction. Comparing the fiber 3D reconstruction images reveals that the fibers of the composites with 0.2% and 0.4% of the CNCs tended more to be parallel to the tensile direction. Highly inclined fibers usually tend to reduce their ability to bridge cracks (Tosun-Felekoğlu et al., 2014). A proper content of the CNCs increased the yield stress and plastic viscosity of the matrix, which could help to break down the agglomerate of the PVA fibers, so fibers could be well dispersed. However, at a CNC content higher than 0.2%, the addition of the CNCs gave rise to too high yield stress and plastic viscosity of the matrix, which might impose a negative impact on the dispersion of the PVA fibers. The probability of the appearance of weakest cross-sections might be higher at either too high or too low fiber volume fractions in local sections, which decreased the ductility of the ECC.

A fluorescence technology was proposed to evaluate the dispersion of the fibers in the 2D plane (Torigoe et al., 2003; Yeon et al., 2009). Since the 3D image reconstruction technique has been utilized to detect the porosity and internal defects of cementitious composites, it is also feasible to reconstruct the fibers inside cementitious composites in 3D images (Liu et al., 2013). In the current work, although the dispersion of the PVA fibers was evaluated by a qualitative method instead of a quantitative method due to the limitation of the software utilized, the results obtained were still valuable for the application of CNCs and the evaluation of the fiber distribution.

4 Conclusion

This work preliminarily investigates the application of a green renewable nano-material, i.e., cellulose nanocrystals, in preparing engineered cementitious composites. To this end, a series of systematic analyses was conducted to study the effect of the CNCs on the rheology, microstructure, mechanical properties, and fiber distribution of the ECC. The following conclusions can be drawn from the findings of this work:

(1) The addition of the CNCs had an obvious effect on the yield stress and plastic viscosity of the ECC matrix, and the CNCs could be used as a viscosity-enhancing admixture to adjust the viscosity of the fresh cement matrix.
(2) LF-NMR analysis confirmed that the addition of the CNCs effectively reduced the total porosity of the ECC and refined its pore size distribution, improving its compactness.
(3) The average compressive strength of the ECC significantly improved with an increase in the amount of the CNCs owing to their filler effect. At a CNC content of 0.1%, 0.2%, and 0.4%, the compressive strength was enhanced by 19.6%, 26.6%, and 33% respectively. The compressive strength of ECC decreased with the increase of FA content, because a higher replacement of OPC by FA led to a decreasing cement hydration degree.
(4) Raising the CNC content from 0% to 0.4% dropped the tensile strain-hardening capacity of the ECC from 1.6% to 0.5%. However, the corresponding initial cracking strength increased steadily from 3.6 to 5.1 MPa. Further, the incorporation of 0.1% CNCs could effectively compensate for the decrease in strength due to the existence of more FA, while a relatively high level of tensile strain capacity as well as tight crack width remained. Thus, an optimal CNC content of 0.1% was suggested for ECC, which produced an enhanced strength and an acceptable drop in tensile strain capacity.
(5) By the application of X-ray micro-CT, the fiber distribution was investigated through the ROI extraction and 3D reconstruction images. A significant improvement in the fiber distribution could be seen with the addition of the CNCs since they controlled the viscosity of the fresh matrix in a reasonable range.

In future works, it remains to be demonstrated the theory that CNC, as a rod-shaped whisker, might resist microscopic cracks, and it will be difficult for the CNCs distributed in the matrix through the electron microscope. Moreover, the CNCs played an important role in enhancing the strength of the matrix, so engineering the interface between the matrix and fibers to avoid the rupture of PVA fibers is crucial in better meeting the requirement of the pseudo-strain-hardening behavior. It is worth mentioning that the characteristics of CNCs that are conducive to the strength development of ECC have

great potential in the development of high-strength ECC. CNCs can be considered for high-strength ECC developed by PE fibers.

Data availability statement

The original contributions presented in the study are included in the article/supplementary material, further inquiries can be directed to the corresponding authors.

Author contributions

XY: Conceptualization, Methodology, Writing–original draft. J-GR: Investigation, Methodology, Writing–review and editing. L-XL: Conceptualization, Data curation, Writing–review and editing. ZW: Supervision, Writing–review and editing. Q-HZ: Data curation, Formal Analysis, Supervision, Writing–review and editing, Q-LL: Funding acquisition, Supervision, Writing–review and editing.

Funding

The author(s) declare that financial support was received for the research, authorship, and/or publication of this article. This work was supported by the National Natural Science Foundation of China with Grant (No. 52078282).

Conflict of interest

Authors Jian-Guo Ren and Qiao-Ling Liu were employed by Engineering Research Institute of Appraisal and Strengthening of Shandong Jianzhu University Co., Ltd. Author Lian-Xu Li was employed by China Tobacco Shandong Industrial Co., Ltd.

The remaining authors declare that the research was conducted in the absence of any commercial or financial relationships that could be construed as a potential conflict of interest.

Publisher's note

All claims expressed in this article are solely those of the authors and do not necessarily represent those of their affiliated organizations, or those of the publisher, the editors and the reviewers. Any product that may be evaluated in this article, or claim that may be made by its manufacturer, is not guaranteed or endorsed by the publisher.

References

Arain, M. F., Wang, M., Chen, J., and Zhang, H. (2019). Study on PVA fiber surface modification for strain-hardening cementitious composites (PVA-SHCC). *Constr. Build. Mater.* 197, 107–116. doi:10.1016/j.conbuildmat.2018.11.072

Cao, Y., Tian, N., Bahr, D., Zavattieri, P. D., Youngblood, J., Moon, R. J., et al. (2016). The influence of cellulose nanocrystals on the microstructure of cement paste. *Cem. Concr. Compos.* 74, 164–173. doi:10.1016/j.cemconcomp.2016.09.008

Cao, Y., Zavaterri, P., Youngblood, J., Moon, R., and Weiss, J. (2015). The influence of cellulose nanocrystal additions on the performance of cement paste. *Cem. Concr. Compos.* 56, 73–83. doi:10.1016/j.cemconcomp.2014.11.008

Cappellari, M., Daubresse, A., and Chaouche, M. (2013). Influence of organic thickening admixtures on the rheological properties of mortars: relationship with water-retention. *Constr. Build. Mater.* 38, 950–961. doi:10.1016/j.conbuildmat.2012.09.055

Ding, C., Guo, L., Chen, B., Xu, Y., Cao, Y., and Fei, C. (2019). Micromechanics theory guidelines and method exploration for surface treatment of PVA fibers used in high-ductility cementitious composites. *Constr. Build. Mater.* 196, 154–165. doi:10.1016/j.conbuildmat.2018.11.118

Ding, Y., Liu, J. P., and Bai, Y. L. (2020). Linkage of multi-scale performances of nano-CaCO3 modified ultra-high performance engineered cementitious composites (UHP-ECC). *Constr. Build. Mater.* 234, 117418. doi:10.1016/j.conbuildmat.2019.117418

Ghafari, E., Costa, H., and Júlio, E. (2015). Critical review on eco-efficient ultra high performance concrete enhanced with nano-materials. *Constr. Build. Mater.* 101, 201–208. doi:10.1016/j.conbuildmat.2015.10.066

Horikoshi, T., Ogawa, A., Saito, T., and Hoshiro, H. (2006). Properties of polyvinyl alcohol fiber as reinforcing materials for cementitious composites. *Int. RILEM Work. High. Perform. Fiber Reinf. Cem. Compos. Struct. Appl.* 2, 145–153.

Jiang, S., Shan, B., Ouyang, J., Zhang, W., Yu, X., Li, P., et al. (2018). Rheological properties of cementitious composites with nano/fiber fillers. *Constr. Build. Mater.* 158, 786–800. doi:10.1016/j.conbuildmat.2017.10.072

Keskinateş, M., and Felekoğlu, B. (2018). The influence of mineral additive type and water/binder ratio on matrix phase rheology and multiple cracking potential of HTPP-ECC. *Constr. Build. Mater.* 173, 508–519. doi:10.1016/j.conbuildmat.2018.04.038

Kumar, R., and Bhattacharjee, B. (2003). Porosity, pore size distribution and *in situ* strength of concrete. *Cem. Concr. Res.* 33, 155–164. doi:10.1016/S0008-8846(02)00942-0

Li, M., and Li, V. C. (2013). Rheology, fiber dispersion, and robust properties of Engineered Cementitious Composites. *Mater. Struct.* 46, 405–420. doi:10.1617/s11527-012-9909-z

Li, Q., Gao, X., and Xu, S. (2016). Multiple effects of nano-SiO2 and hybrid fibers on properties of high toughness fiber reinforced cementitious composites with high-volume fly ash. *Cem. Concr. Compos.* 72, 201–212. doi:10.1016/j.cemconcomp.2016.05.011

Li, V. C. (2019). *Engineered cementitious composites (ECC): bendable concrete for sustainable and resilient infrastructure*. Berlin, Heidelberg: Springer.

Li, V. C., Wang, S., and Wu, C. (2001). Tensile strain-hardening behavior or polyvinyl alcohol engineered cementitious composite. *ACI Mater. J.* 98, 483–492. doi:10.14359/10851

Li, V. C., Wu, C., Wang, S., Ogawa, A., and Saito, T. (2002). Interface tailoring for strain-hardening polyvinyl alcohol-engineered cementitious composite (PVA-ECC). *ACI Mater. J.* 99, 463–472. doi:10.14359/12325

Liu, J., Li, C., Liu, J., Cui, G., and Yang, Z. (2013). Study on 3D spatial distribution of steel fibers in fiber reinforced cementitious composites through micro-CT technique. *Constr. Build. Mater.* 48, 656–661. doi:10.1016/j.conbuildmat.2013.07.052

Liu, Q., Peng, Y., Liang, L., Dong, X., and Li, H. (2019). Effect of cellulose nanocrystals on the properties of cement paste. *J. Nanomater.* 2019, 1–7. doi:10.1155/2019/8318260

Lu, C., Lu, Z., Li, Z., and Leung, C. K. Y. (2016). Effect of graphene oxide on the mechanical behavior of strain hardening cementitious composites. *Constr. Build. Mater.* 120, 457–464. doi:10.1016/j.conbuildmat.2016.05.122

Ma, H., Cai, J., Lin, Z., Qian, S., and Li, V. C. (2017). CaCO3 whisker modified Engineered Cementitious Composite with local ingredients. *Constr. Build. Mater.* 151, 1–8. doi:10.1016/j.conbuildmat.2017.06.057

Montes, F., Fu, T., Youngblood, J. P., and Weiss, J. (2020). Rheological impact of using cellulose nanocrystals (CNC) in cement pastes. *Constr. Build. Mater.* 235, 117497. doi:10.1016/j.conbuildmat.2019.117497

Pan, J., Cai, J., Ma, H., and Leung, C. K. Y. (2018). Development of multiscale fiber-reinforced engineered cementitious composites with PVA fiber and CaCO3 whisker. *J. Mater. Civ. Eng.* 30, 1–9. doi:10.1061/(ASCE)MT.1943-5533.0002305

Pang, C. M., Leung, C. K. Y., and Sun, W. (2014). Effect of rubber particles on properties of pseudo-ductile cementitious composites. *Adv. Mater. Res.* 936, 1456–1462. doi:10.4028/www.scientific.net/AMR.936.1456

Sahmaran, M., Bilici, Z., Ozbay, E., Erdem, T. K., Yucel, H. E., and Lachemi, M. (2013). Improving the workability and rheological properties of Engineered Cementitious Composites using factorial experimental design. *Compos. Part B Eng.* 45, 356–368. doi:10.1016/j.compositesb.2012.08.015

Struble, L. J., and Jiang, Q. (2004). Effects of air entrainment on rheology. *ACI Mater. J.* 101, 448–456. doi:10.14359/13483

Torigoe, S., Horikoshi, T., Ogawa, A., Saito, T., and Hamada, T. (2003). Study on evaluation method for PVA fiber distribution in engineered cementitious composite. *J. Adv. Concr. Technol.* 1, 265–268. doi:10.3151/jact.1.265

Tosun-Felekoğlu, K., Felekoğlu, B., Ranade, R., Lee, B. Y., and Li, V. C. (2014). The role of flaw size and fiber distribution on tensile ductility of PVA-ECC. *Compos. Part B Eng.* 56, 536–545. doi:10.1016/j.compositesb.2013.08.089

Wang, S., and Li, V. C. (2004). "Tailoring of pre-existing flaws in ECC matrix for saturated strain hardening," in In proceedings of the fifth International Conference on Fracture Mechanics of Concrete and Concrete Structures, Vail, CO, January 12–16, 2004, 1005–1012.

Wang, X., Liu, C., Liu, S., Yan, C., Zhang, J., and Li, H. (2020). Compressive strength of pile foundation concrete in permafrost environment in China. *Constr. Build. Mater.* 247, 118431. doi:10.1016/j.conbuildmat.2020.118431

Xi, B., Zhou, Y., Yu, K., Hu, B., Huang, X., Sui, L., et al. (2020). Use of nano-SiO2 to develop a high performance green lightweight engineered cementitious composites containing fly ash cenospheres. *J. Clean. Prod.* 262, 121274. doi:10.1016/j.jclepro.2020.121274

Xu, S., Lyu, Y., Xu, S., and Li, Q. (2019). Enhancing the initial cracking fracture toughness of steel-polyvinyl alcohol hybrid fibers ultra high toughness cementitious composites by incorporating multi-walled carbon nanotubes. *Constr. Build. Mater.* 195, 269–282. doi:10.1016/j.conbuildmat.2018.10.133

Yang, E. H., Yang, Y., and Li, V. C. (2007). Use of high volumes of fly ash to improve ECC mechanical properties and material greenness. *ACI Mater. J.* 104, 620–628. doi:10.14359/18966

Yeon, B., Kim, J., Kim, J., and Yong, Y. (2009). Quantitative evaluation technique of Polyvinyl Alcohol (PVA) fiber dispersion in engineered cementitious composites. *Cem. Concr. Compos.* 31, 408–417. doi:10.1016/j.cemconcomp.2009.04.002

Zheng, D., Yang, H., Feng, W., Fang, Y., and Cui, H. (2023). Modification mechanism of cellulose nanocrystals in cement. *Cem. Concr. Res.* 165, 107089. doi:10.1016/j.cemconres.2023.107089

frontiers | Frontiers in Materials

TYPE Original Research
PUBLISHED 17 October 2024
DOI 10.3389/fmats.2024.1389840

OPEN ACCESS

EDITED BY
Yao Ding,
Chongqing University, China

REVIEWED BY
Xiaohua Li,
Chongqing University, China
Roberto Nascimbene,
IUSS - Scuola Universitaria Superiore
Pavia, Italy

*CORRESPONDENCE
C. Shawn Sun,
shawn.sun@csun.edu

RECEIVED 22 February 2024
ACCEPTED 01 October 2024
PUBLISHED 17 October 2024

CITATION
Sun CS, Babarinde O, Kuruppuarachchi D and Farzana N (2024) Mitigation of end zone cracks in precast prestressed concrete girders using shape memory alloys.
Front. Mater. 11:1389840.
doi: 10.3389/fmats.2024.1389840

Mitigation of end zone cracks in precast prestressed concrete girders using shape memory alloys

C. Shawn Sun[1]*, Oluwatobi Babarinde[2], Dinesha Kuruppuarachchi[3] and Nahid Farzana[4]

[1]Department of Civil Engineering and Construction Management, California State University, Northridge, CA, United States, [2]Simpson Gumpertz & Heger Inc., Waltham, MA, United States, [3]Crosby Group, San Mateo, CA, United States, [4]Program of Civil Engineering, Louisiana Tech University, Ruston, LA, United States

Precast prestressed concrete girders are widely used in U.S. bridge construction. With advancements in high-performance concrete and new girder designs, these girders are now capable of achieving significantly longer spans. Such spans often require deeper girders and an increased number of prestressing strands. The resulting bursting forces at the girder ends at time of prestress release may cause end zone cracking, especially horizontal web cracks, which can compromise the durability of the girders and potentially lead to rejection by bridge owners. Current practices focus on mitigating these cracks by providing adequate end zone reinforcement, but completely eliminating them remains a challenge, as girders are typically prestressed along their length only. This paper proposes an innovative approach to combat end zone cracking through the application of vertical prestressing at the girder ends using shape memory alloys (SMAs). This method involves heating prestrained SMAs at the beam ends to induce recovery stress, thus generating vertical prestress that enhances splitting resistance and reduces web cracking. The research employed a variety of NiTi SMA reinforcement, including wires, strands, and cables, demonstrating the feasibility of this method through both small-scale and full-scale beam tests. The beam tests demonstrated the shape memory effects of SMAs and the impact of induced prestressing. The findings suggest that properly designed vertical prestress can effectively counteract bursting forces and mitigate concrete cracking.

KEYWORDS

shape memory alloys, vertical prestress, end zone cracking, bursting force, splitting resistance, precast prestressed concrete girder, recovery stress

1 Introduction

According to the Federal Highway Administration, nearly one-quarter of the over half a million U.S. bridges use precast prestressed concrete girders (Sirca and Adeli, 2005). Recent advancements in high-performance concrete and the development of new girder sections and larger strand sizes have greatly influenced this widespread adoption, enabling the construction of bridges with significantly longer spans. These innovations have enabled the construction of bridges with substantially longer spans. However, longer spans typically demand deeper girders and an increased number of prestressing strands. When

FIGURE 1
End zone cracks in a precast prestressed concrete beam (derived from Okumus and Oliva, 2013).

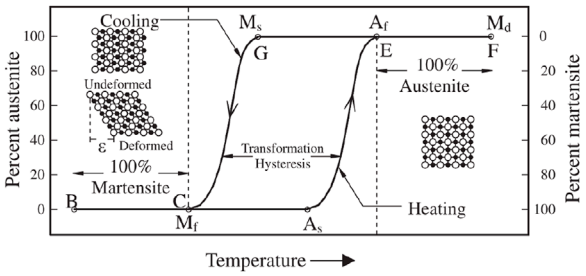

FIGURE 2
Phase transformation and change in SMAs' crystalline structure (sourced from Alam et al., 2007).

TABLE 1 List of SMA wire, strand, and cable.

Item	Description	Area (mm^2)	A_f (°C)
Wire	2.0 mm diameter	3.2	94
Strand	7-wire strand; 2.8 mm diameter	4.8	65
Cable	7-strand cable; 8.4 mm diameter	33.5	65

pretensioned concrete girders are manufactured on a precast bed, the prestressing force in the strands is released to the girder ends through either flame cutting or gradual release using hydraulic jacks (Russell, 2017). This force transition from the strands to the concrete may lead to a significant concentration of stresses, which in turn can cause end-zone cracking (Tadros et al., 2010). A variety of end zone cracks have been identified, including horizontal and inclined cracks in the web, as well as bottom flange cracks (Figure 1). These cracks pose a potential risk to the girders' durability, especially when bridges are located in environments where chloride ions are readily available and can penetrate the concrete, reaching the reinforcement and potentially causing corrosion. As a result, precast producers may need to repair these cracks or face potential rejection of the girders by some owners. In addition, this issue can offset the advantage of low maintenance costs associated with concrete bridge construction by increasing future life cycle expenses. Therefore, addressing these durability concerns is crucial in the design and maintenance of precast concrete bridges.

The prevalent approach to managing the end zone cracks involves ensuring adequate vertical reinforcement in the zone, as established by extensive research, including NCHRP Report 654 by Tadros et al. (2010) which explored the assessment and repair of end zone cracking in prestressed concrete girders. As per the AASHTO LRFD Bridge Design Specifications (AASHTO, 2020), vertical reinforcement is required to counteract four percent of the total prestressing force at the time of prestress release, positioned as close to the girder end as feasible. When girders incorporate a large number of prestressing strands, congested reinforcing configurations become essential to effectively control the cracking. More importantly, the end zone cracks cannot be eliminated, primarily because the girders are prestressed along their lengths only, i.e., there is no prestressing along their heights. As a result, the bursting force at prestress release causes the girder ends to crack. To resolve the problem of end zone cracking, this paper presents an innovative solution using Shape Memory Alloys (SMAs) to apply vertical prestressing at the girder ends.

SMAs are unique materials that undergo a reversible solid-solid phase transformation between two primary phases: martensite and austenite (Ozbulut and Hamilton, 2015). Their distinct property is the ability to endure large deformations and revert to their original shape either by stress removal (superelasticity) or heating (shape memory effect) (Alam et al., 2007). At lower temperatures, SMAs are predominantly in the martensite phase, transforming to austenite upon heating. This transformation is characterized by four distinct temperatures: martensite start (M_s), martensite finish (M_f), austenite start (A_s), and austenite finish (A_f), where the SMA is fully martensitic below M_f and fully austenitic above A_f (Figure 2).

SMAs, widely used in civil engineering, have mechanical properties that significantly vary based on their metal composition. Popular SMAs include NiTi, NiTiNb, and iron-based varieties. Pioneering work by Maji and Negret (1998) utilized NiTi SMAs' shape memory effect for concrete beam prestressing. SMA strands, initially pretensioned, were embedded in mortar beams, and upon curing, activated by heat to induce prestressing. El-Tawil and Ortega-Rosales (2004) tested small mortar beams prestressed with SMA tendons. These prestrained tendons, when heated, generated significant prestressing force in the beams. Their studies comparing 2.5 mm NiTi and 6.3 mm NiTiNb wires found that while NiTi showed substantial recovery stress, NiTiNb was more suitable for permanent applications due to its sustained stress after heat removal. Sherif et al. (2014) explored self-post-tensioning of concrete beams using SMAs, leveraging the heat of hydration from grouts to

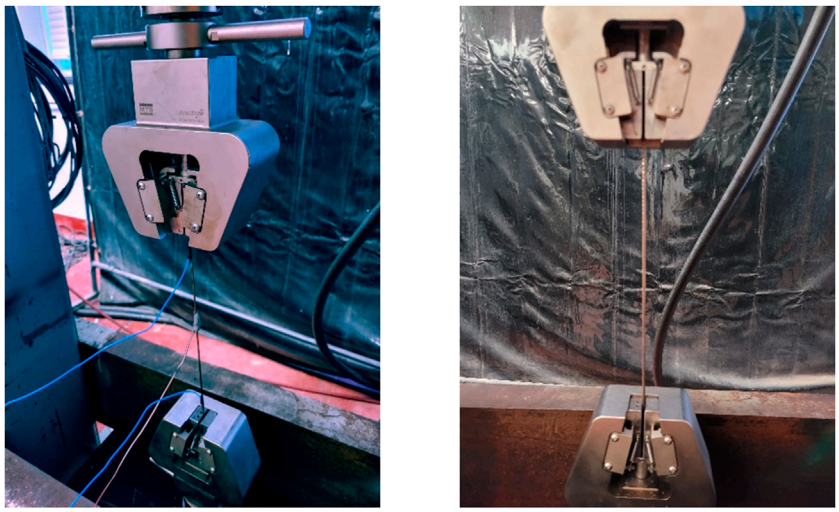

FIGURE 3
Tension test of the SMA wire or strand. **(A)** SMA wire. **(B)** SMA strand.

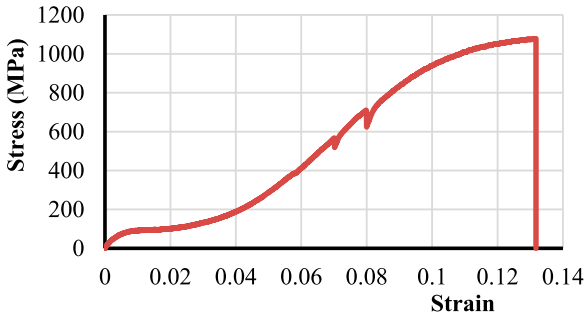

FIGURE 4
Stress-strain diagram of the SMA wire.

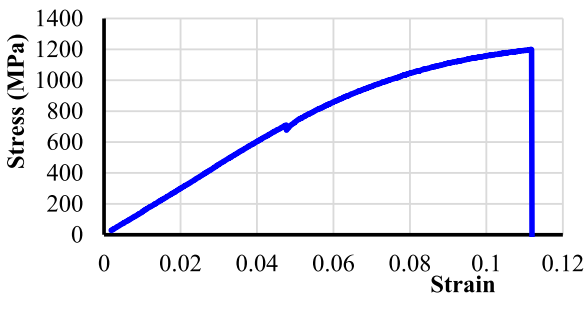

FIGURE 5
Stress-strain diagram of the SMA strand.

activate NiTiNb alloys. This method achieved recovery stresses over 500 MPa post-cooling. Moser et al. (2005) investigated SMA short fibers for prestressing concrete beams. They shaped SMA wires by inelastic elongation into loops and stars, embedding them in mortar prisms. Upon heating the set mortar, the SMAs were activated, generating recovery stress that prestressed the specimens. This process effectively induced compressive stresses of up to 7 MPa, thus demonstrating the effectiveness of SMA fibers in prestressing concrete. These studies collectively illustrate the versatility and efficacy of SMAs in enhancing concrete structures, particularly in prestressing applications. The diverse methods of application and types of SMA used reflect the growing potential of these materials in modern structural engineering.

Soroushian et al. (2001) utilized iron-based SMAs for the repair and strengthening of concrete structures. They demonstrated that these alloys could create post-tensioning forces in structural systems. SMA rods were effectively used to convey corrective forces for the reinforcement and repair of concrete beams, specifically in bridge beams lacking adequate shear strength. Andrawes (2019) developed an innovative Adaptive Prestressing System (APS) for concrete crossties using SMAs. In his research, NiTiNb SMA wires were used to apply prestress at targeted areas of the crossties. Various configurations of SMA prestressing systems, including straight, L-shaped, and U-shaped wires, were tested, confirming the ability of SMA wires to induce prestressing forces precisely where needed. Sinha et al. (2020) proposed a novel post-tensioning method using unbonded near-surface mounted NiTiNb SMA wires. When these wires, prestrained by 2.5%, were Ohmic heated in a constrained environment, they generated a recovery stress of about 500 MPa. This technique was applied to pre-cracked concrete girders, where heating the SMA wires significantly reduced crack widths by up to 74%, showcasing the potential of SMAs in repair of concrete structures.

Numerous researchers have investigated the potential of using SMAs for introducing prestress in concrete beams, primarily focusing on new construction or the repair and strengthening of existing concrete structures. However, the application of SMAs,

FIGURE 6
Tension test of a SMA cable.

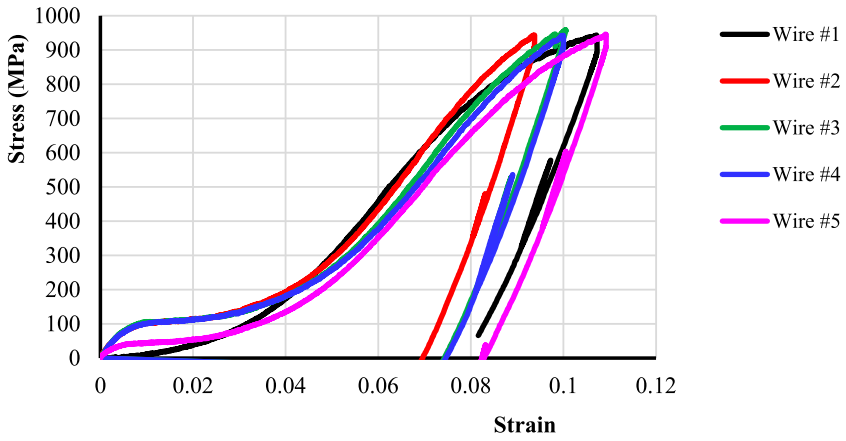

FIGURE 7
Stress-strain diagrams of SMA wires due to loading and unloading.

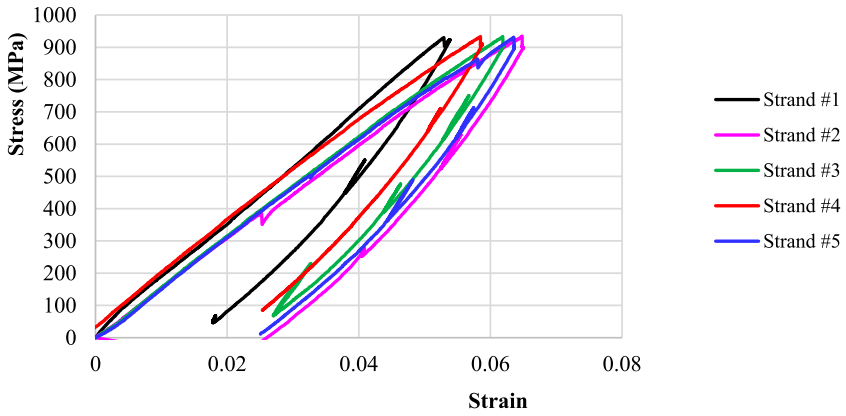

FIGURE 8
Stress-strain diagrams of SMA strands due to loading and unloading.

specifically at the end zones of precast prestressed concrete girders, has not yet been explored. This study marks the first endeavor to evaluate the feasibility of using SMAs to increase splitting resistance at end zones of prestressed concrete girders. By incorporating SMAs to introduce vertical prestressing at the girder ends, this innovative approach is expected to contribute to the development of more durable and reliable prestressed concrete structures. The study was approached in three steps. First, experiments were conducted to characterize the mechanical properties of various SMAs. Next, the effectiveness of SMA in prestressing in small beam specimens was investigated. Finally, a full-scale prestressed concrete girder with SMAs placed at the end zone was studied, incorporating insights

TABLE 2 List of small-scale beams.

Beam no.	SMA reinforcement type	Mortar or concrete	Beam section (mm × mm)	Beam length (mm)	Bonded or unbonded
1	Two wires	Mortar	25 × 25	305	Bonded
2	One strand	Mortar	25 × 25	305	Bonded
3	One cable	Concrete	51 × 51	305	Unbonded
4	One cable	Concrete	51 × 51	305	Bonded

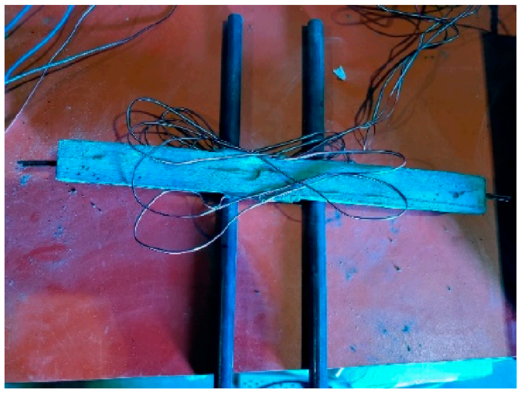

FIGURE 9
Test setup of Beam No. 1.

from the previous steps. This paper presents the experimental studies, results, and discussions.

2 Experimental study

In this study, several suppliers were consulted to source NiTi and NiTiNb SMAs. However, the majority of these suppliers were only able to provide NiTi SMAs in small diameters, with no suitable NiTiNb SMAs available. Consequently, the research team utilized NiTi SMA wires, strands, and cables from a single supplier. Table 1 details these materials, including their descriptions, cross-sectional areas, and austenite finish (A_f) temperatures.

The experimental study included tension tests on SMA wires, strands, and cables to determine their stress-strain relationships. It also featured small-scale beam tests to evaluate the potential of implementing prestressing in concrete beams with SMA components. In addition, a full-scale beam test was performed to explore the effectiveness of SMA cables in mitigating end zone cracking upon prestress release.

2.1 Tension tests of the SMA wires, strands, and cables

An MTS machine with MTS Advantage™ Wedge Grips was used to assess the stress-strain behavior of SMA wires and strands until failure. Each wire or strand was secured with a clear length of 254 mm in-between the grips (Figure 3). The SMA material was kept at ambient temperatures outside of the phase transition range and cut to the desired specimen length. The SMA cable consisted of seven strands, which were separated into individual strands after cutting for testing. During testing, a displacement-controlled approach was adopted, applying a loading rate of 5.1 mm per minute. An initial preload of 89 N was applied to rectify any sag and spiral pre-existing shape present in the wire and strand specimens. Test data was recorded after the load and displacement associated with this low preload were zeroed out. The resulting stress-strain diagrams for the wire and strand are depicted in Figures 4, 5, respectively. It was observed that the wires exhibited an ultimate tensile strength of roughly 1,069 MPa, accompanied by a strain of about 13%. In comparison, the strands demonstrated an ultimate strength of approximately 1,200 MPa with an ultimate strain near 11%.

Due to the limitations of the MTS machine's grips for accommodating the SMA cable, its tensile properties were captured using a hydraulic mono-strand jack setup. This involved positioning ultra-high strength concrete (UHPC) blocks adjacently with the cable threaded through slots within these blocks. One end of the cable was anchored using a chuck, whereas the opposite end was tensioned using the jack, as illustrated in Figure 6. This setup facilitated the testing of two cables up to their failure point, which occurred at load levels around 38.3 kN.

2.2 Prestrained SMA wires, strands, and cables

SMA in the martensite phase subjected to inelastic deformation can recover its original shape with heat application to follow the phase transformation highlighted in Figure 2. Such inelastic deformation is introduced in the mechanical prestraining of SMA specimens. Prestrained SMA, prevented from freely recovering its original shape upon heat application, may be used to introduce counteracting stresses in the end zone of the prestressed girder. SMA specimen prestrained to known residual strain from a loading and unloading cycle will be anchored or bonded into concrete beams.

At ambient temperature, the MTS machine was employed to load and unload the SMA wires and strands, inducing residual strains. The maximum stress levels applied to both wires and strands were intentionally kept slightly below their ultimate tensile strengths to optimize the induction of residual strains. For the unloading phase, a force-control setting was utilized, operating at

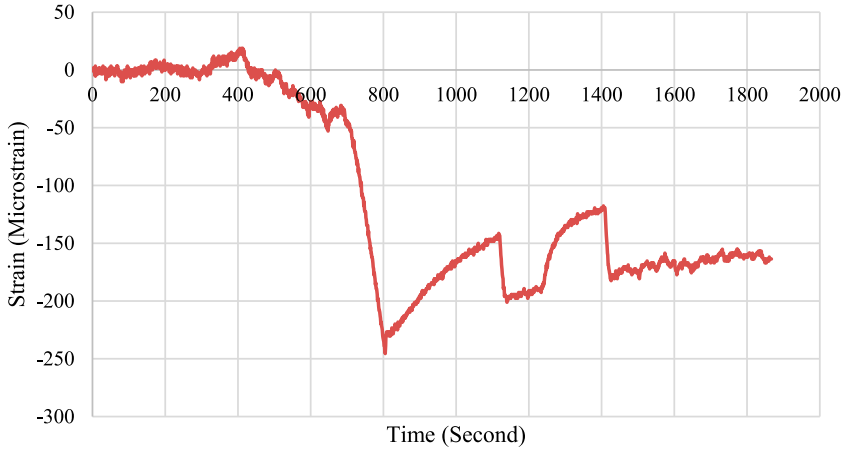

FIGURE 10
Test results of Beam No. 1.

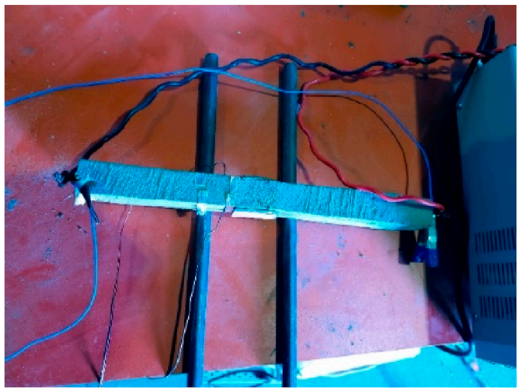

FIGURE 11
Test setup of Beam No. 2.

a rate of 22.2 N per second. This procedure led to the generation of residual strains of approximately 8% in the wires and 2% in the strands, respectively. The stress-strain behaviors of the wires and strands during these loading and unloading cycles are illustrated in Figures 7, 8. This experiment was repeated with five wires and five strands, yielding generally consistent results across samples of the same type. The SMA cables were tensioned using the mono-strand jack up to a force of 34.7 kN and then gradually released, resulting in residual strains. Consequently, the cables exhibited residual strains of about 1.7%.

2.3 Small-scale beam tests

To assess the feasibility of applying prestressing to concrete beams, prestrained NiTi wires, strands, and cables were embedded in small-scale beams made from either Type-M mortar or concrete. The SMA reinforcement was either bonded or unbonded with the mortar or concrete. Table 2 presents the beam details, including SMA reinforcement types, the material used (mortar or concrete), cross-sectional dimensions, beam lengths, and the bonding status of the SMA reinforcement. Mortar was used for Beam Nos. 1 and 2, while concrete was used for Beam Nos. 3 and 4. All beams included bonded SMA reinforcement, except for Beam No. 3, which had unbonded reinforcement. Subsequent sections will delve into the specifics of each specimen type and discuss their respective test outcomes.

The setup for testing Beam No. 1, depicted in Figure 9, incorporated two bundled and mortar-bonded SMA wires. Strain gauges were placed on each side of the beam at midspan to measure axial strain. Figure 10 shows the gauges' average readings over time, in which there was a notable decrease in strain readings around 800 s due to the wires' recovery stress from electrical heating. Initially, the beam experienced a maximum compressive strain of about 250 microstrain. Subsequently, strain levels decreased as the concrete expanded from heating. As the temperature of the concrete gradually decreased, the beam's compressive strain stabilized at approximately 160 microstrain towards the end of the observation period.

The experimental setup for Beam No. 2, illustrated in Figure 11, featured a single SMA strand bonded with mortar. A strain gauge was affixed to each side face of the beam at midspan to monitor axial strain. Figure 12 presents the average strain readings from both gauges over time, following the electrical activation of the strand. The activation resulted in a peak compressive strain in the beam of around 140 microstrain. As the concrete's temperature normalized to ambient conditions, the compressive strain reduced to about 40 microstrain, indicating a considerable loss of the strand's recovery stress.

Figure 13 illustrates the experimental setup for Beam No. 3, featuring an SMA cable within a PVC pipe, unbonded with the concrete. The cable's ends were secured using chucks at both ends of the beam, with one anchor fully seated when the cable was prestrained. Subsequent re-tensioning of the cable to around 3.4 kN compensated for any anchor set loss. Strain gauges were affixed to each side of the beam at midspan to monitor axial strain. Figure 14 depicts the average strain readings over time from these gauges. Upon electrical heating of the cable, the beam experienced a peak compressive strain of 50 microstrain, corresponding to a

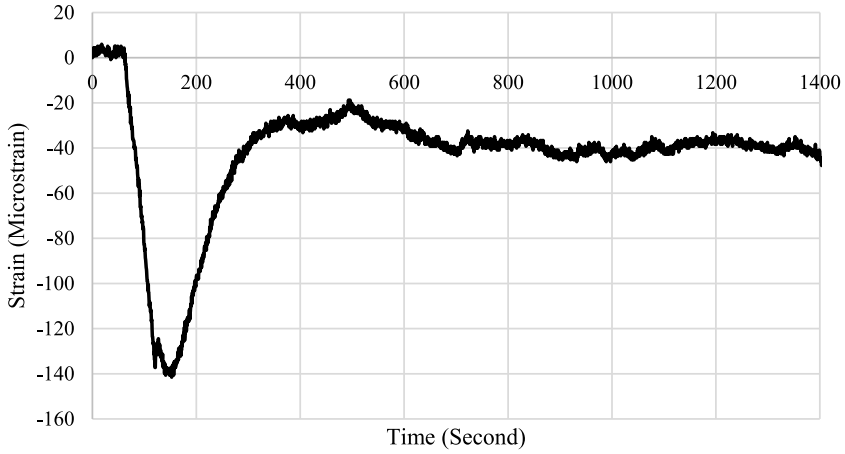

FIGURE 12
Test results of Beam No. 2.

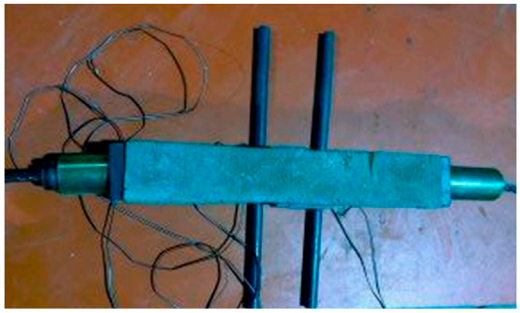

FIGURE 13
Test setup of Beam No. 3.

compressive stress of approximately 1.2 MPa in the concrete beam. This indicated the induced recovery stress generated a compressive force near 3.1 kN. However, this recovery stress diminished once the heating ceased.

Figure 15 presents the setup for Beam No. 4, which incorporates an SMA cable directly bonded to the concrete. Strain gauges were affixed to both sides of the beam at midspan to measure axial strain. The average strain measurements from these gauges over time are depicted in Figure 16. Activation of the SMA cable induced a peak compressive strain of 10 microstrain in the beam, corresponding to a compressive stress of approximately 0.24 MPa in the concrete. This indicated the recovery stress from the SMA cable generated a compressive force of about 0.6 kN. The minimal recovery stress observed is attributed to the beam's short length, which was insufficient to develop the cable. Similarly to Figure 14, the recovery stress gradually diminished after the cessation of heating.

2.4 Full-scale beam test

A concrete beam was constructed in the laboratory to evaluate the effectiveness of SMAs in mitigating end zone cracking at prestress release. Illustrated in Figure 17, the beam section is comparable to an AASHTO Type I beam with simplified flanges to facilitate its fabrication. The beam measures 610 mm in height with a 152 mm wide web. Flanges are 305 mm in width and are 203 mm thick. Provided reinforcement included #13 stirrups in both flanges, pairs of #13 C-bars along the web, and #13 longitudinal bars. The C-bars were spaced at approximately 610 mm along the beam length except at the ends, in which two pairs were placed at 254 mm and 406 mm from each beam end, respectively. The shear reinforcement was intentionally provided far from the beam end to eliminate its contribution to the splitting resistance. The stirrups in the flanges were spaced at 102 mm for a distance of 610 mm from each beam end to provide sufficient confinement for the prestressing strands. Four 15.2 mm-diameter, Grade 1862 strands were placed in flexible polymer plastic tubing in each flange. Figure 18 shows the layout of the prestressing strands and reinforcing bars. One of the beam's ends included three pairs of 13 mm-diameter PVC pipes installed vertically to house the SMA cables.

The beam formwork was removed 3 days after the concrete pour when the concrete strength reached about 23 MPa based on cylinder tests. Four SMA cables were eventually installed at one beam end and the cable ends were anchored by chucks. The first cable was electrically heated prior to installation of the other three cables. The heating was stopped after the cable's temperature reached approximately 100 C and the current was about 39 amps. Afterward, the remaining three cables were placed. Their distances measured to the beam end varied from 89 to 229 mm to allow for evaluation of their effects on the splitting resistance (Figure 19).

The longitudinal steel strands were post-tensioned 4 days after the concrete pour. They were numbered and tensioned in a sequence that ensured symmetry (see Figure 20). The strands were jacked using a hydraulically operated monostrand jack and anchored with strand chucks. Two strain gauges were installed at the end face of the beam web. The strands were tensioned sequentially at one end of the beam, from strand No. 1 to 8 as shown in Figure 20. On average, each strand was tensioned to approximately 60.7 kN. The strands were not fully tensioned to the maximum allowable force due to the relatively low concrete strength at the time of testing.

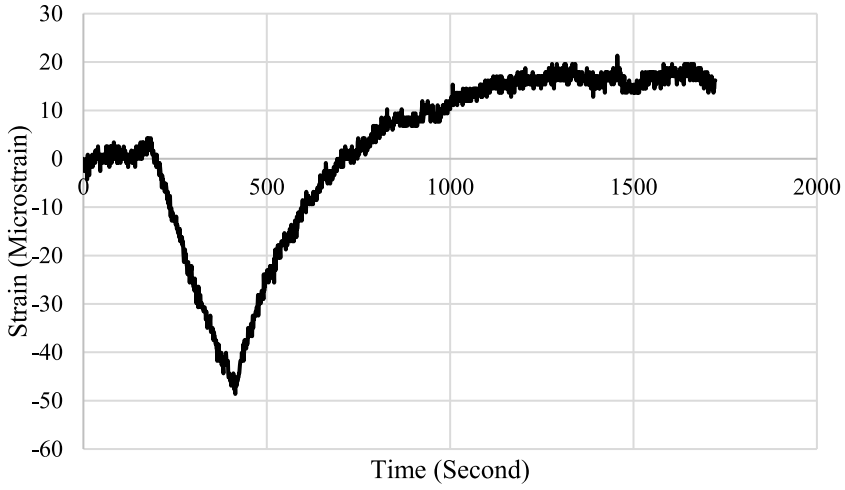

FIGURE 14
Test results of Beam No. 3.

FIGURE 15
Test results of Beam No. 4.

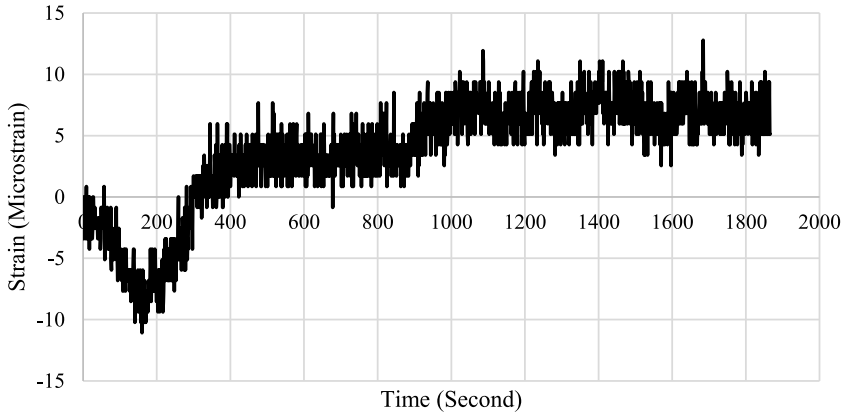

FIGURE 16
Test results of Beam No. 4.

The readings of the two strain gauges at the beam end were collected and plotted in Figures 21–23. Figure 21 shows the gauge readings when Cable 1 was electrically heated. The recovery stress of the SMA cable resulted in strain changes of approximately 15 microstrain at one gauge and 10 microstrain at the other gauge. As an average, these strains corresponded to approximately 0.3 MPa

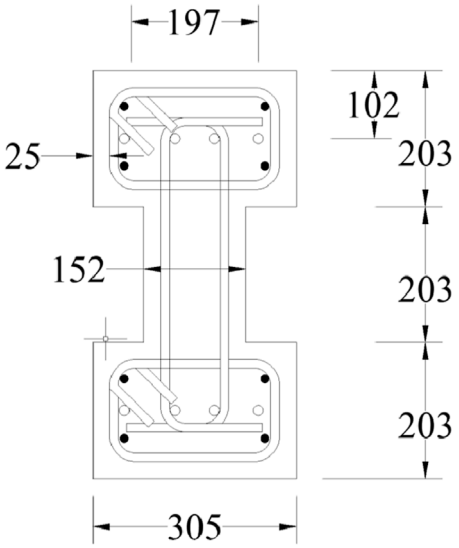

FIGURE 17
Beam section and reinforcement detail.

FIGURE 18
Reinforcement layout.

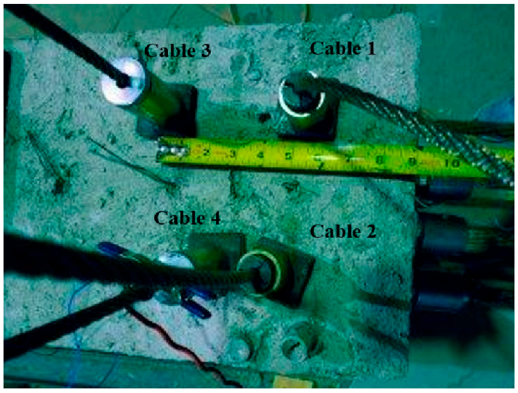

FIGURE 19
Layout of the SMA cables.

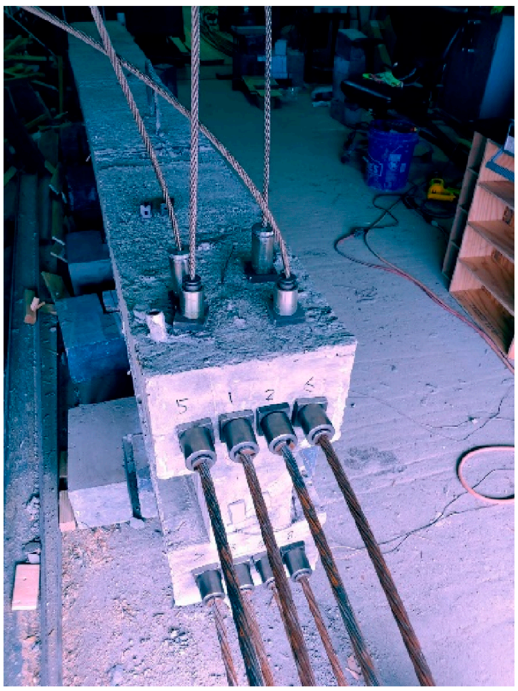

FIGURE 20
Numbering of the steel strands.

compressive stress in the beam web concrete. Similarly, Figure 22 illustrates the gauge readings when Cables 2 to 4 were electrically heated. Activating Cable 2 resulted in approximately 15 microstrain at both gauges. Given their further distance from the beam end, Cables 3 and 4 exerted a less pronounced effect, contributing to around 10 microstrain each. Collectively, the four cables exerted roughly 40 microstrain or 1.0 MPa of compressive stress at the beam's end mid-height. Following the tensioning of all steel strands, an average strain change of 80 microstrain was observed (Figure 23), equating to 1.9 MPa of tensile stress at the instrumented locations. Given that the concrete's modulus of rupture is about 3.0 MPa, the tensile stress generated was insufficient to cause cracking in the web concrete.

3 Discussions

Initially, attempts to heat the SMAs used a heat gun in conjunction with a direct power supply. However, it soon became evident that the heat gun's inability to uniformly distribute heat made it less effective compared to direct electrical heating. Direct electrical heating required a relatively high current, up to 40 amps,

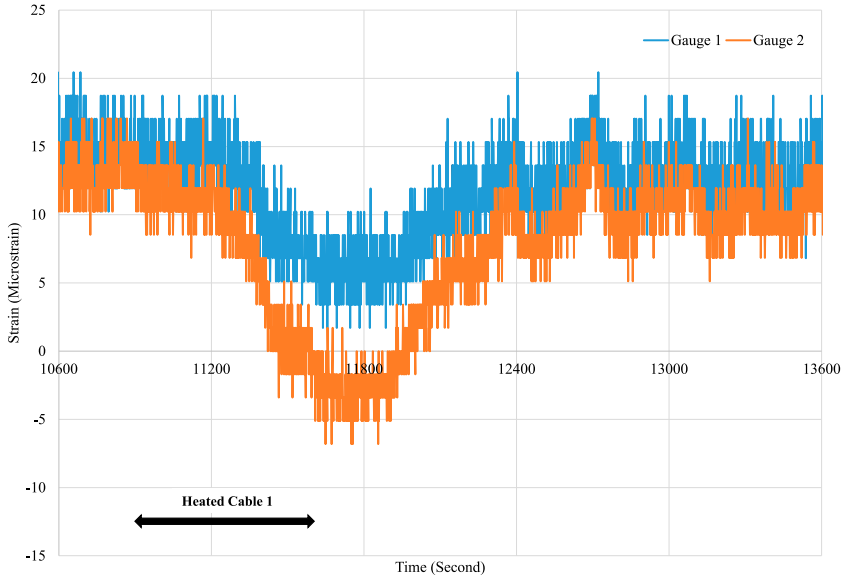

FIGURE 21
Gauge readings due to heating Cable 1.

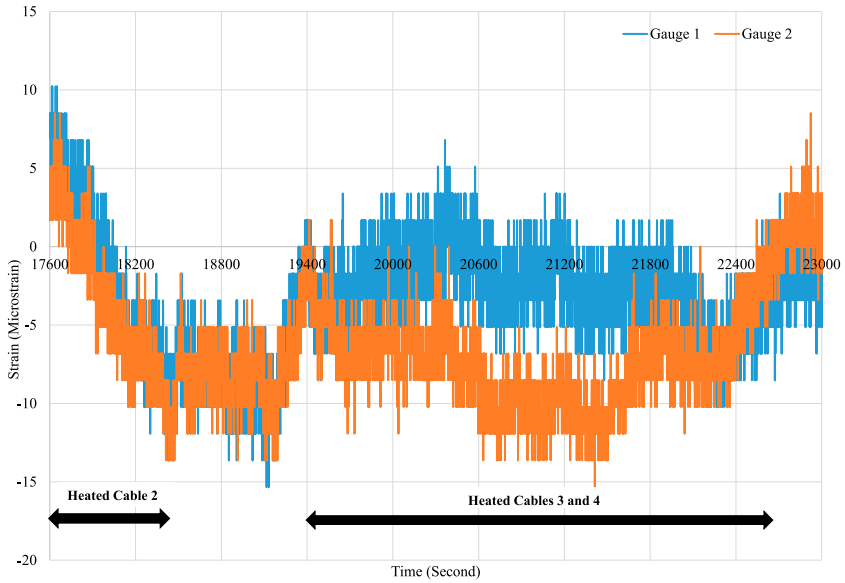

FIGURE 22
Gauge readings due to heating Cables 2 to 4.

to heat the SMAs efficiently and achieve the desired temperature uniformly.

The effectiveness of bonded SMAs in generating prestress in a concrete beam is significantly influenced by the surface conditions of the SMAs. Bending or anchoring the ends of the SMAs can enhance the development of the reinforcement. These modifications improve the interaction between the SMAs and the surrounding concrete matrix, optimizing the engagement and leveraging the recovery stress to maximize the prestressing effect. For unbonded SMAs, the effectiveness of the anchors used should be carefully chosen to achieve the desired prestress. It is important to minimize anchor set losses when implementing an unbonded system to ensure that the intended prestressing force is effectively transferred to the concrete beam. For shorter concrete members, it may be practical to use unbonded SMAs to engage the prestressing force more efficiently.

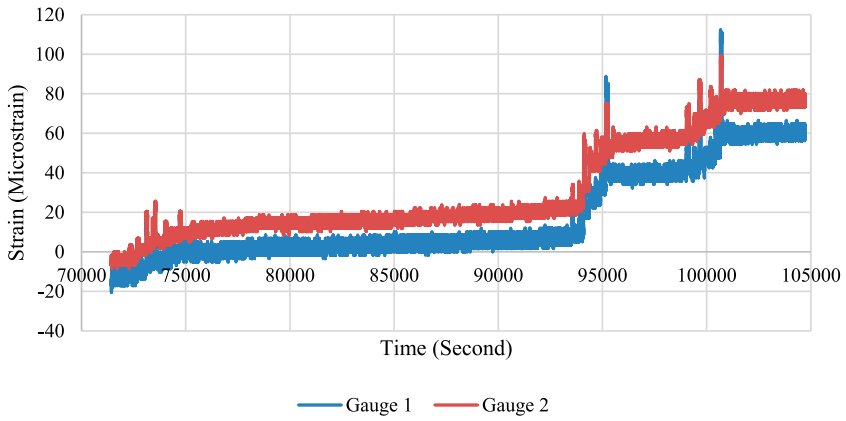

FIGURE 23
Gauge readings due to tensioning steel strands.

In the full-scale beam test, the application of SMA cables resulted in approximately 1.0 MPa of compressive stress in the beam web. This demonstrates that, with a sufficient amount of SMA cables, the induced prestressing force can be substantial and effective in preventing concrete cracking associated with bursting forces at prestress release. Laboratory tests revealed that NiTi SMAs lost a significant portion of their recovery stresses once the applied heat was removed. This finding highlights the potential advantage of using alternative SMAs, such as NiTiNb, which exhibit a wider thermal hysteresis. As recommended by the research of El-Tawil and Ortega-Rosales (2004), NiTiNb SMAs may be more suitable for real-world applications due to their improved performance characteristics in maintaining recovery stresses.

4 Conclusion

This paper investigated the feasibility of using SMAs to introduce vertical prestress at the ends of pretensioned concrete beam girders. The study involved testing small-scale mortar and concrete beams incorporating SMA wires, strands, and cables to assess their shape memory effects and the impact of induced prestressing. Both unbonded and bonded SMAs were evaluated for their effects on resulting compressive strains in the specimens. In addition, a full-scale concrete beam was produced to further assess the effectiveness of SMAs in mitigating end zone cracking caused by the release of prestressing forces. The end zone of the post-tensioned concrete beam was instrumented to measure vertical strains resulting from the SMA's shape memory effects. Based on the laboratory testing results, the following conclusions are drawn:

1. Throughout the small- and full-scale beam tests, it was consistently observed that prestressing forces could be successfully introduced upon the activation of the SMAs. This underscores the potential of SMAs in structural engineering applications, specifically in introducing vertical prestress at the ends of precast prestressed concrete beams. The ability of SMAs to generate prestressing forces upon activation demonstrates their effectiveness and versatility in enhancing the performance and durability of concrete structures.
2. In the full-scale beam test, the SMA cables provided resulted in substantial vertical compressive stress along the beam web. This induced vertical prestress can effectively increase the beam's splitting resistance, thereby reducing the concrete cracking during the release of prestressing forces. The successful application of this prestressing technique underscores its potential to improve the overall structural performance of precast prestressed concrete beams by mitigating issues commonly associated with prestress release.
3. The laboratory tests revealed that the recovery stresses of the NiTi wires, strands, and cables were largely lost once the electrical heating was removed. Despite this limitation, the tests validated the proposed concept of using SMAs to introduce vertical prestress at the ends of precast prestressed concrete beams. However, other types of SMAs that exhibit a wider thermal hysteresis may be more effective in providing a permanent prestressing force.

Data availability statement

The original contributions presented in the study are included in the article/supplementary material, further inquiries can be directed to the corresponding author.

Author contributions

CS: Conceptualization, Funding acquisition, Methodology, Supervision, Writing–original draft, Writing–review and editing. OB: Data curation, Formal Analysis, Writing–review and editing. DK: Data curation, Writing–review and editing. NF: Data curation, Writing–review and editing.

Funding

The author(s) declare that financial support was received for the research, authorship, and/or publication of this article. This work

was supported by the Louisiana Transportation Research Center SIO number DOTLT1000301.

Acknowledgments

The authors would like to thank Louisiana Transportation Research Center for funding this project.

Conflict of interest

Author OB was employed by Simpson Gumpertz & Heger Inc. Author DK was employed by Crosby Group.

The remaining authors declare that the research was conducted in the absence of any commercial or financial relationships that could be construed as a potential conflict of interest.

Publisher's note

All claims expressed in this article are solely those of the authors and do not necessarily represent those of their affiliated organizations, or those of the publisher, the editors and the reviewers. Any product that may be evaluated in this article, or claim that may be made by its manufacturer, is not guaranteed or endorsed by the publisher.

References

AASHTO (2020). *AASHTO LRFD bridge design Specifications*. Ninth Edition. Washington, D.C.

Alam, M. S., Youssef, M. A., and Nehdi, M. (2007). Utilizing shape memory alloys to enhance the performance and safety of civil infrastructure: a review. *Can. J. Civ. Eng.* 34 (9), 1075–1086. doi:10.1139/l07-038

Andrawes, B. (2019). *Adaptive prestressing System for concrete crossties* (No. Rail safety IDEA project 33).

El-Tawil, S., and Ortega-Rosales, J. (2004). Prestressing concrete using shape memory alloy tendons. *Struct. J.* 101 (6), 846–851. doi:10.14359/13460

Maji, A. K., and Negret, I. (1998). Smart prestressing with shape-memory alloy. *J. Eng. Mech.* 124 (10), 1121–1128. doi:10.1061/(asce)0733-9399(1998)124:10(1121)

Moser, K., Bergamini, A., Christen, R., and Czaderski, C. (2005). Feasibility of concrete prestressed by shape memory alloy short fibers. *Mater. Struct.* 38, 593–600. doi:10.1617/14327

Okumus, P., and Oliva, M. G. (2013). Evaluation of crack control methods for end zone cracking in prestressed concrete bridge girders. *PCI J.* 58 (2), 91–105. doi:10.15554/pcij.03012013.91.105

Ozbulut, O., and Hamilton, R. (2015). Smart concrete bridge girders using shape memory alloys. *Mid-Atlantic Univ. Transp. Cent.*

Russell, H. G. (2017). *Control of concrete cracking in bridges (No. Project 20-05, Topic 47-01)*. Washington, DC: The National Academies Press.

Sherif, M., Ozbulut, O., Landa, A., and Hamilton, R. F. (2014). "Self-post-tensioning for concrete beams using shape memory alloys," in *Smart materials, adaptive structures and intelligent systems*, 46155. American Society of Mechanical Engineers, V002T04A014. doi:10.1115/smasis2014-7564

Sinha, A., Tatar, N., and Tatar, J. (2020). Rapid heat-activated post-tensioning of damaged reinforced concrete girders with unbonded near-surface mounted (NSM) NiTiNb shape-memory alloy wires. *Mater. Struct.* 53, 88–15. doi:10.1617/s11527-020-01522-8

Sirca, G. F., and Adeli, H. (2005). Cost optimization of prestressed concrete bridges. *J. Struct. Eng.* 131 (3), 380–388. doi:10.1061/(asce)0733-9445(2005)131:3(380)

Soroushian, P., Ostowari, K., Nossoni, A., and Chowdhury, H. (2001). Repair and strengthening of concrete structures through application of corrective posttensioning forces with shape memory alloys. *Transp. Res. Rec.* 1770 (1), 20–26. doi:10.3141/1770-03

Tadros, M. K., Badie, S. S., and Tuan, C. Y. (2010). *Evaluation and repair proceduresfor precast/prestressed concrete girders with longitudinal cracking in the web, NCHRP Report 654*. Washington, D.C.: Transportation Research Board.

frontiers | Frontiers in Materials

TYPE Review
PUBLISHED 28 October 2024
DOI 10.3389/fmats.2024.1493191

OPEN ACCESS

EDITED BY
Yang Zou,
Chongqing Jiaotong University, China

REVIEWED BY
Yang Yu,
University of New South Wales, Australia
Salvatore Verre,
University of eCampus, Italy

*CORRESPONDENCE
Quan Ma,
1911672@tongji.edu.cn

RECEIVED 08 September 2024
ACCEPTED 30 September 2024
PUBLISHED 28 October 2024

CITATION
Ma Q, Duan Z, Wang J, Yin G and Li X (2024) Frost resistance and improvement techniques of recycled concrete: a comprehensive review.
Front. Mater. 11:1493191.
doi: 10.3389/fmats.2024.1493191

Frost resistance and improvement techniques of recycled concrete: a comprehensive review

Quan Ma[1]*, Zhenhua Duan[1], Jun Wang[2], Gang Yin[3] and Xi Li[2]

[1]College of Civil Engineering, Tongji University, Shanghai, China, [2]China West Construction Group Co., Ltd., China State Construction Engineering Corporation Ltd, Chengdu, China, [3]Linyi Lantai Environmental Protection Technology Co., Ltd, Linyi, China

In the pursuit of sustainable construction practices, the utilization of recycled concrete has emerged as a pivotal strategy, distinguished by its commitment to resource conservation and environmental stewardship. Nevertheless, the inherent micro-porosity and micro-cracking within the old mortar of recycled concrete may lead to weak bonding performance at the interfacial transition zone, culminating in diminished strength, reduced density, and elevated water absorption rates compared to conventional concrete, which critically impairs its performance in cold climates subjected to freeze-thaw cycles. Consequently, this paper provides a structured examination of the frost resistance properties of recycled concrete subjected to freeze-thaw cycling. Initially, the study delineates the mechanisms of frost-induced damage in recycled concrete by synthesizing the degradation pathways observed in both conventional and recycled concrete during freeze-thaw exposure. Subsequently, a detailed analysis is conducted to identify the pivotal factors affecting frost resistance, encompassing the proportion and moisture affinity of recycled aggregates, the addition of silica fume and fly ash, the water-to-cement ratio, and the degree of water saturation. In the final segment, the study compiles and reviews the strategies for bolstering the frost resistance of recycled concrete, including the incorporation of air-entraining admixtures, fiber reinforcement, and aggregate modification approaches. The objective of this research is to offer a thorough comprehension of recycled concrete, with a concentration on the mechanisms of frost damage, the critical determinants of frost resistance, and interventions to augment its resilience against freezing conditions. On this basis, the present paper, in conjunction with the characteristics and current research status of recycled concrete, proposes recommendations for the application of recycled concrete in cold regions. This review is anticipated to facilitate researchers in gaining a comprehensive understanding of the freeze-thaw characteristics of recycled concrete and the measures to enhance its frost resistance. Furthermore, it aims to assist engineering and technical personnel in selecting appropriate treatment methods to improve the frost resistance of recycled concrete in cold regions, thereby promoting the practical engineering application of recycled concrete in such areas.

KEYWORDS

recycled concrete, frost resistance, freeze-thaw cycle, influencing factors, improvement measures

1 Introduction

Concrete is primarily composed of aggregates, binder materials, water, and admixtures. It possesses excellent processing and mechanical properties, which have led to its widespread application in the field of construction. Aggregates are the primary component of concrete, accounting for 60%–80% of the total volume and 70%–85% of the total weight (Muhammad et al., 2024). Traditional concrete heavily relies on the consumption of natural sand and stone, which are non-renewable resources, and this has caused some harm to the natural environment. Previous studies have shown that waste concrete and waste clay bricks constitute the largest volume of construction waste generated during new construction, expansion, reconstruction, and demolition, accounting for 30%–40% of urban waste (Chen et al., 2007). Therefore, utilizing recycled and reprocessed waste materials such as waste concrete (Chandru et al., 2023; Yao et al., 2023), bricks (Chen et al., 2024; Wang et al., 2024), and stone (Shen et al., 2022) aggregates for producing concrete holds great significance for sustainable development.

Frost resistance is a key indicator for assessing its long-term durability in cold environments. However, limitations in disposal technology often result in recycled aggregates having a high amount of attached mortar and microcracks generated during the crushing process. This leads to increased porosity and poorer aggregate quality in recycled concrete (Muhammad et al., 2024; Ren et al., 2024; Tam et al., 2005; Wang et al., 2021; Wang et al., 2014). Furthermore, the interface transition zone (ITZ) in recycled concrete is intricate and less robust compared to that in natural aggregate concrete, making it prone to performance degradation and damage during freeze-thaw cycles (Liu et al., 2019; Sáez Del Bosque et al., 2017; Xiao et al., 2013). As well as, many factors, including the content and water absorption rate of recycled aggregates (Datta et al., 2022; Li T et al., 2024), mineral admixtures (Gunasekara et al., 2020; Li et al., 2012a; Song et al., 2018; Wang et al., 2023a), water-to-cement ratio (Sosa et al., 2021), and water saturation (Luan et al., 2020), can influence its frost resistance. Up to now, scholars have conducted numerous experimental studies and evaluated the frost resistance of these key factors (Guan et al., 2024). Therefore, summarizing the frost damage mechanisms, analyzing its degradation process, and examining how frost resistance indicators change with the number of freeze-thaw cycles can provide valuable insights for researching and applying frost resistance in recycled concrete.

It is crucial to ensure the mechanical performance of recycled concrete in cold environments. Adding air-entraining agents to recycled concrete is an effective method to improve its freeze-thaw resistance (Deng et al., 2021a; Deng et al., 2021b). A large number of uniformly distributed microbubbles are introduced into the concrete by adding an air-entraining agent. These bubbles provide space for the water to expand during freezing, thereby reducing internal stress concentration and the formation of microcracks. Furthermore, the incorporation of fibers can form a three-dimensional network in the concrete, enhancing the crack resistance and spalling resistance of recycled concrete (Guan et al., 2024; Liu et al., 2023; Zhang et al., 2023). Previous studies (Deng et al., 2023; Islam et al., 2022) have shown that the different types of fiber materials have varying effects on improving the frost resistance of recycled concrete. Polypropylene fibers have good flexibility and dispersibility, reducing the formation of microcracks in recycled concrete (Yildizel et al., 2024). However, polypropylene fibers have relatively low strength and modulus, which limits their ability to enhance the frost resistance of concrete. Moreover, steel fibers, with higher strength and toughness, can effectively restrain crack propagation but may increase concrete conductivity. Therefore, selecting the appropriate fiber type based on specific operational conditions is essential. Coating protective agents on recycled aggregates and using chemical adhesives can enhance bond strength between recycled aggregates and fresh concrete, thereby reducing damage during freeze-thaw cycles (Xia et al., 2023; Zheng et al., 2024). However, these methods increase construction costs and require specialized equipment and skills. Therefore, it is necessary to select appropriate modification methods based on engineering conditions to enhance the freeze-thaw resistance of recycled concrete.

This revie summarized the freeze-thaw degradation mechanisms of recycled concrete and discusses the impact of the ITZ on the frost resistance. Subsequently, the key factors, including recycled aggregates, silica fume, water-to-cement ratio, and fly ash affecting the frost resistance are reviewed. Then, this study summarized some improvement techniques (air-entraining, reinforcement fibers, and aggregate modification) to enhance the frost resistance of recycled concrete. This study provides valuable references for improving the durability of recycled concrete structures in cold environments. This will assist researchers and engineering professionals in gaining a comprehensive understanding of the frost resistance of recycled concrete, thereby promoting further in-depth research on the frost resistance of recycled concrete and facilitating its wider application in cold regions.

2 Deterioration mechanisms

2.1 Normal concrete subjected to freeze-thaw cycles

Due to factors such as pore structure and aggregate quality, the material damage after freeze-thaw cycles is extremely complex (Ann et al., 2017; Guo et al., 2022; Kobayashi et al., 2022; Lee et al., 2018; Li Y et al., 2024; Liu and Hansen, 2016). The freeze-thaw damage process does not alter the composition of concrete; thus, its occurrence is primarily due to physical changes (Guo et al., 2022). Currently, the damage mechanisms under freeze-thaw cycles in concrete mainly focused on four representative theories, including the hydraulic pressure theory (Powers, 1945), the osmotic pressure theory (Powers and Helmuth, 1953), the crystallization pressure theory (Scherer, 1999), and the micro-ice crystal model (Setzer, 2001a; Setzer, 2001b). Figure 1 summarizes the principles of these degradation mechanisms, respectively. Among them, the hydraulic and osmotic pressure theories proposed that when water entered the pores of concrete and froze, the volume expansion generated hydrostatic pressure, and the growth of ice crystals led to osmotic pressure, resulting in micro-cracks and damage within the concrete (Gong and Jacobsen, 2019; Wang et al., 2023b). The crystallization pressure theory explains the mechanism of cumulative damage in concrete by detailing the crystallization and pressurization during freezing and the increased water absorption rate during thawing (Liu et al., 2018). The micro-ice crystal theory suggests that the concrete matrix needs to provide additional crystallization pressure

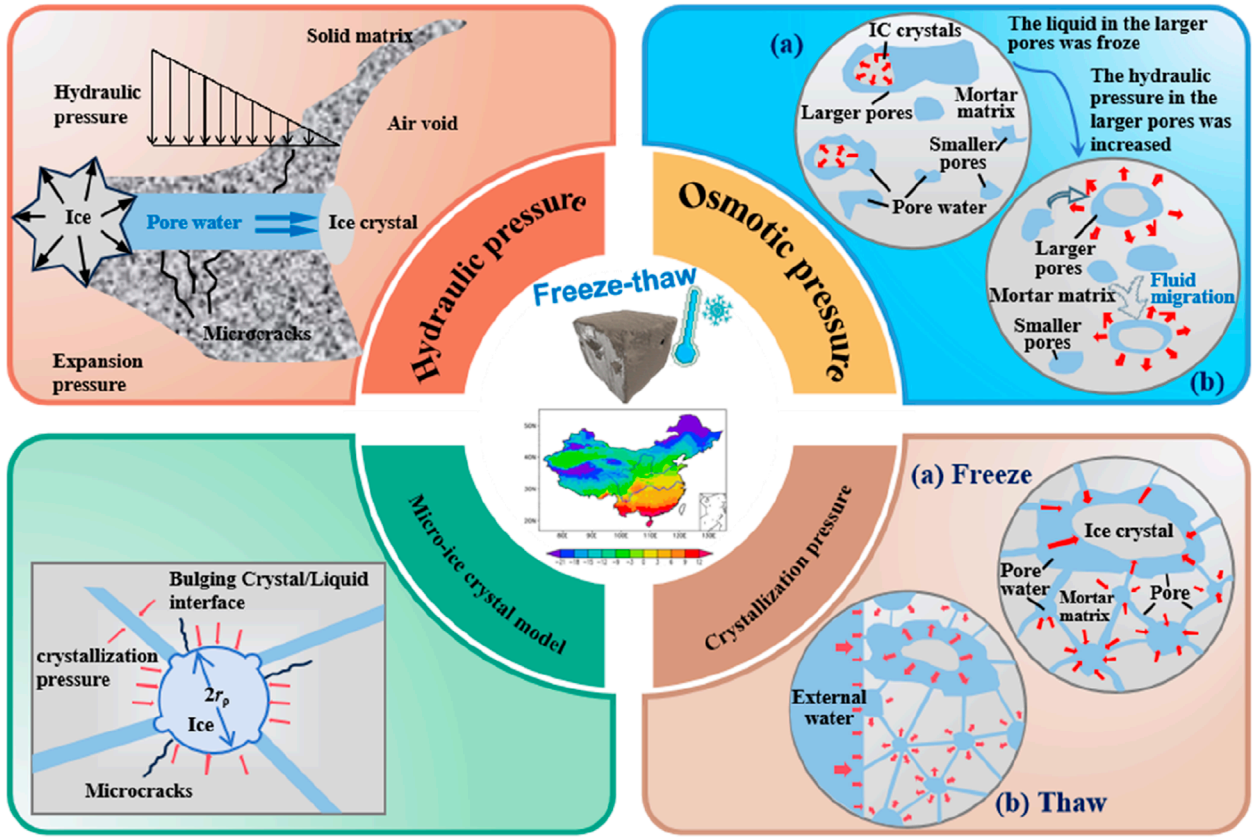

FIGURE 1
Schematic diagram of degradation mechanisms in concrete during freeze-thaw cycles.

to balance the pressure generated by the curvature difference between crystal surfaces and ends (Yan et al., 2014).

2.2 Recycled concrete subjected to freeze-thaw cycles

The internal structure of recycled concrete differs from that of natural concrete, leading to variations in their freeze-thaw damage mechanisms (Luan et al., 2020; Luan et al., 2021). When the moisture content within concrete reaches its critical saturation point, the concrete begins to experience freeze-thaw damage and deterioration. Similarly, the freeze-thaw damage of recycled concrete is also influenced by its sensitivity to internal moisture (Li et al., 2012b; Yang et al., 2024; Yao et al., 2022). Figure 2 illustrates the interface structure inside natural and recycled concrete. Previous studies (Rong et al., 2023; Zhao et al., 2023) have shown that recycled concrete has more complex interface structure, dividing new mortar-mortar interface (ITZ_1), old aggregate-new mortar interface (ITZ_2), and old mortar-old aggregate interface (ITZ_3), respectively. These ITZs exhibit poor performance, resulting increased water absorption and pore structure in recycled concrete (Xiao et al., 2013). Previous studies (Peled et al., 2010; Xiao et al., 2022) have demonstrated that ITZ exhibited characteristics of crystalline looseness and high porosity, especially ITZ_1, with its indentation modulus being 10%–20% lower than that of the surrounding mortar, and its width being 15 μm wider than ITZ_2 and ITZ_3. Therefore, microcracks generated in recycled concrete under freeze-thaw cycles occurred first in weak ITZ and continued to expand, resulting in poor frost resistance (Meng et al., 2024).

Researchers have focused extensively on studying the influence mechanisms of interface structures in recycled concrete on its frost resistance. Most researchers believe that the high-water absorption caused by poor interface quality in recycled concrete is one of the reasons for freeze-thaw damage (Gao et al., 2018; Qiu et al., 2024; Tuyan et al., 2014; Wang et al., 2023c). This is because in the raw materials, old mortar adheres to the surface of recycled aggregates, leading to higher porosity and the generation of microcracks during the crushing process of recycled aggregates (Alabduljabbar et al., 2024). The interface images were observed using a scanning electron microscope by Liu et al. (2019), demonstrating that there were more weak interfaces, microcracks, and pores in the ITZ of recycled concrete. Zheng et al. (2021) demonstrated that when the water-to-cement ratio was high, there were more microcracks in the ITZ around recycled aggregates. This resulted in increased pore water absorption rate and decreased concrete strength. Lin et al. (2023a) found that in recycled concrete, a higher ratio of old mortar-water cement lead to increased porosity, pore size, crystallization pressure, principal stress, and the lower its frost resistance. In addition, scholars have revealed the freeze-thaw damage mechanism

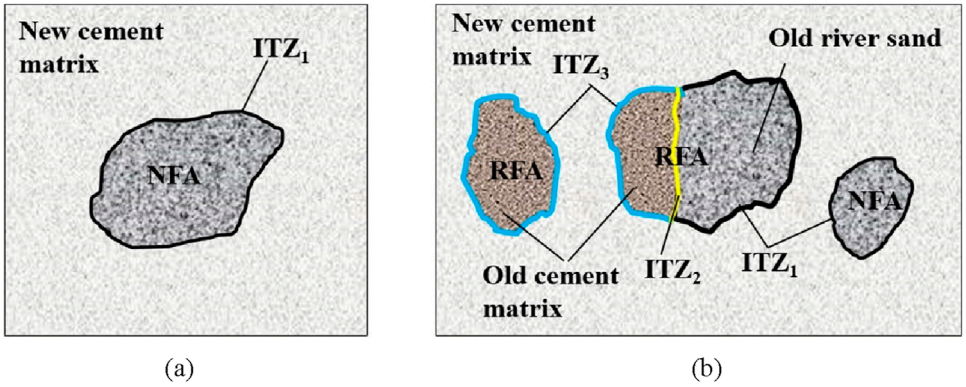

FIGURE 2
Schematic diagram of interface structure for NC and recycled concrete: **(A)** NC, **(B)** recycled concrete (Zhang et al., 2018).

from the perspective of ITZs. Hasholt (2014) found that recycled concrete contained multiple ITZs, generating numerous micro-pores within its interior. During freeze-thaw cycles, smaller pore sizes resulted in faster water absorption rates, increasing the internal osmotic pressure of recycled concrete. Similarly, Xiao et al. (2022) and Zhu et al. (2020) demonstrated that the higher the recycled aggregates content, the higher the porosity and water absorption rate. Luan et al. (2020) found that the critical water saturation was 81%–83% in recycled concrete, which was lower than the critical water saturation range of natural concrete (86%–88%). Therefore, recycled concrete is more prone to freeze-thaw failure than that of natural concrete. In conclusion, scholars generally concur that the high-water absorption rate of recycled aggregates subject the internal small pores in recycled concrete to considerable pressure during the freezing and thawing process. As freeze-thaw cycles increases, the total porosity and micro-cracks between pores increase or expand, establishing channels for the infiltration of external water into the concrete interior. Under high pressure, the weak interface zone of the recycled concrete generates microcracks with the continuous formation and expansion of internal pores, which continuously develop and propagate, ultimately resulting in the loosening of overall internal structures. When the damage accumulates to a certain extent, freeze-thaw damage occurs.

In conclusion, recycled concrete demonstrates a higher incidence of weak ITZs compared to natural concrete, which consequently results in an inferior frost resistance performance. It involved various degradation mechanisms associated with the micro-pore structures in recycled concrete. Therefore, further research is needed to reveal the influence of the ITZ on the mechanism of freeze-thaw damage.

3 Critical influence factors for frost resistance

3.1 Recycled aggregates

3.1.1 Content of recycled aggregates

Generally, the frost resistance of recycled concrete is influenced by the content of recycled aggregates (Bogas et al., 2016; Tran et al., 2022; Wang et al., 2023d; Wang et al., 2023e). Researchers have focused on the recycled fine aggregate (RFA) and conducted corresponding experimental studies. The frost resistance tests were conducted by (Sun and Geng, 2012), and indicated that when the content of RFAs content exceeded 40%, the relative dynamic elastic modulus (RDEM) of the recycled concrete showed a significant decrease, and with the increase in RFAs content, the RDEM decreased more significantly. Bao et al. (2022) examined the frost resistance with varying replacement rates of RFAs. The results showed that the frost resistance was primarily related to the RFAs, showing an initial increase followed by a decrease as the ferronickel slag content increased. When 40% of recycled ferronickel slag fine aggregates were incorporated, the recycled concrete exhibited the best frost resistance, as shown in Figure 3. This is mainly due to the hydration reaction of the active substances in the ferronickel slag, which formed more hydration products and strengthened the ITZ structure within the recycled concrete. Similarly, Saha and Sarker (2020) demonstrated that when ferronickel slag replaced 40% of river sand, the recycled concrete produced more cementitious products, thereby improving its microstructure. The research results of Quan et al. (2022) indicated that the mass loss rates corresponding to molybdenum tailings replacement rates of 0%, 30%, 50%, 70%, and 100% were 0.62%, 0.81%, 0.83%, 0.9%, 1.01%, and 1.11% after 100 freeze-thaw cycles, respectively.

Recycled coarse aggregates (RCAs) exhibited higher porosity and greater absorption capacity compared to RFAs, making them more susceptible to deterioration. For instance, Tuyan et al. (2014) demonstrated that the frost resistance of concrete with crushed limestone recycled aggregates can be significantly decreased. Amorim et al. (2018) observed that the RDEM loss rate of RCA concrete with a 50% content was lower compared to those with 25% and 75% content after 150 freeze-thaw cycles. Additionally, Ji and Wang (2022) found that recycled brick aggregate concrete, with NCA replaced, developed cracks in the ITZ and reduced adhesion between cement mortar and RCAs after 100 freeze-thaw cycles. The substitution of RCAs for NCAs has a negative impact on the frost resistance. Deng et al. (2021) studied the loss rate of flexural strength of RCA concrete after different freeze-thaw cycles and with varying RCA contents. The results showed that the flexural strength loss rate increases with RCA contents, reaching up to 70%,

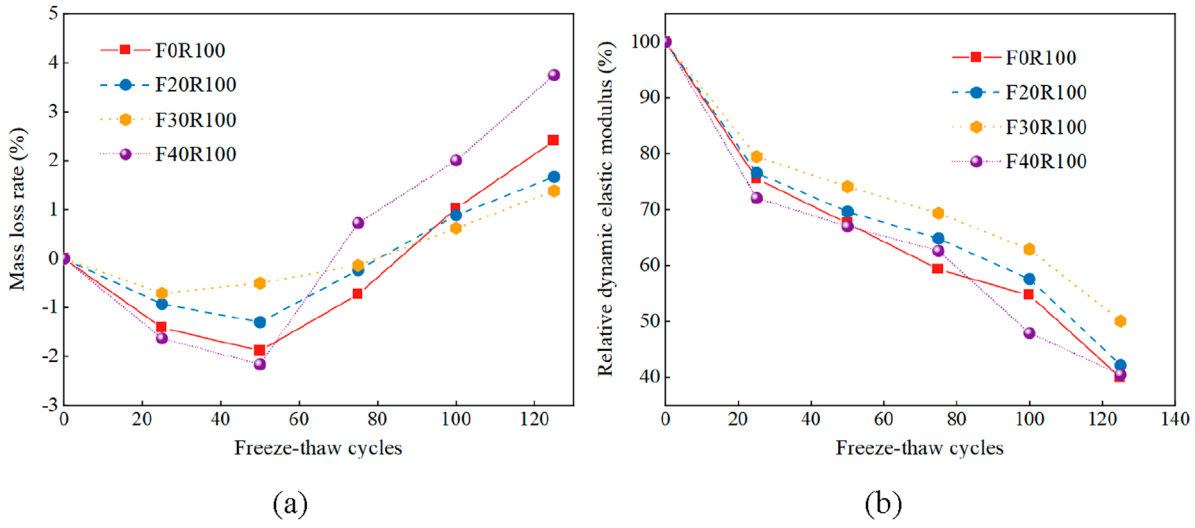

FIGURE 3
The influence of ferronickel slag content on the mass loss rate and RDEM: **(A)** mass loss rate, **(B)** RDEM. Note: F represents nickel-iron slag content; R denotes the recycled coarse aggregate content.

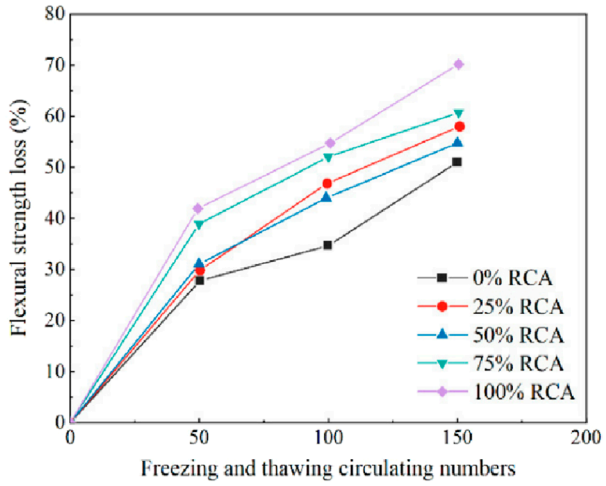

FIGURE 4
Loss rate of flexural strength RCA concrete subjected to freeze-thaw cycles.

as shown in Figure 4. In conclusion, when using RCAs to replace NCAs, the replacement rate should not exceed 50%.

3.1.2 Porosity and absorption of recycled aggregates

The old mortar in recycled aggregate and microcracks may increase water absorption and porosity, thereby reducing frost resistance. Studies have demonstrated that the water absorption of recycled aggregates are approximately 6–10 times that of natural aggregates (Levy and Helene, 2004). According to (Omary et al., 2016), as the water absorption and porosity increase, the strength and density of recycled aggregates decrease. Consequently, the freeze-thaw resistance and splitting tensile strength of recycled aggregate concrete are notably lower than those of natural aggregate concrete. This is because recycled aggregates retain old mortar and develop micro-cracks. Moreover, RFAs exhibited higher porosity compared to RCAs, likely due to more old cement mortar in RFAs. Xia and Zhao (2024) found that the frost damage in recycled concrete was primarily caused by the defects of recycled aggregates. This is because the old mortar contains numerous tiny and loose pore structures with high-water absorption, resulting in micro-cracks propagation and new micro-cracks generation in the new mortar under frost heave forces. Gokce et al. (2004) found that microcracks in recycled concrete first concentrated on the old mortar adhered to the RCA after absorbing water. Subsequently, these cracks rapidly developed and penetrated the new mortar, ultimately leading to freeze-thaw failure. Literature (Ghorbani et al., 2019; Peceño et al., 2019; Wei et al., 2022) indicated that large-sized RCAs were difficult to disperse uniformly in concrete, and increased the porosity of RCA concrete, reducing the frost resistance. Figure 5 illustrates the development of the ITZ in RCA concrete during freeze-thaw cycles. It can be seen that ITZ became fragmented and porous after 300 freeze-thaw cycles, as shown in Figure 5A. The width of the ITZ increased as microcracks gradually expanded and connected with the pores, forming cross-cracks after 400 freeze-thaw cycles, as shown in Figure 5C. In conclusion, frost resistance can be influenced by factors such as water absorption, porosity, and particle size. Therefore, the next step in research should focus on developing effective modification methods for recycled aggregates to enhance the frost resistance.

3.2 Mineral admixture

The frost resistance could be improved by incorporating mineral admixtures, including silica fume (Avet et al., 2019; Bu et al., 2022), fly ash (Şimşek et al., 2022; Yu et al., 2021; Yuan et al., 2024), slag

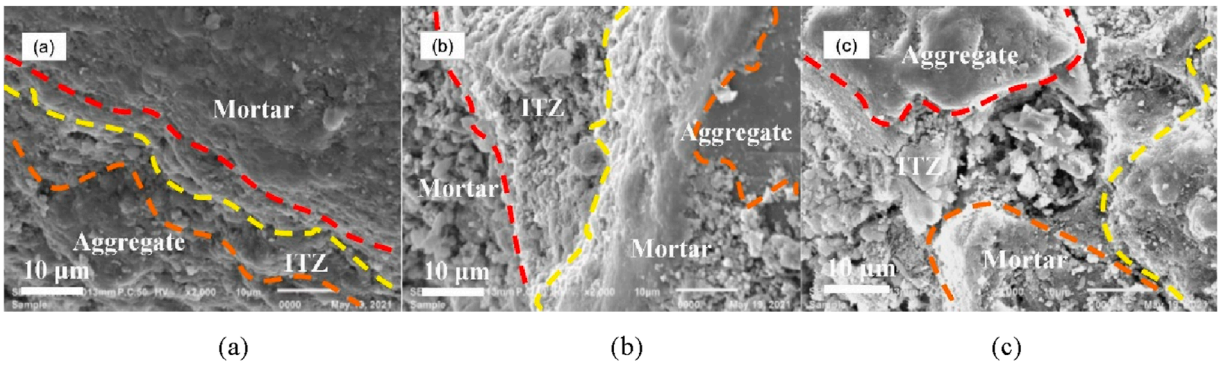

FIGURE 5
ITZ SEM images of RCA concrete at different freeze-thaw cycles: **(A)** 0 cycles, **(B)** 350 cycles, **(C)** 400 cycles (Wei et al., 2022).

(El-Hawary et al., 2021; Lee et al., 2021; Li et al., 2019), and rice husk ash (Ma et al., 2024; Wang et al., 2017; Zhang et al., 2022). On the one hand, it is possible to fill the micro-pores within recycled concrete, increasing its density. On the other hand, the active components of mineral admixtures could promote secondary hydration reactions in recycled concrete, thereby enhancing its frost resistance (Cheng et al., 2018; Mardani-Aghabaglou et al., 2019).

3.2.1 Silica fume

Silica fume (SF) is a finely-grained volcanic ash material. It enhances the durability of concrete by filling internal pores, increasing density, and reducing water absorption. Incorporating the right amount of SF enhances cement hydration and boosts the density of the ITZ in recycled concrete (Oertel et al., 2014; Scrivener et al., 2015). Bai et al. (2023a) investigated the fracture properties of recycled concrete after partially replacing cement with SF. After 125 freeze-thaw cycles, the fracture damage parameters were 0.256 and 0.247 for SF replacement rates of 0% and 9%, respectively. The fracture damage parameter was relatively small when the silica fume content was 9%, indicating a reduction in microcrack density and improved frost resistance after the addition of SF. Wang et al. (2023) found that after 400 freeze-thaw cycles, recycled concrete with 3%, 5%, 8%, 11%, 13%, and 16% SF content showed 16%, 20.0%, 28.0%, 36%, 40%, and 32% increase in splitting tensile strength compared with recycled concrete with 0% SF content, respectively. It can be seen that excessive addition of SF will weaken its effect on improving frost resistance. This is because unhydrated SF particles may cause shrinkage cracks and insert into the hydration products, resulting in a decrease in the bonding strength of the mortar, as shown in Figure 6.

3.2.2 Fly ash

Fly ash is a fine, greyish-white powder rich in silicate and aluminate minerals. Incorporating fly ash into concrete could improve its density (Posi et al., 2016), strength (Lam, 2020), and durability (Corinaldesi, 2012), while also lowering costs and environmental impact. Previous studies have demonstrated that incorporating fly ash into recycled concrete could improve microstructures (Sunayana and Barai, 2021), fill and reduce pores, increase compactness, and delay hydration reactions (Yang et al., 2024), thereby enhancing the frost resistance. Yu et al. (2021) utilized discarded concrete and clay bricks as raw materials, blending them in a 7:3 ratio to produce recycled brick-concrete aggregate, and investigated the frost resistance incorporating both recycled brick-concrete aggregate and fly ash under conditions of freeze-thaw cycling and combined action with sodium chloride. The experimental outcomes indicated that incorporating 15% fly ash content could notably enhance the compressive strength of the recycled concrete, frost resistance, and resistance to chloride-induced synergistic erosion. Nazeer et al. (2024) observed that fly ash would cause a positive effect on the frost resistance. Their findings indicate that using 10% fly ash in recycled concrete leads to a noticeable decrease in the rates of compressive strength loss and mass loss, as depicted in Figure 7. Similarly, LI et al. (2017a) study the influence of fly ash dosage on the frost resistance by substituting cement with fly ash at equal weight percentages of 0%, 20%, and 40%, respectively, to prepare RCA concrete specimens. The tested results demonstrated that the frost resistance was enhanced by incorporating fly ash into RCA concrete. Moreover, the additional pores provided by the RCA in the paste contributed to this enhancement to some extent. Therefore, the utilization of an appropriate amount of fly ash can reduce the loss of RDEM loss and compressive strength in RCA concrete.

Some scholars argue that adding fly ash will reduce its frost resistance performance of recycled concrete. Bu et al. (2023) studied the microstructure, mechanical properties, flexural toughness, and frost resistance with partial fly ash content, including 0%, 10%, 30%, 50%, and 70% in cement. The findings showed that as fly ash content increased, the mass loss settlement initially decreased and then increased. Conversely, the RDEM loss initially increased and then decreased. Completing 100 freeze-thaw cycles, recycled concrete with a 50% fly ash content exhibited the best mechanical properties, with a significant decrease in mechanical properties at higher or lower replacement rates. Similarly, Cheng et al. (2017) found that the RDEM of recycled concrete specimens without fly ash decreased slowly after 300 freeze-thaw cycles. However, specimens incorporating 10% and 30% fly ash experienced a marked acceleration in RDEM reduction rates after 200 freeze-thaw cycles, whereas those with 50% fly ash showed a pronounced increase in RDEM reduction rates following 150 freeze-thaw cycles, as detailed

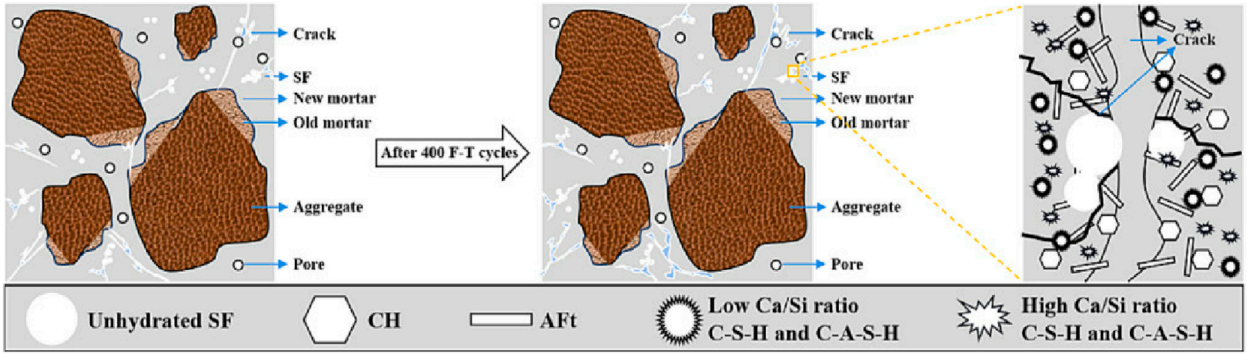

FIGURE 6
Schematic diagram of the mechanism of excessive silica fume under freeze-thaw cycles (Wang et al., 2023c).

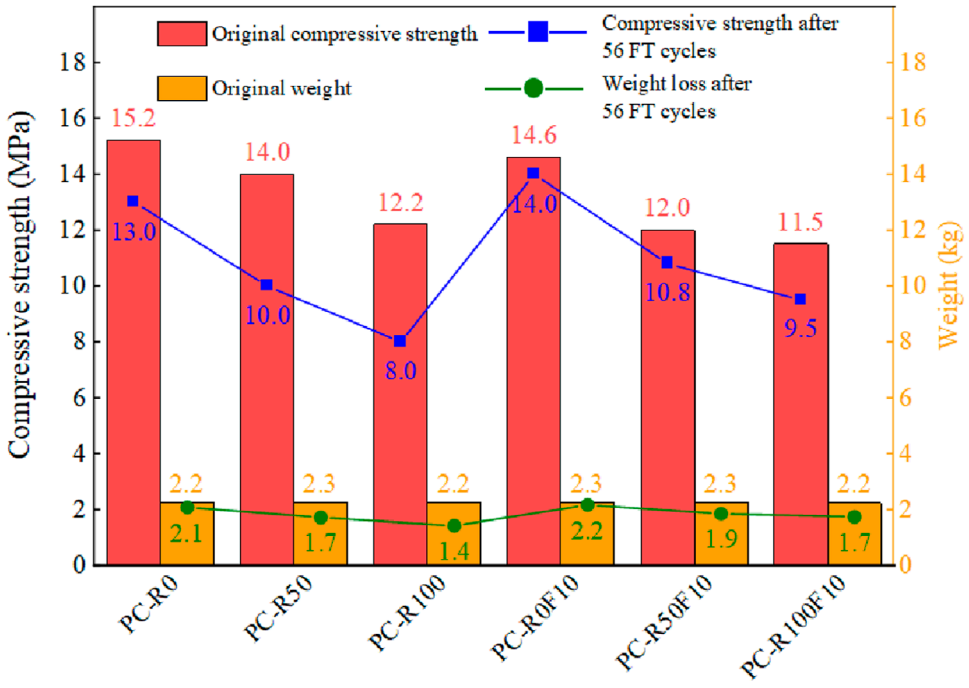

FIGURE 7
The influence of fly ash on the frost resistance. Note: PC signifies cement, R denotes the recycled aggregate content, and F indicates the fly ash content.

in Figure 8. Furthermore, Wu et al. (2019) also founded that the incorporation of fly ash resulted a negative impact on the frost resistance.

In summary, the amount of fly ash incorporation needs to be determined based on specific engineering requirements and the quality of the fly ash. Overusing or underusing fly ash in concrete may negatively impact its performance.

3.2.3 Multiple mineral admixtures

Some researchers have utilized a combination of various mineral admixtures to develop recycled concrete, aiming to explore the effects of composite mineral admixtures on its frost resistance. For instance, Chen et al. (2023) conducted freeze-thaw cycling tests by integrating fly ash (FA) and ground granulated blast furnace slag (GGBS) individually or simultaneously into concrete containing 0%, 35%, and 50% RCAs, replacing part of the cement. The results indicate that the hydration product $Ca(OH)_2$ effectively activated the pozzolanic reactions between fly ash and ground granulated blast furnace slag. Fly ash and ground granulated blast furnace slag act as catalysts in recycled concrete, accelerating the formation of C-S-H gel and enhancing freeze-thaw resistance. Consequently, while RCAs may reduce the frost resistance, incorporating ground granulated blast furnace slag and fly ash as partial substitutes for cement can help alleviate the adverse effects of RCAs on frost resistance. In particular, using fly ash and ground granulated blast furnace slag together as partial replacements for cement significantly

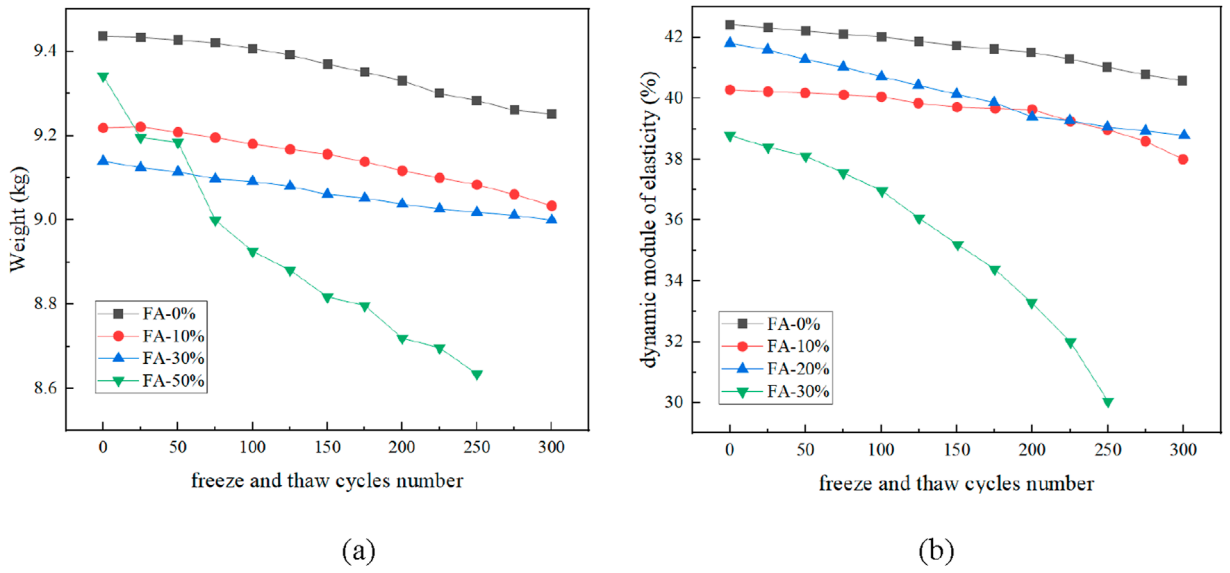

FIGURE 8
The influence of fly ash content on the frost resistance: **(A)** effects of freeze-thaw cycles on weight; **(B)** effects of freeze-thaw cycles on dynamic modulus of elasticity.

enhances the frost resistance of RCA concrete. The synergistic effect of ground granulated blast furnace slag and fly ash occurs at a ratio of 15% by weight, as detailed in Figure 9. Cheng et al. (2024) selected fly ash, silica fume, and granulated blast furnace slag to prepare five distinct cementitious systems of recycled concrete through various combinations of quantities. The experimental outcomes revealed that a superimposed effect was formed due to the full utilization of the morphological effects and micro-filler effects of silica fume, fly ash, and granulated blast furnace slag within the concrete matrix. This synergistic interaction reduced the porosity of recycled concrete, effectively hindering the free water into its interior, and consequently enhancing the frost resistance. Moreover, mineral admixtures can improve the internal structure of recycled concrete and mitigate the damage caused by pore water pressure expansion. The research results of Guo et al. (2020) indicate that self-compacting concrete blended with fly ash, slag, silica fume, and recycled aggregates showed a strength loss similar to that of normal self-compacting concrete.

In general, the concurrent use of multiple mineral admixtures in concrete production enhances the performance of recycled concrete more effectively than using single mineral admixtures alone. In other words, the selection of a combination of various mineral admixtures and the determination of appropriate mixing ratios can significantly enhance the frost resistance of recycled concrete.

3.3 Water-to-cement ratio

The water-to-cement ratio is a crucial factor affecting the frost resistance of recycled concrete. Scholars have conducted experimental studies on the frost resistance of recycled concrete under different water-to-cement ratios. Bogas et al. (2016) carried out rapid freeze-thaw tests by partially or entirely replacing natural fine aggregates (NFAs) with RFAs. The results indicated that the frost resistance of recycled concrete primarily depended on the water-to-cement ratio, with lower ratios correlating to better performance. Atasham Ul Haq et al. (2024) utilized recycled brick aggregate to produce recycled concrete specimens with water-to-cement ratios of 0.65, 0.5, and 0.35, with replacement levels of 0%, 25%, 50%, and 100%. The results showed the recycled concrete made with a water-to-cement ratio of 0.65 exhibited a significantly higher mass loss rate than those with ratios of 0.5 and 0.35. Luo et al. (2015) showed that reducing the water-to-cement ratio led to a denser concrete matrix and reduced the mass loss rate.

Increasing the water-to-cement ratio increases the number and volume of capillary pores in concrete, allowing more water to freeze within the cement paste. Therefore, reducing the water-to-cement ratio of recycled concrete is beneficial for improving its frost resistance. This effect is particularly pronounced in specimens with higher water-to-cement ratios and greater contents of recycled aggregates (Tuyan et al., 2014). Yildirim et al. (2015) designed three levels of recycled aggregate saturation (0%, 50%, and 100%) and three water-to-cement ratios (0.7, 0.6, and 0.5), while controlling the proportion of recycled aggregates at different levels, to study the durability of recycled concrete. The tested results indicated that the mass loss rate of all specimens decreased with the decrease in water-to-cement ratio after 300 freeze-thaw cycles. Likewise, Meng et al. (2021) demonstrated that recycled concrete with high RCA content exhibits poor frost resistance. However, by reducing the water-to-cement ratio, the RDEM of the specimens rapidly decreased at the end of the respective experiments. This indicates that reducing the water-to-cement ratio improves the frost resistance of recycled concrete to some extent. The RDEM results for the concrete specimens are presented in Figure 10.

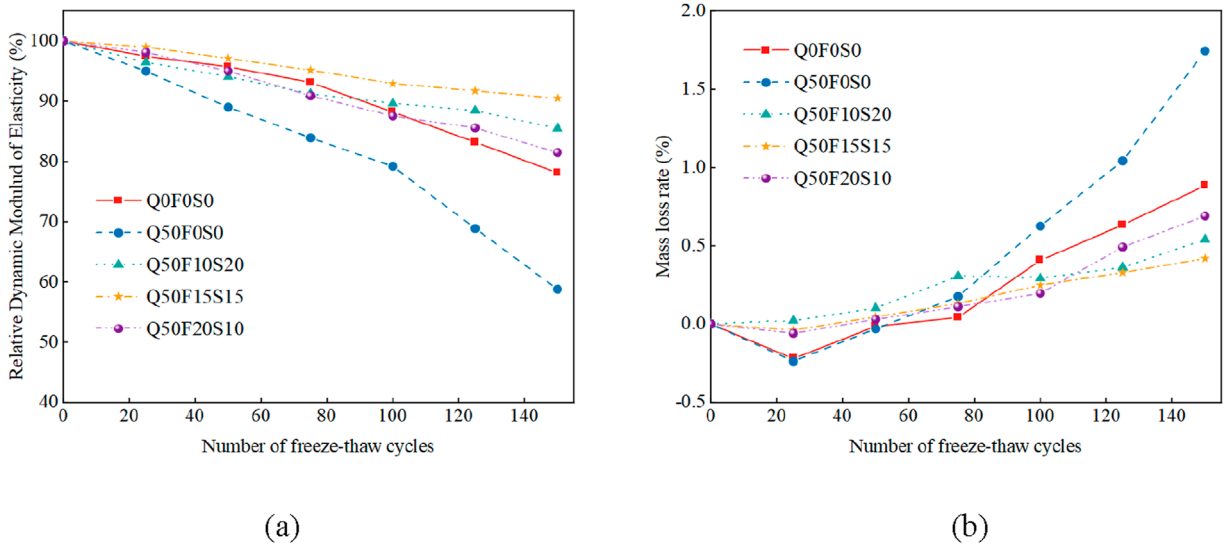

FIGURE 9
Synergistic effects of FA and GGBS on the mass loss rate and REDM of recycled concrete: **(A)** RDEM loss rate; **(B)** Mass loss rate. Note: Q represents the of RCA content; F and S represents FA and GGBS, respectively.

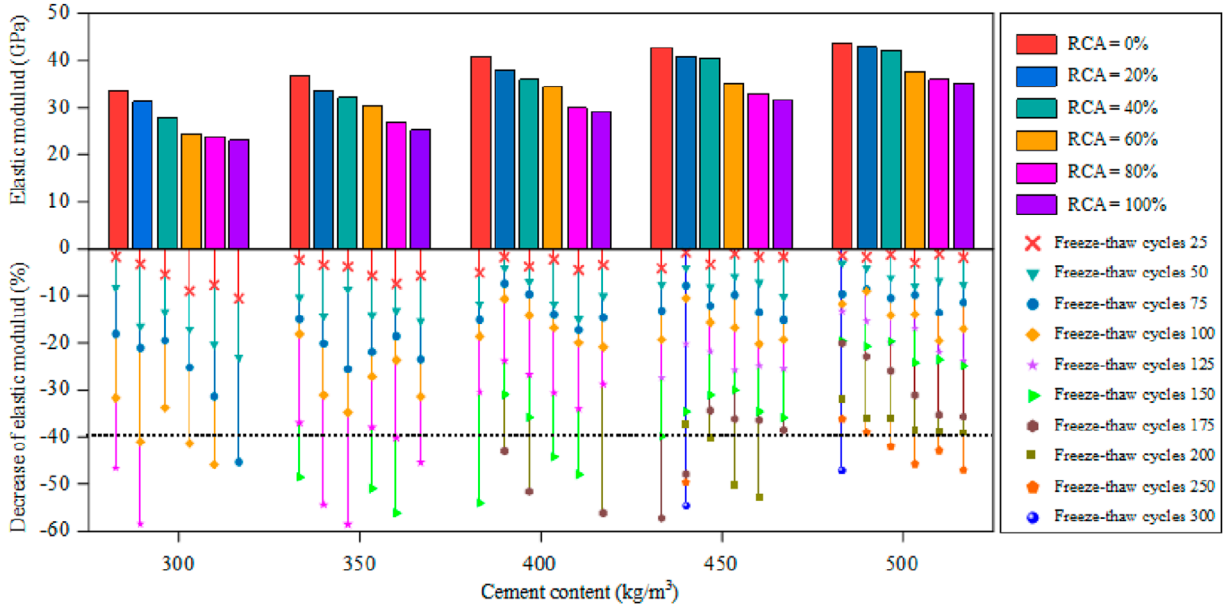

FIGURE 10
Decrease of elastic modulus under different recycled coarse aggregate and freeze-thaw cycles (Yuan et al., 2023).

3.4 Water saturation of recycled aggregates

The water saturation of recycled aggregates could affect the pore structure, reducing the frost resistance of recycled concrete. As a porous medium, recycled aggregates have a high-water absorption rate (Khoury et al., 2019). Pretreating recycled aggregates with water will result in a certain degree of internal curing effect in recycled concrete. Previous studies (Marchi et al., 2023; Pickel et al., 2017; Yang et al., 2022) have shown that internal curing can reduce water consumption, enhance the degree of hydration in concrete, reduce cracks, and ensure the long-term stability of concrete structures.

Scholars have studied the effect of water saturation of recycled aggregates on the internal curing efficiency of recycled concrete. Deng et al. (2021) indicated that the incorporation of RCAs significantly affected the distribution and quality of different pores. Prior to the commencement of freeze-thaw cycles, due to the higher porosity and water absorption rate of recycled aggregates, pre-wetting provided a certain degree of internal

curing for the concrete by supplying water within the aggregate pores. Consequently, recycled aggregate concrete exhibited higher flexural strength compared to natural aggregate concrete. Similarly, de Oliveira and Vazquez (1996) investigated the effect of water saturation on the mechanical properties and durability of recycled concrete. The results showed that recycled concrete made with saturated and dried recycled aggregates exhibited poor frost resistance. Conversely, recycled concrete containing semi-saturated recycled aggregates exhibited better frost resistance, attributed to a denser and stronger interface transition zone. Specifically, the semi-saturated recycled aggregates provided sufficient moisture for internal curing, promoting further hydration of the ITZ and thereby enhancing the frost resistance. Yildirim et al. (2015) found that during the curing process of concrete, water stored in the pores of porous aggregates is gradually released, promoting the hydration of cement. Therefore, achieving an optimal water saturation level for recycled aggregates can improve the frost resistance to some extent. Similarly, El-Hawary and Al-Sulily (2020) have found that recycled concrete specimens containing 50% pre-moistened RCAs exhibit improved frost resistance compared to mixtures without recycled aggregate. In addition, specimens with 50% pre-moistened RCAs and RFAs showed a significant increase in RDEM, indicating that the internal curing provided by pre-moistened recycled aggregates effectively improves the frost resistance. Furthermore, the optimal water saturation of recycled aggregates can still exert their internal curing function in complex environmental conditions, enhancing the frost resistance. For instance, Lei et al. (2018) investigated the effects of mechanical repetitive loading and its interaction with complex environments on the performance of recycled aggregate concrete. The results indicated that pre-saturated recycled aggregates facilitated the hydration of new and old mortar adhered to the recycled aggregates at the ITZ during the curing stage. Figure 11 illustrates variation of RDEM of pre-saturated recycled aggregate concrete with freeze-thaw cycles. In this figure, A represents not recycled aggregate, B represents 50% RCAs and RFAs content, C represents 50% RFAs content, and D represents 50% RCAs content. The numeral "1" represents a water-cement ratio of 0.4, and "75%" indicates that the ambient humidity was 75%. The figure shows that pre-moistened recycled aggregates enhance the frost resistance of concrete, indicating the effectiveness of their internal curing mechanism.

In summary, recycled aggregates, as a type of porous material with high porosity and strong water absorption capacity, when used at an appropriate water saturation level for preparing fresh mixed concrete, will gradually release moisture during the curing process of the concrete. This moisture release provides a certain level of internal curing within the concrete structure, thereby promoting cement hydration and improving the ITZ of the concrete structure.

4 Improvement techniques for frost resistance of recycled concrete

4.1 Incorporating air-entraining agent

The use of air-entraining admixtures can enhance the workability, internal cohesion, and plasticity of concrete, and reduce segregation and water loss, particularly in terms of frost resistance (Huaishuai et al., 2017; Li and Qin, 2013; Long et al., 2013). Incorporating air-entraining admixtures is considered the most effective method for enhancing concrete's frost resistance at a fixed water-to-cement ratio. This is because when recycled concrete is mixed with air-entraining admixtures, numerous small, closed spherical air bubbles can be formed within the concrete (Liu et al., 2011). During the freeze-thaw cycle, air bubbles were absorbed and some water was released, alleviating the hydrostatic pressure and osmotic stress on the concrete, thereby reducing the extent of damage caused by ice crystal expansion.

Liu et al. (2016) investigated the frost resistance made with non-aerated and aerated recycled aggregates concrete. The results showed that the strength loss of recycled concrete containing both aerated and non-aerated aggregates was intermediate between that of concrete with only aerated aggregates and that with only non-aerated aggregates. Tarhan and Şahin (2021) investigated the scaling behavior of recycled concrete incorporating different air-entraining admixtures (0.06%, 0.13%, 0.20%) and recycled aggregate content. The results showed that in the absence of any recycled aggregates, the control group with 0.13% air-entraining admixture had the highest scaling rate. Among the mixtures with the same percentage of recycled aggregates, the mixture containing 0.06% air-entraining admixture typically exhibited the least scaling and the weakest signs of deterioration. These results indicate that the pores generated by the air-entraining admixture assist in reducing the pressure buildup caused by the expansion of liquid water and ice crystals. Furthermore, the spherical air void structure formed after incorporating air-entraining admixture is an important reason for the impact on the frost resistance. Deng et al. (2021) found that the addition of air-entraining admixtures had little effect on the mass loss rate of recycled concrete but helped to increase its RDEM. Similarly, Olanike (2014) found that air-entraining admixtures played a significant role in preventing the RDEM of recycled concrete from decreasing after freeze-thaw cycles. In addition, Zhang et al. (2024) found that the mass loss rates of recycled concrete with a 50% recycled aggregate content were 1.31%, 1.18%, and 2.36% after 200 freeze-thaw cycles when 0.01%, 0.03%, and 0.05% air-entraining agents (MR50-A1/A3/A5) were added, as shown in Figure 12. In the figure, R50 denotes recycled concrete with a 50% replacement rate of recycled aggregates, while MR50 refers to the R50 concrete that has been modified by the addition of nano-silica. This indicates that even a small amount of aerated admixture can help reduce the mass loss under salt-based freeze-thaw conditions.

In summary, the incorporation of air-entraining admixtures can significantly enhance the frost resistance. This improvement is mainly seen in the reduction of RDEM loss and the decrease in scaling and mass loss rates.

4.2 Incorporating reinforcing fibers

The incorporation of fiber-reinforced materials into recycled concrete is a common approach to enhance frost resistance. Commonly used fiber-reinforced materials include steel fibers (GAO et al., 2007), polypropylene fibers (Tošić et al., 2022), glass fibers (Bhikshma and Kumar, 2015), carbon fibers (Zaid and Zamir Hashmi, 2021), and basalt fibers (Guo et al., 2023; Kang et al.,

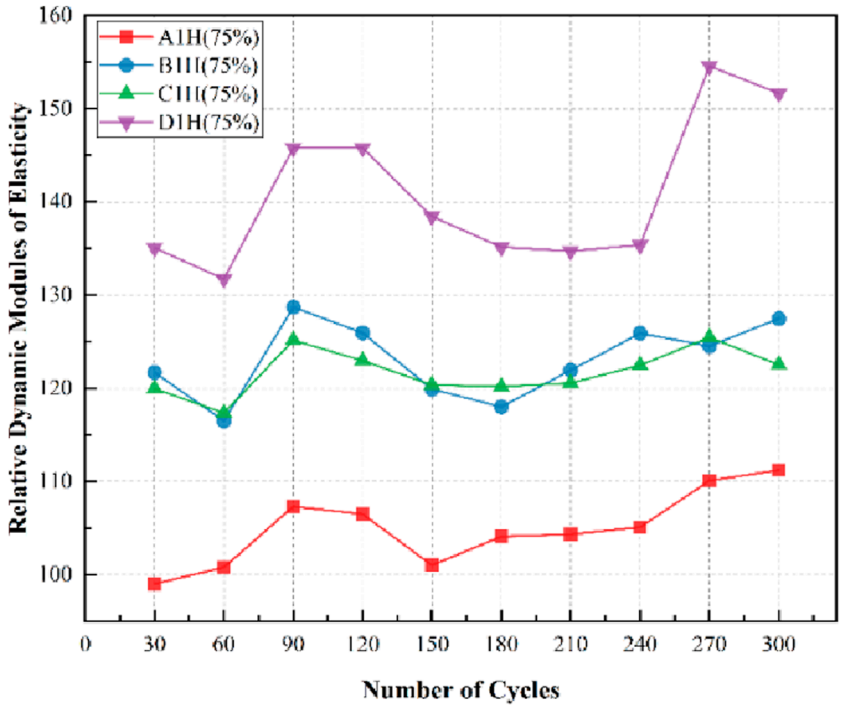

FIGURE 11
Impact of water saturation of recycled aggregates on frost resistance of recycled concrete.

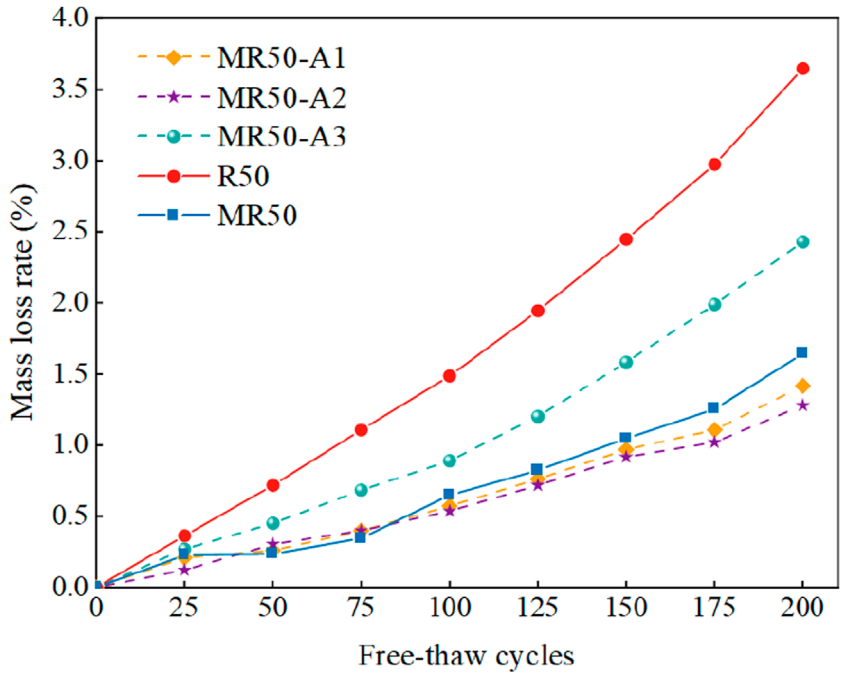

FIGURE 12
Mass loss rate of recycled concrete with different air-entraining agents after freeze-thaw cycles. Note: R50 signifies a replacement rate of 50% with recycled aggregate; MR50 refers to the R50 concrete that has been modified with nano-silica; MR50-A1 denotes the R50 concrete that has been modified with nano-silica and incorporates 0.01% of an air-entraining agent.

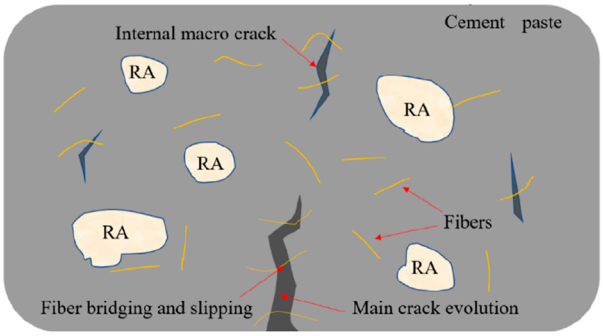

FIGURE 13
Bridging mechanism of reinforcing fibers on concrete cracks.

2024). Bai et al. (2023b) carried out freeze-thaw cycle tests on recycled concrete with different carbon fiber contents and analyzed the microscopic damage mechanisms. The test results indicated that carbon fibers hindered the entry of external water into the interior of recycled concrete, thus restraining the volume expansion of water during freezing. Furthermore, the presence of carbon fibers effectively resisted the tensile forces generated by concrete expansion and cracking, inhibiting crack formation and reducing the concrete's mass loss. Zheng et al. (2022) found that the three-dimensional network structure formed by polypropylene fibers within the recycled concrete matrix could withstand some tensile stresses caused by freeze-thaw cycles, limiting the expansion and contraction of recycled concrete and mitigating the damage. Adding 0.10% polypropylene fibers to recycled concrete could simultaneously improve the strength and frost resistance. Yuan et al. (2024) incorporated basalt fibers into recycled concrete to enhance its frost resistance. The experimental results showed that basalt fibers led to the formation of a spatial network structure within the recycled concrete, thereby strengthening the interaction between aggregate particles and between the aggregates and the binding matrix. After 100 freeze-thaw cycles, recycled concrete specimens without basalt fibers (0 kg/m^3) showed a significant mass loss, reaching the critical failure threshold. In contrast, specimens with different basalt fiber contents exhibited relatively minor mass loss. References (Gao et al., 2020; Liu et al., 2024) also confirmed the microscopic mechanism of action of fiber-reinforced materials in enhancing the frost resistance. In conclusion, the bridging and filling effects of fibers increase the interaction forces between aggregates and between aggregates and the matrix. On the other hand, they reduce the tensile forces required for the expansion of microcracks within recycled concrete, thereby enhancing the material's frost resistance. The bridging mechanism of reinforcing fibers on concrete cracks is illustrated in Figure 13.

The effects of different fiber materials on enhancing the frost resistance of recycled concrete are inconsistent. Mahboob et al. (2024) added steel fibers, plastic fibers, and kenaf fibers into recycled concrete and conducted freeze-thaw cycle tests. The results showed that after 300 freeze-thaw cycles, the recycled concrete with fiber-reinforced materials had significantly lower mass loss rates and RDEM losses than traditional recycled concrete. Furthermore, compared to plastic fibers and kenaf fibers, steel fibers exhibited excellent microstructural protection. However, Pehlivanlı et al. (2015) demonstrated that steel fibers have weak bonding with the mortar matrix, limiting their performance. Mastali et al. (2016) found that adding glass fibers to recycled concrete could improve its frost resistance. However, glass fibers are relatively fragile and prone to breakage during incorporation, which leads to uneven distribution within the recycled concrete matrix and suboptimal performance. In contrast, Ramesh and Eswari (2021) found that basalt fibers maintained excellent mechanical properties under freeze-thaw cycles and exhibited better shear and tensile strengths than other fiber-reinforced materials, such as polypropylene. Furthermore, scholars have also studied the impact of incorporating mixed fibers on the frost resistance. For example, Ahmed and Lim (2023) prepared recycled concrete with basalt, polypropylene, and glass fibers, either individually or in combination. The study found that incorporating mixed fibers could significantly enhance the frost resistance. Similarly, Yuan et al. (2023) found that recycled concrete with a controlled proportion of basalt fibers and steel fibers exhibits better frost resistance compared to concrete with only a single type of fiber. The research data is shown in Figure 14. It is not difficult to see from the figure that after 150 freeze-thaw cycles, recycled concrete specimens (S1.5BF3.5/5.5/7.5) with a volume fraction of 1.5% steel fibers and a basalt fiber content of 3.5/55/7.5 kg/m^3 exhibit superior compressive strength compared to all single basalt reinforced concrete specimens. This improvement is primarily due to the synergistic use of different fiber types, which reduces fiber aggregation and enhances the frost resistance.

In summary, the bridging and filling functions of fibers in recycled concrete help to suppress the tensile stresses generated by freeze-thaw cycles, thereby enhancing the frost resistance. The type and performance of fiber materials are key factors affecting the frost resistance of recycled concrete. Furthermore, compared to incorporating a single type of fiber, the incorporation of multiple types of fibers typically further improves the frost resistance. Therefore, the rational introduction of fibers can effectively enhance the frost resistance of recycled concrete to some extent.

4.3 Aggregate modification

The mortar attached to recycled aggregates limits the promotion and use of recycled concrete. Therefore, modifying recycled aggregates to remove the surface of old mortar or enhance the performance of the ITZ is expected to enhance the frost resistance of recycled concrete. Existing methods for removing old mortar from the recycled aggregates include acid washing (Tanta et al., 2022), mechanical grinding (Lin et al., 2023b), thermal grinding (Kalinowska-Wichrowska et al., 2020), microwave heating (Xiao et al., 2012), and pulsed discharge treatment (Inoue et al., 2009), among others. Wang J et al. (2017) treated recycled concrete aggregates by immersing them in an acetic acid solution, finding that immersion in a 3% acetic acid solution for 24 h could soften the attached mortar, while a concentration of acetic acid above 3% would exert a blocking effect. Tam et al. (2007) treated recycled concrete aggregates with hydrochloric and phosphoric acid, respectively, and the results showed that the water absorption rate of the aggregates decreased by 12%, 9.8%, and 8.3% compared to the untreated state,

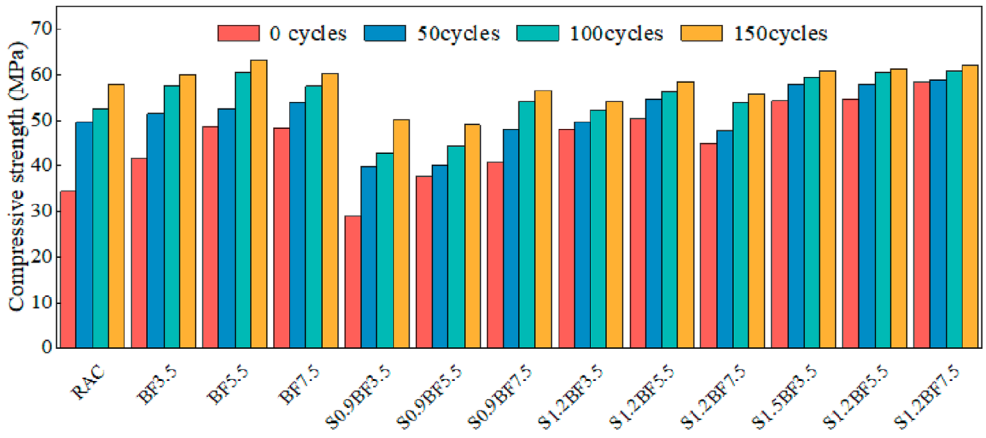

FIGURE 14
Compressive strength of recycled concrete with different reinforcing fibers after freeze-thaw cycles. Notes: BF denotes basalt fiber, and S represents steel fiber.

respectively. However, the use of acid solutions to treat recycled concrete aggregates may damage the structure of natural aggregates containing limestone. Therefore, further optimization of the acid-washing process is required. Pepe et al. (2014) utilized mechanical grinding to treat recycled aggregates, and the results indicated that the water absorption rate was related to the treatment time. Sui and Mueller (2012) heated recycled concrete aggregates at temperatures ranging from 100°C to 600°C and then performed mechanical grinding, finding that treatment at approximately 300°C and sufficient grinding time could grind the apparent density of the recycled aggregates to be close to that of natural coarse aggregates. However, both the mortar attached and the natural aggregate would be worn during the grinding stage. Akbarnezhad et al. (2011) used microwave heating to treat recycled aggregates, and the content of the attached mortar and water absorption rate was reduced by 48% and 33%, respectively, after treatment. With the addition of mechanical friction, the content of the attached mortar and water absorption rate could be further reduced to 85% and 76%, respectively. Pulsed discharge treatment of recycled aggregates is considered one of the most effective treatment methods. Habibzai and Shigeishi (2020) used pulsed discharge to recover natural coarse aggregates and recycled fine aggregates. They discovered that after an appropriate number of discharge treatments, the attached mortar could be completely removed. Inoue et al. (2009) repeatedly discharged recycled concrete, and it was found that the quality of the recycled concrete aggregates increased with the increase in the number of treatments, and the water absorption rate could be reduced from 8% to less than 1%.

By filling the pores within the mortar and the ITZ, it is possible to increase the density of the mortar, reduce surface defects, and thereby enhance the performance of recycled aggregates. Microbially-induced calcium carbonate precipitation can form a protective layer, reducing the erosion caused by the external environment on the aggregate and enhancing the durability of the aggregate. Wang T et al. (2017) reinforced and modified recycled concrete aggregates using spherical *bacillus*, and the results indicated that the mass of the reinforced aggregates increased by 2.5%, with a maximum reduction in water absorption of 20%. Similarly, Qiu et al. (2014) demonstrated that the organic matter in the calcium carbonate induced by bacteria can reduce the wettability of the aggregate surface, decreasing water absorption in treated recycled aggregates. Coating the recycled aggregate surface with mortar repairs the pores and cracks in both the mortar and the ITZ. Hu et al. (2021) applied a zeolite powder-cement (ZP-C) slurry to the surface of RCAs and immersed them. The results demonstrated that a decrease in water absorption of 19.8% and 16.5% for the treated recycled aggregates, respectively. In addition, Zou et al. (2021) modified recycled aggregates using silane coupling agents. The results showed that after 200 freeze-thaw cycles, the mass loss rate was 54.7% lower than that of the unmodified group, and the RDEM was 26.1% higher, as shown in Figure 15. Kou and Poon (2010) strengthened recycled concrete aggregates by immersing them in different concentrations of polyvinyl alcohol solution, and the results showed that the higher the concentration of the polyvinyl alcohol solution, the higher the density and the lower the water absorption of the recycled concrete aggregates.

Accelerated carbonation involves introducing CO_2 into recycled concrete aggregates, leading to a chemical reaction with substances such as calcium hydroxide, calcium silicate hydration products, and calcium aluminate hydration products within the attached mortar, resulting in the formation of calcium carbonate precipitates, aluminates, and silicates (Leemann et al., 2023). This process reduces the porosity and water absorption rate, significantly enhancing the frost resistance. Liang et al. (2024) investigated the influence of incorporating CO_2 curing on the properties of RAC subjected to freeze-thaw cycles. The results indicated that the CO_2 curing method with $Ca(OH)_2$ pre-soaking had the most significant effect on enhancing the frost resistance of recycled concrete. This resulted in a RDEM ranging from 65.27% to 67.71%. Similarly, Li et al. (2017b) investigated the frost resistance of recycled concrete with CO_2 curing periods of 0, 3, and 7 days. The experimental results showed that after 300 freeze-thaw cycles, carbonated recycled concrete exhibited a lower mass loss rate compared to non-carbonated recycled concrete. This is because carbonation mitigates

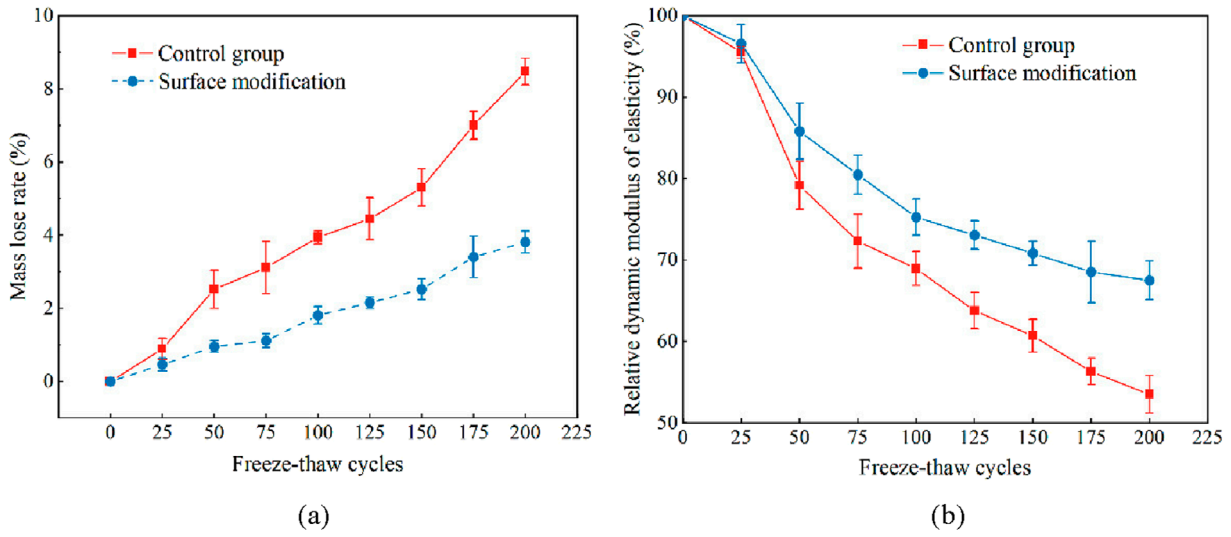

FIGURE 15
Average index of freeze-thaw durability of recycled concrete: **(A)** mass loss rate *versus* freeze-thaw cycles and **(B)** RDME *versus* freeze-thaw cycles (Zou et al., 2021).

the negative effects of high initial porosity and other defects in recycled coarse aggregates during early freeze-thaw cycles and enhances the dispersion of water pressure during later cycles. Moreover, compared to recycled concrete cured for 3 days, recycled concrete cured for 7 days showed a lower mass loss rate and a higher RDEM. It can be observed that extending the CO_2 curing time can improve the frost resistance. Peng et al. (2023) found that increasing the CO_2-cured recycled aggregates content at the same freeze-thaw cycle number reduces the mass loss rate of recycled concrete. In addition, they found that during the CO_2 curing process, the phase transformation occurring inside the material leads to the roughness of the loose ITZ between the matrix and the recycled aggregates, which is the main reason for improving the frost resistance. In summary, carbonation modification relies on the content of carbonizable substances within the attached mortar. However, for recycled concrete aggregates with long service life, the carbonizable substances content in the old mortar and ITZ is extremely low, which limits the efficiency of carbonation modification.

5 Conclusions and remarks

This paper reviews the primary influencing factors on the freeze-thaw resistance of recycled concrete, including the content of recycled aggregate, mineral admixtures, water-to-cement ratio, and water saturation levels, and provides a comprehensive evaluation. Additionally, it briefly summarizes the freeze-thaw damage mechanisms in recycled concrete and outlines several methods for improving its freeze-thaw resistance.

1 The ITZ is a crucial factor affecting the frost resistance of recycled concrete. This is because the ITZ of recycled concrete is complex, and its mechanical properties are poor. Since the internal micropore structure of recycled concrete is influenced by the quality, type, and amount of recycled aggregates, the freeze-thaw damage mechanism in recycled concrete is more complex than that of ordinary concrete, necessitating further investigation.
2 Recycled aggregates are influenced by their production processes, often exhibiting high paste attachment rates on the surface of the aggregates and weak ITZs. This often results in a generally inferior quality of the aggregates. Under freeze-thaw cycling conditions, the frost resistance of recycled concrete typically declines gradually with increasing amounts of recycled aggregates. However, incorporating an appropriate amount of mineral admixtures positively enhances the frost resistance. Extensive testing has shown that a low water-to-cement notably improves frost resistance. Additionally, studies have indicated that an optimal water saturation level of recycled aggregates can provide internal curing effect, further enhancing frost resistance in recycled concrete.
3 Under freeze-thaw actions, the random and isotropic distribution characteristics of fibers play a notable role in the frost resistance of recycled concrete. Additionally, air-entraining agents, commonly used as admixtures, effectively enhance the workability, cohesiveness, and plasticity of concrete while reducing segregation and bleeding. In terms of enhancing the frost resistance of recycled concrete, the impact of air-entraining agents is particularly pronounced. Furthermore, internal modification strategies such as silane treatment and CO_2 curing of recycled aggregates also clearly elevate frost resistance, complementing external strengthening measures like fiber additions or admixture use, thus warranting widespread promotion.
4 In general, the inclusion of admixtures and additives significantly affects the frost resistance of recycled concrete. The careful use of these materials can enhance the frost resistance. However, current research lacks a unified

quantification for the use of various admixtures and additives, such as silica fume, fly ash, rice husk ash, and air-entraining agents. Moreover, there are no standardized measures for improving the frost resistance of recycled concrete, such as the incorporation of fibers, internal curing, or modification of aggregates, meriting further exploration.

Based on existing research findings, the following recommendations are proposed to facilitate the application and promotion of recycled concrete in cold regions.

1 The incorporation rate of recycled aggregates significantly affects the frost resistance of recycled concrete. Based on current research, it is recommended that the content of recycled fine aggregates should not exceed 40% when replacing natural fine aggregates. When substituting natural coarse aggregates with recycled coarse aggregates, the recommended replacement rate should not exceed 50%.
2 In practical engineering, mineral admixtures are frequently used to replace a portion of the binding materials to achieve the objectives of cost reduction and performance enhancement. The addition of an appropriate amount of mineral admixtures can improve the frost resistance of recycled concrete. It is recommended to consider the impact of the dosage of mineral admixtures on the frost resistance of recycled concrete and determine the optimal amount of mineral admixtures.
3 The water-to-cement ratio is a significant factor influencing the frost resistance of recycled concrete. It is recommended to use a lower water-to-cement ratio in the mix design to achieve better frost resistance in recycled concrete.
4 An appropriate degree of water saturation can play a positive role in enhancing the frost resistance of recycled concrete. It is recommended to determine the optimal water saturation level of recycled aggregates to improve their frost resistance.
5 Air-entraining agents have a favorable effect on improving the frost resistance of recycled concrete. It is recommended to select an appropriate dosage to ensure that recycled concrete has good frost resistance. Moreover, an appropriate fiber content can also contribute to a significant improvement in its frost resistance.
6 The old mortar on the surface of recycled aggregates significantly influences the frost resistance of recycled concrete. It is recommended to choose an appropriate method to remove the old mortar from the surface of recycled aggregates or strengthen the recycled aggregates.

Author contributions

QM: Data curation, Formal Analysis, Investigation, Writing–original draft. ZD: Conceptualization, Funding acquisition, Supervision, Writing–review and editing. JW: Project administration, Validation, Writing–review and editing. GY: Formal Analysis, Writing–review and editing. XL: Conceptualization, Validation, Writing–review and editing.

Funding

The author(s) declare that no financial support was received for the research, authorship, and/or publication of this article.

Conflict of interest

Authors JW and XL were employed by China State Construction Engineering Corporation Ltd.

Author GY was employed by Linyi Lantai Environmental Protection Technology Co., Ltd.

The remaining author declares that the research was conducted in the absence of any commercial or financial relationships that could be construed as a potential conflict of interest.

Publisher's note

References

Ahmed, W., and Lim, C. W. (2023). Multicriteria performance assessment of sustainable recycled concrete produced via hybrid usage of basalt, polypropylene and glass fiber. *Constr. Build. Mater* 397, 132462. doi:10.1016/j.conbuildmat.2023.132462

Akbarnezhad, A., Ong, K. C. G., Zhang, M. H., Tam, C. T., and Foo, T. W. J. (2011). Microwave-assisted beneficiation of recycled concrete aggregates. *Constr. Build. Mater* 25, 3469–3479. doi:10.1016/j.conbuildmat.2011.03.038

Alabduljabbar, H., Farooq, F., Alyami, M., and Hammad, A. W. (2024). Assessment of the split tensile strength of fiber reinforced recycled aggregate concrete using interpretable approaches with graphical user interface. *Mater Today Commun.* 38, 108009. doi:10.1016/j.mtcomm.2023.108009

Amorim, N. S., Silva, G., and Ribeiro, D. V. (2018). Effects of the incorporation of recycled aggregate in the durability of the concrete submitted to freeze-thaw cycles. *Constr. Build. Mater* 161, 723–730. doi:10.1016/j.conbuildmat.2017.12.076

Ann, K. Y., Kim, M. J., Hwang, J. P., Cho, C., and Kim, K. H. (2017). Chloride transport in OPC concrete subjected to the freeze and thaw damage. *Adv. Mater Sci. Eng.* 2017, 8212856. doi:10.1155/2017/8212856

Atasham Ul Haq, M., Xia, P., Khan, S., Tahir, M., Hassam, M., Gong, F., et al. (2024). Characterizations and quantification of freeze-thaw behaviors of recycled brick aggregate concrete. *J. Build. Eng.* 86, 108821. doi:10.1016/j.jobe.2024.108821

Avet, F., Sofia, L., and Scrivener, K. (2019). Concrete performance of limestone calcined clay cement (LC3) compared with conventional cements. *Adv. Civ. Eng. Mater* 8, 275–286. doi:10.1520/ACEM20190052

Bai, W., Song, Z., Yuan, C., Guan, J., Xie, C., Huang, H., et al. (2023a). Study on mechanical properties and damage mechanism of recycled concrete containing silica fume in freeze–thaw environment. *Constr. Build. Mater* 375, 130872. doi:10.1016/j.conbuildmat.2023.130872

Bai, W., Wang, X., Yuan, C., Guan, J., Cao, K., and Xie, C. (2023b). Study on dynamic mechanical properties and meso-damage mechanism of carbon fibers recycled aggregate concrete under freeze-thaw environment. *J. Build. Eng.* 79, 107768. doi:10.1016/j.jobe.2023.107768

Bao, J. W., Zheng, R., Yu, Z. H., Zhang, P., Song, Q., Xu, J. G., et al. (2022). Freeze-thaw resistance of recycled aggregate concrete incorporating ferronickel slag as fine aggregate. *Constr. Build. Mater* 356. doi:10.1016/j.conbuildmat.2022.129178

Bhikshma, V., and Kumar, K. P. (2015). Study on flexural behavior of recycled aggregate concrete beams using glass fibers.

Bogas, J. A., de Brito, J., and Ramos, D. (2016). Freeze–thaw resistance of concrete produced with fine recycled concrete aggregates. *J. Clean. Prod.* 115, 294–306. doi:10.1016/j.jclepro.2015.12.065

Bu, C., Liu, L., Lu, X., Zhu, D., Sun, Y., Yu, L., et al. (2022). The durability of recycled fine aggregate concrete: a review. doi:10.3390/ma15031110ER

Bu, N., Liu, R., Fang, W., Zhao, H., and Bai, R. (2023). Study on mechanical properties and frost resistance of recycled fly ash concrete for construction. *J. Funct. Mater.* 54. doi:10.3969/j.issn.1001-9731.2023.05.030

Chandru, U., Bahurudeen, A., and Senthilkumar, R. (2023). Systematic comparison of different recycled fine aggregates from construction and demolition wastes in OPC concrete and PPC concrete. *J. Build. Eng.* 75, 106768. doi:10.1016/j.jobe.2023.106768

Chen, C., Lu, C., Lu, C., Wei, S., Guo, Z., Zhou, Q., et al. (2023). Synergetic effect of fly ash and ground-granulated blast slag on improving the chloride permeability and freeze–thaw resistance of recycled aggregate concrete. *Constr. Build. Mater* 365, 130015. doi:10.1016/j.conbuildmat.2022.130015

Chen, J. S., Huang, C. C., Chu, P. Y., and Lin, K. Y. (2007). Engineering characterization of recycled asphalt concrete and aged bitumen mixed recycling agent. *J. Mater Sci.* 42, 9867–9876. doi:10.1007/s10853-007-1713-8

Chen, X., Guo, Y., Gong, T., Zhang, L., Zhang, H., Qin, M., et al. (2024). Study on preparation and performance of brick-concrete recycled sand powder autoclaved aerated concrete. *J. Build. Eng.* 91, 109671. doi:10.1016/j.jobe.2024.109671

Cheng, S., Shui, Z., Yu, R., Zhang, X., and Zhu, S. (2018). Durability and environment evaluation of an eco-friendly cement-based material incorporating recycled chromium containing slag. *J. Clean. Prod.* 185, 23–31. doi:10.1016/j.jclepro.2018.03.048

Cheng, X., Pinghua, Z., and Xinjie, W. (2024). Effects of mineral admixtures on frost resistance and renewability of recycled aggregate concrete. *Bull. Chin. Ceram. Soc.* 43, 956–964. doi:10.16552/j.cnki.issn1001-1625.2024.03.007

Cheng, Y., Shang, X., and Zhang, Y. (2017). Experimental research on durability of recycled aggregate concrete under freeze-thaw cycles. *J. Phys. Conf. Ser.* 870, 12018. doi:10.1088/1742-6596/870/1/012018

Corinaldesi, V. (2012). Mechanical performance and durability of fly ash recycled aggregate concretes. *Adv. Mater. Res.* 538-541, 1568–1572. doi:10.4028/www.scientific.net/AMR.538-541.1568

Datta, S. D., Sobuz, M. H. R., Akid, A. S. M., and Islam, S. (2022). Influence of coarse aggregate size and content on the properties of recycled aggregate concrete using non-destructive testing methods. *J. Build. Eng.* 61, 105249. doi:10.1016/j.jobe.2022.105249

Deng, Q., Zhang, R., Liu, C., Duan, Z., and Xiao, J. (2023). Influence of fiber properties on abrasion resistance of recycled aggregate concrete: length, volume fraction, and types of fibers. *Constr. Build. Mater* 362, 129750. doi:10.1016/j.conbuildmat.2022.129750

Deng, X., Gao, X., Wang, R., Gao, M., Yan, X., Cao, W., et al. (2021a). Investigation of microstructural damage in air-entrained recycled concrete under a freeze–thaw environment. *Constr. Build. Mater* 268, 121219. doi:10.1016/j.conbuildmat.2020.121219

Deng, X. H., Liu, Y. Y., and Wang, R. (2021b). Investigating freeze-proof durability of air-entrained C30 recycled coarse aggregate concrete. *Arch. Civ. Eng.* 67, 507–524. doi:10.24425/ace.2021.137182

de Oliveira, M. B., and Vazquez, E. (1996). The influence of retained moisture in aggregates from recycling on the properties of new hardened concrete. *Waste Manag.* 16, 113–117. doi:10.1016/S0956-053X(96)00033-5

El-Hawary, M., and Al-Sulily, A. (2020). Internal curing of recycled aggregates concrete. *J. Clean. Prod.* 275, 122911. doi:10.1016/j.jclepro.2020.122911

El-Hawary, M., Al-Yaqout, A., and Elsayed, K. (2021). Freezing and thawing cycles: effect on recycled aggregate concrete including slag. *Int. J. Sustain Eng.* 14, 800–808. doi:10.1080/19397038.2021.1886374

Gao, D., Zhang, L., Zhao, J., and You, P. (2020). Durability of steel fibre-reinforced recycled coarse aggregate concrete. *Constr. Build. Mater* 232, 117119. doi:10.1016/j.conbuildmat.2019.117119

Gao, Q., Ma, Z., Xiao, J., and Li, F. (2018). Effects of imposed damage on the capillary water absorption of recycled aggregate concrete. *Adv. Mater Sci. Eng.* 2018, 2890931. doi:10.1155/2018/2890931

Gao, D., Lou, Z., and Wang, Z. (2007). Experimental research on the compressive strength of steel fiber recycled concrete. *J. Zhengzhou Univ.* 28, 5–10. doi:10.1360/yc-007-0745

Ghorbani, S., Sharifi, S., Ghorbani, S., Tam, V. W., de Brito, J., and Kurda, R. (2019). Effect of crushed concrete waste's maximum size as partial replacement of natural coarse aggregate on the mechanical and durability properties of concrete. *Resour. Conservation Recycl.* 149, 664–673. doi:10.1016/j.resconrec.2019.06.030

Gokce, A., Nagataki, S., Saeki, T., and Hisada, M. (2004). Freezing and thawing resistance of air-entrained concrete incorporating recycled coarse aggregate: the role of air content in demolished concrete. *Cem. Concr. Res.* 34, 799–806. doi:10.1016/j.cemconres.2003.09.014

Gong, F., and Jacobsen, S. (2019). Modeling of water transport in highly saturated concrete with wet surface during freeze/thaw. *Cem. Concr. Res.* 115, 294–307. doi:10.1016/j.cemconres.2018.08.013

Guan, T., Zhang, L., Zheng, Y., Guan, J., Zhang, Y., and Zhang, Y. (2024). Frost resistance and damage evolution model of basalt fiber-reinforced recycled concrete based on recycled coarse aggregate strengthening and vibration mixing processes. *J. Build. Eng.* 91, 109627. doi:10.1016/j.jobe.2024.109627

Gunasekara, C., Zhou, Z., Law, D. W., Sofi, M., Setunge, S., and Mendis, P. (2020). Microstructure and strength development of quaternary blend high-volume fly ash concrete. *J. Mater Sci.* 55, 6441–6456. doi:10.1007/s10853-020-04473-1

Guo, J., Sun, W., Xu, Y., Lin, W., and Jing, W. (2022). *Damage Mech. Model. Concr. Freeze–Thaw Cycles a Rev.*, doi:10.3390/buildings12091317

Guo, Y., Liu, Y., Wang, W., Wang, K., Zhang, Y., and Hou, J. (2023). Effect of basalt fiber on uniaxial compression-related constitutive relation and compressive toughness of recycled aggregate concrete. doi:10.3390/ma16051849

Guo, Z., Jiang, T., Zhang, J., Kong, X., Chen, C., and Lehman, D. E. (2020). Mechanical and durability properties of sustainable self-compacting concrete with recycled concrete aggregate and fly ash, slag and silica fume. *Constr. Build. Mater* 231, 117115. doi:10.1016/j.conbuildmat.2019.117115

Habibzai, R., and Shigeishi, M. (2020). Quality evaluation of pulsed power recycled sand by electrical resistivity method. *Int. J. GEOMATE* 19, 66–75. doi:10.21660/2020.75.84833

Hamman, A., Ismail, M., and Roushdy, M. (2021) Incorporation of perlite and recycled aggregates for internal concrete curing. *Int. Conf. Transp. Dev.*, 225–234. doi:10.1061/9780784483541.021

Hasholt, M. T. (2014). Air void structure and frost resistance: a challenge to Powers' spacing factor. *Mater Struct.* 47, 911–923. doi:10.1617/s11527-013-0102-9

Hu, H., He, Z., Fan, K., Shibro, T., Liu, B., and Shi, J. (2021). Properties enhancement of recycled coarse aggregates by pre-coating/pre-soaking with zeolite powder/calcium hydroxide. *Constr. Build. Mater* 286, 122888. doi:10.1016/j.conbuildmat.2021.122888

Huaishuai, S., Zhiheng, W., Peng, Z., Tiejun, Z., Guoxi, F., and Guosheng, R. (2017). Bond behavior of steel bar in air-entrained RCAC in fresh water and sea water after fast freeze-thaw cycles. *Cold Reg. Sci. Technol.* 135, 90–96. doi:10.1016/j.coldregions.2016.11.005

Inoue, S., Araki, J., Aoki, T., Maeda, S., Iizasa, S., Takaki, M., et al. (2009). Coarse aggregate recycling by pulsed discharge inside of concrete. *Acta Phys. Pol. A* 115, 1107–1109. doi:10.12693/APhysPolA.115.1107

Islam, M. J., Islam, K., Shahjalal, M., Khatun, E., Islam, S., and Razzaque, A. B. (2022). Influence of different types of fibers on the mechanical properties of recycled waste aggregate concrete. *Constr. Build. Mater* 337, 127577. doi:10.1016/j.conbuildmat.2022.127577

Ji, Y., and Wang, D. (2022). Durability of recycled aggregate concrete in cold regions. *Case Stud. Constr. Mater* 17, e01475. doi:10.1016/j.cscm.2022.e01475

Kalinowska-Wichrowska, K., Pawluczuk, E., and Bołtryk, M. (2020). Waste-free technology for recycling concrete rubble. *Constr. Build. Mater* 234, 117407. doi:10.1016/j.conbuildmat.2019.117407

Kang, J., Chen, X., Yu, Z., and Wang, L. (2024). Study on the fatigue life and toughness of recycled aggregate concrete based on basalt fiber. *Mater Today Commun.* 40, 109397. doi:10.1016/j.mtcomm.2024.109397

Khoury, E., Cazacliu, B., and Remond, S. (2019). Control of effective water in recycled aggregate concrete using power curves of the mixer. *Mater Today Commun.* 21, 100721. doi:10.1016/j.mtcomm.2019.100721

Kobayashi, K., Miura, S., Oshima, E., and Yun, H. (2022). Mechanisms of high frost scaling resistance of SHCC. *Constr. Build. Mater* 324, 126300. doi:10.1016/j.conbuildmat.2021.126300

Kou, S., and Poon, C. (2010). Properties of concrete prepared with PVA-impregnated recycled concrete aggregates. *Cem. Concr. Compos.* 32, 649–654. doi:10.1016/j.cemconcomp.2010.05.003

Lam, N. N. (2020). Influence of fly ash and recycled AAC waste for replacement of natural sand in manufacture of autoclaved aerated concrete. *IOP Conf. Ser. Earth Environ. Sci.* 505, 12001. doi:10.1088/1755-1315/505/1/012001

Lee, S., Jang, S. Y., Kim, C. Y., Ahn, E. J., Kim, S. P., Gwon, S., et al. (2018). Effects of redispersible polymer powder on mechanical and durability properties of preplaced aggregate concrete with recycled railway ballast. *Int. J. Concr. Struct. Mater* 12, 69. doi:10.1186/s40069-018-0304-1

Lee, S., Park, S., Kim, D., and Kang, J. (2021). Effect of freeze–thaw cycles on the performance of concrete containing water-cooled and air-cooled slag. doi:10.3390/app11167291ER

Leemann, A., Münch, B., and Wyrzykowski, M. (2023). CO2 absorption of recycled concrete aggregates in natural conditions. *Mater Today Commun.* 36, 106569. doi:10.1016/j.mtcomm.2023.106569

Lei, B., Li, W., Tang, Z., Tam, V. W. Y., and Sun, Z. (2018). Durability of recycled aggregate concrete under coupling mechanical loading and freeze-thaw cycle in salt-solution. *Constr. Build. Mater* 163, 840–849. doi:10.1016/j.conbuildmat.2017.12.194

Levy, S. M., and Helene, P. (2004). Durability of recycled aggregates concrete: a safe way to sustainable development. *Cem. Concr. Res.* 34, 1975–1980. doi:10.1016/j.cemconres.2004.02.009

Li, J., and Qin, C. L. (2013). Strengths investigation of air entrained recycled fine aggregate mortar. *Appl. Mech. Mater.* 253-255, 432–435. doi:10.4028/www.scientific.net/AMM.253-255.432

Li, T., Nogueira, R., de Brito, J., and Liu, J. (2024). A simple method to address the high water absorption of recycled aggregates in cementitious mixes. *Constr. Build. Mater* 411, 134404. doi:10.1016/j.conbuildmat.2023.134404

Li, W., Lu, K., and Walz, J. Y. (2012a). Effects of added kaolinite on the strength and porosity of freeze-cast kaolinite–silica nanocomposites. *J. Mater Sci.* 47, 6882–6890. doi:10.1007/s10853-012-6631-8

Li, W., Pour-Ghaz, M., Castro, J., and Weiss, J. (2012b). Water absorption and critical degree of saturation relating to freeze-thaw damage in concrete pavement joints. *J. Mater Civ. Eng.* 24, 299–307. doi:10.1061/(ASCE)MT.1943-5533.0000383

Li, Y., Jin, K., Lin, H., Shen, J., Shi, J., and Fan, M. (2024). Analysis and prediction of freeze-thaw resistance of concrete based on machine learning. *Mater Today Commun.* 39, 108946. doi:10.1016/j.mtcomm.2024.108946

Li, Y., Wang, R. J., Li, S. Y., and Zhao, Y. (2017b). Assessment of the freeze-thaw resistance of concrete incorporating carbonated coarse recycled concrete aggregates. *J. Ceram. Soc. Jpn.* 125, 837–845. doi:10.2109/jcersj2.17111

Li, Z., Liu, L., Yan, S., Zhang, M., Xia, J., and Xie, Y. (2019). Effect of freeze-thaw cycles on mechanical and porosity properties of recycled construction waste mixtures. *Constr. Build. Mater* 210, 347–363. doi:10.1016/j.conbuildmat.2019.03.184

Liang, C., Wang, S., Cai, Z., Yin, Y., Gao, Y., Guo, M., et al. (2024). Effects of CO2 curing methods on frost resistance and mechanical properties of recycled aggregate concrete. *Case Stud. Constr. Mater* 20, e02973. doi:10.1016/j.cscm.2024.e02973

Lin, Y., Feng, X., and Zhang, Z. (2023a). Microscopic simulation of thermo-mechanical behaviors in recycled concrete under freeze–thaw action. *Constr. Build. Mater* 409, 133892. doi:10.1016/j.conbuildmat.2023.133892

Lin, Y., He, T., and Da, Y. (2023b). Influence of self-grinding modification on the properties of recycled coarse aggregate and recycled concrete. *Mater. Rev.* 37.

Liu, G., Hunger, M., Tošić, N., and de la Fuente, A. (2023). Effect of free and embedded polypropylene fibres recovered from concrete recycling on the properties of new concrete. *Constr. Build. Mater* 409, 134145. doi:10.1016/j.conbuildmat.2023.134145

Liu, J., Shang, Y., Miao, C., and Ran, Q. (2011). Effects of air entraining manners of polycarboxylate-type water reducer on the properties of concrete. *J. Build. Mater.* 14, 528–531. doi:10.3969/j.issn.1007-9629.2011.04.018

Liu, K., Yan, J., Hu, Q., Sun, Y., and Zou, C. (2016). Effects of parent concrete and mixing method on the resistance to freezing and thawing of air-entrained recycled aggregate concrete. *Constr. Build. Mater* 106, 264–273. doi:10.1016/j.conbuildmat.2015.12.074

Liu, L., Qin, S., and Wang, X. (2018). Poro-elastic–plastic model for cement-based materials subjected to freeze–thaw cycles. *Constr. Build. Mater* 184, 87–99. doi:10.1016/j.conbuildmat.2018.06.197

Liu, R., Xiao, H., Liu, J., Guo, S., and Pei, Y. (2019). Improving the microstructure of ITZ and reducing the permeability of concrete with various water/cement ratios using nano-silica. *J. Mater Sci.* 54, 444–456. doi:10.1007/s10853-018-2872-5

Liu, Z., and Hansen, W. (2016). A geometrical model for void saturation in air-entrained concrete under continuous water exposure. *Constr. Build. Mater* 124, 475–484. doi:10.1016/j.conbuildmat.2016.07.113

Li, Y., Wang, R., and Zhao, Y. (2017a). Effect of coupled deterioration by freeze-thaw cycle and carbonation on concrete produced with coarse recycled concrete aggregates. *J. Ceram. Soc. Jpn.* 125, 36–45. doi:10.2109/jcersj2.16183

Long, T., Dong, S. H., Cui, S. M., and Wang, Q. (2013). Compressive behaviour of recycle concrete cubes after freeze-thaw cycles. *Adv. Mater. Res.* 671-674, 1865–1868. doi:10.4028/www.scientific.net/AMR.671-674.1865

Luan, H., Wu, J., and Pan, J. (2020). Saline water absorption behavior and critical saturation degree of recycled aggregate concrete during freeze-thaw cycles. *Constr. Build. Mater* 258, 119640. doi:10.1016/j.conbuildmat.2020.119640

Luan, H., Wu, J., and Pan, J. (2021). Freeze-thaw durability of recycled aggregate concrete: an overview. *J. Wuhan Univ. Technology-Mater. Sci. Ed.* 36, 58–69. doi:10.1007/s11595-021-2378-x

Luo, X. W., Yao, H. L., and Lu, Z. (2015). Production of recycled concrete and its material properties. *Mater. Res. Innovations* 19, S1–S147. doi:10.1179/1432891715Z.0000000001392

Ma, W., Lv, B., Wang, Y., Huang, L., Yan, L., and Kasal, B. (2024). Freeze-thaw, chloride penetration and carbonation resistance of natural and recycled aggregate concrete containing rice husk ash as replacement of cement. *J. Build. Eng.* 86, 108889. doi:10.1016/j.jobe.2024.108889

Mahboob, A., Hassanshahi, O., Safi, M., and Majid, T. A. (2024). Experimental investigation of eco-friendly fiber-reinforced concrete using recycled and natural fibers, integrated with recycled aggregates. *Adv. Compos Mater*, 1–30. doi:10.1080/09243046.2024.2322799

Marchi, T., Garcia Diaz, E., Salgues, M., Souche, J. C., and Devillers, P. (2023). Internal curing capacity of recycled coarse aggregates incorporated in concretes with low water/cement ratios. *Constr. Build. Mater* 409, 133893. doi:10.1016/j.conbuildmat.2023.133893

Mardani-Aghabaglou, A., Yüksel, C., Beglarigale, A., and Ramyar, K. (2019). Improving the mechanical and durability performance of recycled concrete aggregate-bearing mortar mixtures by using binary and ternary cementitious systems. *Constr. Build. Mater* 196, 295–306. doi:10.1016/j.conbuildmat.2018.11.124

Mastali, M., Dalvand, A., and Sattarifard, A. R. (2016). The impact resistance and mechanical properties of reinforced self-compacting concrete with recycled glass fibre reinforced polymers. *J. Clean. Prod.* 124, 312–324. doi:10.1016/j.jclepro.2016.02.148

Meng, D., Wu, X., Quan, H., and Zhu, C. (2021). A strength-based mix design method for recycled aggregate concrete and consequent durability performance. *Constr. Build. Mater* 281, 122616. doi:10.1016/j.conbuildmat.2021.122616

Meng, T., Lai, Z., Yang, X., Dai, D., Jia, Y., and Yu, H. (2024). An approach to effectively improve the properties of recycled concrete aggregate and recycled brick aggregate by micro-nano particle reconstruction. *Constr. Build. Mater* 421, 135669. doi:10.1016/j.conbuildmat.2024.135669

Muhammad, F., Harun, M., Ahmed, A., Kabir, N., Khalid, H. R., and Hanif, A. (2024). Influence of bonded mortar on recycled aggregate concrete properties: a review. *Constr. Build. Mater* 432, 136564. doi:10.1016/j.conbuildmat.2024.136564

Nazeer, M., Kapoor, K., and Singh, S. P. (2024). Impact of recycled concrete aggregates on the strength and durability properties of pervious concrete. *Mag. Concr. Res.* 76, 272–291. doi:10.1680/jmacr.23.00089

Oertel, T., Hutter, F., Helbig, U., and Sextl, G. (2014). Amorphous silica in ultra-high performance concrete: first hour of hydration. *Cem. Concr. Res.* 58, 131–142. doi:10.1016/j.cemconres.2014.01.008

Olanike, A. O. (2014). Experimental investigation into the freeze-thaw resistance of concrete using recycled concrete aggregates and admixtures. *Ratio (Oxf)* 85, 120. doi:10.13189/cea.2014.020404

Omary, S., Ghorbel, E., and Wardeh, G. (2016). Relationships between recycled concrete aggregates characteristics and recycled aggregates concretes properties. *Constr. Build. Mater* 108, 163–174. doi:10.1016/j.conbuildmat.2016.01.042

Peceño, B., Arenas, C., Alonso-Fariñas, B., and Leiva, C. (2019). Substitution of coarse aggregates with mollusk-shell waste in acoustic-absorbing concrete. *J. Mater Civ. Eng.* 31, 4019077. doi:10.1061/(ASCE)MT.1943-5533.0002719

Pehlivanlı, Z. O., Uzun, İ., and Demir, İ. (2015). Mechanical and microstructural features of autoclaved aerated concrete reinforced with autoclaved polypropylene, carbon, basalt and glass fiber. *Constr. Build. Mater* 96, 428–433. doi:10.1016/j.conbuildmat.2015.08.104

Peled, A., Castro, J., and Weiss, J. (2010). Atomic force microscopy examinations of mortar made by using water-filled lightweight aggregate. *Transp. Res. Rec.* 2141, 92–101. doi:10.3141/2141-16

Peng, X., Shi, F., Yang, J., Yang, Q., Wang, H., and Zhang, J. (2023). Modification of construction waste derived recycled aggregate via CO2 curing to enhance corrosive freeze-thaw durability of concrete. *J. Clean. Prod.* 405, 137016. doi:10.1016/j.jclepro.2023.137016

Pepe, M., Toledo Filho, R. D., Koenders, E. A. B., and Martinelli, E. (2014). Alternative processing procedures for recycled aggregates in structural concrete. *Constr. Build. Mater* 69, 124–132. doi:10.1016/j.conbuildmat.2014.06.084

Pickel, D., Tighe, S., and West, J. S. (2017). Assessing benefits of pre-soaked recycled concrete aggregate on variably cured concrete. *Constr. Build. Mater* 141, 245–252. doi:10.1016/j.conbuildmat.2017.02.140

Posi, P., Thongjapo, P., Thamultree, N., Boontee, P., Kasemsiri, P., and Chindaprasirt, P. (2016). Pressed lightweight fly ash-OPC geopolymer concrete containing recycled lightweight concrete aggregate. *Constr. Build. Mater* 127, 450–456. doi:10.1016/j.conbuildmat.2016.09.105

Powers, T. C. (1945). Working hypothesis for further studies of frost resistance of concrete. *ACI J. Proc.* 41. doi:10.14359/8684

Powers, T. C., and Helmuth, R. A. (1953). Theory of volume changes in hardened portland-cement paste during freezing.

Qiu, J., Li, L., Li, L., Luan, X., Guan, X., and Niu, G. (2024). Study on the deterioration characteristics and mechanisms of recycled brick-concrete aggregate concrete under load-freeze-thaw coupling. *Constr. Build. Mater* 413, 134817. doi:10.1016/j.conbuildmat.2023.134817

Qiu, J., Tng, D. Q. S., and Yang, E. (2014). Surface treatment of recycled concrete aggregates through microbial carbonate precipitation. *Constr. Build. Mater* 57, 144–150. doi:10.1016/j.conbuildmat.2014.01.085

Quan, X. Y., Wang, S. L., Li, J. T., Luo, J., Liu, K. N., Xu, J., et al. (2022). Utilization of molybdenum tailings as fine aggregate in recycled aggregate concrete. *J. Clean. Prod.* 372. doi:10.1016/j.jclepro.2022.133649

Ramesh, B., and Eswari, S. (2021). Mechanical behaviour of basalt fibre reinforced concrete: an experimental study. *Mater. Today Proc.* 43, 2317–2322. doi:10.1016/j.matpr.2021.01.071

Ren, Q., Pacheco, J., de Brito, J., and Hu, J. (2024). Analysis of the influence of the attached mortar's geometry on the mechanical behaviour of recycled aggregate concrete through mesoscale modelling. *Eng. Fract. Mech.* 297, 109876. doi:10.1016/j.engfracmech.2024.109876

Rong, X. L., Li, L., Zheng, S. S., Wang, F., Huang, W. Y., Zhang, Y. X., et al. (2023). Freeze–thaw damage model for concrete considering a nonuniform temperature field. *J. Build. Eng.* 72, 106747. doi:10.1016/j.jobe.2023.106747

Sáez Del Bosque, I. F., Zhu, W., Howind, T., Matías, A., Sánchez De Rojas, M. I., and Medina, C. (2017). Properties of interfacial transition zones (ITZs) in concrete containing recycled mixed aggregate. *Cem. Concr. Compos.* 81, 25–34. doi:10.1016/j.cemconcomp.2017.04.011

Saha, A. K., and Sarker, P. K. (2020). Mitigation of the potential alkali-silica reaction of FNS using around FNS as a supplementary binder. *Adv. Cem. Res.* 32, 537–546. doi:10.1680/jadcr.19.00035

Scherer, G. W. (1999). Crystallization in pores. *Cem. Concr. Res.* 29, 1347–1358. doi:10.1016/S0008-8846(99)00002-2

Scrivener, K. L., Lothenbach, B., De Belie, N., Gruyaert, E., Skibsted, J., Snellings, R., et al. (2015). TC 238-SCM: hydration and microstructure of concrete with SCMs. *Mater Struct.* 48, 835–862. doi:10.1617/s11527-015-0527-4

Setzer, M. J. (2001a). Micro-ice-lens formation in porous solid. *J. Colloid Interface Sci.* 243, 193–201. doi:10.1006/jcis.2001.7828

Setzer, M. J. (2001b). Mechanical stability criterion, triple-phase condition, and pressure differences of matter condensed in a porous matrix. *J. Colloid Interface Sci.* 235, 170–182. doi:10.1006/jcis.2000.7317

Shen, W., Wu, J., Du, X., Li, Z., Wu, D., Sun, J., et al. (2022). Cleaner production of high-quality manufactured sand and ecological utilization of recycled stone powder in concrete. *J. Clean. Prod.* 375, 134146. doi:10.1016/j.jclepro.2022.134146

Şimşek, O., Pourghadri Sefidehkhan, H., and Gökçe, H. S. (2022). Performance of fly ash-blended Portland cement concrete developed by using fine or coarse recycled concrete aggregate. *Constr. Build. Mater* 357, 129431. doi:10.1016/j.conbuildmat.2022.129431

Song, H., Xie, W., Liu, J., Cheng, F., Gasem, K. A. M., and Fan, M. (2018). Effect of surfactants on the properties of a gas-sealing coating modified with fly ash and cement. *J. Mater Sci.* 53, 15142–15156. doi:10.1007/s10853-018-2679-4

Sosa, M. E., Villagrán Zaccardi, Y. A., and Zega, C. J. (2021). A critical review of the resulting effective water-to-cement ratio of fine recycled aggregate concrete. *Constr. Build. Mater* 313, 125536. doi:10.1016/j.conbuildmat.2021.125536

Sui, Y., and Mueller, A. (2012). Development of thermo-mechanical treatment for recycling of used concrete. *Mater Struct.* 45, 1487–1495. doi:10.1617/s11527-012-9852-z

Sun, J., and Geng, J. (2012). Effect of particle size and content of recycled fine aggregate on frost resistance of concrete. *J. Build. Mater.* 15, 382–385. doi:10.3969/j.issn.1007-9629.2012.03.017

Sunayana, S., and Barai, S. V. (2021). Partially fly ash incorporated recycled coarse aggregate based concrete: microstructure perspectives and critical analysis. *Constr. Build. Mater* 278, 122322. doi:10.1016/j.conbuildmat.2021.122322

Tam, V. W. Y., Gao, X. F., and Tam, C. M. (2005). Microstructural analysis of recycled aggregate concrete produced from two-stage mixing approach. *Cem. Concr. Res.* 35, 1195–1203. doi:10.1016/j.cemconres.2004.10.025

Tam, V. W. Y., Tam, C. M., and Le, K. N. (2007). Removal of cement mortar remains from recycled aggregate using pre-soaking approaches. *Resour. Conservation Recycl.* 50, 82–101. doi:10.1016/j.resconrec.2006.05.012

Tanta, A., Kanoungo, A., Singh, S., and Kanoungo, S. (2022). The effects of surface treatment methods on properties of recycled concrete aggregates. *Mater. Today Proc.* 50, 1848–1852. doi:10.1016/j.matpr.2021.09.223

Tarhan, Y., and Şahin, R. (2021). Effect of recycled concrete aggregate, air entraining admixture and maximum aggregate particle size on the behavior of concrete under freeze-thaw cycles. *J. Green Build.* 16, 217–233. doi:10.3992/jgb.16.2.217

Tošić, N., Peralta Martínez, D., Hafez, H., Reynvart, I., Ahmad, M., Liu, G., et al. (2022). Multi-recycling of polypropylene fibre reinforced concrete: influence of recycled aggregate properties on new concrete. *Constr. Build. Mater* 346, 128458. doi:10.1016/j.conbuildmat.2022.128458

Tran, D. L., Mouret, M., Cassagnabère, F., and Phung, Q. T. (2022). Effects of intrinsic granular porosity and mineral admixtures on durability and transport properties of recycled aggregate concretes. *Mater Today Commun.* 33, 104709. doi:10.1016/j.mtcomm.2022.104709

Tuyan, M., Mardani-Aghabaglou, A., and Ramyar, K. (2014). Freeze–thaw resistance, mechanical and transport properties of self-consolidating concrete incorporating coarse recycled concrete aggregate. *Mater Des.* 53, 983–991. doi:10.1016/j.matdes.2013.07.100

Wang, C., Wang, J., Liu, X., Cai, Y., and Zhang, Y. (2023a). Orthogonal experimental design for compressive strength of recycled coarse aggregate concrete with silica fume-slag-fly ash hybrid micro-powders. *Constr. Build. Mater* 408, 133669. doi:10.1016/j.conbuildmat.2023.133669

Wang, D., Xu, Y., Zheng, Y., and Wu, Y. (2023b). Effect of freeze–thaw cycles on physical and mechanical properties of concrete with different replacement rates of recycled coarse aggregate. *Int. J. Pavement Res. Technol.* doi:10.1007/s42947-023-00397-6

Wang, H., Zhu, P., Yan, X., Liu, H., Zhu, L., and Wang, X. (2023c). Effect of silica fume on frost resistance and recyclability potential of recycled aggregate concrete under freeze–thaw environment. *Constr. Build. Mater* 409, 134109. doi:10.1016/j.conbuildmat.2023.134109

Wang, J., Vandevyvere, B., Vanhessche, S., Schoon, J., Boon, N., and De Belie, N. (2017). Microbial carbonate precipitation for the improvement of quality of recycled aggregates. *J. Clean. Prod.* 156, 355–366. doi:10.1016/j.jclepro.2017.04.051

Wang, T., Xue, Y., Zhou, M., Lv, Y., Chen, Y., Wu, S., et al. (2017). Hydration kinetics, freeze-thaw resistance, leaching behavior of blended cement containing co-combustion ash of sewage sludge and rice husk. *Constr. Build. Mater* 131, 361–370. doi:10.1016/j.conbuildmat.2016.11.087

Wang, W., Wang, S., Peng, L., Wang, N., Meng, T., Zhao, Y., et al. (2024). Preliminary investigation and life cycle assessment of artificial reefs with recycled brick-concrete aggregates. *Constr. Build. Mater* 432, 136618. doi:10.1016/j.conbuildmat.2024.136618

Wang, Y., Hu, Z., and Liu, J. (2023d). Freeze-thaw resistance of concrete containing azodicarbonamide expansive agent. *Constr. Build. Mater* 367, 130335. doi:10.1016/j.conbuildmat.2023.130335

Wang, Y., Liu, J., Zhu, P., Liu, H., Wu, C., and Zhao, J. (2021). Investigation of adhered mortar content on recycled aggregate using image analysis method. *J. Mater Civ. Eng.* 33, 4021225. doi:10.1061/(ASCE)MT.1943-5533.0003864

Wang, Y., Xie, M., and Zhang, J. (2023e). Mechanical properties and damage model of modified recycled concrete under freeze-thaw cycles. *J. Build. Eng.* 78, 107680. doi:10.1016/j.jobe.2023.107680

Wang, Z., Zeng, Q., Wang, L., Yao, Y., and Li, K. (2014). Effect of moisture content on freeze–thaw behavior of cement paste by electrical resistance measurements. *J. Mater Sci.* 49, 4305–4314. doi:10.1007/s10853-014-8126-2

Wei, D., Zhu, P., Yan, X., Liu, H., Chen, C., and Wang, Z. (2022). Potential evaluation of waste recycled aggregate concrete for structural concrete aggregate from freeze-thaw environment. *Constr. Build. Mater* 321, 126291. doi:10.1016/j.conbuildmat.2021.126291

Wu, Y., Gao, K., and Wu, B. (2019). Influence of fly ash on the compressive strength of concrete containing recycled aggregate. *Emerg. Mater Res.* 8, 483–491. doi:10.1680/jemmr.18.00013

Xia, G., and Zhao, Y. (2024). Interface parameters of recycled aggregate concrete considering the distribution of old mortar content. *Case Stud. Constr. Mater* 20, e03262. doi:10.1016/j.cscm.2024.e03262

Xia, P., Yang, L., Wang, S., Gong, F., Cao, W., and Zhao, Y. (2023). Improved freeze-thaw modification of recycled concrete aggregate originally from frost resistive concrete. *Cem. Concr. Compos.* 144, 105302. doi:10.1016/j.cemconcomp.2023.105302

Xiao, J., Li, W., and Poon, C. (2012). Recent studies on mechanical properties of recycled aggregate concrete in China—a review. *Sci. China Technol. Sci.* 55, 1463–1480. doi:10.1007/s11431-012-4786-9

Xiao, J., Li, W., Sun, Z., Lange, D. A., and Shah, S. P. (2013). Properties of interfacial transition zones in recycled aggregate concrete tested by nanoindentation. *Cem. Concr. Compos.* 37, 276–292. doi:10.1016/j.cemconcomp.2013.01.006

Xiao, J., Wu, L., and Fan, Y. (2012). Test on modification of recycled coarse aggregate by microwave heating. *Concrete*, 55–57. doi:10.3969/j.issn.1002-3550.2012.07.018

Xiao, Q., Wu, Z., Qiu, J., Dong, Z., and Shi, S. (2022). Capillary water absorption performance and damage constitutive model of recycled concrete under freeze–thaw action. *Constr. Build. Mater* 353, 129120. doi:10.1016/j.conbuildmat.2022.129120

Yan, W. J., Niu, F. J., and Zhang, X. J. (2014). Advances in studies on concrete durability and countermeasures against freezing-thawing effects. *Sci. Cold Arid. Reg.* 6, 398–408. doi:10.3724/SP.J.1226.2014.00398

Yang, G., Li, Q., Guo, Y., Liu, H., Zheng, S., and Chen, M. (2022). Study on the mechanical properties and durability of recycled aggregate concrete under the internal curing condition. doi:10.3390/ma15175914

Yang, W., Liu, L., Wu, W., Zhang, K., Xiong, X., Li, C., et al. (2024). A review of the mechanical properties and durability of basalt fiber recycled concrete. *Constr. Build. Mater* 412, 134882. doi:10.1016/j.conbuildmat.2024.134882

Yang, Y., Xu, J., Zhan, B., Gao, P., Yu, Q., Li, R., et al. (2024). Study on hydration characteristics and mechanism of recycled powder-cement binary and multivariate systems. *Constr. Build. Mater* 420, 135646. doi:10.1016/j.conbuildmat.2024.135646

Yao, T., Tian, Q., Zhang, M., Qi, S., Wang, C., Ruan, M., et al. (2023). Experimental research on the preparation and properties of foamed concrete using recycled waste concrete powder. *Constr. Build. Mater* 407, 133370. doi:10.1016/j.conbuildmat.2023.133370

Yao, X., Pei, Z., Zheng, H., Guan, Q., Wang, F., Wang, S., et al. (2022). Review of mechanical and temperature properties of fiber reinforced recycled aggregate concrete. doi:10.3390/buildings12081224ER

Yildirim, S. T., Meyer, C., and Herfellner, S. (2015). Effects of internal curing on the strength, drying shrinkage and freeze–thaw resistance of concrete

containing recycled concrete aggregates. *Constr. Build. Mater* 91, 288–296. doi:10.1016/j.conbuildmat.2015.05.045

Yildizel, S. A., Uzun, M., Arslan, M. A., and Ozbakkaloglu, T. (2024). The prediction and evaluation of recycled polypropylene fiber and aggregate incorporated foam concrete using Artificial Neural Networks. *Constr. Build. Mater* 411, 134646. doi:10.1016/j.conbuildmat.2023.134646

Yu, Y., Wang, J., Wang, N., Wu, C., Zhang, X., Wang, D., et al. (2021). Combined freeze-thaw and chloride attack resistance of concrete made with recycled brick-concrete aggregate. doi:10.3390/ma14237267

Yuan, S., Li, K., Luo, J., Yin, W., Chen, P., Dong, J., et al. (2024). Research on the frost resistance performance of fully recycled pervious concrete reinforced with fly ash and basalt fiber. *J. Build. Eng.* 86, 108792. doi:10.1016/j.jobe.2024.108792

Yuan, X., Dai, M., Li, M., and Liu, F. (2023). Study of the freeze–thaw resistance for composite fiber recycled concrete with sulphate attack exposure. doi:10.3390/buildings13041037ER

Zaid, O., and Zamir Hashmi, S. R. (2021). Experimental study on mechanical performance of recycled fine aggregate concrete reinforced with discarded carbon fibers. *Front. Mater* 8.

Zhang, H., Ji, T., Zeng, X., Yang, Z., Lin, X., and Liang, Y. (2018). Mechanical behavior of ultra-high performance concrete (UHPC) using recycled fine aggregate cured under different conditions and the mechanism based on integrated microstructural parameters. *Constr. Build. Mater* 192, 489–507. doi:10.1016/j.conbuildmat.2018.10.117

Zhang, H., Luo, G., Bao, J., Zhang, P., Lv, H., Li, Y., et al. (2024). Improving the salt frost resistance of recycled aggregate concrete modified by air-entraining agents and nano-silica under sustained compressive loading. *Case Stud. Constr. Mater* 20, e03170. doi:10.1016/j.cscm.2024.e03170

Zhang, W., Liu, H., and Liu, C. (2022). Impact of rice husk ash on the mechanical characteristics and freeze–thaw resistance of recycled aggregate concrete. doi:10.3390/app122312238ER

Zhang, Y., Zhou, G., and Zheng, Y. (2023). Effect of fiber type on the mechanical properties and durability of hardened concrete. *J. Mater Sci.* 58, 16063–16088. doi:10.1007/s10853-023-09021-1

Zhao, H., Wang, S., Wang, R., Shen, L., and Wang, Q. (2023). Utilization of raw coal gangue as coarse aggregates in pavement concrete. *Constr. Build. Mater* 378, 131062. doi:10.1016/j.conbuildmat.2023.131062

Zheng, C., Li, S., Hou, Y., and Jin, B. (2022). *Frost resistance of fiber-reinforced self-compacting recycled concrete* 61, 711–725. doi:10.1515/rams-2022-0269

Zheng, M., Zhang, L., and Feng, Y. (2024). A review on silane and siloxane materials: enhancing durability of cementitious materials through surface treatments. *J. Mater Sci.* 59, 10119–10139. doi:10.1007/s10853-024-09771-6

Zheng, Y., Zhuo, J., and Zhang, P. (2021). A review on durability of nano-SiO2 and basalt fiber modified recycled aggregate concrete. *Constr. Build. Mater* 304, 124659. doi:10.1016/j.conbuildmat.2021.124659

Zhu, P., Hao, Y., Liu, H., Wang, X., and Gu, L. (2020). Durability evaluation of recycled aggregate concrete in a complex environment. *J. Clean. Prod.* 273, 122569. doi:10.1016/j.jclepro.2020.122569

Zou, D., Wang, Z., Shen, M., Liu, T., and Zhou, A. (2021). Improvement in freeze-thaw durability of recycled aggregate permeable concrete with silane modification. *Constr. Build. Mater* 268, 121097. doi:10.1016/j.conbuildmat.2020.121097

Frontiers in Materials

Investigates the discovery and design of materials for future application

A multidisciplinary journal that explores the breadth of materials science, engineering and mechanics - from carbon-based materials to smart materials.

Discover the latest Research Topics

See more →

Frontiers

Avenue du Tribunal-Fédéral 34
1005 Lausanne, Switzerland
frontiersin.org

Contact us

+41 (0)21 510 17 00
frontiersin.org/about/contact